AD-A127 502 TRANSVERSE AND QUANTUM EFFECTS IN SUPERFLUORESCENCE; PUMP DYNAMICS FOR TH..(U) POLYTECHNIC INST OF NEW YORK BROOKLYN DEPT OF MECHANICAL AND A.. F P MATTAR 1/3

UNCLASSIFIED 11 APR 83 POLY-M/AE-83-4 ARO-16800.19-PH F/G 20/6 NL

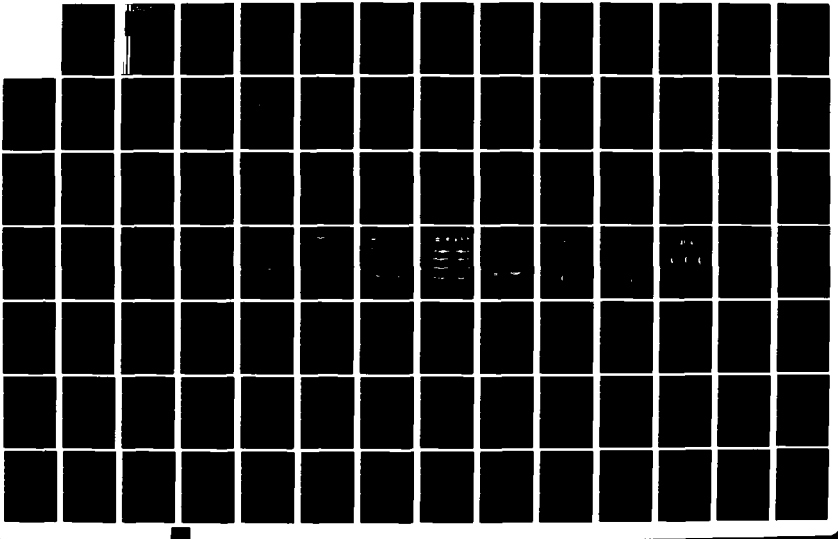

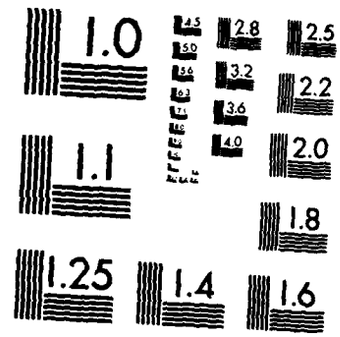

Polytechnic Institute of New York

TRANSVERSE AND QUANTUM EFFECTS IN SUPERFLUORESCENCE; PUMP DYNAMICS FOR THREE-LEVEL SUPERFLUORESENCE; AN ALGORITHIM FOR TRANSVERSE, FULL TRANSIENT EFFECTS IN OPTICAL BI-STABILITY IN A FABRY-PEROT CAVITY

F. P. MATTAR
Mechanical & Aerospace Engineering
and Spectroscopy Lab, M.I.T.

The U.S. Army Research Office
Contract DAAG 29-79-C-0148

Poly-M/AE 83-4

FINAL REPORT

FOR CONTRACT DAAG 29-79-C-0149
(From Sept. 79 to Jan. 83)

on

TRANSVERSE EFFECTS ON LIGHT-MATTER INTERACTION IN SUPERFLUORESCENCE AND OPTICAL BISTABILITY: TRANSVERSE AND QUANTUM EFFECTS IN SUPERFLUORESCENCE; PUMP DYNAMICS FOR THREE-LEVEL SUPERFLUORESCENCE; AN ALGORITHM FOR TRANSVERSE, FULL TRANSIENT EFFECTS IN OPTICAL BISTABILITY IN A FABRY-PEROT CAVITY

to

Physics Program

The U.S. Army Research Office

by

Farres P. Mattar†
Department of Mechanical & Aerospace Engineering
Polytechnic Institute of New York
Brooklyn, NY 11201

M/AE 83-4
April 1983

† Also visitor to Spectroscopy Lab, M.I.T.
(from 1980-Present)

Two- and Three-Level Superfluoresence Calculations and an algorithm for Optical Bistability

F.P. Mattar

Abstract

I. Methodology

Computational methodologies were developed to treat rigorously (i) transverse boundary in an inverted (amplifying) media; (ii) to treat quantum fluctuations in an initial boundary conditions in the light-matter interactions problem; (iii) construct a two-laser three-level code to study light control by light effect; (iv) construction of a data base that (a) would manage the production of different types of laser calculations: cylindrical, cylindrical with atomic frequency broadening, cartesian geometry; all of the above with quantum mechanical initiation), (b) allow parametric comparison within the same type of calculations, by establishing a unifying protocol of software storage, of the various refinements of the model could be contrasted among themselves and with experiment; (v) construct an algorithm for counterbeam transient studies for optical bistability and optical oscillator studies.

II. Physics

A. Transverse effects were shown to be inherent to the problem of superfluorescence. By refining the propagational model advocated by Feld, we were able to simulate correctly Gibbs, et al's Cs data for the first time. The mean field approach was shown not to directly relevant to the Cs data. The interplay of quantum fluctuations and transverse dynamic effects lead to Fresnel variation of the time delay statistic in conformity with experiments.

B. The previously studied as totally independent effects superradiance and swept-gain superradiance were shown to be strongly related to and to evolve assymptotically from the first one to the second one. Output energy stabilization was obtained by balancing the gain (from the inverted medium) with the dynamic diffraction loss (from the finiteness of the beam).

C. The Study of three-level systems exhibited that injected coherent-pump initial characteristic (such as on-axis area, temporal and radial width and shape) injected at one frequency can have significant deterministic effects on the evolution of the superfluorescence at another frequency and its pulse delay time, peak intensity, temporal width and shape. The importance of Resonant Coherent Roman processes was clearly demonstrated in an example where the evolving superfluorescence pulse temporal width τ_s is much less than the reshaped coherent pump width τ_p eventhough the two pulses temporarily overlap (i.e., the superfluorescence process gets started late and terminates early with respect to the pump time duration). The results of the three-level calculations are in quantitative agreement with observations in CO_2 pumped CH_3F.

Collaborations:

(i) Physics

(a) two levels superfluorescence

- Prof. Hyatt M. Gibbs (previously at Bell Lab, now at the Optical Science Center at the University of Arizona)
- Dr. Samuel L. McCall (Bell Lab)
- Prof. Michael S. Feld (M.I.T.)
- Edward A. Watson (MSc. student under Prof. H. Gibbs who helped implementing the fluctuations in the cylindrical program exported to Arizona)

(b) two-level swept-gain superradiance and three-level pump dynamics

- Dr. Charles M. Bowden (MICOM)
- (ii) Numerics
- Prof. Gino Moretti (Polytechnic Institute of New York) for the Counter beam propagation.
- (iii) structure software and system programming
- Richard E. Francoeur (Mobil International Division)
- Pierre Cadieux (system routine for data bases)
- Michel Cormier (user interface for data base)
- Yve Claude (pagination of the program to simulate on CDC the virtual memory facility existing on IBM)

ACKNOWLEDGEMENT

The counterbeam algorithm development as well as the co-propagation code and the software programs for the data base were jointly sponsored by the Office of Naval Research N000-14-80-C-0174.

The hospitality of Dr. H.M. Gibbs at Bell Lab, that of Prof M.S. Feld at the spectroscopy Lab and that of Dr. C.M. Bowden at MICOM is greatly appreciated. Their energetic and enthusiastic collaboration have accelerated the rate of progress of my research. The hospitality of Prof. L. Zahar at the Laboratoire de Modelisation Numerique in Montreal is also appreciated.

The continuous encouragements of Prof. G. Moretti and H.A. Haus is joyfully acknowledged.

Official Presentations at Meetings during the Tenure of the Contract

1 - The International Conference on laser 80, New Orleans, Dec. 30 (2 papers) (proceedings published by STS, MacLean, Virginia 1982).

2 - The International Conferences on Excited states and Multiresonant Nonlinear optical processes in Solid, Aussois, France, March 81, (Abstract digest, ed. by D. Chemla published for CNET by les Editious de Physique, France).

3 - The European Conference on Atomic Physics, Heidelberg, April 81, (Abstract digest ed. by J. Kowalski, G. Zuputlitz and K.G. Weber European Physical Society Geneva, 1981).

4 - Los Alamos Conference on Optics, Los Alamos, 1981, Proceedings published by the Society of Photo-Optic Instrumentation Engineers (SPIE), Belligham, Washington 1981, vol 288 pp. 353-363 and pp. 364 - 371.

5 - The Twelfth Annual Pittsburg Modeling and Simulation Conference (May 1981), ed. W. Vogt and M. Mickle Proceedings published by the Instrument Society of America, Pittsburgh, Pennsylvania.

6 - The International Conference on Optical Bistability Proceedings ed. by C.M. Bowden, M. Ciftan and H.R. Robl (Plenum Press, New York 1981) p. 503 (invited).

7 - U.S. Army Research Office Workshop On Coupled Nonlinear Oscillators Los Alamos Center for Nonlinear Series, 1981 (invited).

8 - The Fifth International Laser Spectroscopy meetings, VICOLS, (two post-deadlines) Jasper, Alberta, Canada (1981), ed. by B. Stoicheff et al. (Springer Verlag 1982).

9 - The Annual Meeting of the Optical Society at Orlando, Florida 1981 (two papers), see abstracts in J. Opt. Soc. Am 71, 1589 (1981).

10 - The Annual Meeting DEAP of the APS, NY, Dec (1981), 3 Abstracts.

11 - The International Conference on Laser 81, New Orleans, Dec, 81 (1 invited, 3 contributed), proceedings published by STS, MacLean, Virginia, 1982.

12 - The Maxborn Centenary Conference, Edinburgh, Scotland, Sep 1982 (3 papers), ed. by the Institute of Physics, U.K., proceedings to be published by SPIE, Belligham, Washington, 1983.

13 - The Fourth International Symposium of Gaz-Dynamic Lasers by M. Onorato, the Polytechnic Institute of Torino (2 papers), Proceedings in press.

14 - The XII International Conference on Quantum Electronics, Munich, June, 1982 (1 invited paper, 1 contributed paper), see Appl. Phys. (Springer-Verlag) June and Dec issues 1982.

Refereed Papers from the work and methodologies developed during the tenure of the research

1. Adaptive Stretching and Rezoning As Effective Computational Techniques for Two-Level Paraxial Maxwell-Bloch Simulation; Computer Physics Communications 20 (1980) 139-163, North Holland Publishing Company (with M.C. Newstein).

2. Coherent Propagation Effects in Multilevel Molecular Systems; Proceedings of the International Conference on Lasers '80, December 15-19, 1980 p. 270-279 (with C.D. Cantrell, F.A. Rebentrost, and W.H. Louisell).

3. Swept-gain Superradiance in Two- and Three-level Systems with Transverse Effects and Diffraction; International Conference on Excited States and Multiresonant Nonlinear Optical Processes in Solids pub. Les editiousde Physique, France (with C.M. Bowden).

4. Transverse Effects in Burnham-Chiao Ringing and Superfluorescence; Proceedings of the International Conference on Lasers '80, December 15-19, 1980 (with H.M. Gibbs and Optical Sciences Center, University of Arizoa, p. 777, 782 Tuscon, AZ).

5. Transverse Effects in Superfluorescence; Vol. 46, No. 17, p. 1123-1126 Physical Review Letters, April, 1981 (with H,M, Gibbs, S.L. McCall and M.S. Feld).

6. Transient Counter-Beam Propagation in a Nonlinear Farby-Perot Cavity; Computer Physics Communications 23 (1981) 1-17, North-Holland Publishing Company (with G. Moretti and R.E. Franceour).

7. Fluid Formulation of High Intensity Laser Beam Propagation Using Lagrangian Coordinates; Computer Physics Communications 22 (1981) 1-11 North-Holland Publishing Company (with J. Teichmann).

8. Effects of Propagation, Transverse Mode Coupling, Diffraction, and Fluctuations on Superfluorescence Evolution; SPIE Vol. 288-Proceedings of the Los Alamos Conference on Optics, 1981, p. 353,363 by the Society of Photo-Optical Instrumentation Engineers, Box 10, Bellingham, WA.

9. Transverse Effects in Swept-gain Superradiance: Evolution from the Superradient State; SPIE Vol. 288-Proceedings of the Los Alamos Conference on Optics, 1981, p. 364,371 by the Society of Photo-Optical Instrumentation Engineers, Box 10, Bellingham, WA (with C.M. Bowden).

10. Effects of Propagation, Transverse Mode Coupling and Diffraction on Nonlinear Light Pulse Evolution; Optical Bistability (1981) Edited by Charles M. Bowden, Mikael Ciftan and Herman R. Robl, Pub. Plenum, NY p. 503,555.

11. Transverse and Phase Effects in Light Control By Light: Pump Dynamics in Superfluorescence; Proceedings of the International Conference on Lasers '81, December 14-18, 1981.

12. A Production System for the Management of a Results Functions Bank and a Special Application: The Laser Project ; Published in the proceedings of the International Conference on Laser '81, ed. by C.B. Collins (STS, MacLean Virginia 1982) pp. 1055-1115 (with M. Cormier, Y. Claude and P. Cadieux).

13. Light Control by Light with an Example in Coherent Pump Dynamics, Propagation, Transverse & Diffraction Effects in Three-Level Superfluorescence; IEEE International Quantum Electronics Conference, Munich (1982), Abstracts Digest Appl. Physics Dec (1982) Springer-Verlag (with C.M. Bowden).

14. Distortions of a CW Light Beam Propagating Through Gas: Self Lensing and Spatial Ringings; Max Born Centenary Conference, Edinburgh (Sep. 1982), (paper 36901), proceedings to be published by SPIE, Bellingham WA (1983) (with M. LeBerre, E. Ressayre and A. Tallet).

15. Coherent Pump Dynamics, Propagation, Transverse, and Diffraction Effects in Three-Level Superfluorescence and control of light by light; Physical Review A, Vol. 27, No. 1, Jan. 1983, p. 345-359 (with C.M. Bowden).

16. Quantum Fluctuations and Transverse Effects in Superfluorescence; Physical Review A, Vol. 27, No. 3, March, 1983 p. 1427-1434 (with E.A. Watson, H.M. Gibbs, M. Cormeier, Y. Claude, S.L. McCall and M.S Feld).

17. Coherrent Pump Dynamics, Propagation, Transverse, and Diffraction Effects in Three-Level Superfluorescence and control of light by light; Topics of current physicsL Multiple Photou Dissociation of Polyatomic Molecules, ed. C.D. Cantrell, Springer Verlag (In Press, 1983).

REPRINTED FROM PROCEEDINGS OF THE INTERNATIONAL CONFERENCE ON LASERS '80, DECEMBER 15-19, 1980

TRANSVERSE EFFECTS IN BURNHAM-CHIAO RINGING AND SUPERFLUORESCENCE

F.P. Mattar*
Polytechnic Institute of New York
Brooklyn, New York 11201

H.M. Gibbs
Bell Labs
Murray Hill, NJ 07974

and
Optical Sciences Center†
University of Arizona
Tucson, AZ 85721

ABSTRACT

Dynamic diffraction coupling is examined in superfluorescence experiments using semi-classical model with initial tipping angle. Effects of Fresnel number and of the radial dependence of initial polarization and atom density on ringing, delay, and intensity are reported.

Semi-classical Treatment of Superfluorescence and Propagation Effects

Analytic solutions[1] of superfluorescence pulse shapes have been obtained only by neglecting propagation effects. Such solutions are somewhat academic in that all experiments so far use extended samples for which propagation effects play a major role. Furthermore, a sample of volume less than λ^3 would experience dipole-dipole dephasing[2] which would destroy SF or at least greatly modify it from the analytic descriptions.

Propagation effects can be taken into account fully in pulse propagation problems by numerically integrating coupled Maxwell-Bloch equations. Such semi-classical calculations have been carried out[3] and found in good agreement with self-induced transparency experiments[3c,4] many years ago.

An identical semi-classical approach was taken in the first simulation of SF.[5] SF begins by spontaneous emission which requires a quantized field description. In a semi-classical model a purely inverted medium does not radiate in the absence of an external electromagnetic field. Consequently, in order to apply the semi-classical formalism to SF, the quantum initiation process was swept into a single initial polarization tipping angle θ_o or into a randomly fluctuating initial polarization.[5] More recent work has studied the quantum fluctuations both theoretically[6] and experimentally.[7]

The need to include propagation effects in SF simulations was first shown by Skribanowitz, Herman, MacGillivray, and Feld.[5] Their SF data in HF often contained pulses with substantial ringing in sharp contrast with the sech^2 symmetrical single-pulse output predicted by the propagationless analytic solutions. Skribanowitz et al. were influenced strongly by the work of Burnham and Chiao[3e] who predicted ringing when small area pulses propagate through absorbers. In fact the Burnham-Chiao or McCall[3d] simulations for π-θ_o area pulse propagation in absorbers or for θ_o area pulses in inverted media are identical to all of the early SF simulations. Namely, the calculations were uniform-plane-wave one-way treatments. No transverse variables were included. I.e., the following equations were numerically integrated:

$$\dot{u} = (\omega_o - \omega)v - u/T_2' \tag{1}$$

$$\dot{v} = -(\omega_o - \omega)u - v/T_2' - w\kappa E \tag{2}$$

$$\dot{w} = -(w + 1)/T_1 + v\kappa E \tag{3}$$

$$\frac{\partial E}{\partial z} + \frac{1}{c}\frac{\partial E}{\partial t} = -\frac{2\pi\omega n p v}{c} \tag{4}$$

where u,v,w are the Bloch components of the pseudo polarization vector, E is the slowly varying envelope of the electromagnetic field, n is the density of atoms with electric dipole transition moment p, $\kappa = 2p/\hbar$, and T_2' and T_1 are the coherence and energy relaxation times, respectively.

*Work jointly supported by the Research Corporation, the International Division of Mobil, the University of Montreal, and the U.S. Army Research Office (Durham).
†Present address.

Such simulations, which are just solutions of the sine-Gordon equation when relaxation is negligible, predict very strong ringing where each ring can be 50% as intense as the preceeding ring. Ringing that pronounced has never been observed. MacGillivray et al.[5] introduced a linear loss term $-K\mathcal{E}$ to the right side of Eq. (4) to account for linear diffraction losses. A value KL = 2.5 reduced the ringing to that observed, but the corresponding Fresnel number is 0.08 compared with their experimental value of order unity. At any rate their simulations showed clearly that the polarization and electric field vary appreciably along the sample, i.e., propagation effects are very important and a mean-field approximation is unjustified.

Initiation by Quantum Fluctuations

The Cs experiment[8a] provided much more quantitative data on pulse shapes and densities for SF under near-ideal conditions. Attempts to simulate those data by uniform-plane-wave simulations were made by Gibbs & Vrehen[8b] and by Saunders, Bullough, and collaborators.[9] They found much more pronounced ringing and longer (as much as twice) delays than observed. Relaxation, inhomogeneous dephasing, and diffraction were too weak in the Cs case to account for these discrepancies. At that time the proper value of θ_o was under discussion. It was found that large θ_o's of order $1/\sqrt{\mu N}$ did improve the fits substantially but not completely. (The shape factor[1b] μ is typically 10^{-5}.) It is now generally accepted from theoretical calculations and a small area injection experiment[10] that $\theta \simeq 2/\sqrt{N}$. That formula yields $\theta_o \simeq 10^{-4}$ for the Cs experiment, resulting in far too much ringing and too long delays. But determining the appropriate θ_o was very significant; by fixing that parameter, the need for other explanations of the ringing and delay-time discrepancies was underscored. And the likelihood that two-way effects were very important was greatly reduced because complicated, two-way computations by Saunders, Bullough, Hassan, and Feuillade[9] as well as MacGillivray and Feld[11] revealed insignificant reduction of ringing by two-way competition for $\theta_o = 10^{-4}$. Only for very large θ_o, of order 0.1, were two-way effects found to appreciably reduce ringing.

Those quantized-field studies of θ_o led naturally to another significant numerical calculation, namely a study of fluctuations in the output pulse shape as a result of the quantum nature of SF initiation. A distribution of initial θ_o's consistent with the quantized-field results was used to initiate the usual coupled Maxwell-Bloch simulations. The resulting distribution[12] of delay times is in good agreement with those observed by Vrehen[7] and with an analytic expression for the variance.[6a]

These fluctuation results also reduced the discrepancy between experimental and simulation densities for the same delay. It became clear that the data presented in Ref. 8, which simulations were trying to reproduce, were selected for approximately minimum delay at a given density. It was estimated that the average delay was about 30% longer than the pulses presented in Ref. 8.[10] The density in the simulation would then need to be 1.3 times higher, so that a 2X discrepancy is reduced to less than the +60% quoted uncertainty in the density.

Transverse Effects

At this stage of the numerical simulations the primary discrepancy between the Cs data and the one-way uniform-plane-wave computations with $\theta_o = 2/\sqrt{N}$ lay in pulse shapes. MacGillivray and Feld noted quite some time ago, that a Gaussian inversion profile results in a distribution of delay times and that a Gaussian average of plane-wave solutions predicts a highly asymmetric output pulse. The ringing is largely removed, but the averaging of the large ringing results in a composite output with a tail much longer than observed.

Encouraged by the importance of dynamic transverse effects in self-induced transparency numerical simulations[13] and actual experiments,[14] we have allowed one transverse degree of freedom in SF simulations. One must add to the righthand side of Eq. (4),

$$i \frac{1}{4FL} \nabla_t^2 \mathcal{E} \tag{5}$$

where $\nabla_t^2 = \frac{1}{\rho} \frac{\partial}{\partial \rho} \left(\rho \frac{\partial}{\partial \rho} \right), \rho = r/r_p$, r_p is the radius of the initial inversion density at half maximum, L is the sample length, and $F = \pi r_p^2 / \lambda L$ is the Fresnel number. $\mathcal{E}$ is, of course, complex so that phase variations introduced by diffraction can be included consistently. Thus, neither the mean-field approximation[1c] no the substitution[5] of a loss term for diffraction coupling is used. Instead, self-consistent numerical methods[15] are adopted which take into account fully both propagation and transverse (both spatial profile and Laplacian coupling) effects. Thus our model possesses a degree of realism long hoped for.[16]

These transverse simulations are in much better agreement with the Cs data as shown in Fig. 1.[17] Each simulation density n_o was adjusted to roughly reproduce the observed delay using $\theta_o = 2/\sqrt{n_o \pi r_p^2 L}$. The inversion density radial dependence was $n_o(r) = n_o \exp[-(\ln 2) r^2/r_p^2]$. These transverse simulations fit the data much better than the Gaussian average of plane-wave solutions for at least two reasons. First, the diffraction coupling between the minimum-delay center portion of the excited cylinder and the outer cylindrical "shells" causes the delay times of the latter to be reduced. This allows more of the cylinder to emit at the same time; the overall delay is lengthened slightly, but the asymmetry is also reduced. See Fig. 2. Second, relaxation included in Fig. 1 was found to reduce the asymmetry more than was anticipated from their rather

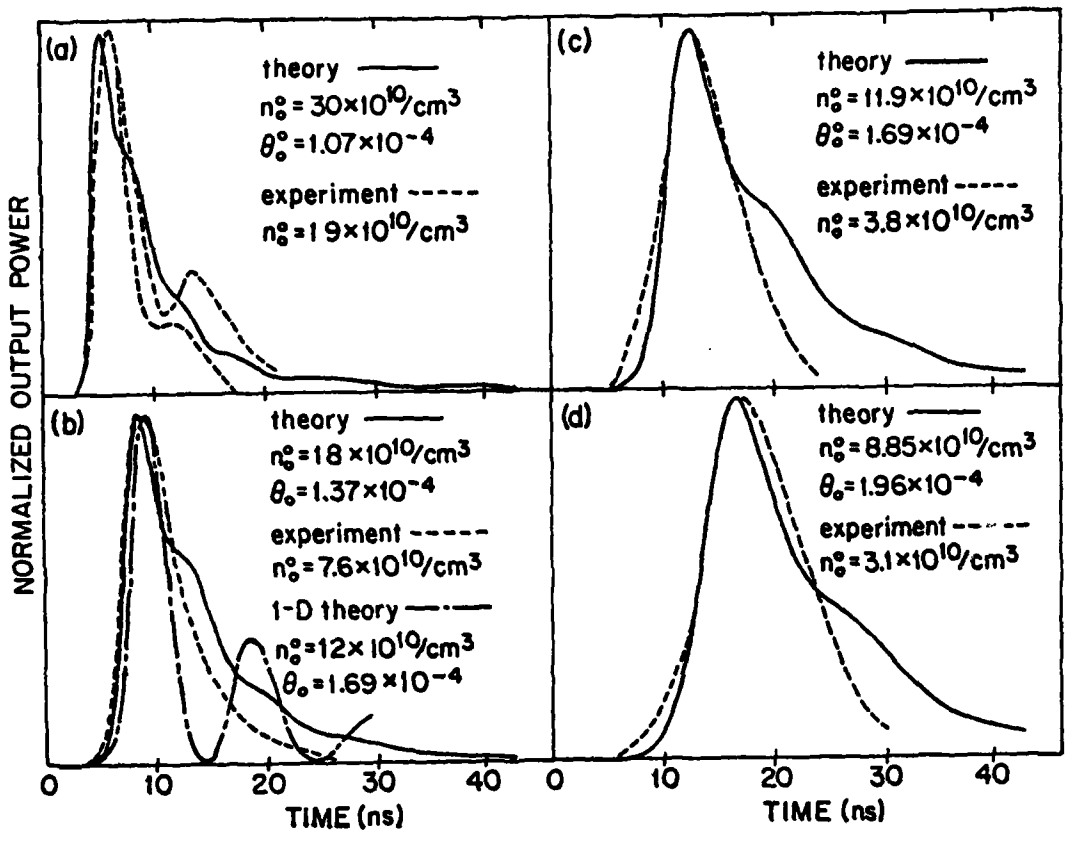

Figure 1. Theoretical fits to Cs data of Ref. 8a. The two experimental curves in (a) indicate typical shot-to-shot variations. The 1-D curve in (b) is the fit of Ref. 8b to the one-dimensional theory. $F = \pi r_p^2/\lambda L = 1$, $L = 2$ cm, $T_1 = 70$ ns, $T_2' = 80$ nsec, $\lambda = 2.931\mu$, $\tau_o = 551$ ns, θ_o uniform Gaussian, inversion $n_o(r) = n_o^o \exp[-\ell n2(r/r_p)^2]$.

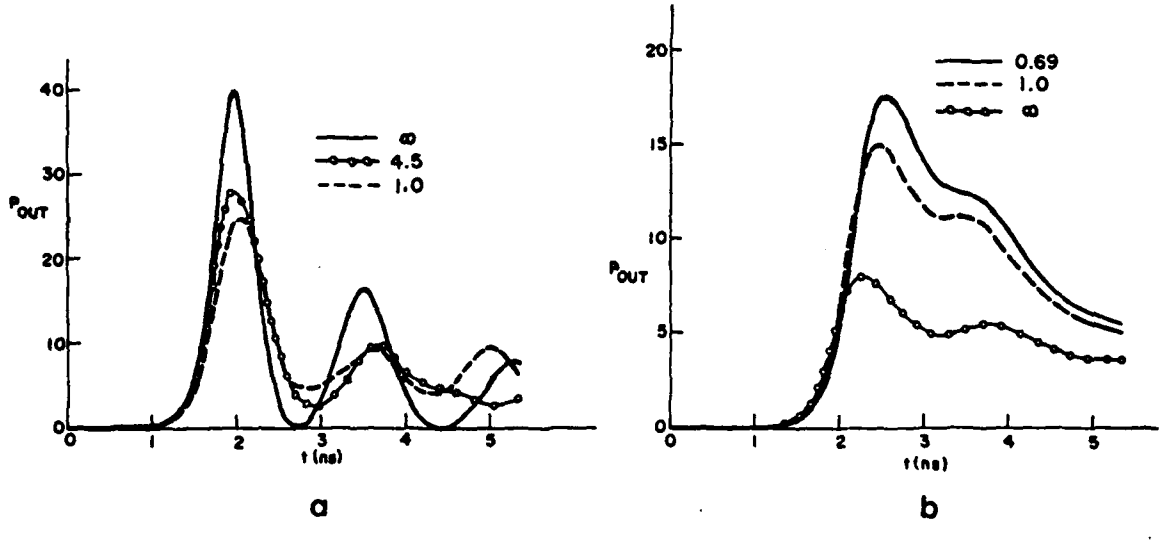

Figure 2. Total energy coherently emitted per unit atom in arbitrary units, as a function of time with Fresnel number as the labelling parameter. $\theta_o = 10^{-4}$ for all radii, $\tau_R = 8\pi\tau_o/3n_o^o\lambda^2 L = 0.046$ ns, and $L = 5.23$ cm. (a) Uniformly inverted cylinder: inversion constant out to ρ_o and zero beyond with $F = \pi\rho_o^2/\lambda L$. The output is accepted only out to ρ_o. (b) Gaussian inversion cylinder with F and $n_o(r)$ defined as in Fig. 1.

long times of T_1 = 70ns and T_1' = 80ns. Although there is still more of a tail in the simulations than the data, the agreement is rather good and far better than the uniform-plane-wave attempts.

The ratio of the simulation density to the experimental density ranges from 1.63 to 2.85 in Fig. 1. It was mentioned before that the average delays for the experimental densities were about 1.3 times longer than the selected pulses. One would then expect to use 1.3 times higher simulation densities in that case, reducing the ratio to 1.25 to 2.2. The quantum calculations[6] actually yield $\theta_0 = (2/\sqrt{N})\ (\ell n(2\pi N)^{1/8})^{1/2}$, not just $2/\sqrt{N}$, which is a 9% correction, reducing the ratio to 1.14 to 2.0. Since the assigned experimental uncertainties are +60%, -40% the agreement is fairly good. If one chooses $\theta_0 = 6/\sqrt{N}$, which agreed better with the small injection experiment, the ratio ranges from 1.01 to 1.78, in still better agreement.

Burnham-Chiao Ringing

Fig. 3 illustrates that this model of SF predicts appreciable ringing if one observes the output with a detector much smaller than the output diameter. This suggests that the single-pulse symmetric Cs SF pulses have substructure in space and time which retains the strong ringing predicted by the uniform-plane-wave approach. The extended cylinder of unit Fresnel number F does not emit its energy in one single cooperative superfluorescence burst after all. In fact, simulations reveal that ringing is reduced by decreasing F. This allows emission from the cylinder's axis to diffract to the outer cylindrical shells in a shorter distance. Consequently, F somewhat less than one may be better than F equal to one for single pulse emission, contrary to the usual arguments.

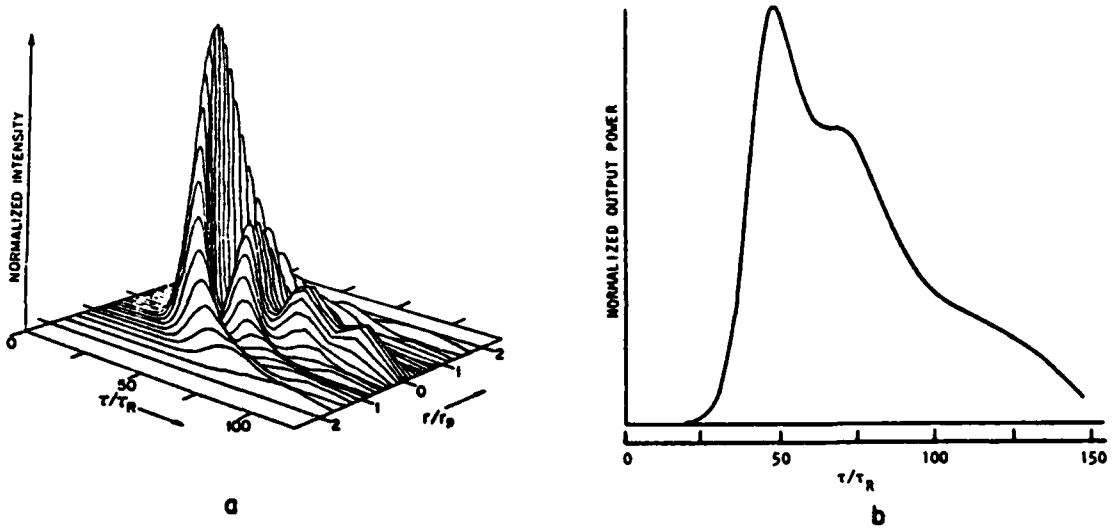

Figure 3. Energy as a function of (a) transverse coordinate $\rho = r/r_p$ and time and (b) only time after integration over ρ. Notice that strong ringing is predicted for a small-aperture detector in the center of the beam although very little ringing is in evidence after radial averaging. $\theta_0 = 2.38 \times 10^{-4} \exp(-\rho^2/2)$, τ_R = 4.9 ns, F = 1, L = 22.4 cm, and transverse Gaussian inversion profile. As F is decreased, ringing is washed out into smaller and smaller ρ.

Future Work

It must be emphasized that this transverse simulation of SF contains approximations; strictly speaking it is a solution of the propagation of a small-area uniform-plane-wave coherent pulse through an inverted medium with a Gaussian transverse inversion profile. Experiments could be performed under such conditions and our semi-classical description should be complete. The transverse SF simulation should be extended to explore more thoroughly the quantum and three-dimensional aspects of SF. Quantum fluctuations in the initiation should be included in the transverse calculation to examine the fluctuations in output shape and delay. The initiation should not be inserted as a homogeneous tipping of all the individual polarization vectors phased to emit a plane wave in the forward direction. Ideally the initiation and calculation should allow three spatial degrees of freedom so that transverse modes can compete. The strong ringing on axis, as predicted above, may not persist with three-dimensional fluctuations. Two transverse effects previously observed in Cs might emerge. It was found at high densities, approximately for sample lengths longer than the Arecchi-Courtens[18] coherence length, that SF from a Fresnel-one sample fluctuates and shows little or no correlation between the pulse shapes at two different transverse positions.[19] And large Fresnel-number SF is emitted over the full geometrical angle with only small fluctuations.[19]

References

1. (a) R.H. Dicke, Phys. Rev. 93, 99 (1954) and in Proceedings of the Third International Conference on Quantum Electronics, (Paris, 1963), P. Grivet and N. Bloembergen, eds., (Columbia University Press, NY, 1964).

   (b) N.E. Rehler and J.H. Eberly, Phys. Rev. A 3, 1735 (1971).

   (c) R. Bonifacio, P. Schwendimann, and F. Haake, Phys. Rev. A 4, 302 and 854 (1971). R. Bonifacio and L.A. Lugiato, Phys. Rev. A 11, 1507 and 12, 587 (1975).

2. R. Friedberg, S.R. Hartmann, and J.T. Manassah, Phys. Lett. 40A, 365 (1972). R. Friedberg and S.R. Hartmann, Opt. Commun. 10, 298 (1974).

3. (a) J.P. Wittke and P.J. Warter, J. Appl. Phys. 35, 1668 (1964).

   (b) F.T. Arecchi and R. Bonifacio, IEEE J. Quantum Electron. QE-1, 169 (1965).

   (c) S.L. McCall and E.L. Hahn, Phys. Rev. Lett. 18, 908 (1967) and Phys. Rev. 183, 457 (1969).

   (d) S.L. McCall, Dissertation, University of California, 1968.

   (e) D.C. Burnham and R.Y. Chiao, Phys. Rev. 188, 667 (1969).

   (f) F.A. Hopf and M.O. Scully, Phys. Rev. 179, 399 (1969).

   (g) A. Icsevgi and W.E. Lamb, Jr., Phys. Rev. 185, 517 (1969).

4. R.E. Slusher and H.M. Gibbs, Phys. Rev. A 5, 1634 (1972) and 6, 1255 (1972).

5. N. Skribanowitz, I.P. Herman, J.C. MacGillvray, and M.S. Feld, Phys. Rev. Lett. 30, 309 (1973). I.P. Herman, J.C. MacGillivray, N. Sribanowitz, and M.S. Feld in Laser Spectroscopy, R.G. Brewer and A. Mooradian, eds. (Plenum, NY, 1974). J.C. MacGillivray and M.S. Feld, Phys. Rev. A 14, 1169 (1976).

6. (a) M.F.H. Schuurmans, D. Polder, and Q.H.F. Vrehen, J. Opt. Soc. Am. 68, 699 (1978). D. Polder, M.F.H. Schuurmans, and Q.H. Vrehen, Phys. Rev. A 19, 1192 (1979).

   (b) R. Glauber and F. Haake, Phys. Lett. 68A, 29 (1978).

   (c) F.A. Hopf, Phys. Rev. A 20, 2054 (1979).

7. Q.H.F. Vrehen in Laser Spectroscopy IV (Springer-Verlag, Berlin, 1979), H. Walther and K.W. Rothe, eds., 471.

8. H.M. Gibbs, Q.H.F. Vrehen, and H.M.J. Hikspoors.

   (a) Phys. Rev. Lett. 39, 547 (1977) and

   (b) in Laser Spectroscopy III (Springer-Verlag, Berlin, 1977), J.L. Hall and J.L. Carlsten, eds., p. 213

9. (a) R. Saunders, S.S. Hassan, and R.K. Bullough, J. Phys. A 9, 1725 (1976).

   (b) R.K. Bullough, R. Saunders, and C. Feuillade in Coherence and Quantum Optics IV (Plenum, NY, 1978), L. Mandel and E. Wolf, eds., 263.

10. Q.H.F. Vrehen and M.F.H. Schuurmans, Phys. Rev. Lett. 42, 224 (1979).

11. J.C. MacGillivray and M.S. Feld, Phys. Rev. A, to be published.

12. F. Haake, H. King, G. Schroder, J. Haus, R. Glauber, and F. Hopf, Phys. Rev. Lett. 42, 1740 (1979). F. Haake, J. Haus, H. King, G. Schroder, R. Glauber, Phys. Rev. Lett. 45, 558 (1980).

13. N. Wright and M.C. Newstein, Opt. Commun. 9, 8(1973). F.P. Mattar and M.C. Newstein, Opt. Commun. 18, 70 (1976).

14. H.M. Gibbs, B. Bolger, F.P. Mattar, M.C. Newstein, G. Forster, and P.E. Toschek, Phys. Rev. Lett. 37, 1743 (1976). J.J. Bannister, H.J. Baker, T.A. King, and W.G. McNaught, Phys. Rev. Lett. 44, 1062 (1980).

15. F.P. Mattar, Appl. Phys. 17, 53 (1978). F.P. Mattar and M.C. Newstein, Comp. Phys. Comm. 20, 139 1980.

16. See panel discussion in C.M. Bowden, D.W. Howgate, and H.R. Robl, eds., Cooperative Effects in Matter and Radiation (Plenum Press, NY, 1977). Q.H.F. Vrehen in Coherence and Quantum Optics IV, L. Mandel and E. Wolf, eds., (Plenum Press, NY, 1978). M.S. Feld and J.C. MacGillivray in Advances in Coherent Nonlinear Optics, M.S. Feld and V.S. Letokhov, eds., (Springer-Verlag, Berlin, 1980).

17. F.P. Mattar, H.M. Gibbs, S.L. McCall, and M.S. Feld, to be published.

18. F.T. Arecchi and E. Courtens, Phys. Rev. A 2, 1730 (1970).

19. Q.H.F. Vrehen, H.M.J. Hikspoors, and H.M. Gibbs, in Coherence and Quantum Optics IV (Plenum, NY, 1978), L. Mandel and E. Wolf, eds., p. 543.

Jarro P. Matter

PROCEEDINGS
OF THE

INTERNATIONAL CONFERENCE
ON

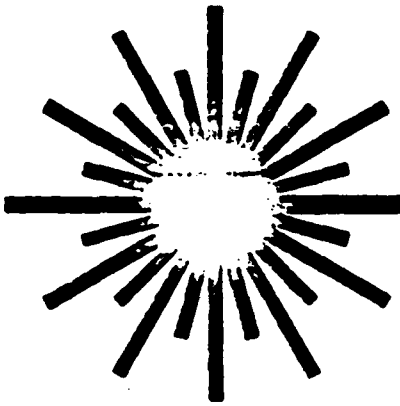

LASERS '80

NEW ORLEANS, LOUISIANA DECEMBER 15-19, 1980

Carl B. Collins, *Editor*

CONFERENCE SPONSORED BY
THE SOCIETY FOR OPTICAL & QUANTUM ELECTRONICS

STS PRESS • McLEAN, VA • 1981

REPRINTED FROM PROCEEDINGS OF THE INTERNATIONAL CONFERENCE ON LASERS '80, DECEMBER 15-19, 1980

Coherent Propagation Effects in Multilevel Molecular Systems*

C. D. Cantrell
Center for Quantum Electronics & Applications
University of Texas at Dallas
Richardson, Texas 75080 USA

F. A. Rebentrost
Projektgruppe für Laserforschung
Max-Planck Gesellschaft zur Förderung der Wissenschaften E.V.
D-8046 Garching bei München, Federal Republic of Germany

W. H. Louisell
Department of Physics
University of Southern California
Los Angeles, California 90007 USA

F. P. Mattar
Polytechnic Institute of New York
Brooklyn, New York 11201 USA

Abstract

We discuss coherent propagation effects in vapors of polyatomic molecules under conditions of multiple photon excitation, including the generation of new frequencies and the development of transverse effects such as self-focusing and self-defocusing. We give a discussion of the adiabatic-following approximation for multilevel systems, and discuss the generation of new frequencies in this limit as well as in the limit of an instantaneously-switched-on pulse.

Introduction

The multiple-photon excitation of polyatomic molecules has attracted much attention since the demonstration of isopotic selectivity in the multiple-photon dissociation of BCl_3 [1] and SF_6, [2] particularly after these processes were shown to occur in the absence of collisions [3]. In the ensuing debate [4] as to the origins of the multiple-photon excitation and dissociation of polyatomic molecules, little has been said about the possible influence of coherent propagation effects and other collective processes upon the interpretation of the experimental measurements of energy absorption that have been carried out to date. It has recently been suggested [5] that the generation of near-resonant sidebands as the result of propagat in a multilevel molecular gaseous medium may be responsible for a number of effects that have previously been ascribed to a hypothesized rapid intramolecular relaxation of energy, such as the observed pumping of nearly all rotational states by laser pulses of modest intensity [6]. Also, the recent discovery of strong self-focusing in SF_6 under conditions of collisionless multiple-photon excitation calls into question most of the measurements of energy deposition that have been reported in the literature to date [7]. Under these circumstances we have chosen to review the current status of propagation calculations in multilevel systems, both from the point of view of generation of new frequencies and from the point of view of transverse effects such as self-focusing and self-defocusing. Following a brief introduction to the current understanding of the energy levels of polyatomic molecules such as SF_6, we summarize the derivation of the Schrödinger equation for multilevel systems and the propagation equation for the optical electric field under the slowly-varying-amplitude-and-phase approximation (SVAPA). We then discuss the generation of new frequencies and transverse effects in two limits: the limit of a rapidly-switchedon pulse and the limit of an adiabatically-switched-on pulse. In the limit of a rapidly-switched-on pulse, sidebands are generated that are nearly resonant with all the molecular radiative transitions that are accessible from the initial molecular state [5,8]; the sideband amplitude saturates at a constant value after a finite propagation distance. In the limit of an adiabatically-switched-on pulse, a sideband spectrum is generated by the process of self-phase modulation [9]. Finally, we present numerical results concerning the generation of new frequencies by a system that models some of the qualitative characteristics of SF_6 irradiated by a rapidly-switched-on pulse.

Practical applications where coherent propagation effects in multilevel molecular systems may be important include laser chemistry and isotope separation, and the propagation of powerful laser beams through the earth's atmosphere. In laser-induced chemistry and isotope separation the generation of additional frequencies, whether for rapidly-switched-on pulses or adiabatically-switched-on pulses, will result in a reduction of isotopic or chemical-bond selectivity and an overall increase of multiple-photon excitat Transverse effects such as self-focusing or self-defocusing will alter the volume illuminated by a laser during multiple-photon absorption experiments and will thereby affect the calculation of the number of laser photons absorbed per molecule. On a practical scale, self-focusing may define a fundamental limit t the optical path length that can be utilized in industrial laser chemistry or isotope separation, and may thereby limit the useful through-put of an industrial plant. For the problem of atmospheric propagation,

*Research at UTD partially supported by the National Science Foundation under Grant No. CHE-8017324

the generation of additional frequencies will result in an increase of absorption and hence a reduction of transmission for pulsed laser beams with respect to that calculated for low-intensity CW beams. Self-focusing and self-defocusing will, of course, have an important effect on beam quality and the ultimate achievable far-field irradiance.

Energy Levels of Polyatomic Molecules

From the point of view of calculations of coherent propagation, the dominant feature of the energy levels of polyatomic molecules is the splitting of these levels by vibrational and rotational effects [4]. Originally it was supposed that multiple-photon excitation of polyatomic molecules would be very difficult owing to the general tendency of the spacing of the vibrational energy levels of an anharmonic oscillator to decrease with increasing excitation energy. However, early force-field studies of polyatomic molecules such as SF_6 that possess degenerate modes of vibration indicated that the splitting of the degenerate excited vibrational levels of these molecules by vibrational anharmonic effects could provide an important compensation for the anharmonicity of the vibration, and thereby increase the probability for finding a nearly resonant ladder of states for multiple-photon excitation [10]. These early calculations have recently been strikingly confirmed by experiment [11]. Rotational compensation of anharmonicity--in other words, the compensation of vibrational anharmonicity by a change of rotational energy--has also been suggested as an important factor in the occurrence of nearly resonant pathways for the excitation of polyatomic molecules [12]. The pathways for excitation to an excited state with three vibrational quanta in SF_6 are indicated schematically in Fig. 1. In the numerical calculations reported in this paper, we shall use a model of the excited states and transition moments of SF_6 that was recently reviewed by Cantrell, Letokhov and Makarov [1(c)]. In this model we employ effective states $|n\ell JR\rangle$ that represent grouped states of the real SF_6 molecule, with with energy levels given by

$$E(n\ell JR) = n\nu_3 + n(n-1)X_{33} + [\ell(\ell+1) - 2n]\, G_{33} + B_0 J(J+1) + B_0\zeta_3\{R(R+1) - J(J+1) - \ell(\ell+1) + 2n\} \quad (1)$$

where n is the number of vibrational quanta; ℓ is the vibrational angular momentum number; J is the total angular momentum of molecules; R is the rotational angular momentum of the molecular framework; B_0 is the rotational constant of the ground state of the molecule; ζ_3 is the magnitude of the vibrational angular momentum in units of h; ν_3 is the molecular vibrational frequency corrected for anharmonicity; X_{33} is a vibrational anharmonicity constant; and G_{33} describes the anharmonic splitting. The transition moments in this model are

$$\mu_{n\ell JR;\ n+1,\ \ell'J'R} = (1/3)^{1/2} \langle\mu_{01}\rangle\langle n\ell \| \hat{q} \| n+1,\ \ell'\rangle\, W(\ell'\ell J'J'1R) \quad (2)$$

where $\langle\mu_{01}\rangle$ is the dipole transition moment reported in the literature; W is a Racah coefficient; and the reduced matrix element $\langle n\ell \| \hat{q} \| n+1,\ \ell'\rangle$ is given in the review [1(c)]. A detailed account of other improved models for the energy levels of SF_6 for purposes of calculations of multiple-photon excitation will be published elsewhere.

Equations for Propagation

The propagation of a plane quasimonochromatic electromagnetic wave may be described in the slowly varying amplitude and phase approximation (SVAPA) by the equation

$$\frac{\partial \mathcal{E}(z,t')}{\partial z} = \frac{k}{2n^2\varepsilon_0}\,\mathcal{P} \quad (3)$$

where $\mathcal{E} = E'\exp(i\phi)$ is the complex electromagnetic field with envelope E' and phase ϕ; z is the propagation distance; $t' = t - nz/c$ is the retarded time; n is the linear index of refraction; $k = 2\pi n/\lambda$ is the propagation constant; and

$$\mathcal{P} = 2iN \sum_{m,A,B} \tilde{c}_{mA}\, \tilde{c}^{*}_{m-1,B}\, \mu_{mA;m-1,B} \quad (4)$$

$$= (S+iC)\, e^{i\phi} \quad (5)$$

is the slowly varying complex polarization. The complex amplitude $\mathcal{P}$ is related to the real dipole moment per unit volume $P = N\langle\mu\rangle$, where μ is the molecular dipole operator, by the equations

$$P = 2\mathrm{Re}(De^{i\zeta}) \quad (6)$$

$$= C\cos\zeta + S\sin\zeta \quad (7)$$

where

$$\rho = 2iDe^{i\phi} \tag{8}$$

and

$$\zeta = kz - \omega t + \phi \tag{9}$$

$$= -\omega t' + \phi \tag{10}$$

In Eq. (4), the subscripts m and A denote, respectively, the vibrational quantum number and the set of remaining quantum numbers needed to specify the effective state. The amplitudes c_{mA} of the states $|mA\rangle$ have been subjected to the transformation

$$c_{mA} = \tilde{c}_{mA} e^{-im\omega t'} \tag{11}$$

which results in the Schrödinger equation

$$\frac{\partial \tilde{c}_{mA}}{\partial t'} = i\Delta_{mA} \tilde{c}_{mA} + \frac{i}{2\hbar} \sum_B \{\mathcal{E}^* \mu_{mA;m+1,B} \tilde{c}_{m+1,B} + \mathcal{E} \mu_{mA;m-1,B} \tilde{c}_{m-1,B}\} \tag{12}$$

$$\Delta_{mA} = m\omega - E_{mA}/\hbar \tag{13}$$

which must be solved in order to calculate the polarization ρ, Eq. (4). Preliminary accounts of results obtained by the self-consistent numerical solution of Eqs. (3) and (12) have recently appeared [8] and a more detailed discussion is in preparation.

Excitation of a Multilevel System by a Pulse with Finite Risetime

When all the detunings Δ_{mA} for $m \neq 0$ are large compared to the Rabi frequency [1(c)]

$$\omega_R = \frac{\langle \mu_{01} \rangle}{2\sqrt{3}\hbar} |\mathcal{E}|, \tag{14}$$

then the amplitudes $\tilde{c}_{mA}$ of the states $|mA\rangle$ that are connected by dipole-allowed transitions with the initial (ground) state $|0B\rangle$ may be calculated by first-order time-dependent perturbation theory. For an incident pulse

$$\mathcal{E}(t') = \frac{E_0 e^{-\gamma t'}}{1+e^{-t'/t_0}} \tag{15}$$

which describes a laser pulse with a risetime t_0 and a fall time γ^{-1}, an analytical expression for the amplitudes of the states with $m=1$ may be obtained provided that

$$0 < \gamma t_0 < 1. \tag{16}$$

In this case the solution of Eq. (12) in first-order time-dependent perturbation theory for the initial condition $\tilde{c}_{0B} = 1$, $\tilde{c}_{mA} = 0$ $(m \neq 0)$,

$$\tilde{c}_{mA}(t') = \frac{i}{2\hbar} \exp(i\Delta_{mA} t') \int_{-\infty}^{t'} \exp(-i\Delta_{mA} t'') \mu_{mA,0B} \mathcal{E}(t'') dt'' , \tag{17}$$

may be explicitly evaluated [8(a)] with the result

$$\tilde{c}_{mA}(t' \to \infty) = -\left(\frac{\mu_{mA,0B} E_0}{2\hbar}\right) \frac{2\pi t_0 \exp(i\Delta_{mA} t')}{e^{-w} - e^{w}} \tag{18}$$

where

$$w = \pi(\Delta_{mA} - i\gamma) t_0 \tag{19}$$

In the limit of a rapid rise ($|\Delta_{mA}| t_0 \ll 1$) and a slow fall ($\gamma t_0 \ll 1$),

$$\tilde{c}_{mA}(t' \to \infty) \cong \exp(i\Delta_{mA}t') \frac{\mu_{mA,0B}E_0}{2\hbar\Delta_{mA}} \tag{20}$$

and the polarization becomes (assuming that only m=1 is excited)

$$\mathcal{P} = 2iN \sum_{A} \frac{[\mu_{mA,0B}]^2 E_0}{2\hbar\Delta_{mA}} \exp(i\Delta_{mA}t') \tag{21}$$

This is identical with earlier estimates based on the approximation of an instantaneously switched-on pulse. In the opposite limit of a slow rise ($|\Delta_{mA}|t_0 >> 1$) and a slow fall ($\gamma t_0 << 1$),

$$\tilde{c}_{mA}(t') \cong \frac{\varepsilon\pi\mu_{mA,0B}E_0 t_0 \exp[(i\Delta_{mA}t' - \pi\Delta_{mA}t_0)\varepsilon]}{2\hbar} \tag{22}$$

where ε = sign (Δ_{mA}), and the polarization becomes

$$\mathcal{P} \cong \frac{i\pi N\varepsilon}{\hbar} \sum_{A} |\mu_{mA,0B}|^2 E_0 t_0 \exp[(i\Delta_{mA}t' - \pi\Delta_{mA}t_0)\varepsilon] \; . \tag{23}$$

In other words, the amplitude of the sideband at the frequency $\omega - \Delta_{mA} = E_{mA}/\hbar$ is reduced in this case by the factor $\exp(-\pi|\Delta_{mA}|t_0)$. This general conclusion for multilevel systems establishes an analytical foundation for qualitatively similar conclusions arrived at by numerical methods in the special case of a two-level system by Eberly, Konopicki and Shore [13].

The Adiabatic-Following Approximation for Multilevel Systems

For a general pulse (for which $|\Delta_{mA}|$ need not be large compared to ω_R), and in the sudden approximation, in which the incident field $\mathcal{E}(0,t')$ is 0 for $t' \leq 0$, and is E_0 for $t' > 0$, then at the entrance face of the medium ($z = 0$) the Schrödinger equation (12) is (for $t' > 0$) that of a system evolving under the influence of a time-independent effective Hamiltonian whose matrix elements are

$$H^{eff}_{mA;mA} = \delta_{AB}\Delta_{mA}$$

$$H^{eff}_{mA;(m-1)B} = (2\hbar)^{-1}\mathcal{E}\mu_{mA;(m-1)B} \tag{24}$$

In this case it is natural to introduce the eigenvectors $|\lambda\rangle$ of H_{eff},

$$H^{eff}|\lambda\rangle = \lambda|\lambda\rangle \tag{25}$$

which are known as the "dressed" states. In the sudden approximation, the molecular system is initially (at $t' = 0+\varepsilon$) in that superposition of dressed states that results in the initial state just prior ($t'=0-\varepsilon$) to the switching on of the field $\mathcal{E}$:

$$\psi(0)\rangle = \sum_{\lambda} \langle\lambda|\psi(0)\rangle|\lambda\rangle \tag{26}$$

Subsequently each dressed state $|\lambda\rangle$ evolves with the time dependence $\exp(i\lambda t')$, so that

$$c_{mA}(t') = \sum_{\lambda} \exp(im\omega t' - i\lambda t')\langle mA|\lambda\rangle\langle\lambda|\psi(0)\rangle \tag{27}$$

In this case the macroscopic polarization induced by $\mathcal{E}(t')$ is (at z=0, before $\mathcal{E}$ is modified by propagation)

$$\mathcal{P}(0,t') = \sum_{\lambda\lambda'} \rho_{\lambda\lambda'} \exp[i(\lambda-\lambda')t'] \tag{28}$$

where

$$\rho_{\lambda\lambda'} = 2iN \sum_{m,A,B} \sum_{n,p} \sum_{C,D} \tilde{c}_{mC}(0)\, \tilde{c}^{*}_{pD}(0)\langle m-1,B|\lambda'\rangle\langle\lambda'|pD\rangle \langle nC|\lambda\rangle\langle\lambda|mA\rangle \tag{29}$$

Eqs. (28) and (29) show explicitly the generation of sidebands at every frequency $\lambda' - \lambda$ for every possible pair of "dressed" states λ, λ'.

In the opposite limit, in which the detuning Δ_{mA} is large compared to the reciprocal of the shortest time in which the field $\mathcal{E}$ changes significantly, then the phase of the polarization P generated by the medium quickly becomes the same as the phase of E. This statement, which is evident from the general discussion of adiabacitity in the textbook of Laudau and Lifshitz [14], and from the calculations of Arecchi and Bonifacio [15], and which has been discussed more recently for a two-level system by Eberly, Konopicki, and Shore [13], may easily be established by using the language of dressed states [8(a)]. When the field is switched on adabiatically slowly on the time scale of the reciprocal of the minimum detuning, then the system remains in that "dressed" state that is correlated with the initial eigenstate of the system $|\lambda_0\rangle \rightarrow |\psi(-\infty)\rangle$ at infinite time in the past, i.e., with the initial eigenstate in the presence of a vanishing optical field. In this approximation the Schrödinger-picture amplitudes are

$$c_{mA}(t') = \langle mA|\lambda_0\rangle e^{-i\lambda_0 t' - im\omega t'} \tag{30}$$

(where λ_0 and $|\lambda_0\rangle$ are (adiabatic) functions of t'), and the polarization in this approximation is

$$\mathcal{P}(0,t') = 2iN \sum_{m,A,B} \langle mA|\lambda_0\rangle\langle m-1,B|\lambda_0\rangle \mu_{mA;(m-1)B} \tag{31}$$

Since the components $\langle mA|\lambda\rangle$ of the dressed-state eigenvectors $|\lambda\rangle$ in the basis $|mA\rangle$ may be chosen to be real, the polarization given by (31) is pure imaginary. Comparison with (5) (with $\phi=0$) shows that in this case $S(t')=0$, i.e., that

$$P(0,t') = C(0,t')\cos\zeta \quad , \tag{32}$$

so that the macroscopic polarization adiabatically "follows" the field $E(0,t') = E'(0,t')\cos\zeta$. An explicit evaluation of the eigenvectors $|\lambda\rangle$ and eigenvalues λ for a two-level system shows that Eq. (31) is identical in that case with the adiabatic-following approximation of Grischkowsky et al. For a two-level system the dressed-state eigenvalues are

$$\lambda_{\substack{1\\(2)}} = \frac{\Delta}{2} \pm \frac{1}{2}[\Delta^2 + 4\Omega^2]^{1/2} \tag{33a}$$

where $\Omega = \mu_0 E'/2\hbar$. The eigenvalue $\lambda_1(\lambda_2)$ is correlated with the upper (lower) level as $E'\rightarrow 0$. The eigenvector correlated with the initial (i.e., ground) state at $E'=0$ is

$$\langle 0|\lambda_2\rangle = \frac{|\Omega|}{[\lambda_2^2+|\Omega|^2]^{1/2}} \tag{33b}$$

$$\langle 1|\lambda_2\rangle = \frac{|\Omega|}{\Omega}\frac{\lambda_2}{[\lambda_2^2+|\Omega|^2]^{1/2}} \tag{33c}$$

so that the polarization for a two-level system initially in the ground state is, in the approximation of Eq. (31),

$$\mathcal{P} = 2iN\frac{\Omega\lambda_2}{[(\lambda_2)^2+\Omega^2]^{1/2}} = -2iN\mu\frac{\Omega}{[\Delta^2+4\Omega^2]^{1/2}} \tag{34}$$

which is identical with the adiabatic-following approximation of Grischkowsky et al. [16]. Thus Eq. (31) defines an adiabatic-following approximation for multilevel systems. We reiterate that this approximation is valid only sufficiently far from resonance, i.e., when $[(\Delta_{mA})_{min}]^{-1}$ is small compared to the risetime of $E'(t')$.

It is evident that in the adiabatic-following situation described by Eq. (31) no resonant sidebands are generated. However, frequencies other than the incident frequency ω will still be present in the field radiated by the system,

$$\mathcal{E}_{rad}(z,t') = \frac{k}{2n^2\epsilon_0}\int_0^z \mathcal{P}(z',t')dt' \quad , \tag{35}$$

due to the phenomenon of self-phase modulation [9,17]. In the adiabatic-following limit it is possible to define the nonlinear susceptibility $\chi(E')$ as follows:

$$\chi(E') = \frac{P(0,t')}{E(0,t')} = \frac{C(0,t')}{E'(0,t')} = \frac{2ReD(0,t')}{E'(0,t')} \tag{36}$$

where D may be read off from Eqs. (4) and (8). We note that χ as defined in (36) contains all powers of E'. Eq. (36) is not restricted in validity to a particular order of perturbation theory. However, under some circumstances one may expand the nonlinear index of refraction

$$n^{NL} = (1+\chi)^{1/2} \tag{37}$$

approximately in the usual way:

$$n^{NL} \cong n_0 + \frac{1}{2} n_2 (E')^2 \tag{38}$$

We shall report a detailed numerical calculation of n^{NL}, n_0 and n_2 as functions of ω in a separate publication. However, we note here that for a system of length L the field (35) radiated by the medium initially (for sufficiently small z) grows as $kL\, n_2(E')^2$, so that the Fourier amplitude of $\mathcal{E}_{rad}$ at a detuning $\Delta\omega$ will be inversely proportional to the second derivative of $[E'(t')]^2$ at the stationary-phase points:

$$\tilde{\mathcal{E}}_{rad}(\Delta\omega) \propto \left| \frac{d^2}{dt'^2}[E'(t')]^2 \right|^{-1/2}_{\Delta\omega = -kn_2 L(d(E')^2/dt')/2n_0} \tag{39}$$

This is, of course, the phenomenon of self-phase modulation, which is well known in quasi-two-level systems [17]. The bandwidth of frequencies generated by self-phase modulation will exceed the original laser bandwidth $\Delta\omega_0$ provided that

$$\frac{1}{\Delta\omega_0} \left| \frac{d}{dt'} \left\{ \frac{kn_2[E']^2}{2n_0} \right\} \right|_{max} kL \geq 1 \tag{40}$$

Preliminary estimates made with Eq. (40) indicate that the bandwidth of frequencies generated by self-phase modulation exceeds $\Delta\omega_0$ under the conditions of most multiple-photon absorption experiments performed to date [9].

Transverse effects (self-focusing and self-defocusing) will occur in the case of a rapidly-switched-on pulse (i.e., for nearly resonant excitation) for a multilevel system as well as for the two-level systems that have been the subject of previous studies. We are now conducting numerical calculations of transverse effects in pulse propagation for multilevel systems, using previously developed numerical techniques [18]. One of these techniques is a perturbation approach that correctly describes the initial self-focusing behavior without the numerical complexity associated with a full coherent self-focusing calculation. The perturbation method uses two plane-wave pencils, one located on the axis of the (cylindrically symmetric) beam, the other slightly off-axis and with smaller intensity. It may be shown analytically that these pencils move with different velocities, and that the initial self-focusing is directly attributable to this difference of velocities.

However, in the limit of a slowly-switched-on pulse (i.e., for nonresonant excitation) the transverse effects associated with pulse propagation in multilevel systems may be discussed using the nonlinear index of refraction, Eq. (37). Whenever the expansion (38) is valid, then transverse effects may be calculated using standard theoretical approaches that take (38) as a point of departure. We shall give a discussion of transverse effects based on this approach in a future publication. Here we content ourselves with the observation that the spatial growth rate α of the mode of the self-focusing instability with maximum growth rate [19] is such that

$$\alpha L \geq 1 \tag{41}$$

provided that

$$\frac{n_2[E']^2}{2n_0} kL \geq 1. \tag{42}$$

Self-focusing effects may be expected to play an important role whenever (42) is satisfied, as it appears to be in many multiple-photon absorption experiments [7].

For a real molecular system subject to a thermal distribution of initial states, some molecules will satisfy the criterion for rapidly-switched-on pulses and other molecules will satisfy the criterion for

adiabatically-switched-on pulses. Under these circumstances the calculation must be pursued along differ lines for different classes of initial conditions. The dynamics of those molecules that are excited clos to resonance must be described using the full Schrödinger Eq. (12), while the dynamics of molecules excit far from resonance may be described by Eqs. (30)-(31). Calculations using this technique will be reporte elsewhere.

Numerical Studies of Pulse Propagation in Multilevel Systems

Since Eqs. (3) and (12) are (formally) two ordinary differential equations in the different independ variables z,t', coupled by the (nonlinear) polarization $\mathcal{P}(z,t')$, the self-consistent numerical solution (3) and (12) may be obtained by essentially the same methods used for pulse propagation in two-level syst by Hopf and Scully [20] and Icsevgi and Lamb [21]. In broad outline, the method consists of integrating (12) to find $\tilde{c}_{mA}(z,t')$ and eventually $\mathcal{P}(z,t')$ (Eq. (4)) as functions of t' for a given (fixed) value of z using the (known) dependence of $\mathcal{E}(z,t')$ on t' at the position z. Eq. (3) is then integrated one spatial step Δz for each (discrete) value of t' to find the field $\mathcal{E}(z+\Delta z,t')$ as a function of t' at the new posit $z+\Delta z$. Equation (12) may now be integrated to find $\tilde{c}_{mA}(z+\Delta z,t')$ as a function of t' at $z+\Delta z$, and so on.

The choice of a numerical algorithm for the solution of equations such as (3) and (12) has been care studied by Icsevgi and Lamb [21], who found the modified Euler predictor-corrector method to be fast and give acceptable accuracy. Since our problem involves substantially more time points (values of t') than were employed by Icsevgi and Lamb, we chose the slightly more accurate Hamming predictor-corrector method [22] for the integration of (12), but retained the modified Euler method for (3). In fact, the differenc between results obtained with the Hamming and modified Euler predictor-corrector methods in the integrati of (12) in test calculations were not significant. In all cases we used iteration to provide the initial values at two successive temporal or spatial steps required to start the predictor-corrector algorithm [21].

The temporal and spatial step sizes h_t and h_s were chosen to be sufficiently small that further refin ment did not significantly affect the solution, but large enough to minimize computational time given the desired accuracy. It may be shown that Eqs. (12) display an absolute instability for time-step sizes h_t such that

$$|\Delta_{mA}|_{max}\, h_t > 1. \tag{43}$$

The necessity to avoid this instability (even for the amplitude $\tilde{c}_{mA}$ of a state for which $|\Delta_{mA}|$ is so large in comparison with ω_R that $|\tilde{c}_{mA}|$ is always $\ll 1$) imposes a maximum acceptable value of h_t that (for weak fields) may be very small given the other physically relevant time scales in the problem, such as $(\omega_R)^{-1}$.

For the molecular energy levels and laser frequencies used in our calculations, the choice

$$h_t = \frac{1}{200}\,\frac{2\pi}{\omega_R} \tag{44}$$

gave acceptable results without requiring too much computational effort at low values of ω_R. Typical numerical results for the amplitude $|\mathcal{E}|/E_0$ and phase ϕ/π of a pulse

$$\mathcal{E}(0,t') = \begin{cases} 0, & t' < 0 \\ E_0, & t' \geq 0 \end{cases} \tag{45}$$

are shown in Fig. 2.

In order to investigate the frequencies introduced into the pulse as the result of propagation, we calculated the spectrum of the field radiated by the medium, Eq. (35). Since the field calculated self-consistently is $\mathcal{E}(z,t')$, and since Eq. (3) may be rephrased as the integral equation

$$\mathcal{E}(z,t') = \mathcal{E}_{inc}(t') + \mathcal{E}_{rad}(z,t') \tag{46}$$

(where $\mathcal{E}_{rad}$ is to be calculated using the self-consistently determined polarization $\mathcal{P}$), we see that

$$\mathcal{E}_{rad}(z,t') = \mathcal{E}(z,t') - \mathcal{E}_{inc}(t') \tag{47}$$

To calculate the spectrum of $\mathcal{E}_{rad}(z,t')$, we have calculated the numerical Fourier transform of the auto-correlation function

$$G(t_0,T) = T^{-1}\int_{t_0}^{t_0+T} \mathcal{E}^*_{rad}(t')\,\mathcal{E}_{rad}(t'+T)\,dt'. \tag{48}$$

Since the generation of sidebands is a non-adiabatic phenomenon, the autocorrelation $G(t_0,T)$ and its Fourier transform will depend on t_0. We have chosen $t_0=0$ in the spectrum of Fig. 3, which corresponds to the same conditions as in Fig. 2.

Using this technique we have calculated the sideband spectra for systems consisting of two, four, and ten energy levels, as functions of the propagation distance z and the laser electric field E_0, and for a variety of functional forms for the incident pulse $\mathcal{E}_{inc}(t')$ [8(a)]. The energy levels are as follows: (a) two-level system: The levels $(n\ell JR) = (00J_0J_0)$ and $(1,1,J_0-1,J_0)$. Our numerical results for this case appear to be in qualitative agreement with the previously published calculations of Eberly, Konopicki and Shore [13]. A quantitative comparison is impossible, owing to the fact that the vertical scale indicating the magnitude of the Fourier transform of $G(t_0,T)$ was omitted from their Figs. 2-4. (b) Four-level system: the levels $(n\ell JR) = (0,0,J_0,J_0)$, and $(1,1,J,R)$ with $J = J_0$, $J_0 \pm 1$. This system is an example of a general family of systems with a common lower level, and in which the upper levels are not radiatively connected among each other. Our calculations reported in Ref. 8(a) are the first calculations of which we are aware that treat the general problem of transient phenomena in pulse propagation in this type of system. Earlier pulse-propagation calculations on a three-level system with a common upper level pumped by a transition from one of the two lower levels addressed primarily the problem of gain on the transition that was not pumped initially [23]. The published calculation of distortionless pulse propagation in a three-level system by Higginbotham et al. [24] actually assumed two of the levels to be degenerate, thereby eliminating many of the effects we wish to investigate. The investigation of pulse propagation in degenerate systems by Hopf, Rhodes and Szöke [25] concerned an ensemble of two-level systems, and not a truly multilevel system of the type considered here. (c) Ten-level system: the levels $(n\ell JR) = (0,0,J_0,J_0)$; $(1,1,J,J_0)$ with $J = J_0, J_0 \pm 1$; $(2,0,J_0,J_0)$; and $(2,2,J,J_0)$ with $J = J_0 - 2, \ldots, J_0 + 2$. This is an example of a general type of energy-level scheme in which each level with vibrational quantum number n is connected radiatively to several levels with $n' = n \pm 1$. Our results reported in Ref. 8 and in Figs. 2-3 here are the first published calculations of pulse-propagation phenomena in such a system.

References

1. R. V. Ambartzumian, V. S. Letokhov, E. A. Ryabov and N. V. Chekalin, ZhETF Pis. Red. 20, 597 (1974).
2. R. V. Ambartzumian, Yu. A. Gorokhov, V. S. Letokhov, and G. N. Makarov, ZhETF Pis. Red. 21, 375 (1975) [JETP Lett. 21, 171 (1975); J. L. Lyman, R. J. Jensen, J. Rink, C. P. Robinson and S. D. Rockwood, Appl. Phys. Lett. 27, 87 (1975).
3. M. J. Coggiola, P. A. Schulz, Y. T. Lee and Y. R. Shen, Phys. Rev. Lett. 38, 17 (1977); P. Kolodner, C. Winterfeld and E. Yablonovitch, Optics Commun. 20, 119 (1977).
4. For reviews, see: (a) V. S. Letokhov and C. B. Moore, Sov. J. Quant. Electron. 6, 129 and 259 (1976). (b) C. D. Cantrell, S. M. Freund and J. L. Lyman, pp. 485-576 in The Laser Handbook, Vol. 3, edited by M. L. Stitch (Amsterdam, North-Holland Publishing Com., 1979). (c) C. D. Cantrell, V. S. Letokhov and A. A. Makarov, pp. 165-269 in Coherent Nonlinear Optics: Recent Advances, edited by V. S. Letokhov and M. S. Feld (Berlin, Springer-Verlag, 1980).
5. A. A. Makarov, C. D. Cantrell and W. H. Louisell, Optics Commun. 31, 31 (1979).
6. S. S. Alimpiev, V. N. Bagratashvili, N. V. Karlov, V. S. Letokhov, V. V. Lobko, A. A. Makarov, B. G. Sartakov, and E. M. Khokhlov, ZhETF Pis. Red. 25, 582 (1977); A. S. Akhmanov, V. N. Bagratashvili, V. Yu. Baranov, Yu. R. Kolomisky, V. S. Letokhov, V. D. Pismenny and E. A. Ryabov, Optics Commun. 23, 357 (1977).
7. A. V. Nowak and D. O. Ham, Optics Lett. (in press).
8. (a) C. D. Cantrell, F. A. Rebentrost and W. H. Louisell, Optics Commun. (in press); (b) C. D. Cantrell, W. H. Louisell and J. F. Lam, pp 138-141 in Laser-Induced Processes in Molecules, edited by K. L. Kompa and S. D. Smith (Berlin, Springer-Verlag, 1979).
9. The possible role of self-phase modulation in generating sidebands has been considered independently and previously by D. O. Ham (private communication).
10. C. D. Cantrell and H. W. Galbraith, Optics Commun. 18, 513 (1976) and 21, 374 (1977); C. C. Jensen, W. B. Person, B. J. Krohn and J. Overend, Opt. Commun. 20, 275 (1977).
11. C. W. Patterson, B. J. Krohn and A. S. Pine, Optics Lett. 6, 39 (1981).
12. R. V. Ambartzumian, Yu. A. Gorokhov, V. S. Letokhov, G. N. Makarov, and A. A. Puretzky, ZhETF Pis. Red. 23, 26 (1976) [JETP Lett. 23, 22 (1976)].
13. J. H. Eberly, M. J. Konopicki, and B. W. Shore, Optics Commun. 35, 76 (1980).
14. L. D. Landau and E. M. Lifshitz, Quantum Mechanics: Non-Relativistic Theory, 2nd edition (London, Pergamon Press, 1965), pp. 140-142.
15. F. T. Arecchi and R. Bonifacio, IEEE J. Quant. Elect. QE-1, 169 (1969).
16. D. Grischkowsky, pp. 437-452 in Laser Applications to Optics and Spectroscopy, edited by S. F. Jacobs et al. (Reading, Addison-Wesley, 1975).
17. F. Shimizu, Phys. Rev. Lett. 19, 1097 (1967).
18. (a) F. P. Mattar and M. C. Newstein, IEEE J. Quant. Electron. QE-13, 507(1977). (b) H. M. Gibbs, B. Bölger, F. P. Mattar, M. C. Newstein, G. Forster and P. Toschek, Phys. Rev. Lett. 37, 1743 (1976). (c) F. P. Mattar, Appl. Phys. 17, 53 (1978). (d) F. P. Mattar and M. C. Newstein, Computer Physics Commun. 20, 139 (1980).
19. B. R. Suydam, IEEE J. Quant. Electron. QE-10, 837 (1974) and QE-11, 225 (1975).
20. F. A. Hopf and M. O. Scully, Phys. Rev. 179, 399 (1969).
21. A. Icsevgi and W. E. Lamb, Jr., Phys. Rev. 185, 517 (1969).
22. R. W. Hamming, Introduction to Applied Numerical Analysis (New York, McGraw-Hill, 1971), pp. 203-214.
23. C. D. Cantrell, F. A. Hopf, G. W. Rhodes and M. O. Scully, Appl. Optics 15, 1651 (1976).
24. J. Higginbotham, R. T. Deck and D. G. Ellis, Phys. Rev. A 16, 2089 (1977).
25. F. A. Hopf, C. K. Rhodes and A. Szöke, Phys. Rev. B 1, 2833 (1977).

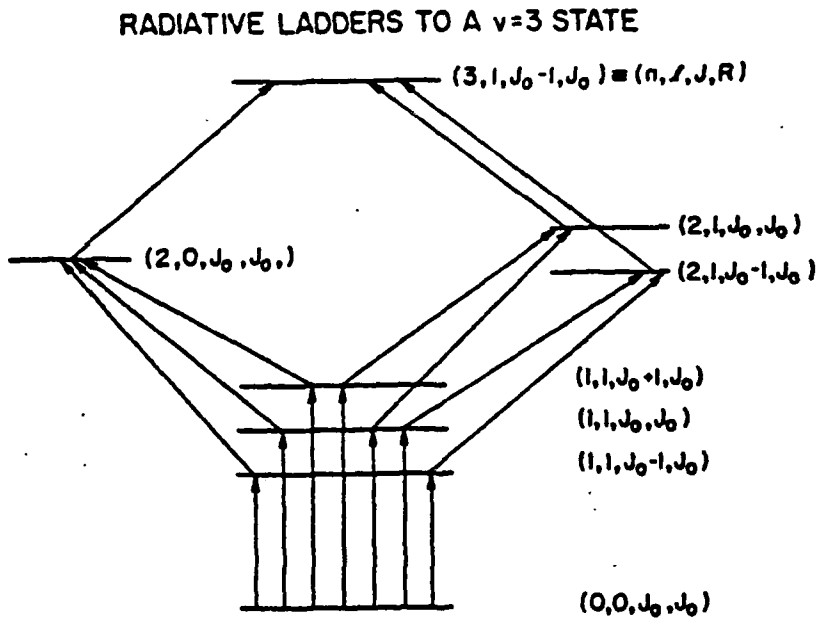

Figure 1: Schematic diagram of dipole-allowed transitions (indicated by arrows) that begin on a given effective state [4(c)] $(n\ell JR) = (0,0,J_0,J_0)$ and end on $(3,1,J_0 - 1, J_0)$.

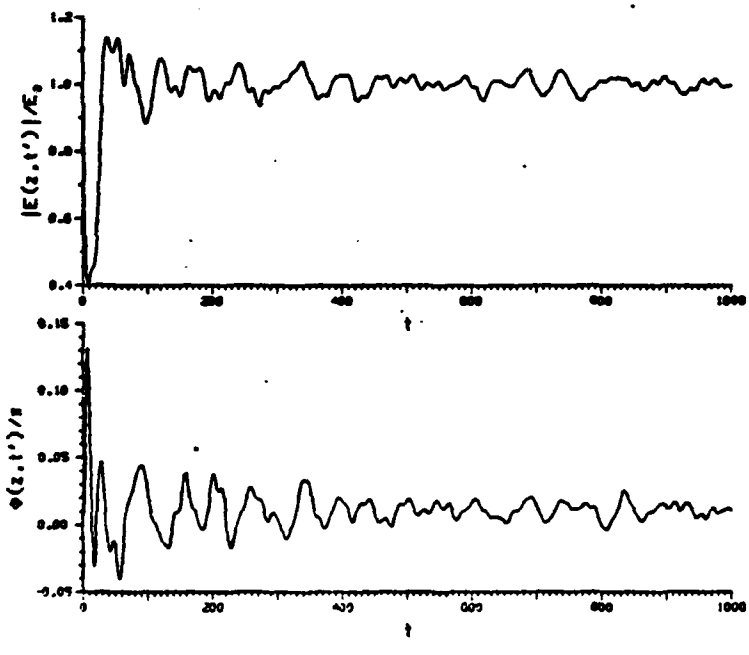

Figure 2: The normalized amplitude and phase of $\mathcal{E}(z,t')$ for z = 50 cm, and for the ten-level system shown in [8(a)], Fig. 1. Parameters are: $\langle\mu_{01}\rangle = 0.388$ D, $N = 3.54 \times 10^{15}$ cm^{-3}, $E_0 = 10^3$ sV cm^{-1} (3×10^3 V cm^{-1}), $X_{33} = -2.54$ cm^{-1}, $G_{33} = 0.303$ cm^{-1}, $T_{33} = 0$, $J_0 = 68$, $\nu_\ell/c = \omega/2\pi c = 946$ cm^{-1}.

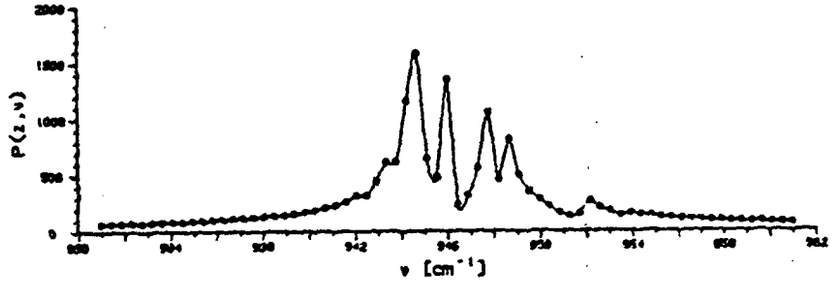

Figure 3: Power spectrum of the field shown in Fig. 2. The units of the vertical axis are $(\text{sV cm}^{-1})^2$, and the resolution of the numerical Fourier transform is 0.44 cm^{-1}. The initial time t_0 was taken as zero in Eq. (48).

International Conference on Excited states and Multiresonant nonlinear optical processes in solids

Digest of Technical Papers

Aussois, French Alps
March 18-20, 1981

LES ÉDITIONS DE PHYSIQUE
Avenue du Hoggar
Zone Industrielle de Courtaboeuf

Swept-gain superradiance in two- and three-level systems with transverse effects and diffraction (*)

F. P. Mattar and C. M. Bowden (**)

Aerodynamics Laboratory, Polytechnic Institute of New York, Farmingdale, New York 11735, U.S.A.

(**) Research Directorate, US Army Missile Laboratory, US Army Missile Command, Redstone Arsenal, Alabama 35898, U.S.A.

Abstract. — Results of numerical calculations using computational methods developed earlier to efficiently treat transverse as well as longitudinal reshaping associated with single-stream and two-way pulse propagation and generation effects in cooperative light-matter interactions, using the semiclassical model, are presented. Specifically, the results are presented and discussed for the two- as well as three-level system for a traveling excitation for both Gaussian and uniform gain distributions. Conditions are established for lethargic and highly nonlinear soliton pulse evolution through the asymptotic large Z regime.

Summary. — Computational methods based upon he Bloch-Maxwell semiclassical model were developed arlier [1] to efficiently treat transverse as well as ongitudinal reshaping and diffraction associated with ingle-stream and two-way pulse propagation and eneration effects in cooperative interaction between ie radiation field and a medium consisting of a ollection of two-level atoms. Results of the calcula- on are presented for pulse evolution as a function f propagation distance Z in the two-level system for traveling excitation with both Gaussian and uniform ain distributions with a *classical* initial tipping angle istribution. We present the conditions under which ie system evolves from a superfluorescent condi- on [2], where the atoms are contained within a ooperation volume, to an asymptotic steady-state [3] r sufficiently large propagation distance Z where oliton behavior is exhibited. The steady-state condi- on is interpreted in terms of the asymptotic behavior the principal mode pulse area and stabilization of the ntire pulse shape. Pulse areas greater than π are own to occur because of multiple pulse generation id self-focusing. Furthermore, it is shown that ffraction plays a much greater role in the results for e swept-gain superradiance regime [3] than for the nditions for which superfluorescence occurs [2]. ie results of our numerical calculations for the symptotic large Z regime are compared with the e-dimensional analytical results for swept-gain perradiance [3].

The numerical code was extended [1] to represent a collection of three-level atoms in the presence of two laser fields, consistent with the usual parity considerations [4, 5]. Results are presented for traveling excitation corresponding to optical pumping for both Gaussian and uniform radial gain distributions and several different temporal functions for the excitation. Superfluorescence is shown to occur for conditions analogous to those for the two-level case [1]; however, two-photon (coherent Raman) effects play a strong role in pulse delay and shape characteristics, as predicted from earlier analytical work [4, 5]. Pulse evolution characteristics are shown to depend upon the excitation temporal function dependence and radial function dependence as well as temporal duration and total area.

We show also in this case the conditions under which the system evolves to an asymptotic, steady-state condition at sufficiently large Z in terms of the principal mode pulse area and total pulse shape stabilization. As in the case of two-level swept-gain superradiance, strong self-focusing and multiple pulse generation is indicated.

Finally, results for simulton [6] behavior in the three-level system is presented with two injection signals and also with one injection signal (the optical pump) and a uniform tipping angle (determined from a thermal population distribution) which allows the second pulse to evolve. The latter conditions correspond most realistically in the large [7] region with experimental conditions for swept-gain superradiance reported in the literature [7, 8]. Results of the calculation are presented and compared with the experimental data.

*) Work jointly sponsored by the Research Corporation, the ernational Division of Mobil Corporation, the University of ontreal, the US Army Research Office, DAAG29-79-C-0148, Office of Naval Research, NOOO-14-80-C-0174, and Battelle lumbus Laboratories contract DAAG29-76-D-0100.

References

[1] MATTAR, F. P., *Effects of Propagation, Transverse Mode Coupling and Diffraction on Nonlinear Light Pulse Evolution*, in *Optical Bistability*, edited by C. M. Bowden, M. Ciftan and H. R. Robl (Plenum Press, NY, 1981), in press.

[2] MATTAR, F. P., GIBBS, H. M., MCCALL, S. L. and FELD, M. S., *Transverse Effects in Superfluorescence*, submitted for publication.

[3] BONIFACIO, R., HOPF, F. A., MEYSTRE, P. and SCULLY, M. O., *Phys. Rev.* A 12 (1975) 2568.

[4] BOWDEN, C. M. and SUNG, C. C., *Phys. Rev.* A 18 (1978) 1558.

[5] BOWDEN, C. M. and SUNG, C. C., *Phys. Rev.* A 20 (1979) 2033.

[6] KONOPNICKI, M. J., DRUMMOND, P. D. and EBERLY, J. H., *Theory of Lossless Propagation of Simultaneous, Different-Wavelength Optical Pulses*, private communication.

[7] EHRLICH, J. J., BOWDEN, C. M., HOWGATE, D. W., LEHNIGK, S. H., ROSENBERGER, A. T. and DETEMPLE, T. A., in *Coherence and Quantum Optics*, edited by L. Mandel and E. Wolf (Plenum Press, NY, 1978), Vol. 4, p. 555.

[8] ROSENBERGER, A. T., DETEMPLE, T. A., BOWDEN, C. M. and SUNG, C. C., *Superrddiance and Swept-Gain Superradiance in CH_3F*, in *Proceedings of Tenth International Quantum Electronics Conference*, 1978.

Computer Physics Communications 20 (1980) 139–163

ADAPTIVE STRETCHING AND REZONING AS EFFECTIVE COMPUTATIONAL TECHNIQUES FOR TWO-LEVEL PARAXIAL MAXWELL–BLOCH SIMULATION *

F.P. MATTAR ** and M.C. NEWSTEIN ***
Polytechnic Institute of New York, Brooklyn, NY 11201, USA

The methods, developed in gas dynamics, which make possible the detailed calculation of the coherent interaction of short optical pulses with a nonlinear active resonant medium are presented. This paper extends earlier work by giving a rigorous and self-consistent solution of the coupled nonlinear Maxwell–Bloch equations including transverse and time-dependent phase variations. In addition, the onset of an on-resonance self-focusing and beam degradation were predicted in absorbers and in amplifiers. To accurately handle such severe energy redistribution, dynamic nonuniform computational grids were found to be necessary. The self-focusing result agrees very well with a previous perturbation treatment and with recent experiments in sodium, neon and iodine, whereas severe beam distortion, when rigorously addressing the problem of transverse boundary, was observed in high-power lasers utilized in inertial fusion experiments. The formation of dynamic self-action effects is due to the combined effects of diffraction and the inertial response of the active medium.

1. Introduction

When an intense laser beam propagates through a resonant active medium, the absorptive and dispersive properties of the medium affect the shape of the laser beam profile, thus altering the characteristic structure of the medium [1–6]. This modified matter will then reaffect the field profile. The resulting cross-modulation of light by matter and matter by light is a continuous self-sustained phenomenon.

The current research was undertaken in an effort to answer detailed questions relating to the coherent exchange of energy, nonlinear phase distortion, and beam quality in high-power laser transmission; the method was chosen to develop a suitable theory and realistic numerical computer code based on close collaboration with experimentalists [6–20]. It is believed that real-life experiments would depart from the predictions of previous plane-wave analysis as sketched in fig. 1. The interplay of diffraction coupling and the medium response will *inevitably* redistribute the beam energy spatially and temporally [21–23]. This transient beam reshaping profoundly affects a device that relies on this nonlinear interaction effect.

This modeling encompasses self-phase modulation, dynamic longitudinal and transverse reshaping, and coherent energy exchange in an inertial medium. Effective mathematical transformations which are consistent with the physics make attainable a heretofore unachievable solution [24–29].

Light propagating in free space experiences diffraction spreading which alters the beam shape [30,31]. In the complicated nonlinear problem, the interaction intertwines the various parts of the beam; the beam transverse dimensions change drastically. As the transmission distance increases from the launching aperture, one is inevitably faced with substantial numerical difficulties. For example, a numerical paraxial code using a uniform, radial grid can suffer a serious drawback which would make the cost of the calculation prohibitive. The number of points required would need to be increased tremendously if the transient beam undergoes severe self-divergence or self-convergence. It is therefore imperative that the transverse mesh be sufficiently small to correctly sample the oscillations of the field amplitude and phase.

* Work jointly supported by F.P. Mattar, the Research Corporation, the International Division of Mobil, the University of Montreal and the US Army Research Office DAAG29-79-C-0148.
** Aerodynamics Laboratories.
*** Electrical Engineering.

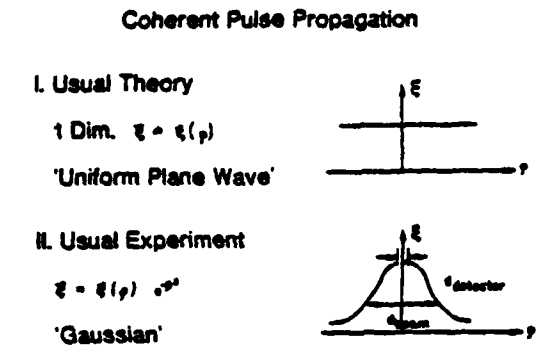

Fig. 1. The state of the art in coherent pulse propagation is displayed. The theoretical effort was restricted to a uniform plane wave prior to the work of Newstein and colleagues; whereas the usual experiment was carried out using a Gaussian beam. To simulate a uniform plane wave, the detector diameter was selected as small as possible when compared to the Gaussian beam diameter.

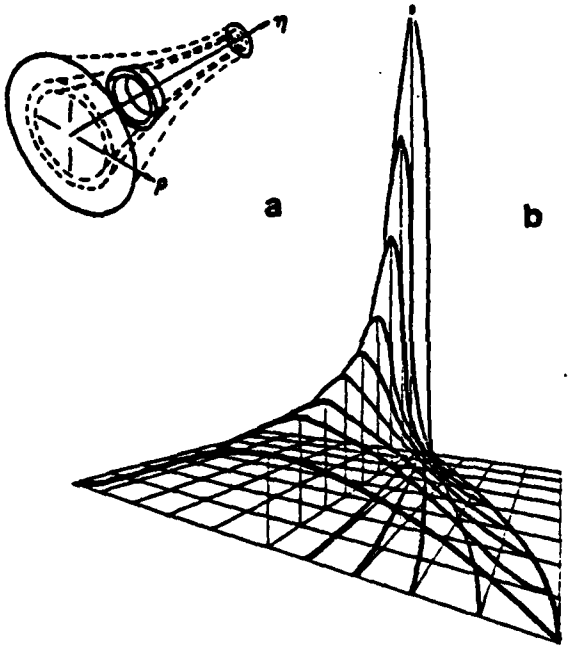

Fig. 2. (a) Isometric representation of the beam cross-section as it experiences self-focusing: The cross-section decreases as a function of the propagation distance; (b) An isometric display of the time integrated field energy as a function of ρ and η to illustrate the resolution limitation associated with uniform mesh.

If, for self-focused beams, a fixed, transverse mesh is used, there may be in the vicinity of the focal region a lack of resolution as displayed in fig. 2. A nonnegligible loss of computational effort in the wings of the beam also occurs. In an effort to maintain accuracy and efficiency, the governing equations were integrated using a simple coordinate transformation which was revised at suitable intervals to allow the numerical grid to follow the pulsed-beam behavior. The mesh network will expand or contract accordingly.

The interdependent nature of each aspect of the problem requires a thorough comprehension of the

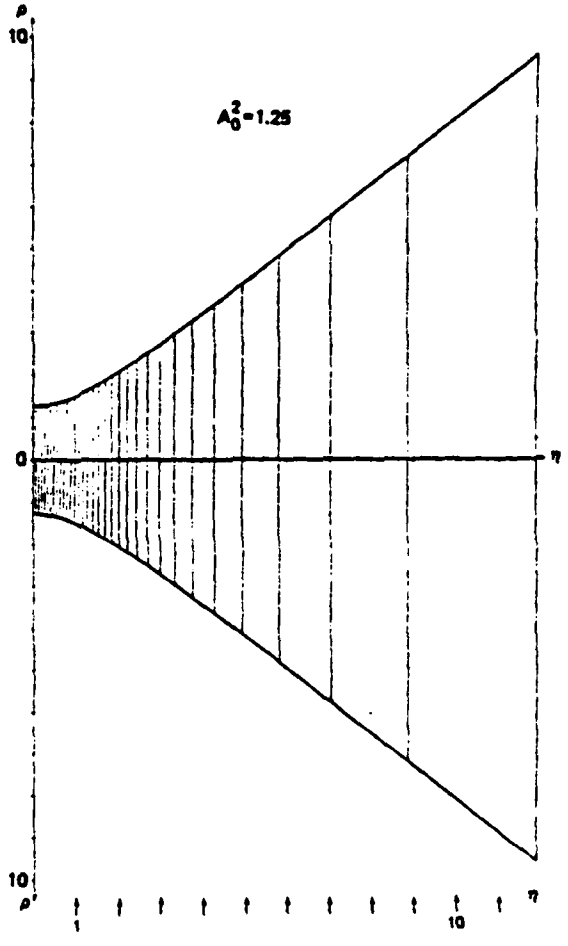

Fig. 3. Two-dimensional prescribed rezoning for ρ and η. As the beam narrows the density of transverse points and the transmission planes increase simultaneously.

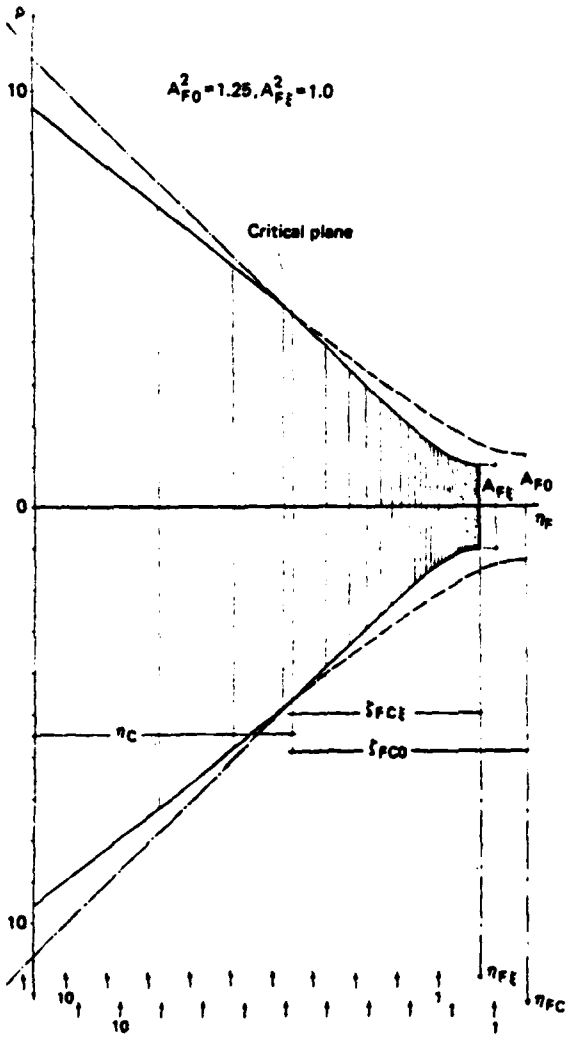

Fig. 4. Self-adjusted two-dimensional rezoning for ρ and η to follow more closely the actual beam characteristics. The (normalizing) Gaussian reference beam is redefined during the calculation.

relevant physics. In setting up variable grids there is an important factor to be considered: one must address any transverse energy distribution while analyzing the longitudinal alterations (figs. 3 and 4). If a variable longitudinal mesh, $\Delta\eta$, is introduced without carrying a variable, radial mesh, $\Delta\rho$, to handle large increments along the direction of propagation, one inevitably faces a steadily decreasing $\Delta\eta$ step as the beam starts to break up. This effect will intensify to such an extent that $\Delta\eta$ crashes to an increasingly smaller value and the calculation must be discontinued.

It is noteworthy that the choice of $\Delta\eta$ and $\Delta\rho$ is restrictively subjected to the definition of the Fresnel number [65]. The smaller the Fresnel number the smaller must be the ratio $[\Delta\eta/(\Delta\rho)^2]$ so that the numerical instability criterion obtained by linearized theory, is always satisfied.

Besides the coordinate modification, a change in the dependent variables is introduced in terms of renormalizing factors (such as the reference beam waist, wave-front curvature and field amplitude) to extract the radial dependence of the phase front and any important source of amplitude variation. As a result of the phase factorization, the new dependent functions vary more gradually in the new coordinate system: what one calculates, therefore, is a deviation from a reference Gaussian beam. As soon as the localized computational mesh departs significantly from the physical beam waist, the renormalization procedure is refreshed using pertinent moment properties of the physical quantities. Thus, the grid can be coarser, less extensive and more efficient.

Another major obstable is the cumulative memory effect in the response of the medium to the laser beam. For computational efficiency, the temporal grid will be nonuniformly stretched as indicated by *either* curve in fig. 10. In such an involved computation the calculational efficiency of the algorithm is of crucial importance. A brute force finite difference treatment of the governing equations is not feasible.

The adoption of nonuniform meshing techniques defined in connection with aerodynamics problems has proven to be very foresightful. These numerical methods, designed by Moretti [25–29], discriminate between different domains of dependence on different physical parameters; a higher degree of accuracy in the actual physical problem thus became feasible.

2. Physical background

The great interest in understanding the transmission of intense ultra-short pulses through a nonlinear medium is due to their application in laser-induced energy release via fusion of hydrogen iso-

topes. These pulses are assumed to be so short that no appreciable pumping (or other energy-exchange processes) can occur during the pulse. The resonant medium is thus left in a state of nonequilibrium after the pulse passes. When designing high power laser systems, one must verify that no beam distortion could evolve. Any departure from the desired uniform illumination of the target could prevent the fusion mechanism from taking place. One controls the cumulative interplay of beam diffraction with the medium inertia to avoid triggering the onset of any substantial self-action phenomena.

This model is readily deduced from the Maxwell–Bloch equations while taking into account the mutual influence of the transient beam and the resonant two-level atoms. The intense traveling electric field is treated classically, whereas, the two-level system is analyzed quantum mechanically. In particular, the medium response is described using the density matrix formalism [6,31]. None of the simplifying approximations (such as adiabatic following [17], or rate equation [18]), is introduced; instead an exact self-consistent numerical approach is developed.

This first nonplanar study simulates more accurately the experimental configurations than the previous restrictive one-dimensional theoretical attempts. The model takes into account the interplay of diffraction, time-dependent phase, nonlinear atomic inertia and initial matter and field boundary conditions.

This modeling, evolved from a close collaboration with various experimentalists, can lead to a better understanding of the basic cooperative effects in light-matter interactions. Extensions of this study may also help select optimum design configuration for superfluorescence [38–43], optical bi-stability [41–47], and double coherent transients [48–52]. Further benefits may include the development of new methods to generate ultra-short pulses as required for optical information transmission and optical communication.

3. Equations of motion

In the slowly varying envelope approximation the dimensionless semi-classical field-matter equations [6,22,23] (which describe our system in a cylindrical geometry with azimuthal symmetry), are:

$$-iF\,\nabla_T^2 e + \partial e/\partial\eta = \mathcal{P}\,, \tag{1}$$

$$\partial\mathcal{P}/\partial\tau = eW - (i\,\Delta\Omega + 1/\tau_2)\mathcal{P} \tag{2}$$

and

$$\partial W/\partial\tau = -1/2(e^*\mathcal{P} + e\mathcal{P}^*) - (W - W_0)/\tau_1\,, \tag{3}$$

where

$$e = (2\mu/\hbar)\,\tau_p e' \qquad \text{and} \qquad \mathcal{P} = (2/\mu)\mathcal{P}'\,,$$

$$E = \mathrm{Re}[e' \exp\{i((\kappa/c)\,z - \omega t)\}\,];$$

with

$$\kappa/c = \omega$$

and

$$\nabla_T^2 e = \left[\frac{1}{\rho}\frac{\partial}{\partial\rho}\left(\rho\,\frac{\partial e}{\partial\rho}\right)\right];$$

after applying L'Hopital's rule, the on-axis Laplacian reads:

$$\nabla_T^2 e = 2\partial^2 e/\partial\rho^2\,;$$

and

$$P = i\,\mathrm{Re}[\mathcal{P}' \exp\{i((\kappa/c)\,z - \kappa t)\}\,]\,.$$

The complex field amplitude e, the complex polarization density $\mathcal{P}$, and the energy stored per atom W, are normalized functions of the transverse coordinate $\rho = r/r_p$, the longitudinal coordinate $\eta = z\alpha_{eff}$, and the retarded time $\tau = (t - zn/c)/\tau_p$. The time scale is normalized to the input pulse length, τ_p and the transverse dimension scales to the input beam spatial width r_p. The longitudinal distance is normalized to the effective absorption length [7], $(\alpha_{eff})^{-1}$, where

$$\alpha_{eff} = \left[\frac{\omega\mu^2 N}{n\hbar c}\right]\tau_p \rightarrow [=\alpha'\tau_p]\,, \tag{4}$$

here, ω is the angular carrier frequency of the optical pulse, μ is the dipole moment of the resonant transition, N is the number density of resonant molecules, and n is the index of refraction of the background material. The dimensionless quantities $\Delta\omega = (\omega - \omega_0)\tau_p$, $\tau_1 = T_1/\tau_p$, and $\tau_2 = T_2/\tau_p$ measure the offset of the optical carrier frequency ω from the central frequency of the molecular resonance ω_0, the thermal relaxation time T_1, and the polarization dephasing time T_2, respectively.

Even in their dimensionless forms, the various

quantities have a direct physical significance. Thus $\mathcal{P}$ is a measure of the component of the transverse oscillating dipole moment ($\mathcal{P}$ has the proper phase for energy exchange with the radiation field). In a two-state system, in the absence of relaxation phenomena, a resonant field will cause each atom to oscillate between the two states, $W = -1$ and $W = +1$, at a Rabi circular frequency $f_R = e/\tau_p = (\mu/h)e'$. Thus e measures how far this state-exchanging process proceeds in a fwhm pulse length τ_p.

The dimensionless parameter, F, is given by $F = \lambda(\alpha_{eff})^{-1}/(4\pi r_p^2)$. The reciprocal of F is the Fresnel number associated with an aperture radius r_p and a propagation distance $(\alpha_{eff})^{-1}$. The magnitude of F determines whether or not one can divide the transverse dependence of the field into "pencils", (one per radius ρ), which may be treated in the plane-wave approximation. The diffraction coupling term and the nonlinear interaction terms alternately dominate depending on whether $F > 1$ or $F < 1$.

As outlined by Haus et al. [19], the acceptance of eq. (3), as describing the coupling of the material to the electric field, implies certain approximations. Eq. (3) shows that the product $e\mathcal{P}$ of the electric field, e, and the polarization, $\mathcal{P}$, causes a time rate of change of the population difference (i.e., in medium energy) leading to saturation effects: inertial effects *are* considered.

4. Energy consideration

From the field-matter relations (1)–(3) one obtains the energy current equation:

$$+iF\,\nabla_T(e\nabla_T e^* - e^*\nabla_T e) + \partial_\eta = (e^*\mathcal{P} + e\mathcal{P}^*)\,,$$

$$\nabla \cdot J = -2[\partial_\tau W + (W - W_0)/\tau_1]\,, \qquad (5)$$

where, using the polar representation of the complex envelope, we have

$$e = A\exp[+i\phi]\,, \qquad (6)$$

$$J_z = A^2 \qquad (7)$$

and

$$J_T = 2FiA^2\,\partial\phi/\partial\rho\,. \qquad (8)$$

The components J_z and J_T represent the longitudinal and transverse energy current flow. Thus, the existence of transverse energy flow is clearly associated with the radial variation of the phase of the complex field amplitude e. When J_T is negative [i.e., $\partial\phi/\partial\rho > 0$], self-induced focusing dominates diffraction spreading. Since $\partial\phi/\partial\rho$ determines the direction and speed of energy flow, it is reasonable to monitor either a phase gradient or the transverse energy current for a central diagnostic as the calculation proceeds.

One may rewrite the continuity eq. (5) in the laboratory frame to recover its familiar form:

$$\nabla \cdot J = -\frac{\partial}{\partial\tau}\left[2W + \frac{n}{c\tau_p\alpha_{eff}}A^2\right] - 2\frac{W - W_0}{\tau_1}\,. \qquad (9)$$

5. Outline of numerics

The retarded time τ refers to the actual arrival time in a stationary frame of the front of the pulse at the position z. This coordinate transformation, from t to τ, fig. 5a, allows an accurate numerical scheme to be developed for which the increment in η and τ need not be related in any special way.

Herein, the equations of motion are solved in the near-field region of an optical pulse, initially Gaussian

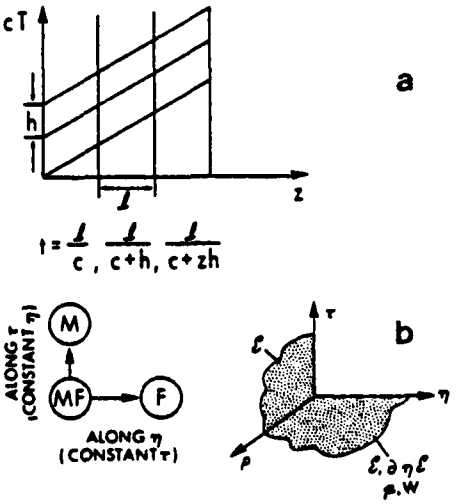

Fig. 5. Graph (a) displays the retarded time concept; (b) outlines the numerical approach: a marching problem along η for the field simultaneously with a temporal upgrading of the material variables along τ.

in both ρ and τ. This amounts to a mixed initial boundary-value problem. The initial configurations of the laser beam and the resonant medium are specified subject to certain conditions for $\tau \geq 0$ which must be satisfied at all space points. Furthermore, the field boundary condition at $\eta = 0$ is time-dependent. See fig. 5b. For the numerical solution, a temporal-spatial mesh of grid points is used to represent the $\rho\eta\tau$ space. At a given plane η, the values of the various dependent variables are obtained for all stations. This is repeated until the desired propagation length has been traversed.

The basic numerical algorithm consists of a combined explicit/implicit method. The MacCormack [24] two-level predictor–corrector, nonsymmetrical finite-difference scheme is used to advance the field equation along the direction of propagation, η, while the modified Euler three-level, predictor–corrector scheme is used to update the material variable in time-retarded time τ. The mutual light-matter influence is a mixture of a boundary value (for advancing the field) and an initial value problem (for calculating the atomic responses) [9]. To improve accuracy and speed up convergence, cross-coupling is accentuated. With such steps, the scheme becomes as flexible as a strongly-implicit algorithm. The final field value, rather than the predicted one as done classically [6–10, 25, 20, 22], is used to correct the material variable, and the final material values instead of the predicted ones are used to correct the field. The final variables are obtained as solutions of a set of five, simultaneous, algebraic equations.

6. Details of numerical procedure

An outline of the numerical method is illustrated using two simplified equations that are representative of the full set describing the propagation and atomic dynamics effects. Here, the material variables are denoted by M; either of the electric field variables is denoted by F. Both variables are complex quantities which are functions of the propagational coordinate, η, the transverse spatial coordinate and τ, the retarded time. With M_e, the equilibrium value of M, one can write the representative equations as:

$$-\mathrm{i}\,\nabla_T^2 F + \frac{\partial F}{\partial \eta} = M\,, \tag{23}$$

with

$$\nabla_T^2 F = \frac{1}{\rho}\left\{\frac{\partial}{\partial \rho}\left(\rho\,\frac{\partial F}{\partial \rho}\right)\right\}, \tag{24}$$

$$\frac{\partial M}{\partial \tau} = FM + M + M_e\,, \tag{25}$$

subject to the initial and boundary conditions:

1. for $\tau \geq 0$: $F = 0$, $M = M_0$ known function to take into account the pumping effects;
2. for $\eta = 0$: F is given as known function of τ and ρ;
3. for all η and τ: $[\partial F/\partial \rho]_{\rho=0}$ and $[\partial F/\partial \rho]_{\rho=\rho_{max}}$ vanish, with ρ_{max} defining the extent of the region over which the numerical solution is to be determined).

The derivatives in (23) appear only with respect to space variables; time enters only implicitly, through the right-hand side terms. Conversely, the derivative in (25) is a time derivative only, and the space influence is provided by the right-hand side terms. Thus the equations can be considered as somewhat uncoupled and separate integration procedures are adopted. We cannot be sure that the accuracy of the integration procedure is of the second order in $\Delta\eta$ and $\Delta\rho$ as well as in $\Delta\tau$ for the material variables, and similarly for the field variable with respect to $\Delta\tau$. This algorithm uses the two-level nonsymmetric, MacCormack explicit predictor–corrector finite difference scheme for marching the electric field F along η and the three-level modified Euler scheme to integrate along τ the material variables. To ensure second-order accuracy in all space and time increment steps simultaneously for all the dependent physical, field and material variables, the final field F instead of the predicted F is used to evaluate the final M; and the final M instead of the predicted M, to correct the field variable F. For simplification a quasi-linearization (see Moretti's treatment of the chemical kinetics problem [26]) is introduced as follows:

$$FM = -F_i M_i + F_i M + F M_i\,, \tag{26}$$

where i means the "initial value" and can reasonably be denoted by the predicted values. This approach follows readily the Taylor expansion of the product FM:

$$FM = (FM)_i + \left[\frac{\partial}{\partial F}(FM)\right]_i (F - F_i)$$

$$+\left[\frac{\partial}{\partial M}(FM)\right]_i (M - M_i) + \ldots \quad (27)$$

truncated at first-order terms.

Mathematically, this algorithm reads as follows: with

$$F(j\,\Delta\eta,\, m\,\Delta\rho,\, k\,\Delta\tau) \equiv F^j_{m,k}\,, \quad (28)$$

$$LF = i\,\nabla_T^2 F = (i/\rho)\{\partial/\partial\rho(\rho F)\}\,, \quad (29)$$

the predicted field can be written as:

$$\tilde{F}^{j+1}_{m,k} = F^j_{m,k} + \Delta\eta[M^j_{m,k} - L^F M^j_{m,k}]\,, \quad (30)$$

whereas the corrected field reads as follows:

$$F^{j+1}_{m,k} = \tfrac{1}{2}\,[(F^j_{m,k} + \tilde{F}^{j+1}_{m,k}) + \Delta\eta(M^{j+1}_{m,k} - L^B \tilde{F}^{j+1}_{m,k})]\,, \quad (31)$$

L^F and L^B are the forward and backward differencing of the transverse Laplacian operator cylindrical coordinates with azimuthal symmetry.

The material variables are integrated in the following manner. The predicted values are defined as:

$$\tilde{M}^{j+1}_{m,k+1} = M^{j+1}_{m,k-1} + 2\,\Delta\tau[F^{j+1}_{m,k} M^{j+1}_{m,k} - M^{j+1}_{m,k} + M_e]\,, \quad (32)$$

while the corrected values are given by:

$$M^{j+1}_{m,k+1} = \tfrac{1}{2}(M^{j+1}_{m,k} + \tilde{M}^{j+1}_{m,k+1}) + \Delta\tau\{(-\tilde{F}^{j+1}_{m,k+1}\tilde{M}^{j+1}_{m,k+1}) + F^{j+1}_{m,k+1}\tilde{M}^{j+1}_{m,k+1} + \tilde{F}^{j+1}_{m,k+1} M^{j+1}_{m,k+1} + (\tilde{M}^{j+1}_{m,k+1} + M_e)\}\,. \quad (33)$$

Rearranging, one has

$$F^{j+1}_{m,k+1} = a_1 + b_1 F^{j+1}_{m,k+1} + q_1 M^{j+1}_{m,k+1}\,, \quad (34)$$

$$M^{j+1}_{m,k+1} = a_2 + b_2 F^{j+1}_{m,k+1} + q_2 M^{j+1}_{m,k+1}\,, \quad (35)$$

which is a set of linear algebraic equations that can readily be solved by straightforward elimination.

The numerical code has been tested systematically by insuring the reproduction of analytical results of problems such as free-space propagation [31], Gaussian beam propagation through lenselike media [32], Bloch's solution at the input plane for an on-resonance real field [6] and coupled uniform plane-wave calculations for an input 2π hyperbolic secant [6–11]. Identical results were obtained solving these problems expressed in the eikonal and transport form [1], and the three-dimensional results have been compared qualitatively and quantitatively with an analytic perturbation in the reshaping region [22,40].

7. Importance of boundary conditions

When the laser beam travels through an amplifier, the transverse boundary has an increasingly *crucial* effect in contrast to the absorber situation. The laser field which resonates with the pre-excited transition experiences gain; whereas, the laser field which encounters a transition initially at ground state, experiences resonant absorption and losses. A more significant portion of the pulse energy is diffracted outwardly in the amplifier than in the absorber [23].

In resonant, nonlinear, light–matter interactions, the velocity profile is not uniform across the beam. The intensity at a particular radius as well as the initial state of the transition dictates the distinct delay/advance that the "pencil" will experience at a particular radius. Consequently, these boundary reflection conditions tend to play a substantial role in the amplifier calculations and could obscure the emergence of any new physical effects. Hence, acceptable results are achieved only by carefully coupling the internal points analyzed with the boundary points [27].

Special care is required to reduce the boundary effect to a minimum. By using nonuniform grids and confining the active medium by radially-dependent absorbing shells one can construct an effective, reliable algorithm, locally consistent with the physics of the problem: i.e., the boundary condition to be discussed below is an absorbing surface. This condition represents an actual experimental approach in which the laser amplifier is coated to circumvent any spurious reflections.

Mathematically, this approach is implemented by introducing a radially-dependent loss distribution. The loss coefficients obey a Gaussian-dependence peaking at the wall itself. Three forms of loss were studied: Ohmic linear form, cubic Kerr loss, and reduction in the nonlinear gain of the active medium.

For strongly amplifying media, the transverse boundary could still cause computational difficulties for self-diverging beams, because it is difficult to select, beforehand, the functional location of the boundary. An alternate approach to the problem would be to extend the transverse grid to infinity as displayed in fig. 6. In practice, the most effective treatment of the dynamic, transverse, boundary consists of implementing an absorbing surface while concurrently considering an infinite physical domain and

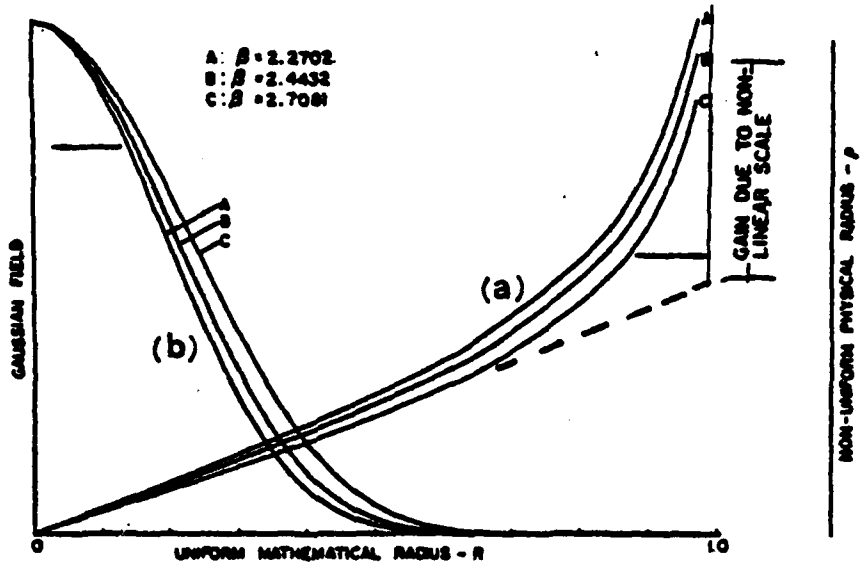

Fig. 6. (a) Non-uniform stretching of the transverse coordinate; (b) Contrast the Gaussian beam dependence with the non-uniform physical radius.

mapping it on a finite computation region.

Hence, the desired transformation process for the transverse coordinate is:

$$\xi = \tanh(\beta\rho), \qquad 0 < \xi < 1, \qquad N_B > N_A, \tag{36}$$

$$\xi = (k-1)/N_B, \qquad 1 < k < N_B, \tag{37}$$

$$\rho_{max} = \rho(N_A), \tag{38}$$

$$\rho = \left(\frac{1}{2\beta}\right) \log\left(\frac{1+\xi}{1-\xi}\right), \tag{39}$$

with

$$\beta = \frac{1}{2\rho(N_A)} \log\left[\frac{1+\xi(N_A)}{1-\xi(N_A)}\right], \tag{40}$$

with $\rho(N_A)$ denoting the actual maximum radius where the active medium is still present. In the region extending from $\rho(N_A)$ to $\rho(N_B)$ there is no amplifying medium; instead, there *is* an absorbing layer.

The mapping derivatives can also be defined analytically as follows:

$$\partial\xi/\partial\rho = \beta(1-\xi^2) = \beta\,\mathrm{sech}^2(\beta\rho) \tag{41a}$$

and

$$\partial^2\xi/\partial\rho^2 = 2\beta^2\xi(1-\xi^2). \tag{41b}$$

on axis:

$$\nabla_{T\rho}^2\xi \to \infty. \tag{41c}$$

The diffraction coupling term becomes:

$$\nabla_T^2 e = \frac{\partial^2 e}{\partial\xi^2}\frac{\partial\xi^2}{\partial\rho^2} + \frac{\partial e}{\partial\xi}(\nabla_{T\rho}^2\xi), \tag{41d}$$

with the on-axis contribution

$$[\nabla_T^2 e]_{\rho=0} = \frac{\partial^2 e}{\partial\xi^2}\left(\frac{\partial\xi}{\partial\rho}\right)^2 + \lim_{\rho\to 0}\frac{1}{\rho}\left(\frac{\partial e}{\partial\rho}\right)\frac{\partial\xi}{\partial\rho}$$

$$= 2\frac{\partial^2 e}{\partial\xi^2}\left(\frac{\partial\xi}{\partial\rho}\right)^2 = 2\beta^2\left(\frac{\partial^2 e}{\partial\xi^2}\right). \tag{41e}$$

In fig. 7, the first and second radial derivatives and the Laplacian term are drawn. Fig. 8 contrasts in the stretched radial coordinate system, the transverse coupling and the electric field.

When using the above, the numerical domain sensitivity and the dependence of the physical param-

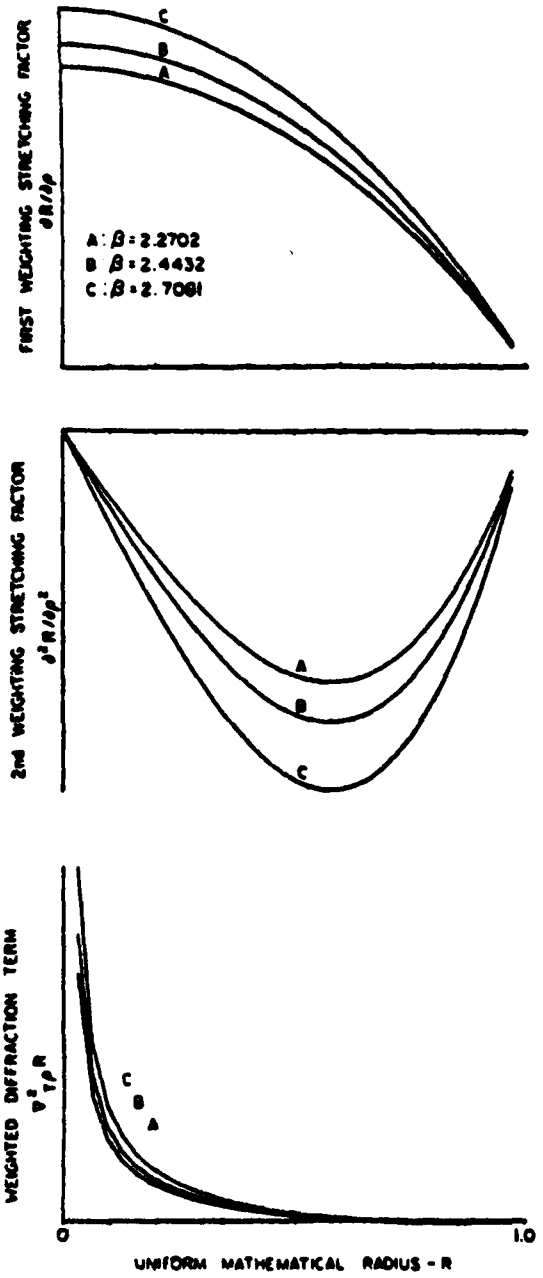

Fig. 7. This graph illustrates the dependence of the radial mapping and the derivatives on the different parameters versus the uniform mathematical radius.

eters on the boundary conditions can readily be assessed.

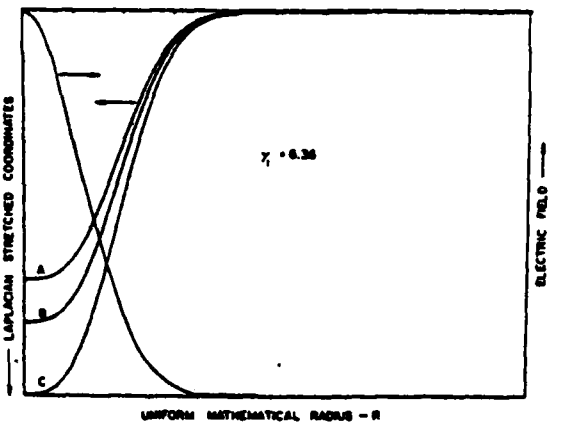

Fig. 8. This figure contrasts the Laplacian dependence for a given Gaussian profile for various non-uniform radial point densities.

8. Prescribed stretching

Proper handling of the differential equations of motion is possible provided there are enough mesh points to insure adequate resolution where phase gradients change very rapidly. However, to keep the computing costs at a minimum a nonuniform grid is used.

It is defined by widely-spaced computational nodes in the area most distant from the plane of interest and densely clustered nodes in the critical region of rapid change; the latter being in the neighborhood of maxima and minima or, for multi-dimensional problems, in the vicinity of saddle points.

Consequently, resolution is sought only where it is needed. The costs involving computer time and memory size dictate the maximum number of points that can be economically employed. In planning such a variable mesh size, the following [28], must be kept in mind:

(a) The stretching of the mesh should be defined analytically so that all additional weight coefficients appearing in the equations of motion in the computational space, and their derivatives, can be evaluated exactly at each node. This avoids the introduction of additional truncation errors in the computation.

(b) To assure a maximum value of ΔT, the mathematical grid step, the minimum value of $\Delta\tau$, the

physical time increment, should be chosen at each step according to necessity. This means that the minimum value of $\Delta\tau$ must be a function of the pulse function steepness.

(c) The minimum value of $\Delta\tau$ should occur inside the region of the highest gradient which occurs near the pulse peak.

For example, following Moretti's approach, if $T = \tanh(\alpha\tau)$ (42a) and α must be larger than 1, the entire semi-axis τ greater than zero can be mapped on the interval $0 < T < 1$ with a clustering of points in the vicinity of $\tau = 0$, for evenly-spaced nodes in t.

This mapping has several advantages. It introduces into the equations of motion new coefficients which are defined analytically and have no singularities. It avoids interpolation at the common border of meshes differently spaced. The computation is formally the same in the 'T' space as it was in the τ space. Some additional coefficients, due to the presence of the stretching function, appear and are easily defined by coding the stretching function in the main program. By a proper choice of the function and by letting some parameters (such as α, above) vary as functions of the propagation distance according to physical needs, the accumulation of points can be obtained where necessary at any distance of propagation. In the laser problem, we use a slightly modified stretching function:

$$\tau = \tau_c + (\alpha/2)\log(T/(1-T)) \tag{42b}$$

where α is a stretching factor which makes points more dense around τ_c, the centre of gravity of the transformation. In particular,

$$\alpha = \tau_{\text{window}}/\log(N_{\text{up}} - 2) \tag{43}$$

with N_{up} is the number of uniform points in the mathematical grid, and τ_{window} is the temporal window

$$\tau_{\text{window}} = (\tau_{\max} - \tau_{\min}), \tag{44}$$

τ_c is an arbitrary point used to define the centre of transformation so that the change of the coordinate will be optimum for more than one plane along the direction of propagation. Fig. 9 illustrates the transformation and its different dependence on the particular choice of its parameters.

Note that a derivative of the mapping function produced by the gradual variation along the 'T' axis is also defined analytically, namely $\partial\tau/\partial T = (\alpha/2)[T(1-T)]^{-1}$ (44b). In response the computational grid remains unchanged while the physical grid (and the associated weighting factors) can change appreciably.

Should one need to study the laser field build-up due to initial random noise polarization (for superradiance), or to an initial tapping angle (for super-

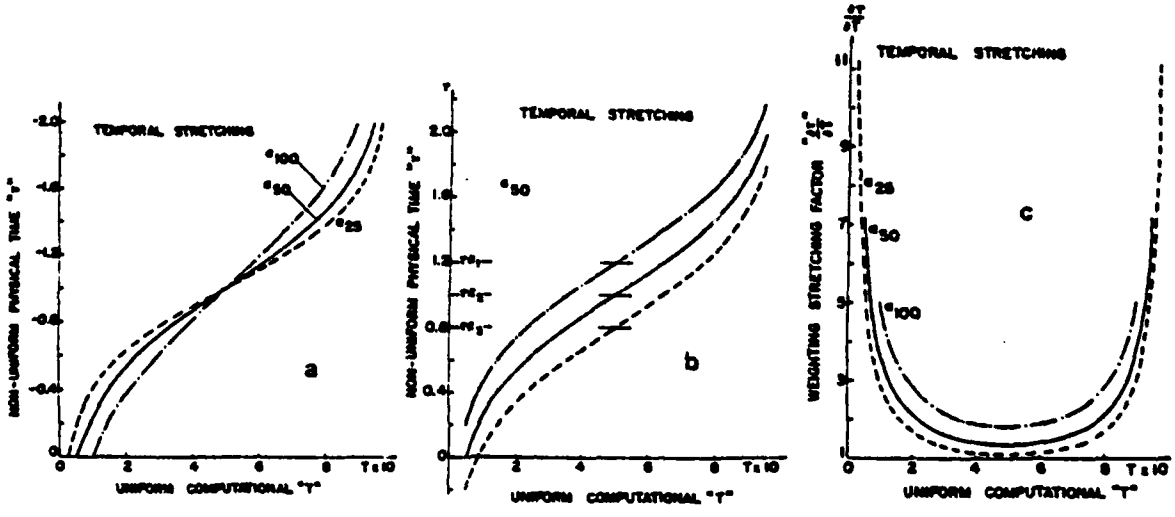

Fig. 9. Dependence of prescribed stretching and its derivatives on the point densities and the centre of transformation.

fluorescence), one must utilize a different stretching [66]. This stretching is similar to the one defined for treating radial boundary conditions. The mesh points are clustered near the beginning (small τ); their density decreases as τ increases. Note that the Fresnel number for the super-fluorescence simulation was selected to be one [66], in accordance with present experiments.

9. Adaptive stretching in time

As the energy continues to shift back and forth between the field and the medium, the pulse velocity is modified disproportionately across the beam cross-section. This retardation/advance phenomenon in absorber/amplifier can cause energy to fall outside the temporal window. Furthermore, due to nonlinear dispersion, the various portions of a pulse can propagate with different velocities, causing pulse compression. This temporal narrowing can lead to the formation of optical shock waves. The quality of the temporal resolution becomes critical. To maintain computational accuracy a more sophisticated stretching than that described in section 8 is needed. The accumulation centre of the nonlinear transformation used to stretch the time coordinate should be made to vary along the direction of propagation. This adaptive stretching will insure that the redistribution of mesh points properly matches the shifted pulse (fig. 10).

Here the transformation (42) from τ to T is applied about a centre τ_c which is a function of η:

$$\tau = \tau_c(\eta) + \frac{\alpha}{2}\log\frac{T}{1-T}\,. \tag{45}$$

The stretching factor α could also be a function of η (fig. 19b) with

$$\tau_c(\eta + \Delta\eta) = \tau_c(\eta) + [\tau_{pk}(\eta) - \tau_{pk}(\eta - \Delta\eta)]\,, \tag{46}$$

where $\tau_{pk}(\eta)$ is determined from the previous plane η as the time at which the electric field on axis is maximum. The time delay/advance accumulated in

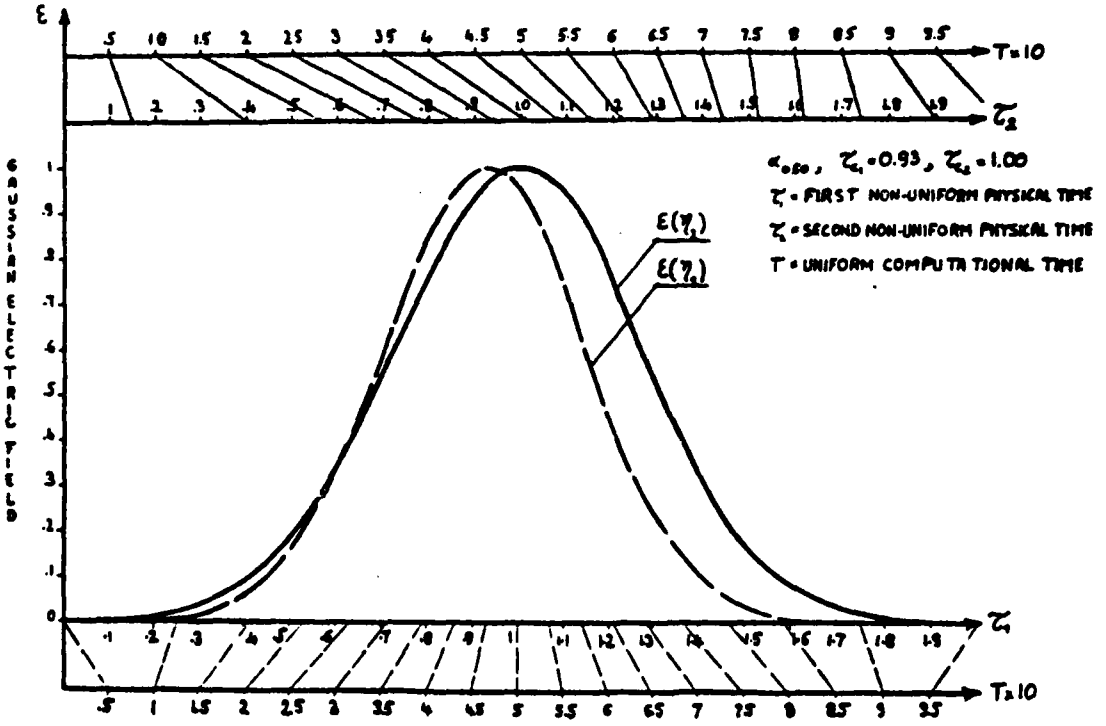

Fig. 10. Adaptive stretching with different centres of transformation.

the interval $\Delta\eta$

$$\Delta\tau = \tau_{pk}(\eta) - \tau_{pk}(\eta\,\Delta\eta) \tag{47}$$

measures the velocity of the peak relative to the speed of light:

$$v/c = 1/[c(\Delta\tau/\Delta\eta) + 1]\,. \tag{48}$$

The equations are very similar to those of section 3, with an extra term added:

$$-iF\,\nabla^2_{T\rho}e + \partial_\eta e + \frac{\partial e}{\partial T}\left[-\frac{\partial T}{\partial \tau}\right]_{\tau_c}\frac{d\tau_c}{d\eta} = \mathcal{P}\,. \tag{49}$$

The role played by the time coordinate is different. Previously the field equation did *not* contain an explicitly dependent term.

10. Rezoning

The main difficulty in modeling laser propagation through inhomogeneous and nonlinear media stems from the difficulty of preassessing the mutual influence of the field on the atomic dynamics and the effect of the induced polarization on the field propagation. Strong beam distortions are expected to occur based on a perturbational treatment of initial trends. One must normalize out the critical oscillations to overcome the economical burden of an extremely fine mesh size. To insure such accuracy and speed in the computation, a judicious choice of coordinate system and appropriate changes in the dependent variables, which can either be chosen a priori or automatically redefined during the computation, must be considered (fig. 11) [33–37].

This procedure removes the necessity for sampling the high frequency oscillations induced in the phase by self-lensing phenomena. The coordinate transformation alters the independent variables and thereby causes the dependent variables to take a different functional form. The new dependent variables are numerically identical to the original physical amplitudes at equivalent points in space and time.

The requirements of spatial rezoning will be satisfied by simultaneously selecting a coordinate transformation (from the original coordinates ρ and η to new coordinates ξ and z) and an appropriate phase and amplitude transformation. The chosen transformation will share the analytical properties of an ideal Gaussian beam propagating in a vacuum. Using Kogelnik and Li's notation [30], the Gaussian solution of the free-space ($\mathcal{P} = 0$) equation

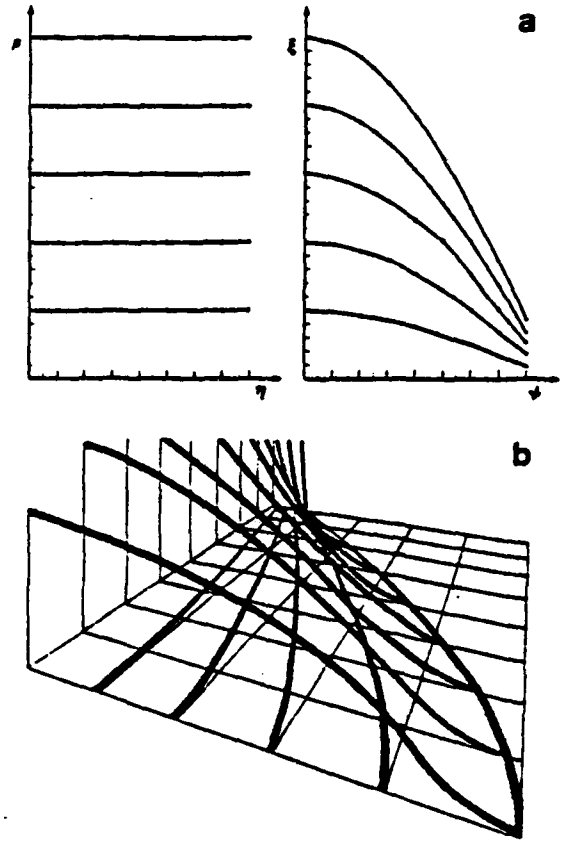

Fig. 11. (a) The concept of the prescribed rezoning; (b) a close-up of the non-uniform mapped grid of fig. 2b.

$$2i\,\partial_\eta e + \nabla^2_{T\rho}e = 0 \tag{50}$$

is well known and may be written as:

$$e(\rho, \eta, \tau) = a(\eta, \tau)^{-1}\exp\left\{\psi(\eta, \tau) - \rho^2\left(\frac{1}{a^2(\eta, \tau)} + \frac{ikn_0}{2R(\eta, \tau)}\right)\right\}, \tag{51}$$

where

$$\psi(\eta, \tau) = \arctan(\eta/ka_0^2)\,, \tag{52}$$

$$a(\eta, \tau) = a_0\sec\psi\,, \tag{53}$$

$$R(\eta, \tau) = \eta \operatorname{cosec} \psi \,. \tag{54}$$

The parameter a is the measure of the transverse scale, and

$$a_0 = a(0, \tau) \tag{55}$$

is the width of the initial intensity distribution. The parameter a shrinks or expands as the beam converges or diverges. It is logical to require the transverse mesh to vary as a varies. Therefore, the variable

$$\xi = \rho / a(\eta, \tau) \tag{56}$$

is introduced (fig. 11). More specifically, stability and convergence are assured if the ratio $[\Delta\eta/(\Delta\rho)^2]$ is appropriately defined, according to the Fresnel number chosen, and kept constant throughout the calculation.

Accordingly, one must introduce a new axial variable z so that this parameter automatically remains constant as ρ varies. This should increase the density of η planes around the focus of the laser field where the irradiance sharply increases in magnitude causing a more extensive and severe field-material interaction to occur. This is accomplished by introducing

$$z = \psi \tag{57}$$

and using a constant Δz. This has the effect of making the extent of real space related to the size of the vacuum beam.

In terms of ξ and z the field equation now appears as

$$\frac{1}{a^2(z)} \left[2\mathrm{i}\, \partial_z e - 2\mathrm{i}\xi(\tan z)\, \partial_\xi e + \nabla^2_{T\xi} e\right] = \mathrm{i}c_1 \,, \tag{58}$$

where c_1 is a constant.

For the field and polarization envelopes, the variables B and S are defined as:

$$\begin{Bmatrix} e \\ P \end{Bmatrix} = [a_0^{-1} \cos z] \begin{Bmatrix} B \\ S \end{Bmatrix} \exp\left[+\mathrm{i}\,\frac{\xi^2}{2} \tan z - \mathrm{i}z\right] . \tag{59}$$

The quadratic phase and amplitude variation have been removed. The new field then takes the form:

$$\{1/a^2(z)\}\, [2\mathrm{i}\, \partial_z B + \nabla^2_{T\xi} B + (2 - \xi^2) B] = \mathrm{i}c_1 S \,. \tag{60}$$

B and S vary more slowly in their functional values than their predecessors allowing the numerical procedure to march the solution forward in a more economical fashion by using larger meshes. They are numerically treated in an almost identical fashion to e and $\mathcal{P}$. Strongly nonlinear media require, however, a more sophisticated approach.

11. Adaptive rezoning

The foregoing concepts may be generalized by repeating the simple coordinate and analytical function transformations along the direction of propagation at each integration step. The feasibility of such automatic rezoning has been demonstrated by Hermann and Bradley in their CW analysis of thermal blooming [33] and by Moretti in supersonic flow calculations [28,29].

In particular, the change of reference wavefront technique consists of tracking the actual beam features and then readjusting the coordinate system. An adaptation of Hermann and Bradley's technique to a cylindrical geometry is presented herein.

The new axial coordinate z is defined, as before, as

$$z = \arctan(\eta / k a_0^2) \tag{61}$$

and

$$\partial_\eta z = (1/k a^2) \,. \tag{62}$$

Previously, the centre of the transformation where the radial mesh points were most tightly bunched, was at the focus ($z = \eta = 0$). Now the transformation will be defined in terms of an auxiliary axial variable z_ξ as a function of z, which is calculated adaptively in a way that reflects and compensates the changing physical situation. The relationship $z_\xi(z)$ will be defined later in this section.

The radial coordinate ξ is then defined similarly as

$$\xi = \rho / a_\xi(z_\xi) \tag{63}$$

with an auxiliary axial coordinate z_ξ different from z. For stability reasons, $(\Delta z_\xi / \Delta\xi^2)$ must be a constant. From

$$z_\xi = \psi \tag{64}$$

this leads to:

$$a_\xi(z_\xi) = a_{0\xi} / \cos z_\xi \,, \tag{65}$$

$$\mathrm{d}\eta = k a_0^2 [\tan(z + \mathrm{d}z) - \tan z] \tag{66}$$

$$= k a_{0\xi}^2 [\tan(z_\xi + \mathrm{d}z_\xi) - \tan z_\xi] \,, \tag{67}$$

which gives:

$$\partial_z z_\xi = a^2/a_\xi^2 , \tag{68}$$

and also leads to an expression for dz_ξ:

$$\tan(dz_\xi) = a^2 \tan(dz)/\{a_\xi^2 + \tan(dz) \times [a^2 \tan z_\xi - a_\xi^2 \tan z]\} . \tag{69}$$

This enables one to find appropriate values for a/a_ξ. $a_{0\xi}$ is then defined by writing:

$$a_\xi(z_\xi + dz_\xi) = a_{0\xi}/\cos(z_\xi + dz_\xi) . \tag{70}$$

In this adaptive rezoning scheme, the physical solution near the current z plane is described better by a Gaussian beam of neck radius $a_{\xi 0}$ whose focal point is a distance z_ξ away than by an initially assumed Gaussian beam with parameters a_0 and z. With this transformation the field equation (50) in terms of z and ξ becomes

$$2i\,\partial_z e + \frac{a^2}{a_\xi}\,[\nabla_\xi^2 e - 2i\xi \tan z(\partial_\xi e)] = ic_1^2 a_\xi \mathcal{P} . \tag{71}$$

To remove the unwanted oscillations, new dependent variables B and S are introduced by $e = GB$ and $\mathcal{P} = GS$, where

$$G = a_\xi^{-1} \exp\left\{+\frac{i}{2}\,\xi^2 \tan z_\xi\, iz_\xi\right\} . \tag{72}$$

All the values at the end of the previous interval (η plane) are indicated with a subscript p. The electric field e is given in the old representation as $e = G_p B_p$, and in the new representation as $e = GB$; where G_p is dependent on $z_{\xi p}$ and G on z_ξ, and B is given by

$$B_p = B \exp[+i(\alpha\xi^2 + \beta\xi^4)] . \tag{73}$$

The best match is obtained by requiring that $\phi(B)$, the phase of B, should vary radially as little as possible.

$$\phi(B) = \phi(B_p) + \phi(G_p) - \phi(G) = (\alpha\xi^2 + \beta\xi^4 + \ldots) + (\tfrac{1}{2}\xi^2 \tan z_{\xi p} - z_{\xi p}) - (\tfrac{1}{2}\xi^2 \tan z_\xi z_\xi) , \tag{74}$$

where α is the curvature.

α and β are determined in a appropriate manner from B_p so that a new variable B has *no* curvature. It is clear that the new value of z_ξ at the present new plane under consideration is derived from the old value by

$$z_\xi = \arctan(2\alpha + \tan z_{\xi p}) , \tag{75}$$

with the new neck radius $a_{0\xi}$

$$a_{0\xi} = a_\xi \cos z_\xi . \tag{76}$$

The equation for B is then:

$$2i\,\partial_z B + \frac{a^2}{a_\xi^2}\,\{\nabla_T^2 B + (2 - \xi^2)B\} = ic_1 a^2 S . \tag{77}$$

By using this final differential equation, the new equation varies *less* in its functional values than does the original.

The instantaneous local parameters α and β of the quadratic wave front are determined by fitting the calculated $\phi(\xi)$ of B_p to a quartic in ξ; a reasonable approach is that the intensity-weighted square of the phase gradient:

$$\int B^2 [\partial_\rho(\alpha\xi^2 + \beta\xi^4 + \psi)]^2\, \xi\, d\xi = \text{minimum} , \tag{78}$$

where ψ is the phase of the field variable $B = A \exp(-i\psi)$ [79]. The minimization of the phase gradient is weighted by the beam intensity. Consequently, the curvature at the highest intensity portion of the beam contributes the most.

The following different moment integrals are introduced

$$M_n = \int \{\xi^{2n} B^2\}\, \xi\, d\xi , \qquad \gamma_n = \int \{B^2 \xi^{(2n-1)} \partial_\xi \psi\}\, \xi\, d\xi , \tag{80}$$

using the relation

$$B^2 \partial_\xi \psi = -\mathrm{Im}\{B^* \partial_\xi B\} , \tag{81}$$

$$\gamma_n = -\mathrm{Im} \int \{B^* \partial_\xi B)\, \xi^{(2n-1)}\}\, \xi\, d\xi , \tag{82}$$

by taking partial derivatives with respect to the α's and β's, one obtains

$$\alpha = -(M_2\gamma_2 - M_3\gamma_1)/E$$

and

$$\beta = (M_1\gamma_2 - M_2\gamma_1)/2E ,$$

where

$$E = 2(M_2^2 - M_1 M_3) . \tag{83}$$

The distinctive advantage of these stretching and adjustable rezoning techniques stems, as suggested by Moretti, from the fact that they automatically define the mapping and all related derivatives analytically.

12. Numerical results

In this section are outlined basic results, obtained with and without rezoning and stretching, and illustrating why the more sophisticated techniques required less computational effort.

The first part of this investigation which dealt with absorbing material led to the discovery of new physical phenomena which promise to have significant applications for proposed optical communications systems. It had been shown that spontaneous focusing can occur in the absence of lenses, and that the focusing can be controlled by varying the medium parameters. The second part of this analysis dealt with amplifiers.

The dependence of the propagation characteristic on the Fresnel number F^{-1} associated with an effective atomic length, on the on-axis input pulse "area", on the relaxation times and on the off-line centre frequency shift have been studied. Furthermore, particular care was exercised to ensure a perfectly smooth Gaussian beam [23,54–59] thereby eliminating any possibility of small scale self-focusing build-up [60–63].

The effect of coherent self-focusing is illustrated in fig. 12. The time integrated pulse 'energy' per unit area is plotted for various values of the transverse coordinate, as a function of the propagation distance. Two orientations are shown to display the energy redistribution as the laser beam is transmitted in the nonlinear resonant absorber. The necessity of a non-uniform mesh is quite evident.

The three-dimensional numerical calculations [23, 56–59] substantiate the physical picture based on time changes in the phase. It can be perceptually visualized in selected frames from a computer movie simulation of the numerical model output data.

In fig. 13 the isometric plots are drawn against the retarded time for various transverse coordinates at four specific regions of the propagation process: (a) the reshaping region where the perturbation treatment holds; (b) the build-up region; (c) the focal region; and (d) the post-focal region. While in fig. 14 a rotation of isometric plots is displayed to emphasize the radially dependent delay resulting from the coherent interaction. Positive values of the transverse energy current correspond to outward flow and nega-

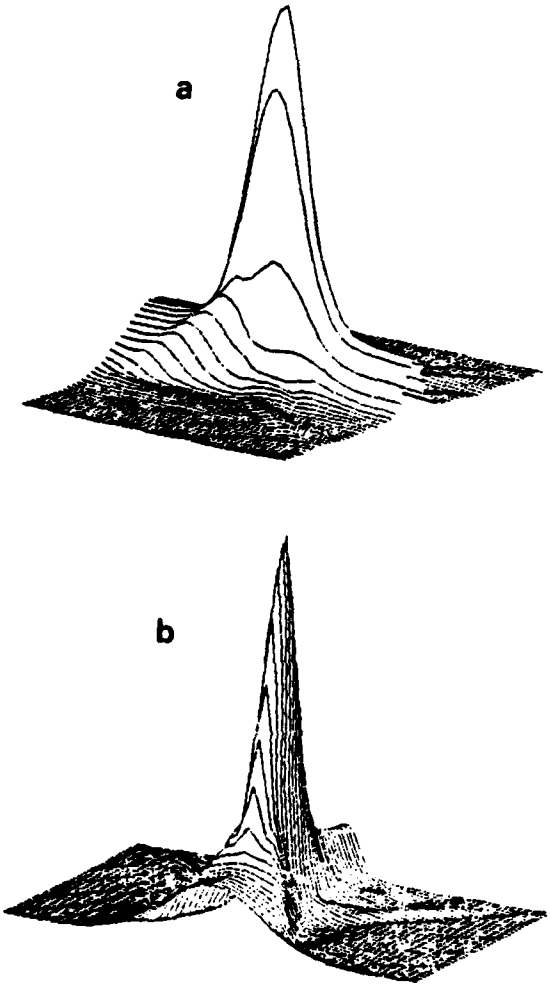

Fig. 12. The energy per unit area $\{\int_0^1 |e(\rho, \eta, \tau')|^2 d\tau\}$ the fluency is displayed as a function of the distance in the direction of propagation for various values of the coordinates transverse to the direction of propagation. To illustrate the gradual inward energy flow the $\pi/2$ reorientation is also displayed. The longitudinal orientation illustrates the gradual boosting mechanism that the field energy experiences as it flows radially towards the beam axis (while η increases). The second angle displays the severe beam distortion in its cross-section as a function of η.

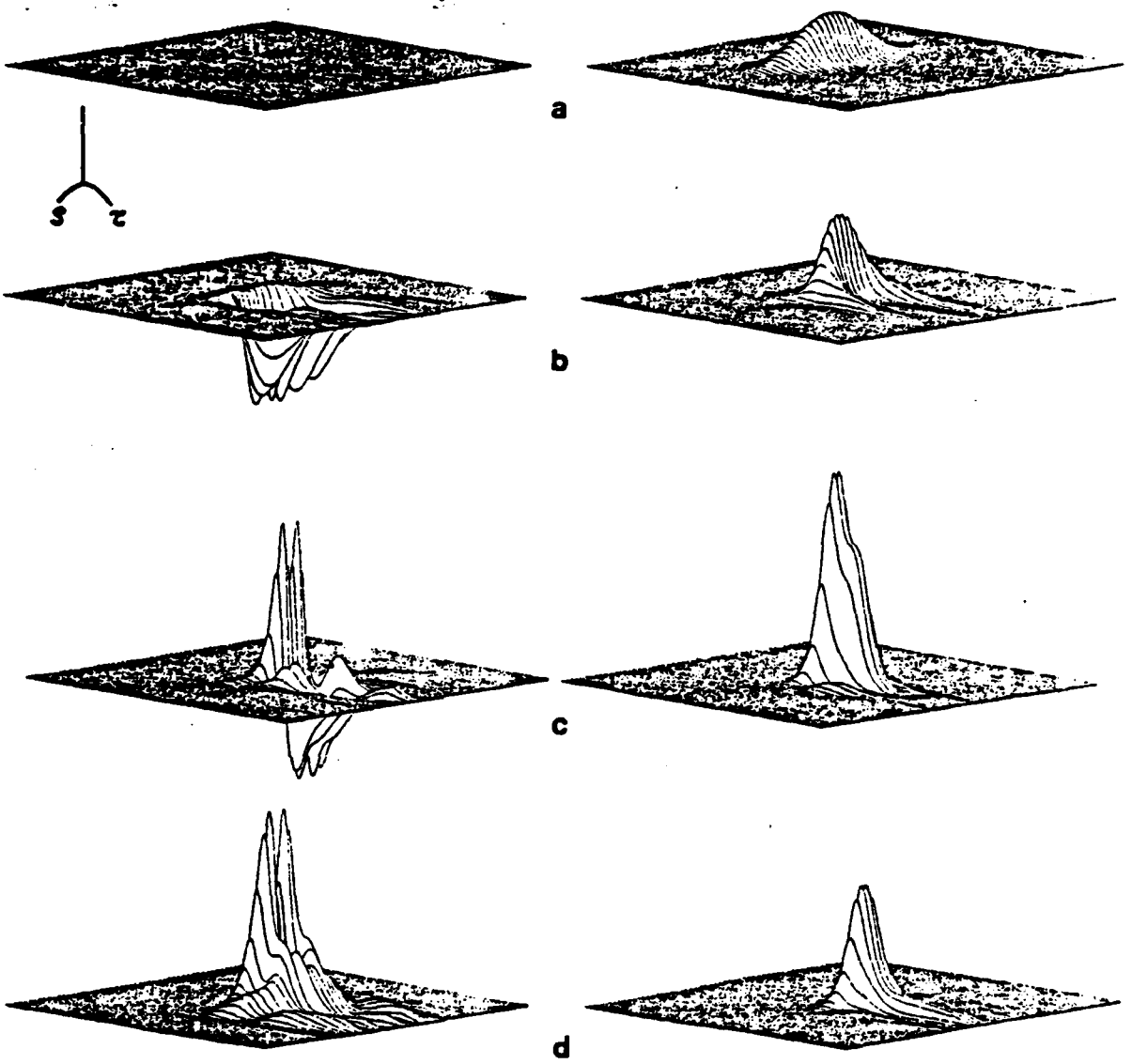

Fig. 13. Isometric plots of the absorber field energy and transverse energy flow, against the retarded time for various transverse coordinates at four regions: (a) reshaping, (b) build-up region, (c) focal region, (d) post-focal region.

tive values to inward flow. The results of the top two graphs in the right and left columns are also in agreement with the physical picture related to the analytic perturbation discussed elsewhere [23,65].

The burn pattern, iso-irradiance level contours (against τ and ρ) for different propagation distances are shown in fig. 15. Severe changes in the beam cross-section are taking place as a function of the propagating distance. At the launching front, the beam is smooth and symmetric; as the beam propagates into the nonlinear resonant medium the effect of the nonlinear inertia takes place.

The general format for presenting three-dimensional coherent pulse propagation in an amplifying

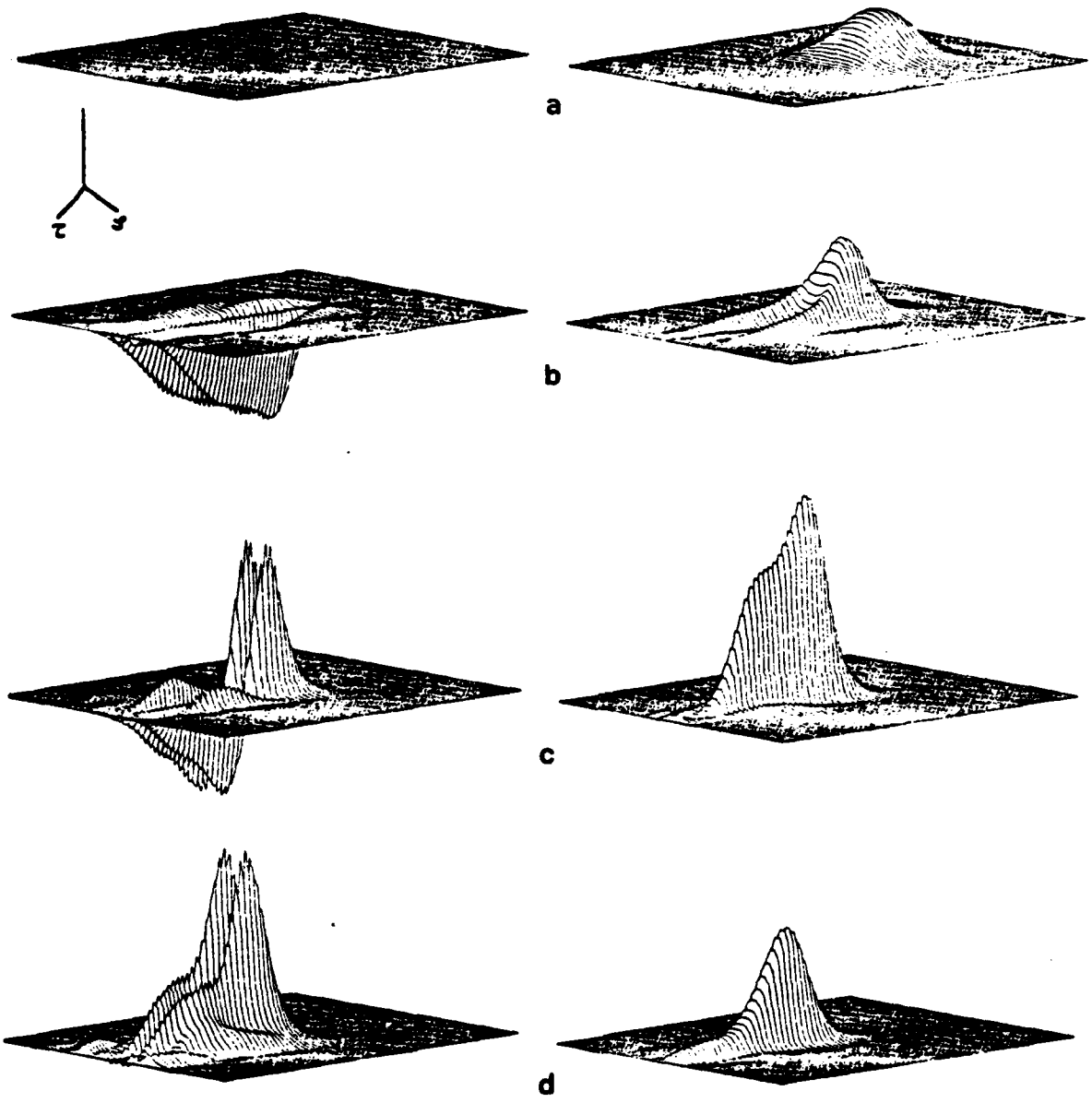

Fig. 14. Isometric plots of the absorber field energy and transverse energy flow profile for various time slices at the four regions of interest.

medium will be the same as for the absorber.

In the right hand side of fig. 16 the field energy is displayed isometrically against the retarded time for various radii at the previously defined five critical regions of propagation and are constrasted with their profile plotted in the left hand side of fig. 16 for various instants of time. In fig. 17, one can see from the contour energy levels that the peak of the pulse is

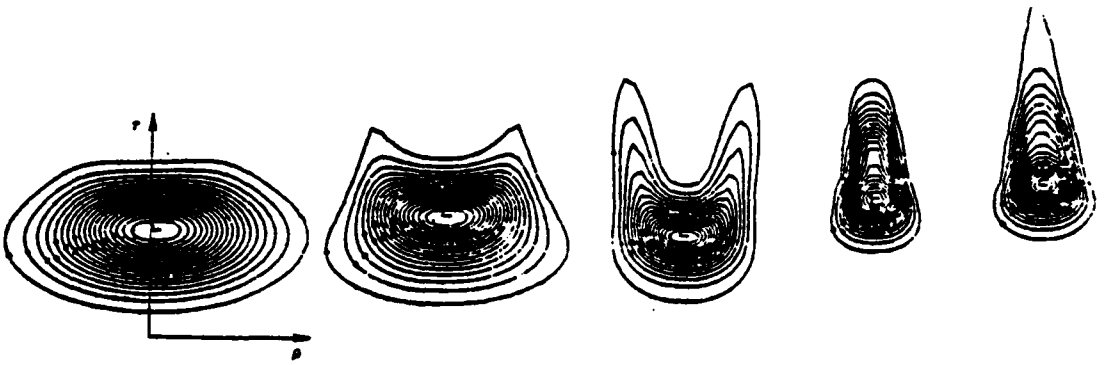

Fig. 15. Absorber field energy contour plots for the four propagation regions of interest. Notice the temporal delay associated with the coherent exchange of energy between light and matter, as well as the beam cross-section narrowing.

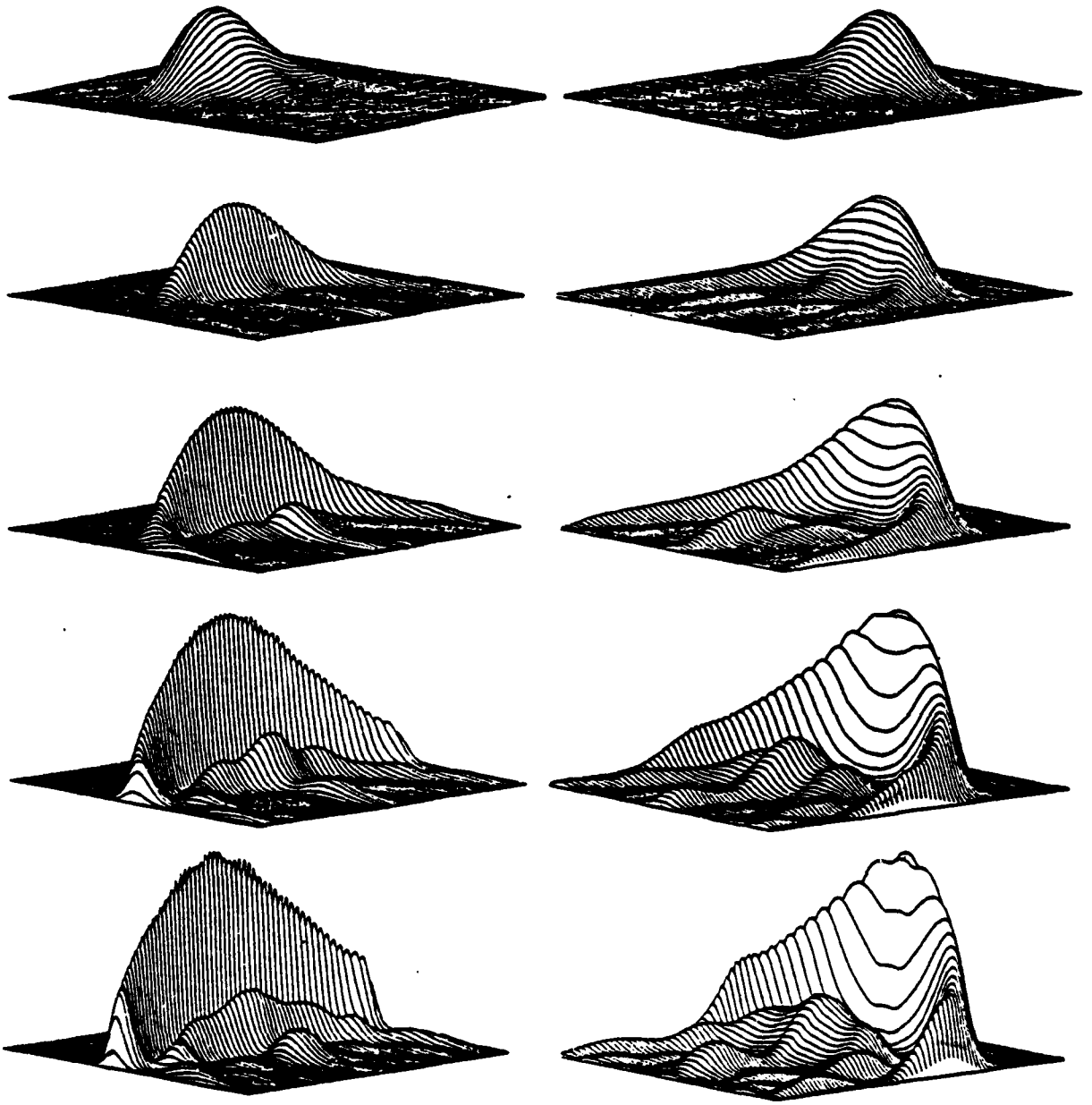

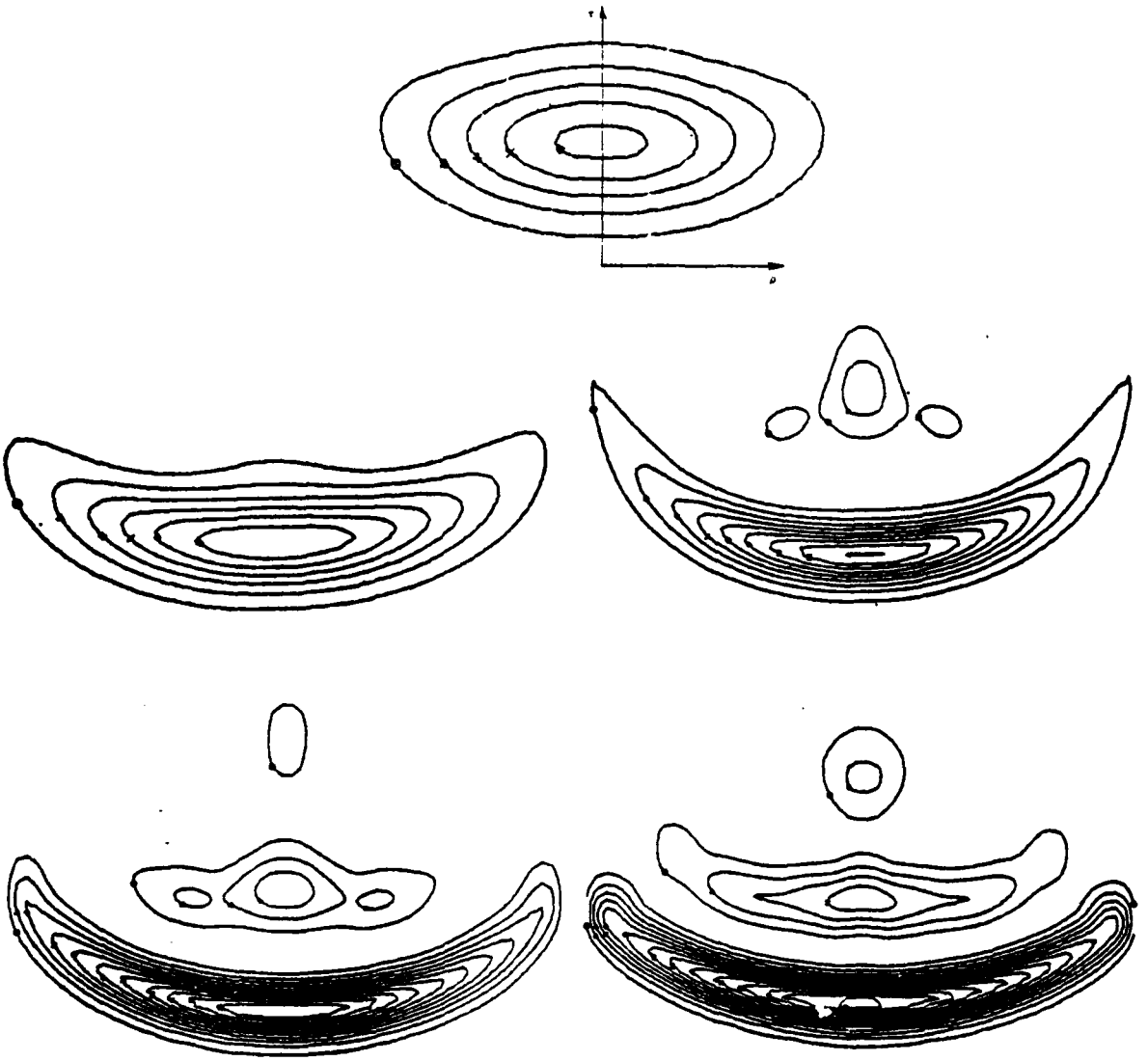

Fig. 17. Amplifier field energy contour plots for the four propagation regions of interest. Notice the temporal advance associated with the coherent exchange of energy between light and matter, as well as the beam cross-section narrowing.

advanced with respect to a frame moving with the velocity of light. It is seen that the smaller area propagates slower than the larger areas.

The effect of the radial boundary is illustrated in figs. 18 to 20. Nonuniform radial stretching was adopted during the computation. Isometrics of the field energy and the energy current are plotted versus τ for different radii in fig. 18 and versus ρ for

Fig. 16. Isometric plots of the amplifier field energy versus the retarded time for various transverse coordinates contrasted to its profile for various time at distinct propagational region.

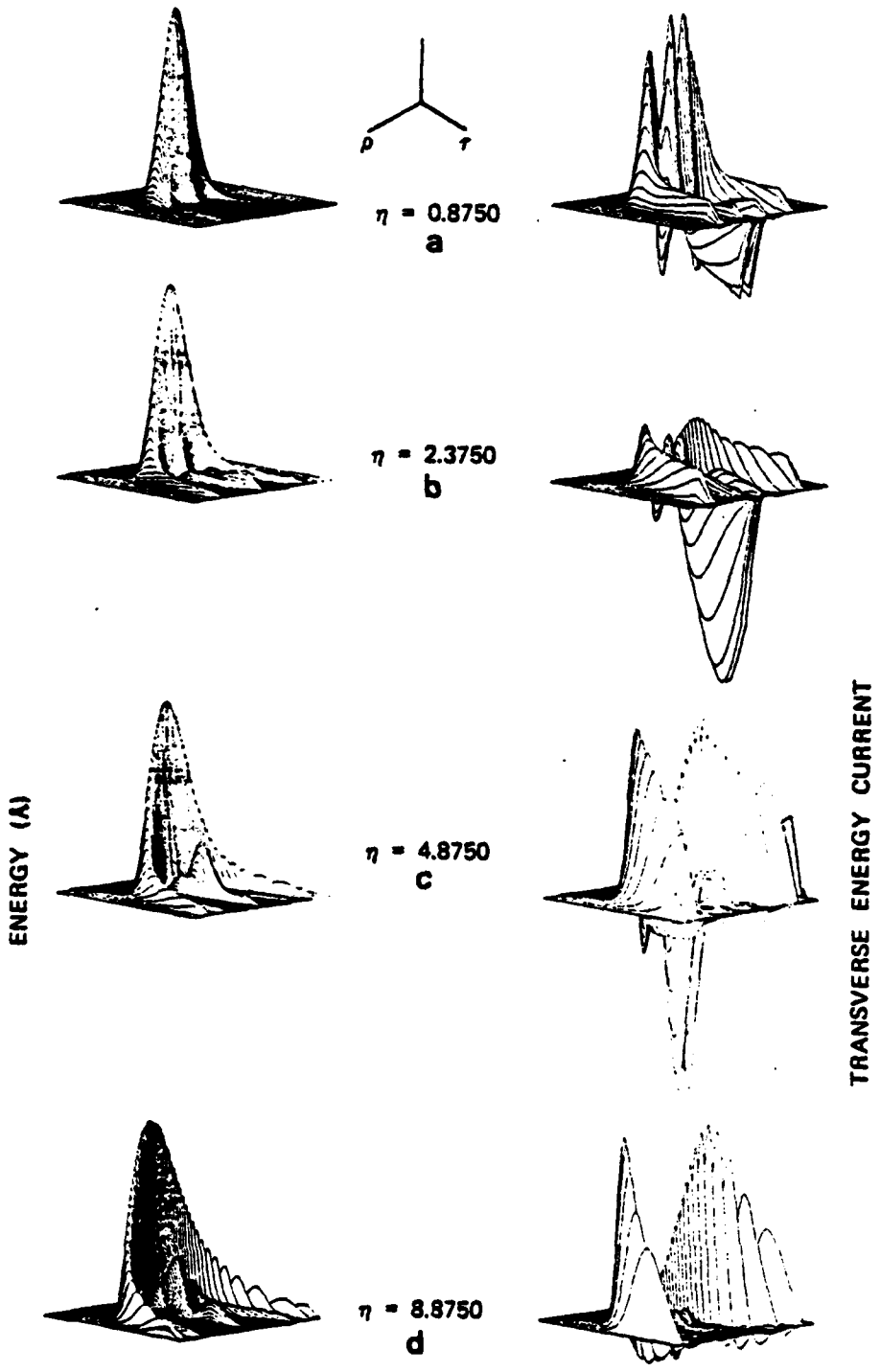

Fig. 18. Isometric plots of the amplifier field energy and transverse energy flow, against the retarded time for various transverse coordinates at four regions: (a) reshaping, (b) build-up region, (c) focal region, (d) post-focal region, with stretched radial coordinate for proper accounting of the transverse boundary condition.

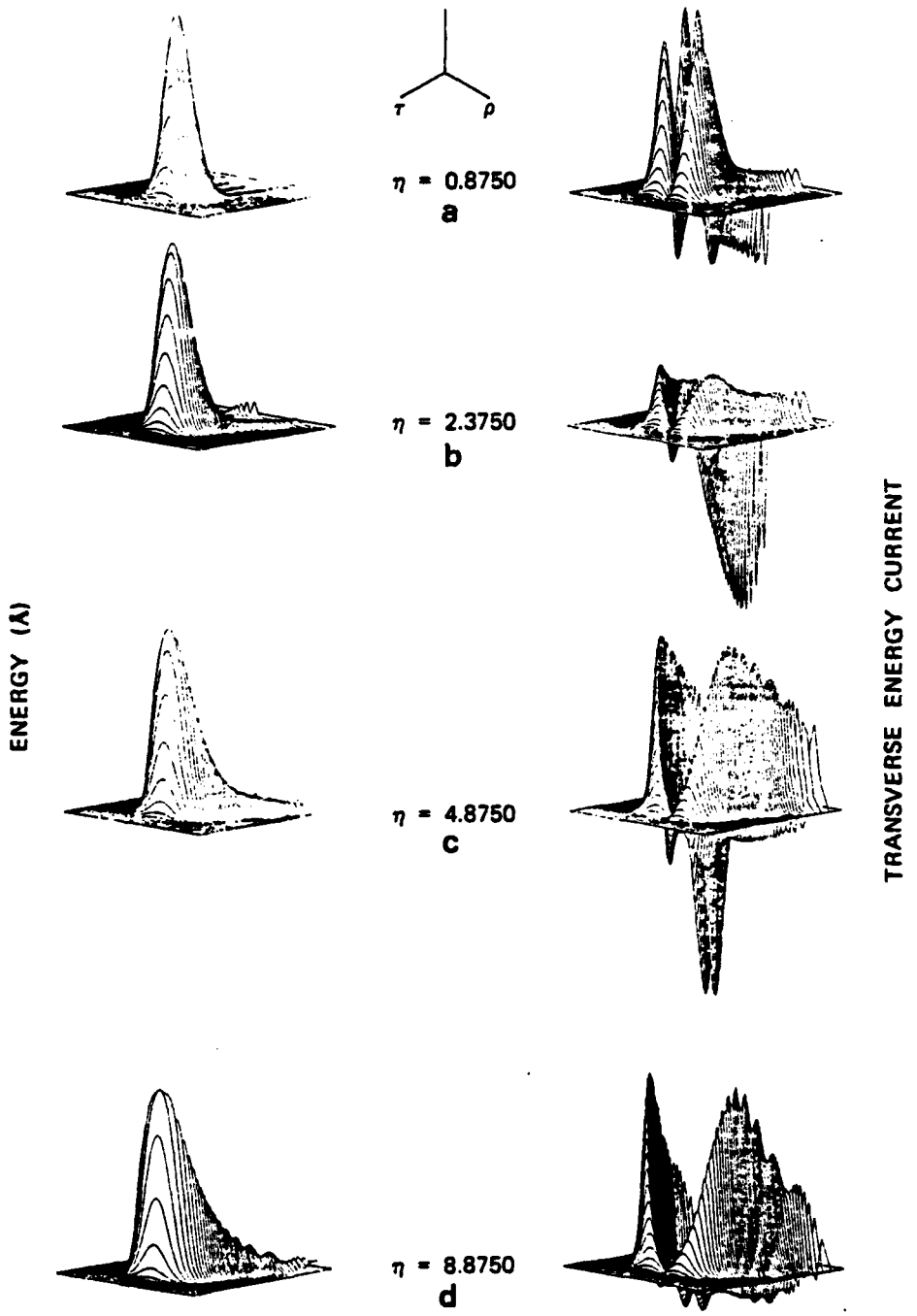

Fig. 19. Isometric plots of the amplifier field energy and transverse energy flow profile for various time slices at the four regions of interest, with stretched radial coordinate for proper accounting of the transverse boundary condition. No severe reflection or abrupt variation in the field energy, at the wall boundary, is observed.

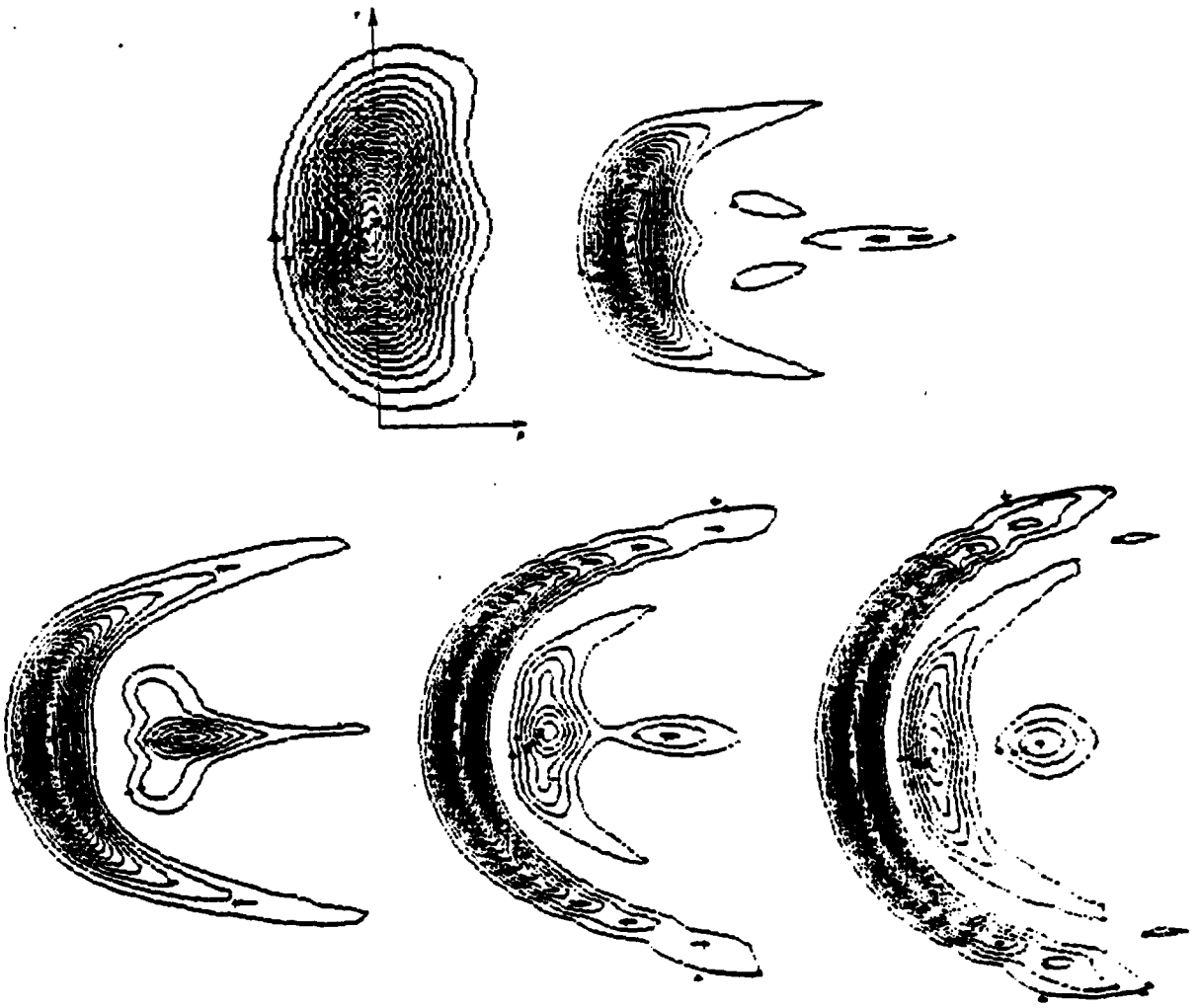

Fig. 20. Amplifier field energy contour plots for the four propagation regions of interest. Notice the temporal advance associated with the coherent exchange of energy between light and matter, as well as the beam cross-section narrowing, with stretched radial coordinate for proper accounting of the transverse boundary condition. No severe reflection or abrupt variation in the field energy, at the wall boundary, is observed.

various instants of time in fig. 19. From the energy current graphs, one discovers out that a focusing phase is *not* an exclusive property of a resonant absorber.

Fig. 20 displays the contour energy levels where the enhancement of diffraction by the pre-excited two-level atomic medium is clearly evident.

13. Concluding remarks

Most features of the numerical model used to study temporal and transverse reshaping effects of short optical pulses propagating in active nonlinear resonant media have been presented. The experiment strives to achieve a rigorous analysis of this nonlinear

interaction with maximum accuracy and minimum computational effort. The applicability of computational methods developed in gas and fluid dynamics to the detailed evolution of optical beams in nonlinear media has been demonstrated. By introducing adaptive stretching and rezoning transformations, the calculations improved considerably.

In particular, self-adjusted rezoning and stretching techniques consisting of repeated applications of the same basic formula were reviewed as a convenient device for generating computational grids for complex nonlinear interactions. The techniques are well-suited for easy programming because the mapping functions and all related derivatives are defined analytically as much as possible. Enhancement of speed and accuracy was realized by improving the integration technique/algorithm which turned out to be general and simple in its application compared with its analogue, the two-dimensional Lagrangian approach. Furthermore, this method has been applied to a number of situations with and without homogeneity in the resonant properties of the atomic medium. Note that the theoretical predictions defined with this code, when applied to absorbing media, were quantitatively ascertained [56,59] by independent experimental observations in sodium, neon and iodine, respectively [53,55,67], and recent independent perturbational [60,61,63] and computational analysis [62]. The design of the first of these experiments dealing with sodium vapor, was based on qualitative ideas, quantitative analysis and numerical results obtained with the code described in this paper.

Although the topic of this paper has been most widely received in optical radiation physics, we believe that this methodology, drawn from aerodynamics, will prove functional for a wide variety of nonlinear time-dependent equations in such fields as chemical kinetics and oil reservoir simulations.

14. Summary

The mathematical modeling of the coherent transmission of ultra-short optical pulses in a two-level, atomic gaseous medium, which can sustain amplification and/or absorption is presented. The main purpose was to understand how inertial nonlinearity affects the propagation of intense ultra-short light beams. Previously, this effect had been intractable.

The results of this analysis served as a guide to real-life, coherent light–matter interaction experiments. The equations with radial and phase variations included, are implemented using a two-dimensional, time-dependent, finite-difference computer code with two population densities, an inertial-medium polarization density and adaptive propagation capabilities. The importance of dynamic transverse effects, namely, diffraction coupling and a reflecting radial boundary, in the evolution of both initial ground-state and inverted media with different Fresnel numbers, has also been assessed.

Calculations using an Eulerian code predicted and elucidated an on-resonance, transient, whole-beam, self-lensing phenomenon in absorbers. This effect was subsequently ascertained by experimental observations in sodium and neon. Conversely, calculations concerning amplifiers depicted longitudinal pulse break-up, which degraded beam quality, as substantiated in high-power laser experiments. Significant phase modulation and transverse spreading may explain the mechanism that limits the useful output of long amplifiers. Parametric computations illustrated that these self-action phenomena can be controlled by tuning the various system parameters.

Accuracy and computational economy are achieved simultaneously by dynamically redistributing the computational Eulerian grid points according to the physical requirements of the nonlinear interaction. Evenly-spaced computational grids are related to variable grids in a physical space by a range of stretching and rezoning techniques. This mapping consists of either an a priori coordinate transformation or an adaptive transformation based on the actual physical solution. Both stretching in time and rezoning in space alleviate the computational effort. The propagation problem is then reformulated in terms of coordinates that will automatically accommodate any change in the beam profile. This attempt permits the construction of a computer code capable of being physically meaningful at every mode point.

The dynamic grid obtained through self-adjusted mapping techniques removes the main disadvantage of insufficient resolution from which Eulerian codes generally suffer. Furthermore, the advantages of grid sensitivity are obtained while circumventing the traditional impediments associated with the Lagrangian methods.

Acknowledgements

F.P. Mattar would like particularly to express his appreciation to his thesis adviser Professor M.C. Newstein and to his mentors Professor H.A. Haus and Professor Gino Moretti for their unselfish guidance in the physics and numerics of the work. He has benefited from enlightening discussions with Dr. H.M. Gibbs, Dr. S.L. McCall, Professor J.H. Marburger, Dr. D.C. Brown and Professor P.E. Toschek on the physics and Dr. J. Hermann, Dr. B.R. Suydam and Dr. J. Fleck on the numerics. He is indebted to H.M. Gibbs for his faith in the work that led to the first experimental verification of the coherent on-resonance self-focusing. The hospitality of Professor J. Teichman at University of Montreal and Dr. T.C. Cattrall at Mobil which made the computations possible, is gratefully acknowledged. F.P. Mattar wishes to thank Dr. C. Hazzi and D.J. Steele for their extended patience, unselfish support and continuous encouragements during his convalescence. Furthermore, the editing efforts of D.J. Steele; the art work of Kerop Studio in Cairo, of P. Florence and D.J. Steele in New York; and the skillful and laborious word processing effort of E. Cummings are appreciated.

References

[1] S.A. Akhamanov, A.-P. Sukhorukov and P.V. Kokhlov, Laser handbook, ed. F. Arrechi (North-Holland, Amsterdam, 1972) p. 1151.
[2] G. Askary'yan, Sov. Phys. JET P42 (1962) 1568; Usp. Fiz. Naul. 111 (1973) 249.
[3] B.R. Suydam, Los Alamos Scientific Lab., Tech. Rep. L4-5003-MS (March 1973) p. 1.
[4] O. Svelto, Progress in optics XII, ed. E. Wolf (North-Holland, Amsterdam, 1974) p. 1.
[5] J. Marburger, Progress in quantum electron, vol. 4 (Pergamon Press, London, New York, 1975) p. 35.
[6] S.L. McCall and E.L. Hahn, Bull. Am. Phys. Soc. 10 (1965) 1189; Phys. Rev. Lett. 18 (1967) 908; Phys. Rev. 183 (1969) 457; Phys. Rev. A2 (1970) 870.
[7] H.M. Gibb and R.E. Slusher, Appl. Phys. Lett. 18 (1971) 505; Phys. Rev. A5 (1972) 1634; Phys. Rev. A6 (1972) 2326.
[8] F.A. Hopf and M.O. Scully, Phys. Rev. 179 (1969) 399.
[9] A. Icsevgi a d W.E. Lamb, Jr., Phys. Rev. 185 (1969) 517.
[10] E. Courtens, In: Proc. Chania Conf. (1969) unpublished, and in: Laser handbook, ed. F. Arrechi (North-Holland, Amsterdam, 1972).
[11] G. Lamb, Rev. Mod. Phys. 43 (1971) 99.
[12] R.E. Slusher, Progress in optics XII, ed. E. Wolf (North-Holland, Amsterdam, 1974) p. 53.
[13] L.A. Poluektov, Yu.M. Popov and V.S. Roitoeig, Sov. Phys. Usp. 17 (1975) 673.
[14] P. Kryuokow and V. Letokov. Sov. Phys. Ups. 12 (1970) 641.
[15] A. Zembrod and T. Gruhl, Phys. Rev. Lett. 27 (1971) 287.
[16] (a) C.K. Rhodes and A. Szöke, Phys. Rev. 184 (1969) 25.
(b) C.K. Rhodes, A. Szöke and A. Javan, Phys. Rev. Lett. 21 (1968) 1151.
(c) F.A. Hopf, C.K. Rhodes and A. Szöke, Phys. Rev. B1 (1970) 2833.
[17] D. Grischkowsky, Phys. Rev. Lett. 24 (1970) 866. D. Grischowsky and J. Armstrong, in: Proc. 3rd Conf. on Quantum optics, Univ. of Rochester (1972) p. 829.
[18] A. Javan and P.L. Kelley, IEEE J. Quantum Electron. QE-2 (1966) 470.
[19] H.A. Haus and T.K. Gustafson, IEEE J. Quantum Electron. QE-4 (1968) 519.
[20] J.C. Diels and E.L. Hahn, Phys. Rev. A8 (1973) 1084, A10 (1974) 2501.
[21] N.D. Wright, Pulse propagation in nonlinear resonant media, Ph.D. Dissertation, Polytechnic Institute of New York (February 1974).
[22] N. Wright and M.C. Newstein, (a) Opt. Commun. 9 (1973) 8; (b) IEEE J. Quantum Electron. QE-10 (1974) 743.
[23] M.C. Newstein and F.P. Mattar, Proc. 7th Conf. on Numerical simulation of plasmas, Courant Institute, New York Univ. (June 1975) p. 223; 10th Congress of the International Commission of Optics, Prague, Czechkoslovakia (1975); Recent advances in optical physics, B. Havelka and J. Blabla, distributed by the Soc. of Czechkoslovak Math. and Phys. (1976) p. 199; 10th Intern. Conf. of Quantum Electronics, Amsterdam (1976), see Opt. Commun. 18 (1976) 70 and IEEE J. Quantum Electron. QE-13 (1977) 507; Cooperative effects in matter and radiation, eds. C.M. Bowden, D.W. Howgate and H.R. Robl (Plenum Press, New York, 1977) p. 139; Proc. of the Cooperative effects Session of the US Army Symp. of New concepts in high energy lasers, Invited paper, Huntsville, Alabama (December 1976).
[24] R.W. MacCormack, AIAA Hypervelocity impact Conf. (1969) paper 69–354; Lecture notes in physics (Springer Verlag, Berlin, 1971) p. 151.
[25] G. Moretti, Proc. 1974 Heat Transfer and Fluid Mechanics Institute, (Stanford University Press, Stanford, 1974); POLY-AE/AM Report No. 74-9; POLY-AE/AM Report No. 74-23 (December 1974); PIBAL Report No. 73-18 (August, 1973); PIBAL Report No. 69-26 (July 1969); PIBAL Report No. 70-48 (November 1970); PIBAL Report No. 71-25 (September 1971); POLY-AE/AM Report No. 74-15 (September 1974); Proc. Symp. Transsonicum II, Göttingen, Fed. Rep. Germany,

8–13 Sept. 1975 (Springer-Verlag, Berlin, 1976) p. 439; (POLYAE/AM Report No. 76-06).
[26] G. Moretti, Proc. IBM Scientific Computing Symp. on Large scale problems in physics, IBM Research Center, Yorktown Heights, New York (December 1963).
[27] G. Moretti, PIBAL Report No. 68-15 (1968); POLY-AE/AM Report No. 74-15 (September 1974).
[28] G. Moretti, PIBAL Report No. 69-25 (July 1969); PIBAL Report No. 69-26 (July 1969).
[29] G. Moretti, Proc. ASME Symp. on Numerical/laboratory computer methods in fluid mechanics, published by ASME (December 1976); POLY M/AE Report No. 76-06 (1976).
[30] H. Kogelnik and T. Li, Appl. Opt. 5 (1969) 1550.
[31] H. Kogelnik, Appl. Opt. 4 (1965) 1562.
P.K. Tien, J.P. Gordon and J.R. Whinnery, Proc. IEEE 53 (1965) 129.
A. Yariv. Quantum Electronics (Interscience, New York, 1975).
[32] W. Lamb, Jr., Phys. Rev. 134A (1964) 1429.
[33] L. Bradley and J. Hermann, MIT-Lincoln Lab. Tech. report LTP-10 (July 1971) and Internal note on Change of reference wavefront in the MIT CW Nonlinear Optics Propagation Code (Fall 1974) private communication to F.P. Mattar for which he is grateful.
[34] P.B. Ulrich, NRL Report 7706 (May 1974).
[35] H.J. Breaux, Ballistic Research Laboratories, Aberdeen Proving Ground, Maryland; BRL Report 1723 (1974).
[36] J.A. Fleck, Jr., J.R. Morris and M.D. Feit, Lawrence Livermore Laboratory, Livermore, CA, Part I: LLL Report UCRL-51372 (1975); Preprint of Technical Report, Lawrence Livermore Laboratory, University of California, UCRL-52071 (May 1976).
[37] F.P. Mattar, Appl. Phys. 17 (1978) 53.
[38] R.H. Dicke, Phys. Rev. 93 (1954) 99; in: Quantum Electronics: Proc. 3rd Intern. Congr., Paris, eds. P. Grivet and N. Bloembergen (Dunod, Paris and Columbia Univ. Press, New York, 1965).
[39] N.E. Rehler and J.H. Eberly, Phys. Rev. A3 (1971) 1735.
[40] J.H. Eberly, Am. J. Phys. 40 (1972) 1374.
For a pedagogical review on superfluorescence/superradiance, see L. Allen and J.H. Eberly, Optical resonance and two-level atoms (Wiley, New York, 1975).
[41] Q.H.F. Vrehen, H.M.J. Hikspoors and H.M. Gibbs, Phys. Rev. Lett. 38 (1977) 764, 39 (1977) 547; Laser Spectroscopy III, eds. J.L. Hall and J.L. Carlsten (Springer-Verlag, Berlin, 1977).
[42] M.S. Feld, in: Fundamental and Applied Laser Physics: Proc. Esfahan Symp., eds. M.S. Feld, N.A. Kurnit and A. Javan (Wiley, New York, 1973).
[43] J.C. MacGillivray and M.S. Feld, Phys. Rev. A14 (1976) 1169.
[44] A. Szöke, V. Daneau, J. Goldhar and N.A. Kurnit, Appl. Phys. Lett. 15 (1969) 376.
[45] S.L. McCall, Phys. Rev. A9 (1974) 1515.
[46] S.L. McCall, H.M. Gibbs, G.G. Churchill and T.N.C. Venkatesan, Bull. Am. Phys. Soc. 20 (1975) 636; J. Opt. Soc. Am. 65 (1975) 1184; Phys. Rev. Lett. 36 (1976) 1135.
[47] F.S. Felber and J.H. Marburger, Appl. Phys. Lett. 28 (1976) 731.
[48] R. Brewer and E.L. Hahn, Phys. Rev. A11 (1975) 1641.
[49] M. Sargent III and P. Horwitz, Phys. Rev. A13 (1976) 1962.
[50] J.T. Ackerhalt, J.H. Eberly and B.W. Shore, Phys. Rev. A19 (1977) 248.
[51] F.P. Mattar and J.H. Eberly, Proc. Physics and chemistry of laser-induced process in molecules, Edinburgh, 1978 eds. K.L. Kompa and S.C. Smith (Springer-Verlag, Berlin, 1979) p. 61.
[52] M. Konopnicki and J.H. Eberly, 10th Pittsburg Annual Simulation and Modeling Conf., Pittsburg (1979).
[53] H.M. Gibbs, B. Bolger and L. Baade, 9th Intern. Conf. of Quantum Electronics (1976), see: Opt. Commun. 18 (1976) 199.
[54] G. Forster and P.E. Toschek, post-deadline paper of the Quantum Optics Session of the Spring Annual Meeting of the German Physical Society, Hanover, Fed. Rep. Germany (February 1976).
[55] W. Krieger, G. Gaida and P.E. Toschek, Z. Phys. B25 (1976) 297.
[56] H.M. Gibbs, B. Bolger, F.P. Mattar, M.C. Newstein, G. Forster and P.E. Toschek, Phys. Rev. Lett. 37 (1976) 1743 (prepared by H.M. Gibbs).
[57] F.P. Mattar, G. Forster and P.E. Toschek, Spring meeting of the German Physical Society, Mainz, Fed. Rep. Germany (February 1977) (prepared by P.E. Toschek); Kvantovaya Electronika (Moscow) 5 (1978) 1818 (prepared by P.E. Toschek).
[58] F.P. Mattar, M.C. Newstein, P. Serafim, H.M. Gibbs, B. Bolger, G. Forster and P. Toschek, 4th Rochester Conf. of Coherence and quantum optics, Rochester, New York (June 1977) eds. R. Mandel and E. Wolf (Plenum Press, New York, 1978) p. 143 (prepared by H.M. Gibbs).
[59] F.P. Mattar, Kvantovaya Electronika (Moscow) 4 (1977) 2520.
[60] L.A. Bol'shov, V.V. Likhanskii and A.O. Napartovich, Zh. Eksp. Teor. Fiz. 72 (1977) 1769.
[61] M.J. Ablowitz and Y. Kodama, Phys. Lett., Clarkson College preprint, Fall 1978, to be published.
[62] L.A. Bol'shov, T.K. Kirichenko and A.P. Favolsky, USSR Academy of Sciences – Mathematics Division, preprint, Fall 1978, Institute of Applied Mathematics 3A (1978) p. 53, in Russian.
[63] L.A. Bol'shov and V.V. Likhansky, Zh. Eksp. Teor. Fiz. 75 (1978) 2047, in Russian (US translation: Sov. Phys. J. Exp. Theoret. Phys. 48 (1979) 1030.
[64] F.P. Mattar, Ω10 Technical Note 63, Lab. for Laser Energetics, Univ. of Rochester, Rochester, NY (March 1976).
[65] F.P. Mattar, Ph.D. Dissertation, Polytechnic Institute of New York, NY (December 1975) available from Ann Arbor, Michigan.
[66] F.P. Mattar and H.M. Gibbs, Aerodynamics Labs. – Technical Report, Polytechnic Institute of New York (April 1980).
[67] J.J. Bannister, H.J. Baker, T.A. King and W.G. McNaught, Phys. Rev. Lett. 44 (1980) 1062.

Transverse Effects in Superfluorescence

F. P. Mattar
Aerodynamics Laboratory, Polytechnic Institute of New York, Brooklyn, New York 11201, and Spectroscopy Laboratory, Massachusetts Institute of Technology, Cambridge, Massachusetts 02139

and

H. M. Gibbs[a] and S. L. McCall
Bell Laboratories, Murray Hill, New Jersey 07974

and

M. S. Feld
Spectroscopy Laboratory and Physics Department, Massachusetts Institute of Technology, Cambridge, Massachusetts 02139
(Received 14 November 1980)

Dynamic diffraction coupling is examined in superfluorescence with use of a semiclassical model in which diffraction and transverse density variations are rigorously included. The Cs data are correctly simulated for the first time.

PACS numbers: 42.65.Gv, 32.50.+d

Superfluorescence[1] (SF) is the process by which coherent emission occurs from an ensemble of two-level atoms all intially in the upper state. An important question in SF experiments is why the output pulse is sometimes smooth, but at other times exhibits multiple structure or ringing. Strong ringing or pulsing has been observed by several groups, including the initial HF-gas studies.[2] Recent Cs experiments,[3] however, never show ringing at low densities, whereas at higher densities, highly fluctuating multiple pulsing is usually observed, and is believed to arise from transverse-mode competition. Strong Burnham-Chiao ringing[4] is predicted by plane-wave models,[5] which neglect variations transverse to the propagation direction. We find that inclusion of transverse effects, both *spatial averaging* and Laplacian *diffraction*, substantially alters the one-dimensional Cs predictions,[3b] leading to greater conformity with the Cs data.

The initial SF state is prepared by rapidly inverting a sample of three-level atoms by transferring population from the ground state to the upper state with a short light pulse, creating a cylindrical region of excited atoms.[2] SF pulse emission subsequently occurs between this excited state and the intermediate state. There is no optical cavity and stray feedback is negligible.

This study employs the semiclassical approach to explore the influence of transverse effects, using the average value[6] of the initial tipping angle.[4,5a] Both longitudinal fluctuations[6] and transverse flucutations, as influenced by diffraction, will be discussed elsewhere.

Transverse effects are expected to influence the pulse shapes in at least two ways, one of which is *spatial averaging*. In SF experiments the initial inversion density $n_0(r)$ is radially dependent since the pump light pulse typically has a Gaussian-like profile.[7] In the absence of diffraction this cylinder can be thought of as a set of concentric cylindrical shells, each with its own density, tipping angle, and delay time.[8] The radiation will be a sum of plane-wave intensities; when the entire output signal is viewed the ringing averages out, resulting in an asymmetric pulse with a long tail.[9]

A second transverse effect, *diffraction*, causes light emitted by one shell to affect the emission from adjacent shells. This coupling mechanism, which causes transverse energy flow, is more important for samples with small Fresnel numbers F.

SF is inherently a transverse-effect problem even for large-F samples since the off-axis modes are not discriminated against. This work is the first to correctly include this crucial element.

Our analysis adopts the coupled Maxwell-Schrödinger equations, which fully take into account propagation and transverse effects. Previous approaches examined transverse effects in the mean-field approximation[10] or included a loss term in the Maxwell equation to describe diffraction.[2,5] Thus our model possesses a long sought for degree of realism.[11]

The simulations are based upon an extension of a model[12] which describes transverse effects observed in self-induced transparency experiments.[13] For simplicity the influence of the backward wave, which is negligible,[14] is not considered, and cylindrical symmetry is assumed. The equations of motion are[12]

$$\partial\xi/\partial z - i(4FL)^{-1}\nabla_T^2\xi = (4\pi^2/\lambda)\mathcal{P}, \quad (1a)$$

$$\partial\mathcal{P}/\partial\tau + \mathcal{P}/T_2 = (\mu^2/\hbar)n\xi, \quad (1b)$$

$$\partial n/\partial\tau + n/T_1 = -\mathrm{Re}(\mathcal{P}\xi^*/\hbar), \quad (1c)$$

where ξ and $\mathcal{P}$ are the slowly varying complex amplitudes of the electric field and polarization, respectively, n is the inversion density, $\tau = t - z/c$ is the retarded time, μ is the transition dipole moment matrix element, and T_1 and T_2 are the population relaxation and polarization dephasing times. Diffraction is taken into account by the Laplacian term $\nabla_T^2\xi = (1/\rho)(\partial/\partial\rho)\rho\,\partial\xi/\partial\rho$, where $\rho = r/r_\rho$, with Fresnel number $F = \pi r_\rho^2/\lambda L$. r_ρ is the radius of the initial inversion density at half maximum, and L is the sample length. The boundary conditions are $\partial\xi/\partial r = 0$ on the axis ($r = 0$) and at $r = \infty$. To insure that (1) the entire field is accurately simulated, (2) no artificial reflections are introduced at the numerical boundary $r_m \gg r_\rho$, and (3) fine diffraction variations near the axis are resolved, the sample cross section is divided into nonuniform cells, and is surrounded by an absorbing shell.

Equations (1) are numerically integrated subject to the initial conditions $n = n_0\cos\theta_0$ and $\mathcal{P} = \mu n_0 \sin\theta_0$, which correspond to an initial tipping angle θ_0. The initial inversion density in the experiment is radially dependent; r dependence of n_0 and/or θ_0 is allowed for in the computations.

Figure 1(a) displays results where spatial averaging is present but diffraction is absent, by setting $F = \infty$ in Eq. (1a). In this figure the emitted power of SF pulses is plotted for samples with uniform and Gaussian profiles of $n_0(r)$ and $\theta_0(r)$. First, we study ringing reduction due to spatial averaging of independent concentric shells, each emitting in a plane-wave fashion. The case in which θ_0 and n_0 are both constant (curve i), the uniform plane-wave limit, exhibits strong ringing.[4,5] In curve ii, in which n_0 is Gaussian $\{n_0(r) = n_0^0 \exp[-\ln 2(r/r_\rho)^2]\}$ and θ_0 is uniform, the ringing is largely averaged out, resulting in an asymmetric pulse with a tail. An essentially identical result (curve iii) is obtained for the case in which n_0 and θ_0 are both Gaussian $\{\theta_0 = \theta_0^0 \times \exp[0.5\ln 2(r/r_\rho)^2]\}$, showing that the ringing is predominantly removed by a Gaussian n_0 regardless of the radial dependence of θ_0. This is expected, since the output-pulse parameters are all dependent only on $|\ln\theta_0|$.[5] As shown in Fig. 1(b), with uniform n_0 and θ_0 but with diffraction included, the output pulse is almost symmetrical

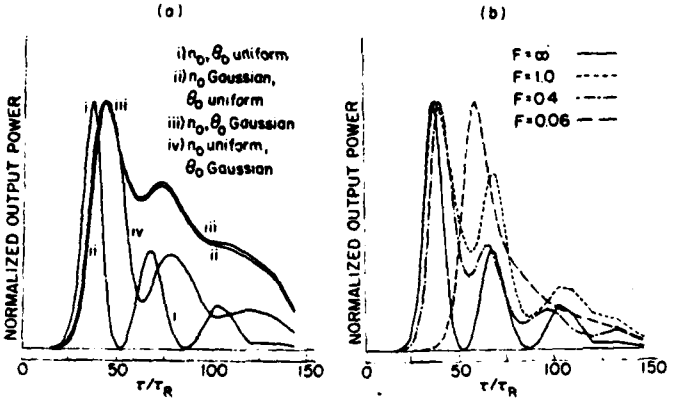

FIG. 1. (a) Normalized SF output power vs τ/τ_R, $\tau_R = \hbar\lambda/4\pi^2\mu^2 n_0^0 L = 8\pi\tau_0/3n_0^0\lambda^2 L$. ($\tau_R$ is the same as that defined in Ref. 5a. It appears smaller by a factor of 3 because it uses the "partial" radiative lifetime τ_0 instead of the observed one, $T_{2\rho}$.) $\theta_0^0 = 2\times 10^{-1}$, $T_1 = T_2 = T_2^* = \infty$, $L/c\tau_R = 3.9$, and $F = \infty$ (see text). (b) Same as (a) but with diffraction included and uniform $n_0(r)$ and $\theta_0(r)$.

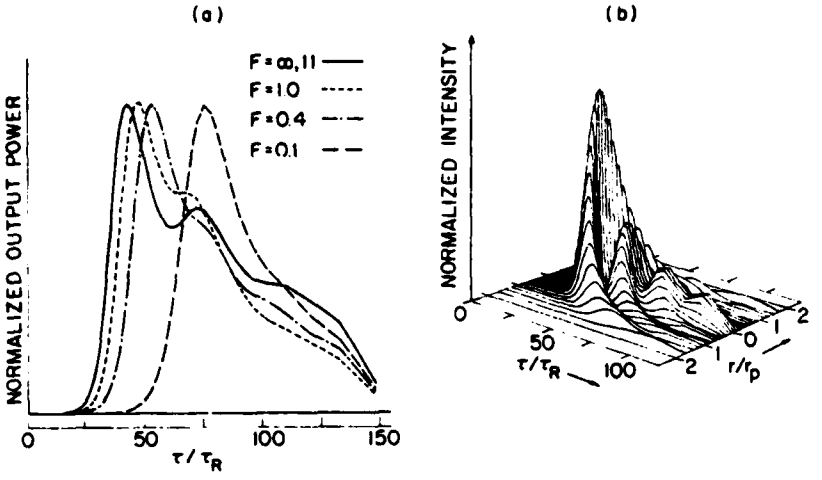

FIG. 2. Influence of diffraction on SF pulse shapes. Parameters are the same as in Fig. 1(a), with n_0 Gaussian and θ_0 uniform. (a) Emitted power; (b) isometric graph of intensity for the $F=1$ case of (a).

and also nearly free of ringing for $F \leq 0.4$.

Figure 2(a) studies the effect of diffraction on the SF pulse shapes by varying F, with use of a Gaussian n_0 as in Fig. 1(a), curve ii. Reducing F curtails the oscillatory structure and makes the output pulses more symmetrical, since the outer portions of the gain cylinder are stimulated to emit earlier because of diffraction from the inner portions. Thus diffraction becomes more important as F decreases.

Figure 2(b) is an isometric graph of the intensity buildup for a sample with $F=1$. The radial variations of intensity peaks, delay, and ringing illustrate how different gain shells contribute independently to the net power. Each shell exhibits a different Burnham-Chiao ringing pattern. Accordingly, their contributions to the net signal interfere and reduce the ringing. However, the central portion of the output pulse should exhibit strong plane-wave ringing. In fact, the ringing observed in the HF-gas experiments[2] may have been just that, since the detector viewed a small area in the near field of the beam.

Figure 3 compares the normalized Cs SF data of Refs. 3 and 11b (for which $F \simeq 0.7$ with uncertainty ranging from 0.35 to 1.4) to the theory (including relaxation terms). The data were fitted with use of a Gaussian n_0 and a uniform θ_0 with nominal value[6] $\theta_0 = 2(n_0{}^0 \pi r_p{}^2 L)^{1/2}$, $n_0{}^0$ being adjusted to yield the observed delays (1.6–2.8 times the experimental n_0 values). However, in Ref. 3 the curve published at each density was the one with the *shortest* delay. The *average* delay is ~30% greater at each density.[15] Thus the *effective* ratios of our computed densities to the experimental ones range from 1.2 to 2.2, compared with the +60%, −40% quoted experimental uncertainties.

The quantum calculations[6] actually yield $\theta_0 = (2/\sqrt{N})[\ln(2N)^{1/8}]^{1/2}$, a 9% correction which further reduces the range to 1.14–2.0. If one sets $\theta_0 = 6/\sqrt{N}$, as suggested by the small injection experi-

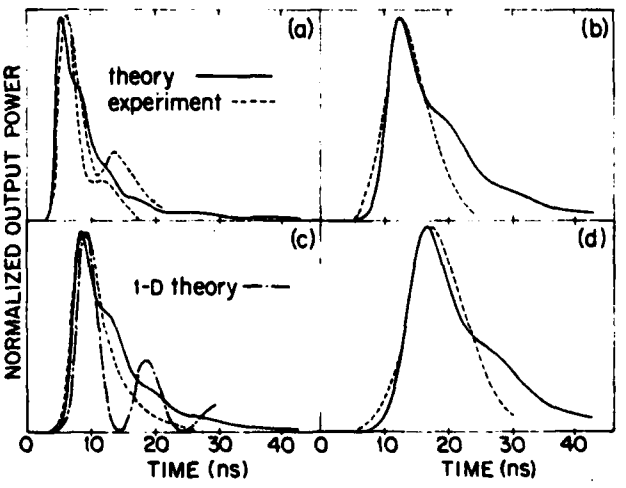

FIG. 3. Theoretical fits to Cs data of Ref. 3. The two dashed-line curves in (a) indicate typical experimental shot-to-shot variations. $F = 1$, $L = 2$ cm, $T_1 = 70$ ns, $T_2 = 80$ ns, $\lambda = 2.931\ \mu$m, $\tau_0 = 551$ ns, θ_0 is uniform or Gaussian, and $n_0(r)$ is Gaussian. The following give $\theta_0{}^0$(fit), $n_0{}^0$(fit), $n_0{}^0$(exp), with $\theta_0{}^0$ in units of 10^{-1}/cm^3 and $n_0{}^0$ in units of 10^{10}/cm^3: (a) 1.07, 31, 19; (b) 1.37, 18, 7.6; (c) 1.69, 11.9, 3.8; (d) 1.96, 8.85, 3.1. The broken-line curve in (b) is the one-dimensional fit of Ref. 3b, with $\theta_0{}^0 = 1.69$ and $n_0{}^0 = 12$.

ment,[15] the range is 1–1.8, in still better agreement.

The calculated shapes are in good agreement with the data, and are within the range of shot-to-shot fluctuations [Fig. 3(a)]. The *only* discrepancy is that the simulations predict more of a tail than observed in the experiments. For comparison, Fig. 3(b) also plots the fit in Ref. 3b of the one-dimensional Maxwell-Schrödinger theory.[4] As can be seen, the present theory gives a more accurate fit, illustrating the necessity of including transverse effects. The pulse tails are further curtailed by reducing F within the range of experimental uncertainties[11b] (which used a $1/e$ rather than a half width at half maximum definition of r_p). Note that often a Fresnel number F', defined as $r_p^2/\lambda L$, is used; diffraction effects become important when $F'=1$ (i.e., when $F=0.36$).

In conclusion, SF experiments are described much more accurately by including transverse effects. Our calculations do not include short-scale-length phase and magnitude fluctuations in θ_0, which result in multiple transverse-mode initiation of the SF process, leading to multidirectional output emission with hot spots. This effect, which is expected to be important only for large-F samples (since diffraction singles out a smooth phase front in small-F samples), is under study.

This work was supported in part by the Research Corporation, Mobil Oil Corporation, the University of Montreal, the U. S. Army Research Office, and the U. S. National Science Foundation.

---

[a]Present address: Optical Sciences Center, University of Arizona, Tucson, Ariz. 85721.

[1]This effect if also known as *superradiance* and *Dicke superradiance*, although these terms are also used to describe coherent emission from samples with initial polarization.

[2]N. Skribanowitz, I. P. Herman, J. C. MacGillivray, and M. S. Feld, Phys. Rev. Lett. 30, 309 (1973).

[3a]H. M. Gibbs, Q. H. F. Vrehen, and H. M. J. Hikspoors, Phys. Rev. Lett. 39, 547 (1977).

[3b]H. M. Gibbs, Q. H. F. Vrehen, and H. M. J. Hikspoors, in *Laser Spectroscopy III*, edited by J. L. Hall and J. L. Carlsten (Springer-Verlag, Berlin, 1977), p. 213.

[4]S. L. McCall, Ph.D. thesis, University of California at Berkeley, 1968 (unpublished); D. C. Burnham and R. Y. Chiao, Phys. Rev. 188, 667 (1969).

[5a]J. C. MacGillivray and M. S. Feld, Phys. Rev. A 14, 1169 (1976).

[5b]R. Saunders, S. S. Hassan, and R. K. Bullough, J. Phys. A 9, 1725 (1976).

[6]F. Haake, J. Haus, H. King, G. Schroder, and R. Glauber, Phys. Rev. Lett. 45, 558 (1980); D. Polder, M. F. H. Schuurmans, and Q. H. F. Vrehen, Phys. Rev. A 19, 1192 (1979), and references therein.

[7]In general, $n_0(r)$ will not be Gaussian even if the pump profile is, since saturation flattens $n_0(r)$ near its center, with Gaussian wings. However, our numerical results show that the exact shape of $n_0(r)$ is not critical.

[8]See Ref. 5a, Eq. (49); J. A. Hermann, Phys. Lett. 69A, 316 (1979); McCall (Ref. 4); Burnham and Chiao (Ref. 4); Polder, Schuurmans, and Vrehen (Ref. 6).

[9]J. C. MacGillivray and M. S. Feld, Phys. Rev. A 23, 1334 (1981); M. S. Feld and J. C. MacGillivray, in *Coherent Nonlinear Optics*, edited by M. S. Feld and V. S. Letokhov (Springer-Verlag, Berlin, 1980); Gibbs, Vrehen, and Hikspoors, Ref. 3b.

[10]R. Bonifacio, J. D. Farina, and L. M. Narducci, Opt. Commun. 31, 377 (1979). This paper uses the mean-field theory (MFT), which neglects propagation and predicts no ringing for the low-density Cs regime. Therefore the mode-competition transverse effects that they treat apply only to high-density MFT oscillatory SF and are not directly relevant to the Cs data.

[11a]Panel discussion, in *Cooperative Effects in Matter and Radiation*, edited by C. M. Bowden, D. W. Howgate, and H. R. Robl (Plenum, New York, 1977).

[11b]Q. H. F. Vrehen, in *Cooperative Effects in Matter and Radiation*, edited by C. M. Bowden, D. W. Howgate, and H. R. Robl (Plenum, New York, 1977).

[12]F. P. Mattar and M. C. Newstein, IEEE J. Quantum Electron. 13, 507 (1977), and Comput. Phys. Commun. 20, 139 (1980); F. P. Mattar, Appl. Phys. 17, 53 (1978).

[13]H. M. Gibbs, B. Bolger, F. P. Mattar, M. C. Newstein, G. Forster, and P. E. Toschek, Phys. Rev. Lett. 37, 1743 (1976); J. J. Bannister, H. J. Baker, T. A. King, and W. G. McNaught, Phys. Rev. Lett. 44, 1062 (1980).

[14]Plane-wave studies of R. Saunders and R. K. Bullough (in Ref. 11) and J. C. MacGillivray and M. S. Feld [Ref. 9, and Phys. Rev. A 23, 1334 (1981)] show that for realistic values of θ_0 the mutual influence of the two counterpropagating waves is negligible.

[15]Footnote 13 of Q. H. F. Vrehen and M. F. H. Schuurmans, Phys. Rev. Lett. 42, 224 (1979).

Computer Physics Communications 23 (1981) 1–17
North-Holland Publishing Company

TRANSIENT COUNTER-BEAM PROPAGATION IN A NONLINEAR FABRY–PEROT CAVITY *

F.P. MATTAR **, G. MORETTI
Aerodynamics Laboratory, Polytechnic Institute of New York, Brooklyn, NY 11201, USA

and R.E. FRANCEOUR
The International Division, Mobil, New York, NY 10017, USA

Received 10 December 1980

By adapting Moretti's self-consistent numerical approach to integrating the Euler equation of compressible flow, a unified complete temporal and spatial description of superfluorescence and optical bi-stability was undertaken. (The simulation includes material initialization as well as refractive transverse and longitudinal field boundary conditions appropriate to the cylindrical laser cavity). The respecting of physical causality in Moretti's method was maintained; but by using an improved derivative estimator at both the predictor and corrector levels, the overall accuracy was improved.

The physical model includes nonplanar two-way Maxwell–Bloch propagation with spontaneous sources. The problem of dynamic transverse effects as they relate to soliton collisions is addressed. The calculations are based upon an extension of Mattar's previous semi-classical model for diffraction and phase effects in self-induced transparency at thick optical absorptions.

The computational algorithm relies on the use of characteristics, but is strictly a finite-difference scheme. This explicit scheme involves the simultaneous integration along the time coordinate for both forward and backward wave. However, directional derivatives must be considered to appropriately take into account the mutual influence of the two light beams without violating the laws of forbidden signals. Particular case is exercised to maintain at least a second-order accuracy using one-sided approximations to spatial derivatives. Each forward/backward field derivative will be related to its respective directional history. A numerical approach in which the discretization is not consistent with these physical facts will inevitably fail. Thus the numerical algorithm must discriminate between different domains of dependence of different physical parameters.

The physical process can now be analyzed with a degree of realism not previously attainable. Significant agreement with experimental observations is reported from the planar or time-independent analysis counterpart confined to the central portion of the beam.

1. Introduction

The modelling of longitudinal and transverse coherent pulse reshaping that occurs when forward- and backward-travelling beams interact coherently with a medium resonant to the pulse-carrier frequency and with each other is presented. The physical system is characterized by a pulse duration much shorter than all the atomic relaxation lifetimes and dephasing times. In addition, the field is large enough so that significant exchange of energy between the light pulse and matter takes place in a time that is short compared to a relaxation time.

The response of the resonant medium is not instantaneous but cumulative (i.e., it is associated with the past history of the applied field). Hence, the inertial response of the medium is not describlable in terms of an intensity-dependent susceptibility. Instead it necessitates a more general functional of the applied field. The treatment differs from earlier theoretical and experimental studies where a rate-equation approximation was considered. Consequently, a semiclassical formulism, similar to the one used by McCall and Hahn [1] in their analysis of self-induced transparency, must be adopted. The physical model is based on counter-propagating travelling-wave equations, derived from Maxwell's equations including transverse [2,3] and transient phase variation [4], and a two-model

* Work supported in part by the Research Corporation, the Army Research Office, the Office of Naval Research and the International Division of Mobil.
The concept of this analysis was proposed at ICO-11 Madrid (September 1978) ed. J. Buescos, Proc. distributed by the Spanish Optical Society, Madrid.
** Author is also presently with Lab. Laser Spectroscopy, MIT, Cambridge, MA 02139, USA.

0010-4655/81/0000–0000/$02.50

[5,6] version of the Bloch's [7] equations describing a distribution of two-level homogeneously broadened atomic systems. Furthermore, the simplifying mean-field approximation is not considered; instead, an exact numerical approach that adapts computational methodologies gained in solving fluid dynamics problems is developed.

In the slowing-varying-envelope approximation, both the phase and amplitude variations of a linearly-polarized field in the transverse direction are described by two scalar wave equations, one for each mode: forward-travelling propagation. Each equation is driven by the appropriate polarization associated with the nonlinear inertial response of the active medium. The dynamic crosscoupling of the two waves appears explictly in the two-mode analogue of the traditional single-mode Bloch's equations describing the material system. The presence of the longitudinal mirrors will further enhance the mutual influence of the two beams. Variations in polarization and population over wavelength distances are treated by means of expansions in spatial Fourier series. The Fourier series are truncated after the third or fifth harmonic. As McCall [6] and Fleck [5] outlined it, the number of terms needed is influenced by the relative strength of the two crossing beams and the importance of pumping and relaxation processes in restoring depleted population differences.

Counter-propagational studies have been previously considered for pulses with infinite transverse extent (i.e., uniform planes) by Marburger and Felber [8] in connection with nonresonant nonlinearities. Two-mode one-dimensional analysis involving resonant interactions have been tackled by McCall [5], Fleck [6], Saunder and Bullough [9], and more recently by Eberly, Whitney and Konopnicki [10]. However, restrictive assumptions were made relating to the allowed form of the temporal field variations. Since the experimental arrangements often do not satisfy the uniform plane-wave condition, the detailed nature of transverse behavior (using rigorous Laplacian coupling) must be worked out. This present three-dimensional treatment assumes azimuthal cylindrical symmetry.

Furthermore, the interplay of diffraction coupling (through the Laplacian term), and the medium response will inevitably redistribute the beam energy spatially and temporally [11–14]. This transient two-stream beam reshaping profoundly affects a device that relies on this nonlinear light–matter interaction effect. Several physical effects such as strong self-phase modulation, spectral broadening, self-steepening and self-focusing that have been separately studied, combine here to affect the behavior diversely during different positions and times of the pulse evolution. Due to the essential complexity of the governing equations of motion, only effective numerical methods which are consistent with the physics can make attainable a heretofore unachievable solution.

An extension of an efficient numerical approach [15–17] was developed by Mattar to study the transverse energy flow associated with beam variations in the single mode SIT problem. The latter code, which simulates the rigorous interplay of diffraction (Laplacian term) and the inertial two-level atom (Bloch equation) response, had led to the discovery of a new transient on-resonance self-lensing phenomenon which was subsequently verified in sodium [18], neon [19] and more recently in iodine [20] vapour in laboratory experiments. Accurate comparison over a wide domain of physical dependencies was reported [21]. Consequently, the numerics of diffraction and Bloch equations will only be briefly outlined.

In the standing-wave problem, the two waves are integrated simultaneously along t the physical time: no retarded time [22] (or Galilean) transformation as in SIT will be introduced.

To ensure proper handling of the two-stream effect, special attention must be exercised. For causality reasons, as advanced by Moretti [23], only directional resolution for spatial derivatives of each stream (forward and backward field) must be sought. This is achieved by using one-sided discretization techniques. The forward field derivative will be approximated by a different set of points than those used for the backward field derivative. The spatial derivative of the forward field is discretized using points which lie to the left as all preceding forward waves have propagated in the same left–right direction. The backward field is approximated by points positioned to the right. As a result, each characteristic (information carrier) is related to its respective directive history. Thus, violation of the law of forbidden signals is prevented.

Once the basic effects are observed and assessed using straightforward orthogonal computational meshes, nonuniform grids which alleviate the calculational effort [24–28], will be implemented. (The nonuniform grid permits greater point concentrations in the temporal and spatial regions of main interest.)

The prime goals of this study are to achieve an understanding of beam effects in soliton collision [29], and to

relate this situation to the single stream SIT problem and to observations in super-fluorescence [30–33] and optical bi-stability [34,35] experiments. Furthermore, one readily investigates the dependence of the counter-propagation transmission characteristics on pulse and beam shape, on the relaxation times, the resonance frequency offset, the input pulse area(s) on-axis and, the Fresnel number, the mirror reflectivity, the initial tipping angle. The outline of this paper is as follows: in section 2 are the standing-wave Maxwell–Bloch equations and the initial and boundary condition. Section 3 presents the law of forbidden signals. The accuracy of the predictor/corrector scheme is presented in section 4. The effect of improving the derivative estimator on the overall numerical scheme is described in section 5, while section 6 presents the theory of approximating linear operators. In section 7, three-point estimator formulae for the first derivative of a function are derived. Section 8 describes the treatment of the longitudinal boundary condition. Section 9 presents the three-point estimate as an example for the four-point estimator for the Laplacian of a function. Section 10 concludes the paper.

2. Equation of motion

In the slowly-varying-envelope approximation, the dimensionless field–matter equations are:

$$-iF\nabla_T^2 e^+ + \frac{\partial e^+}{\partial \tau} + \frac{\partial e^+}{\partial z} = +g^+\langle P\exp(-ikz)\rangle\,, \tag{2.1}$$

$$-iF\nabla_T^2 e^- + \frac{\partial e^-}{\partial \tau} - \frac{\partial e^-}{\partial z} = +g^-\langle P\exp(+ikz)\rangle\,, \tag{2.2}$$

with g^+ and g^- the nonuniform gain associated to the pump experienced by the forward (e^+) and backward (e^-) travelling wave. The quantities in the r.h.s. undergo rapid spatial variations; $\langle\ \rangle$ represents the spatial average of these quantities over a period of half a wavelength

$$\frac{\partial P}{\partial \tau} + (-i(\Delta\Omega) + \tau_2^{-2})\,P = +\{W(e^+ + e^-)\}\,, \tag{2.3}$$

$$\frac{\partial W}{\partial \tau} + \tau_1^{-1}(W^e - W) = -\tfrac{1}{2}(P + P^-)(e^+ + e^-)\,. \tag{2.4}$$

Equivalently

$$\frac{\partial P}{\partial \tau} + (-i(\Delta\Omega) + \tau_2^{-1})\,P = W[e^+\exp(-ikz) + e^-\exp(+ikz)]\,, \tag{2.5}$$

$$\frac{\partial W}{\partial \tau} + \tau_1^{-1}(W^e - W) = -\tfrac{1}{2}(Pe^{+*}\exp(ikz) + Pe^{-*}\exp(-ikz) + \text{c.c.})\,, \tag{2.6}$$

with

$$e^{\pm} = (2\mu\tau_p/\mu)\,e^{\pm}\,, \tag{2.7}$$

$$P = (P'/2\mu)\,, \tag{2.8}$$

$$E^{\pm} = \mathrm{Re}\{e^{\pm}\exp[i(\omega t \mp kz)]\} \tag{2.9}$$

and

$$P = \mathrm{Re}\{ip'\exp(i\omega t)\}\,. \tag{2.10}$$

The complex field amplitude $e^{\pm}$, the complex polarization density P' and the energy stored per atom are func-

tions of the transverse coordinate

$$\rho = r/r_p \,, \tag{2.11}$$

the longitudinal coordinate

$$z = \alpha_{eff} z \tag{2.12}$$

and the physical time

$$\tau = t/\tau_p \,. \tag{2.13}$$

The time scale is normalized to a characteristic time of the forward input pulse τ_p, and the transverse dimension scales to a characteristic spatial width r_p of the forward input transient beam. The longitudinal distance is normalized to the effective absorption length [37].

$$\alpha_{eff}^{-1} = 8\pi\omega\mu^2 N\tau_p/nhc \,. \tag{2.14}$$

In this expression ω is the angular carrier frequency of the optical pulse, μ is the dipole moment of the resonant transition, N is the number density of resonant molecules and can sustain radial variations, and n is the index of refraction of the background material. The dimensionless quantities

$$\Delta\Omega = (\omega - \omega_0)\,\tau_p \,, \tag{2.15}$$

$$\tau_1 = T_1/\tau_p \,, \tag{2.16}$$

$$\tau_2 = T_2/\tau_p \,, \tag{2.17}$$

measure the offset of the optical carrier frequency ω from the central frequency of the molecular resonance ω_0, the thermal relaxation time T_1, and the polarization dephasing relaxation time T_2, respectively. The dimensionless parameter F (which is the gain to loss ratio) is given by

$$F = \lambda\alpha_{eff}^{-1}/4\pi r_p^2 \tag{2.18}$$

and is the reciprocal of the Fresnel number associated with an aperture of radius r_p and a propagation distance (α_{eff}^{-1}). The magnitude of F determines whether or not it is possible to divide up the transverse dependences of the fields into "pencils" (one pencil for each radius) which may be treated in the plane-wave approximation. The diffraction coupling term and the nonlinear interaction terms alternately dominate depending on whether $F < 1$ or $F > 1$.

The presence of opposing waves leads to a quasi-standing wave pattern in the field intensity over a half wavelength. To effectively deal with this numerical difficulty, one decouples the material variables using Fourier series [5,6] namely

$$P = \exp(-ikz) \sum_{p=0}^{\infty} P^{+}_{(2p+1)} \exp(-i2pkz) + \exp(+ikz) \sum_{p=0}^{\infty} P^{-}_{(2p+1)} \exp(+i2pkz) \,, \tag{2.19}$$

$$W = W_0 + \sum_{p=1}^{\infty} [W_{2p} \exp(-i2pkz) + \text{c.c.}] \,, \tag{2.20}$$

with W_0 a real number. By substituting in the travelling equation of motion one obtains

$$\partial_\tau P_1^+ + P_1^+/\tau_2 = W_0 e^+ + W_2 e^- \,, \tag{2.22}$$

$$\partial_\tau P_3^+ + P_3^+/\tau_2 = W_2 e^+ + W_4 e^- \,, \tag{2.23}$$

... ...

$$\partial_\tau P^+_{(2p+1)} + P^+_{(2p+1)}/\tau_2 = W_{2p}e^+ + W_{2(p+1)}\,e^- \text{, and} \tag{2.24}$$

$$\partial_\tau P^-_1 + P^-_1/\tau_2 = W_0 e^- + W^*_2 e^+ , \tag{2.25}$$

$$\partial_\tau P^-_3 + P^-_3/\tau_2 = W_2 e^- + W^*_4 e^+ , \tag{2.26}$$

$$\ldots \qquad \ldots$$

$$\partial_\tau P^-_{(2p+1)} + P^-_{(2p+1)}/\tau_2 = W^*_{2p}e^- + W^*_{2(p+1)}e^+ , \tag{2.27}$$

$$\partial_\tau W_0 + (W_0 - W^e_0)/\tau_1 = -\tfrac{1}{2}(e^{-*}P^-_1 + e^{+*}P^+_1 + \text{c.c.}) , \tag{2.28}$$

$$\partial_\tau W_2 + W_2/\tau_1 = -\tfrac{1}{2}(e^{-*}P^+_1 + e^{+*}P^+_3 + e^+P^{-*}_1 + e^-P^{-*}_3) , \tag{2.29}$$

$$\partial_\tau W_{2p} + W_{2p}/\tau_1 = -\tfrac{1}{2}(e^{-*}P^+_1 + e^+P^+_{2p+1} + e^+P^{-*}_{2p+1} + e^{-*}P^{-*}_{2p+1}) . \tag{2.30}$$

The field propagation and atomic dynamic equation are subjected to the following initial and boundary conditions.

1. Initial

For $\tau \geqslant 0$,

$$e^\pm = 0 , \tag{2.31}$$

$$W_0 = W^e_0 , \tag{2.32}$$

a known function to take into account the pumping effects. For SIT soliton collision

$$P^\pm_{(2p+1)} = 0 , \qquad \text{for all } p , \tag{2.33}$$

while for the superfluorescence problem

$$P^\pm_{(2p+1)} \tag{2.34}$$

is defined in terms of a non-uniform initial tipping angle that reflects the radial variations of the atomic density – its value can either be deterministic or fluctuating.

2. Longitudinal

For $z = 0$ and $z = L$: e^+ and e^- are given in terms of a known incident function

$$e_{I0} \tag{2.35}$$

and

$$e_{IL} \tag{2.36}$$

of τ and ρ. Should enclosing mirrors to delineate the cavity be considered in the analysis, one must deal with the following longitudinal boundary equations

$$e^+ = \sqrt{(1-R_1)}\,e_{I0} + \sqrt{R_1}\,e^- , \qquad \text{at } z = 0 , \tag{2.37}$$

$$e^- = \sqrt{(1-R_2)}\,e_{IL} + \sqrt{R_2}\,e^+ , \qquad \text{at } z = L , \tag{2.38}$$

where R_1, R_2 and $(1-R_1)$, $(1-R_2)$ are the respective reflectivity and transmitting factor associated with each left and right mirror.

3. Transverse

For all z and τ $[\partial e^\pm/\partial\rho]_{\rho=0}$ and $[\partial e^\pm/\partial\rho]_{\rho=\rho_{max}}$ vanishes. ρ_{max} defines the extent of the region over which the numerical solution is to be determined. To avoid unphysical reflection from the transverse boundary, one

must, for amplifier calculations, use stretched (nonuniform) radial grids (i.e., consider a quasi-infinite physical domain and map it on a finite computation region) and confine the pre-excited active medium by radially-dependent absorbing shells [17]. Note that this condition represents an actual experimental approach in which the laser amplifier is coated to circumvent any spurious reflections.

3. The law of forbidden signals

The concept of the physical law of forbidden signals and how it affects two-stream flow discretization problems was originally written by Moretti to handle the numerical integration of Euler equations. The method, referred to as the λ-scheme, was presented elsewhere [38]. However, since it represents the basis of our present algorithm, we felt useful to summarize here its salient features.

In any problem involving wave propagation, the equations describe the physical fact that any point at a given time is affected by signals sent to it by other points at previous times. Such signals travel along lines which are known as the 'characteristics' of the equations.

For example, a point such as A in fig. 1 is affected by signals emanating from B (forward wave) and from C (backward wave), while point A′ will be the recipient of signals launched from A and D.

Similar wave trajectories appear in our present problem, but the slopes of the lines can change in space and time.

It is clear that the slopes of the two characteristics which carry the information necessary to define the forward and backward propagating variables at every point, are of different signs; they $\lambda_{1,2}$, are numerically equal to $\pm c/n$. For such a point, A (fig. 2), the domain of dependence is defined by point B and point C, the two characteristics being defined by AC and AB, respectively, to a first degree of accuracy. When discretizing the partial differential equations for computational purposes, point A must be made dependent on points distributed on a segment which brackets BC, for example on points D, E and F of fig. 2. Such a condition is necessary for stability but it must be loosely interpreted. Suppose, indeed, that one uses a scheme in which a point such as A is always made to depend on D, E and F, indiscriminately (this is what happens in most of the schemes currently used, including the MacCormack method). Suppose, now, that the physical domain of dependence of A is the segment BC of fig. 3. The information carried to A from F is not only unnecessary, it is also untrue. Consequently, the numerical scheme, while not violating the CFL stability rule, would violate the law of forbidden signals. Physically, it would be much better to use information from D and E to define A, even if this implied lowering the nominal degree of accuracy of the scheme. In other words, to say that a given scheme, using points D, E and F, has a second-order accuracy is meaningless since a wrong scheme has no accuracy whatsoever.

In two-wave propagation problems treated by relaxation methods, the need for a switching of the discretization scheme in passing from forward (advanced) to backward (retarded) points is evidently related to the law of forbidden signals.

The sensitivity of results to the numerical domain of dependence as related to the physical domain of dependence explains why computations which use integration schemes such as MacCormack's [40,41] show a progressive deterioration as the AC line of fig. 2 becomes parallel to the T-axis ($\lambda_1 \to 0$), even if λ_1 is still negative [38]. The information from F actually does not reach A; in a coarse mesh, such information may be drastically different from the actual values (from C) which affect A. On the other hand, since the CFL rules must be satisfied and

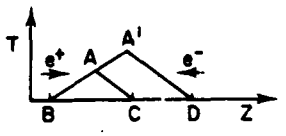

Fig. 1.

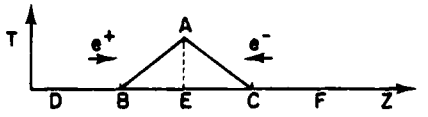

Fig. 2.

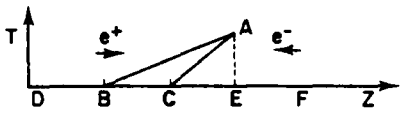

Fig. 3.

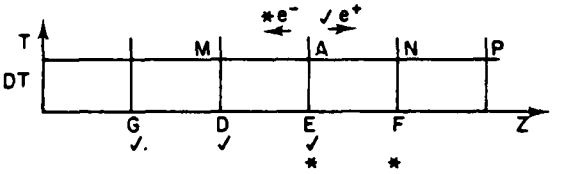

Fig. 4.

F is the nearest point to C on its right, the weight of such information should be minimized. Moretti's λ-scheme, relying simultaneously on the two field equations, provides us with such a possibility.

Every spatial derivative of the forward field is approximated by using points which lie on the same side of E as C, and every derivative of the backward scattered field is approximated by using points which lie on the same side of E as B. By doing so, not only is each characteristic related with information which is only found on the same side of A from which the characteristic proceeds, but such information is appropriately weighted with factors. These depend on the slopes of the characteristic so that the contribution of points located too far outside the physical domain of dependence is minimized. A one-level scheme which defines

$$\partial e^+/\partial z = (e^+_E - e^+_D)/\Delta z\,, \qquad \text{(forward wave)}\,, \tag{3.1}$$

$$\partial e^-/\partial z = (e^-_F - e^-_E)/\Delta z\,, \qquad \text{(backward wave)}\,, \tag{3.2}$$

is Gordon's scheme [42], accurate to first order. To obtain a scheme with second-order accuracy, Moretti considered two levels, in a manner very similar to MacCormack's [40]. More points, as in fig. 4, must be introduced. At the predictor level following Moretti's scheme one defines

$$\partial \tilde{e}^+/\partial z = (2e^+_E - 3e^+_D + e^+_G)/\Delta z\,, \qquad \text{(forward wave)}\,, \tag{3.3}$$

$$\partial \tilde{e}^-/\partial z = (e^-_F - e^-_E)/\Delta z\,, \qquad \text{(backward wave)}\,. \tag{3.4}$$

At the corrector level, one defines

$$\partial \dot{e}^+/\partial z = (\tilde{e}^+_A - \tilde{e}^+_M)/\Delta z\,, \qquad \text{(forward wave)} \tag{3.5}$$

and

$$\partial \dot{e}^-/\partial z = (-2\tilde{e}^-_A + 3\tilde{e}^-_N + \tilde{e}^-_P)/\Delta z\,. \tag{3.6}$$

It is easy to see that, if any function f is updated as

$$\tilde{f} = f + f_T \Delta T \tag{3.7}$$

at the predictor level, with the T-derivatives defined as in (2.21) and the z-derivatives defined as in (3.3), (3.4) and as

$$f(T + \Delta T) = \tfrac{1}{2}(f + \tilde{f} + f_T \Delta T) \tag{3.8}$$

at the corrector level, with the T-derivatives defined again as in (2.1), (2.2), and the z-derivatives defined as in (3.5), (3.6), the value of f at $T + \Delta T$ is obtained with second-order accuracy. The updating rule (3.7) and (3.8) are the same as in the MacCormack scheme.

At the risk of increasing the domain of dependence, but with the goal of modularising the algorithm, we have used three- and four-point estimators for each first and second derivative, respectively. We have also extended Moretti's algorithm to a nonuniform mesh to handle the longitudinal refractive (left and right) mirrors: the same one-sided differencing (to satisfy the law of causality) is used for both predictor and corrector steps. Nevertheless, we derived, using the theory of estimation, conveniently presented by Hamming [43], second order derivative estimators at both the predictor and corrector levels. As a result, the overall accuracy of Moretti's scheme was increased.

4. Order of error for straight-line predictor/corrector

We consider the following predictor/corrector scheme as suggested by MacCormack

predict: $$\tilde{f}_{n+1} = f_n + \delta \tilde{f}_n' , \tag{4.1}$$

correct: $$\hat{f}_{n+1} = \tfrac{1}{2}(\tilde{f}_{n+1} + f_n + \delta \tilde{f}'_{n+1}) , \tag{4.2}$$

where $\tilde{f}$ indicates predicted, $\hat{f}$ corrected and f exact values. Assume that the derivative estimator for prediction has an error of order p and that for correction of order c, so that:

$$\tilde{f}_n' = f_n' + O(\delta^p) \tag{4.3}$$

$$\hat{f}'_{n+1} = f'_{n+1} + O(\delta^c) \tag{4.4}$$

where $O(\delta^i)$ is a sum involving terms in δ to the power i or higher. Combining (4.1) with (4.3) and (4.2) with (4.4) we get:

predict: $$\tilde{f}_{n+1} = f_n + \delta f_n' + O(\delta^{p+1}) , \tag{4.5}$$

correct: $$\hat{f}_{n+1} = \tfrac{1}{2}[\tilde{f}_{n+1} + f_n + \delta f'_{n+1} + O(\delta^{c+1})] . \tag{4.6}$$

The Taylor series expansion for f_{n+1} is:

$$f_{n+1} = f_n + \delta f_n' + \frac{\delta^2}{2} f_n'' + O(\delta^3) . \tag{4.7}$$

Combining (4.7) and (4.5) we get the predictor error $\tilde{\epsilon}_{n+1}$ as follows:

$$\tilde{\epsilon}_{n+1} = f_{n+1} - \tilde{f}_{n+1} = f_n + f_n' + \frac{\delta^2}{2} f_n'' + O(\delta^3) - f_n - \delta f_n' + O(\delta^{p+1})$$

$$= \left(\frac{f_n''}{2}\right)\delta^2 + O(\delta^{p+1}) . \tag{4.8}$$

Thus

$$\tilde{\epsilon}_{n+1} = O(\delta^2) , \qquad \text{for all } p \geqslant 1 . \tag{4.9}$$

Consider now the corrector error:

$$\tilde{\epsilon}_{n+1} = f_{n+1} - \hat{f}_{n+1} = f_n + \delta f_n' + \frac{\delta^2}{2} f_n'' + O(\delta^3) - \tfrac{1}{2}\tilde{f}_{n+1} - \tfrac{1}{2} f_n - \frac{\delta}{2} f'_{n+1} + O(\delta^{c+1})$$

$$= \tfrac{1}{2} f_n + (f_n' - \tfrac{1}{2} f'_{n+1})\,\delta + \frac{f_n''}{2}\delta - \tfrac{1}{2}[f_n + \delta f_n' + O(\delta^{p+1})] + O(\delta^{c+1})$$

$$= \left(\frac{f_n' - f_n''}{2}\right)\delta + \frac{f_n''}{2}\delta^2 + O(\delta^{c+1}) + O(\delta^{p+1}) . \tag{4.10}$$

But

$$f'_{n+1} = f_n' + \delta f_n'' + O(\delta^3) . \tag{4.11}$$

Thus

$$\left(\frac{f_n' - f'_{n+1}}{2}\right)\delta = -\frac{f_n''}{2}\delta^2 + O(\delta^2) . \tag{4.12}$$

Whence

$$\tilde{\epsilon}_{n+1} = O(\delta^3) + O(\delta^{c+1}) + O(\delta^{p+1}) \tag{4.13}$$

or

$$\hat{\epsilon}_{n+1} = O(\delta^{\min(3,c+1,p+1)}) . \tag{4.14}$$

Thus the order of error for the predictor/corrector is the minimum of 3, $c+1$ and $p+1$. If $c = 2$ and $p = 2$, their

Table 1
Comparison table between weighting coefficients for derivative estimators using Hamming's estimation theory and Moretti's law of forbidden signals

Hamming: $\tilde{f}'_n = f'_n + O(\delta^2) \rightarrow \tilde{f}'_n = f'_n + O(\delta^2)$

Moretti: $\tilde{f}'_n = f'_n + \frac{5f''_n}{2}\delta + O(\delta^2) \rightarrow f'_n = \tilde{f}'_n - \frac{5f''_n}{2}\delta + O(\delta^2)$

Moretti	Hamming
Predictor	
$f_{n+1} = f_n + \delta f'_n + \frac{f''_n}{2}\delta^2 + O(\delta^3)$	$\tilde{f}_{n+1} = f_n + \delta f'_n + O(\delta^3)$
$\tilde{f}_{n+1} = f_n + \delta f'_n + \frac{5f''_n}{2}\delta^2 + O(\delta^3)$	$\tilde{f}_{n+1} - f_{n+1} = -\frac{f''}{2}\delta^2 + O(\delta^3)$
$\tilde{f}_{n+1} - f_{n+1} = 2f''\delta^2 + O(\delta^3)$	
Corrector	
$\hat{f}_{n+1} = \frac{1}{2}(\tilde{f}_{n+1} + f_n + \tilde{f}'_{n+1})$	$\hat{f}_{n+1} - f_n = \frac{1}{2}f_n + \frac{\delta}{2}f'_n + O(\delta^3)$
$\tilde{f}_{n+1} - f_{n+1} = \frac{1}{2}f_n + \frac{\delta}{2}f'_n + \frac{5f''_n}{2}\delta^2 + O(\delta^3)$	$+ \frac{1}{2}f_n + \frac{\delta}{2}f'_{n+1} + O(\delta^3)$
$+ \frac{1}{2}f_n + \frac{\delta}{2}f'_{n+1} + \frac{f''_{n+1}}{4}\delta^2 + O(\delta^3)$	$- f_n - \delta f'_n - \frac{f''_n}{2}\delta^2 + O(\delta^2)$
$+ f_n - \delta f'_n - \frac{f''_n}{2}\delta^2 + O(\delta^3)$	$= \left(\frac{f'_{n+1} - f'_n}{2}\right)\delta - \frac{f''_n}{2}\delta^2 + O(\delta^3)$
$= \left(\frac{f'_{n+1} - f'_n}{2}\right)\delta + \left(\frac{5f''_{n+1} - 3f''_n}{4}\right)\delta^2 + O(\delta^3)$	$= \left(\frac{f''_n}{2} - \frac{f''_n}{2}\right)\delta^2 + O(\delta^3)$
but	
$f'_{n+1} = f'_n + f''_n + \frac{\delta^2}{2}f'''_n + O(\delta^3)$	$= O(\delta^3)!$
$= \left(\frac{f''_n}{2} + \frac{5f''_{n+1} - 2f''_n}{4}\right)\delta^2 + O(\delta^3)$	
$= \left(\frac{5f''_{n+1} - f''_n}{4}\right)\delta^2 + O(\delta^3)$	

second-order errors effectively cancel out. From the above, it is clear that for maximum accuracy with the straight-line predictor/corrector, the derivative estimators for both prediction and correction should guarantee at least second-order accuracy. Anything above second-order accuracy, however, will not necessarily improve the results.

5. The effect of prediction error on correction error for a weighted formula estimator of the correction derivative

We investigate derivative estimator formulae of the type:

$$\hat{f}'_n = \sum_i \alpha_i f_n(s_i). \tag{5.1}$$

Let $\delta = \max_i(|x_{i+1} - x_i|)$ and assume

$$\hat{f}'_n = f'_n + O(\delta^c), \tag{5.2}$$

so that (5.1) has error c.

In applying a straight-line predictor/corrector with such an estimator for the corrector, we observe that the error in the estimated corrector derivative, since it based on predicted values, will also depend on the error of prediction. From (4.9) we know that the error in predicted values is $O(\delta^2)$ for any reasonable derivative estimator. Thus we may write:

$$\tilde{f}_{n+1}(x_i) = f_{n+1}(x_i) + O(\delta^2). \tag{5.3}$$

Applying formula (5.1) to (5.3) we get:

$$\tilde{f}'_{n+1} = \sum_i \alpha_i f_{n+1}(x_1) = \sum_i \alpha_i f_{n+1}(x_i) + O(\delta^2). \tag{5.4}$$

Thus, using (5.2):

$$f'_{n+1} = \hat{f}'_{n+1} + O(\delta^c) + O(\delta^2) = \hat{f}'_{n+1} + O(\delta^{\min(c,2)}). \tag{5.5}$$

Therefore the effective error of the corrected derivative cannot be increased beyond 2 for a straight-line corrector. It makes no sense to use a formula of type (5.1) with $c > 2$. From the theory of estimation, conveniently presented by Hamming [43], this means that only three weighting factors $\alpha_1, \alpha_2, \alpha_3$ need be used. See table 1 for comparison between weighting coefficients.

6. Approximating linear operators

Let $\bar{x} = (x_1, x_2, x_3, ..., x_m)$, $x_i < x_j$ for $i \neq j$. Consider the function f and let $f(x)$ and W be the column vectors

$$f(\bar{x}) = \begin{pmatrix} f(x_1) \\ f(x_2) \\ f(x_3) \\ \cdot \\ \cdot \\ \cdot \\ f(x_m) \end{pmatrix}, \qquad W = \begin{pmatrix} w_1 \\ w_2 \\ w_3 \\ \cdot \\ \cdot \\ \cdot \\ w_m \end{pmatrix}. \tag{6.1}$$

Let L be a linear operator. We seek a vector W such that:

$$f = W \cdot f(\bar{x}) + O(\delta^m),$$

where $\delta = \max_i (|x_{i+1} - x_i|), i = 1, ..., m-1$. We approximate f by a polynomial P_f of order $m-1$ which agrees, exactly with f at points $x_1, x_2, x_3, ..., x_m$:

$$P_x(x) = \sum_{j=1}^{m} L_{jm}(x) f(x_j) , \tag{6.2}$$

where L_{jm} are the Lagrange polynomials for x. It can easily be shown that

$$f(x) = P_f(x) + R(f, \bar{x}; x) , \tag{6.4}$$

where the remainder term $R(f, X; x)$ is

$$R(f, \bar{X}; x) = \frac{f^{(m)}(0)}{m!} \prod_{i=1}^{m} (x - x_i) \leqslant O(\delta^m) , \tag{6.5}$$

for some $\theta: x_1 \leqslant \theta \leqslant x_m$. Let λ_{ij} be the coefficients of L_{jm} so that

$$L_{jm}(x) = \sum_{i=0}^{m-1} \lambda_{ij} x^i , \tag{6.6}$$

yielding

$$f(x) = \sum_{j=1}^{m} f(x_j) \sum_{i=0}^{m-1} \lambda_{ij} x^i + R(f, X; x) . \tag{6.7}$$

Applying L to both sides of (3.7), we get

$$Lf(x) = \sum_{j=1}^{m} f(x_j) \sum_{i=0}^{m-1} \lambda_{ij} Lx^i + LR(f, X; x) . \tag{6.8}$$

Define the column vector M_m as:

$$M_m(x) = \begin{pmatrix} 1 \\ x \\ x^2 \\ \cdot \\ \cdot \\ \cdot \\ x^m \end{pmatrix} ,$$

and let $\Lambda_m(\bar{X})$ be the matrix of coefficients of the Lagrange polynomials on $\bar{X}$. Then (6.8) may be rewritten as:

$$Lf(x) = (\Lambda_m(\bar{X}) \cdot LM_m(x))^{\mathrm{T}} \cdot f(\bar{X}) + LR(f, \bar{X}; x) , \tag{6.9}$$

where superscript T represents the matrix transpose operations. We propose the vector

$$W = \Lambda_m(\bar{X}) \cdot LM_m(x) \tag{6.10}$$

as our weighting vector. Note that this vector is independent of the function f.

Eq. (6.9) represents a formula for estimating a linear operation on a function given the function's values at a set of points. Unfortunately, little can be said at this point about the error term $LR(f, \bar{X}, x)$ for arbitrary L. Let us concentrate our attention now on derivative operators. In this case:

$$\frac{\mathrm{d}}{\mathrm{d}x} R(f, \bar{X}; x) = \frac{\mathrm{d}}{\mathrm{d}x} \left(\frac{f^{(m)}(\theta)}{m!} \prod_{i=1}^{m} (x - x_i) \right)$$

$$= \frac{1}{m!}\left[f^{(m+1)}(\theta)\frac{d\theta}{dx}\prod_{i=1}^{m}(x-x_i) + f^{(m)}(\theta)\frac{d}{dx}\prod_{i=1}^{m}(x-x_i)\right]$$

$$= \frac{1}{m!}\left[f^{(m+1)}(\theta)\frac{d\theta}{dx}\prod_{i=1}^{m}(x-x_i) + f^{(m)}(\theta)\left\{\prod_{i=2}^{m}(x-x_i) + \sum_{j=1}^{m-1}\prod_{i=1}^{j}(x-x_i)\right\}\right], \tag{6.11}$$

since θ is in general a function of x. Let us further restrict ourselves to cases where $x = x_k$ for some k. If we assume that $f^{(m)}(\theta(x_k))$, $f^{(m+1)}(\theta(x_k))$ and $(d\theta/dx)|_{x=x_k}$ are defined, then the first term above cancels yielding

$$\frac{d}{dx}R(f, X; x)|_{x=x_k} = \frac{f^{(m)}((x_k))}{m!}\left[\prod_{i=2}^{m}(x_k - x_i) + \sum_{j=1}^{m-1}\prod_{i=1}^{j}(x_k - x_i)\right]. \tag{6.12}$$

If $k = 1$, then all the terms under the summation sign will vanish yielding:

$$\frac{d}{dx}R(f, X; x)|_{x=x_1} = \frac{f^{(m)}(\theta(x_1))}{m!}\prod_{i=2}^{m}(x_1 - x_i), \tag{6.13}$$

$$\frac{d}{dx}R(f, X; x)|_{x=x_1} = \frac{f^{(m)}(\theta(x_1))}{m!}\prod_{k\neq i=1}^{m}(x_1 - x_i). \tag{6.14}$$

The absolute value of this error term is clearly $\leqslant O(\delta^{m-1})$. Thus if m is the order of approximation of formula (5.7), then $m - 1$ is the order of approximation of formula (5.9) for the first derivative operator. Similarly, it can be shown under suitable conditions on $\theta(x)$ and $f^{(l)}(\theta(x))$ that

$$\left|\frac{d^n}{dx^n}R(r, \bar{X}; x)\right|_{x=x_k} \leqslant O(\delta^{m-n}). \tag{6.15}$$

7. A three point estimator formula for the first derivative of a function

From the results of section 6, we know that a three point formula of type 6.9 should yield an error of order 2. To define the Lagrange coefficient matrix, define the fundamental polynomials as:

$$\pi_j(x) = \prod_{j=i=1}^{3}(x - x_i). \tag{7.1}$$

Then the three point Lagrange coefficient matrix is

$$\Lambda_3 = \begin{pmatrix} \frac{x_2x_3}{\pi_1(x_1)} & \frac{-x_2 - x_3}{\pi_1(x_1)} & \frac{1}{\pi_1(x_1)} \\ \frac{x_1x_3}{\pi_2(x_2)} & \frac{-x_1 - x_3}{\pi_2(x_2)} & \frac{1}{\pi_2(x_2)} \\ \frac{x_1x_2}{\pi_3(x_3)} & \frac{-x_1 - x_2}{\pi_3(x_3)} & \frac{1}{\pi_3(x_3)} \end{pmatrix}. \tag{7.2}$$

Let D_1, D_2 and D_3 be the weighting vectors of formula (6.10) for the derivative at points x_1, x_2 and x_3, respectively. Since

$$\frac{d}{dx}M_3(x) = \begin{pmatrix} 0 \\ 1 \\ 2x \end{pmatrix}, \tag{7.3}$$

we have

$$\frac{\mathrm{d}}{\mathrm{d}x}f(x)\Big|_{x=x_i} = \left(\Lambda_3 \cdot \begin{pmatrix} 0 \\ 1 \\ 2x_i \end{pmatrix}\right)^{\mathrm{T}} f\begin{pmatrix} x_1 \\ x_2 \\ x_3 \end{pmatrix}, \tag{7.4}$$

or

$$D_i = \Lambda_3 \cdot \begin{pmatrix} 0 \\ 1 \\ 2x_i \end{pmatrix}, \tag{7.5}$$

which yields the forward, central and backward differencing estimators, respectively,

$$D_1 = \left(\frac{2x_1 - x_2 - x_3}{\pi_1(x_1)}, \quad \frac{x_1 - x_3}{\pi_2(x_2)}, \quad \frac{x_1 - x_2}{\pi_3(x_3)}\right), \tag{7.6}$$

$$D_2 = \left(\frac{x_2 - x_3}{\pi_1(x_1)}, \quad \frac{2x_2 - x_1 - x_3}{\pi_2(x_2)}, \quad \frac{x_2 - x_1}{\pi_3(x_3)}\right), \tag{7.7}$$

$$D_3 = \left(\frac{x_3 - x_2}{\pi_1(x_1)}, \quad \frac{x_3 - x_1}{\pi_2(x_2)}, \quad \frac{2x_3 - x_1 - x_2}{\pi_3(x_3)}\right). \tag{7.8}$$

To simplify the expressions, we introduce the following

$$\delta_1 = x_2 - x_1\,, \quad \delta_2 = x_3 - x_2\,, \quad \delta = \tfrac{1}{2}(x_3 - x_1) = \tfrac{1}{2}(\delta_1 + \delta_2)\,, \tag{7.9}$$

$$p_1 = \frac{1}{2}\left(\frac{\delta_1}{\delta_2} - 1\right) \to \frac{\delta_1}{\delta_2} = 2\rho_1 + 1\,, \qquad p_2 = \frac{1}{2}\left(\frac{\delta_2}{\delta_1} - 1\right) \to \frac{\delta_2}{\delta_1} = 2\rho_2 + 1\,.$$

The fundamental polynomials then become:

$$\pi_1(x_1) = (x_1 - x_2)(x_1 - x_3) = \delta_1(\delta_1 + \delta_2)\,, \quad \pi_2(x_2) = (x_2 - x_1)(x_2 - x_3) = -\delta_1\delta_2\,,$$
$$\pi_3(x_3) = (x_3 - x_1)(x_3 - x_2) = (\delta_1 + \delta_2)\,\delta_2\,. \tag{7.10}$$

The weight vectors for our estimation formulae then become:

$$D_1 = \left(\frac{-2\delta_1 - \delta_2}{\delta_1(\delta_1 + \delta_2)}, \quad \frac{\delta_1 + \delta_2}{\delta_1\delta_2}, \quad \frac{-\delta_1}{(\delta_1 + \delta_2)\delta_2}\right) = \frac{1}{\delta_1 + \delta_2}\left(-2 - \frac{\delta_2}{\delta_1}, \quad \frac{(\delta_1 + \delta_2)^2}{\delta_1\delta_2}, -\frac{\delta_1}{\delta_2}\right) \tag{7.11}$$

$$= \frac{1}{\delta}(-(3 + 2\rho_2)\,, 2\rho_1 + 1 + 2 + 2\rho_2 + 1\,, -(1 + 2\rho_1)) = \frac{1}{\delta}(-(\tfrac{3}{2} + \rho_2), 2 + (\rho_1 + \rho_2), -(\tfrac{1}{2} + \rho_1))\,,$$

$$D_2 = \left(\frac{-\delta_2}{\delta_1(\delta_1 + \delta_2)}, \quad \frac{\delta_2 - \delta_1}{\delta_1\delta_2}, \quad \frac{\delta_1}{(\delta_1 + \delta_2)\delta_2}\right)$$

$$= \frac{1}{\delta_1 + \delta_2}\left(-\frac{\delta_2}{\delta_1}, \frac{\delta_2^2 - \delta_1^2}{\delta_1\delta_2}, \frac{\delta_1}{\delta_2}\right) = \frac{1}{\delta}(-(\tfrac{1}{2} + \rho_2), \rho_2 - \rho_1, \tfrac{1}{2} + \rho_1)\,, \tag{7.12}$$

$$D_3 = \left(\frac{\delta_2}{\delta_1(\delta_1 + \delta_2)}, \frac{\delta_1 + \delta_2}{-\delta_1\delta_2}, \quad \frac{\delta_1 + 2\delta_2}{(\delta_1 + \delta_2)\delta_2}\right)$$

$$= \frac{1}{\delta_1 + \delta_2}\left(+\frac{\delta_2}{\delta_1}, \quad \frac{-(\delta_1 + \delta_2)^2}{\delta_1\delta_2}, \quad 2 + \frac{\delta_1}{\delta_2}\right) = \frac{1}{\delta}((\tfrac{1}{2} + \rho_2)\,, \quad -(2 + \rho_1 + \rho_2)\,, \quad \tfrac{3}{2} + \rho_1)\,. \tag{7.13}$$

8. Treatment of longitudinal boundary

When treating any point within the cavity or at either longitudinal boundary (where a partially reflecting mirror is situated) there is no problem. But, for example, at $z = 0$, e^+ is determined by eq. (2.35) and not through previous predictor/corrector formulae (7.11)–(7.13) as only e^- is calculated at $z = 0$ in that manner. However, for a point one increment ($\delta = \Delta z$) from the left mirror, one encounters difficulties calculating the forward wave. The second needed point, which is vital to the formulae, would fall outside the cavity. An identical difficulty arises from the counterpart backward wave with respect to the right hand mirror. The field traveling from the right is defined at $z = L$ by eq. (2.36).

To deal with this situation one has to modify the predictor/corrector schemes so that an increment δ^2 is used instead of δ. The loss of that second point, which reduces the accuracy of the derivative estimator maintains near the mirror the same order accuracy. One must compensate this loss by locally reducing the mesh size.

9. A three point estimator formula for the Laplacian of a function

We seek a weighting vector $L = \begin{pmatrix} l_1 \\ l_2 \\ l_3 \end{pmatrix}$ such that

$$\nabla^2 f\Big|_x = \left(\frac{\partial^2 f}{\partial x^2} + \frac{1}{x}\frac{\partial f}{\partial x}\right)\Big|_x = L \cdot f\begin{pmatrix} x_1 \\ x_2 \\ x_3 \end{pmatrix}. \tag{9.1}$$

Because of the linearity of all operations, this may be rewritten:

$$\nabla^2|_x = {}^2D \cdot f(\bar{x}) + \tfrac{1}{2}D \cdot f(\bar{x}), \tag{9.2}$$

where D is the weighting vector for the first derivative derived in the previous section, and ${}^2D$ is the weighting vector for the second derivative. To find ${}^2D$, we note:

$${}^2D\begin{pmatrix} 1 \\ x_2 \\ x \end{pmatrix} = \begin{pmatrix} 0 \\ 0 \\ 2 \end{pmatrix}, \tag{9.3}$$

so that our equations become, using the notation of the previous sections:

$$\left(\Lambda_3\, {}^2D\begin{pmatrix} 1 \\ x \\ x^2 \end{pmatrix}\right)^{\mathrm{T}} = \left(\frac{2}{\delta_1(\delta_1+\delta_2)}, \frac{-2}{\delta_1\delta_2}, \frac{2}{(\delta_1+\delta_2)\delta_2}\right)$$

$$= \frac{2}{\delta^2}\left(1+\frac{\delta_2}{\delta_1}, -\left(2+\frac{\delta_1}{\delta_2}+\frac{\delta_2}{\delta_1}\right), \frac{\delta_1}{\delta_2}+1\right) = \frac{4}{\delta^2}\left(1+\frac{\rho_2}{2}, \left(2+\frac{\rho_1+\rho_2}{2}\right), \quad 1+\frac{\rho_1}{2}\right). \tag{9.4}$$

Note that this formula is independent of x. Combining (9.4) with previous results, we get the following weighting vectors for our Laplacian:

$$L_1 = \frac{4}{\delta^2}\left(1-\frac{3}{2}\left(\frac{\delta}{2x_1}\right)+\frac{\rho_2}{2}\left(1-\frac{\delta}{2x_1}\right)-\left(2-2\left(\frac{\delta}{2x_1}\right)+\frac{(\rho_1+\rho_2)}{2}\left(1-\frac{\delta}{2x_1}\right)\right), \quad 1-\frac{1}{2}\left(\frac{\delta}{2x_1}\right)+\frac{\rho_1}{2}\left(1-\frac{\delta}{2x_1}\right)\right), \tag{9.5}$$

$$L_2 = \frac{4}{\delta^2}\left(1-\frac{1}{2}\left(\frac{\delta}{2x_2}\right)+\frac{\rho_2}{2}\left(1-\frac{\delta}{2x_2}\right), \quad -\left(2+\frac{\rho_1}{2}\left(1+\frac{\delta}{2x_2}\right)+\frac{\rho_2}{2}\left(1\frac{\delta}{2x_2}\right)\right), \quad 1+\frac{1}{2}\left(\frac{\delta}{2x_2}\right)+\frac{\rho_1}{2}\left(1+\frac{\delta}{2x_2}\right)\right), \tag{9.6}$$

$$L_3 = \frac{4}{\delta^2}\left(1+\frac{1}{2}\left(\frac{\delta}{2x_3}\right)+\frac{\rho_2}{2}\left(1+\frac{\delta}{2x_3}\right), \quad -\left(2+2\left(\frac{\delta}{2x_3}\right)+\left(\frac{\rho_1+\rho_2}{2}\right)\left(1-\frac{\delta}{2x_3}\right)\right),\right.$$

$$1+\frac{3}{2}\left(\frac{\delta}{2x_3}\right)+\frac{\rho_1}{2}\left(1+\frac{\delta}{2x_3}\right)\Big). \tag{9.7}$$

If we introduce the variables

$$r_1=\frac{\rho_1}{2}=\frac{1}{2}\left(\frac{\delta_1}{2}-1\right), \tag{9.8}$$

$$r_2=\frac{\rho_2}{2}=\frac{1}{2}\left(\frac{\delta_2}{\delta_1}-1\right), \tag{9.9}$$

$$d=\frac{\delta}{2}=\frac{1}{2}\left(\delta_1+\delta_2\right). \tag{9.10}$$

The formula simplifies to:

$$L_1=\frac{1}{d^2}\left(1-\frac{3}{2}\frac{d}{x_1}+r_2\left(1-\frac{d}{x_1}\right),-\left(2-2\frac{d}{x_1}+(r_1+r_2)\left(1-\frac{d}{x_1}\right)\right),\quad 1-\frac{1}{2}\frac{d}{x_1}+r_1\left(1-\frac{d}{x_1}\right)\right), \tag{9.11}$$

$$L_2=\frac{1}{d^2}\left(1-\frac{1}{2}\frac{d}{x_1}+r_2\left(1-\frac{d}{x_2}\right),-\left(2+r_1\left(1+\frac{d}{x_2}\right)+r_2\left(1-\frac{d}{x_2}\right)\right),\quad 1+\frac{1}{2}\frac{d}{x_2}+r_1\left(1+\frac{d}{x_2}\right)\right), \tag{9.12}$$

$$L_3=\frac{1}{d^2}\left(1+\frac{1}{2}\frac{d}{x_3}+r_2\left(1+\frac{d}{x_3}\right),-\left(2+2\frac{d}{x_3}+(r_1+r_2)\left(1-\frac{d}{x_3}\right)\right),\quad 1+\frac{3}{2}\frac{d}{x_3}+r_1\left(1+\frac{d}{x_3}\right)\right). \tag{9.13}$$

It should be noted that, since the Laplacian involves a second derivative and only three points are used, the above formulae will lead to error term of first order in δ (or d).

This section can be readily extended to a four-point estimator. The details of the derivation can be found in ref. [44].

10. Concluding remarks

Most features of the numerical model used to study temporal and transverse reshaping effects of short optical pulses counter-propagating in a nonlinear Fabry–Perot entry have been presented. The derivation of the differencing formulae was summarized. The experiment strives to achieve a rigorous analysis of this nonlinear interaction with maximum accuracy and minimum computational effort. The applicability of Moretti λ-scheme developed in gas dynamics to this laser physics problem has been demonstrated. Extension of his method to nonuniform grids were carried out. To facilitate the legibility, maintainability and portability of the program, as well as the implementation of further extensions of the planar wave theory, structural modular programming techniques have been used. The resultant code is concise and easy to follow. Results of this algorithm will be presented elsewhere.

Acknowledgements

The authors wish to thank S. Chitlaru for helping deriving the tedious four-point Laplacian formulae. F.P. Mattar would like particularly to express his appreciation to Drs. H.M. Gibbs and S.L. McCall for their unselfish guidance and enlightening discussions in the physics of this work. The hospitality of Dr. T.C. Cattrall at Mobil which made the computations possible is gratefully acknowledged. Furthermore, F.P.M. would also like to

thank Dr. C. Hazzi and D.J. Steele for their extended patience, unselfish support and continuous encouragement during his convalescence. The skillful word processing effort of E. Cummings is joyfully appreciated.

References

[1] S.L. McCall and E.L. Hahn, Phys. Rev. Lett. 18 (1967) 308; Phys. Rev. 183 (1969) 487, A2 (1970).
[2] N. Wright and M.C. Newstein, Opt. Commun. 1 (1973) 8; IEEE J. Quantum Elec. QE-10, (1974) 743.
[3] M.C. Newstein and F.P. Mattar, J. Opt. Soc. Am. 65 (1975) 1181; Opt. Commun. 18 (1976) 70; Recent Advances in optical physics, eds. B. Havelka and J. Blabla, (Soc. of Czechoslovak Math. and Phys., Prague, 1975) p. 299; IEEE J. Quantum Elec. QE-13 (1977) 507.
[4] J.-C. Diels and E.L. Hahn, Phys. Rev. A8 (1973) 1084, A10 (1974) 2501.
[5] S.L. McCall, Phys. Rev. A9 (1974) 1515.
[6] J.A. Fleck, Jr., Phys. Rev. B1 (1970) 84.
[7] R.P. Feyman, F.L. Vernon, Jr. and R.W. Hellwarth, J. Appl. Phys. 28 (1957) 43.
E.L. Hahn, Heritage of the Block equations in quantum optics, to appear in The Felix Bloch Festschrift 75 Birthday.
[8] J.H. Marburger and F.S. Felber, Appl. Phys. Lett. 28 (1976) 731; Phys. Rev. A17 (1978) 335.
[9] R. Sanders and R.K. Bullough, in: Cooperative effects in matter and radiation, eds. C.M. Bowden, D.W. Howgate and H.R. Robl (Plenum, New York, 1977) p. 209.
[10] J.H. Eberly, K.G. Whitney and M. Konopnicki, unpublished Final Research Report to Office of Naval Research (Fall 1977) for research conducted at University of Rochester, Rochester, NY.
[11] H.M. Gibbs, B. Bölger, F.P. Mattar, M.C. Newstein, G. Forster and P.E. Toschek, Phys. Rev. Lett. 37 (1976) 1743.
[12] F.P. Mattar, M.C. Newstein, P.E. Serafim, H.M. Gibbs, B. Bölger, G. Forster and P.E. Toschek, Coherence and quantum optics IV, eds. L. Mandel and E. Wolf (Plenum, New York, 1977) p. 143.
[13] J.H. Marburger, Progress in quantum electronics, vol. 4, eds. J.H. Sanders and S. Stenholm (Pergamon Press, London, New York, 1975) p. 35.
[14] J.H. Marburger, Theory of self-focusing with counter-propagating beams (CW Theory in Kerr cubic nonlinearity medium), preprint.
[15] M.C. Newstein and F.P. Mattar, Proc. 7th Conf. Numerical simulation of plasmas (Courant Inst. of Mathematical Studies, New York, 1975) p. 273.
[16] F.P. Mattar, Appl. Phys. 17 (1978) 53.
[17] F.P. Mattar and M.C. Newstein, Comput. Phys. Commun. 20 (1980) 139.
[18] H.M. Gibbs, B. Bölger and L. Baade, Opt. Commun. 18 (1976) 199.
[19] G. Forster and P.E. Toschek, Spring Annual Meeting of the German Physical Society, Hanover, Fed. Rep. Germany (February 1976).
W. Krieger, G. Gaide and P.E. Toschek, Z. Phys. B25 (1976) 197.
[20] J.J. Bannister, H.J. Baker, T.A. King and W.G. McNaught, Phys. Rev. Lett. 44 (1980) 1062; XI Intern. Conf. of Quantum Electronics, Boston (June 1980).
[21] See refs. [11,12], as well as F.P. Mattar and M.C. Newstein, (ref. [9], p. 139).
F.P. Mattar, Kvantovaya Electronika 4 (1977) 2520.
F.P. Mattar, G. Forster and P.E. Toschek, Kvantovaya Electronika 5 (1978) 1819.
[22] F.A. Hopf and M.O. Scully, Phys. Rev. 179 (1969) 399.
[23] G. Moretti, AIAA 14 (1976) 894; Poly-M/AE Tech. Rep. 78–22 (1980), Polytechnic Institute of New York.
[24] G. Moretti, PIBAL Rep. 70–20 (1970); Proc. ASME Symp. numerical Lab computer methods in fluid mech., ASME (Dec. 1976), Poly M/AE Tech. Rep. 76–06 (1976), Polytechnic Institute of New York.
[25] L. Bradley and J. Hermann, MIT Lincoln Lab Rep. LTP-10 (1971); and internal note On Changes of reference wavefront in the MIT CW nonlinear optics propagation code (1974) (private communication to F.P. Mattar).
[26] P.B. Ulrich, Naval Research Lab. NRL Rep. 7706 (1974).
[27] J.A. Fleck, Jr., J.R. Morris and H.D. Feit, Appl. Phys. 10 (1976) 129, 14 (1977) 99.
[28] G.T. Moore and F.J. McCarthy, J. Opt. Soc. Am. 67 (1977) 221, 228.
[29] D.W. Dolfi and E.L. Hahn, Phys. Rev. A (1980), to appear.
[30] H.M. Gibbs, see ref. [9], p. 61; and lecture on Superfluorescence experiments, 1977 NATO/ASI on Coherence in spectroscopy and modern physics.
Q.H.F. Vrehen, see ref. [9], p. 78; Laser spectroscopy IV, eds. H. Walther and I.W. Rothe.
H.M.J. Hikspoors and H.M. Gibbs, see ref. [12], p. 543.

[31] Q.H.F. Vrehen, H.M.J. Hikspoors and H.M. Gibbs, Phys. Rev. Lett. 38 (1977) 764, 39 (1977) 547; Laser spectroscopy III, eds. by J.I. Hall and J.I. Carlsten (Springer-Verlag, Berlin, 1977).
[32] J.C. MacGillivray and M.S. Feld, Phys. Rev. A14 (1974); ref. [9], p. 1.
M.S. Feld and J.C. MacGillivray, in: Advances in coherent nonlinear optics, eds. M.S. Feld and V.S. Letokhov (Springer-Verlag, Berlin, 1981).
[33] F.P. Mattar, H.M. Gibbs, S.L. McCall and M.S. Feld, Phys. Rev. Lett. 46 (1981) 1123, and European Conf. on Atomic physics (April 1981) paper W10, eds. J. Kowalski, G. zu Putlitz and H.B. Weber, publ. European Phys. Soc.
[34] T.N.C. Venkatesan, Opt. News 5 (1979) 6; J. Opt. Soc. Am. 65 (1975) 1184; Phys. Rev. Lett. 36 (1976) 1135;
US patents no. 012 699 (1975) and no. 121 167 (1976), lecture on optical bistability and differential gains at 1977 NATO/ASI on Coherence in spectroscopy and modern physics (Plenum, New York, 1975).
[35] T.N.C. Venkatesan and S.L. McCall, Appl. Phys. Lett. 30 (1977) 282.
H.M. Gibbs, S.L. McCall, T.N.C. Venkatesan, A.C. Gossard, A. Passner and W. Wiegmann, IEEE J. Quantum Electron. QE-15 (1979) 108D; Appl. Phys. Lett. 35 (1979) 451.
S.L. McCall and H.M. Gibbs, Opt. Commun. (1980).
H.M. Gibbs, S.L. McCall and T.N.C. Venkatesan, Special issue on Optical feedback in Opt. Eng., to be published.
[36] T. Bischofberger and Y.R. Shen, Appl. Phys. Lett. 32 (1978) 156; Opt. Lett. 4 (1979) 40, 175 Phys. Rev. A19 (1979) 1169.
[37] H.M. Gibbs and R.E. Slusher, Appl. Phys. Lett. 18 (1971) 505; Phys. Rev. A5 (1972) 1634, A6 (1972) 2326.
[38] G. Moretti, Comput. Fluids 7 (1979) 191.
B. Gabutti, La stabilita de una schema all differenze finite per le equazioni della fluide dinamica, Politechnico di Milano, preprint.
[39] G. Moretti, PIBAL Rep. 68–15 (1968), Polytechnic Institute of New York.
[40] R.W. MacCormack, AIAA hypervelocity impact Conf. (1969) paper 69–554.
[41] R.W. MacCormack, Lecture notes in physics (Springer-Verlag, Berlin, 1971) p. 151.
[42] P. Gordon, General Electric Final Rep. NOL Contract ≠N60921-7164 (1968).
[43] R.W. Hamming, Numerical methods for scientists and engineers (McGraw-Hill, New York, Maidenhead, 1962).
[44] F.P. Mattar, G. Moretti and R.E. Franceour, POLY-M/AE ADL Technical Report 80–12 (1980).

Computer Physics Communications 22 (1981) 1–11
North-Holland Publishing Company

FLUID FORMULATION OF HIGH INTENSITY LASER BEAM PROPAGATION USING LAGRANGIAN COORDINATES *

F.P. MATTAR **
Aerodynamics Laboratory, Polytechnic Institute of New York,
and
Physics Department, University of Montreal, Montreal, Canada

J. TEICHMANN
Physics Department, University of Montreal, Montreal, Canada

Received 28 June 1979; in revised form 6 October 1980

The complete mathematical modeling of nonlinear light-matter interaction is presented in a hydrodynamic context. The field intensity and the phase gradient are the dependent variables of interest. The resulting governing equations are a generalization of the Navier–Stokes equations. This fluid formulation allows the insights and the methodologies which have been gained in solving hydrodynamics problems to be extended to nonlinear optics problems. To insure effective numerical treatment of the anticipated nonlinear self-lensing phenomena, a self-adjusted nonuniform redistribution, along the direction of propagation, of the computation points according to the actual local requirements of the physics must be used. As an alternative to the application of adaptive rezoning techniques in conjunction with Eulerian coordinates, Lagrangian variables are used to provide automatically the desired nonlinear mapping from the physical plane into the mathematical frame. In this paper we propose a method suitable for the solution of the described problem in one-dimensional cases as well as in two-dimensional cases with cylindrical symmetry. To overcome the numerical difficulties related to the inversion of the Jacobian, an analytical algorithm based on the paraxial approximation was developed.

1. Introduction

When sufficiently strong optical beams propagate through nonlinear media, significant self-action phenomena [1] can occur and the propagation characteristics are significantly altered from the vacuum propagation [2]. In particular, self-lensing associated with the nonlinear index of refraction of the medium appears. The corresponding nonlinear beam distortion due to the nonlinear interaction can be rigorously solved only by using appropriate numerical methods since the equations are far too complicated to be handled by any known analytical techniques.

Should the beam focus along the direction of propagation, its transverse dimensions will drastically change at the focal point from what it was at the aperture. It becomes necessary that the transverse dimensions of the three-dimensional grids shrink/expand in size as the focal point is approached/passed [3–8,17].

For the nonlinear interaction, the actual desired shrinkage/expansion of the transverse mesh cannot be guessed a priori; it must be locally determined by the solution to the problem itself. It is therefore necessary to have the

* A numerical algorithm associated with the hydrodynamic analogy of quantum mechanics was previously developed by the same authors, using explicit finite differencing methods in Eulerian coordinates as well as splitting and self-adaptive rezoning. The paper was presented at the Second International Symposium on Gas Flow and Chemical Lasers, Western Hemisphere (1979) held on 11–15 September 1978, at the Von Karman Institute of Fluid Dynamics in Belgium.

** Partially supported by the Research Corporation, the Army Research Office, the Office of Naval Research and the International Division of Mobil. Present address: Laser Spectroscopy Laboratory, MIT, Cambridge, MA, USA.

0010–4655/81/0000–0000/$02.50

three-dimensional space grid changing concomitantly with the actual beam shape and size and the local wave-front. To avoid oscillatory behavior associated with the decomposing of the electric field into its real and imaginary parts, it is necessary to describe the field using the modulus and the phase [9–12].

The present paper deals with the hydrodynamic analogy [11,12] of the problem of nonlinear propagation.

In this approach, the evolution of the beam is interpreted in terms of a flowing fluid whose density is proportional to the gradient of the phase. This description allows the treatment of more slowly varying dependent variables and yields equations of motion that are similar and equivalent to those obtained by the method of moments used for the average description of the beam propagation characteristics [1,13–15]. Furthermore, this scheme could allow even larger and coarser marching mesh sizes if it were used simultaneously with an automatically adaptive nonuniform rezoned coordinate system. The set of governing equations thus obtained is a generalization of the Navier–Stokes equations [16–18] that describe a compressible fluid subjected to an internal potential which depends solely and nonlinearly upon the fluid density and its derivatives. This internal potential is often referred to as the quantum mechanical potential.

A further transformation of the dependent variable, namely the use of the natural logarithm of the density, is also introduced [17] to simplify the numerics. To generate an effective and reliable computational code with modest storage requirements, one usually introduces mapping techniques which consist of various function and coordinate transformations. An alternative method to this systematic is the adoption of Lagrangian coordinates. The Lagrangian approach [19] operates with the displacement of a fluid element, following the temporal evolution of its trajectory. In this way, one easily finds the evolution of the phase and the energy in the plane transverse to the direction of the beam propagation. Hence, the system of Lagrangian trajectories corresponds to the automatic self-adaptive nonuniform rezoning and mapping techniques used in the usual Eulerian system; it should also ensure an optimum redistribution of the computational points during the calculation in the various regions of interest. Furthermore, the number of equations is reduced (in comparison to the Eulerian description), and the coupling between the different variables is strengthened, thus accelerating the rate of convergence of the algorithms.

The organization of this paper is as follows: section 2 presents the equations of motion. Section 3 is devoted to the energy conservation and the motivation for an identification of physical variables. Section 4 introduces the fluid description. Section 5 reviews the method of moments. Section 6 summarizes the proposed algorithm based on the Lagrangian formulation. Section 7 presents the conclusion.

2. Equations of motion

For the class of problems describing the propagation of optical signals, the slowly varying envelope approximation is usually adopted, namely [1]

$$E(r, t) = \mathrm{Re}\left\{e(r, t) \exp\left[\mathrm{i}\left(\frac{\omega_0}{c} z - \omega_0 t\right)\right]\right\}, \tag{1}$$

where z designates the propagation direction. Assuming that the complex amplitude $e(r, t)$ changes by a small fractional amount, temporally in the optical period $2\pi/\omega_0$ and spatially in the optical wavelength $2\pi c/\omega_0$, the field equation becomes first order in z and t and reduces, for a linearly polarized light, to the quasi-optics equation

$$-\frac{\mathrm{i}}{2\omega_0} \frac{c}{n_0} \nabla_{\mathrm{T}}^2 e + \frac{\partial}{\partial z} e + \frac{n_0}{c} \frac{\partial}{\partial t} e = \gamma |e^2| e. \tag{2}$$

Here, n_0 is the linear index of refraction of the background material, γ is proportional to the nonlinear part of the refractive index n_2, $n = n_0 + n_2 |e|^2 e$. The differential operator ∇_{T}^2 is the transverse Laplacian in Cartesian coordinates. The time scale is normalized to a characteristic time τ_p of the input pulse and the transverse dimen-

sion scales to a characteristic spatial width r_p of the input pulse. The input beam is supposed to have azimuthal symmetry. By introducing a moving frame of reference,

$$\eta = z, \quad \tau = t - (n_0/c)z \tag{3}$$

the quasi-optics equation (2) reduces to the nonlinear Schrödinger equation:

$$-\frac{i}{2\omega_0}\frac{c}{n_0}\nabla_T^2 e + \frac{\partial}{\partial\eta}e = \gamma|e^2|e. \tag{4}$$

3. Energy relations

By multiplying eq. (4) by e^* and adding the complex conjugate, one obtains (with $\gamma = \gamma_1 + i\gamma_2$)

$$\frac{i}{2\omega_0}\frac{c}{n_0}(e\nabla_T^2 e^* - e^*\nabla_T^2 e) + \frac{\partial}{\partial\eta}|e^2| = 2\gamma_1|e^4| \tag{5}$$

or equivalently

$$\nabla_T \cdot J_T + \partial J_z/\partial\eta = 2\gamma_1|e^4|, \tag{6}$$

where $J_z = |e^2| = A^2$,

$$J_T = (2\omega_0 n_0)^{-1} c\nabla_T \cdot (e\nabla_T e^* - e^*\nabla_T e) = (c/n_0\omega_0)[A^2(\nabla_T\phi)].$$

In the last relation, the polar representation of the complex envelope was used:

$$e = A\exp(i\phi), \tag{7}$$

where A and ϕ are the real functions of coordinates.

The components J_z and J_T represent the longitudinal and transverse energy density flow. Thus, the existence of the transverse energy density current is related to the transverse gradient of the phase ϕ of the complex field (7). When $J_T < 0$ (i.e., $\nabla_T\phi < 0$), self-induced focusing dominates the spreading due to diffraction [20]. The choice of the intensity A^2 and the gradient of the phase ϕ as new variable is physically enlightening and eliminates most of the oscillatory phase difficulties [2] associated with the use of real and imaginary parts of the electric field.

4. Fluid description

Let the nonlinear polarization on the r.h.s. of eq. (4) be written as

$$P^{NL} = (\chi_R + i\chi_I)e = \chi_{NL}e, \tag{8}$$

where χ_R and χ_I are real functions of A. Using eq. (7), one obtains from eq. (4) the transport the the eikonal equations ($n_0 = k_0 c/\omega_0$) [21]:

$$k_0\frac{\partial}{\partial\eta}A^2 + \nabla_T \cdot [A^2\nabla_T\phi] = -\frac{4\pi\omega_0^2}{c^2}\chi_I A^2, \tag{9}$$

$$2k_0\frac{\partial}{\partial\eta}\phi + \left[(\nabla_T\phi)^2 - \frac{A\cdot\nabla_T^2 A}{A^2}\right] = \frac{4\pi\omega_0^2}{c^2}\chi_R. \tag{10}$$

The transport equation (9) expresses the conservation of beam energy over the transverse plane. When $\chi_I = 0$, the

total power is conserved along the direction of propagation. The eikonal equation (10) describes the evolution of the surface of constant phase. It has the form of the Hamilton–Jacobi equation for the two-dimensional motion of particles having unit mass and moving under the influence of potential [1] given by

$$V = -\frac{1}{2k_0^2}(\nabla_T^2 A)A^{-1} - \frac{2\pi}{n_0^2}\chi_R, \tag{11}$$

if $k_{0z}z$ is regarded as time coordinate and $k_{0x}x$, $k_{0y}y$ as spatial coordinates. Furthermore, if one adopts A^2 and $\nabla_T\phi$ as new dependent variables, the equations of motion become similar to the continuity and momentum transport equations of ordinary hydrodynamics.

By defining

$$\mathbf{v} = k_0^{-1}\nabla_T\phi, \quad \rho = A^2 \tag{12}$$

and supposing $\chi_I = 0$, eqs. (9) and (10) can be written as

$$\frac{\partial \mathbf{v}}{\partial \eta} + (\mathbf{v}\cdot\nabla_T)\mathbf{v} = \frac{1}{2k_0^2}\nabla_T[\rho^{-1/2}(\nabla^2\sqrt{\rho})] + \frac{\gamma_2}{k_0}(\nabla_T\rho), \tag{13}$$

$$\frac{\partial \rho}{\partial \eta} + \nabla_T\cdot(\rho\mathbf{v}) = 0. \tag{14}$$

These equations are the momentum and continuity transport equations of a fluid with a pressure $P = (\nabla_T^2\sqrt{\rho})/\sqrt{\rho}$. It should be emphasized that this pressure depends here solely on the "fluid density" and not on the "velocity". Eq. (13) can be rearranged into

$$\frac{\partial}{\partial \eta}(\rho\mathbf{v}) + \nabla_T\cdot(\rho\mathbf{v}\mathbf{v}) = \frac{1}{2k_0^2}\nabla_T\cdot\left[\tfrac{1}{2}(\nabla_T^2\rho)\mathbf{I} - \frac{1}{2\rho}(\nabla_T\rho)(\nabla_T\rho)\right] + \frac{\gamma_2}{k_0}\rho(\nabla_T\rho), \tag{15}$$

where $\mathbf{I}$ is the unit tensor.

5. The averaged description of wave beams in nonlinear media, the method of moments

The existence of constants of motion and conservation laws, even in a limited number, is very useful for obtaining insight into the dynamics of the self-action phenomena associated with the propagation process. To analyze the nonlinear quasi-optic propagation, Vlasov et al. [13] extended the method of moments, originally developed in connection with the transport theory. In this theory the problem of finding a certain distribution $f(\xi)$ is replaced by that of determining the moments $M_n = \int_{-\infty}^{+\infty}\xi^n f(\xi)\,d\xi$ of this distribution, which are usually more easily calculated than the function $f(\xi)$ itself. Knowledge of all the moments allows the use of known methods to reconstruct the form of the function $f(\xi)$. A simple expression for estimating the width of the diffracted beam is derived in terms of the zero, first-order moment and second-order centrifugal moment integrals of the incident field. These moments are integrated over the full beam cross-section and are, therefore, functions of the propagation coordinate only. The theory of moments only holds when the susceptibility is a function of $|e|^2$, (i.e., when the nonlinear index of refraction is a cubic or fifth-order power in the field).

The starting point of the method of moments is the recognition that the existence of a hierarchy of conservation equations [13,15]

$$\frac{\partial w}{\partial t} = -\nabla\cdot J, \quad \frac{\partial}{\partial t}J = c^2\nabla\cdot\mathbf{T}, \quad \frac{\partial}{\partial t}[\mathrm{Tr}(\mathbf{T})] = -\nabla\cdot Q, \tag{16}$$

implies a relation between the conserved quantities and the time derivatives of the moments of w. Here, w is scalar, J and Q are vectors and $\mathbf{T}$ is a symmetric tensor of second rank having the trace $\mathrm{Tr}(\mathbf{T})$. The first three

moments of w are defined as follows:

$$W = \int_V \mathrm{d}V\, w, \quad \boldsymbol{S} = \frac{1}{W}\int_V \mathrm{d}V\, \boldsymbol{r} w, \quad (Q_{\mathrm{eff}})^2 = \frac{1}{W}\int_V \mathrm{d}V\, r^2 w. \tag{17}$$

The integrals are taken over the volume in which the field quantities are defined, and $\boldsymbol{r}$ is the position vector. Using the Gauss theorem, it can readily be shown that

$$\frac{\mathrm{d}W}{\mathrm{d}t} = \frac{\mathrm{d}^2\boldsymbol{S}}{\mathrm{d}t^2} = \frac{\mathrm{d}^3}{\mathrm{d}t^3}(Q_{\mathrm{eff}}^2) = 0.$$

In deriving these results, it was assumed that

$$\hat{\boldsymbol{n}} \cdot \boldsymbol{J} = \hat{\boldsymbol{n}} \cdot \boldsymbol{Q} = \hat{\boldsymbol{n}} \cdot \mathbf{T} = 0$$

on the closed boundary Σ with normal $\hat{\boldsymbol{n}}$ of the volume V. If Σ is at infinity, all integrals converge. It thus follows that

$$W = W_0, \quad \boldsymbol{S} = \boldsymbol{S}_0 + \boldsymbol{\upsilon} \cdot t \quad \text{and} \quad (Q_{\mathrm{eff}}^2) = Q_0^2 + 2c_1 t + c_2 t^2, \tag{18}$$

where $\boldsymbol{S}_0 = \boldsymbol{S}(t=0)$, $Q_0 = Q(t_0)$ and

$$\boldsymbol{\upsilon} = \frac{1}{W_0}\int_V \mathrm{d}V\, \boldsymbol{J}|_{t=0}, \quad c_1 = \frac{1}{S_0}\int_V \mathrm{d}V\, \boldsymbol{r} \cdot \boldsymbol{J}|_{t=0}, \quad c_2 = -\frac{1}{W_0}\int_V \mathrm{d}V\, \mathrm{Tr}(\mathbf{T})|_{t=0}.$$

The relations (18) have a simple physical meaning: the energy W of the field is conserved, the energy center $\boldsymbol{S}$ moves along a straight line with a constant speed $\boldsymbol{\upsilon}$ and the square of the effective radius of the bunch, Q_{eff}^2, varies according to a parabolic law (for $t \to \infty$, $Q_{\mathrm{eff}} \approx t$). It can readily be verified that the conserved quantities satisfy

$$\boldsymbol{\upsilon} = \frac{\partial}{\partial t}\int_V \mathrm{d}V\, \boldsymbol{r} w \quad \text{and} \quad c_2 = \frac{\partial^2}{\partial t^2}\int_V \mathrm{d}V\, r^2 w. \tag{19}$$

The hierarchy of conservation laws is satisfied by Maxwell's vacuum equation when W is the density of electromagnetic energy, $\boldsymbol{J}$ is the Poynting vector and $\mathbf{T}$ is the Maxwell stress tensor.

Using the transformation (7) and introducing the fluid quantities (12), one obtains for the quasi-optics equation (4) where $t \to \eta$, $\nabla \to \nabla_{\mathrm{T}}$ and $\gamma_1 = 0$

$$w = \rho, \quad \boldsymbol{J} = \rho\boldsymbol{\upsilon},$$

$$T_{\alpha\beta} = -\frac{1}{4k_0^2\rho}\left[(\nabla_\alpha\rho)(\nabla_\beta\rho) - \rho\upsilon_\alpha\upsilon_\beta + \frac{1}{4k_0^2}\delta_{\alpha\beta}(\nabla_{\mathrm{T}}^2\rho) + \frac{\gamma_2}{2k_0}\delta_{\alpha\beta}\rho^2\right], \qquad \alpha,\beta = x,y,$$

$$\mathrm{Tr}(\mathbf{T}) = \frac{1}{2k_0^2}\left[(\nabla_{\mathrm{T}}^2\rho) - \tfrac{1}{2}\rho^{-1}(\nabla_{\mathrm{T}}\rho)^2 - 2k_0^2\rho(\boldsymbol{\upsilon}\cdot\boldsymbol{\upsilon}) + 2k_0\gamma_2\rho^2\right],$$

$$Q = \frac{1}{2k_0^2}\left\{\nabla_{\mathrm{T}}[\nabla_{\mathrm{T}} \cdot (\rho\boldsymbol{\upsilon})] - (\nabla_{\mathrm{T}}\rho)(\nabla_{\mathrm{T}}\cdot\boldsymbol{\upsilon}) + \boldsymbol{\upsilon}[(\nabla_{\mathrm{T}}^2\rho) - \tfrac{1}{2}\rho^{-1}(\nabla_{\mathrm{T}}\rho)^2 - 2k_0^2\rho(\boldsymbol{\upsilon}\cdot\boldsymbol{\upsilon})]\right\} + \frac{2}{k_0}\gamma_2\rho^2 \ . \tag{20}$$

The equation of the effective beam radius is now

$$Q_{\mathrm{eff}}^2 = Q_0^2 + 2c_1\eta + c_2\eta^2 \tag{21}$$

with the following constants of motion:

$$W_0 = \int_\Sigma \mathrm{d}\sigma\, \rho|_{\eta=0}$$

$$Q_0^2 = \frac{1}{W_0}\int_\Sigma d\sigma\, r^2 \rho|_{\eta=0}$$

$$c_1 = \frac{1}{W_0}\int_\Sigma d\sigma\, r\cdot(\rho v)|_{\eta=0}$$

$$c_2 = -\frac{1}{W_0}\frac{1}{2k_0^2}\int_\Sigma d\sigma\{(\nabla_T^2\rho) - \tfrac{1}{2}\rho^{-1}(\nabla_T\rho)^2 - 2k_0^2\rho(v\cdot v) + 2\gamma_2 k_0\rho^2\}|_{\eta=0}. \tag{22}$$

The beam quantities (20) verify the conservation relations (16). The invariant c_1 is related to the transverse energy current. In terms of amplitude and phase, the integrand is $A^2(r\cdot\nabla_T\phi)$. This shows that when the transverse current of energy, which is proportional to the transverse gradient of the phase ϕ, is negative ($\nabla_T\phi<0$), self-induced lensing dominates diffraction spreading. It should be pointed out that these results only are valid for a nonconfined beam of finite power. The integrals in the x,y plane around the outside boundary of the beam cross-section can only vanish if both e and $\nabla_T e$ vanish. This is not possible on a finite boundary unless e vanishes everywhere. For a finite beam the boundary should recede to infinite. In the numerical solution it is necessary to introduce a perfect conducting wall. The surface integrals remain finite, although small. For this reason numerical solution will disagree with the average mean square radius calculated from the method of moments by a small finite difference.

A similar hierarchy of moments was derived via the quasi-particle approach [22]. An alternative to the Schrödinger picture [13] discussed here is the Heisenberg picture proposed in ref. [23]. Although both methods give the same expectation values, the Heisenberg picture is believed to be simpler.

The method of moments as outlined here represents a local check to the numerical analysis giving the average estimate for quantities related to e^2.

6. The Lagrangian formulation

Let us summarize the fluid equations taking the quasi-optics relation (4) with the nonlinear polarization term in the form (9). One has for $\chi_I \neq 0$ (nonzero gain or absorption)

$$\frac{\partial}{\partial\eta}\rho + \nabla_T\cdot(\rho v) = \frac{1}{k_0}\chi_I\rho, \quad \rho\left[\frac{\partial}{\partial\eta}v + (v\cdot\nabla_T)v\right] = \frac{1}{2k_0^2}\rho\nabla_T[\rho^{-1/2}\nabla_T^2(\rho^{1/2}) + \chi_R]. \tag{23}$$

The second equation can be rewritten as

$$\rho\left[\frac{\partial}{\partial\eta}v + (v\cdot\nabla_T)v\right] = \frac{1}{4k_0^2}\nabla_T[\rho\nabla_T^2(\ln\rho)] + \frac{\rho}{2k_0^2}\nabla_T\chi_R$$

or, by analogy with usual "fluid" equations, as

$$\rho\left[\frac{\partial}{\partial\eta} + (v\cdot\nabla_T)\right]v = \nabla_T P + \frac{\rho}{2k_0^2}\nabla_T\chi_R, \tag{24}$$

where the scalar function P is defined as

$$P = \frac{1}{4k_0^2}[\rho\nabla_T^2(\ln\rho)]. \tag{25}$$

To elaborate the appropriate computational code, we transform eqs. (23) and (24) into the Lagrangian coordinates [19].

The two hydrodynamic equations (23) may be rewritten in the Eulerian coordinates ($\chi_I = 0$) in the form

$$\frac{D}{D\eta}\rho + \rho\nabla_T \cdot \upsilon = 0, \qquad \rho\frac{D}{D\eta}\upsilon = \nabla_T P,$$

where $D/D\eta = \partial/\partial\eta + \upsilon \cdot \nabla_T$ is the Eulerian derivative describing the motion of the fluid element in a given point of the laboratory frame of reference. Let us transform eq. (23) into Lagrangian coordinates in which the observer moves with the fluid element. In this way, the local derivative $\partial/\partial\eta$ becomes equal to the total derivative $D/D\eta$ although the new coordinates will be related to the initial position of the fluid element [24].

6.1. The one-dimensional case

Let X, η be the Eulerian coordinates and $X = X_0$ ($\eta = 0$ define the Lagrangian coordinate X_0. The speed υ is defined in the one-dimensional case as $\upsilon = \partial X/\partial\eta$.

The transformation relations are as follows:

$$X = X(X_0, \eta_L) = X_0 + \int_0^{\eta_L} d\eta'_L\, \upsilon(X_0, \eta'_L), \qquad \eta = \eta_L. \tag{26}$$

It thus follows that

$$\frac{\partial}{\partial X} = \left(\frac{\partial X}{\partial X_0}\right)^{-1}\frac{\partial}{\partial X_0}, \qquad \frac{\partial}{\partial \eta_L} = \frac{\partial}{\partial\eta} + \frac{\partial X}{\partial\eta}\frac{\partial}{\partial X}.$$

The first equation (23) gives for $\chi_I = 0$

$$\frac{\partial\rho}{\partial\eta_L} + \rho\left(\frac{\partial X}{\partial X_0}\right)^{-1}\frac{\partial}{\partial X_0}\frac{\partial X}{\partial\eta_L} = 0,$$

which integrates to the mass conservation law

$$\rho = \rho_0(\partial X/\partial X_0)^{-1}. \tag{27}$$

The second equation (24) transforms with the help of (27) into

$$\rho_0\frac{\partial^2 X}{\partial\eta_L^2} = \frac{\partial}{\partial X_0}P + \frac{1}{2k_0^2}\rho_0\left(\frac{\partial X}{\partial X_0}\right)^{-1}\frac{\partial}{\partial X_0}\chi_R. \tag{28}$$

Using eq. (27), the scalar function P reads in Lagrangian coordinates

$$P = \frac{1}{4k_0^2}\left\{\rho\left[2\left(\frac{\partial X}{\partial X_0}\right)^{-4}\left(\frac{\partial^2 X}{\partial X_0^2}\right)^2 - \left(\frac{\partial X}{\partial X_0}\right)^{-3}\left(\frac{\partial^3 X}{\partial X_0^3}\right)\right]\right\} \tag{29}$$

and eq. (28) gives, using eq. (29),

$$\frac{\partial^2 X}{\partial\eta_L^2} = \frac{1}{4k_0^2}\left\{-\left(\frac{\partial X}{\partial X_0}\right)^{-5}\left(\frac{\partial^2 X}{\partial X_0^2}\right)\left[2\left(\frac{\partial X}{\partial X_0}\right)^{-1}\left(\frac{\partial^2 X}{\partial X_0^2}\right)^2 - \left(\frac{\partial^3 X}{\partial X_0^3}\right)\right]\right.$$
$$\left. + \left(\frac{\partial X}{\partial X_0}\right)^{-4}\left[7\left(\frac{\partial X}{\partial X_0}\right)^{-1}\left(\frac{\partial^2 X}{\partial X_0^2}\right)\left(\frac{\partial^3 X}{\partial X_0^3}\right) - 8\left(\frac{\partial X}{\partial X_0}\right)^{-2}\left(\frac{\partial^2 X}{\partial X_0^2}\right)^3 - \left(\frac{\partial^4 X}{\partial X_0^4}\right)\right] + 2\left(\frac{\partial X}{\partial X_0}\right)^{-1}\frac{\partial}{\partial X_0}\chi_R\right\}. \tag{30}$$

The system of fluid equations (23) reduces to a single equation in X which has a second-order derivative in variable η and derivatives in X_0 up to fourth order.

For a nonlinear media with a nonvanishing χ_I, the first equation (23)

$$\frac{\partial}{\partial\eta}\rho + \upsilon\frac{\partial}{\partial X}\rho + \rho\frac{\partial}{\partial X}\upsilon = \frac{1}{k_0}\chi_I\rho$$

is transformed into

$$\frac{\partial}{\partial \eta_L}\left[\ln\left(\rho\frac{\partial X}{\partial X_0}\right)\right]=\frac{1}{k_0}\chi_I$$

which by integration gives

$$\rho\left(\frac{\partial X}{\partial X_0}\right)=\rho_0\exp\left\{\frac{1}{k_0}\int_0^{\eta_L}\mathrm{d}\eta'_L\,\chi_I\right\}. \tag{31}$$

With this dependence of ρ on η_L, the second equation (24) reads

$$\rho_0\exp\left\{\frac{1}{k_0}\int_0^{\eta_L}\mathrm{d}\eta_L\,\chi_I\right\}\frac{\partial^2 X}{\partial\eta_L^2}=\frac{\partial}{\partial X_0}P+\frac{1}{2k_0^2}\rho_0\left(\frac{\partial X}{\partial X_0}\right)^{-1}\left(\frac{\partial}{\partial X_0}\chi_R\right)\exp\left\{\frac{1}{k_0}\int_0^{\eta_L}\mathrm{d}\eta'_L\,\chi_I\right\}. \tag{32}$$

6.2. Two-dimensional case in cylindrical geometry

In cylindrical coordinates, the system (23) reads

$$\frac{\partial}{\partial\eta}\rho+v_r\frac{\partial}{\partial r}\rho+\rho\frac{1}{r}\frac{\partial}{\partial r}(rv_r)=\frac{1}{k_0}\rho\chi_I,$$

$$\rho\left(\frac{\partial}{\partial\eta}v_r+v_r\frac{\partial}{\partial r}v_r\right)=\frac{1}{4k_0^2}\frac{\partial}{\partial r}\left\{\rho\frac{1}{r}\frac{\partial}{\partial r}\left[r\frac{\partial}{\partial r}(\ln\rho)\right]\right\}+\frac{\rho}{2k_0^2}\frac{\partial}{\partial r}\chi_R. \tag{33}$$

Introducing the Lagrangian variables r_{0L}, η_L

$$r_E=r_E(r_{0L},\eta_L),\quad \eta_E=\eta_L,$$

we find the solution of the first relation (38) in the form (for $\chi_I=0$)

$$\rho=\rho_0\left(\frac{\partial r_E}{\partial r_{0L}}\right)^{-1}\frac{r_{0L}}{r_E}. \tag{34}$$

Let us define the fluid "pressure" by analogy with previous cases as

$$P=\frac{1}{4k_0^2}\left\{\rho\frac{1}{r_E}\frac{\partial}{\partial r_E}\left[r_E\frac{\partial}{\partial r_E}(\ln\rho)\right]\right\}. \tag{36}$$

The scalar P is explicitly

$$P=\frac{1}{4k_0^2}\rho\left(\frac{\partial r_E}{\partial r_{0L}}\right)^{-2}\left[2\left(\frac{\partial r_E}{\partial r_{0L}}\right)^{-2}\left(\frac{\partial^2 r_E}{\partial r_{0L}^2}\right)^2-\left(\frac{\partial r_E}{\partial r_{0L}}\right)^{-1}\left(\frac{\partial^3 r_E}{\partial r_{0L}^3}\right)-\frac{1}{r_E}\left(\frac{\partial^2 r_E}{\partial r_{0L}^2}\right)\right]. \tag{37}$$

Finally, the eq. (36) becomes

$$\begin{aligned}\frac{\partial^2 r_E}{\partial\eta_L^2}=\frac{1}{4k_0^2}\Bigg\{&\left[-\left(\frac{\partial r_E}{\partial r_{0L}}\right)^{-2}\left(\frac{\partial^2 r_E}{\partial r_{0L}^2}\right)-\frac{1}{r_E}\right]\left[2\left(\frac{\partial r_E}{\partial r_{0L}}\right)^{-4}\left(\frac{\partial^2 r_E}{\partial r_{0L}^2}\right)^2-\left(\frac{\partial r_E}{\partial r_{0L}}\right)^{-3}\left(\frac{\partial^3 r_E}{\partial r_{0L}^3}\right)\right.\\&\left.-\frac{1}{r_E}\left(\frac{\partial r_E}{\partial r_{0L}}\right)^{-2}\left(\frac{\partial^2 r_E}{\partial r_{0L}^2}\right)\right]+\left(\frac{\partial r_E}{\partial r_{0L}}\right)^{-2}\left[7\left(\frac{\partial r_E}{\partial r_{0L}}\right)^{-3}\left(\frac{\partial^3 r_E}{\partial r_{0L}^3}\right)\left(\frac{\partial^2 r_E}{\partial r_{0L}^2}\right)-8\left(\frac{\partial r_E}{\partial r_{0L}}\right)^{-4}\left(\frac{\partial^2 r_E}{\partial r_{0L}^2}\right)^3\right.\\&\left.-\left(\frac{\partial r_E}{\partial r_{0L}}\right)^{-2}\left(\frac{\partial^4 r_E}{\partial r_{0L}^4}\right)+\frac{1}{r_E^2}\left(\frac{\partial^2 r_E}{\partial r_{0L}^2}\right)+\frac{2}{r_E}\left(\frac{\partial r_E}{\partial r_{0L}^2}\right)^2-\frac{1}{r_E}\left(\frac{\partial r_E}{\partial r_{0L}}\right)^{-1}\left(\frac{\partial^3 r_E}{\partial r_{0L}^3}\right)\right]\Bigg\}+\frac{1}{2k_0^2}\left(\frac{\partial r_E}{\partial r_{0L}}\right)^{-1}\frac{\partial}{\partial r_{0L}}\chi_R.\end{aligned} \tag{38}$$

In the case of the imaginary part of χ, $\chi_I \neq 0$ we have by analogy with eq. (32)

$$\frac{\partial^2 r_E}{\partial \eta_L^2} = \left(\rho_0 \frac{r_{0L}}{r_E}\right)^{-1} \exp\left\{-\frac{1}{k_0}\int_0^{\eta_L} d\eta'_L\, \chi_I(\eta'_L)\right\} \frac{\partial}{\partial r_{0L}} P + \frac{1}{2k_0^2}\left(\frac{\partial r_E}{\partial r_{0L}}\right)^{-1} \frac{\partial}{\partial r_{0L}} \chi_R. \tag{39}$$

Details of the two-dimensional case in Cartesian coordinates can be found in ref. [25].

The evolutional equations (30) and (38) are rather complex due to the presence of the inverse displacement gradient Jacobian J_{ij}. In order to obtain the evolutional equation more accessible to numerical analysis, we limit ourselves to the paraxial approximation, assuming that the beam convergence or divergence, respectively, due to the nonlinear polarization remains small. Let us introduce the Lagrangian displacement ξ [26]

$$\boldsymbol{x} = \boldsymbol{x}_0 + \boldsymbol{\xi}, \quad |\boldsymbol{\xi}| \ll |\boldsymbol{x}_0|, \quad J_{ij} = \frac{\partial X_i}{\partial X_{0j}} = \delta_{ij} + \frac{\partial \xi_i}{\partial X_{0j}}. \tag{40}$$

The value of any function (field) defined on $\boldsymbol{x}$, resulting from the displacement $\boldsymbol{\xi}$ may be expanded in power series of $\boldsymbol{\xi}$ either in form of Eulerian expansions defined at $\boldsymbol{x}(\eta)$, either in form of Lagrangian expansions defined at $\boldsymbol{x}_0(\eta)$. Introducing the Eulerian expansions

$$\rho(\boldsymbol{x}) = \rho_0(\boldsymbol{x}) + \delta_1\rho(\boldsymbol{x}) + \delta_2\rho(\boldsymbol{x}) + \ldots, \qquad \boldsymbol{v}(\boldsymbol{x}) = \boldsymbol{v}_0(\boldsymbol{x}) + \delta_1\boldsymbol{v}(\boldsymbol{x}) + \delta_2\boldsymbol{v}(\boldsymbol{x}) + \ldots$$

into the system (23) and expressing the first and second order changes δ as functions of the displacement $\boldsymbol{\xi}$, we obtain the following hierarchy of evolutional equations [24]. (We assume $\partial/\partial\eta\, \boldsymbol{v}_0 = 0$, $\chi_I = \chi_R = 0$):

0th order: $$(\boldsymbol{v}_0 \cdot \nabla_T)\boldsymbol{v}_0 = \frac{1}{2k_0^2}\nabla_T\{\rho_0^{-1/2}\nabla_T^2\rho_0^{1/2}\}; \tag{41}$$

1st order:

$$\ddot{\boldsymbol{\xi}} + 2(\boldsymbol{v}_0 \cdot \nabla_T)\dot{\boldsymbol{\xi}} + (\boldsymbol{v}_0 \cdot \nabla_T)[(\boldsymbol{v}_0 \cdot \nabla_T)\boldsymbol{\xi} - (\boldsymbol{\xi} \cdot \nabla_T)\boldsymbol{v}_0] + \{[(\boldsymbol{v}_0 \cdot \nabla_T)\boldsymbol{\xi} - (\boldsymbol{\xi} \cdot \nabla_T)\boldsymbol{v}_0] \cdot \nabla_T\}\boldsymbol{v}_0$$
$$= \frac{1}{4k_0^2}\nabla_T\{\rho_0^{-3/2}[\nabla_T \cdot (\rho_0\boldsymbol{\xi})]\nabla_T^2\rho_0^{1/2} - \rho_0^{-1/2}\nabla_T^2[\rho_0^{-1/2}\nabla_T \cdot (\rho_0\boldsymbol{\xi})]\}; \tag{42}$$

2nd order:

$$(\boldsymbol{\xi} \cdot \nabla_T)[\ddot{\boldsymbol{\xi}} + (\boldsymbol{v}_0 \cdot \nabla_T)\dot{\boldsymbol{\xi}} - (\dot{\boldsymbol{\xi}} \cdot \nabla_T)\boldsymbol{v}_0] + \dot{\xi}_i\dot{\xi}_j\frac{\partial^2\boldsymbol{v}_0}{\partial X_{0i}\,\partial X_{0j}}$$
$$+ \{[(\boldsymbol{\xi} \cdot \nabla_T)\boldsymbol{v}_0] \cdot \nabla_T\}[\dot{\boldsymbol{\xi}} + (\boldsymbol{v}_0 \cdot \nabla_T)\boldsymbol{\xi} - (\boldsymbol{\xi} \cdot \nabla_T)\boldsymbol{v}_0] + \{(\boldsymbol{\xi} \cdot \nabla_T)[\dot{\boldsymbol{\xi}} + (\boldsymbol{v}_0 \cdot \nabla_T)\boldsymbol{\xi} - (\boldsymbol{\xi} \cdot \nabla_T)\boldsymbol{v}_0] \cdot \nabla_T\}\boldsymbol{v}_0$$
$$+ \tfrac{1}{2}(\boldsymbol{v}_0 \cdot \nabla_T)\xi_i\xi_j\frac{\partial^2\boldsymbol{v}_0}{\partial X_{0i}\,\partial X_{0j}} + \tfrac{1}{2}\left\{\left[\xi_i\xi_j\frac{\partial^2\boldsymbol{v}_0}{\partial X_{0i}\,\partial X_{0j}}\right] \cdot \nabla_T\right\}\boldsymbol{v}_0$$
$$= \frac{1}{8k_0^2}\nabla_T\left\{\rho_0^{-3/2}\left[[\nabla_T \cdot (\rho_0\boldsymbol{\xi})]\nabla_T^2[\rho_0^{-1/2}\nabla_T \cdot (\rho_0\boldsymbol{\xi})] + \rho_0\left[\frac{\partial\xi_i}{\partial X_{0j}}\frac{\partial\xi_j}{\partial X_{0i}} + (\nabla_T \cdot \boldsymbol{\xi})^2\right]\nabla_T^2\rho_0\right.\right.$$
$$+ \left[2(\boldsymbol{\xi} \cdot \nabla_T)[\nabla_T \cdot (\rho_0\boldsymbol{\xi})] - \xi_i\xi_j\frac{\partial^2\rho_0}{\partial X_{0i}\,\partial X_{0j}} - 2\rho_0\,\mathrm{det}\frac{\partial\xi_i}{\partial X_{0j}}\right]\nabla_T^2\rho_0\Big] + \rho_0^{-1/2}\nabla_T^2\left[\rho_0^{1/2}\left[-(\nabla_T \cdot \boldsymbol{\xi})^2\right.\right.$$
$$\left.\left.\left.\left. - \frac{\partial\xi_i}{\partial X_{0j}}\frac{\partial\xi_j}{\partial X_{0i}}\right] - 2\rho_0^{-1/2}(\boldsymbol{\xi} \cdot \nabla_T)[\nabla_T \cdot (\rho_0\boldsymbol{\xi})] + \rho_0^{-1/2}\xi_i\xi_j\frac{\partial^2\rho_0}{\partial X_{0i}\,\partial X_{0j}} + 2\rho_0^{1/2}\,\mathrm{det}\left(\frac{\partial\xi_i}{\partial X_{0j}}\right)\right]\right\}; \tag{43}$$

for dispersive media $\chi_i \neq 0$, $\chi_R \neq 0$ and the integration of the first equation (23) results in

$$\rho = \rho_0(\det J_{ij})^{-1}\exp\left[(1/k_0)\int_0^{\eta} d\eta'\,\chi_I\right]. \tag{44}$$

The r.h.s. of the second evolution equation should then be completed by an additional term

$$\frac{1}{2k_0^2}\{\nabla_T \chi_R - (\nabla_T \cdot \xi)\nabla_T \chi_R\}. \tag{45}$$

In case of an azimuthally symmetric beam we introduce cylindrical coordinates assuming that the azimuth ϕ is ignorable. Then

$$\det J = \frac{r}{r_0}\frac{\partial r}{\partial r_0}.$$

Under the assumption of the paraxial approximation, $r = r_0 + \xi$ the hierarchy of evolutional relations reads ($\chi_I = \chi_R = 0$):

$$v_{0r}\frac{\partial}{\partial r_0}v_{0r} = \frac{1}{2k_0^2}\frac{\partial}{\partial r_0}\left\{\rho_0^{-1/2}\frac{\partial^2}{\partial r_0^2}\rho_0^{1/2}\right\}, \tag{46}$$

$$\ddot{\xi} + 2v_{0r}\frac{\partial}{\partial r_0}\dot{\xi} + v_{0r}^2\frac{\partial^2}{\partial r_0^2}\xi - v_{0r}\xi\frac{\partial^2}{\partial r_0^2}v_{0r} + v_{0r}\left(\frac{\partial}{\partial r_0}\xi\right)\left(\frac{\partial}{\partial r_0}v_{0r}\right) - \xi\left(\frac{\partial}{\partial r_0}v_{0r}\right)^2$$
$$= \frac{1}{8k_0^2}\frac{\partial}{\partial r_0}\left\{\rho_0^{-3/2}\left[-\tfrac{3}{2}\rho_0^{-1}\left(\frac{\partial\rho_0}{\partial r_0}\right)^2 + \left(\frac{\partial^2\rho_0}{\partial r_0^2}\right) + 2\frac{\partial\rho_0}{\partial r_0}\frac{\partial}{\partial r_0} - 2\rho_0\frac{\partial^2}{\partial r_0^2}\right]\mathrm{div}(\rho_0\xi)\right\}, \tag{47}$$

$$\xi\frac{\partial}{\partial r_0}\left[\ddot{\xi} + v_{0r}\frac{\partial\dot{\xi}}{\partial r_0} - \dot{\xi}\frac{\partial v_{0r}}{\partial r_0}\right] + \xi\dot{\xi}\frac{\partial^2 v_{0r}}{\partial r_0^2} + \tfrac{1}{2}v_{0r}\frac{\partial}{\partial r_0}\left(\xi^2\frac{\partial^2 v_{0r}}{\partial r_0^2}\right)$$
$$+\left[\xi v_{0r}\frac{\partial^2}{\partial r_0^2} - 2\xi\frac{\partial v_{0r}}{\partial r_0}\frac{\partial}{\partial r_0}\right]\left[\dot{\xi} + v_{0r}\frac{\partial\xi}{\partial r_0} - \xi\frac{\partial v_{0r}}{\partial r_0}\right] + \tfrac{1}{2}\xi^2\frac{\partial v_{0r}}{\partial r_0}\frac{\partial^2 v_{0r}}{\partial r_0^2}$$
$$= \frac{1}{8k_0^2}\frac{\partial}{\partial r_0}\left\{\rho_0^{-3/2}\left[[\mathrm{div}(\rho_0\xi)]\frac{\partial^2}{\partial r_0^2}[\rho_0^{-1/2}\,\mathrm{div}(\rho_0\xi)] - 2\rho_0\frac{\partial^2}{\partial r^2}\left[\rho_0^{-1/2}\frac{\partial}{\partial r_0}[\mathrm{div}(\rho_0\xi)]\right.\right.\right.$$
$$+\rho_0^{1/2}\frac{\xi}{r_0}\frac{\partial\xi}{\partial r_0} - \tfrac{1}{2}\rho_0^{-1/2}\xi^2\frac{\partial^2\rho_0}{\partial r_0^2} + \rho_0^{1/2}\frac{\xi^2}{r_0^2} + \rho_0^{1/2}\left(\frac{\partial\xi}{\partial r_0}\right)^2\Big]$$
$$\left.\left.+\left(\frac{\partial^2}{\partial r_0^2}\rho_0^{1/2}\right)\left[2\xi\frac{\partial}{\partial r_0}[\mathrm{div}(\rho_0\xi)] + 2\rho_0\frac{\xi}{r_0}\frac{\partial\xi}{\partial r_0} - \xi^2\frac{\partial^2\rho_0}{\partial r_0^2} + 2\rho_0\left(\frac{\xi^2}{r_0^2}\right) + 2\rho_0\left(\frac{\partial\xi}{\partial r_0}\right)^2\right]\right]\right\}. \tag{48}$$

A generalization of these equations for the dissipative case, $\chi_I \neq 0$, $\chi_R \neq 0$ is straightforward.

In the two methods presented, the set of starting transport equations is combined, via the Lagrangian displacement X on ξ in the case of paraxial approximation, into one equation for X or ξ, respectively. This equation [eqs. (30) or (38), eqs. (47), (43) or (47), (48)] is further elaborated using a suitable differencing scheme. The virtue of the present analysis consists in the fact, that only one variable has to be calculated. This differs our method from Lagrangian analysis, carried out in the past [24].

7. Conclusion

By writing the paraxial scalar wave equation in a conservation form, one finds that it has the structure of the hydrodynamics equation. On the basis of this analogy, the intensity of the laser beam, $|e|^2$, can be interpreted as the density ρ, while the phase, ϕ, as the velocity potential (v = grad ϕ) of a hydrodynamic flow process subjected to a pressure, which – in contrast to classical hydrodynamics – depends on derivatives of the fluid density.

It is noteworthy that this hydrodynamic approach to intense laser propagation in nonlinear media removes the rapid numerical oscillations encountered when the field is described by its real and imaginary parts: the new independent variables change much more slowly.

During the nonlinear interaction, significant reshaping and beam distortion take place. To achieve accuracy and efficiency simultaneously, one must resort to nonuniform grids which self-adjust according to the local requirements of the physics. Thus, the Lagrangian description – as opposed to the Eulerian description, which would have required mapping and adaptive rezoning techniques – is adopted.

The continuity and velocity equations reduce to only one evolution equation for the Lagrangian displacement. The resulting governing equation involves derivatives $\partial r/\partial r_0$ up to the fourth order. To overcome the numerical difficulties associated to the inversion of the Jacobian, an analytical algorithm valid in the paraxial limit was further presented.

The object of this communication was to illustrate a novel transfer of effective computational techniques gained in fluid and aerodynamics to optical physics [8] by emphasizing the fluid equivalency. The main goals of this study were to (1) propose an algorithm which is totally consistent with the subtle physics requirements; and (2) to readily gain additional physical insights in this essential nonlinear light–matter interaction.

It is noteworthy that a recent independent research effort also dealt with the hydrodynamic analogy in a Lagrangian description for nonlinear propagation in the atmosphere. However, an explicit algorithm was adopted [26].

Acknowledgements

This work was partially supported by DREV under Contract No. 85076-00219, F.P. Mattar gratefully acknowledges useful discussions with Dr. B.R. Suydam, Professor G. Moretti and Professor Dr. J. Deletrez on the numerical aspect of the problem.

References

[1] J.H. Marburger, Progr. Quant. Electron. 4 (1976) part I.
[2] H. Kogelnik and T. Li, Appl. Opt. 5 (1966) 1550.
[3] L. Bradley, J. Hermann, MIT Lincoln Lab. Techn. Rep. (1971).
[4] P.B. Ulrich, Naval Res. Lab. Techn. Rep. NRL 7382 (1971).
[5] H.J. Breaux, Ball. Res. Lab. BRL Rep. 1723 (1974).
[6] J.A. Fleck, J.R. Morris and M.J. Feit, LLL Rep. UCRL-51372 (1975).
[7] J.A. Fleck, J.R. Morris and M.J. Feit, LLL Rep. UCRL-52071 (1976).
[8] F.P. Mattar, Appl. Phys. 17 (1978) 63.
[9] A.J. Glass, LLL Annual Laser Fusion Rep., Basic Studies (1973–1974).
[10] O. Rossignol, DREV Rep. R-4029 (1976).
[11] E. Madelung, Z. Phys. 40 (1926) 322.
[12] H.E. Wilhelm, Phys. Rev. D1 (1970) 2278.
[13] S.N. Vlasov, V.A. Petrishev and V.I. Talanov, Izv. Vysshikh Uchebn. Zavedenii Radiofiz. 14 (1971) 1353.
[14] B.R. Suydam, IEEE J. Quant. Electron. 10 (1974) 837.
[15] J.E. Lam, B. Lipman and F.D. Tappert, Phys. Fluids 20 (1977) 1179.
[16] R.W. MacCormack, AIAA Hypervelocity Impact Conf., paper No. 69-354 (1969).
[17] G. Moretti, PIBAL Reps. 69-25 (1969), 69-26 (1969), 70-20 (1970), 70-48 (1970), 72-37 (1972), 74-15 (1974), 76-06 (1976).
[18] P.J. Roache, Computational fluid dynamics (Hermosa, New Mexico, 1972).
[19] R. Courant and K.O. Friedrich, Supersonic flow and shock waves (Interscience, New York, 1948).
[20] F.P. Mattar and M.C. Newstein, in: Cooperative effects in matter and radiation, eds. C.M. Bowden, D.W. Howgate and H. Robl (Plenum, New York, 1977) p. 139; Comput. Phys. Commun. 20 (1980) 139.
[21] S.A. Akhmanov, R.V. Khokhlov and A.P. Sukhorukov, in: Laser handbook, eds. F.T. Arrechi and E.O. Schults-DuBois (North-Holland, Amsterdam, 19/2) p. 1151.
[22] N. Marcuvitz, IEE Trans. Electron. Dev. ED-17 (1970) 252.
[23] M.C. Newstein and D. Ramakrishnan, Rep. POLY-MRI-1394-78 (1978).
[24] F.P. Mattar and J. Teichman, IEEE Conf. Plasma Science, Montreal (1979).
[25] F.P. Mattar and J. Teichman, Physics Dept., University of Montreal, Techn. Rep. UDM-PL 79/1 (1979).
[26] J. Teichmann and F. Mattar, Proc. IXth Conf. Numer. Simulation in Plasmas, Evanson, Illinois (1980).
[27] M. Lax, J. Battch and G.P. Agrawal, Channeling of Intense Electromagnetic Beams, preprint, Physics Dept. at CCNY, New York (1980).

Reprinted from SPIE Vol. 288—Los Alamos Conference on Optics

Transverse effects in swept-gain superradiance: evolution from the superradiant state

C. M. Bowden
U.S. Army Missile Laboratory
U.S. Army Missile Command, Redstone Arsenal, Alabama 35898

F. P. Mattar*
Aerodynamics Laboratory, Polytechnic Institute of New York
Brooklyn, New York 11201
Laser Spectroscopy Laboratory, Massachusetts Institute of Technology
Cambridge, Massachusetts 02139

Abstract

Results of numerical calculations are presented and analyzed for pulse generation and subsequent stabilization in large propagation distance z , for a collection of two-level absorbers which are swept-excited by an impulse inversion along the z-direction at the speed of light in the medium. The calculation is performed using the coupled Maxwell-Bloch formalism and for the conditions that $T_2 = T_1$, $T_2 >> \tau_c$, $g/\kappa >> 1$, where T_2 is macroscopic dipole moment dephasing time, T_1 is the longitudinal relaxation time for the absorber, τ_c is the characteristic superradiant cooperation time among the absorbers and g/κ is the linear gain, g , to diffraction loss, κ, ratio. Results of the calculation for nonlinear pulse evolution and propagation for one spacial dimension (planar case) is compared with the results for the comparable case where transverse mode coupling is included.

Introduction

In 1975, Bonifacio, Hopf, Meystre and Scully[1](hereafter referred to as BHMS) predicted the conditions for which steady-state pulses having characteristics of superradiance (intensity $\sim\rho^2$, temporal width $\sim 1/\rho$, where ρ is the density of absorbers, and pulse envelope varying in time as hyperbolic secant with characteristic delay of the peak from the excitation) can be generated in swept-gain amplifiers. They obtained and analyzed steady-state solutions of the coupled Maxwell-Bloch equations in the retarded time frame in one spacial dimension z in the limit $z \to \infty$, for the initial condition that impulse inversion occurs at $\tau = 0$, where $\tau = t - z/c$, in the retarded time. Exact analytical results under these conditions were obtained by BHMS for homogeneously-broadened systems for two special cases, $T_2 << T_1$ and $T_1 = T_2$, where T_2 and T_1, are the transverse and longitudinal atomic relaxation times, respectively.

Subsequent theoretical work which followed the initial work of BHMS[1] addressed to the quantum mechanical aspects of pulse buildup from noise and the role of spontaneous emission in the small signal regime for a system with small Doppler width[2] and for a homogeneously-broadened system.[3] Further theoretical work analyzed the effects of coherent pumping, for the excitation, on pulse buildup, both numerically[4] and analytically[5,6,7]. The first reported detailed experimental study of swept-gain superradiance[4,5] was for CO_2-pumped CH_3F.

Since Dicke's initial prediction[8] for the circumstances under which a macroscopic volume of atoms can radiate collectively (collective, spontaneous relaxation), a large amount of theoretical and experimental effort has been devoted to the subject of superradiance.[9] Experimental arrangements for the study of superradiance has been identical with that for swept-gain superradiance.[9,10] Even though the two phenomena stem from entirely different physical processes, the same physical model should account for both, each being a limiting case essentially in terms of the length of the active volume of atoms. Indeed, the first reported experimental study of swept-gain superradiance[4] also constituted a study of the evolution from superradiant response of the system through swept-gain superradiance as a function of the length of the active volume along the propagation axis.[10] The experimental results indicate a continuous transition from conditions supportive of superradiance or superfluorescence through swept-gain superradiance in the asymptotic regime of large propagation length z.

In this paper we analyze numerically, and interpret analytically, the evolution of the response of a collection of two-level absorbers to swept impulse excitation, from the small volume, superradiant regime, through the asymptotic, steady-state propagation at sufficiently large propagation distances z. We also determine the effects of transverse mode coupling on the pulse generation[11,12] and propagation.[13]

*Work partially supported by ARO, ONR, Battelle, University of Montreal, and Research Corporation.

The model is presented in the next section and the analytical results for swept-gain superradiance in the planar regime obtained previously by BHMS[1] are briefly reviewed. A comparison is made between conditions for the observation of single pulse superfluorescence[14] and swept-gain superradiance.[1] Results of the numerical calculations are presented and discussed in Section III for the evolution of pulse area with propagation distance z for the single spacial dimension. The evolution from superradiance to steady-state swept-gain superradiance and their connection is explicitly analyzed and discussed. Results for a comparable case incorporating transverse mode coupling with a Guassian gain profile are presented and compared with results for the planar, one spacial dimension calculation. It is shown that the effects of self-focusing can be much more important in the swept-gain, steady-state condition than for the particular corresponding conditions for superradiance. The results of our calculation are summarized in the last section and future work connected with these results is outlined.

II. Coupled Maxwell-Bloch model for swept-gain superradiance

BHMS showed[1] that if a volume of two-level absorbers is gain-swept at the speed of light in the active medium by a traveling impulse excitation, a solitary pulse is generated from noise amplification in the amplifying medium and reaches a steady-state at sufficiently large propagation distance z, provided the gain, g, to loss, κ, ratio satisfies the condition $g/\kappa > 1$. The solitary pulse is characterized by superradiant-like features with respect to pulse shape, intensity, temporal width, and delay of the peak of the pulse envelope from the impulse excitation.

They considered the coupled Maxwell-Bloch equations in the retarded time frame, which is a frequently used model for pulse propagation and generation in nonlinear media,

$$\frac{\partial P}{\partial \tau} = \varepsilon \Delta - \frac{P}{T_2} \tag{2-1}$$

$$\frac{\partial \Delta}{\partial \tau} = -\varepsilon P - \frac{\Delta}{T_1} \tag{2-2}$$

$$\frac{\partial \varepsilon}{\partial z} = \alpha P - \kappa \varepsilon . \tag{2-3}$$

In the above equations, P is the dimensionless macroscopic transverse polarization per atom, Δ is the inversion for the two-level atom, T_2 and T_1, are the dephasing and relaxation times for the polarization and atomic inversion, respectively. The third equation, (2-3), is the linearized Maxwell equation[15] in the retarded time frame in the slowly varying envelope (SVEA) and rotating wave approximation for the pulse envelope E. Here, the electromagnetic field envelope, E , is normalized to give the Rabi frequency[15] ε ,

$$\varepsilon = \frac{\mu_0 E}{\hbar} \tag{2-4}$$

where μ_0 is the matrix element of the transition dipole moment between the pair of atomic energy levels and E is the electromagnetic field envelope which is a function of the propagation coordinate z and retarded time τ ,

$$\tau = t - z/c . \tag{2-5}$$

The other quantities involved in Eqs. (2-1) - (2-3) are

$$\alpha = \frac{g}{T_2} = \frac{3}{4\pi} \frac{\lambda^2 \rho}{\tau_0} \tag{2-6}$$

where g is the gain and λ is the wavelength of the carrier frequency of the single mode radiation field envelope, ρ is the atomic density and τ_0 is the spontaneous atomic relaxation time. The loss term in (2-3) defined by κ is the linear loss which arises because of diffraction as well as other dissipative processes.

BHMS considered the steady-state solutions of (2-1) - (2-3), i.e., the solutions under the condition

$$\varepsilon(z \to \infty, \tau) = \lim_{z \to \infty} \left\{ \varepsilon(0,\tau) e^{-\kappa z} + \alpha \int_0^z dz' \, e^{-\kappa(z-z')} \, P(z',\tau) \right\} \tag{2-7}$$

and the initial condition

$$\Delta(\tau = 0) = 1. \tag{2-8}$$

Equation (2-7) leads immediately to the adiabatic relation between the field and polarization,

$$\varepsilon(z \to \infty, \tau) = \frac{\alpha}{\kappa} P(z \to \infty, \tau) . \tag{2-9}$$

This last expression can be used to eliminate P from (2-1) and (2-2) and steady-state solutions are found by solving the resulting pair of nonlinear differential equations.

Exact analytical results were obtained by BHMS for two distinct cases, $T_2 << T_1$ and $T_2 = T_1$. For $T_2 << T_1$:

$$\varepsilon(\tau) = \frac{1}{\tau_s'} \operatorname{sech} \frac{\tau}{\tau_s'} \tag{2-10}$$

where

$$\tau_s' = T_2 \left[(g-\kappa)/\kappa\right]^{-1} \tag{2-11}$$

For $g >> \kappa$, we see from (2-10), (2-11), and (2-6) that the intensity I of the steady-state pulse, $I \sim E^2$, varies as the density squared, $I \sim \rho^2$, whereas (2-10) and (2-11) indicate that the width τ_s' varies inversely as the density $\tau_s' \sim 1/\rho$. Also, from (2-11) the pulse width is always less than T_2 whenever $g > \kappa$. For $T_2 = T_1$:

The set of equations (2-1) - (2-3) reduces to the generalized sine-Gordon equation[1]

$$\frac{\partial^2 \phi(\xi,z)}{\partial \xi \partial z} + \kappa \frac{\partial \phi(\xi,z)}{\partial \xi} = \alpha \sin \phi(\xi,z) \tag{2-12}$$

where

$$\xi = \frac{1}{\gamma}\left(1 - e^{-\gamma\tau}\right) \tag{2-13}$$

is the reduced time and

$$\gamma = \frac{1}{T_2} = \frac{1}{T_1} \quad .$$

The angle ϕ is the Bloch angle,

$$\varepsilon = \frac{\partial \phi}{\partial \tau} \quad . \tag{2-14}$$

In the asymptotic regime, the space derivative term in (2-12) vanishes and the resulting solution, using (2-14), is

$$\varepsilon(\tau) = \frac{1}{\tau_s} e^{-\gamma\tau} \operatorname{sech}\left\{\frac{1}{\tau_s}\left[\xi(\tau) - \xi_0\right]\right\} \tag{2-15}$$

where

$$\tau_s = \frac{\kappa T_2}{g} \tag{2-16}$$

and the time delay between the impulse excitation and the peak of the steady-state pulse ξ_0, is given by

$$\xi_0 = \tau_s \log\left[\cot \tfrac{1}{2}\phi_0\right] . \tag{2-17}$$

Here, ϕ_0 is the initial Bloch-angle at $\tau = 0$ to account for quantum noise which drives the atomic excitation away from the completely inverted metastable state.

Again, from (2-15) it is seen that the intensity $I \sim \rho^2$ whereas the pulse width $\tau_w \sim 1/\rho$. It was shown[1] by BHMS that such pulses will evolve provided $g/\kappa > 1$. The area of the pulse θ is defined as the Bloch angle ϕ at infinite time τ , and is obtained by integrating (2-14). From (2-12) in the asymptotic regime, i.e., neglecting the first term on the left,

$$\tan \tfrac{1}{2}\theta = (\tan \tfrac{1}{2}\phi_0)\, e^{g/\kappa} \quad . \tag{2-18}$$

Thus, given an initial Bloch angle ϕ_0, for g/κ sufficiently large, the area θ approaches π , i.e., as large as it can be for a single pulse. The threshold for $\theta \to \pi$ was determined to be

$$\left[g/\kappa\right]_{\text{threshold}} \simeq \log\left(\frac{1}{\phi_0}\right) . \tag{2-19}$$

Any further increase in the gain-to-loss, g/κ, does not increase the pulse area since it is saturated above threshold. However, from (2-15) the intensity continues to vary as the square of the density and the pulse width as inverse density.

The criteria, therefore, for the generation of steady-state pulses is that the active medium be swept-excited at the speed of light in the medium and that $g/\kappa > 1$. The resulting pulses have characteristics of superfluorescence[14], although for different physical reasons. The major difference in realizing the two phenomena is that to produce superfluorescence the medium responds as though it were uniformily excited, i.e., the atoms are contained within a certain cooperation volume, whereas for swept-gain superradiance, the medium "sees" an impulse excitation traveling at the velocity of light in the medium. Table 1 compares the conditions for single pulse superfluorescence in the mean field limit[14], with the corresponding conditions for pulse generation in swept-gain superradiance in the asymptotic regime. It is to be pointed out that the essential physical difference between what has been called superfluorescence[14] and what is termed swept-gain superradiance[1] is that the atomic relaxation for the former occurs by collective, spontaneous relaxation[8], whereas for the latter, individual atomic relaxation occurs by stimulated relaxation due to pulse propagation in the medium.

Table 1. Comparison of Conditions for Superfluorescence in Mean Field Approximation with Swept-Gain Superradiance in Asymptotic Approximation

Superfluorescence Mean-Field Approximation	Swept-Gain Superradiance Asymptotic Approximation
$\frac{\partial \varepsilon(t)}{\partial t} = \alpha P(t) - \kappa' \varepsilon(t)$	$\frac{\partial \varepsilon(z,\tau)}{\partial z} = \alpha P(z,\tau) - \kappa \varepsilon(z,\tau)$
	$\tau = t - z/c$
$\kappa' \varepsilon >> \frac{\partial \varepsilon}{\partial t}$	$\kappa \varepsilon >> \frac{\partial \varepsilon}{\partial z}$
$P = \frac{\kappa'}{\alpha} \varepsilon$	$P = \frac{\kappa}{\alpha} \varepsilon$
$\tau_E < \tau_c < \tau_R < \tau_D < T_1, T_2, T_2^*$	$g/\kappa > 1$
$\tau_E = L/C$	$\tau_E' = (c\kappa)^{-1}$
$\tau_R = \frac{8\pi\tau_o}{3\alpha\lambda^2 L}$	$\tau_s = \frac{\kappa T_2}{g}$
$\tau_D = \tau_R \log\left(\frac{1}{\theta_o^2}\right)$	$\xi_o = \tau_s \log\left[\cot \tfrac{1}{2}\phi_o\right]$
$\tau_C = (\tau_E \tau_R)^{1/2}$	$\tau_C = (\tau_E' \tau_s)^{1/2}$

Here, τ_R is the characteristic superradiance time[14] for $z = L$, τ_D is the delay time[14] of the pulse peak from the excitation, and τ_c is the cooperation time[16] corresponding to the cooperation length ℓ_c, $\tau_c = c\ell_c$. Note that for $L = \ell_c$, $\tau_R = \tau_c$. τ_D is the delay time of the peak of the superradiant pulse from the impulse excitation.

We have calculated the evolution of pulse area for swept-gain superradiance as a function of propagation distance z according to the relations (2-1) - (2-3) for the conditions $T_1 = T_2$, $g/\kappa > \log(1/\phi_o)$ and for $\tau_R << T_2$ where τ_R is the characteristic superfluorescence time. Thus, we have determined the evolution of pulse area from the superfluorescence regime (small z) through the asymptotic swept-gain regime (large z). These results we compare with corresponding calculations taking into account transverse mode coupling and diffraction for a Gaussian gain profile. In this case, the Maxwell equation (2-3) takes the three-dimensional form

$$-iT_2 \mathcal{F}^{-1} \nabla_\sigma^2 \varepsilon + \frac{\partial \varepsilon}{\partial \eta} = d P \qquad (2\text{-}20)$$

where d = radial function describing nonuniformity of gain profile, $\eta = z\alpha$, and

$$\mathcal{F} = \frac{4\pi r_p^2}{\lambda g^{-1}} \tag{2-21}$$

is the Beer's length dependent Fresnel number relevant to propagation effects. Here r_p is the Gaussian gain width at half maximum. The transverse effects arising from (2-20) are related to the planar case using (2-3) by taking the linear field loss κ in the latter to be entirely diffraction-loss, i.e.

$$\kappa = \frac{\lambda}{A} \tag{2-22}$$

where $A = \pi r_p^2$. Thus, the Fresnel number $\mathcal{F}$, (2-21), is

$$\mathcal{F} = \frac{g}{\kappa} \tag{2-23}$$

the gain-to-loss ratio. The results of the calculation and related discussions are presented in the next section.

III. Numerical results for propagation and transverse effects: Evolution from superfluorescence to swept-gain superradiance

First we present the results of numerical integration of (2-1) - (2-3) for the initial condition (2-8) and for $T_1 = T_2$. We have also chosen the values for the system parameters such that the superradiance cooperation time,[16] τ_c , satisfies the condition $\tau_c << T_2$ (see Table 1), where $\ell_c = c\tau_c$ is the maximum length of the sample over which the atoms can cooperate to produce superradiant emission. Also, the gain, g , to loss, κ , ratio, $g/\kappa >> \log (1/\phi_0)$,(see (2-19)), so that results of the last section predict steady-state pulses of area $\theta = \pi$, Eq. (2-18).

The absolute pulse area $|\theta|$,

$$|\theta| = \int_0^\infty |\varepsilon| \, d\tau \tag{3-1}$$

is shown as a function of propagation length z in Figure 1. There are three distinct regimes evident in the pulse area, $|\theta|$, propagation evolution. These are determined by the characteristic times for the system τ_R (Table 1), and τ_s, (2-16).

The first regime, characterized by the smallest values of the propagation distance z, shows a rapid rise of the pulse area, (3-1), with propagation distance z. The area proceeds in z through $|\theta| = \pi$, corresponding to single pulse buildup, to values $|\theta| > \pi$, which eventually corresponds to subsequent ringing, and finally peaks out at $|\theta| \simeq 3\pi$. This behavior is described by the sine-Gordon equation (2-12), with the values of the parameters used in the calculation (see Figure 1). We have, for this particular small z regime,

$$\kappa \frac{\partial \phi}{\partial \tau} << \alpha \sin \phi, \tag{3-2}$$

so (2-12) becomes

$$\frac{\partial^2 \phi}{\partial \tau \partial z} = \alpha \sin \phi \quad , \tag{3-3}$$

where, from (2-13), $\xi \to \tau$ since in this case $\tau/T_2 << 1$. This is just the Burnham-Chiao propagation equation[17] , which yields the well-known solution for pulse buildup from gain with subsequent undamped ringing.

From (2-6) and Table 1, we have

$$\alpha = \frac{1}{2c\tau_c^2} \tag{3-4}$$

where τ_c is the Arecchi-Courtens superradiant cooperation time[16] which corresponds to the superradiant cooperation length $z = \ell_c, \ell_c = c\tau_c$, the maximum length over which the atoms can cooperate collectively to produce superradiant emission. Equation (3-3) yields

$$\frac{d\theta}{dz} = \frac{1}{2\ell_c} \int_0^{z/\ell_c} d\nu \sin \phi \, . \tag{3-5}$$

Here,

$\nu = \tau/\tau_c = z/\ell_c$ and θ, as in (3-1), is related to the Bloch angle ϕ, by $\theta = \phi(\tau = z/c)$. Thus, the initial pulse buildup in Figure 1 is governed by the superradiance time τ_R (Table 1) where $\tau_R \sim z^{-1}$ and $\tau_R = \tau_c$ when $z = \ell_c$, and in this particular case, $\ell_c = 2.68$ cm. The region corresponding to $0 < |\theta| < \pi$ we call the single pulse superradiant regime, $z < \ell_c$, which is subsequently followed by Burnham-Chiao ringing. This initial superradiant pulse buildup occurs in this case because $\tau_c << T_2$.

After several diffraction lengths κ^{-1}, the area (3-1) reaches a maximum and then decays as $e^{-\kappa z}$ to the asymptotic steady-state $\theta = \pi$ pulse predicted analytically in the last section, and shown in Figure 1. This regime is governed by the characteristic time τ_s, (2-16).

The results shown in Figure 1 exhibit the pulse area evolution from pure superradiance, $|\theta| < \pi$, through Burnham-Chiao ringing, each governed by τ_R, to pulse area instability which subsequently decays by linear field loss κ to the asymptotic steady-state π pulse. The necessary and sufficient conditions for evolution from superradiance to π-pulse swept-gain superradiance are that $g/\kappa > \log 1/\phi_o > 1$, $\tau_c << T_2$.

The effects of changes in the value of the linear field loss κ, all other parameters remaining the same, are shown in Figure 2 for four other values of κ and, hence g/κ. It is seen that asymptotic stability in the pulse area is reached for lower z values the higher the value for the loss κ, as one would expect. Also, the higher loss and lower gain-to-loss reduce the amplitude of the pulse area instability peak, again as one would expect. This further suggests that the transition from superradiance to asymptotic swept-gain superradiance can occur without intermediate ringing if $(\kappa c)^{-1} << \tau_c$.

When transverse effects are taken into account in the calculation, Eq. (2-3) is replaced by (2-20). The transverse mode coupling is generated through the first term in (2-20), and its contribution is governed by the Fresnel number $\mathcal{F}$, (2-21) and (2-23). This is not the conventional Fresnel number used in discussions of superradiance and superfluorescence[18], but it is the one which is meaningful[13] throughout the entire propagation regime. Generally, the larger the Fresnel number $\mathcal{F}$, (2-21), the less the importance of contributions from transverse effects, (2-20), i.e., large $\mathcal{F}$ means more nearly plane wave propagation behavior.

We use the values of the parameters and the conditions which gave rise to the one-dimensional results of Figure 1, but choose the cross-sectional area A for a Gaussian initial gain profile from (2-22) and the value of κ used to obtain the results of Figure 1, where r_p is the radial Gaussian width for the gain distribution, and obtain the calculational results shown in Figure 3. Here, we show the pulse area (3-1) as a function of propagation distance z and radial dimension ρ. Energy which intersects the boundary $\rho = \rho_{max}$ is absorbed in the calculation; thus diffraction as well as transverse mode coupling is explicitly treated in the calculation consistent with the conditions imposed by (2-20), (2-21) - (2-23). Thus, the calculation giving the results shown in Figure 3 is the three-dimensional extension of the calculation which gave the results shown in Figure 1. The pulse area (3-1) as a function of z for the on-axis mode is displayed in Figure 4.

It is noted by comparing Figures 1, 3, and 4 that the transverse effects almost completely wash-out the instability in the pulse area buildup which occurs in the one-dimensional calculation, Figure 1. Furthermore, Figures 3 and 4 indicate a different kind of pulse area instability at higher z values which is due to self-focusing. The qualitative effects of self-focusing on pulse propagation can be seen in Figure 5. The results of the three-dimensional calculation indicate, therefore, that a true steady-state may not exist, at least in the sense of the analytical predictions of Section II.

Similar one-spacial dimension calculations for pulse area evolution in swept-gain superradiance, but under the influence of lethargic gain conditions, have been reported by BHMS[19].

IV. Summary and conclusions

We have demonstrated the pulse evolution in one-dimensional propagation from superfluorescence to asymptotic swept-gain superradiance for ideal conditions supportive of superfluorescence[14,18] and π-pulse swept-gain superradiance.[1] The results are shown in Figures 1 and 2. Transverse effects tend to wash-out the early pulse area instability which occurs for the one-dimensional case as seen by comparing Figures 1 and 2 with Figures 3 and 4. However, as noted in Figures 3 and 4, the pulse area shows an instability in the asymptotic region of large z when transverse effects are taken into account. This evidently arises from self-focusing, Figure 5. Thus, in this case, a true steady-state does not exist due to transverse mode coupling effects.

This work is in process of being extended[20,21] to the calculation of the effects of coherent optical pumping and propagation as well as transverse effects for three-level systems[6,7] for three-level superfluorescence and swept-gain superradiance and coherent pulse shaping due to specified pulse injection and propagation in three-level systems.

References

1. Bonifacio, R., Hopf, F. A., Meystre, P., and Scully, M. O., Phys. Rev. A12, 2568. 1975.
2. Hopf, F. A. and Meystre, P., Phys. Rev. A12, 2534. 1975.
3. Hopf, F. A., Meystre, P., and McLaughlin, D. W., Phys. Rev. A13, 777. 1976.

4. Ehrlich, J. J., Bowden, C. M., Howgate, D. W., Lehnigk, S. H., Rosenberger, A. T., and DeTemple, T. A., "Swept-gain Superradiance in CO_2-pumped CH_3F", in Coherence and Quantum Optics IV, edited by L. Mandel and E. Wolf (Plenum, New York), p. 923. 1978.
5. Rosenberger, A. T., DeTemple, T. A., Bowden, C. M., and Sung, C. C., J. Opt. Soc. Am. 68, 700. 1978.
6. Bowden, C. M. and Sung, C. C., Phys. Rev. A18, 1558. 1978.
7. Bowden, C. M. and Sung, C. C., Phys. Rev. A20, 2033. 1979.
8. Dicke, R. H., Phys. Rev. 93, 99. 1954.
9. Cooperative Effects in Matter and Radiation, edited by C. M. Bowden, D. W. Howgate and H. R. Robl, (Plenum, New York). 1977.
10. Vrehen, Q. H. F. and Gibbs, H. M., "Superfluorescence Experiments", in Topics in Current Physics, edited by R. Bonifacio (Springer-Verlag, New York), in press. 1981.
11. Mattar, F. P., "Effects of Propagation, Transverse Mode Coupling and Diffraction on Nonlinear Light Pulse Evolution", in Optical Bistability, edited by C. M. Bowden, M. Ciftan and H. R. Robl (Plenum Press, New York), p. 503. 1981.
12. Mattar, F. P., Gibbs, H. M., McCall, S. L. and Feld, M. S., Phys. Rev. Lett. 46, 1123. 1981. Also, "Transverse Fluctuations in Superfluorescence", European Conference on Atomic Physics, Heidelberg, Germany, April 1981, Paper W10.
13. Mattar, F. P. and Newstein, M.C., "Beam-Profile Effects in Self-induced Transparency: On-resonance Self-focusing of Coherent Optical Pulses in Absorbing Media", in Cooperative Effects in Matter and Radiation, edited by C. M. Bowden, D. W. Howgate and H. R. Robl (Plenum Press, New York), p. 139. 1977.
14. Bonifacio, R. and Lugiato, L. A., Phys. Rev. A11, 1507. 1975. A12, 587. 1975.
15. Optical Resonance and Two-level Atoms, L. Allen and J. H. Eberly (John Wiley, New York). 1975.
16. Arecchi, F. T. and Courtens, E., Phys. Rev. A2, 1730. 1970.
17. Burnham, D. C. and Chiao, R. Y., Phys. Rev. 188, 667. 1969.
18. Vrehen, Q. H. F., reference 9, page 79.
19. Bonifacio, R., Hopf, F. A., Meystre, P. and Scully, M. O., "Theory of a Short Wavelength Swept-gain Amplifier", in Laser Induced Fusion and X-Ray Laser Studies, Physics of Quantum Electronics, VOL III, edited by S. F. Jacobs, M. O. Scully, M. Sargent III, and C. D. Cantrell, III. (Addison-Wesley, London, 1976). p. 487.
20. Mattar, F. P. and Bowden, C. M., "Swept-gain Superradiance in Two- and Three-level Systems With Transverse Effects and Diffraction", International Conference on Excited States and Multiresonant Nonlinear Optical Processes in Solids, Aussois, France, March 18-20, 1981.
21. Mattar, F. P. and Bowden, C. M., to be submitted for publication.

Figures

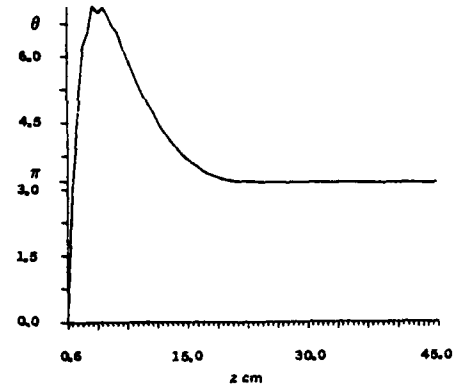

Figure 1. Pulse area $\theta = \int_0^\infty |\varepsilon| d\tau$ vs. propagation distance z for numerical integration of Eqs. (2-1) - (2-3). Values for the parameters used in the calculation are: $g = 291.6\ cm^{-1}$, $\kappa = 2.60 cm^{-1}$, $g/\kappa = 112.15$, $T_1 = T_2 = 70$ nsec, $\phi_0 = 9.42 \times 10^{-4}$, $\tau_c = 89.4$ psec.

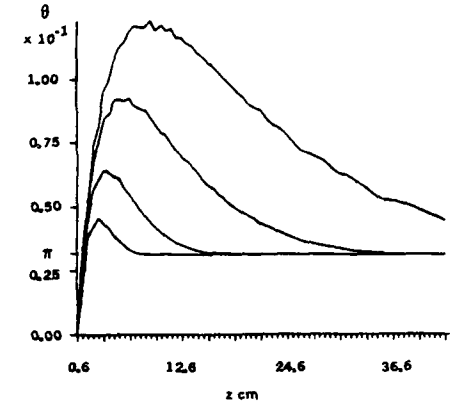

Figure 2. Pulse area $\theta = \int_0^\infty |\varepsilon| d\tau$ vs. propagation distance z for numerical integration of Eqs. (2-1) - (2-3). Values of the parameters used are those of Figure 1 except for κ: 1) $\kappa = 5.2\ cm^{-1}$, $g/\kappa = 56.08$; 2) $\kappa = 10.4\ cm^{-1}$, $g/\kappa = 28.04$; 3) $\kappa = 20.8$, $g/\kappa = 14.02$; 4) $\kappa = 41.6\ cm^{-1}$, $g/\kappa = 7.01$.

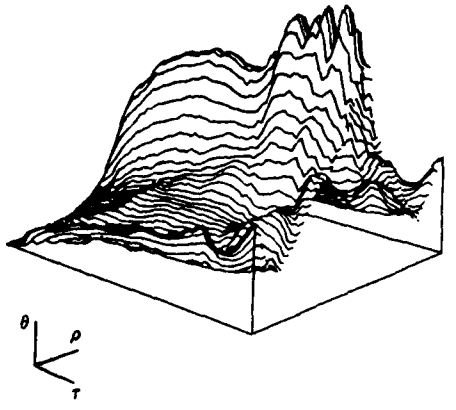

Figure 3. Pulse area θ vs. propagation distance z and radial dimension ρ for numerical integration of Eqs. (2-1), (2-2), and (2-20). Values of the parameters used are those of Figure 1, with the Fresnel number $\mathcal{F}$ chosen according to (2-23) and a Gaussian initial gain profile determined from (2-21),(2-22).

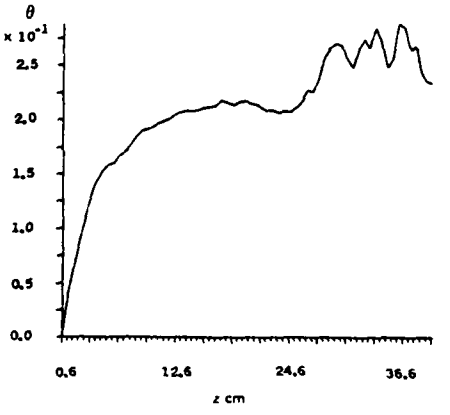

Figure 4. Pulse area θ vs. propagation distance z for the on-axis mode. Values of the parameters are those of Figure 3.

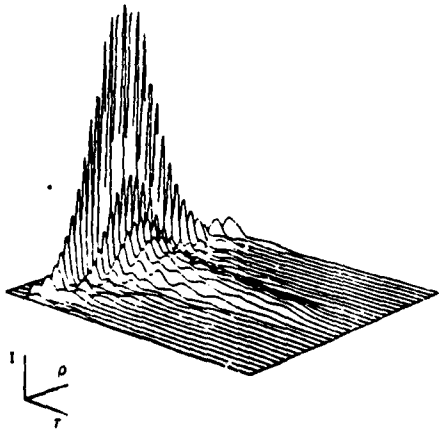

Figure 5. Temporal and radial dependence of pulse intensity at large z.

Reprinted from SPIE Vol 288—Los Alamos Conference on Optics

Effects of propagation, transverse mode coupling, diffraction, and fluctuations on superfluorescence evolution

Farres P. Mattar
Department of Mechanical and Aerospace Engineering
Aerodynamics Laboratory, Polytechnic Institute of New York
Brooklyn, New York 11201
Spectroscopy Laboratory, Massachusetts Institute of Technology
Cambridge, Massachusetts 02139

Abstract

Using proven computational methods developed to efficiently treat transverse and longitudinal dynamic reshaping associated with single-stream propagation effects in cooperative light-matter interactions, a realistic superfluorescence (SF) theory was constructed in close collaboration with experimentalists. A semi-classical model based on the Maxwell-Bloch equations (which rigorously encompasses diffraction, transverse density variations and inhomogeneous broadening) is used. Furthermore, the medium initiation is stimulated by a coherent pulse of an area θ_0 which varies radially, propagates along the rod axis and tips the individual Bloch vectors over an angle θ_0 from its upright position. This effective initiation is treated in using either (a) an homogeneous average tipping angle or (b) instantaneous longitudinal and transverse fluctuations. The Cs datas are correctly simulated for the first time.*

Important remark

At this time, I wish to express my appreciation and give credit to Gibbs, McCall and Feld for their many contributions in the form of numerous relevant discussions, preparatory analytical work and help in selecting details of realistic models based on their close contact with laboratory results. In addition, Dr Gibbs' participation in carrying the calculations accelerated the rate of progress in my research. Let me take this occasion to thank Dr. Gibbs, Dr. McCall and Dr. Feld for their energetic and enthousiastic collaboration.

Introduction

Superfluorescence[1] (SF) is the process by which coherent emission occurs from an ensemble of two-level atoms all initially in the upper state. An important question in SF experiments is why the output pulse is sometimes smooth, but at other times exhibits multiple structure or ringing. Strong ringing or pulsing has been observed by several groups, including the initial HF gas studies[2]. However, recent Cs experiments[3] never show ringing at low densities, whereas at higher densities, highly fluctuating multiple pulsing is usually observed, believed to arise from transverse mode competition[4]. Strong "McCall/Burnham-Chiao" ringing[5] is predicted by semi-classical plane-wave models with initial tipping angle, which neglect variations transverse to the propagation direction. On the other hand, simplified propagationless analytic solutions based on the mean field theory (MFT)[6] of SF pulses have resulted in a symmetrical sech^2 single pulse output. However, such solutions are somewhat academic since all the experiments so far use extended samples for which propagation effects play a major role. Alternatively, when the effective tipping angle is analysed, using quantum mechanics[7], several features of the observed pulses are successfully explained. However, the theory is again far from being complete as several other features, such as the absence of ringing remain unexplained. That is probably as was noted[3,7,10,13] because the one-dimensional model was unrealistic. Specifically, transverse effects are expected to influence the pulse evolution in at least two ways: (a) *spatial averaging* of radiation evolving planarly in concentric shells each with its own density (hence, its own initiation and own delay); and (b) *diffraction coupling* which induces communication between adjacent shells. The first mechanism describes very large Fresnel number F while the second one is very important with small F samples. Inclusion of transverse effects substantially altered the one-dimensional Cs predictions[3b], leading the greater conformity with the Cs data.

The initial SF state is prepared by rapidly inverting a sample of three level atoms by transferring population from the ground state to the upper state with a short light pulse, creating a cylindrical region of excited atoms[2]. SF pulse emission subsequently occurs between this excited state and the intermediate state. There is no optical cavity and stray feedback is negligible.

* This work was supported in part by F.P. Mattar, the Research Corporation, Mobil Oil Corporation, the University of Montreal and the U.S. Army Research and National Science Foundation.

AD-A127 502 TRANSVERSE AND QUANTUM EFFECTS IN SUPERFLUORESCENCE; PUMP DYNAMICS FOR TH..(U) POLYTECHNIC INST OF NEW YORK BROOKLYN DEPT OF MECHANICAL AND A.. F P MATTAR 2/3

UNCLASSIFIED 11 APR 83 POLY-M/AE-83-4 ARO-16880.19-PH F/G 20/6 NL

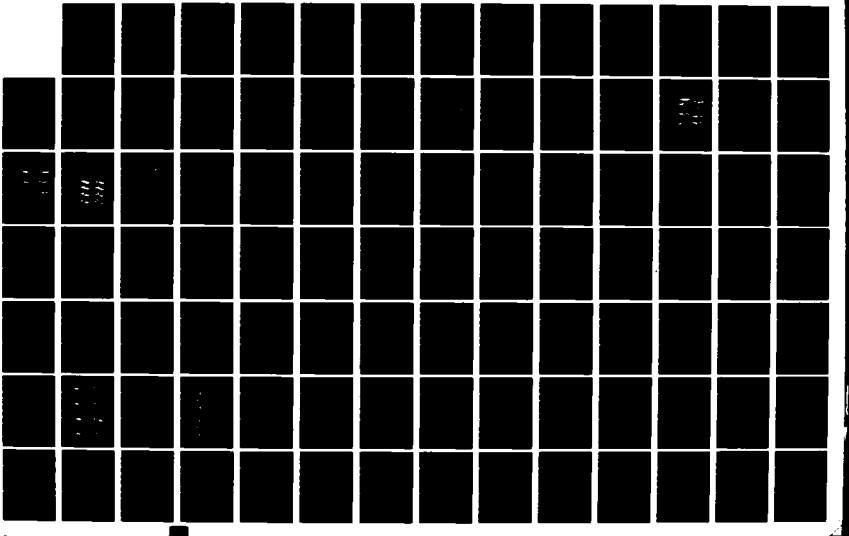

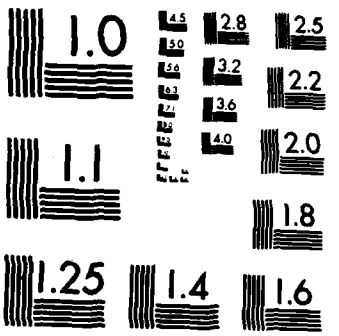

This research employs the semiclassical Maxwell-Bloch approach to explore the influence of transverse effects, using both the average value[4,5a] and statistics[7] of the initial tipping angle[4,5a]. The latter part of the study encompasses both longitudinal fluctuations[7] and transverse fluctuations in the initiating spontaneous emission, as influenced by diffraction.

Transverse effects are expected to influence the pulse shapes in at least two ways, one of which is *spatial averaging*. In SF experiments the initial inversion density, $n_o(r)$, is radially dependent since the pump light pulse typically has a Gaussian-like profile.[8] In the absence of diffraction this cylinder can be thought of as a set of concentric cylindrican shells, each with its own density, tipping angle and delay time[9]. The radiation will thus be a sum of plane-wave intensities; when the entire output-signal is viewed the ringing averages out, resulting in an asymmetric pulse with a long tail.[10]

A second transverse effect, *diffraction*, causes light emitted by one shell to affect the emission from adjacent shells. This cross-coupling mechanism, which causes transverse energy flow, is more important for samples with small Fresnel numbers F.

Furthermore, SF is inherently a *transverse effect* problem even for large F samples since the off-axis modes are not discriminated against. This work is the first to correctly include this crucial element.

Our analysis adopts the coupled Maxwell-Bloch equations, which take fully into account propagation and transverse effects. Previous approaches examined transverse effects in the mean field approximation[11], or included a loss term in the Maxwell equation to describe diffraction.[2,5,12] Thus, our model possesses a long sought after degree of realism.[13a]

Equation of motion

The simulations are based upon an extension of a model[14] which describes transverse effects observed in self-induced transparency experiments.[15] For simplicity the influence of the backward wave, being negligible,[16] is not presently considered, and cylindrical symmetry is assumed. Relaxation of its simplification will be discusses elsewhere[16,17]. The equations of motion are[14]:

$$\frac{\partial \xi}{\partial z} - i\frac{1}{4FL}\nabla_T^2\xi = g\,P \quad \text{(with g, the nonlinear gain, sustaining radial density variations)} \tag{1a}$$

$$\frac{\partial P}{\partial \tau} + P/T_2 = \frac{\mu^2}{\hbar}\xi n \tag{1b}$$

$$\frac{\partial n}{\partial \tau} + \frac{n}{T_1} = -\,\mathrm{Re}(\xi P^*/\hbar) \tag{1c}$$

where ξ and P are the slowly varying complex amplitudes of the electric field and polarization, respectively, n is the inversion density, $\tau = t - z/c$ is the retarded time, μ is the transition dipole moment matrix element and T_1 and T_2 are the population relaxation and polarization dephasing times. Diffraction is taken into account by the Laplacian term $\nabla_T^2\xi = \frac{1}{\rho}\frac{\partial}{\partial\rho}\left(\rho\frac{\partial\xi}{\partial\rho}\right)$ where $\rho = r/r_p$, with Fresnel number $F = \pi r_p^2/\lambda L$, r_p = radius of the initial inversion density at half maximum, and L = sample length. The boundary conditions are $\partial\xi/\partial r = 0$ on the axis (r=0) and at $r = \infty$. To insure that (1) the entire field is accurately simulated, (2) no artificial reflections are introduced at the numerical boundary $r_m >> r_p$, and (3) fine diffraction variations near the axis are resolved; the sample cross-section is divided into nonuniform cells, and is surrounded by an absorbing shell.

Equations (1) are numerically integrated subject to the initial conditions $n = n_o \cos\theta_o$, $P = u + iv = \mu n_o \sin\theta_o (\cos\phi + i\sin\phi)$, which correspond to an initial tipping angle θ_o and a phase (horizontal tilt) angle ϕ. The initial inversion density in the experiment is radially dependent; r-dependence of n_o and/or θ_o is allowed for in the computations.

Numerical results. Figure 1a displays results where spatial averaging is present but diffraction is absent, by setting $F = \infty$ in Eq. (1a). In this figure the emitted power of SF pulses is plotted for samples with uniform and Gaussian profiles of $n_o(r)$ and $\theta_o(r)$ (ϕ is constant). Here, ringing reduction due to spatial averaging of independent concentric shells, (each emitting in a plane-wave fashion), is studied. For a given ϕ, the case of θ_o and n_o both constant (curve i), the uniform plane-wave limit, exhibits strong ringing.[4,5] In curve ii, in which n_o is Gaussian ($n_o(r) = n_o^0 \exp[-\ln 2(r/r_p)^2]$) and θ_o and ϕ are uniform, the ringing is largely averaged out, resulting in an asymmetric pulse with a tail. An essentially identical result (curve iii) is obtained for n_o and θ_o both Gaussian ($\theta_o = \theta_o^0 \exp[0.5\ \ln 2(r/r_p)^2]$), showing that the ringing is predominantly removed by a Gaussian n_o regardless of the radial dependence of θ_o. This is expected since the output pulse

parameters are all dependent only on $|\ell n\ \theta_o|$.[9] As shown in Fig. 1b, with uniform n_o and θ_o but with diffraction included, the output is almost symmetrical and also nearly free of ringing for $F \leq 0.4$.

Figure 2(a) studies the effect of diffraction on the SF pulse shapes by varying F, using Gaussian n_o as in Fig. 1(a), curve ii. Reducing F curtails the oscillatory structure and makes the output pulses more symmetrical, since the diffraction coupling between the minimum-delay center portions of the excited cylinder and the outer cylindrical shell causes the delays of the latter to be reduced. Consequently, outer shells are stimulated to emit earlier. This allows more of the cylinder to emit at the same time; the overall delay is lenghtened slightly and the asymmetry from the Gaussian average is reduced. Thus, diffraction becomes more important as F decreases.

Figure 2(b) is an isometric graph of the intensity build-up for a sample with $F = 1$. The radial variations of intensity peaks, delay and ringing illustrate how different gain shells contribute independently to the net power. Each shell exhibits a different Burnham-Chiao ringing pattern. Accordingly, their contributions to the net signal interfere and reduce the ringing. However, the central portion of the output pulse should exhibit strong plane-wave ringing. In fact, the ringing observed in the HF experiments[2] may have been just that, since the detector viewed a small area in the near field of the beam.

Figure 3 compares the normalized Cs SF data of Ref. 3 and 13b (for which $F \sim 0.7$ with uncertainty ranging from 0.35 to 1.4) to the theory (including relaxation terms). The data were fitted using a Gaussian n_o and a uniform θ_o with nominal value[7] $\theta_o = 2/\sqrt{n_o^g \cdot \pi r_p^2 L}$, n_o being adjusted to yield the observed delays (1.6 to 2.8 times the experimental n_o values). However, in Ref. 3 the curve published at each density was the one having the *shortest* delay. The *average* delay is ~ 30% greater at each density[17]. Thus, the *effective* ratios of our computed densities to the experimental ones range from 1.2 to 2.1, compared with the +60%, -40% quoted experimental uncertainties. The quantum calculations actually yield $\theta_o = (2/\sqrt{n})[\ell n(2n)^{1/8}]^{1/2}$, a 9% correction which further reduces the range to 1.14 - 2.0. Should one adopt Gibbs and Vrehen's decision to set $\theta_o = 6/\sqrt{n}$ following the small injection experiment[16], the range is 1 - 1.8, yet closer agreement. The calculated shapes are in good agreement with the data, and are within the range of shot-to-shot fluctuations (Fig. 3(a)). The only discrepancy is that the simulations predict more of a tail than observed in the experiments. For comparison, Fig. 3(b) also plots the fit in Ref. 3b of the one-dimensional Maxwell-Schrodinger theory[4]. As can be seen, the present theory gives a more accurate fit, illustrating the necessity of including transverse effects. The pulse tails are further curtailed by reducing F within the range of experimental uncertainties[13b] (which used a 1/e rather than a HWHM definition of r_p). Note that often a Fresnel number F' defined as "$r_p^2/\lambda L$" is used; diffraction effects become important when $F' = 1$ (i.e., when $F = 0.36$). If one includes inhomogeneous broadening* one finds that the tail is further reduced as displayed in Fig. 4. The reduction of T_2^* from ∞, to 300 and 32 nsec (for graph. 1, 2 and 3 respectively) shortens the delay, reduces the asymmetry and depresses the tail.

The dependence of the delay measured by the peak location, the pulse width and the peak intensity on the Fresnel numbers F, the radiation time and the tipping angle are illustrated in figure 5.

One can examine fluctuations in the calculations either[1] directly (a) by allowing both in-phase and out of phase components of P to vary randomly according to a normal distribution or (b) through the concept of the tipping angle by including statistics[7a,7b] in $\theta = \theta_o\sqrt{\log(1/x)}$** (with x is a uniform random number) and in ϕ[7c] (varying randomly from $0 \to 2\pi$ in a uniform fashion). An ensemble of these calculations is carried out to simulate shot-to-shot experimental situations; the input θ_o of all these individual segments obeys a Gaussian statistics distribution. Their selection is such that their number can be kept to a minimum[7c].

One finds that those fluctuation calculations *ascertained* the importance of including transverse effects. The influences of a quantum initiation in the transverse simulation clearly appear in the delay reduction, the pulse symmetrisation and the tail curtailment. Figure 6 outlines those statistics results in both planar and non-planar geometries. Figure 7 contrasts the situation in average initial tipping angle with the quantum statistics.

In summary, transverse effects[18,19] are *crucial* for an accurate description of superfluorescence.

* $P = \frac{\sqrt{\pi}}{T_2^*} \int P(\Delta\omega)\ \exp\left[-(T_2^*(\Delta\omega))^2\right]$

** One needs to be careful in not updating the value of θ_o along z (as was accidently introduced into the program but corrected by H.M. Gibbs and E. Watson); otherwise, θ_o fluctuates in a random walk instead of a Gaussian way.

In future work, counter beam propagation in the SF evolution needs to be verified[16]. The initiation and calculations should allow three spatial degrees of freedom (i.e., two transverse dimensions[17]), so that transverse modes can compete. Furthermore, the effect of pump dynamics and reshaping need to be rigorously assessed as outlined in reference [18].

Conclusion

The results provide the first complete explanation of the absence of ringing, and for the first time, quantitative agreement (within measurement uncertainties) with the definitive Cs experiments [3]

Acknowledgement

The system programming assistance of P. Cadieux, M. Cormier and Y. Claude, the editing effort and art work of D.J. Steele, the typing of L. Leclair are joyfully appreciated. The hospitality of Dr. Jiri Teichman of the University of Montreal and Dr. Cattrell at Mobil is particularly appreciated.

References

1. This effect is also known as *superradiance* and *Dicke superradiance*, although these terms are also used to describe coherent emission from samples with initial polarization.
2. N. Skribanowitz, I.P. Herman, J.C. MacGillivray, and M.S. Feld, Phys. Rev. Lett. 30, 309 (1973).
3. H.M. Gibbs, Q.H.F. Vrehen and H.M.J. Hikspoors, (a) Phys. Rev. Lett. 39, 547 (1977); (b) *Laser Spectroscopy III*, J.L. Hall and J.L. Carlsten, eds, (Springer-Verlag, Berlin, 1977) p. 213.
4. S.L. McCall, Ph.D. thesis, Univ. California at Berkeley, 1968 (unpublished); D.C. Burnham and R.Y. Chiao, Phys. Rev. 188, 667 (1969).
5. (a) J.C. MacGillivray and M.S. Feld, Phys. Rev. A 14, 1169 (1976); (b) Ref. 11.
6. R. Bonifacio, P. Schwendimann, Nuovo-Cimento 3, 509 and 512 (1970); R. Bonifacio, P. Schwendimann and F. Haake, Phys. Rev. A 4, 302 (1971) and A 4, 854 (1971); R. Bonifacio and L.A. Lugiato, Phys. Rev. A 11, 1507 and A 12, 587 (1975).
7. (a) F. Haake, J. Haus, H. King, G. Schröder and R. Glauber, Phys. Rev. Lett. 45, 558 (1980); (b) D. Polder, M.F.H. Schuurmans and Q.H.F. Vrehen, Phys. Rev. A 19, 1192 (1979); (c) F.A. Hopf, Phys. Rev. A 20, 2064 (1979); and reference therein.
8. In general $n_o(r)$ will not be Gaussian even if the pump profile is, since saturation flattens $n_o(r)$ near its center, with Gaussian wings. However, our numerical results show that the exact shape of $n_o(r)$ is not critical.
9. See Ref. 5, Eq. (49); J.A. Hermann, Phys. Lett. 69A, 316 (1979); and Refs. 4 and 7(b).
10. J.C. MacGillivray, Sc.D. thesis. M.I.T., 1978 (unpublished); and M.S. Feld and J.C. MacGillivray in *Coherent Nonlinear Optics*, M.S. Feld and V.S. Letokhov, eds. (Springer-Verlag, Berlin, 1980); and Ref. 3b.
11. R. Bonifacio, J.D. Farina and L.M. Narduci, Opt. Comm. 31, 377 (1979). This paper uses the mean field theory (MFT), which neglects propagation and predicts no ringing for the low-density Cs régime: therefore, the mode competition transverse effects that they treat apply *only* to high-density MFT oscillatory SF and are not directly relevant to the Cs data.
12. R. Saunders, S.S. Hassan and R.K. Bullough, J. Phys. A 9, 1725 (1976).
13. *Cooperative Effects in Matter and Radiation*, edited by C.M. Bowden, D.W. Howgate and H.R. Robl, (Plenum Press, New York, 1977): (a) panel discussion, (b) Q.H.F. Vrehen; and Q.H.F. Vrehen and H.M. Gibbs, "Superfluorescence Experiments", in *Topics in Current Physics*, ed. by R. Bonifacio, Springer-Verlag (1981).
14. F.P. Mattar and M.C. Newstein, (a) IEEE J. Quantum Electron QE-13, 507 (1977); (b) Comp. Phys. Comm. 20, 139 (1980) and F.P. Mattar, Appl. Phys. 17, 53 (1978) and "Effects of Propagation, Transverse Mode Coupling and Diffraction on Nonlinear Light Pulse Evolution", in *Optical Bistability*, ed. by C.M. Bowden, M. Ciftan and H.R. Robl (Plenum Press, New York) p. 503.
15. H.M. Gibbs, B. Bolger, F.P. Mattar, M.C. Newstein, G. Forster and P.E. Toschek, Phys. Rev. Lett. 37, 1743 (1976); J.J. Bannister, H.J. Baker, T.A. King and W.G. McNaught, Phys. Rev. Lett. 44, 1062 (1980).
16. Plane-wave studies of R. Saunders and R.K. Bullough (in Ref. 13) and J.C. MacGillivray and M.S. Feld (Ref. 10 and Phys. Rev. A 23, 1334 (1981) show that for realistic values of v_o the mutual influence of the two counter-propagating waves is negligible.
17. P. Cormier, M. Cormier, C. Goutier and F.P. Mattar, twelfth annual Pittsburgh Modeling and Simulation Conference (May 1981), paper 6 G-4.
18. Footnote 13 of Q.H.F. Vrehen and M.F.H. Schuurmans, Phys. Rev. Lett. 42, 224 (1979).
19. F.P. Mattar and H.M. Gibbs, "Transverse Effects in Burnham-Chiao Ringing and Superfluorescence", Laser 80, New Orleans 1980.
20. F.P. Mattar, H.M. Gibbs, S.L. McCall and M.S. Feld, Phys. Rev. Lett. 46, 1123 (1981) and "Transverse and Fluctuation Effects in Superfluorescence", European conference of atomic physics, Heidelberg, April 1981 (paper W10).

21. F.P. Mattar, G. Moretti and R.E. Francoeur, "Transient Counter-beam propagation in a nonlinear Fabry-Perot cavity" (computer Phys. Comm. 22, to be published 1981).
22. F.P. Mattar and C.M. Bowden, "Swept-gain Superradiance in two and three-level systems with Transverse Effects and Diffraction", International Conference on Excited States and Multiresonant Nonlinear Optical Processes in Solids, Aussois, France (March 1981), CNET (and reference therein).

Figure captions

Figure 1. Normalized SF output power vs. τ/τ_R, $\tau_R = \hbar\lambda/4\pi^2\mu^2 n^o_o L = 8\pi\tau_o/3n^o_o\lambda^2 L$. $\theta^o_o = 2\times10^{-4}$, $T_1 = T_2 = T_2^* = \infty$; $L/c\tau_R = 3.9$, (a) $F = \infty$ (see text). (b) Same as (a) but with diffraction included and uniform $n_o(r)$ and $\theta_o(r)$.

Figure 2. Influence of diffraction on SF pulse shapes. Parameters are the same as in Fig. 1a, with n_o Gaussian and θ_o uniform. (a) Emitted power; (b) Isometric graph of intensity for F = 1 case of Fig. 2a.

Figure 3. Theoretical fits to Cs data of Ref. 3. The two curves in (a) indicate typical experimental shot-to-shot variations. F = 1, L = 2 cm, T_1 = 70 ns, T_2 = 80 nsec, λ = 2.931μ, τ_o = 551 nsec, θ_o uniform or Gaussian, $n_o(r)$ is Gaussian. The following give θ^o_o(fit), n^o_o(fit), n^o_o(exp), with θ^o_o in units of 10^{-4} and n^o_o 10^{10}/cm^3: (a) 1.07, 31, 19; (b) 1.37, 18, 7.6; (c) 1.69, 11.9, 3.8; (d) 1.96, 8.85, 3.1. The broken-line curve in (b) is the one-dimensional fit of Ref. 3b, with θ^o_o = 1.69 and n^o_o = 12.

Figure 4. The effect of the inhomogeneous broadening is clearly illustrated T_2^* in graph (a) for Burnham-Chiao ringing (the value T_2^* in curve 1 is infinite while it is 300 ns in curve 2), and is illustrated in graph (b) for the Cs experiment ($T_2^* = \infty$, 300, 32 ns for curves 1, 2, 3 respectively). The power output curve is more symmetric, the peak appears sooner, and the tail is reduced furthermore.

Figure 5. The output power characteristics are the delay (temporal peak location), the peak power (maximum) and the temporal width $\{[\int\tau\, p(\tau)\, d\tau] / [\int p(\tau)\, d\tau]\}$. They are plotted as a function of the inverse Fresnel number for two different tipping angles with infinite relaxation times in graph (a) for large gain typical to the Burnham-Chiao ringing case with relaxation times included, and in graph (b) for the Cs data in graph (c) versus the square logarithm of the tipping angle for uniform, Gaussian and super-Gaussian densities. Graph (d) displays the dependence of the output power curve characteristics as a function of τ_R (equivalently, the inverse square gain) for various relaxation times namely T_1, T_2 = (∞,∞); (70,80); (60,80).

Figure 6. The initiation is simulated using non-uniform random statistics instead of the average tipping angle. Both vertical tipping angle θ_o and horizontal phase angle ϕ are being varied at each and every grid point. θ_o obeys a normal probability distribution as suggested by Glauber & Haake (7a) and Schuurmans, Polder and Vrehen (7b); whereas ϕ varies uniformly between 0 and 2π as suggested by Hopf (7c). An equivalent fluctuation calculation can be carried out by allowing directly a random variation for both in-and out-of-phase components of the polarisation p. Graph (a) and (b) display the uniform plane wave theory for random tipping angles and for random *p* respectively. Graph (c) represents, for a uniform plane wave calculation, an isometric comparison between the output pulse of the various segments of the statistical ensemble at a given propagation length (note that the axes are τ and NBruns). Graph (d) represents the histograms of the tipping angle θ fluctuation and of its phase angle ϕ. Graph (e) represents the histogram on characteristics of the output pulse for a planar simulation with 37 segments (NBruns=37): in curve (i) the peak location (delay); in curve (ii) the magnitude of the pulse peak; and in curve (iii) the pulse width. The result of our delay fluctuations confirmed Haake et al's planar calculations. Graph (f) compares the mutual influence of diffraction and inhomogeneous fluctuation in the tipping angle θ and its phase angle ϕ. Graph (g) displays the isometrics of the output intensity and the associated global histograms for the various segments of the statistical ensembles summarized in Graph (f). Graph (h) duplicates the situation in Graph (f) but with a random P instead of random θ x ϕ; the tail curtailment is maintained. Note the random variation in peak magnitude, peak location and pulse with. *The combined effect of diffraction and statistics shortens the delays, curtails the tail and makes the pulse even more symmetric as experimentally observed in the Cs data.*

Figure 7. The output power is contrasted for various situations where statistics are present directly through *p* (Irand = 4) or through θ and ϕ (Irand = 2) or are absent (Irand = 0); planar and non-planar analyses are represented through Idimen = 1 or 3.

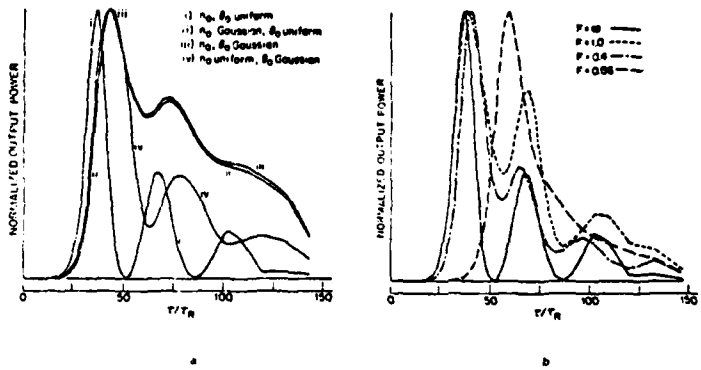

Figure 1

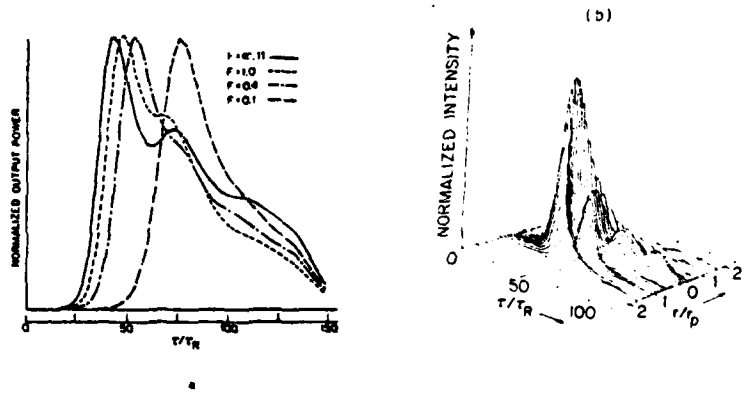

Figure 2

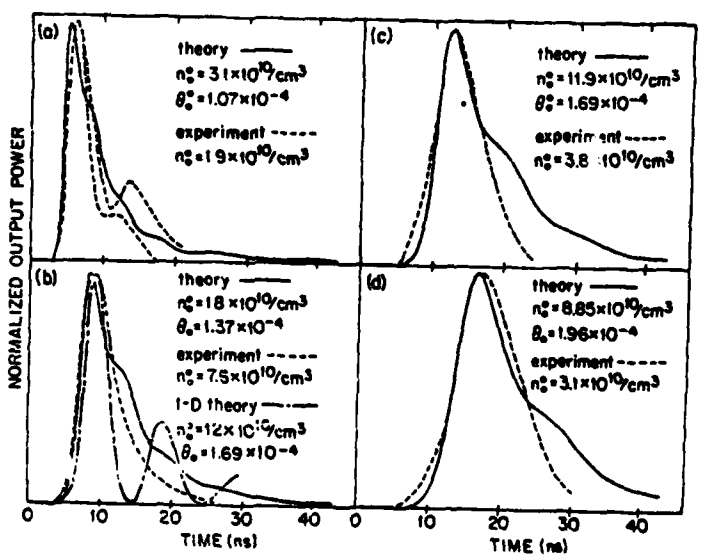

Figure 3

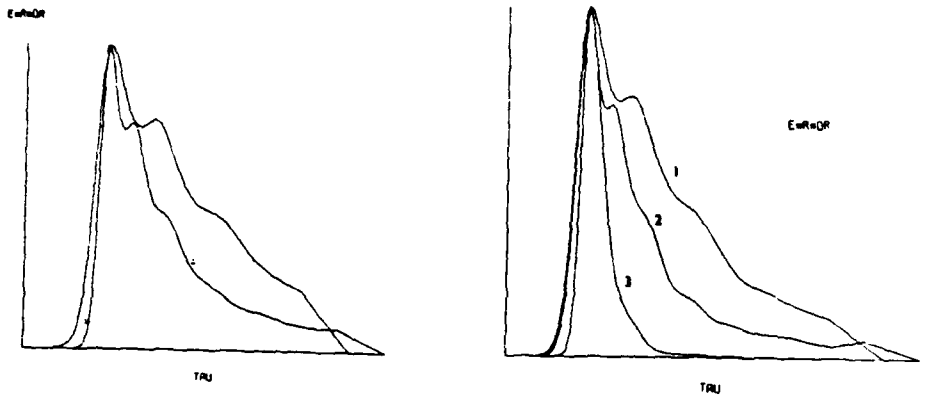

Figure 4

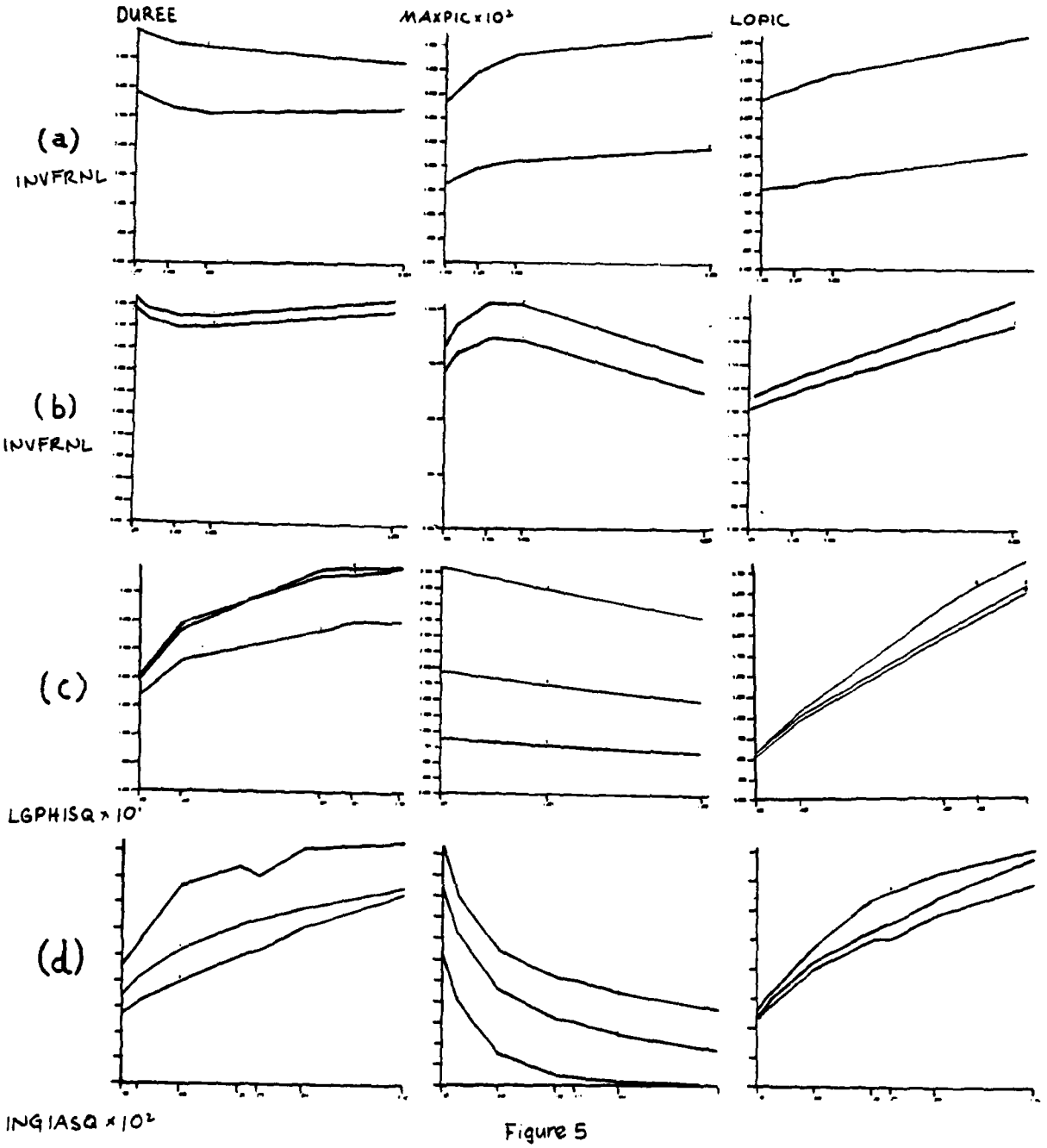

Figure 5

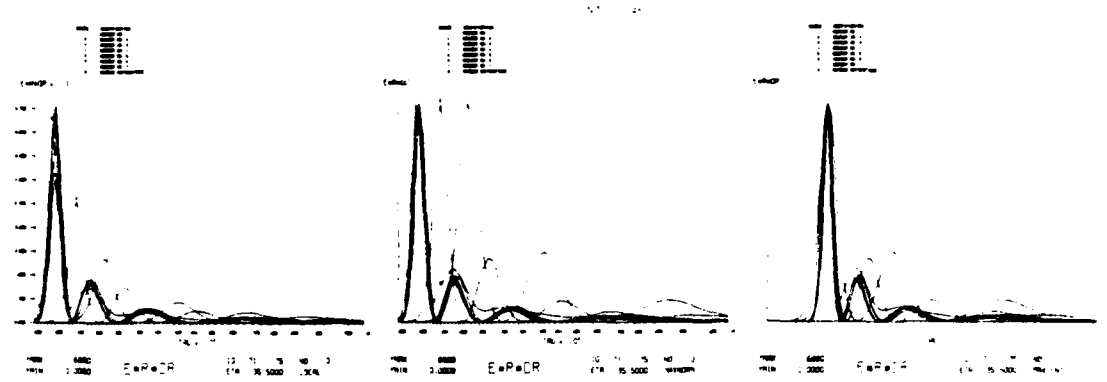

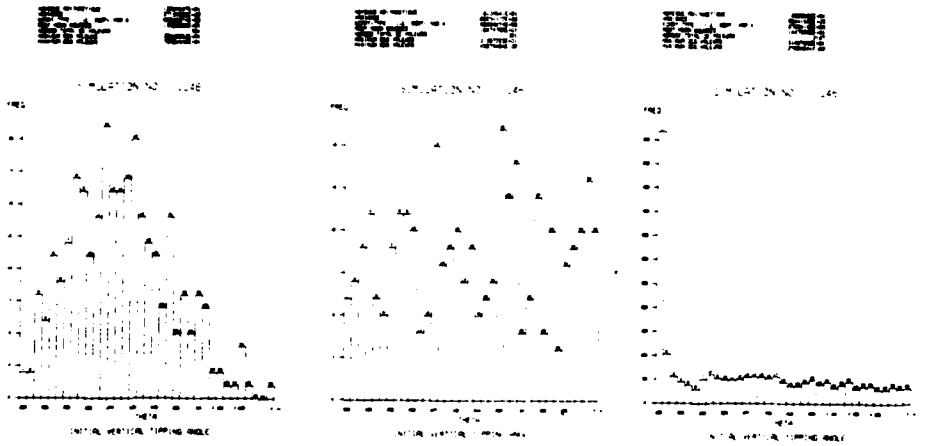

SEGMENT #3 SEGMENT #7 GLOBAL (ALL SEGMENTS)

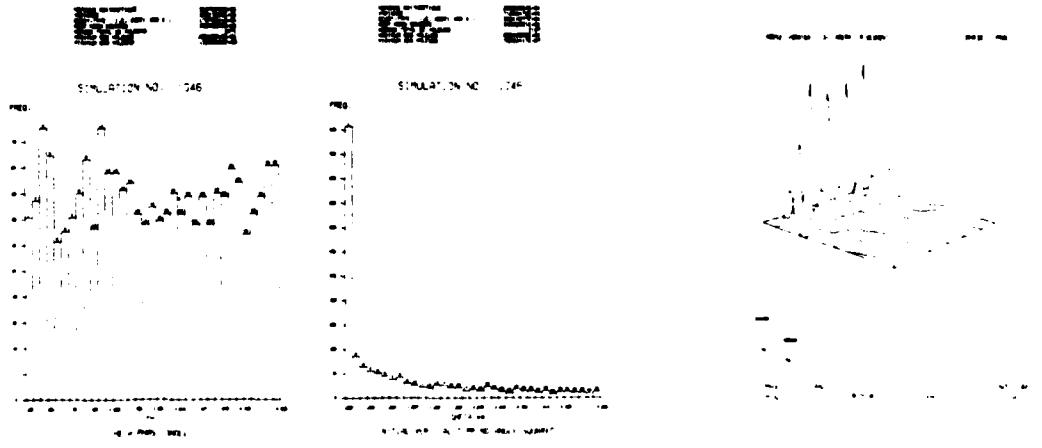

GLOBAL GLOBAL

Figure 6a

Figure 6c

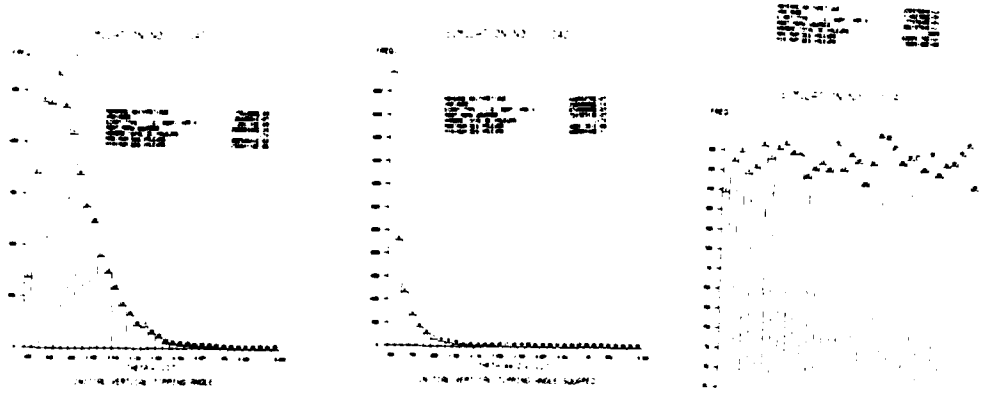

Figure 6d

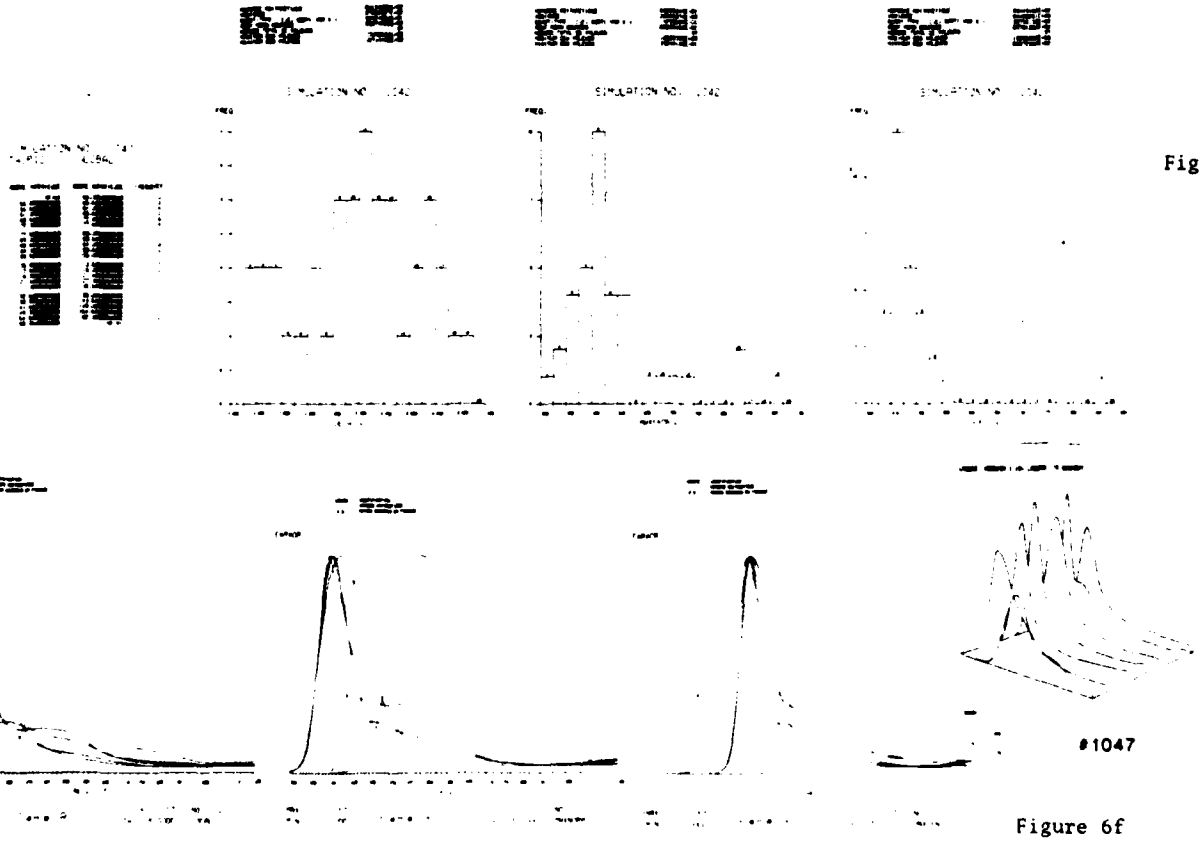

#1047

Figure 6f

#1047

Reprinted from:
OPTICAL BISTABILITY (1981)
Edited by Charles M. Bowden, Mikael Ciftan
and Hermann R. Robl
Book available from: Plenum Publishing Corporation
233 Spring Street, New York, N.Y. 10013

EFFECTS OF PROPAGATION, TRANSVERSE MODE COUPLING AND DIFFRACTION ON NONLINEAR LIGHT PULSE EVOLUTION

F.P. Mattar†

Aerodynamics Laboratory, Polytechnic Institute of New York, Farmingdale, New York 11735

Abstract: The effective computational methods developed to efficiently tackle transverse and longitudinal reshaping associated with single-stream and two-way propagation effects in cooperative light-matter interactions, using the semi-classical model are described. The mathematical methods are justified on physical grounds. Typical illustrative results of propagation in resonant absorbers, amplifiers and superfluorescence systems are presented.

I. INTRODUCTION

This paper reviews the unified mathematical methods developed for three-dimensional simulation of several physical phenomena previously studied independently. The same basic algorithm with some alterations will simulate both superfluorescence[1,2] and optical bistability[3,4]. With extra modifications, it can also analyze four-wave mixing[5] and phase conjugation[6] systems. Further applications include two-way Self-Induced Transparency[7] and Soliton Collision[8] studies.

The proposed model evolved as a result of close collaboration with the experimentalists, H.M. Gibbs[9-13], S.L. McCall[11-13] and recently, M.S. Feld[13], enhancing the rate of progress in the re-

†Work jointly sponsored by the Research Corporation, the International Division of Mobil Corporation, the University of Montreal, the U.S. Army Research Office, DAAG29-79-C-0148 and the Office of Naval Research, N000-14-80-C-0174.

search and leading to a better understanding of basic cooperative effects in light-matter interactions. Quantitative analyses in superfluorescence were obtained and are being developed in optical bistability.

The model encompasses propagation that includes rigorous diffraction[16,15], time-dependent phase variation, off-resonance[16] as well as nonuniform excitation[19] and transverse and longitudinal boundary conditions[18]. (An additional control probe-beam is being developed[21].)

The adoption of proven computational techniques, developed by Moretti[22-24] in aerodynamics, to solve problems in the laser field, is justified by the analogy between fluid and wave propagation problems described. The laser beam evolution can be interpreted in terms of an equivalent flowing fluid[25] whose density is proportional to the laser field intensity, and whose velocity is proportional to the gradient of the field phase. This description allows for the treatment of more slowly varying dependent variables and yields to governing equations of motion, which are a generalization of the Navier-Stokes equations[26]. In the fluid formulation, the equivalent fluid is compressible and is subjected to an internal potential, depending solely and nonlinearly upon the fluid density and its derivatives; this is called the "quantum mechanical potential." Furthermore, the field scalar wave equation mathematically corresponds to a complex heat diffusion equation with a non-uniform functional source; while the Bloch equations, in a rotating frame, are structurally similar to the torque equation[27]. For two-way problems, the simultaneous set of quasi-optic field equations (one for each traveling wave) play the same preponderant role as Euler equations in shock calculations for fluid dynamics problems.

Quite different effects, i.e., self-lensing[28], self-phase modulation[29], self-spectral broadening[30] and self-steepening[31], previously studied separately, combine here to modify the pulse behavior diversely at different positions and times. For example, the interplay of diffraction coupling through the Laplacian term and the inertial response of the non-uniform pre-excited medium will inevitably redistribute the beam energy spatially and temporally[32]. This transient one- or multi-beam transverse reshaping will profoundly affect the performance of any device that relies upon it. Specifically, this pragmatic, three-dimensional analysis helps in the interpretation of recent experimental results in superradiance, superfluorescence, optical bistability and active-mirror amplifiers for laser-fusion. It also accounts for deviations and departures between recent experimental observations and predictions of planar wave theory (see Fig. (1)).

To circumvent excessive memory requirements while insuring adequate numerical resolution, one must resort to nonuniform

meshes. In this large computational problem, the calculational efficiency of the algorithm chosen is of crucial importance. A brute force, finite difference treatment of the governing equations is not feasible. Instead, by using the details of the physical processes to determine where to concentrate the computational effort, accuracy and economy are achieved. For example, if for self-focused beams, a fixed transverse mesh is used, a lack of resolution (see Fig. (2)) may result. A non-negligible loss of computational effort in the wings of the beam will also occur.

Coherent Pulse Propagation

I. Usual Theory

1 Dim. $\xi=\xi(\rho)$

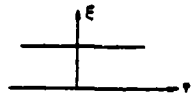

'Uniform Plane Wave'

II. Usual Experiment

$\xi=\xi(\rho)\ e^{-\rho^2}$

'Gaussian'

Fig. 1. The state of the art in coherent pulse propagation is displayed. The theoretical effort was restricted to a uniform plane wave prior to the work of Newstein et al; whereas the usual experiment was carried out using a Gaussian beam. To simulate a uniform plane wave, the smallest possible detector diameter was selected as compared to the Gaussian beam diameter (i.e., (i.e., $d_{detector} << d_{beam}$)

In particular, evenly-spaced computational grid points are related to variable grids in a physical space by adaptive stretching (Fig. (3)) and rezoning (Fig. (4)) techniques. This mapping consists either of an a priori coordinate transformation or an adaptive transformation (Fig. (5)) based on the actual physical solution. Both stretching transformation in time and rezoning techniques in space are used to alleviate the computational effort. The propagation problem is thus reformulated in terms of appropriate coordinates that will automatically accommodate any change in the beam profile[34-40].

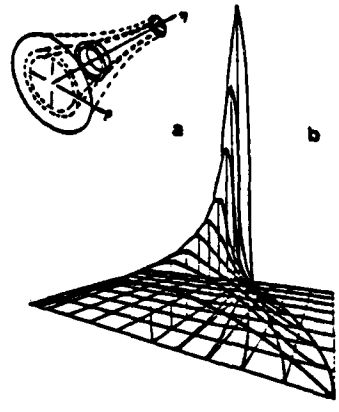

Fig. 2 (a) Isometric representation of the beam cross-section as it experiences self-focusing: The cross-section decreases as a function of the propagation distance; (b) An isometric display of the time integrated field energy as a function of ρ and η to illustrate the resolution limitation associated with uniform mesh.

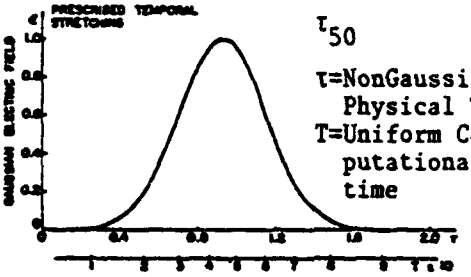

Fig. 3. Non-uniform prescribed temporal stretching.

The resultant dynamic grid removes the main disadvantage of insufficient resolution, where uniform Eulerian codes generally suffer. Furthermore, the advantages of grid sensitivity can be obtained by either using adequate rezoning and mapping in Eulerian coordinates or by simply using traditional Lagrangian methods[41,42]. Thus, the convenience of moderate memory requirements can be combined with the desirable numerical resolution should one rezone the grids. The techniques due to Moretti[33] will economically generate precise results. Although this appears surprising because of the mesh coarseness, his technique succeeds because it discriminates intelligently between the different domains of the critical physical parameters.

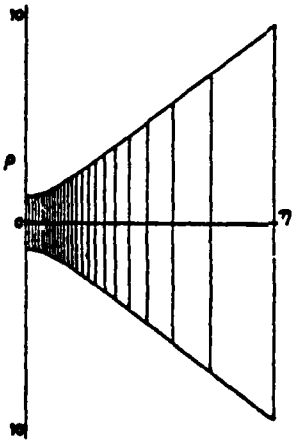

Figure 4. Two-dimensional prescribed rezoning for ρ and η. As the beam narrows the density of transverse points and the transmission planes increase simultaneously.

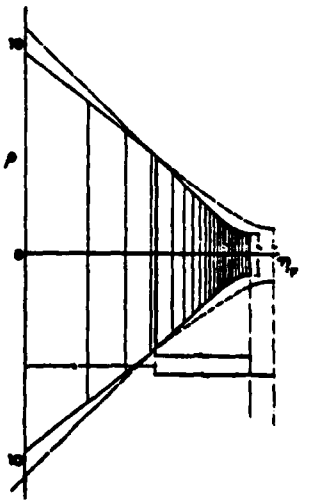

Fig. 5. Self-adjusted two-dimensional rezoning for ρ and η to follow more closely the actual beam characteristics. The (normalizing) Gaussian reference beam is redefined during the calculation.

For the two-beam analysis, our approach relies on one-way nonsymmetric discretizations of the longitudinal and transverse derivatives as well as nonuniform grids. Numerical instrumentation is unavoidable. The role of characteristics as information carriers is emphasized and therefore the law of forbidden signals cannot be violated[43]. The physical subtleties of the nonlinear problem can be adequately implemented.

Interactive graphic software was developed to simplify the physics of extraction from these complex codes. Structural modular programming techniques are used, making the program easier to read, maintain and transport as well as for further extensions and generalizations of the planar wave theory. The resultant code is deceptively simple and easy to follow. This mathematical modeling, motivated by Gibbs' and McCall's experimental work, is engineering physics in its purest sense: its main goal is to obtain a numerical solution to and insight into a real physical problem, instead of reaching a neat analytical solution to an idealized problem of limited applications.

II. SIT/SUPERFLUORESCENCE EQUATIONS OF MOTION

In the slowly varying envelope approximation, the SIT dimensionless, semi-classical field-matter equations[15] (which describe a system in a cylindrical geometry with azimuthal symmetry), are:

$$-iF\,\nabla_T^2 e + \frac{\partial e}{\partial \eta} = \mathcal{P} \tag{1}$$

$$\partial \mathcal{P}/\partial \tau = eW - (i\Delta\Omega + 1/\tau_2)\mathcal{P} \tag{2}$$

and

$$\partial W/\partial \tau = -1/2(e^*\mathcal{P} + e\mathcal{P}^*) - (W-W^e)/\tau_1 \tag{3}$$

where

$$e = (2\mu/h)\tau_p e', \quad \text{and} \quad \mathcal{P} = (2/\mu)\mathcal{P}', \tag{4}$$

$$E = \mathrm{Re}[e'\exp\{i(\kappa/c)z-\omega t)\}]; \tag{5}$$

with W^e the equilibrium value of W, subjected to the initial and boundary conditions.

1. for $\tau \geq 0$: $e = 0$, $W = W_i$, $\mathcal{P} = \mathcal{P}_i$ known function to take into account the pumping effects or the initial tipping angle.

2. for $\eta = 0$: e is given as a known function of τ and ρ;

3. for all η and τ: $[\partial e/\partial\rho]_{\rho=0}$ and $[\partial e/\partial\rho]_{\rho=\rho_{max}}$ vanishes (with ρ_{max} defining the extent of the region over which the numerical solution is to be determined).

with $k/c = \omega$ (6)

and $\nabla_T^2 e = [\ \frac{1}{\rho}\frac{\partial}{\partial\rho}(\rho\ \frac{\partial e}{\partial\rho}\ )]$; (7)

after applying l'Hopital's rule, the on-axis Laplacian reads:

$$\nabla_T^2 = 2\ \frac{\partial^2 e}{\partial\rho^2} \tag{8}$$

$$P = i\ \mathrm{Re}[\mathcal{P}'\ \exp\{i(\kappa/c)z - kt\}]. \tag{9}$$

The complex field amplitude e, the complex polarization density $\mathcal{P}$, and the energy stored per atom W, are normalized functions of the transverse coordinate $\rho = t/t_p$, the longitudinal coordinate $\eta = z \times \alpha_{eff}$, and the retarded time $\tau = (t - zn/c)\tau_p$ (see Fig. (6)). The time scale is normalized to the full width half maximum (FWHM) input pulse length, τ_p and the transverse dimension scales to the input beam spatial width r_p. The longitudinal distance is normalized to the effective absorption length,[44] $(\alpha_{eff})^{-1}$ where

$$\alpha_{eff} = [\frac{\omega\mu^2 N}{n\hbar c}]\tau_p \rightarrow [\alpha'\tau_p] \tag{10}$$

Here, ω is the angular carrier frequency of the optical pulse, μ is the dipole moment of the resonant transition, N is the number density of resonant molecules, and n is the index of refraction of the background material. The dimensionless quantities $\Delta\omega = (\omega - \omega_o)\tau_p$, $\tau_1 = T_1/\tau_p$, and $\tau_2 = T_2/\tau_p$ measure the offset of the optical carrier frequency ω from the central frequency of the molecular resonance ω_o, the thermal relaxation time T_1, and the polarization dephasing time T_2, respectively.

Even in their dimensionless forms, the various quantities have a direct physical significance. Thus ρ is a measure of the component of the transverse oscillating dipole moment (ρ has the proper phase for energy exchange with the radiation field). In a two-level system, in the absence of relaxation phenomena, a resonant field cause each atom to oscillate between the two states,

W=-1 and W=+1, at a Rabi frequency $f_R = e/2\tau_p = (\mu/\hbar)e'$. Thus e measures how far this state-exchanging process proceeds in rp'

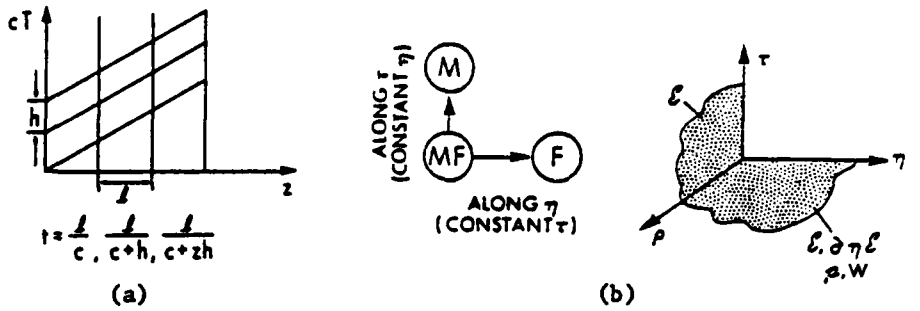

Fig. 6. Graph (a) displays the retarded time concept. Graph (b) outlines the numerical approach: a marching problem along η for the field simultaneously with a temporal upgrading of the material variables along τ.

The dimensionless parameter, F, is given by $F=\lambda(\alpha_{eff})^{-1}/(4\pi r_p^2)$. The reciprocal of F is the Fresnel number associated with an aperture radius r_p and a propagation distance $(\alpha_{eff})^{-1}$. The magnitude of F determines whether or not one can divide the transverse dependence of the field into "pencils" (one per radius ρ), to be treated in the plane-wave approximation.

As outlined by Haus et al[45], the acceptance of equations (1-3) implies certain approximations: eq. (3) shows that the product 'e$\mathcal{P}$' of the electric field e and the polarization $\mathcal{P}$ causes a time rate of change in the population difference leading to saturation effects. Inertial effects <u>are</u> considered.

III. IMPORTANCE OF BOUNDARY CONDITIONS

When the laser beam travels through an amplifier, the transverse boundary has an increasingly <u>crucial</u> effect compared to the absorber situation. The laser field which resonates with the pre-excited transition, experiences gain; the laser which encounters a transition initially at ground state, experiences resonant absorption and losses. A greater portion of the pulse energy is diffracted outwardly in the amplifier than in the absorber[46]. Consequently, these boundary reflection conditions play a substantial role in the amplifier calculations and obscure the emergence of any new physical effects. Acceptable results are achieved <u>only</u>

by carefully coupling the internal points analyzed with the boundary points[47]. Special care is required to reduce the boundary effect to a minimum such as using non-uniform grids and confining the active medium by an absorbing shell.

In practice, the transverse boundary is simulated by implementing an absorbing surface and mapping an infinite physical domain onto a finite computation region (see Fig. (7)). In Fig. (8), the first and second radial derivatives and the Laplacian term are drawn. Figure (9) contrasts in the stretched radial coordinate system, the transverse coupling and the electric field. The numerical domain sensitivity and the physical dependence on the boundary conditions can be readily assessed.

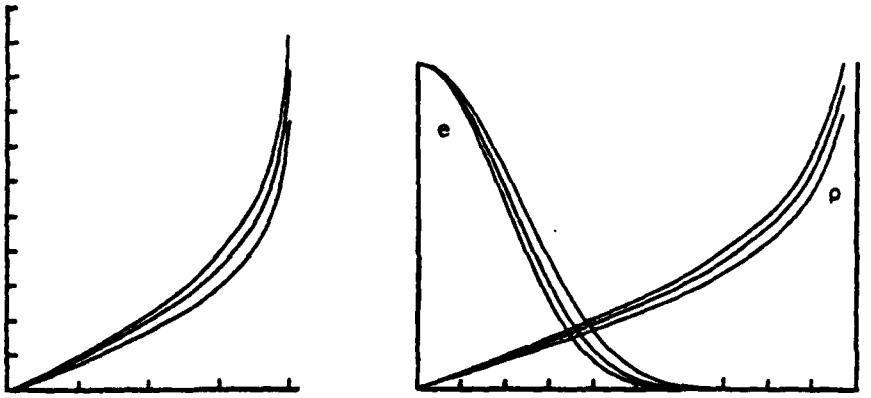

Fig. 7. Graph (a) shows non-uniform stretching of the transverse coordinate. Graph (b) contrasts the Gaussian beam e dependence with the nonuniform physical radius ρ. Both graphs are plotted versus the uniform mathematical radius R.

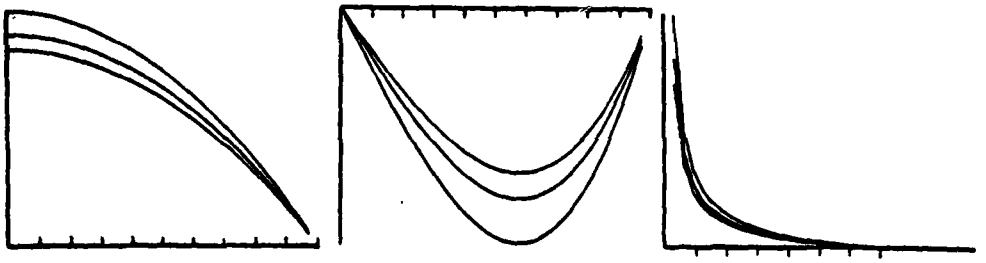

Fig. 8. This graph illustrates the dependence of the radial mapping and the derivatives on the different parameters versus the uniform mathematical radius: First weighting stretching factor $\partial R/\partial\rho$; 2nd weighting stretching factor, $\partial^2 R/\partial\rho^2$; weighted diffraction term, $\nabla^2_{T\rho} R$.

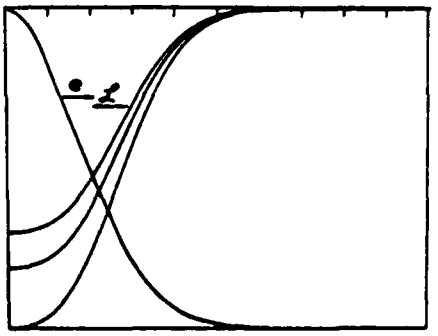

Fig. 9. This figure contrasts the Laplacian dependence '$\mathcal{L}$' for a given Gaussian profile 'e' for various non-uniform radial point densities.

IV. PRESCRIBED STRETCHING

The numerical grid is defined by widely-spaced computational nodes in the area most distant from the plane of interest and by densely clustered nodes in the critical region of rapid change; the latter being in the neighborhood of maxima and minima, or for multi-dimensional problems, in the vicinity of saddle points. Resolution is sought only where it is needed. The costs involving computer time and memory size dictate the maximum number of points that can be economically employed. In planning such a variable mesh size, the following must be kept in mind:

(A) The stretching of the mesh should be defined analytically so that all additional weight coefficients appearing in the equations of motion in the computational space, and their derivatives, can be evaluated exactly at each node. This avoids the introduction of additional truncation errors in the computation.

(B) To assure a maximum value of ΔT, the mathematical grid step, the minimum value of $\Delta\tau$, the physical time increment, should be chosen at each step according to necessity. This means that the minimum value of $\Delta\tau$ must be a function of the pulse function steepness.

(C) The minimum value of $\Delta\tau$ should occur inside the region of the highest gradient which occurs near the pulse peak.

For example, following Moretti's approach,[32] if

$$T=\tanh(\alpha\tau) \tag{11}$$

and α the stretching factor must be larger than 1, the entire semi-axis τ greater than zero can be mapped on the interval $0 < T < 1$

with a clustering of points in the vicinity of $\tau_c = 0$, the center of gravity of the transformation for evenly-spaced nodes in t.

This mapping brings new coefficients into the equations of motion which are defined analytically and have no singularities. It avoids interpolation at the common border of differently spaced meshes. The computation is formally the same in the "T" space as it was in the "τ" space. Some additional coefficients, due to the stretching function, appear and are defined by coding the stretching function in the main program. A slightly modified stretching function is used in the laser problem. Figure (10) illustrates the transformation and its different dependencies on the particular choice of its parameters.

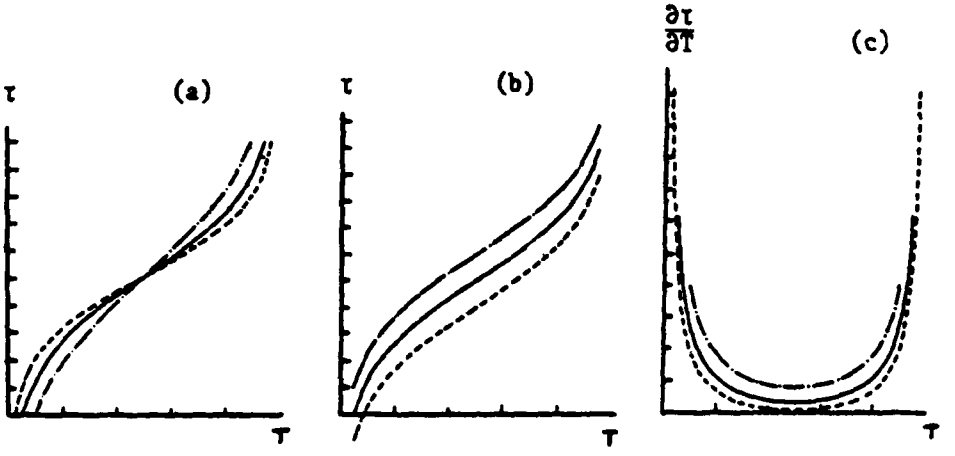

Fig. 10 Dependence of prescribed stretching τ and its derivatives ∂τ/∂T on the point densities and the center of transformation versus the uniform computational T.

The derivative of the mapping function produced by the gradual variation along the "T" axis is also defined analytically. In response, the computational grid remains unchanged while the physical grid (and the associated weighting factors) can change a lot.

Should one need to study the laser field buildup due to initial random noise polarization (for superfluorescence), or an initial tipping angle (for superradiance), one must use a different stretching[32]. This stretching is like the one defined for treating radial boundary conditions. The mesh points are clustered near the beginning (small τ); their density decreases as τ increases.

V. ADAPTIVE STRETCHING IN TIME

As the energy continues to shift back and forth between the field and the medium, the pulse velocity is modified disproportionately across the beam cross-section. This retardation/advance phenomenon in absorber/amplifier can cause energy to fall outside the temporal window. Also, due to nonlinear dispersion, various portions of a pulse can propagate with different velocities, causing pulse compression. This temporal narrowing can lead to the formation of optical shock waves. To maintain computational accuracy, a more sophisticated stretching is needed. The accumulation center of the nonlinear transformation is made to vary along the direction of propagation. This adaptive stretching will insure that the redistribution of mesh points properly matches the shifted pulse, Figure (11).

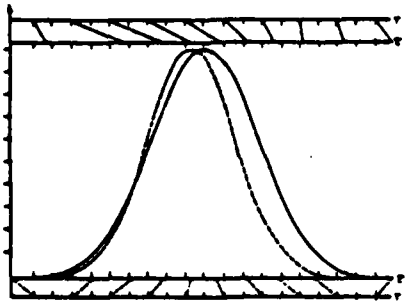

Fig. 11 Adaptive stretching with different centers of transformation.

Here, the transformation from τ to T is applied about a center τ_c which is a function of η. The stretching factor α could also be a function of η.

The field equation is similar to those of Section II, but contains an extra term:

$$-iF\,\nabla^2_{T\rho}e + \partial_\eta e + \frac{\partial e}{\partial T}\left[-\frac{\partial T}{\partial \tau}\right]\tau_c \frac{d\tau_c}{d\eta} = \mathcal{P} \qquad (12)$$

The role played by the time coordinate is different: an explicitly time-dependent term is now included.

VI. REZONING

The main difficulty in modeling laser propagation through inhomogeneous and nonlinear media stems from the difficulty of pre-assessing the mutual influence of the field on the atomic dynamics and vice versa. Strong beam distortions should occur based on a perturbational treatment of initial trends. One must

normalize out the critical oscillations to overcome the economical burden of an extremely fine mesh size. To insure accuracy and speed in the computation, a judicious choice of coordinate systems and appropriate changes in the dependent variables, which can either be chosen a priori or automatically redefined during the computation, must be considered (Figure (12))[33-40].

This coordinate transformation alters the dependent variables and causes them to take a different functional form. The new dependent variables are numerically identical to the original physical amplitudes at equivalent points in space and time.

The requirements of spatial rezoning will be satisfied by simultaneously selecting a coordinate transformation (from the

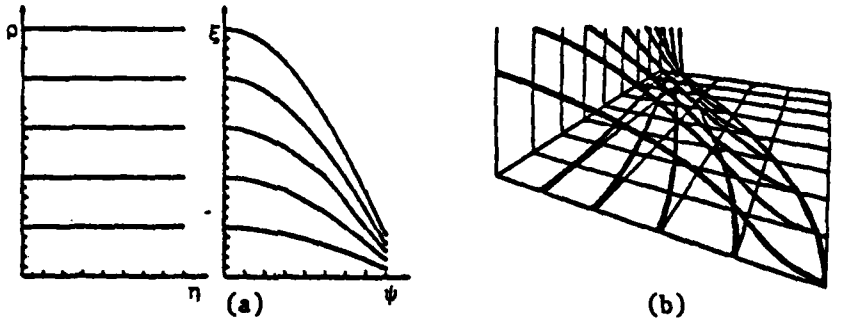

Fig. 12. The concepts of prescribed rezoning are shown in Graph (a); Graph (b) is a close-up of the nonuniform mapped grid of Fig. 2(b).

original coordinates ρ and η to new coordinates ξ and z) and an appropriate phase and amplitude transformation. The chosen function transformation will share the analytical properties of an ideal Gaussian beam propagating in a vacuum.

Since the parameter a, the measure of the transverse scale, shrinks or expands as the beam converges or diverges, it is logical to require the transverse mesh to vary as "a" varies. However, to assure stability and convergence, the ratio $[\Delta\eta/(\Delta\rho)^2]$ must be defined according to the chosen Fresnel number and it must be kept constant throughout the calculation. Accordingly, a new axial variable, z, must be introduced to keep this parameter constant as ρ varies. This should increase the density of η planes around the focus of the laser field where the irradiance sharply increases in magnitude causing a more extensive and severe field-material interaction to occur.

If the quadratic phase and amplitude variation are removed from the field and polarization envelopes, the new field equation

varies more slowly than its predecessor; thus, the numerical procedure allows one to march the solution forward more economically by using larger meshes.

VII. ADAPTIVE REZONING

The foregoing concepts may be generalized by repeating the simple coordinate and analytical function transformations along the direction of propagation at each integration step. Figure (5) and graphs (13a) and (13b) illustrate this self-adjusted mapping in planar and isometric graphs.

The feasibility of such automatic rezoning was demonstrated by Moretti in his conformal mapping of supersonic flow calculations[34], and by Hermann and Bradley in their CW analysis of thermal bloom-

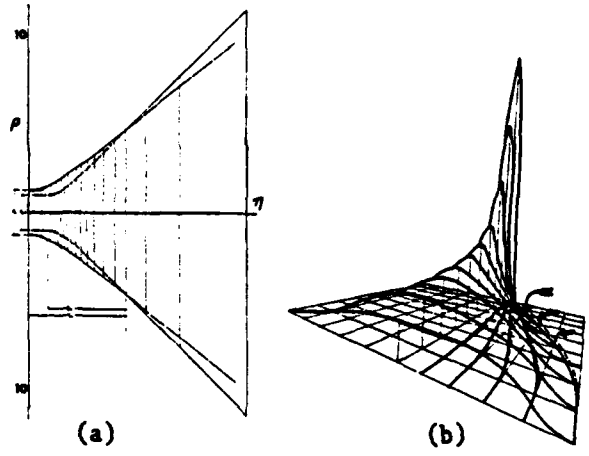

Fig. 13. Graph (a) illustrates the self-adjusted rezoned grid; Graph (b) shows the usefulness of adaptive two-dimensional mapping through isometric representation of the field fluency.

ing[35]. In particular, the change of reference wavefront technique consists of tracking the actual beam features and then readjusting the coordinate system. The new axial coordinate z is defined as before. Previously, the center of the transformation where the radial mesh points were most tightly bunched was at the focus ($z = \eta = 0$). Now the transformation is defined in terms of an auxiliary axial variable z_ξ as a function of z, which is calculated adaptively, in a way that reflects and compensates the changing physical situation.

In this adaptive rezoning scheme, the physical solution near the current z plane is described better by a Gaussian beam of neck radius $a_{\xi 0}$ whose point is a distance z_ξ away than by an initially assumed Gaussian beam with parameters a_0 and z. In addition, to

remove the unwanted oscillations, new dependent variables are introduced without quadratic and quartic radial dependence in the phases of the pulse and polarization envelopes. By minimizing the local field phase gradient the relationship between the auxiliary z_ξ and z is obtained. Thus the rezoning parameters are determined appropriately from the local field variable at the preceding plane, so the new variable at this present point has no curvature. Note that the new equation varies less in its functional values than the original. The numerical computation is significantly improved. Notably, the instantaneous local rezoning parameters of the quadratic wavefront are determined by fitting the calculated phase of the local field to a quartic in the nonuniform radius. More specifically, the intensity-weighted square of the phase gradient integrated over the aperture is minimized. Consequently, the curvature at the highest intensity portion of the beam contributes the most. Various moment integrals of the local field variable and the local transverse energy current will be introduced, to specifically evaluate the adjustable rezoning parameters.

VIII. NUMERICAL RESULTS

This section outlines basic results in SIT, obtained with and without rezoning and stretching, and illustrates why the more sophisticated techniques required less computational efforts.

The first part of this investigation led to the discovery of new physical phenomena which promise to have significant applications for proposed optical communications systems. It had been shown that spontaneous focusing can occur in the absence of lenses, and that the focusing can be controlled by varying the medium parameters. The second part of this analysis dealt with amplifiers.

The dependence of the propagation characteristics on the Fresnel number F^{-1} associated with an effective medium length, on the on-axis input pulse "area," on the relaxation times and on the off-line center frequency shift, has been studied. Furthermore, particular care was exercised to ensure a perfectly smooth Gaussian beam (see Figure (10)) thereby eliminating any possibility of small-scale, self-focusing buildup[48].

The time-integrated pulse "energy" per unit area, $\int_0^\tau |e(\rho,\eta,\tau')|^2 d\tau$, the fluency, is plotted for various values of the transverse coordinate, as a function of the propagation distance (see Fig. 14).

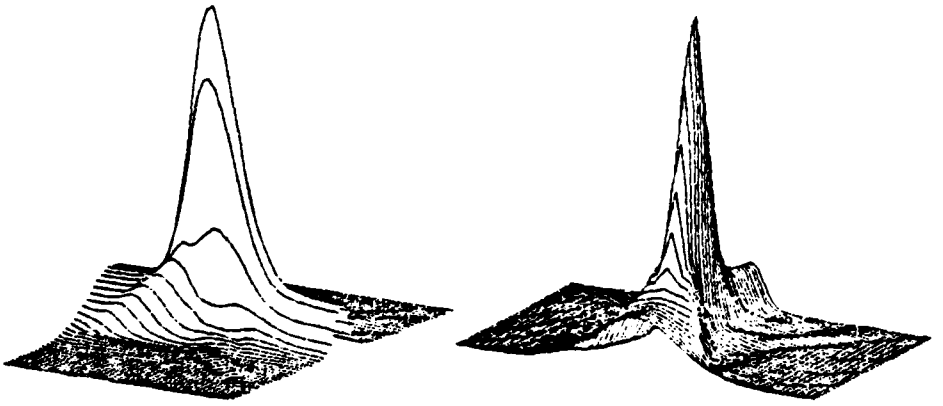

Fig. 14. The longitudinal orientation shown in the left-hand figure illustrates the gradual boosting mechanism that field energy experiences as it flows radially towards the beam axis (while η increases). The second orientation displays the severe beam distortion in its cross-section as a function of η.

The three-dimensional numerical calculations substantiate the physical picture based on a perturbational study of the phase evolution[10,15]. It could be visualized using selected frames from a computer movie simulation of the numerical model output data. In the left-hand curves of Figure (15) the transverse energy current is isometrically plotted against the retarded time for various transverse coordinates at four specific regions of the propagation process: (a) the reshaping region where the perturbation treatment holds; (b) the buildup regions; (c) the focal region; and (d) the post-focal region. The field energy is displayed for the specific regions in the right-most curves of Fig. (15). A rotation of the isometric plots is displayed in Figure (16), to emphasize the radially dependent delay resulting from the coherent interaction. Positive values of the transverse energy current correspond to outward flow, and negative values to inward flow. The results of the reshaping and buildup regions in Figures (15) and (16) agree with the physical picture related to the analytic perturbation discussed elsewhere.

The burn pattern, iso-irradiance level contours (against τ and ρ) for different propagation distances are shown in Figure (17). Severe changes in the beam cross-section are taking place as a function of the propagating distance. At the launching front, the beam is smooth and symmetrical; as the beam propagates into the nonlinear resonant medium, the effect of the nonlinear inertia takes place.

The general format for presenting three-dimensional coherent pulse propagation in amplifying medium will be the same as for the absorber (see Figs. (18) to (21)).

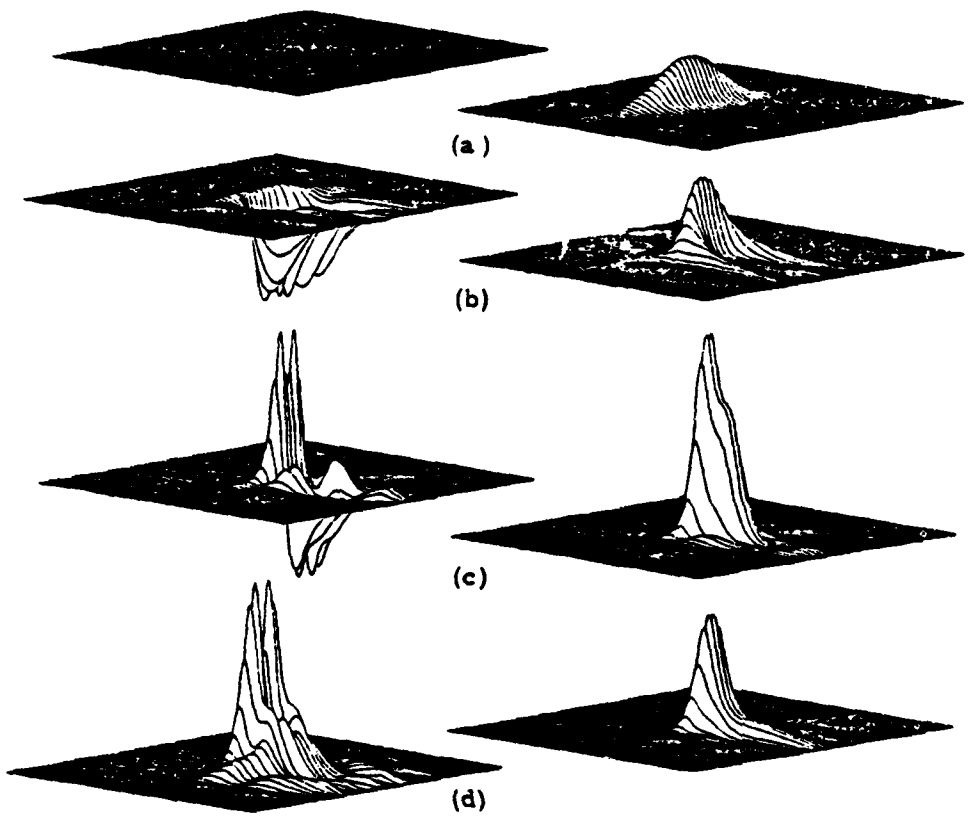

Fig. 15. Isometric plots of the absorber field energy and transverse energy flow, against the retarded time for various transverse coordinates at the four regions of interest.

IX. TRANSVERSE EFFECTS IN SUPERFLUORESCENCE

With the help of Gibbs, the outstanding question dealing with the strong reduction (and elimination) of ringing observed in the low-density Cs [2] experiment from the amount predicted in the one-dimensional calculations [1(b)] was resolved. This was accomplished by developing a rigorous two-dimensional theory of Burnham-Chiao ringing [1b] and superradiance and superfluorescence (SF) in a pre-excited thick medium using a semi-classical formulation [1e] which includes one-way propagation effects as in SIT. The initia-

tion of the SF emission process is characterized by a tipping angle θ_R. When the small signal field gain $\alpha_{eff}L/2$ (or equivalently, the characteristic radiation damping time τ_R of the collective atomic system) is sufficiently large, θ_R, the ratio of the length L to the coherence length L_c, and the Fresnel number $\mathcal{F}$ (equal to area/λL) completely characterize the system behavior. However, L/L_c is not a critical parameter as predicted by the mean field theory.

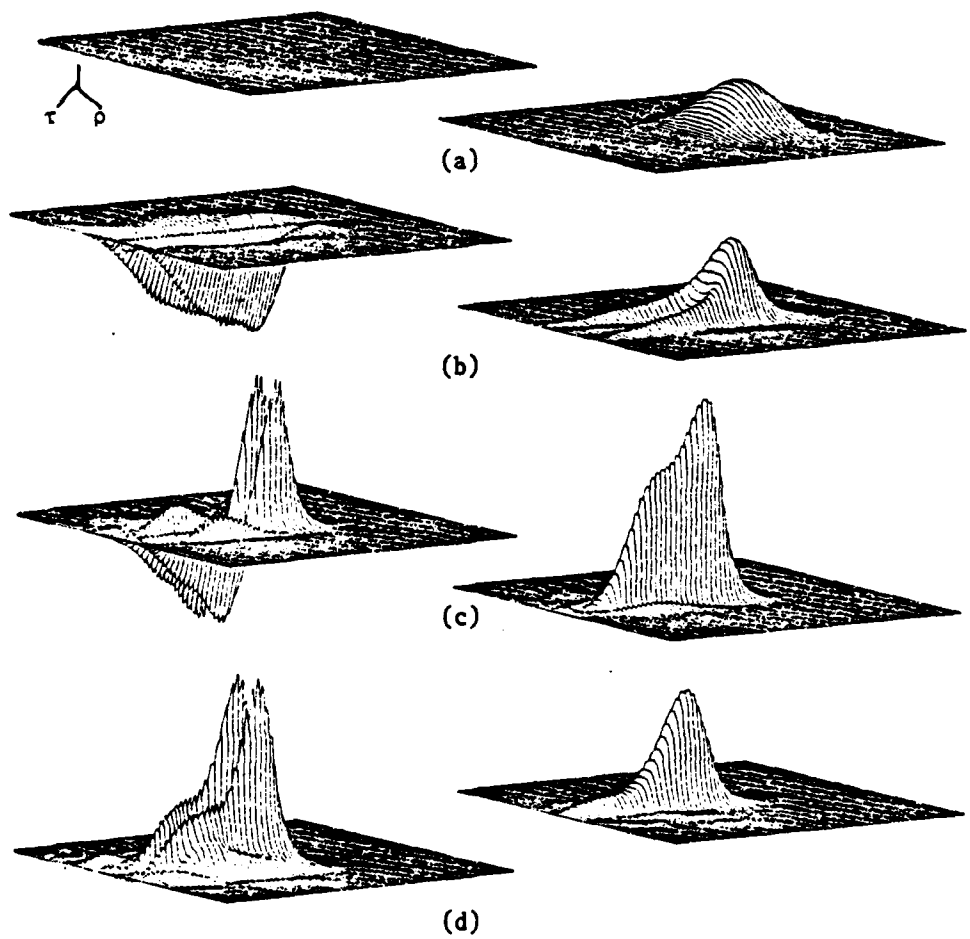

Fig. 16 Isometric plots of the absorber field energy and transverse energy flow profile for various time slices at the four regions of interest.

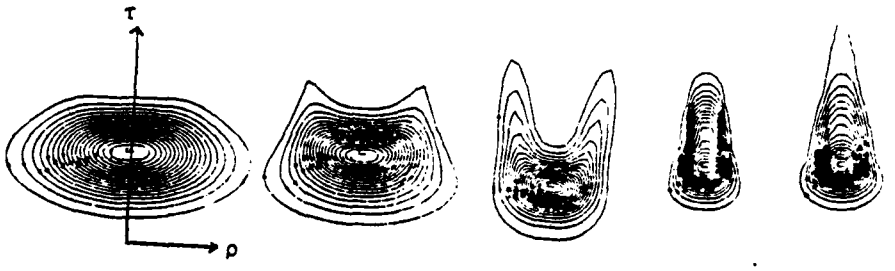

Fig. 17. Absorber field energy contour plots for the four propagation distances. Notice the temporal delay associated with the coherent exchange of energy between light and matter, as well as the beam cross-section narrowing.

Neither the mean-field approximations[1d], nor the substitution of a loss term to account for diffraction coupling[1c,20d], are considered; instead self-consistent methods similar to those developed for SIT studies are adopted[39,46]. The numerical simulation takes fully into account both propagation and transverse (spatial profile and Laplacian coupling) effects.

The previously reported pronounced SF ringing for plane-wave simulation is reproduced for uniform input profile. The reduction of ringing is studied for various radial profiles for the gain $g_R=\alpha_{eff}[c\tau_R]$ (equivalently, the population inversion) and the small input pulse area θ_R[11-13].

The ringing reduction can be explained by two physical mechanisms: (a) a shell (ring) model[32(d)]: spatial averaging of uncoupled planar modes, each associated with a particular shell and subjected to both a distinct θ_R and a radiation time. Radial averaging by a Gaussian gain profile of very large $\mathcal{T}$ eliminates most of the ringing, resulting in an asymmetric pulse with a long tail; and (b) a rigorous diffraction coupling: through the Laplacian term, the adjacent shells interact, causing the field energy to flow transversely across the beam from one region to another.

When diffraction coupling is considered concomitantly with radial variations of θ_R and g_R (i.e., of τ_R), the ringing is more subdued (see Fig. (23)). In other words, reducing $\mathcal{T}$ of a Gaussian profile does reduce the asymmetry (in better agreement with the Cs data) since the outer beam portions are stimulated to emit earlier

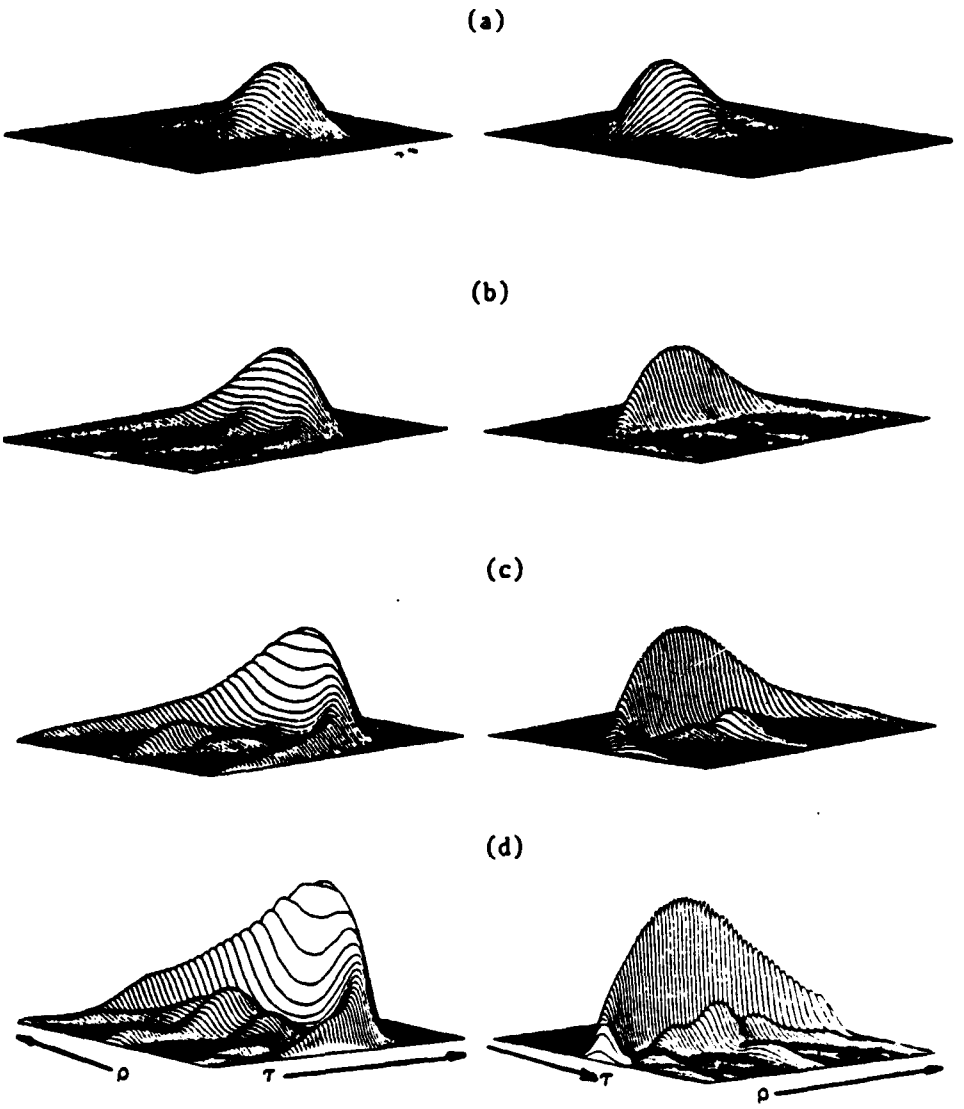

Fig. 18. Isometric plots of the amplifier field energy as a function of τ and ρ for two orientations $\pi/2$ apart at four locations along the propagation direction.

by diffraction from the inner portion. Thus, the effect of the Laplacian coupling is small for large $\mathcal{T}$ but becomes progressively greater at about $\mathcal{T} \leq 1$.

Fig. 19. Amplifier field energy contour plots for the four propagation regions of interest. Note the temporal advance associated with coherent exchange of energy between light and matter (the smaller area propagates more slowly than the larger one), as well as beam cross-section expansion.

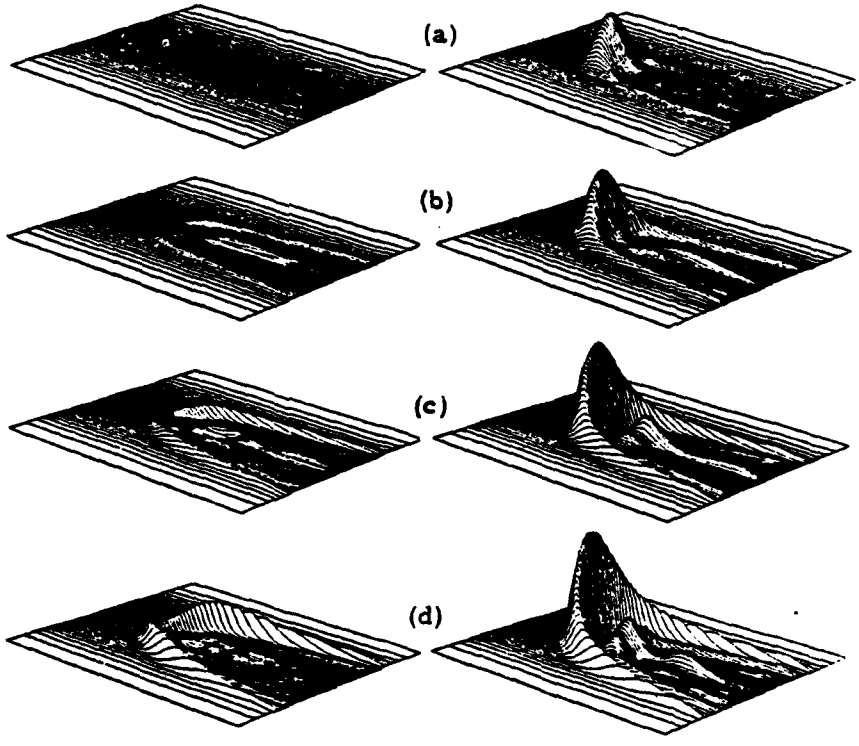

Fig. 20. Isometric plots of amplifier field energy and transverse energy flow against retarded time for various transverse coordinates at four propagation regions studied for absorbers. Stretched radial coordinate was adopted for proper accounting of transverse boundary condition. When these results are compared with those for an absorber, it is evident that a focusing phase is not restricted to the absorber, but develops also for the secondary pulses in amplifying media.

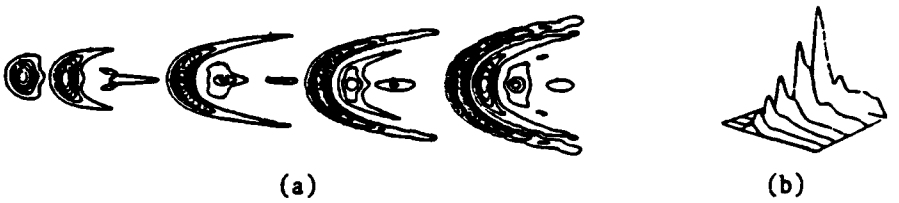

Fig. 21. Amplifier field energy contour plots for four propagation regions of interest with stretched radial coordinates. No severe reflection or abrupt variation in the field energy, at the wall boundary, is observed. The enhancement of diffraction by pre-excited two-level medium is clearly evident.

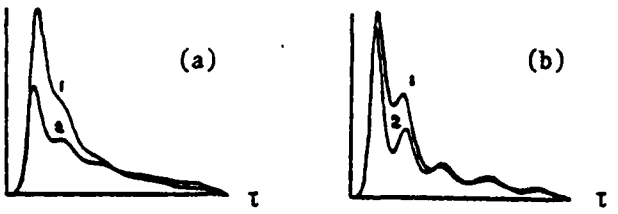

Fig. 22 Contrast the time dependence of the energy after integrating over ρ for the shell model (where θ_R and τ_R are both radially dependent) and the diffraction model (where the Laplacian coupling is rigorously present) for two population inversions: (a) Gaussian $g = g_o \exp[-\rho^2]$, and (b) saturable inversion $g = g_o$ for $\rho < \rho_b$; $g = g_o \exp[-\rho^2]$ for $\rho_b < \rho < \rho_{max}$.

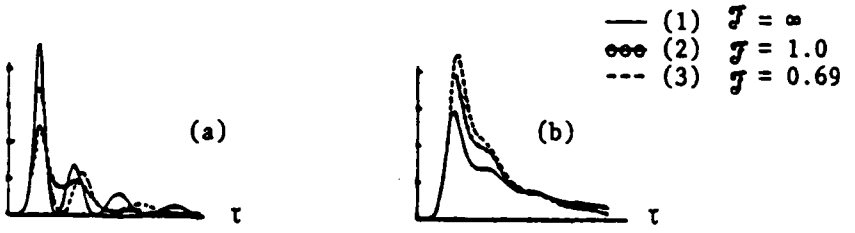

Fig. 23. Total energy per atom as a function of time with $\mathcal{F}$ as the labeling parameter. $\tau_R = 0.046$ ns and $L/L_c = 1.95$. $\theta_R = 3 \times 10^{-3}$ for all radii. (a) Superfluorescence of uniform cylinder or small-area pulse propagation through uniform gain cylinder; (b) Uniform small-area pulse propagation through Gaussian gain medium.

Computer results representing the SF of uniform and nonuniform cylinders (i.e., small-area pulse propagating through a uniform Gaussian gain cylinder) are respectively displayed in Figure (24a) and Figure (24b) for different $\mathcal{J}$. In Figures (25a) and (25b), this initial small-area θ_R is now radially dependent. Figures (26a) and (26b) duplicate the physical situation in Figures (24a) and (24b), but for a smaller initial polarization. The universal superfluorescence scaling law is seen not to hold; the calculated pulse length is much more sensitive to the magnitude of θ_R in the transverse case than it is in the planar case.

The ringing predicted by this two-spatial-dimensional theory agrees more with experimental observations than that predicted by the uniform plane-wave counterpart. Detailed isometric graphs of the field energy buildup show, in Figures (27a), (27b) and (27c) qualitative agreement in peak intensity and peak delay with the ring (shell) model [1c]. Figure (28) illustrates the elimination of ringing under conditions similar to the low-density Cs data for different radial density distributions. Figure (29) contrasts the dependence of the radial gain on a typical $\mathcal{J}$ by various θ_R; Figure (30) illustrates the dependence of the radial gain on a typical θ_R by different $\mathcal{J}$. Figure (31) shows the effect of varying τ_R on this output intensity. Various small-scale ripples were introduced in the gain profile (see Fig. 31).

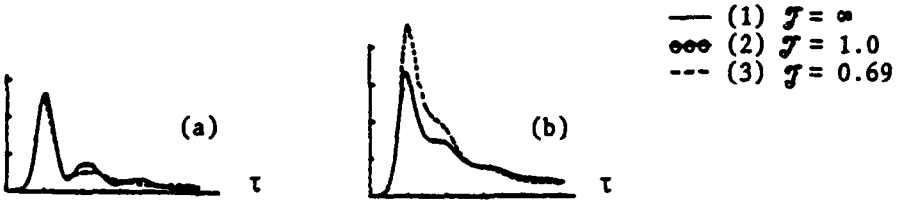

Fig. 24. (a) Propagation of small-area Gaussian profile pulse through uniform cylinders (τ_R = 0.046 ns, L/L_c = 1.35 and θ_R = 3×10^{-3} on-axis). (b) Superfluorescence with Gaussian radial gain (τ_R = 0.046 ns, L/L_c = 1.35 and $\theta_R = 3 \times 10^{-3}$ on-axis).

Ringing is largely removed by a gain medium of $\mathcal{J} = 1$, resulting in an asymmetric output pulse with a long tail. It now seems that a larger θ_R, see Fig. (33a) (unlikely, according to measurement of feedback effects and estimates of Raman effects during the excitation pulse[2d]), or smaller $\mathcal{J}$ (perhaps 0.4 consistent with the range $0.35 < \mathcal{J} < 1.39$ of ref. 1(a) which used a 1/e rather than a half width half maximum (HWHM) definition of r_p), see Fig. (33b),

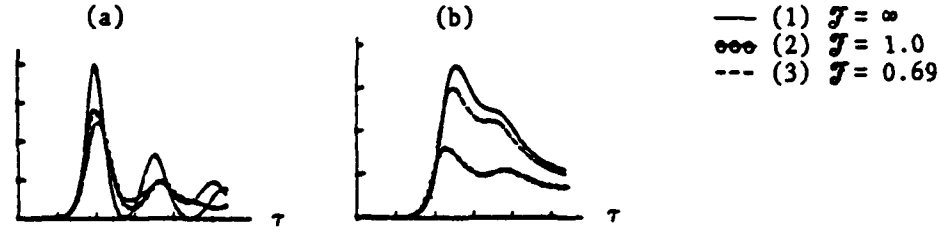

Fig. 25. Same parameters as in Fig. 23 but with a smaller $\theta_R = 10^{-4}$: (a) Small area propagation in a uniformly inverted cylinder. (b) Small-area propagation in a Gaussian inversion cylinder.

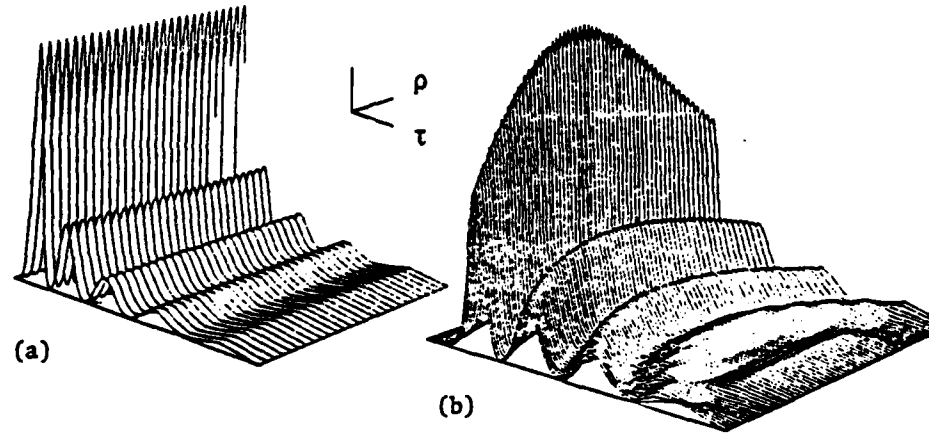

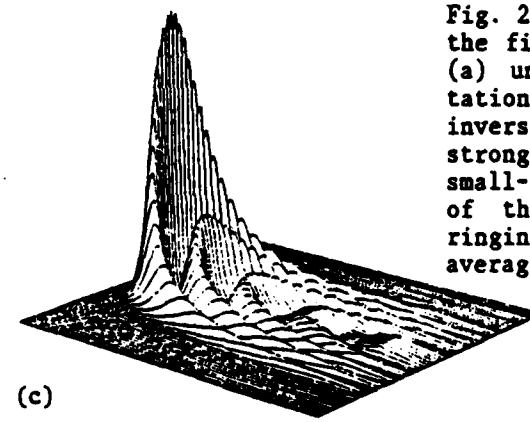

Fig. 26. Isometric representation of the field energy versus ρ and τ, for (a) uniform inversion and pre-excitation; (b) radial θ; (c) Gaussian inversion profile. Notice that strong ringing would be seen by a small-aperture detector in the center of the beam although very little ringing is in evidence after radial averaging.

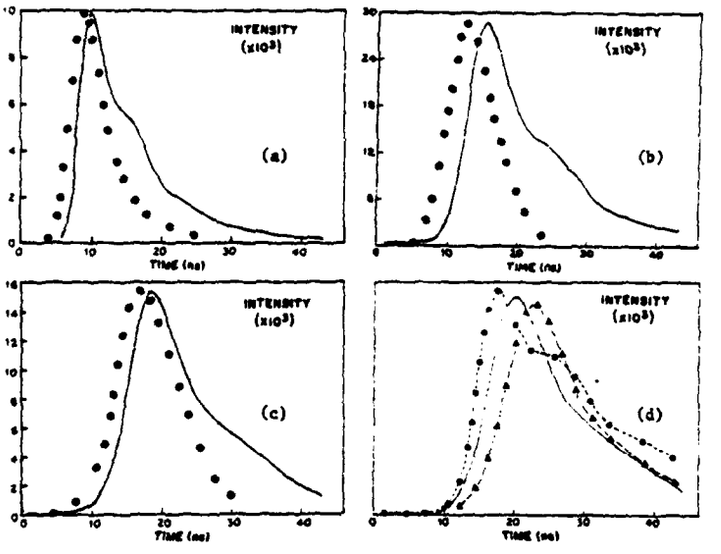

Fig. 27. Comparison of pulse shapes for situations where L/L_c is similar to the low density Cs. Relaxation terms were not included in this analysis. Note the asymmetry associated with an atomic beam of $\mathcal{T} = 1$. (a) $n = 1.9 \times 10^{11}$ cm^{-3}; $\theta_o = 2.64\ \beta\ 10^{-4}$; (b) $n = 18.24\ \beta\ 10^{10}$ cm^{-3}; $\theta_o = 1.37 \times 10^{-4}$; (c) $n = 11.9 \times 10^{10}$; $\theta_o = 1.69 \times 10^{-4}$; (d) $n = 8.75 \times 10^{-4}$; $\theta_o = 1.96 \times 10^{-4}$. Time is measured in nsec.

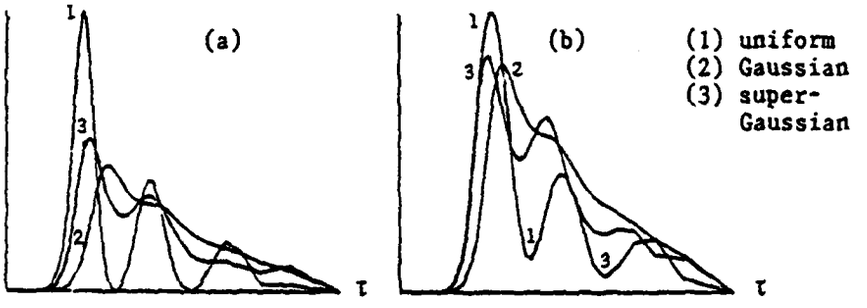

Fig. 28. Contrast of the total energy per unit atom (versus time) for different radiation damping time τ_R for a chosen $\mathcal{T} = 0.7$ and a uniform $\theta_R = 3 \times 10^{-3}$ (for different inversion profiles.

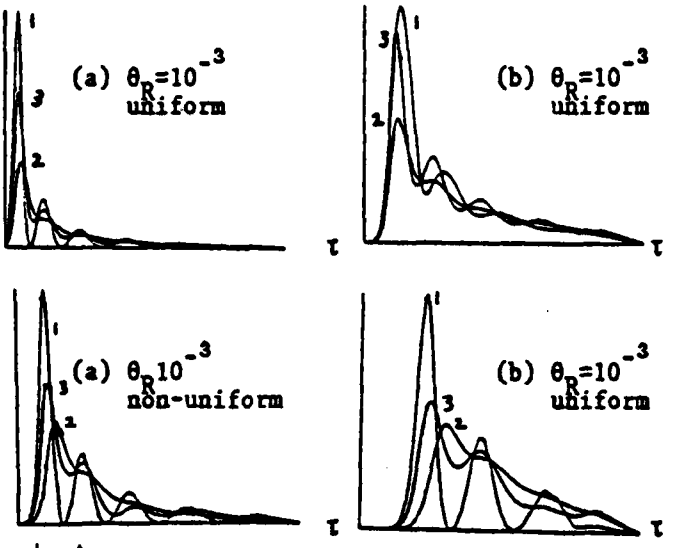

Fig. 29. Contrast of the total energy per unit atoms (versus time) for different inversions (1) uniform, (2) Gaussian (3) saturable Gaussian, and for particular tipping angle profiles. $\theta_R=10^{-3}$ non-uniform τ_R = 0.46 ns and L/L_c = 1.95. $\mathcal{T}$ = 6.

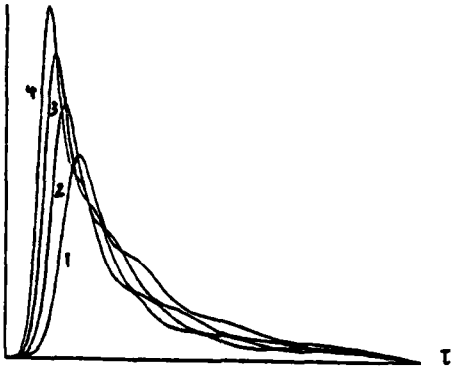

Fig. 30. Contrast of the total energy per unit atom (versus time) for different radiation damping time τ_R for a chosen $\mathcal{T}$ = 0.7, and a fixed tipping angle $\theta_R = 3 \times 10^{-3}$. g_R = 100, 125, 150, 175.

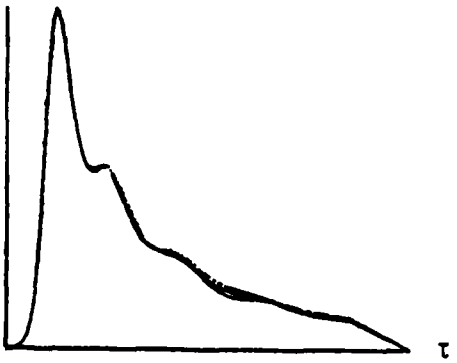

Fig. 31. Display of small-ripple effects in the Gaussian inversion of the cylinder on the total energy per unit atom (versus time) for $\mathcal{T}$ = 0.7, τ_R = 0.46 ns, and L/L_c = 1.95.

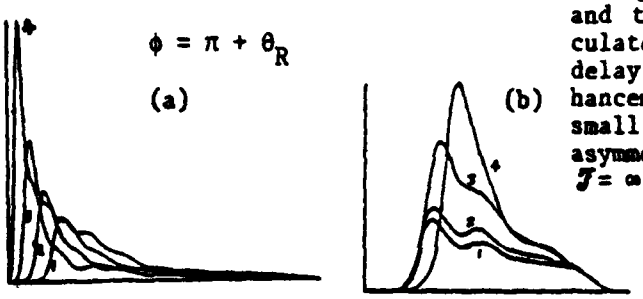

Fig. 32. (a) Emphasizes the effect of large θ_R versus small θ_R on the the pulse shape asymmetry and the ratio of the calculated pulse length to the delay of the peak. (b) Enhancement of the effect of small on the pulse shape asymmetry. $\mathcal{J} = \infty$, 2.76, 0.7, 0.4.

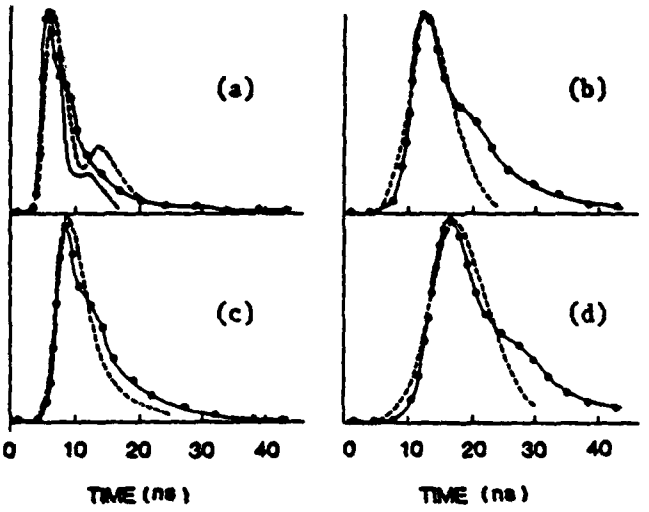

Fig. 33. Comparison of experimental and three-dimensional theoretical superfluorescence pulse shape for several densities N in an atomic beam of 2.0 cm length. The model encompasses rigorous radial dependence of N, τ_R and θ_R, diffraction (through the Laplacian) and relaxation times. $\mathcal{J} = 1$, L = 2 cm, T_1 = 70 ns, T_2 = 80 ns, $\lambda = 2.931\mu$, $\tau(0)$ = 551 nsec, Gaussian and inversion; in the following columns are the on-axis inversion density n in units of 10^{11} cm^{-3}, n of the experiment in the same units and θ_o in 10^{-4} radians: (a) 3.1, 1.9, 1.07; (b) 3.1, 7.6, 1.37; (c) 1.2, 3.8, 1.69; (d) 0.885, 3.1, 1.96.

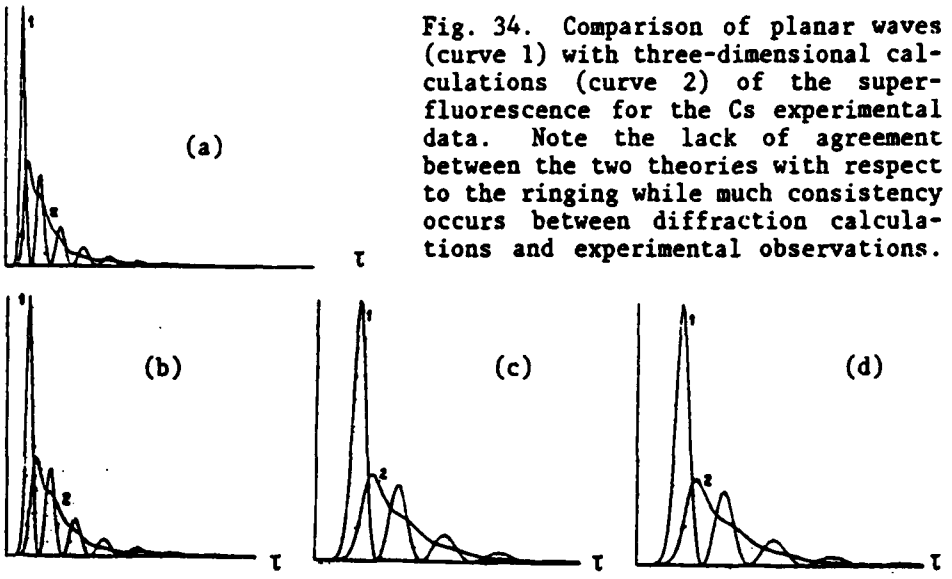

Fig. 34. Comparison of planar waves (curve 1) with three-dimensional calculations (curve 2) of the superfluorescence for the Cs experimental data. Note the lack of agreement between the two theories with respect to the ringing while much consistency occurs between diffraction calculations and experimental observations.

is needed to reduce the asymmetry and pulse width. But when relaxation terms are also included in the analysis and the densities are adjusted within quoted experimental uncertainties, a rather good agreement, (see Fig. (34)) is obtained between theory and experiments for a unity $\mathcal{J}$. These radial effects explain why the observed ringing in superfluorescence is less than that predicted by plane-wave simulations (see Fig. 34). Extensions of the present simulations to two-way propagation and random fluctuation of the tipping angle are planned. The agreement with experimental observations should be improved. [Recently, Bonifacio et al[1d] also reported the suppression of the ringing by using coupled-mode mean-field theory. However, their model does not encompass the propagational effects substantiated by both experimental observation and rigorous three-dimensional Maxwell-Bloch analysis.]

X. FLUID DESCRIPTION

Consider the polar representation of the field

$$e = A \exp(+i\phi) \tag{13}$$

with A and ϕ real amplitude and phase. Also let the nonlinear polarization of the RHS of equation (1) be written as

$$P^{NL} = (\chi_R + i\,\chi_I)e + \chi_{NL}e, \tag{14}$$

where χ_R and χ_I are real functions of A. Using equation (13), one gets from equation (1) the transport and the eikonal equations ($n_o = k_o c/\omega_o$)

$$K_o \frac{\partial}{\partial \eta} A^2 + \nabla_T \cdot [A^2 \nabla_T \phi] = - \frac{4\pi\omega_o^2}{c^2} \chi_I A^2, \tag{15}$$

$$2k_o \frac{\partial}{\partial \eta} \phi + (\nabla_T \phi)^2 - \left[\frac{A \cdot \nabla_T^2 A}{A^2}\right] = \frac{4\pi\omega_o^2}{c^2} \chi_R \tag{16}$$

The transport equation (15) expresses conservation of beam energy over the transverse plane. When $\chi_I = 0$, total power is conserved along the direction of propagation. The eikonal equation (16) describes the evolution of the surface of constant phase. It has the form of the Hamilton-Jacobi equation for the two-dimensional motion of particles having unit mass and moving under the influence of a potential[49] given by

$$V = - \frac{1}{2k_o^2} \cdot (\nabla_T^2 A)\, A^{-1} - \frac{2\pi}{n_o^2} \chi_R$$

if $k_{oz}z$ is regarded as time coordinate and $k_{ox}x$, $k_{oy}y$ as spatial coordinates. Furthermore, if one adopts A^2 and $\nabla_T\phi$ as new dependent variables, the equations of motion become similar to the continuity and momentum transport equations of ordinary hydrodynamics[25,26]. By defining

$$\underset{\sim}{v} = k_o^{-1} \nabla_T \phi, \quad \text{and} \tag{17}$$

$$\rho = A^2 \tag{18}$$

and supposing $\chi_I = 0$, equations (15) and (16) can be written as

$$\frac{\partial \underset{\sim}{v}}{\partial \eta} + (\underset{\sim}{v} \cdot \nabla_T)\underset{\sim}{v} = \frac{1}{2k_o} \nabla_T [\rho^{-1/2} (\nabla_T^2 \sqrt{\rho})] + \frac{\gamma_2}{k_o} (\nabla_T \rho) \tag{19}$$

$$\frac{\partial \rho}{\partial \eta} + \nabla_T \cdot (\rho \underset{\sim}{v}) = 0. \tag{20}$$

These equations are the momentum and continuity transport equations of a fluid with a pressure

$$P = (\nabla_T^2 \sqrt{\rho})/\sqrt{\rho})). \tag{21}$$

It should be emphasized that this pressure depends here solely on the "fluid density" and not on the "velocity". Equation (19) and (20) can be rearranged into

$$\frac{\partial}{\partial \eta}(\rho \underset{\sim}{v}) + \nabla_T \cdot (\rho \underset{\sim}{\underset{\sim}{vv}}) = \frac{1}{2k_o^2}\left[\frac{1}{2}(\nabla_T^2 \rho)\,\underset{\sim}{\underset{\sim}{I}} - \right.$$

$$\left. - \frac{1}{2\rho}(\nabla_T \rho)(\nabla_T \rho)\right] + \frac{\gamma_2}{k_o}\rho(\nabla_T \rho), \tag{22}$$

where $\underset{\sim}{\underset{\sim}{I}}$ is the unit tensor.

XI. EQUATIONS OF MOTION FOR OPTICAL BISTABILITY

In the slowly varying envelope approximation, the dimensionless field-matter equations* are

$$-iF\nabla_T^2 e^+ + \frac{\partial e^+}{\partial \tau} + \frac{\partial e^+}{\partial z} = +g^+ < P^* \exp(ikz)> \tag{23}$$

$$-iF\nabla_T^2 e^- + \frac{\partial e^-}{\partial t} - \frac{\partial e^-}{\partial z} = +g^- <P \exp(+ikz)> \tag{24}$$

with g^+, g^- as the nonlinear form of the gain experienced by the forward (e^+) and backward (e^-) traveling waves associated with the pump. The quantities in the R.H.S. undergo rapid spatial variations; $<\cdots>$ spatial average of these quantities with a period of half a wavelength

$$\frac{\partial P}{\partial t} + (-i\Delta\Omega) + \tau_2^{-1})P = + \{W(e^+ + e^-)\} \tag{25}$$

$$\frac{\partial W}{\partial t} + \tau_1^{-1}(W^e - W) = -\frac{1}{2}(P^+ + P^-)(e^+ + e^-) \tag{26}$$

Equivalently,

$$\frac{\partial P}{\partial t} + (-i(\Delta\Omega) + \tau_2^{-1})P = W[e^+ \exp(-ikz) + e^- \exp(+ikz)] \tag{27}$$

*As an aside, the nonlinear interface bistability effect[4(e)], though potentially important, is not considered.

$$\frac{\partial W}{\partial t} + \tau_1^{-1}(W^e - W) = \frac{1}{2}(Pe^{+*}\exp(ikz) + Pe^{-*}\exp(-ikz) + \underline{c.c.}) \quad (28)$$

with

$$e^{\pm} = (2\mu\tau_p/\hbar)e^{\pm} \quad (29)$$

$$P = (p'/2\mu), \quad (30)$$

$$E^{\pm} = Re\{e^{\pm}\exp[i(\omega t \mp kz)]\} \quad (31)$$

and

$$P = Re\{i\ p'\ \exp(i\omega t)\} \quad (32)$$

The complex field amplitude $e^{\pm}$, the complex polarization density p and the energy stored per atom W are functions of the transverse coordinate

$$\rho = r/r_p, \quad (33)$$

the longitudinal coordinate

$$z = \alpha_{eff} z' \quad (34)$$

and the physical time

$$\tau = t/\tau_p. \quad (35)$$

In the standing-wave problem, the two waves are integrated simultaneously along the physical time, as contrasted to S.I.T. retarded time.[50] Otherwise the physical parameters and variables have the same meaning.

The presence of opposing waves leads to a quasi-standing wave pattern in the field intensity over a half-wave length. To effectively deal with this numerical difficulty one decouples the material variables using Fourier series[18,19] namely,

$$P=\exp(-ikz)\sum_{p=0}^{\infty} P^{+}_{(2p+1)}\exp(-i2pkz)+\exp(+ikz)\sum_{p=0}^{\infty} P^{-}_{(2p+1)}\exp(+i2pkz) \quad (36)$$

$$W = W_o + \sum_{p=1}^{\infty} [W_{2p}\ \exp(-i2pkz) + c.c.] \quad (37)$$

with W_o a real number. Substituting in the traveling equation of motion, one obtains

$$\partial_\tau P_1^+ + P_1^+/\tau_2 = W_o e^+ + W_2 e^- ; \tag{38}$$

$$\partial_\tau P_3^+ + P_3^+/\tau_2 = W_2 e^+ + W_4 e^- ; \tag{39}$$

... ...

$$\partial_\tau P_{(2p+1)}^+ + P_{(2p+1)}^+/\tau_2 = W_{2p} e^+ + W_{2(p+1)} e^- ; \text{ and} \tag{40}$$

$$\partial_\tau P_1^- + P_1^-/\tau_2 = W_o e^- + W_2^* e^+ \tag{41}$$

$$\partial_\tau P_3^- + P_3^-/\tau_2 = W_2 e^- + W_4^* e^+ \tag{42}$$

... ...

$$\partial_\tau P_{(2p+1)}^- + P_{(2p+1)}^-/\tau_2 = W_{2p}^* e^- + W_{2(p+1)}^* e^+ \tag{43}$$

$$\partial_\tau W_o + (W_o - W_o^e)/\tau_1 = -\frac{1}{2}(e^{-*} P_1^- + e^{+*} P_1^+ + \text{c.c.}) \tag{44}$$

$$\partial_\tau W_2 + W_2/\tau_1 = -\frac{1}{2}(e^{-*} P_1^+ + e^{+*} P_3^+ + e^+ P_1^{-*} + e^- P_3^{-*}) \tag{45}$$

$$\partial_\tau W_{2p} + W_{2p}/\tau_1 = -\frac{1}{2}(e^{-*} P_1^+ + e^+ P_{2p+1}^+ + e^+ P_{2p+1}^{-*} + e^{-*} P_{2p+1}^{-*}) \tag{46}$$

The field propagation and atomic dynamic equation are subjected to the following initial and boundary conditions:

1. INITIAL:

for $t \geq 0$

$$e^\pm = 0 \tag{47}$$

$$W_o = W_o^e \quad , \tag{48}$$

where W_o^e is a known function to take into account the pumping effects. For S.I.T. or soliton collision

$$P_{(2p+1)}^\pm = 0, \qquad \text{for all } p \tag{49}$$

while for the superfluorescence problem

$$P^{\pm}_{(2p+1)} \tag{50}$$

is defined in terms of an initial tipping angle θ_R.

2. LONGITUDINAL

For z=0 and z=L: e^+ and e^- are given in terms of a known incident function

$$e_{I0} \tag{51}$$

and

$$e_{IL} \tag{52}$$

of τ and ρ.

If enclosing mirrors delineating the cavity are used in the analysis, one must observe the longitudinal boundary equations

$$e^+ = \sqrt{(1-R_1)}\, e_{I0} + \sqrt{R_1}\, e^- \qquad \text{at } z = 0 \tag{53}$$

$$e^- = \sqrt{(1-R_2)}\, e_{IL} + \sqrt{R_2}\, e^+ \qquad \text{at } z = L \tag{54}$$

where R_1, R_2, $(1-R_1)$ and $(1-R_2)$ are the respective reflectivity and transmitting factor associated with each left and right mirror.

3. TRANSVERSE

For all z and τ $[\partial e^{\pm}/\partial\rho]_{\rho=0}$ and $[\partial e^{\pm}/\partial\rho]_{\rho=\rho_{max}}$ vanish. The previously described transverse boundary conditions (Section II) apply here for each of the fields.

It is noteworthy that the presence of the longitudinal mirrors will enhance the mutual influence of the two beams. Variations in polarization and population over wave-length distances are treated by means of expansions in spatial Fourier series, which are truncated after the third or fifth harmonic. The number of terms needed is influenced by the relative strength of the two crossing beams and by the importance of pumping and relaxation processes in restoring depleted population differences.

XII. CONCEPT OF TWO-WAY CHARACTERISTICS

An easy way to visualize the mutual influence of the two counter-propagating beams is to imagine their respective information carriers in the traveling wave description.

For a light velocity normalized to unity (c/n = 1), by introducing

$$\xi = \frac{1}{2}(t-z) \qquad \text{and} \qquad \eta = \frac{1}{2}(t+z) \tag{55}$$

or equivalently

$$t = \eta + \xi \qquad \text{and} \qquad z = \eta - \xi \ , \tag{56}$$

one obtains the new derivative as

$$\frac{\partial}{\partial t} = \frac{1}{2}\left(\frac{\partial}{\partial \eta} + \frac{\partial}{\partial \xi}\right) \qquad \text{and} \qquad \frac{\partial}{\partial z} = \frac{1}{2}\left(\frac{\partial}{\partial \eta} - \frac{\partial}{\partial \xi}\right) \ . \tag{57}$$

Consequently

$$\frac{\partial}{\partial t} + \frac{\partial}{\partial z} = \frac{\partial}{\partial \eta} \ , \qquad \frac{\partial}{\partial t} - \frac{\partial}{\partial z} = \frac{\partial}{\partial \xi} \ . \tag{58a}$$

The field equation reduces to

$$\frac{\partial e^-}{\partial \xi} = i\nabla_T^2 e^- + P^- \ ; \qquad \frac{\partial e^+}{\partial \eta} = i\nabla_T^2 e^+ + P^+ \ . \tag{58b}$$

This means that the field is integrated along its directional characteristic path. With the polarization having a dynamic functional dependence on the total field the full Bloch equations are required. Furthermore the two oppositely traveling waves must be integrated simultaneously.

$$P^{\pm} = P^{\pm}(P_1^{\pm},\ldots,P_n^{\pm},e^+,e^-) \tag{59}$$

An example of one of the material (Bloch) equations is

$$\frac{\partial P_k^{\pm}}{\partial \xi} + \frac{\partial P_k^{\pm}}{\partial \eta} + \gamma_k P_k = S_k(P_1^{\pm},\ldots,P_{k1}^{\pm},P_{k+1}^{\pm}\ldots P_n^{\pm},e^+,e^-) \tag{60}$$

By identifying as outlined in Courant and Hilbert [50], the characteristics variable, namely

$$\xi = \xi(s) \qquad \text{and} \qquad \eta = \eta(s) \ , \tag{61}$$

or equivalently

$$\xi = \xi_o + s \qquad \text{and} \qquad \eta = \eta_o - s \ . \tag{62}$$

one obtains

$$\frac{\partial \xi}{\partial s} = +1 \qquad \text{and} \qquad \frac{\partial \eta}{\partial s} = -1 \tag{63}$$

which simplifies the Bloch equations as follows:

$$\frac{\partial P_k}{\partial s} + \gamma_k P_k = S_k \tag{64}$$

which can be rigorously[54,55] integrated to give

$$P_k(s+\Delta s) = P_k(s)\exp(-\Delta s/\gamma s) + \int_{s}^{s+\Delta s} \{\exp[-(s-s')\gamma]S_k(s')ds'\} \quad . \tag{65}$$

Illustrating the method of solution (see Fig. (35), arrows indicate integration paths for reducing differential equations to finite difference equations. Paths AB are used for Field Equations, and while Paths CB are used for Material Equations.

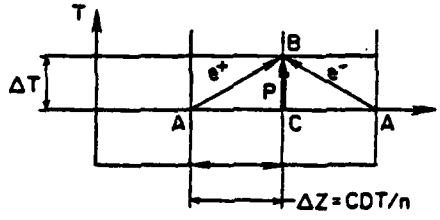

Fig. 35. Illustrates the two-way characteristic and the basis of the computational algorithm.

XIII. THE LAW OF FORBIDDEN SIGNALS

The effect of the physical law of forbidden signals on two-stream flow discretization problems was applied by Moretti to the integration of Euler equations[24,43].

For causality reasons, only directional resolution for spatial derivatives of each stream (forward and backward field) must be sought. This is achieved by using one-sided discretization techniques. The spatial derivative of the forward field is discretized using points lying to the left as all preceding forward waves have propagated in the same left-right direction; while the backward field is approximated by points positioned to the right. As a result, each characteristic (information carrier) is related to its respective directive history. Thus, violation of the law of forbidden signals is prevented.

In any wave propagation problem, the equations describe the physical fact that any point at a given time is affected by signals

sent to it by other points at previous times. Such signals travel along lines known as the "characteristics" of the equations. For example a point such as A in Figure (36) is affected by signals emanating from B (forward wave) and from C (backward wave), while point A' will receive signals launched from A and D. Similar wave trajectories appear in the present problem, but the slopes of the lines can change in space and time.

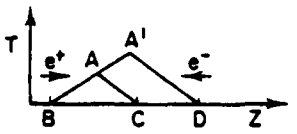

Fig. 36 Displays the role of characteristics as information carriers.

The slopes of the two characteristics carrying necessary information to define the forward and backward propagating variables at every point, are of different sign and are numerically equal to $\pm c/n$. For such a point A, Figure (37), the domain of dependence is defined by point B and C, the two characteristics being defined by AC and AB, to a first degree of accuracy. When discretizing the partial differential equations, point A must be made dependent on points distributed on a segment which brackets BC; e.g., on points D, E and F in Figure (38). This condition is necessary for stability but must be loosely interpreted. Suppose that one uses a scheme where a point A is made dependent on D, E and F, indiscriminately (this is what happens in most schemes currently used, including the MacCormack method). Suppose now, that the physical domain of dependence of A is the segment BC of Figure (38). The information carried to A from F is not only unnecessary;

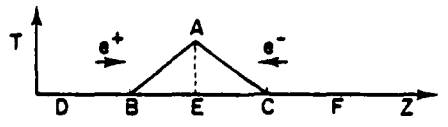

Fig. 37. Illustrates the concept of the law of forbidden signal for two-stream with characteristics of different sign.

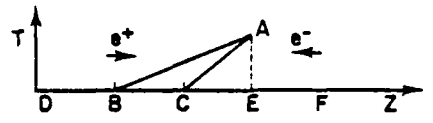

Fig. 38. Illustrates the concept of the causality for two-stream flow with characteristics of same (identical) sign.

it is also undue. Consequently, the numerical scheme, while not violating the Courant-Friedrick-Levy[54] (CFL) stability rule, would violate the law of forbidden signals. Physically, it is much better to use only information from D and E to define A, even if this implies lowering the nominal degree of accuracy of the scheme.

The sensitivity of results to the numerical domain of dependence as related to the physical domain of dependence explains why computations using integration schemes, like MacCormack's[52], show a progressive deterioration as the AC line of Figure (38) becomes parallel to the T-axis ($\lambda_1 \to 0$), even if λ_1 is still negative. The information from F actually does not reach A; in a coarse mesh, such information may be quite different from the actual values (from C) which affect A. On the other hand, since the CFL rules must be satisfied and F is the nearest point to C on its right, the weight of such information should be minimized. Moretti's λ-scheme, relying simultaneously on the two field equations provides such a possibility. Every spatial derivative of the forward field is approximated by using points lying on the same side of E as C, and every derivation of the backward-scattered field is approximated by using points which lie on the same side of E as B. By doing so, each characteristic relates with information found on the same side of A from which the characteristic proceeds also such information is appropriately weighted with factors dependent on the characteristic's slopes, so the contribution of points located too far outside the physical domain of dependence is minimized.

A one-level scheme which defines

$$\frac{\partial e^+}{\partial z} = (e_E^+ - e_D^+)/\Delta z \qquad \text{(forward wave)} \qquad (66)$$

$$\frac{\partial e^-}{\partial z} = (e_F^- - e_E^-)/\Delta z \qquad \text{(backward wave)} \qquad (67)$$

is Gordon's scheme [53], accurate to the first order. To obtain a scheme with second-order accuracy, Moretti considered two levels, in a manner very similar to MacCormack's. More points, as in Fig. (39) must be introduced. At the predictor level following Moretti's scheme one defines

$$\frac{\partial \tilde{e}^+}{\partial z} = (2e_E^+ - 3e_D^+ + e_G^+)/\Delta z \qquad \text{(forward wave)} \qquad (68)$$

$$\frac{\partial \tilde{e}^+}{\partial z} = (e_F^- - e_E^-)/\Delta z \qquad \text{(backward wave)} \qquad (69)$$

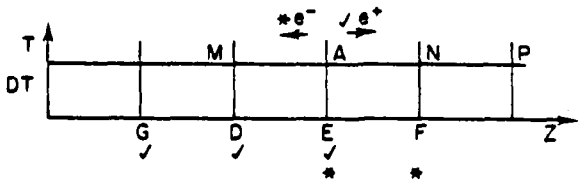

Fig. 39. Displays the computational grid for the λ-scheme.

At the corrector level, one defines

$$\frac{\partial \hat{e}^{+}}{\partial z} = (\tilde{e}_A^{+} - \tilde{e}_M^{+})/\Delta z \qquad \text{(forward wave)} \tag{70}$$

and

$$\frac{\partial \hat{e}^{-}}{\partial z} = (-2\tilde{e}_A^{-} + 3\tilde{e}_N^{-} + \tilde{e}_p^{-})/\Delta z \tag{71}$$

It is easy to see that, if any function f is updated as

$$\tilde{f} = f + f_t \, \Delta t \tag{72}$$

at the predictor level, with the t-derivatives defined as in (23) and (24) and the z-derivatives defined as in (68) and (69) and as

$$f(t+\Delta t) = \frac{1}{2} (f+\tilde{f}+f_t \Delta t) \tag{73}$$

at the corrector level, with the t-derivatives defined again as in (23) and (24), and the z-derivatives defined as in (70) and (71), the value of f at 't+Δt' is obtained with second order accuracy. The updating rule (72) and (73) is the same as in the MacCormack scheme.

At the risk of increasing the domain of dependence, but with the goal of modularizing the algorithm, three- and four-point estimators were used for each first and second derivative respectively. Moretti's algorithm was also extended to non-uniform mesh to handle the longitudinal refractive left and right mirrors: the same one-sided differencing is used for both predictor and corrector steps. Nevertheless, the weights derived, using the theory of estimation, (presented by Hamming[53]), have improved the order of accuracy of the spatial derivative estimator at both predictor and corrector levels. In particular, the derivative estimators are of second order instead of first order as in Moretti's λ-scheme. Specifically, these weights are derived using a development in terms as a sum of Lagrangian polynomials at a set of points. As a result, the overall accuracy of Moretti's predictor/corrector scheme was increased[56] from second to third order. Either forward or backward longitudinal derivatives at both predictor and corrector stages are given for the point x_1, x_2 and x_3 as:

$$D_1 = \left(\frac{2x_1-x_2-x_3}{\pi_1(x_1)} \quad , \quad \frac{x_1-x_3}{\pi_2(x_2)} \quad , \quad \frac{x_1-x_2}{\pi_3(x_3)} \right) \tag{74}$$

$$D_2 = \left(\frac{x_2-x_3}{\pi_1(x_1)} \quad , \quad \frac{2x_2-x_1-x_3}{\pi_2(x_2)} \quad , \quad \frac{x_2-x_1}{\pi_3(x_3)} \right) \tag{75}$$

$$D_3 = \left(\frac{x_3 - x_2}{\pi_1(x_1)} \quad , \quad \frac{x_3 - x_1}{\pi_2(x_2)} \quad , \quad \frac{2x_3 - x_1 - x_2}{\pi_3(x_3)} \right) \tag{76}$$

$$\text{with } \pi_j(x) = \prod_{i \neq j=1}^{3} (x - x_i) \tag{77}$$

Here D_1, D_2 and D_3 represents forward, central and backward differencing estimators for the (first-order longitudinal spatial) derivative.

XIV. TREATMENT OF LONGITUDINAL BOUNDARY

When treating any point within the cavity or at either longitudinal boundary (where a partially reflecting mirror is situated), there is no problem. For example, at $z = 0$, e^+ is determined by equation (53) and not through previous predictor/corrector formulas (68-71), as only e^- is calculated at $z = 0$ in that predictor/corrector manner (68-71). However, for a point one increment ($\delta = \Delta z$) from the left mirror, one encounters difficulties calculating the forward wave. The second needed point, which is vital to the formulas, would fall outside the cavity. An identical difficulty arises from the counterpart backward wave with respect to the right hand mirror. The field traveling from the right is defined at $z = L$ by equation (54).

To deal with this situation one has to modify the predictor/corrector schemes so the increment "δ^2" is used instead of δ. The loss of that second point reduces the accuracy of the derivative estimator. To maintain the same order of accuracy near the mirror, one must compensate for this loss by reducing the mesh size.

XV. NUMERICAL PROCEDURE FOR SHORT OPTICAL CAVITY

An alternate procedure to carry out the computation is to integrate the field along the longitudinal propagational distance. This approach is particularly attractive for a short cavity. It was developed with the help of McCall[57] as an attempt to relax the restrictive relation between the temporal t and spatial meshes z and r. It is presently being implemented and will be outlined here.

The reflecting effect of the partially refracting mirror can be built into the determining equations. Forward and backward field and polarization terms will appear explicitly as driving

sources in each traveling field equation (see Fig. 40). One can readily contrast the two physical situations of long and short cavity. To illustrate the methodology the diffraction is neglected. For no reflection, the fields are described by

$$e^{+}(t+\Delta t,z) = e^{+}(t,z-c\Delta t) + \int_{z-c\Delta t}^{z} dz'\ P^{+}(t+\Delta t - \frac{z-z'}{c}\ ,\ z') \qquad (78)$$

which applies if $z > c\Delta t$. Also

$$e^{-}(t+\Delta t,z) = e^{-}(t,z+c\Delta t) + \int_{z}^{z+c\Delta t} dz'\ P^{-}(t+\Delta t + \frac{z-z'}{c}\ ,\ z') \qquad (79)$$

applies if $L-z > c\Delta t$. For one reflection, the fields are obtained by

$$e^{+}(t+\Delta t,z) = \sqrt{T}\, e_{I0}(t+\Delta t - z/c) + \int_{0}^{z} dz'\ P^{+}(t + \Delta t - \frac{z-z'}{c}\ ,\ z')$$

$$+ \sqrt{R e^{-}}(t,c\Delta t-z) + \sqrt{R}\int_{0}^{c\Delta t-z} dz'\ P^{-}(t+\Delta t- \frac{z+z'}{c},\ z') \qquad (80)$$

whenever $z < c\Delta t$, and if $L-z < c\Delta t$, then one reflection

$$e^{-}(t+\Delta t,z) = \sqrt{T}\, e_{IL}(t+\Delta t - \frac{L-z}{c}) + \sqrt{R}\, e^{i\beta}\, e^{+}(t,2L-z-c\Delta t)$$

$$+ \int_{z}^{L} dz'\ P^{-}(t+\Delta t + \frac{z-z'}{c}\ ,\ z')$$

$$+ \sqrt{R}\, e^{i\beta} \int_{2L-z-c\Delta t}^{L} dz'\ P^{+}(t+\Delta t - \frac{2L-z-z'}{c}\ ,\ z') \qquad (81)$$

In all of the above it is assumed that $c\Delta t < L$ (so that two reflections cannot occur in time Δt). To correctly include the influence of diffraction, appropriate weighting coefficients must be used as summarized below:

(1) For no reflection-correct by $\frac{1}{2}\nabla_T^2(e^{+}c\Delta t)$, $\frac{1}{2}\nabla_T^2(e^{-}c\Delta t)$

(2) For one reflection-

(a) Term $\sqrt{T}\, e_{I0}$ only propagates z ($c\Delta t > z$) so correct only by $z\,\nabla_T^2$

(b) Term $\int_0^z dz'\ P^+$ goes a distance of an average of $(\frac{1}{2})z$; correct by $\frac{z}{2}\nabla_T^2$

(c) Term $e^-(t,c\Delta t-z)$ goes a distance of $c\Delta t$; full correction by $c\Delta t-z$

(d) Term $\sqrt{R}\int_0^{c\Delta t-z} dz'\ P^-$ goes $\frac{c\Delta t-z}{c} + z$; correct bya distance of $\frac{c\Delta t+z}{2}\nabla_T^2$

(e) Term $\sqrt{T}$ goes $\underline{e^{IL}}$ goes a distance of (L-z); correct by $(1/2)(L-z)\nabla_T^2$

(f) Term $\sqrt{R}\ e^{i\beta}\ e^+$ goes full distance; correct $\frac{1}{2}\ c\Delta t\ \nabla_T^2$

(g) Term $\int_z^L dz'\ P^-$ goes a distance of $\frac{L-z}{2}$; correct by $\frac{1}{2}\ (L-z)\ \nabla_T^2$

(h) Term $\sqrt{R}\ e^{i\beta}\int_{2L-z-c\Delta t}^{L} dz'\ P^+$ goes a distance of $\frac{(L-z)+c\Delta t}{2}$ on the average; correct $\frac{L-z+c\Delta t}{2}\nabla_T^2$

and similarly for any time correction.

Instead of the usual predictor/corrector weighting of 1/2 for each of predicted and corrected values, a more complicated procedure must be used.

XVI. TWO-LASER THREE-LEVEL ATOM

An extension of the SF calculations presented in Section IX should include such pump dynamics and its depletion on a three-level system similar to the model suggested by the Bowden et al[59]. The simulation of the dynamic interactions of two intense, ultrashort laser pulses propagating simultaneously through a gas of three-energy level atoms was considered[60]. The rigorous diffrac-

tion and cross-modulation interplay of the two laser beams with the inertial response of the doubly resonant medium is studied using an extension of the numerical algorithm developed for SIT analysis. It is expected that by altering the pump characteristics, one encodes information in the pulse that evolves in the nonlinear media resulting in a light by light control. An intermediate study will be Double Coherent Transients[61,62]. Another benefit of this study would be an analysis of Wall's[63] scheme for optical bistability in a coherently-driven three-level atomic system. However, some material equation modifications must be made as the novel mechanism relies on the nonlinear absorption resonances associated with a population trapping, coherent superposition of the ground sublevel. When one defines dimensionless variables in a parallel manner to SIT, the physical problems are described by the following equations: τ_{pa} and τ_{pb} are the pulse τ_p of laser a and laser b respectively. Q is the quadrupole slowly varying envelope.

$$-iF\,\nabla_T^2\, e_{a,b} + \partial_\eta\, e_{a,b} = g_{a,b}\, P_{a,b} \tag{82}$$

with

$$g_{a,b} = (\mu_a/\mu_b)\ (\tau_{pa}/\tau_{pb})^{1/2} \tag{83}$$

$$\partial_\tau P_a = e_a\, W_a - i(\Delta\Omega_a)P_a - P_a/\tau_{2a} + \tfrac{i}{2}\, e_b^*\, Q \tag{84}$$

$$\partial_\tau P_b = e_b\, W_b - i(\Delta\Omega_b)\, P_b - P_b/\tau_{2b} - \tfrac{i}{2}\, e_a^*\, Q \tag{85}$$

$$\partial_\tau Q = -i[(\Delta\Omega_a+\Delta\Omega_b)]Q + \tfrac{i}{2}\,(e_a\, P_b - e_b\, P_a) - Q/\tau_{2ab} \tag{86}$$

$$\partial_\tau W_a = -\tfrac{i}{2}(e_a^*\, P_a + e_a\, P_a^*) - (W_a - W_a^e)/\tau_{1a} + \tfrac{1}{4}(e_b^*\, P_b + e_b\, P_b^*) \tag{87}$$

$$\partial_\tau W_b = -\tfrac{1}{2}(e_b^*\, P_b + e_b\, P_b^*) - (W_b - W_b^e)/\tau_{1b} + \tfrac{1}{4}(e_a^*\, P_a + e_a\, P_a^*) \tag{88}$$

If one uses the identity

$$W_a + W_b = W_{ab} \tag{89}$$

a further equation (not absolutely necessary) is introduced:

$$\partial_\tau W_{ab} = +\,1/4[(e_a^* P_a + e_a P_a) + (e_b^* P_b + e_b P_b^*)] - (w_{ab} - W_{ab}^e)/\tau_{ab} \tag{90}$$

when $W_{a,b}^e$ and W_{ab}^e are the equilibrium values of $W_{a,b}$ and W_{ab}, subjected for infinite relaxation times to a conservation of probability

$$\partial_\tau\{|P_a|^2 + |P_b|^2 + |Q|^2 + (W_a^2 + W_b^2 + W_{ab}^2)\} = \text{zero}. \quad (91)$$

Equivalently:

$$|P_a|^2 + |P_b|^2 + |Q|^2 + 2/3(W_a^2+W_b^2+W_{ab}^2) = |P_{a,i}|^2 + |P_{b,i}|^2 + |Q_i|^2 + 2/3(W_{a,i}^2+W_{b,i}^2+W_{ab,i}^2). \quad (92)$$

Figure (40) illustrates W_a, W_b and W_{ab} as a function of time for a particular radius in the reshaping region.

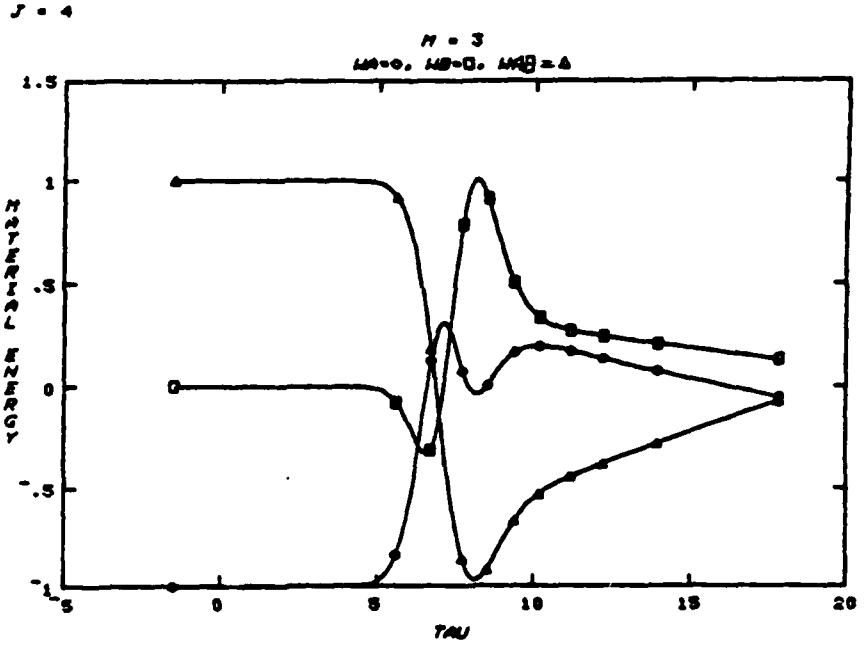

Fig. 40. Contrast of the material energy for a double self-induced transparency calculation.

Numerical Refinements

If the two laser beams which propagate concomitantly are severely disparate from each other, the normal stretching technique must be generalized into a double stretching transformation[60c] to ensure that the nonuniform temporal grids simultaneously match the two different pulses. No spatial rezoning is as yet designed.

Prescribed Double Stretching

Due to the essential nonlinear nature of the cooperative effects associated with a coherent light-matter interaction, dif-

ferent speeds are associated with pulses of different strengths. So particular attention must be given to deal effectively with two concomitant longitudinal speeds (one for each laser). Mathematically this is

$$T = a\tau + b \sin \omega_s \tau$$

$$\frac{\partial T}{\partial \tau} = a + b\,\omega_s \cos \omega_s \tau$$

and is shown in Fig. 41. Evenly spaced grid points in T are clearly related to non-uniform variable grid points in the physical time τ.

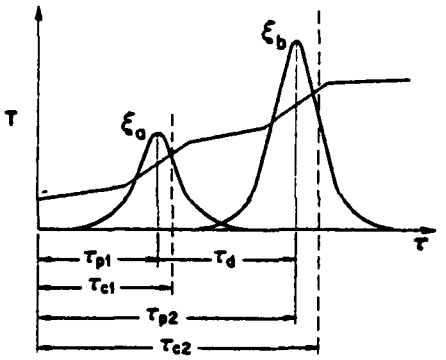

Fig. 41. Displays the prescribed double stretching.

ω_s	0	$\pi/2$	π	$3\pi/2$	2π
$\cos \omega_s \tau$	1	0	-1	0	1
$\partial T/\partial \upsilon$	$a + b\omega_s$	a	$a - b\omega_s$	a	$a + b\omega_s$

For $\omega_s \tau = \pi$, $\partial T/\partial \tau$ is minimum.

Several noteworthy facts must not be overlooked, i.e., (i) ω_s is related to the frequency of oscillations; and (ii) the steepness of the slopes must depend on the concentration points.

The various stretching parameters are given by

$$a = 1/2 \left[\frac{\partial T}{\partial \tau}\Big|_{max} + \frac{\partial T}{\partial \tau}\Big|_{min}\right]$$

$$b = \{1/2\ \omega_s\} \left[\frac{\partial T}{\partial \tau}\Big|_{max} - \frac{\partial T}{\partial \tau}\Big|_{min}\right]$$

$$\omega_s(\tau_{c2} - \tau_{c1}) = 2\pi \Rightarrow \omega_s\ \tau_d = 2\pi$$

If τ_d increases, ω_s decreases - a smaller frequency yields to a larger b, if τ_d decreases, ω_s increases - a larger frequency yields to a smaller b parameter.

To ensure monotonicity of the function T in τ (so that multivalued possibilities are excluded), an important condition which must never be violated (see Fig. 42), is

$$g = \frac{\partial T}{\partial \upsilon}\Big|_{min} \equiv (a - b\omega) > 0$$

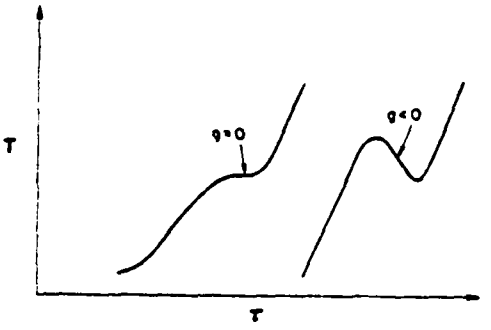

Fig. 42. Displays the limitations on the parameter choice to the double stretching transformation.

Adaptive Double Stretching

Following the spirit of adjusted stretching for a single pulse, described in Section V, the sampling frequency ω_s can vary along the direction of propagation η.

Prescribed Triple Stretching

For a correct treatment of the pulses propagating concomitantly while one of the two lasers may have broken up into two small pulses, successive double stretchings are applied

Step 1 $\qquad \zeta = A\ x^2 + Bx$

from $x = x_2,\ \zeta = \zeta_o = Ax_2^2 + Bx_2$

$x = x_3,\ \zeta = 2\zeta_o = Ax_3^2 + Bx_3$

and $x = 0,\ \zeta = 0.$

$\zeta_1 - \zeta_2 = \zeta_2 - \zeta_3 = 0 - \zeta_1$

one gets, $A = \dfrac{\zeta_o(x_3 - 2x_2)}{x_3 x_2 (x_2 - x_3)}$ and $B = \dfrac{\zeta_o(2x^2{}_2 - x^2{}_3)}{x_2 x_3 (x_2 - x_3)}$;

Step 2 $Y = a\,\zeta + b \sin \omega_s\, \zeta$

Cumulative step $Y = a(Ax^2 + Bx) + b \sin \omega_s\, (Ax^2 + Bx)$

$Y_x = a(2x\,A + B) + b\omega_s\, (2Ax + B) \cos\, (Ax^2 + B)$

$= (2Ax + B)\, (a + b\omega_s \cos\, (Ax^2 + B))$.

The coefficients are readily found (see Fig. 43).

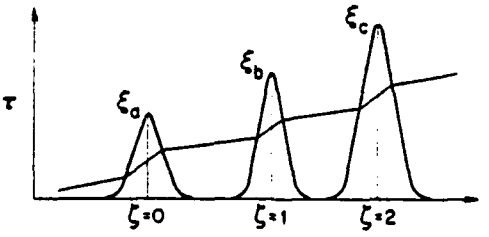

Fig. 43. Illustrates a prescribed triple stretching.

XVII. CONCLUDING REMARKS

Most of the features of the numerical model used to study temporal and transverse reshaping effects of single and multiple short optical pulses propagating concomitantly in active, nonlinear, resonant media have been presented. The calculations strive to achieve a rigorous analysis of this nonlinear interaction with maximum accuracy and minimum computational effort. The applicability of computational methods developed in gas and fluid dynamics to the detailed evolution of optical beams in nonlinear media have been demonstrated.

By introducing adaptive stretching and rezoning transformations wherever possible, the calculations improved considerably.

In particular, self-adjusted rezoning and stretching techniques consisting of repeated applications of the same basic formulae were reviewed as a convenient device for generating computational grids for complex nonlinear interactions. The techniques are well-suited for each programming because the mapping functions and all related derivatives are defined analytically as much as possible. Enhancement of speed and accuracy was realized by improving the integration technique/algorithm which was general and simple in its application compared with its analogue, the two-dimensional Lagrangian approach[42].

This method was applied to a number of SIT situations with and without homogeneity in the resonant properties of the atomic medium. Note that the theoretical predictions defined with the single stream SIT code, when applied to absorbing media, were quantitatively found[64] by independent experimental observations[65], and recent independent perturbational[66] and computational analysis[67]. The design of the first of these experiments dealing with sodium vapor, was based on qualitative ideas, quantitative analysis and numerical results obtained with the code described in this paper. More recently, King et al also reported[68] the experimental observation in iodine atomic vapor of the coherent on-resonance self-focusing. This is a novel manifestation of the phenomenon as it deals with a magnetic dipole instead of an electric dipole moment.

Also, the severe beam distortion and on-axis pulse break-up, when the problem of transverse boundary is rigorously addressed, was observed in high power lasers used in Laser Fusion experiments.

With the help of Gibbs and McCall, we have resolved the major discrepancies between planar calculations (as done by Hopf et al[69]) and the Cs experimental observations. The main sources of these discrepancies[60] were the occurrence of transverse effects in the experiments and the uncertainty in the tipping angle values.

Optical bistability shares with the previous SIT and SF the same basic physical features; however, the initial and boundary conditions are different and complicate the problem. Nevertheless, the similarities predominate; therefore, a unified numerical description with some modifications can apply to all these problems. This new computational approach, based on the concept of absolute consistency of the numerics with the physics, should be successful.

ADDENDUM

An alternate solution to eliminate rapid oscillations from the two-mode Bloch equation without recourse to harmonic expansion could be to adopt Moore and Scully[71] multiple-scaling perturbation

expansion. They have applied the techniques of multiple-scaling perturbation theory, described in hydrodynamics textbooks, to the free-electron laser problem and the pico-second transient phenomena.

ACKNOWLEDGMENTS

F.P. Mattar thanks his thesis advisor Professor M.C. Newstein, his mentors Professors H.A. Haus and Gino Moretti, for their guidance in the physics and numerics of the work. He has benefitted from discussions with Drs. H.M. Gibbs, S.L. McCall, J.H. Marburger, D.C. Brown, P.E. Toschek, and M.S. Feld in the physics; and J. Hermann, B.R. Suydam and J. Fleck, on the numerics. He is indebted to Dr. Gibbs for his faith in the work that led to the first experimental verification of the coherent on-resonance self-focusing. The hospitality of Dr. J. Teichman at the Univ. of Montreal and Dr. T.C. Cattrall at Mobil, (which made the computations possible), is gratefully acknowledged. F.P. Mattar particularly thanks Dr. C. Hazzi and D.J. Steele for their patience, support and encouragement during his convalescence. Furthermore, the editing efforts of D.J. Steele the artwork of Kerop Studio in Cairo, W. Roberts and D.J. Steele in New York; and the skillful and laborious word processing efforts of E. Cummings are joyfully appreciated.

REFERENCES

1. (a) R.H. Dicke, Phys. Rev. 93, 99 (1954) and in Proc. Third Int. Conf. on Quant. Elec., Paris, 1963, ed. by P. Grivet and N. Bloembergen (Columbia University Press, N.Y., 1964); (b) D.C. Burnham and R.Y. Chiao, Phys. Rev. 188, 667 (1979) and S.L. McCall, Ph.D. thesis, Univ. of California, Berkeley (1968); (c) J.C. MacGillivray and M.S. Feld, Phys. Rev. A14, 1169 (1976); (d) R. Bonifacio and L.A. Lugiato, Phys. Rev. A11, 1507 and 12 587 (1975).
2. (a) Cooperative Effects in Matter and Radiation, ed. by C.M. Bowden, D.W. Howgate and H.R. Robl (Plenum Press, N.Y., 1977), and (ii) panel discussion compiled by M. Konopnicki and A.T. Rosenberg, p. 360, (ii) H.M. Gibbs, p. 61 and (iii) Q.H.F. Vrehen, p. 79; (b) lecture on Superfluorescence experiments, 1977 NATO/ASI on Coherence in Spectroscopy and Modern Physics (Plenum Press, N.Y., 1977); (c) Q.H.F. Vrehen, Coherence and Quantum Optics IV, ed. by L. Mandel and E. Wolf (Plenum Press, N.Y., 1978), pp. 78 and Laser Spectroscopy IV, ed. H. Walther and I.W. Rothe; (d) Q.H.F. Vrehen, H.M.J. Hikspoors and H.M. Gibbs, Phys. Rev. Lett. 38, 764 (1977), Phys. Rev. Lett. 39, 547 (1977) and Laser Spectroscopy III, ed. by J.I. Hall and J.I. Carlsten, Springer-Verlag (1977);

(e) Q.H.F. Vrehen and M.F.H. Schuurmans, Phys. Rev. Lett. 42, 224 (1979).

3. (a) H. Seidel, Bistable optical circuits using saturable absorber within a resonant cavity, U.S. Patent 3 610 731 (1969); (b) H.M. Gibbs, S.L. McCall and T.N.C. Venkatesan, Optics News 5, 6 (1979), J. Opt. Soc. Am. 65, 1184 (1975), Phys. Rev. Lett. 36, 1135 (1976) (U.S. patents #012,699 [1975] and #121,167 [1976], lecture on Optical Bistability and Differential Gains at 1977 NATO/ASI on Coherence in Spectroscopy and Modern Physics (Plenum Press, 1977); (c) A. Szöke, V. Daneu, J. Goldher, and N.A. Kurint, Appl. Phys. Lett. 15, 376 (1969).
4. (a) T.N.C. Venkatesan and S.L. McCall, Appl. Phys. Lett. 30, 282 (1977), H.M. Gibbs, S.L. McCall, T.N.C. Venkatesan, A.C. Gossard, A. Passner and W. Wiegmann, CLEA/1978 (IEEE J. Quantum Electronics 15, 108D [1979]) and Appl. Phys. Lett. 35, 451 (1979); S.L. McCall and H.M. Gibbs (to be published in Opt. Comm. 1980) and H.M. Gibbs, S.L. McCall and T.N.C. Venkatesan (to be published in special issue on Optical Feedback in Opt. Eng.); (b) T. Bischofberger and Y.R. Shen, Appl. Phys. Lett. 32, 156 (1978), Opt. Lett. 4, 40 & 175 (1979) and Phys. Rev. A19, 1169 (1979); (c) P.W. Smith, J.P. Hermann, W.J. Tomlinson and P.J. Maloney, Appl. Phys. Lett. 35, 846 (1979); (d) Proc. of the Int'l Optical Bistability Conf., Asheville, North Carolina (June 1980), ed. C.M. Bowden, M. Ciftan and M.R. Robl, to be published (to be published) by Plenum Press.
5. R. W. Hellwarth, J. Opt. Soc. Am. 67, 1 (1977) and IEEE J. Quantum Electron., 15, 101 (1979).
6. A. Yariv, IEEE J. Quantum Electron., 14, 650 (1978) and Compensation for Optical Propagation Distortion through Phase Adaptation (preprint Caltech 1979).
7. (a) S.L. McCall, Ph.D. thesis, Univ. of California, Berkeley (1968); (b) J.-C. Diels, Ph.D. thesis, Univ. of Calif. Berkeley (1973); (c) A. Icsevgi and W.E. Lamb, Jr., Phys. Rev. 185, 517 (1969).
8. D.W. Dolfi and E.L. Hahn (to appear in Phys. Rev. a, 1980).
9. H.M. Gibbs, B. Bölger, F.P. Mattar, M.C. Newstein, G. Forster and P.E. Toschek, Phys. Rev. Lett. 37, 1743 (1976).
10. F.P. Mattar, M.C. Newstein, P. Serafim, H.M. Gibbs, B. Bölger, G. Forster and P. Toschek, Fourth Rochester Conf. of Coherence and Quantum Optics, Rochester, NY (June 1977), Plenum Press, ed., L. Mandel and E. Wolf, p. 143-164 (1978).
11. F.P. Mattar, H.M. Gibbs, Laser 1980, New Orleans(1980).
12. S.L. McCall, F.P. Mattar, and H.M. Gibbs, Optics in Four-Dimensions, Encenade, Mexico (1980).
13. F.P. Mattar, H.M. Gibbs, S.L. McCall and M.S. Feld submitted to Phys. Rev. Lett. and Phys. Rev. A.

14. N. Wright and M.C. Newstein, Opt. Commun., 9, 8 (1973) and IEEE J. Quantum Electron., 10, 743 (1974).
15. M.C. Newstein and F.P. Mattar, Proc. 7th Conf. Numerical Simulation of Plasmas (Courant Institute, NYU, June 1975, p. 223; and Proc. of 10th Congress of the Int'l Commission of Optics, Prague, Czechoslovakia (1975), Recent Advances in Optical Physics, p. 199, B. Havelka and J.Blabla, distributed by the Soc. of Czechoslovak Math. and Phys. (1976); IX Int'l Conf. of Quantum Electronics, Amsterdam (1976), see Opt. Comm. 18, 70 (1976), and IEEE J. Quantum Electron, 13, 507 (1977) and see ref. 2(a) 139.
16. J.C. Diels and E.L. Hahn, Phys. Rev. A8, 1084 (1973) and Phys. Rev. A10, 2501 (1974).
17. (a) S.L. McCall and E.L. Hahn, Phys. Rev. Lett. 28, 308 (1967), Phys. Rev. 183, 487 (1969) and Phys. Rev. A2 (1970); (b) A. Icsevgi and W.E. Lamb, Jr., Phys. Rev. 185, 517 (1969).
18. S.L. McCall, Phys. Rev. A9, 1515 (1974).
19. (a) J.A. Fleck, Jr., Appl. Phys. Lett. 13, 365 (1968); (b) J.A. Fleck, Jr., Phys. Rev. B1, 84 (1970); (c) See Ref. 1(c) and ref. (11)
20. (a) S.L. McCall and H.M. Gibbs (to be published in Optics Comm. 1980); (b) H.J. Carmichael (to be published in Optica Acta (1980) and H.J. Carmichael and G.P. Agrawal, Inhomogeneous Broadening and Mean Field Approximation for Optical Bistability in a Fabry-Perot (preprint 1979); Steady State Formulation of Optical Bistability for a Doppler Broadened Medium in a Fabry-Perot (preprint 1980); (c) J.H. Marburger and F.S. Felber, Appl. Phys. Lett. 28, 831 (1976) and Phys. Rev. A17, 335 (1978); (d) R. Sanders and R.K. Bullough in Cooperative Effects in Matter and Radiation, ed. by C.M. Bowden, D.W. Howgate and H.R. Robl, 209, Plenum Press (1977); and R. Saunders, S.S. Hassan and R.K. Bullough, J. Phys. A9, 1725 (1976); (e) J.H. Eberly, K.G. Whitney and M. Konopnicki, unpublished Final Research Report to ONR (Fall 1977) Rochester, NY; (f) P. Meystre, Opt. Comm. 26, 277 (1978) and R. Bonifacio and P. Meystre, Opt. Comm. 27, 147 (1978); and F.A. Hopf and P. Meystre (to be published in Opt. Comm.).
21. (a) C.M. Bowden and C.C. Sung, Phys. Rev. A18, 1558 (1978) and Phys. Rev. A20, 2033 (1979); (b) R. Brewer and E.L. Hahn, Phys. Rev. A11, 1641 (1975); (c) M. Sargent III and P. Horwitz, Phys. Rev. A13, 1962 (1976); (d) N.S. Feld, Frontiers in Laser Spectroscopy, 2, 203 (Les Houches Lectures 1976), Ed. R. Balian, S. Haroche and S. Liberman, North Holland (1977); (e) F.P. Mattar and J.H. Eberly, Proc. of the Physics and Chemistry of Laser- Induced Process in Molecules, Edinburgh (1978) ed. by K.L. Kompa and S.C. Smith, 61, Springer-Verlag (1979); (f) M. Konopnicki and J.H. Eberly, Proc. 10th Pittsburgh Annual Simulation and Modeling Conf., Pittsburgh (1979) ed. Vogt and Publ. Instrument Soc. of America (ISA), Pittsburgh, PA.

22. G. Moretti, Polytechnic Institute of New York Rept 69-25, 1969; Polytechnic Institute of New York Rept 69-26, 1969; Proc. of the 1974 Heat Transfer and Fluid Mechanics Inst., Stanford Univ. Press, 1974, Polytechnic Institute of New York-AE/AM Rept 74-9; (POLY-AE/AM Rept 74-23); Polytechnic Institute of New York Rept 73-18, 1973; Polytechnic Institute of New York Rept 69-26, 1969; Polytechnic Institute of New York Rept 70-48, 1970; Polytechnic Institute of New York Rept 71-25, 1971; POLY-AE/AM Rept 74-15, 1974; Proc. Symposium Transsonicum II, Gottingen, Germany, September 8-13, 1975, Springer-Verlag, Berlin, 439 (2976); (Polytechnic Institute of New York-AE/AM Rept 76-06).
23. G. Moretti, The Chemical Kinetics Problem in the Numerical Analyses of Nonequilibrium Flows, Proc. of the IBM Scientific Computing Symposium on Large Scale Problems in Physics, Dec. 1963, IBM Research Ctr, Yorktown Heights, NY); and Polytechnic Institute of New York Rept 68-15 (1968). Polytechnic Institute of New York-AE.AM Rept 74-15, 1974.
24. G. Moretti, AIAA 14, 834 (1976), and Computers and Fluids 7, 191 (1979).
25. (a) E. Madelung, Z. Physik 40, 322 (1966). (b) H.E. Wilhelm, Phys. Rev. D1, 2278 (1970). (c) M. Jammer, The Philosophy of Quantum Mechanics 21, J. Wiley (1974).
26. (a) F.P. Mattar, Proc. of the Ninth Conf. of Numerical Methods in Plasma, Monterey, California (June 1978). Lawrence Livermore Lab. (LLL) Tech. Rept 78-004. (b) F.P. Mattar, J. Teichman, L. Bissonnette and R.W. MacCormack, Proc. of the Second Int'l Symp. on Gas Flow and Chemical Lasers, ed. J. Wendt, Western Hemisphere Pub. (1979).
27. R.P. Feyman, F.L. Vernon, Jr. and R.W. Hellwarth, J. Appl. Phys. 28, 43 (1957); and E.L. Hahn, Heritage of the Bloch Equations in Quantum Optics, to appear in The Felix Bloch Festschrist 75 Birthday.
28. (a) G. Askary'yan, Sov. Phys. JET P42, 1568 (1962) Moscow; and Usp. Fiz. Nauk., 111, 249, October 1973. (b) S.A. Akhamanov, A-P. Sukhorukov, and P.V. Kokhlov, Laser Handbook, F. Arrechi, Ed., Amsterdam, The Netherlands: North Holland, 1972, 1151. (c) B.R. Suydam, Self-Focusing in passive media I, Los Alamos Scientific Lab, Tech. Rep. L4-5002-MS, March 1973, and IEEE J. Quant. Elec. 10, 837 (1974), and IEEE J. Quant. Elec. 11, 225 (1975).
29. (a) J.H. Marburger, Progress in Quantum Electronics, 4, 35 ed. J.M. Sanders and Stenholm, Pergamon Press (1975), and Theory of Self-focusing with Counter-propagating Beams, preprint (1979). (b) O. Svelto, Progress in Optics XII, E. Wolf, ed. Amsterdam, The Netherlands: North Holland, 1974, 1.
30. Ibid Ref. 16.
31. T. Gustafson, J.-P. Taran, H.A. Haus, J. Lifsitz and P. Kelley, Phys. Rev. 177, 60 (1969).

32. (a) F.P. Mattar, Kvantovaya Electronika 4, 2520 (1977). (b) S.L. McCall and H.M. Gibbs (ibid ref. 20(a) and ref. 4(d)). (c) D.A.B. Miller and S.D. Smith, Opt. Comm. 31, 101 (1979) and D.A.B. Miller, S.D. Smith and A. Johnston, Appl. Phys. Lett. 35, 658 (1979). (d) M.S. Feld and J.C. MacGillivray in Advances in Coherent Nonlinear Optics, ed. M.S. Feld and V.S. Letokhov (to be published by Springer-Verlag, 1980). (e) R. Bonifacio, J.D. Farina and L.M. Narducci, Opt. Commun. 31, 377 (1979).
33. G. Moretti, Polytechnic Institute of New York Rept 69-25, 1960; Polytechnic Institute of New York Rept 69-26, 1969.
34. G. Moretti, Proc. of the ASME Symp. on Numerical/Laboratory Computer Methods in Fluid Mechanics, ASME, Dec. 1976. Polytecnhic Institute of New York -M/AE Rept 76-06.
35. L. Bradley and J. Hermann, MIT-Lincoln Lab Tech. Rept LTP-10 (July 1971) and Internal note on Change of reference wavefront in the MIT CW Nonlinear Optics Propagation Code (Fall 1974) private communication.
36. P.B. Ulrich, NRL Rept 7706 (May 1974).
37. H.J. Breaux, Ballistic Research Labs, Aberdeen Proving Ground, Maryland; BRL Rept 1723 (1974).
38. J.A. Fleck, Jr., J.R. Morris and M.D. Feit, Appl. Phys, 10, 129 (1976) and 14, 99 (1977).
39. F.P. Mattar, Appl. Phys. 17, 53 (1968) Springer-Verlag.
40. K.G. Whiteney, G.L. Nader, and P.B. Ulrich, Naval Research Lab. Washington, DC, NRL Rept 8074 (1977).
41. W.A. Newcomb, Nuclear Fusion, Suppl. 2, 451 (1962).
42. F.P. Mattar and J. Teichmann, IEEE Conf. Plasma Science, Montreal (1979) and submitted to Comp. Phys. Comm.
43. (a) G. Moretti, AIAA 14, 894 (1976) and Poly-M/AE Tech. Rep. 78 (1980), PINY; (b) B. Gabutti, La stabilita de una schema alle differenze finite per le equazioni della fluide dinamica (preprint, Polytechnico di Milano).
44. H.M. Gibbs and R. E. Slusher, Appl. Phys. Lett. 18, 505 (1971), Phys. Rev. A5, 1634 (1972) and Phys. Rev. A6, 2326 (1972).
45. H.A. Haus and T.K. Gustafson, IEEE J. Quant. Elec. 4, 519 (1968).
46. F.P. Mattar and M.C. Newstein, PINY Rept. ADL-M/AE 79-63 (1979) (to be published in Comp. Phys. Comm. 1980).
47. G. Moretti, Polytechnic Institute of New York Rept 68-15 (1968). Polytechnic Institute of New York-AE. AM Rept 74-15, 1974.
48. (a) V.I. Bespalov and V.I. Talanov, Soviet Phys., JETP letters, 3, 471 (1966), Eng. Trans. 3, 307. (b) V.I. Talanov, Soviet Phys. JETP Letters 2,218 (1965) Eng. Trans. 2, 138 and Zh. Eksp. Teor. Fiz. Pisma. Red. 11, 303, Eng. Trans. 133, JETP letters, 1970. (c) B.R. Suydam, Laser Induced Damage in Optical Material, 1973 NBS special publication 387, 42 and IEEE J. Quant. Elec. 10, 837 (1973) and IEEE J. Quant. Elec.

11, 225 (1975). (d) J.B. Trenholme, (LLL) Laser Fusion program 2nd 1973 semi-annual program report, 47 (UCRL-60021-73-2). (e) N.B. Baranova, N.E. Bykovskii, B. Ya. Zel'dovich and Yu. V. Senatskii, Kvant. Elektron. 1, 2435 (1974). (f) D.C. Brown, The Physics of High Peak Power Nd-Glass Lasers, Springer-Verlag (to be published in the Spring 1980). (g) L.A. Gol'shov, V.V. Likhanskii and A.O. Napartovich, Zh. Eksp. Teor. Fiz. 72, 769 (197~) Moscow. (h) M.J. Ablowitz and Y. Kodama, Phys. Lett. (1979). (i) L.A. Bol'shov, T.K. Kirichenko, A.P. Favolsky, U.S.S.R. Acad. of Sci., Math. Div. preprint, Fall 1978), Inst. of Appl. Math. 1978, 53 (3A) in Russian.

49. W.G. Wagner, H.A. Haus and J.H. Marburger, J. Phys. Rev. (1970).
50. R. Courant and K.O. Friedrichs, Supersonic Flow and Shock Waves, NY Interscience (1948).
51. F.A. Hopf and M.O. Scully, Phys. Rev. 179, 399 (1969).
52. R.W. MacCormack, AIAA Hypervelocity Impact Conf., 1969, paper 69-554 and Lecture Notes in Physics, Springer-Verlag, 151 (1971).
53. P. Gordon, General Electric Final Rep. NOL Contrace #N60921-7164 (1968).
54. R.W. Hamming, Numerical Methods for Scientists and Engineers, McGraw-Hill Book Co. (1962).
55. (a) B.R. Suydam, A Laser Propagation Code, Los Alamos Sci. Lab., LA-5607-MS Tech. Informal Rept (1974). (b) F.P. Mattar (with the help of Dr. B.R. Suydam, LASL) Eighth Conf. on Numerical Simulation of Plasmas, Monterey, Calif. (June 1978). Distributed by the Univ. of Calif./LLL, Livermore, Calif. (rept Conf-780612).
56. F.P. Mattar and R.E. Francoeur, Transient Counter-Beam Propagation in a Nonlinear Fabry Perot County (Long Sample), PINY, ADL-M/AE Tech. Rept. 80-12 (1980) and Proc. of the Ninth Conf. of Numerical Simulation of Plasma (ed. G. Knorr and J. Denavit) Northwestern Univ. Evanston, IL, 1980.
57. F.P. Mattar and S.L. McCall, Transient Counter-Beam Propagation In a Nonlinear Fabry Perot County II. Short Sample, PINY, ADL-M/AE Tech. Rept. 80-15 (1980).
58. (a) Ibid ref. 1(c); (b) Ibid ref. 2
59. Ibid ref. 21(a).
60. (a) Ibid ref. 21(d); (b) Ibid ref. 21(e); (c) F.P. Mattar, Proc. 10th Pittsburgh Annual Simulation and Modeling Conf., Pittsburgh (1979), ed. W. Vogt and M. Mickle, Publ. ISA, Pittsburgh, PA.
61. R.G. Brewer, (1975) in Frontiers in Laser Spectroscopy, ed. R. Balian, S. Haroche and S. Liberman 338 (North Holland 1977).
62. V.S. Letkhov and B.D. Sov. J. Quant. Elec. 4, 11 (1975).
63. D. Walls (ref. 4(d)).

64. (a) H.M. Gibbs, B. Bölger, F.P. Mattar, M.C. Newstein, G. Forster and P.E. Toschek, Phys. Rev. Lett. 37, 1743 (1976) (prep. by H.M. Gibbs); (b) Ref. (10); (c) F.P. Mattar, G. Forster and P.E. Toschek, Spring meeting of the German Phys. Soc., Mainz, F.R. Germany (Feb. 1977). Kvantovaya Electronika 5, 1819 (1978).
65. (a) H.M. Gibbs, B. Bölger and L. Baade, IX Int'l Conf.of Quant. Elec. (1976), Opt. Comm. 18, 199 (1976). (b) G. Forster and P.E. Toschek, Quantum Optics Session of the Spring Annual Meeting of the German Phys. Soc., Hanover, F.R. Germany (Feb. 1976). (c) W. Krieger, G. Gaida and P.E. Toschek, Z. Physik B25, 297 (1976).
66. (a) L.A. Bol'shov, V.V. Likhanskii and A.O. Napartovich, Zh. Eksp. Teor. Fiz. 72, 1769 (1977) Moscow; (b) M.J. Ablowitz and Y. Kodama, Phys. Lett. A70, 83 (1979); (c) L.A. Bolshov and V.V. Likhansky, Zhurnal Eksperimental'noi i Teoreti cheskii Fiziki, 75, 2947 (1978) in Russian (Eng. trans.: Sov. Phys. Jrnl of Exp. and Theo. Phys. 48, 1030 (1979)).
67. L.A. Bol'shov, T.K. Kirichenko, A.P. Favolsky, (USSR Acad. of Sci., Math. Div. preprint, Fall 1978), Inst. of Appl. Math. 1978, 53 (3A) in Russian.
68. J.J. Bannister, H.J. Baker, T.A. King and W. G. McNaught, Phys. Rev. Lett. 44, 1062 (1980) and XI Int'l Conf. of Quant. Elec., Boston (1980).
69. F.A. Hopf (private communication).
70. (See ibid ref. 11-13.)
71. G.T. Moore and M.O. Scully, Coherent Dynamics of a Free-Electron Laser with Arbitrary Magnet Geometry. I-General Formulation, Opt. Sci. Ctr, Univ. of Arizona, preprint (brought to the author's attention by Professor F.A. Hopf).

REPRINTED FROM PROCEEDINGS OF THE INTERNATIONAL CONFERENCE ON LASERS '81, DECEMBER 14-18, 1981
PRINTED IN USA

TRANSVERSE AND PHASE EFFECTS IN LIGHT CONTROL BY LIGHT: PUMP DYNAMICS IN SUPERFLUORESCENCE

F. P. Mattar*

Mechanical and Aerospace Engineering Dept., Polytechnic Institute of New York, Brooklyn, NY 11201
and Spectroscopy Laboratory, Massachusetts Institute
of Technology, Cambridge, MA 02139

and

C. M. Bowden

Research Directorate, US Army Missile Laboratory
US Army Missile Command, Redstone Arsenal, Huntsville, AL 35898

and

Y. Claude and M. Cormier

Dept d'Imformatique, Université de Montreal, Montreal, PQ, Canada

Abstract

Calculational results and analysis are presented and discussed for the effects of coherent pump dynamics, propagation, transverse and diffraction effects on superfluorescent (SF) emission from an optically-pumped three-level system. The full, co-propagational aspects of the injected pump pulse together with the SF which evolves are explicity treated in the calculation. It is shown that the effect of increasing the injection signal area exhibits a similar effect on the evolved SF delay time as either increasing the gain, or F^{-1}, (F is the Fresnel number per effective gain). All else being equal, it is demonstrated that alteration of the temporal as well as radial shape of the injected pump pulse has a profound effect upon the shape of SF as well as the sharpness of the rise of the pulse, its delay time, peak intensity and temporal width. For conditions of sufficiently large gain and large injection pulse area, SF which evolves and the propagating pump pulse eventually occur in the same time frame (overlap). It is shown that under these conditions the SF can be significantly temporally narrower than the pump and of significantly larger peak intensity. Thus, by choosing the shape of the injected pump envelope and/or its area, the SF shape, delay time, peak intensity and temporal duration can be altered. Thus, deterministic control of the characteristics of the evolving SF pulse is demonstrated by selecting appropriate characteristics of the injected pulse signal at a different frequency.

Introduction

Superfluorescence[1] (SF), is the dynamical radiation process which evolves from a collection of atoms or molecules prepared initially in the fully inverted state, and which subsequently undergoes collective, spontaneous relaxation[2]. Since Dicke's early work[2], much theoretical and experimental effort has been devoted to this subject[3].

With the exception of the more recent work of Bowden and Sung[4], all theoretical treatments have dealt exclusively with the relaxation process from a prepared state of complete inversion in a two-level manifold of atomic energy levels, and thus do not consider the dynamical effects of the pumping process. Yet, all reported experimental work[5-10] has utilized optical pumping on a minimum manifold of three atomic or molecular energy levels by laser pulse injection into the nonlinear medium, which subsequently superfluoresces.

It was pointed out by Bowden and Sung[4] that for a system otherwise satisfying the conditions for superfluorescent emission, unless the characteristic superradiance time[1], τ_R, is much greater than the pump pulse temporal duration, τ_p, i.e., $\tau_R >> \tau_p$, the process of coherent optical pumping on a three-level system can have dramatic effects on the SF. This is a condition which has not been realized over the full range of reported data. Also, Bowden and Sung's analysis was restricted to the uniform plane wave regime; it cannot account for the inevitable spatial and temporal beam energy redistribution (as in physical system). Transverse fluency is associated with radial density variations and diffraction coupling, it leads to communication among the various parts of the beam.

In this paper, we present calculational results and analysis for the effects of coherent pump dynamics, propagation, transverse and diffraction effects on SF emission from an optically-pumped three-level system. The full, nonlinear, co-propagational aspects of the injected pump pulse, together with the SF which evolves are explicitly treated in the calculation. Not only do our results relate strongly to previous calculations and experimental results in SF, but we introduce and demonstrate a new concept in nonlinear light-matter

* Jointly supported by the US Army Research Office DAAG29-79-C-0148, the Office of Naval Research N000-14-80-C-0174, and Battelle Colombus

interactions, which we call light control by light. We show how characteristics of the SF can be controlled by specifying certain characteristics of the injection pulse.

Equations of motion

The model upon which the calculation is based is comprised of a collection of identical three-level atoms, each having the energy level scheme shown in Figure 1. The $1 \leftrightarrow 3$ transition is induced by a coherent electromagnetic field injection pulse of frequency ω_o nearly tuned to the indicated transition. The properties of this pumping pulse are specified initially in terms of the initial and boundary conditions. The transition $3 \leftrightarrow 2$ evolves by spontaneous emission at frequency ω_o. It is assumed that the energy level spacing is such that $\varepsilon_3 > \varepsilon_2 >> \varepsilon_1$ so that the fields at frequencies ω_o and ω can be treated by separate wave equations. The energy levels $2 \leftrightarrow 1$ are not coupled radiatively due to parity considerations, and spontaneous relaxation from $3 \leftrightarrow 2$ is simulated by the choice of a small, but nonzero initial transverse polarization characterized by the parameter $\phi_o \sim 10^{-4}$. Our results do not depend upon nominal deviations of this parameter. The initial condition is chosen consistent with the particular choice of ϕ_o, with nearly all the population in the ground state, and the initial values of the other atomic variables chosen consistently[4,11].

We use the electric dipole and rotating wave approximations and couple the atomic dipole moments to clasical field amplitudes which are determined from Maxwell's equations. The Hamiltonian which describes the field-matter interaction for this system[4] comprising N atoms, is,

$$H = \hbar \sum_{r=1}^{3} \sum_{j=1}^{N} \varepsilon_{rj} R_{rr}^{(j)} - \frac{i\hbar}{2} \sum_{j=1}^{N} [\Omega^{(j)} R_{32}^{(j)} e^{-i(\omega t - \underline{k}\cdot\underline{r}_j)} - \Omega^{(j)*} R_{23}^{(j)} e^{i(\omega t - \underline{k}\cdot\underline{r}_j)}] - \frac{i\hbar}{2} \sum_{j=1}^{N} [\omega_R^{(j)} R_{31}^{(j)}$$

$$X \; e^{-i(\omega_o t - \underline{k}_o\cdot\underline{r}_j)} - \omega_R^{*(j)} R_{13}^{(j)} \; e^{i(\omega_o t - \underline{k}_o\cdot\underline{r}_j)}] \; , \qquad (1)$$

The first term on the right-hand side of Eq. (1) is the free atomic system Hamiltonian, with atomic level spacings ε_{rj}, $r = 1,2,3$; $j=1,2,\ldots,N$. The second term on the right-hand side describes the interaction of the atomic system with the fluorescence field associated with the $3 \leftrightarrow 2$ transition, whereas the last term on the right in (1) described the interaction between the atomic system and the coherent pumping field. The fluorescence field and the pumping field have amplitudes $\Omega^{(j)}$ and $\omega_R^{(j)}$, respectively, in terms of Rabi frequency, at the position of the j^{th} atom, $\underline{r}_j$. The respective wave vectors of the two fields are k and k_o and the carrier frequencies are ω and ω_o. It is assumed that the electromagnetic field amplitudes vary insignificantly over the atomic dimensions and that all of the atoms remain fixed during the time frame of the dynamical evolution of the system.

The atomic variables in (1) are the canonical operators [4] $R_{k\ell}^{(j)}$ which obey the Lie algebra defined by the commutation rules [12-14]

$$[R_{ij}^{(m)}, R_{\ell k}^{(n)}] = R_{ik}^{(m)} \delta_{\ell j}\delta_{mn} - R_{\ell j}^{(m)} \delta_{ik}\delta_{mn} \qquad (2)$$

$i,j, = 1,2,3$; $m,n = 1,2,\ldots,N$. The Rabi rates, $\Omega^{(j)}$ and $\omega_R^{(j)}$ are given in terms of the electric field amplitudes $E^{(j)}$ and $E_o^{(j)}$, respectively, and the matrix elements of the transition dipole moments, $\mu_{32}^{(j)}$ and $\mu_{31}^{(j)}$ by

$$\Omega^{(j)} = \frac{E^{(j)} \mu_{32}^{(j)}}{\hbar} \; , \qquad (3a)$$

$$\omega_R^{(j)} = \frac{E_o^{(j)} \mu_{31}^{(j)}}{\hbar} \; , \qquad (3b)$$

where we have considered only one linear polarization for the two fields and propagation in the positive z direction.

It is convenient to canonically transform (1) to remove the rapid time variations at the carrier frequencies ω and ω_o and the rapid spacial variations in the wave vectors k and k_o. We assume that the field envelopes $\Omega^{(j)}$ and $\omega_R^{(j)}$ vary much more slowly than the periods ω^{-1} and ω_o^{-1}, respectively. In the trans-

formed representation, we are thus dealing with slowly varying field amplitudes and atomic operators. The desired transformation U is unitary and is described in ref. 12.

$$\tilde{H}_T = U\ H\ U^{-1}$$

The equations of motion for the atomic variables are calculated from the transformed Hamiltonian according to

$$i\dot{R}_{k\ell}^{(j)} = [H_T, R_{k\ell}^{(j)}] \tag{5}$$

This set of equations constitutes the equation of motion for the density operator ψ for the system in the slow-varying operator representation. By imposing the canonical unitary transformation, we, in fact, transformed to a slow-varying operator representation which is consistent with the slowly-varying enveloped approximation to be imposed later on in the Maxwell's equations coupled to the hierarchy of nonlinear, first-order equations, (5).

The following hierarchy of coupled nonlinear equations of motion is obtained for the atomic variables:

$$\dot{R}_{33}^{(j)} = \frac{1}{2}\ [\Omega^{(j)}\ R_{32}^{(j)} + \Omega^{*(j)}\ R_{23}^{(j)}] + \frac{1}{2}\ [\omega_R^{(j)}\ R_{31}^{(j)} + \omega_R^{*(j)}\ R_{13}^{(j)}] - \gamma_{11}[R_{33}^{(j)} - R_{33}^{(e)}]\ , \tag{6a}$$

$$\dot{R}_{22}^{(j)} = -\ \frac{1}{2}\ [\Omega^{(j)}\ R_{32}^{(j)} + \Omega^{*(j)}\ R_{23}^{(j)}] - \gamma_{11}\ [R_{22}^{(j)} - R_{22}^{(e)}]\ , \tag{6b}$$

$$\dot{R}_{11}^{(j)} = -\ \frac{1}{2}\ [\omega_R^{(j)}\ R_{31}^{(j)} + \omega_R^{*(j)}\ R_{13}^{(j)}] - \gamma_{11}\ [R_{11}^{(j)} - R_{11}^{(e)}]\ , \tag{6c}$$

$$\dot{R}_{32}^{(j)} = i\delta^{(j)}\ R_{32}^{(j)} + \frac{1}{2}\ \Omega^{*(j)}\ [R_{22}^{(j)} - R_{33}^{(j)}] + \frac{1}{2}\ \omega_R^{*(j)}\ R_{12}^{(j)} - \gamma_1\ R_{32}^{(j)}\ , \tag{6d}$$

$$\dot{R}_{12}^{(j)} = i\delta^{(j)}\ R_{12} - \frac{1}{2}\ [\Omega^{*(j)}\ R_{13} + \omega_R^{(j)}\ R_{32}] - \gamma_1\ R_{12}^{(j)}\ , \tag{6e}$$

$$\dot{R}_{13}^{(j)} = i\Delta^{(j)}\ R_{13}^{(j)} + \frac{1}{2}\ \Omega^{(j)}\ R_{12} - \frac{1}{2}\ \omega_R^{(j)}\ [R_{33}^{(j)} - R_{11}^{(j)}] - \gamma_1\ R_{13}^{(j)}\ . \tag{6f}$$

In Eqs. (6), we have added phenomenological relaxation γ_{11} and dephasing γ_1 and taken these to be uniform, i.e., the same parameters for each transition. For the diagonal terms, $R_{kk}^{(j)}$, the equilibrium values are designated as $R_{kk}^{(e)}$, the same for all atoms.

Since the equations (6) are linear in the atomic variables $R_{k\ell}^{(j)}$, they are isomorphic to the set of equations of motion for the matrix elements of the density operator ψ. We shall treat the Eqs. (6) from this point as c-number equations. Further, we assume that all the atoms have identical energy level structure and also, we drop the atomic labels j, so it is taken implicitly that the atomic and field variables depend upon the special coordinates as well as the time.

It is convenient to introduce a new set of variables in terms of the old ones. We let

$$W_{k\ell} = R_{kk} - R_{\ell\ell}\ , \quad k > \ell\ , \tag{7a}$$

$$R_{k\ell} = \frac{1}{2}\ (U_{k\ell} + i\ V_{k\ell})\ , \quad k > \ell\ , \tag{7b}$$

where $U_{k\ell}$, $V_{k\ell}$, and $W_{k\ell}$ are real variables, and $U_{k\ell} = U_{\ell k}$, $V_{k\ell} = V_{\ell k}$,

$$\Omega = X + iY\ , \tag{7c}$$

$$\omega_R = X_o + iY_o\ , \tag{7d}$$

where X, Y, X_o and Y_o are real variables.

The resulting equations of motion for the real variables $\{W_{k\ell}, U_{k\ell}, V_{k\ell}\}$ are

$$\dot{W}_{31} = \frac{1}{2}\ \{X\ U_{32} - YV_{32}\} + \{X_o U_{31} - Y_o V_{31}\} - \gamma_{11}[W_{31} - W_{31}^{(e)}]\ , \tag{8a}$$

$$\dot{W}_{32} = \{X\ U_{32} - YV_{32}\} + \frac{1}{2}\ \{X_o U_{31} - Y_o V_{31}\} - \gamma_{11}[W_{32} - W_{32}^{(e)}]\ , \tag{8b}$$

$$\dot{U}_{32} = -\ \delta V_{32} - XW_{32} + \frac{1}{2}\ [X_o U_{21} - Y_o V_{21}] - \gamma_1\ U_{32}\ , \tag{8c}$$

$$\dot{V}_{32} = \delta U_{32} + \gamma W_{32} - \tfrac{1}{2}\,[X_o V_{21} + Y_o U_{21}] - \gamma_1 V_{32} \quad , \tag{8d}$$

$$\dot{U}_{31} = \Delta V_{31} + \tfrac{1}{2}\,[X U_{21} + Y V_{21}] - X_o W_{31} - \gamma_1 U_{31} \quad , \tag{8e}$$

$$\dot{V}_{31} = -\Delta U_{31} + \tfrac{1}{2}\,[X V_{21} - Y U_{21}] + Y_o W_{31} - \gamma_1 V_{31} \quad , \tag{8f}$$

$$\dot{U}_{21} = \delta V_{21} - \tfrac{1}{2}\,[X U_{31} - Y V_{31}] - \tfrac{1}{2}\,[X_o U_{32} - Y_o V_{32}] - \gamma_1 U_{21} \quad , \tag{8g}$$

$$\dot{V}_{21} = -\delta U_{21} - \tfrac{1}{2}\,[X V_{31} + Y U_{31}] + \tfrac{1}{2}\,[X_o V_{32} + Y_o U_{32}] - \gamma_1 V_{21} \quad . \tag{8h}$$

In obtaining Eqs. (8), we have made use of the invarient, tr ψ = I,

$$I \equiv R_{11}^{(j)} + R_{22}^{(j)} + R_{33}^{(j)} \quad . \tag{9}$$

It is noted that $\dot{I} = 0$ is satisfied identically in (6a)-(6c) for $\gamma_{11} \to 0$. For $\gamma_{11} \neq 0$, the condition (9) together with (6a)-(6c) constitutes the statement of conservation of atomic density, i.e., particle number.

The Eqs. (8) are coupled to Maxwell's equations through the polarizations associated with each transition field. It is easily determined that the Maxwell's equations in dimensionless form in the slowly-varying envelope approximation and in the retarded time frame can be written in the following form

$$\tfrac{1}{2} F_p^{-1} \nabla_\rho^2 \begin{Bmatrix} -X_o \\ Y_o \end{Bmatrix} + \frac{\partial}{\partial \eta_p} \begin{Bmatrix} Y_o \\ X_o \end{Bmatrix} = d \begin{Bmatrix} -U_{31} \\ V_{31} \end{Bmatrix} , \tag{10a}$$

$$\tfrac{1}{2} F_s^{-1} \nabla_\rho^2 \begin{Bmatrix} -X \\ Y \end{Bmatrix} + \frac{\partial}{\partial \eta_s} \begin{Bmatrix} Y \\ X \end{Bmatrix} = d \begin{Bmatrix} -U_{32} \\ V_{32} \end{Bmatrix} \quad . \tag{10b}$$

In the above equations, we have assumed cylindrical symmetry, thus the transverse Laplacian which accounts for diffraction coupling is:

$$\nabla_\rho^2 = \frac{1}{\rho} \frac{\partial}{\partial \rho} \left(\rho \frac{\partial}{\partial \rho}\right) \tag{11}$$

The first term on the left-hand side in (10a,b) accounts for transverse communication effects across the beam with normalized radial coordinate $\rho = r/r_p$ where r is the radial distance and r_p is a characteristic spatial width. In (10), $\eta_{p_s} = z\,\alpha_{\substack{eff \\ p_s}}$ where $\alpha_{\substack{eff \\ p_s}}$ is the on-axis effective gain,

$$\alpha_{\substack{eff \\ p_s}} = \frac{\left\{\begin{matrix}\omega \\ \omega_o\end{matrix}\right\}\left\{\begin{matrix}\mu_{32} \\ \mu_{31}\end{matrix}\right\}^2 N}{n \hbar c} \left\{\begin{matrix}\tau_p \\ \tau_s\end{matrix}\right\} \tag{12}$$

where $\left\{\begin{matrix}\tau_p \\ \tau_s\end{matrix}\right\}$ are characteristic times for the system, N is the atomic number density (assumed longitudinally homogeneous) and n is the index of refraction (assumed identical for each transition wavelength). The quantity

$$d = \frac{N(r)}{N_o} \tag{13}$$

governs the relative radial population density distribution for active atoms and is taken as either Gaussian with full width r_p or uniform, in which case r_p corresponds to $\rho_{max} = 1$. The Gaussian distribution would be associated with an atomic or molecular beam with propagation along the beam axis. For the cases treated here, it was found that there is no significant difference in the results for a uniform density distribution with injection pulse of initial radial width at half maximum, r_o, and a Gaussian radial density variation with $r_o = r_p$. For the latter case, the effective gain g_{eff} is appropriately adjusted such that both the radially integrated gain and the total effective gain, $g_{eff}L$, remain invariant between the two cases, where L is the length of the medium in the direction of propagation. In obtaining (10-13), we have extended Mattar et. al (14) Theoretical analysis for two-level SF. Equations (10) are written in the retarded time,

τ, frame where $\tau = t - nz/c$. From this point on, $\cdot$ in Eqs. (8) is taken to be $\cdot = \partial/\partial\tau$. Finally, the first factors on the first terms in (10) are the reciprocals of the "gain length" Fresnel numbers defined by

$$F_{p_s} \equiv \frac{\pi r_p^2}{\lambda_{p_s} g_{eff}^{-1}} \quad , \tag{14}$$

where

$$g_{eff} = \frac{\alpha_{eff}}{\frac{\tau_p}{\tau_s}} \quad . \tag{15}$$

It is seen from (10) that for sufficiently large Fresnel number, F, the corrections due to transverse effects become negligible. Note that F corresponds to a gain to less ratio. The "gain length" Fresnel numbers F are related to the usual Fresnel numbers $\mathcal{F} = \pi r_p^2/\lambda L$, where L is the length of the medium by

$$F/\mathcal{F} = g_{eff} L \ . \tag{16}$$

i.e., the total gains of the medium. In the computation, diffraction is also explicity taken into account by the boundary condition that $\rho = \rho_{max}$ corresponds to completely absorbing walls.

The initial conditions are chosen to establish a small, but nonzero transverse polarization for the $3 \leftrightarrow 2$ transition with almost the entire population in the ground state. This requires the specification of two small parameters, $\varepsilon \sim 10^{-4}$, for the ground state initial population deficit, and $\delta \sim 10^{-4}$ for the tipping single for the initial transverse polarization for the $3 \leftrightarrow 2$ transition. The derivation for the initial values for the various matrix elements is presented elsewhere [12], and the results are as follows:

$$W_{31} = 2\varepsilon - 1 \tag{17a}$$

$$W_{32} = \varepsilon \tag{17b}$$

$$U_{32} = 0 \tag{17c}$$

$$V_{32} = \varepsilon\delta \tag{17d}$$

$$U_{31} = m \sin \phi_p \tag{17e}$$

$$V_{31} = m \cos \phi_p \tag{17f}$$

$$U_{21} = -2 V_{31} \tag{17g}$$

$$V_{21} = 2 U_{31} \quad , \tag{17h}$$

where $m = \cos^{-1}(2\varepsilon - 1)$ and the phase ϕ_p is arbitrary, and we have chosen the phase ϕ_s to be zero.

Numerical Results

Calculational methods applied to this model and discussed elswehere[13,15] were used to compute the effects on SF pulse evolution for various conditions for the injection signal, thus demonstrating control of the SF signal by control of the input signal. Some examples follow.

In Figure 2 is shown the transverse integrated SF pulse intensity vs. retarded time τ (curve 2) together with the transverse integrated pump pulse intensity vs. τ (curve 1) for a gain and propagation depth chosen so that the pulses temporally overlap. Under these conditions the two pulses strongly interact with each other via the nonlinear medium, and the two-photon process (resonant coherent Raman - RCR) which transfers population directly between levels 2 and 1, makes strong contributions to the mutual pulse development[4]. The importance of the RCR in SF dynamical evolution in an optically-pumped three-level system was pointed out for the first time in reference 4. Indeed, in the extreme case, the SF pulse evolution demonstrated here has greater nonlinearity than SF in a two-level system which has been prepared initially by an impulse excitation. What is remarkable is that this is an example where the SF pulse temporal width τ_s is much less than the pump width τ_p, i.e., the SF process gets started late terminates early with respect to the pump time duration. Pulses of this type have been observed[16] in CO_2-pumped CH_3F.

Figure 3 is a comparison of the radially integrated SF pulses at equal propagation depth for three different values for the input pulse radial shape parameter v, where the initial condition for the pump transition field amplitude $X_o(\rho)$ is $X_o(\rho) = X_o(0) \exp[-(r/r_p)^v]$. Since all other parameters are identical

for the three curves, this shows that the peak intensity increases with increasing ν whereas the temporal width and delay time decreases. Also, it is clear that the SF pulse shape varies with ν. In connection with each of the SF curves shown, there is less than ten percent overlap with the injected pulse. These results thus demonstrate the control of the SF shape, delay time, peak intensity and temporal width by control of the injection pulse radial shape. In Figure 4, we contrast for different ν (as in Fig. 3) isometric of the pump and superfluoresance outputs to display the importance of spatial profile (ν=1,2,3: exponential, Gaussian and hyper-Gaussian).

The effect on the SF pulse of variation of the input pulse temporal shape parameter σ, is shown in Figure 5 which compares SF pulses at the same penetration depth as given in Figure 3, for two different values of σ. Here $X_o(\rho) = X_o(0) \exp [-(\frac{\tau}{\tau_p})^{\sigma}]$. It is seen that the variation from a Gaussian, σ = 2, to a super-Gaussian, σ = 4, temporal input pump pulse shape causes almost a factor of two increase in the peak SF intensity with a significant reduction in temporal width and no discernible shift in the time delay. This situation is in marked contrast with that shown in Figure 3 for the effect of pump radial shape variation. As in the previous case, there is less than ten percent overlap between the SF pulses and the pump pulse.

Figure 6 shows the SF pulses at equal penetration for various values for the initial temporal width τ_p of the injected Gaussian π-pulses. All other parameters for the pulse propagation are equal. Again, there is less than ten percent overlap between the SF pulses shown and the pump pulse. Thus, reducing the initial temporal width of the injection pulse causes a shift of the SF delay time and temporal width to higher values, and a decrease in the SF peak intensity.

Figures 7 and 8 illustrates the Fresnel dependence of the SF buildings. Figure 7 represents the radially integrated output SF energy while Figure 8 displays isometrically, versus τ and ρ, the SF energy. As the initial spatial width of the injected Gaussian pump increases r_p, the associated Fresnel number decreases, the delay strengthens, the SF peak intensity reduces and the SF pulse gets more symmetrical.

The effect on the SF pulse of the on-axis area of the Gaussian pump pulse is shown in Figure 9 for the same penetration depth as for Figure 3. It is seen here that the effect of increasing the initial on-axis area of the pump pulse is to decrease the SF pulse temporal width and delay time and to increase the intensity. As before, the overlap in this case between the SF and pump pulses is less than ten percent.

Figure 10 illustrates the dependence of SF output on the shape (form) of the input pump pulse whether it is full Gaussian pump, half-front Gaussian or reflected-half Gaussian. The shorter delay and the stronger SF output are associated with the full Gaussian followed by the reflected-half Gaussian pump and the (rising) front half Gaussian pump respectively.

In Fig. 11, the effect of varying N, the atomic density, on the SF build-up is shown. Note that N enters in the definition of α_{eff} then in F_{p_s}. The more dense N becomes, (the larger is the effective gain), the more intense is the SF build-up and the shorter becomes the relative delay. Thus, the overlap between the SF and the pump pulses increases with N. Furthermore, the nonlinear contribution of the two-photon effects increases significantly.

Conclusion

We have shown here eight ways of shaping the SF pulse by controlling corresponding properties of the injection pulse in coherent optical pumping on a three-level system, where propagation, transverse effects and diffraction are precisely taken into account. We have demonstrated also, in Figure 1, the highly nonlinear effect of generation of an SF pulse of much narrower temporal width and larger peak Rabi rate than the pump pulse under conditions where the two pulses completely temporally overlap after suitable propagation and pulse reshaping. An additional significant nonlinear to the SF emission in this case is due to the competing two-photon process with the direct process[4]. We have thus demonstrated by numerical simulation, the nonlinear control of light at one frequency with light of another frequency.

By changing the material characteristics such is the dipole moment of species on the associated transition frequency, one finds that the SF pump dynamics are modified [12]. The effect of increasing them is similar to the effects associated with augmenting N.

Acknowledgment

The diligent Word Processing efforts of Jerry Marciw are joyfully acknowledged.

REFERENCES

1. R. Bonifacio and L. A Lugiato, Phys. Rev. A11, 1507 (1975); 12, 587 (1975).
2. R. H. Dicke, Phys. Rev. 93, 99 (1954).

3. See papers and references contained in Cooperative Effects in Matter and Radiation, edited by C. M. Bowden, D. W. Howgate and H. R. Robl, (Plenum, New York, 1977).

4. C. M. Bowden and C. C. Sung, Phys. Rev. A18, 1558 (1978); Phys. Rev. A20, 2033 (1979).

5. N. Skribanowitz, I. P. Herman, J. C. MacGillivray and M. S. Feld, Phys. Rev. Lett. 30, 309 (1973).

6. H. M. Gibbs, Q. H. F. Vrehen and H. M. J. Hickspoors, Phys. Rev. Lett. 39, 547 (1977).

7. Q. H. F. Vrehen, in Cooperative Effects in Matter and Radiation, edited by C. M. Bowden, D. W. Howgate and H. R. Robl (Plenum, New York, 1977), p. 79.

8. M. Gross, C. Fabre, P. Pillet and S. Haroche, Phys. Rev. Lett. 36, 1035 (1976).

9. A. Flusberg, F. Mossberg and S. R. Hartmann, in Cooperative Effects in Matter and Radiation, edited by C. M. Bowden, D. W. Howgate and H. R. Robl (Plenum, New York, 1977), p. 37.

10. A. T. Rosenberger and T. A. DeTemple, Phys. Rev. A24, 868 (1981).

11. F. T. Hioe and J. H. Eberly, Phys. Rev. Lett. 47, 838 (1981).

12. F. P Mattar and C. M. Bowden in preparation for Topics in Current Physics: Multiple Photon Dissociation of Polyatomic Molecules ed. C. D Cantrell (Springer Verlag 1982).

13. F. P. Mattar, in Optical Bistability, edited by C. M. Bowden, M. Ciftan and H. R. Robl (Plenum, New York, 1981), p. 503; in "Proceedings, 10th Simulation and Modeling Conference, Pittsburg, 1978", edited by W. Vogt ad M. Mickle, Publ. Inst. Soc. Am. (1979), Pittsburgh, PA; and in Appl. Phys. 17, 57 (1978).

14. F. P. Mattar, H. M. Gibbs, S. L. McCall and M. S. Feld, Phys. Rev. Lett. 46, 1123 (1981).

15. F. P. Mattar and M. C. Newstein, in Cooperative Effects in Mattar and Radiation, edited by C. M. Bowden, D. W. Howgate and H. R. Robl, (Plenum, New York, 1977), p. 139.

16. T. A. DeTemple, private communication.

FIGURE CAPTIONS

Figure 1. Model three-level atomic system and electromagnetic field tunings under consideration. For the results reported here, the injected pulse is tuned to the $1 \leftrightarrow 3$ transition.

Figure 2. Radially integrated intensity profiles for the SF and injected pulse at Z = 5.3 cm penetration depth. The injected pulse is initially Gaussian in r and τ with widths $r_o = 0.24$ cm and $\tau_p = 4$ nsec, respectively, and initial on-axis area $\theta = \pi$. Further, $(\varepsilon_3-\varepsilon_1)/(\varepsilon_3-\varepsilon_2) = 126.6$; $g_p = 17\ cm^{-1}$; $g_s = 641.7\ cm^{-1}$; $F_p = 8400$; $F_s = 2505$; $T_1 = 80$ nsec; $T_2 = 70$ nsec, where T_1 and T_2 are taken to be the same for each transition.

Figure 3. Radially integrated intensity profiles of SF pulses at a propagation depth Z = 5.3 cm for three different values for the input radial shape parameter v. The injected pulse is initially Gaussian in τ, and has radial and temporal widths as for Figure 2 with initial on-axis area $\theta = 2\pi$. In this case, $g_p = 14.2\ cm^{-1}$; $g_s = 758.3\ cm^{-1}$; $F_s = 2960$; $F_p = 7017$, with all other parameters the same as for Figure 2. Here, curve 1, v = 2; curve 2, v = 3; curve 3, v = 4, (see text).

Figure 4. Isometric SF intensity (τ versus ρ) at a propagation depth Z = 5.3 cm for three different values for use input radial shape parameter ν. This figure complements Figure 3.

Figure 5. Radially integrated intensity profiles of SF pulses at a propagation dept Z = 5.3 cm for two different values for the input pulse temporal shape parameter σ. The injected pulse is initially Gaussian in r, and has radial and temporal widths as for Figure 2 with initial on-axis area $\theta = 3\pi$. In this case, $g_s = 641.7\ cm^{-1}$; $F_s = 2505$ and all other parameters are the same as for Figure 3. Here curve 1, $\sigma = 2$; curve 2, $\sigma = 4$ (see text).

Figure 6. Radially integrated intensity profiles of SF pulses for five different values for the temporal width, τ_p of the injected signal: curve 1, $\tau_p = 4$ nsec; curve 2, $\tau_p = 3.3$ nsec; curve 3, $\tau_p = 2.9$ nsec; curve 4, $\tau_p = 2.5$ nsec; curve 5, $\tau_p = 2.2$ nsec.

Figure 7. Radially integrated intensity profile of SF pulses at a propagation depth Z = 5.3 cm for five different values of the spatial width r_p of the injected pump (thus of the associated Fresnel number): curve 1, $\mathcal{F} = 0.69$; curve 2, $\mathcal{F} = 0.40$; curve 3, $\mathcal{F} = 0.24$; curve 4, $\mathcal{F} = 0.17$ and curve 5, $\mathcal{F} = 0.10$.

Figure 8. Contrast of SF (top line) and Pump (botton line) Energy isometric versus τ and ρ at a propagation depth Z = 5.3 cm for different values of the Pump Fresnel number (associated with the initial spatial width of the injected signal): curve 1, $\mathcal{F}$ = 4.0; curve 2, $\mathcal{F}$ = 2.26; curve 3, $\mathcal{F}$ = 1.0; curve 4, $\mathcal{F}$ = 0.69; curve 5, $\mathcal{F}$ = 0.40; curve 6, $\mathcal{F}$ = 0.27 and curve 7, $\mathcal{F}$ = 0.10.

Figure 9. Radially integrated intensity profiles of SF pulses for three different values for the initial on-axis injection pulse area θ_p; curve 1, $\theta_p = \pi$; curve 2, $\theta_p = 2\pi$; curve 3, $\theta_p = 3\pi$ All other parameters are the same as for Figure 2, except for $g_s = 291.7\ cm^{-1}$ and $F_s = 1138.7$.

Figure 10. Radially integrated intensity profile of SF pulses for three different form of the injected pump: curve 1, front half Gaussian form; curve 2, full Gaussian and curve 3, reflected half Gaussian.

Figure 11. Radially integrated intensity profile of SF pulses for three different atomic density N. From curve a to curve d, the density ratios are: b/a = 1.4, c/a = 1.8, d/a = 2.2.

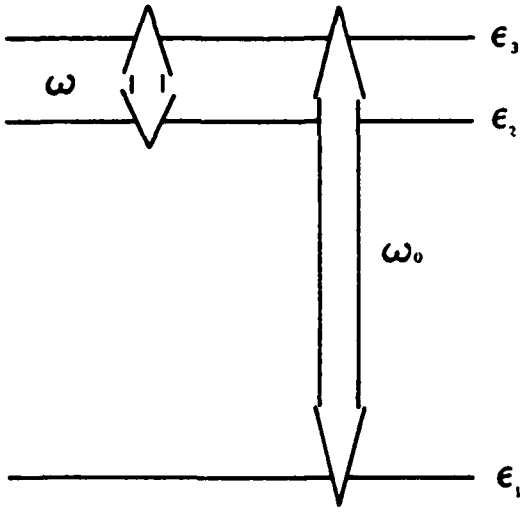

Figure 1

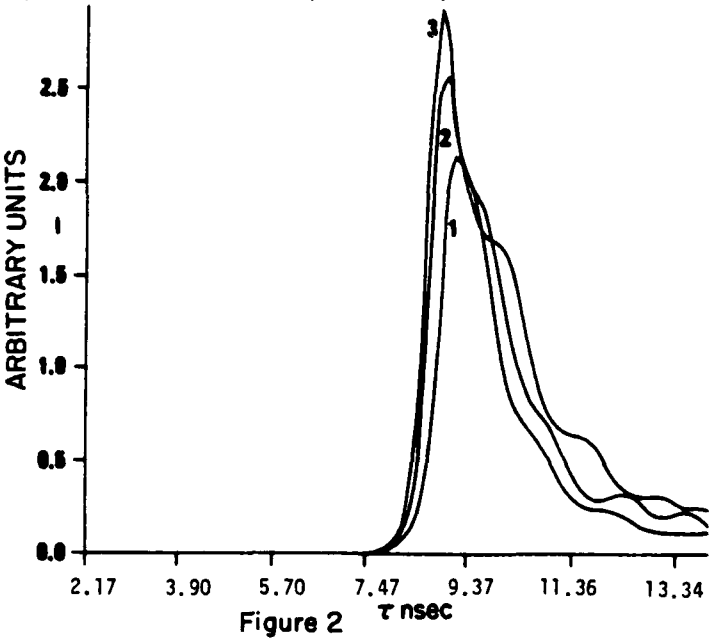

Figure 2

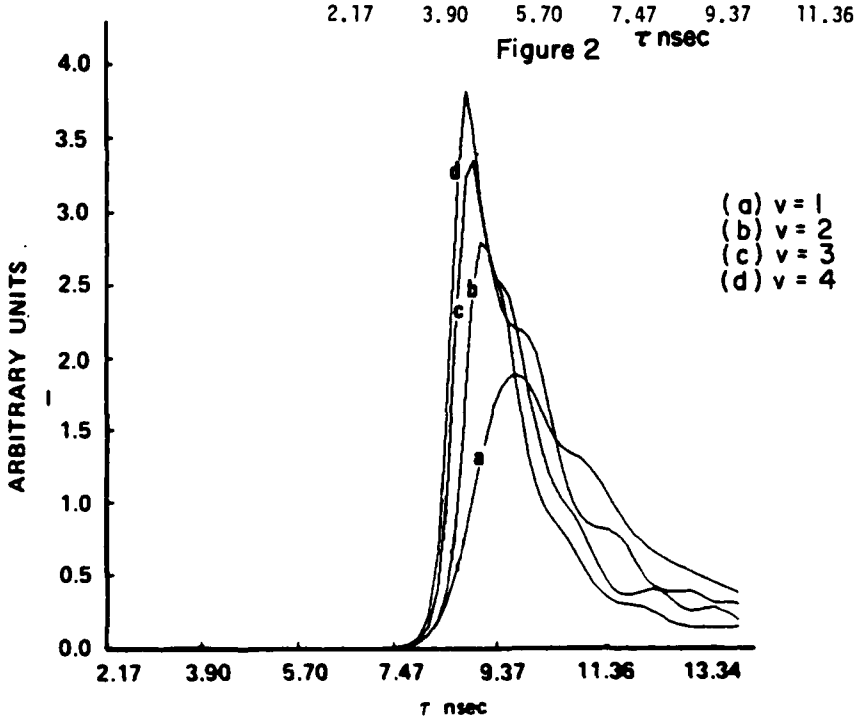

Figure 3

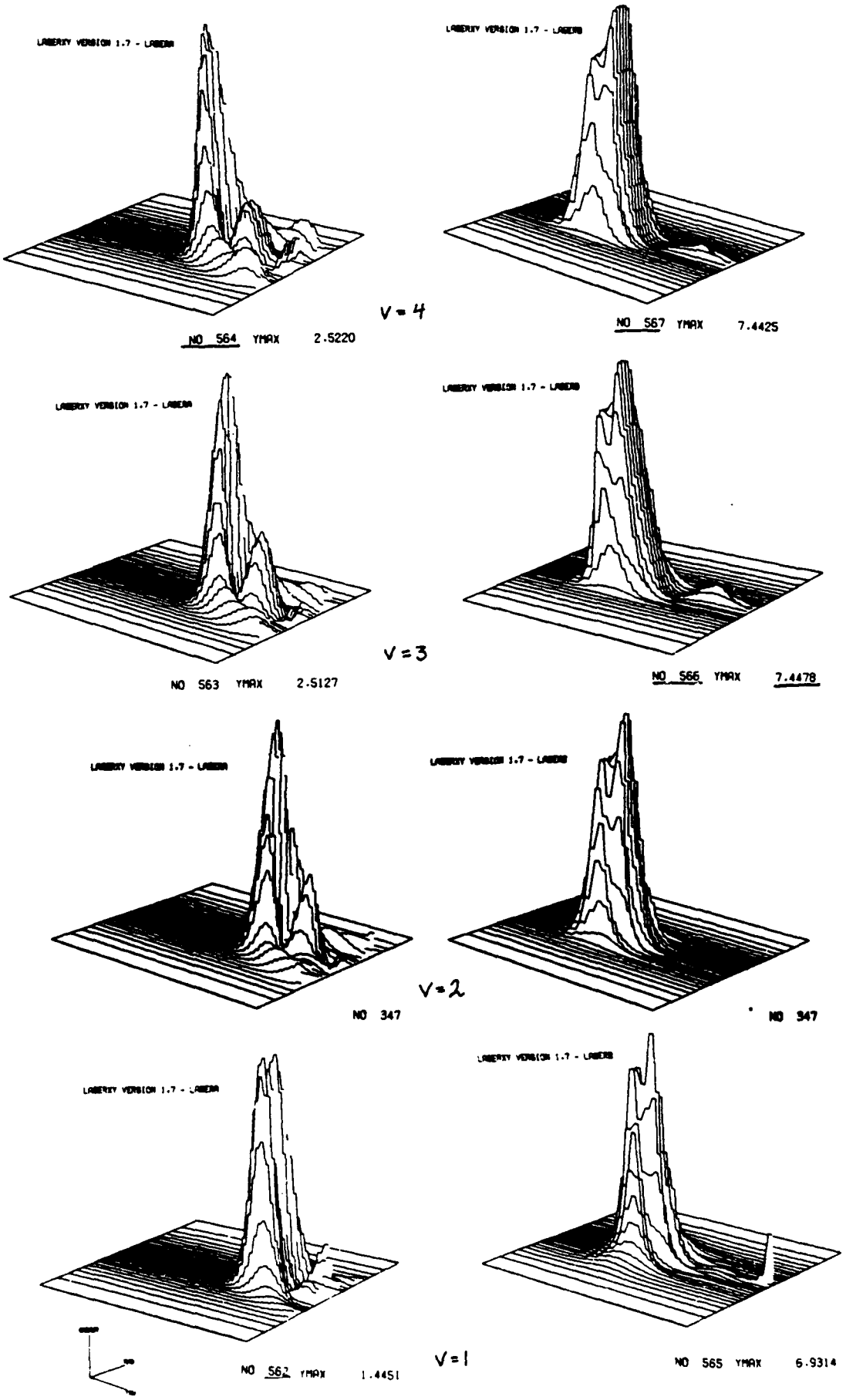
LASERVIEW VERSION 1.7 - LASERA
LASERVIEW VERSION 1.7 - LASERB
V = 4
NO 564 YMAX 2.5220
NO 567 YMAX 7.4425
LASERVIEW VERSION 1.7 - LASERA
LASERVIEW VERSION 1.7 - LASERB
V = 3
NO 563 YMAX 2.5127
NO 566 YMAX 7.4478
LASERVIEW VERSION 1.7 - LASERA
LASERVIEW VERSION 1.7 - LASERB
V = 2
NO 347
NO 347
LASERVIEW VERSION 1.7 - LASERA
LASERVIEW VERSION 1.7 - LASERB
V = 1
NO 562 YMAX 1.4451
NO 565 YMAX 6.9314
ENERGY

Figure 4

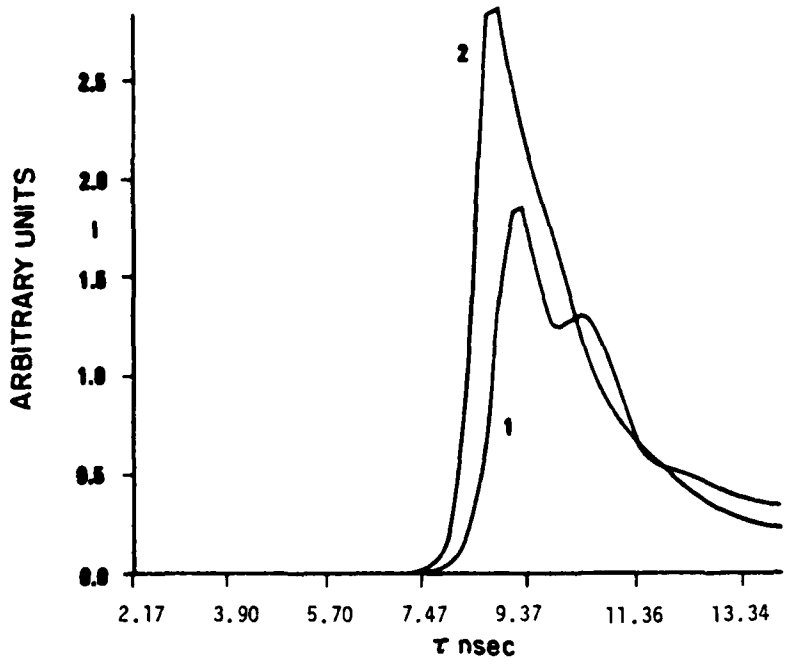

Figure 5

FIGURE 6

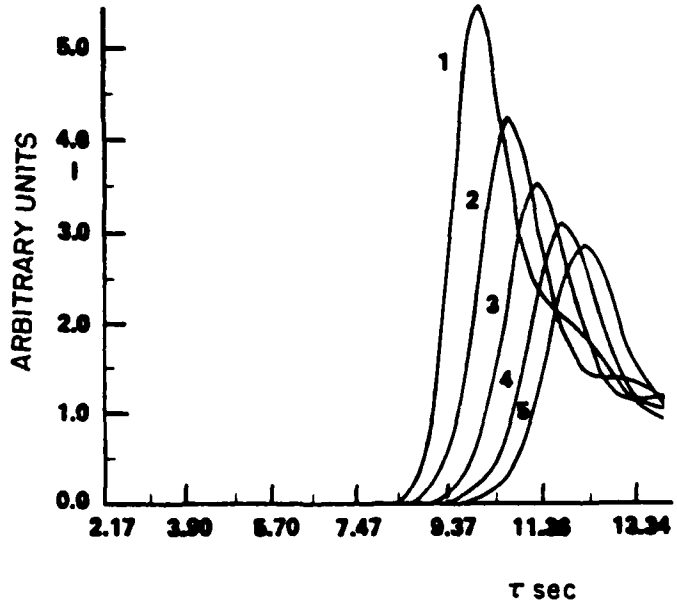

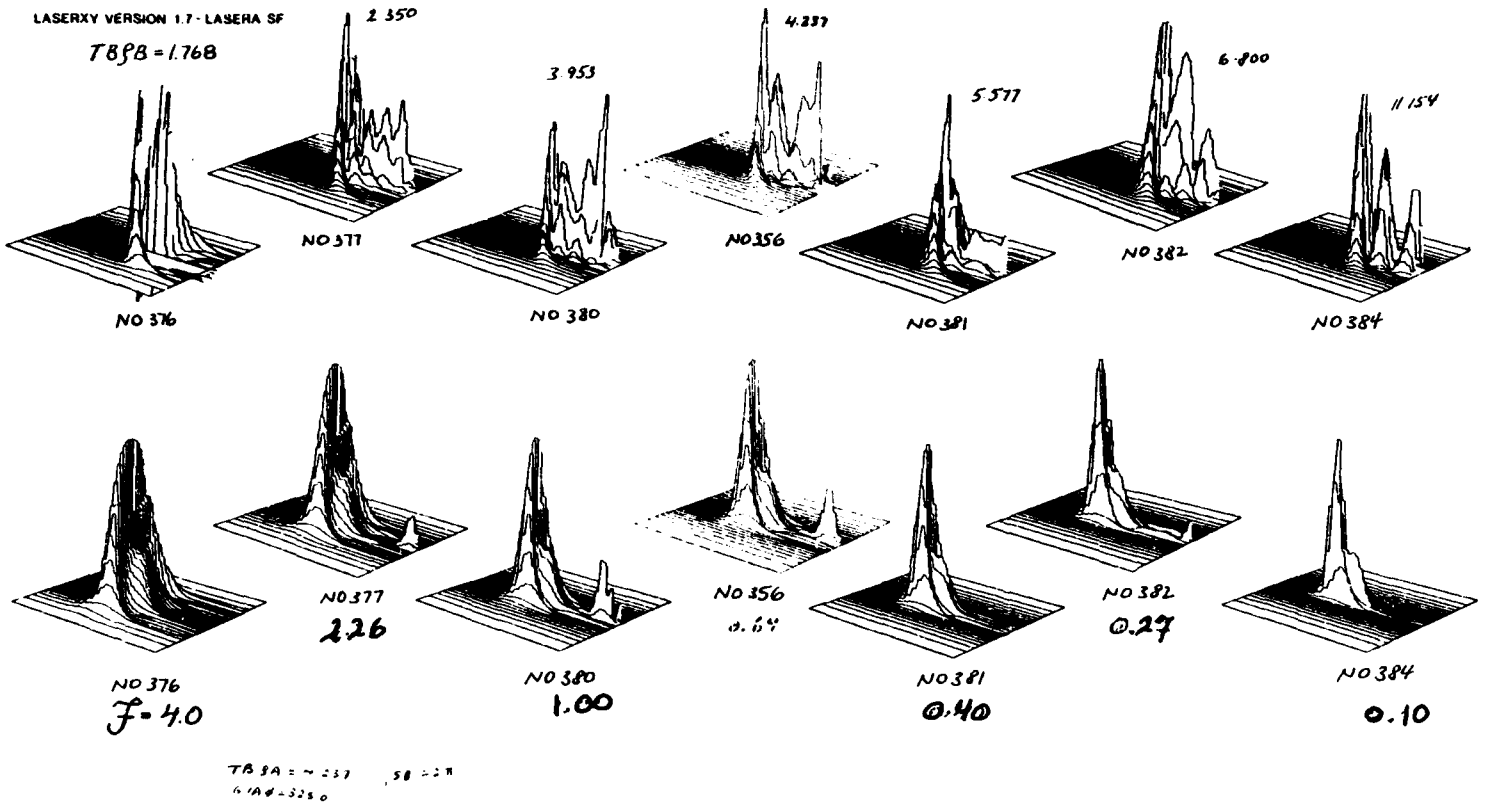
LASERXY VERSION 1.7 - LASERA SF
TBPB = 1.768
2.350
3.953
4.237
5.577
6.800
11.154
NO 376
NO 377
NO 380
NO 356
NO 381
NO 382
NO 384
NO 376
F = 4.0
NO 377
2.26
NO 380
1.00
NO 356
0.64
NO 381
0.40
NO 382
0.27
NO 384
0.10

Figure 8

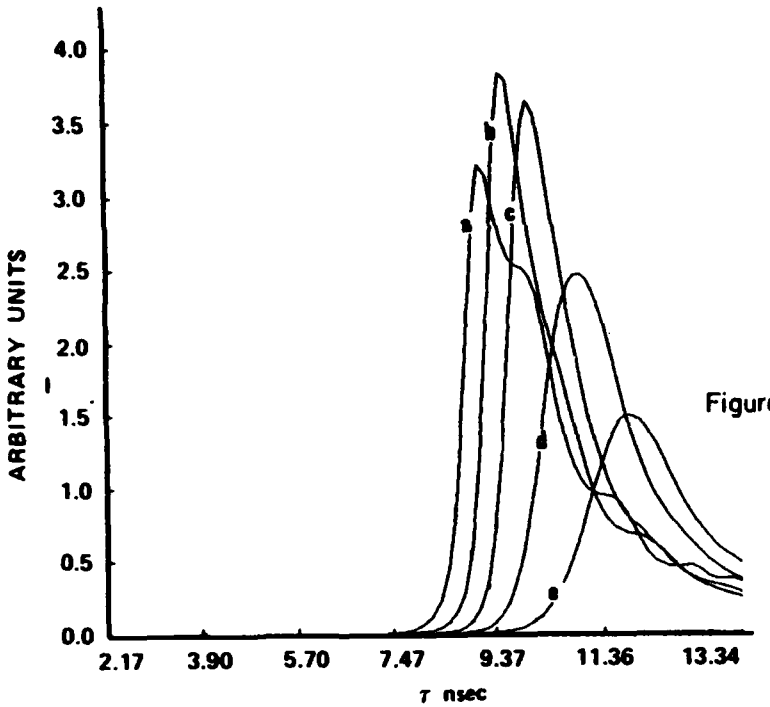

Figure 7

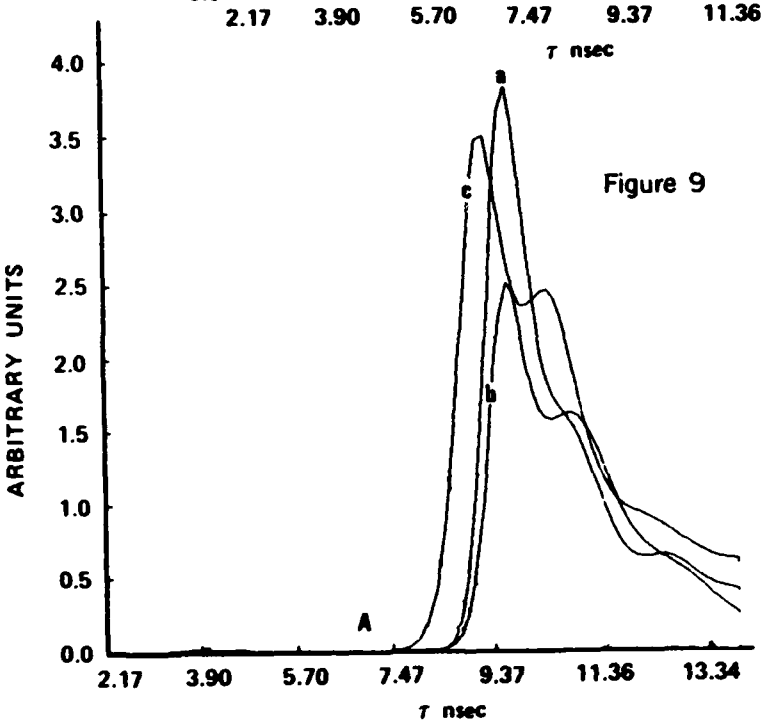

Figure 9

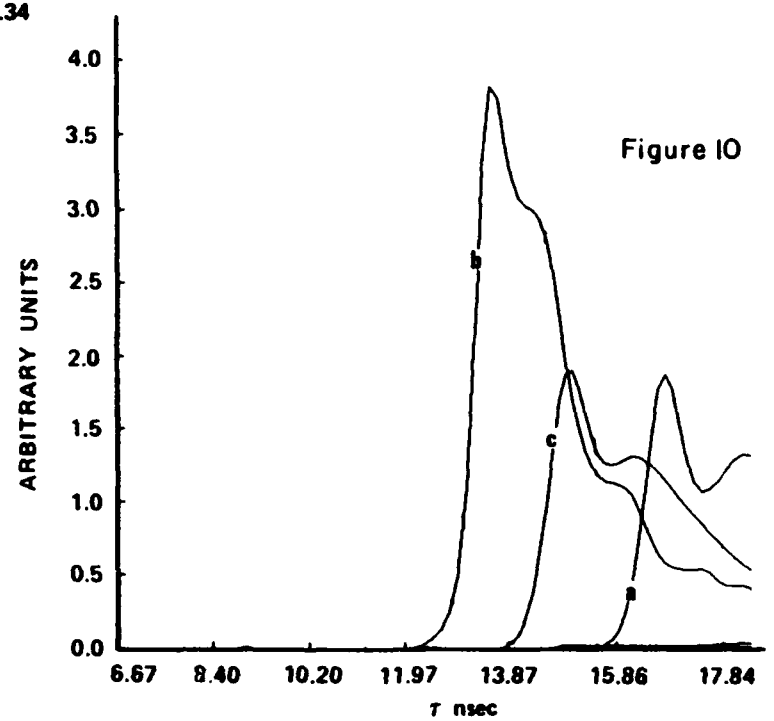

Figure 10

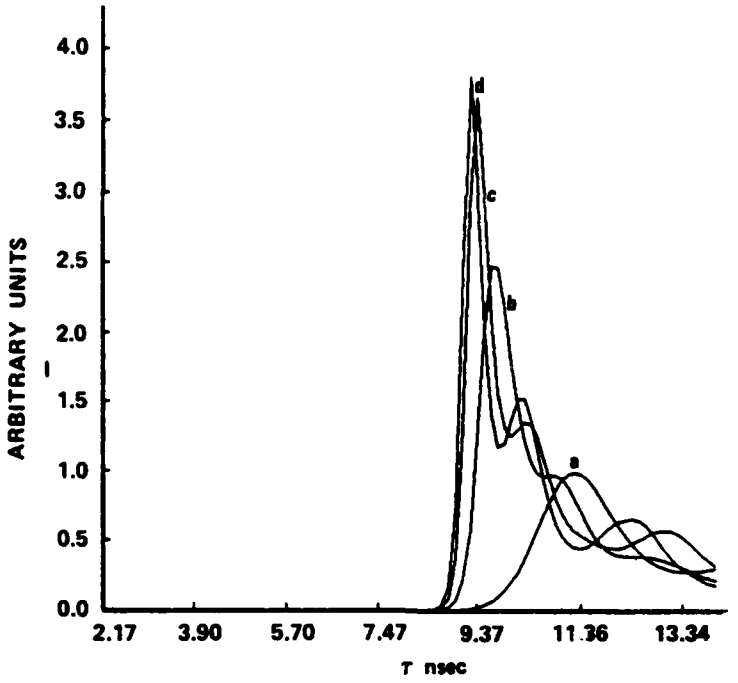
4.0
3.5
3.0
2.5
2.0
1.5
1.0
0.5
0.0
ARBITRARY UNITS
I
d
c
b
a
2.17
3.90
5.70
7.47
9.37
11.36
13.34
T nsec

Figure II

DEPARTMENT OF MECHANICAL
AND AEROSPACE ENGINEERING

A PRODUCTION SYSTEM FOR THE MANAGEMENT OF A RESULTS FUNCTIONS BANK AND A SPECIAL APPLICATION: THE LASER PROJECT+

BY: M CORMIER, Y. CLAUDE, P. CADIEUX
AND F. MATTAR (POLYTECHNIC INSTITUTE
OF TECHNOLOGY AND SPECTROSCOPY
LABORATORY, MASSACHUSETTS INSTITUTE
OF TECHNOLOGY)

+ Presented at the International Conference
on Laser '81, New Orleans, Dec. 1981

Spring 1982

Poly M/AE Report No. 82-8

A PRODUCTION SYSTEM FOR THE MANAGEMENT OF A RESULTS FUNCTIONS BANK AND A SPECIAL APPLICATION: THE LASER PROJECT

M. Cormier, Y. Claude, P. Cadieux
Dept. d'Informatique et Recherche operationnelle
Universite de Montreal, Montreal, Canada

&

F.P. MATTAR*
Dept. of Mechanical and Aerospace Engineering
Polytechnic Institute of New York, Brooklyn, New York 11201, U.S.A.
and
Spectroscopy Laboratory
Massachusetts Institute of Technology
Cambridge, Mass. 02139, U.S.A.

ABSTRACT

This document presents the system developed to support the numerical laser modeling project at the Universite de Montreal in conjunction with the Polytechnic Institute of New York. This tool represents a mechanism for practical parametric simulation studies of real-life experiments in quantum Electronics. The goal of this system is to offer a reliable, adaptable and easy tool to the production and study of laser simulations, a study mainly done through drawings and comparisons of functions. Organized around SIMRES and DATSIM type files, this system encompasses software packages which control file access, application programs and the very laser programs. The SIMRES files are self-descriptive and can store in the same direct access file all the information relative to a simulation. The SIMRES package is used to generate a SIMRES file while the XTRACT package permits the reading of the information stored on a SIMRES file. The DATSIM files regroup on one file, permanently located on disk, a summary of the SIMRES files (because of their size these must be filed away on a magnetic type). The DATSIM package permits the reading and the writing procedures of the DATSIM files. This document also presents three of the principal application programs: the DEFPARM program which helps the user to construct parameter games for the simulation programs, the DESRES program which plots the simulation results, and the SYNTH program which makes the comparisons. Finally, the document presents the different laser programs.

* Jointly supported by F.P.Mattar, the U.S. Army Research Office, the U.S. Office of Naval Research, the U.S. Science Foundation Research Corporation, Battelle Colombus Lab. and the Canadian Defense Research Establishment at Valcartier.

I - INTRODUCTION

The laser numerical modeling project began over three years ago at the University of Montreal. A first production system, which permitted generation of laser simulations and graphic representation of the results was then set up.

This first system was based on a fixed structure of the result files, and the programs using this structure were consequently not very flexible.

Eventually, new needs appeared (catalogs and comparisons) and their implementation made the system more complex and less efficient as these new possibilities could not always be adequately integrated. Finally, new models were introduced to the system for which the fixed format was not adequate.

A second system, more flexible and more powerful, was undertaken in May 1981. The object of this document is to present this new system. It consists, on the one hand, of a nucleus, made of general packages, which permits the creation and manipulation of result files consisting of functions of arbitrary dimensionality; and on the other, of a set of programs adapted to precise tasks (graphic representation of the results, comparisons).

The order of the sections goes from the general to the particular.

Section two presents the objectives which oriented the design and implementation of the system.

Section three gives a comprehensive view of the system.

Section four presents the different packages forming the nucleus.

Section five presents the programs which generate the various products (drawings, catalogs) of the laser modeling project.

The conclusion returns to the objectives presented in section two and discusses to what extent they have been attained.

II - OBJECTIVES

The design of the different packages composing the production system for the laser numerical modeling project has been elaborated from the following goals:

- modularity
- flexibility
- reliability
- efficiency
- transportability
- adequate documentation

2.1 MODULARITY

Modularity implies that a job is divided into tasks and that execution of a given task is confined within a set of routines.

By proceeding, such a task is isolated from the rest of the program. The use of packages is modular since they are indenendent from the programs and can therefore be used in various ways in various programs.

2.2 FLEXIBILITY

Flexibility is the quality of a software which not only answers a precise need but also adapts to a range of similar problems.

Software products must therefore be given a maximum of generality and flexibility in view of current and future needs. Ideally, a software should handle the general case.

But in reality, it is often neither possible nor desirable; and restrictions are necessary.

In such cases, flexibility is then measured by the facility with which the software can be modified in order to bypass its limitations or restrict their impact.

2.3 RELIABILITY

Reliability combines two major aspects.

The first aspect is that a software must give the control back to the operating system only if it wishes to do so. This means that a software must prevent conditions (such as memory overflow) where the operating system would otherwise force it to stop.

The second aspect is that when a routine or a program does return results, these must be correct; otherwise no results are produced and an error message is returned.

2.4 EFFICIENCY

When designing a software, the limited and often costly resources given by an operating system, often shared by many users, must be taken into account.

Techniques which minimize factors such as computation time, memory requirements and disk access are thus essential. Moreover, reduced use of the resources may have a positive impact on the turnaround time, and then again, the optimisations will directly benefit the user.

2.5 TRANSPORTABILITY

It is often difficult to produce perfectly transportable software products. Nevertheless, techniques can be used to increase software transportability. Thus, machine dependent and installation dependent features must be banned. In some cases, it is impossible to do so (such as in I/O routines) and critical actions must be isolated in routines which can easily be modified to adapt to other environments.

2.6 ADEQUATE DOCUMENTATION

Three types of documentation are necessary to describe a given system adequately:

Comments within the source code are necessary to maintain and modify the software.

A separate technical manual complements the internal documentation with a higher level description giving the overall design philosophy and indicating the global structure and interdependencies between the various procedures or programs.

Finally, a user's guide is needed to indicate clearly how the software is to be used.

III - A COMPREHENSIVE VIEW OF THE SYSTEM

The system supporting the laser modeling project has been developped on a pair of CDC CYBER 173 computers at the Centre de Calcul of the Université de Montréal. It consists of programs and packages written in FORTRAN IV. The three major tasks accomplished by the system are:

- generation of simulation results,
- drawings of the results of an individual simulation,
- comparisons of results between simulations.

3.1 GENERATION OF RESULTS

The study of lasers is done with programs simulating the spacial and temporal evolution of a laser impulse, in conformity with a given numerical model. Initially, there was only one program which was using a single laser cylindrical model. Eventually, with developments in the physics theory, the initial model was improved (it now takes into account Doppler effects, oscillatory phenomena, ...) and new models were developped (2-laser model, Cartesian model). There are now many laser simulation programs, each being the starting point of a data-base of results associated with the model.

Each simulation is controlled by a set of parameters defining the material and the field through which the laser impulse propagates. These parameters are given to the laser programs as FORTRAN NAMELISTs. For each model, simulations are identified through a unique number. This number is included in the NAMELISTs as a special parameter. The results of a simulation are written on SIMRES type files (SIMulation RESults). Each file is identified through a root to which a suffix is added; the root corresponds to the identifier of the program which produced the simulation, and the suffix is the simulation number.

SIMRES files contain general information (name of the originating program, version number of the program, creation date of the file, ...), the list of the simulation parameters, and the results of the simulation. The way results of a simulation are handled can be summarized in the following manner:

- The programs evaluate functions of varying dimensionality and the parameters of the simulation determine at what points these functions must be evaluated.

- Values of the functions are kept in SIMRES files for a given sample of evaluation points.

As can be seen, all the information relative to a simulation is kept on a single entity, i.e. the SIMRES file. In this basic scheme (NAMELISTs, simulation programs, SIMRES files), DATSIM type files and the program DEFPARM were added. The program DEFPARM (DEFinition PARa-Meters) is used to assist the user in writing NAMELISTs. It is an interactive program which allows the user to describe a simulation of a family of simulations by using a compact syntax, and in return produces the corresponding NAMELISTs. Although this program may not be essential, its advantage is to relieve the user of the chore of writing often repetitive NAMELISTs.

It also avoids trivial errors such as syntax errors in NAMELISTs and errors in parameter names.

The emergence of DATSIM files is linked to a context of intense production. Moreover, to be efficient at a production level, it is necessary that any information concerning any given produced simulation be available. SIMRES files being too large and too numerous to be all kept on disk, a mechanism has been laid to transfer data between disk and tape. This archival system is essential, but it considerably slows the access to information. To be efficient, we must then compromise and keep on disk some high priority informations concerning all produced simulations.

The informations are gathered in a data base consisting of DATSIM type files (DATa SIMulation). DATSIM files contain, for every simulation produced by the program:

- general informations, identical to those on SIMRES files,
- values of the simulation parameters,
- evaluation points and values of the functions used in comparisons.

The program MAJDTS (Mise-A-Jour-update, DaTSim) reads useful informations on a SIMRES file and writes them on the SIMRES file. It is noteworthy that the information contained in the DATSIM file is used by the program DEFPARM to get the numbers to be assigned to new simulations.

The configuration of the system, as regards to the production of simulations is given at figure 3.1.

The suffixes 1CFS, 2CFS, 1PS, 1P4S refer to the different laser models (these will be explained in Section 5).

Consider model 1CFS (1-laser Cylindric Frequency Statistics model). The program DEFPARM takes the specifications from the user, validates them and writes on the file SX1CFS (Simulations to be eXecuted) the data needed to produce the simulations requested. Then, the program LR1CFS (LaseR) reads the appropriate date on the file SX1CFS, generates the simulation and produces a SIMRES file whose identifier is LR1CFS (no) ((no): simulation number).

Finally, the file LR1CFS (no) gives the program MAJDTS the information needed to register the simulation on the file DT1CFS (DaTsim) which contains a summary of the simulations carried out with the model 1CFS.

3.2 DRAWINGS OF A SIMULATION

The study of the simulation results requires graphic support in order to visualize the profiles of the functions evaluated by the simulation programs. The program DESRES (dessin-drawing, simres) has been designed to offer such assistance. This program can be used either in batch or interactive mode.

Drawings needed are specified by using a syntax whose structure is similar to that of a program and allows inner loops on simulations, functions, selection criteria, etc. The user can thus indicate in a short way what drawings he wishes to have.

The commands given by the user are analysed by the program DESRES, which breaks them up in single units, using the package XTRACT. The SIMRES files then give all the information needed to identify and produce the drawings. There are four types of drawings available:

- 2-dimensional representation of a function,
- 3-dimensional representation of a function,
- 2-dimensional projection of a 3-d representation.

The 3-D projections and the level curves are performed by the program TRASURF (CACM sept /74).

Figure 3.2 presents the portion of the system which carries out the production of drawings.

3.3 COMPARISONS OF RESULTS BETWEEN SIMULATIONS

The program SYNTH (SYNTHesis) has been designed to allow comparisons of results between simulations. A comparison is done by superposing on one drawing 2-dimensional representations of either functions coming from different simulations or functions for which each point comes from a different simulation. The program SYNTH is a powerful tool; it can be used in both interactive and batch mode and its scope includes the three following applications:

- Comparison inside one simulation.

- Comparisons between simulations of a same model, bringing out the role of certain parameters in 2 or more laser models, and the role each laser plays.

- Comparisons between the different models to demonstrate their impact. The user specifies the work to be done either by defining the objects to be compared and the comparison criteria or by indicating where to search for the objects to be compared and how to organize the comparison. In this last case, part of the search procedure needed for the definition of the comparison is done by the SYNTH program.

After validating and accepting the request, the SYNTH program produces the necessary headings identifying the comparison (by isolating the fixed parameters from the variable ones) then effects the drawings corresponding to the comparison.

The running of a comparison requires all the information needed at the same time on one disk. It is at this level that the DATSIM files are useful as they give access to the parameter list of all the simulations already produced and to certain functions often used in the comparisons. Nevertheless, the data on the DATSIM files are not always sufficient, the user therefore must revert to the archival procedures of the needed SIMRES files.

This structure is presented in figure 3.3.

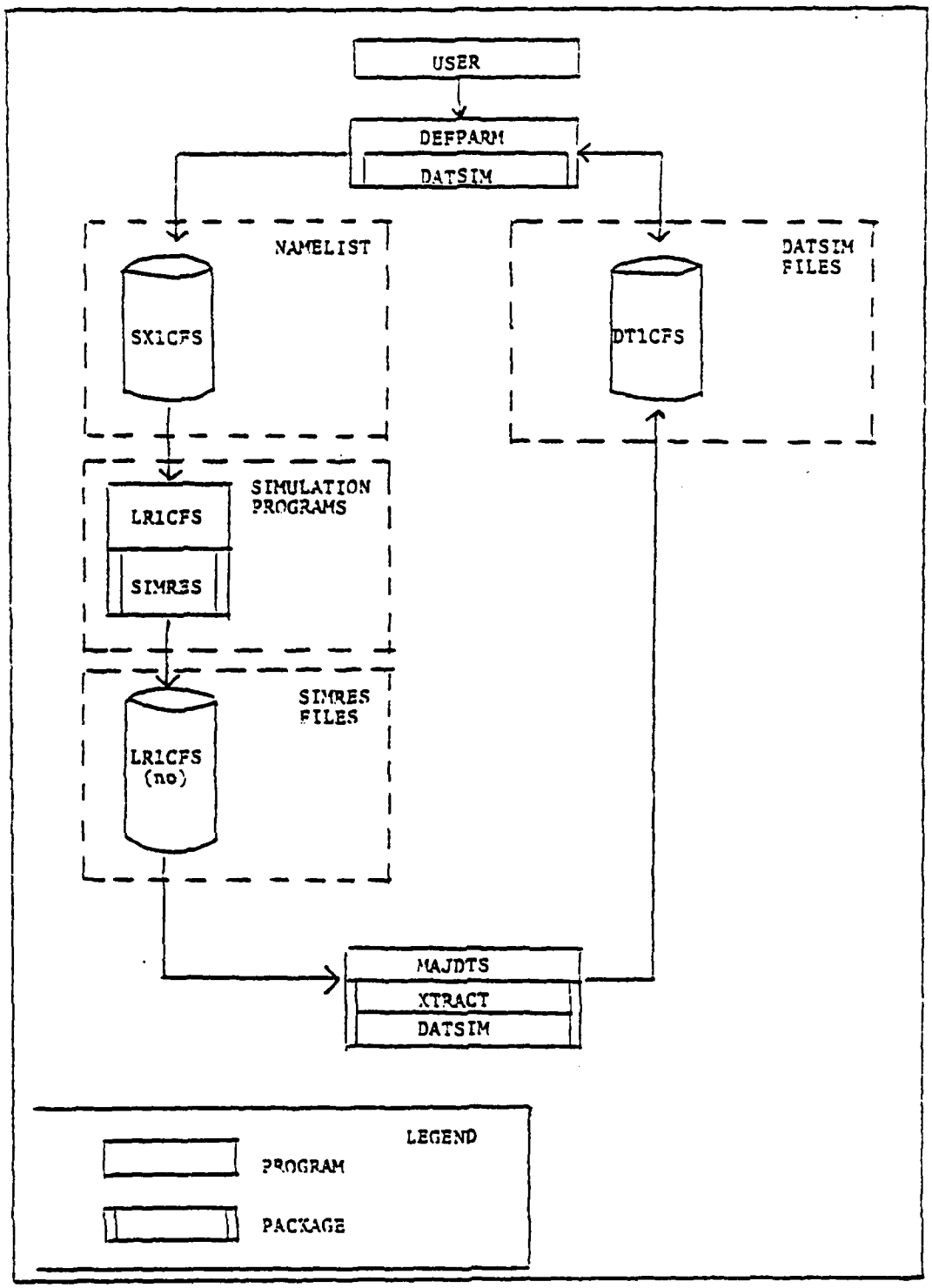

FIGURE 3.1 - SIMULATIONS PRODUCTION

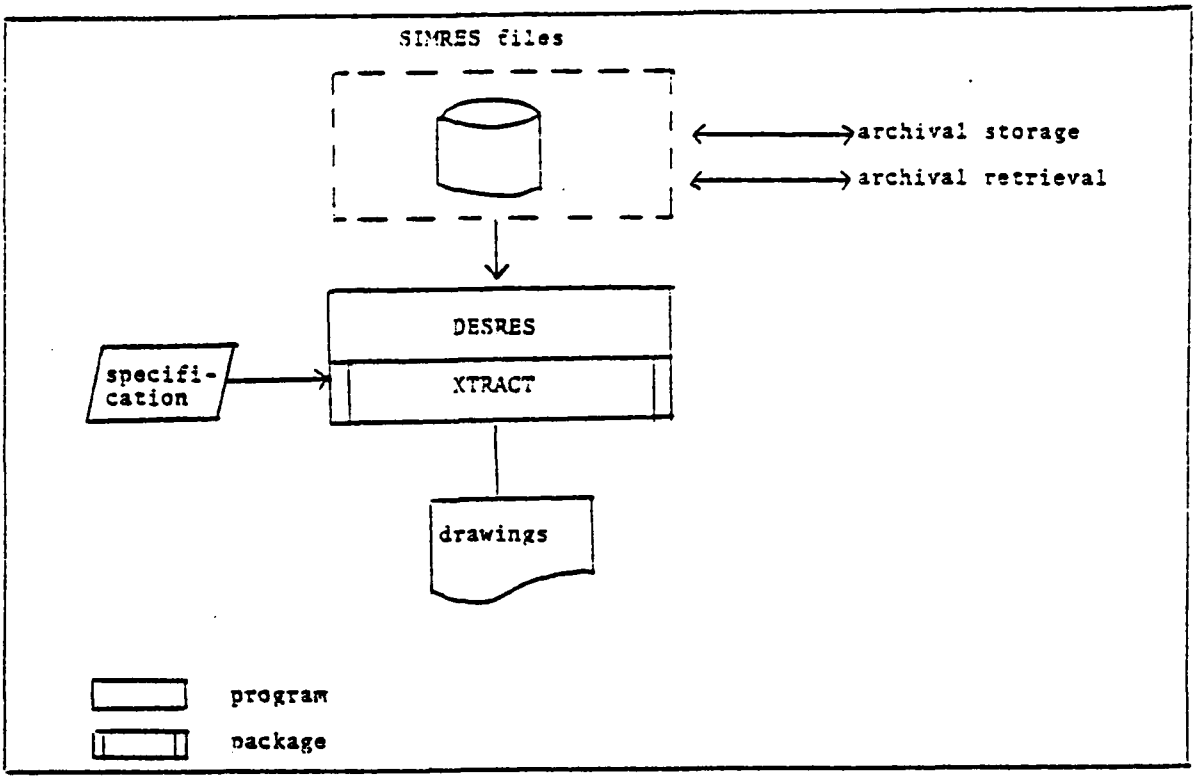

FIGURE 3.2 - PRODUCTION OF DRAWINGS

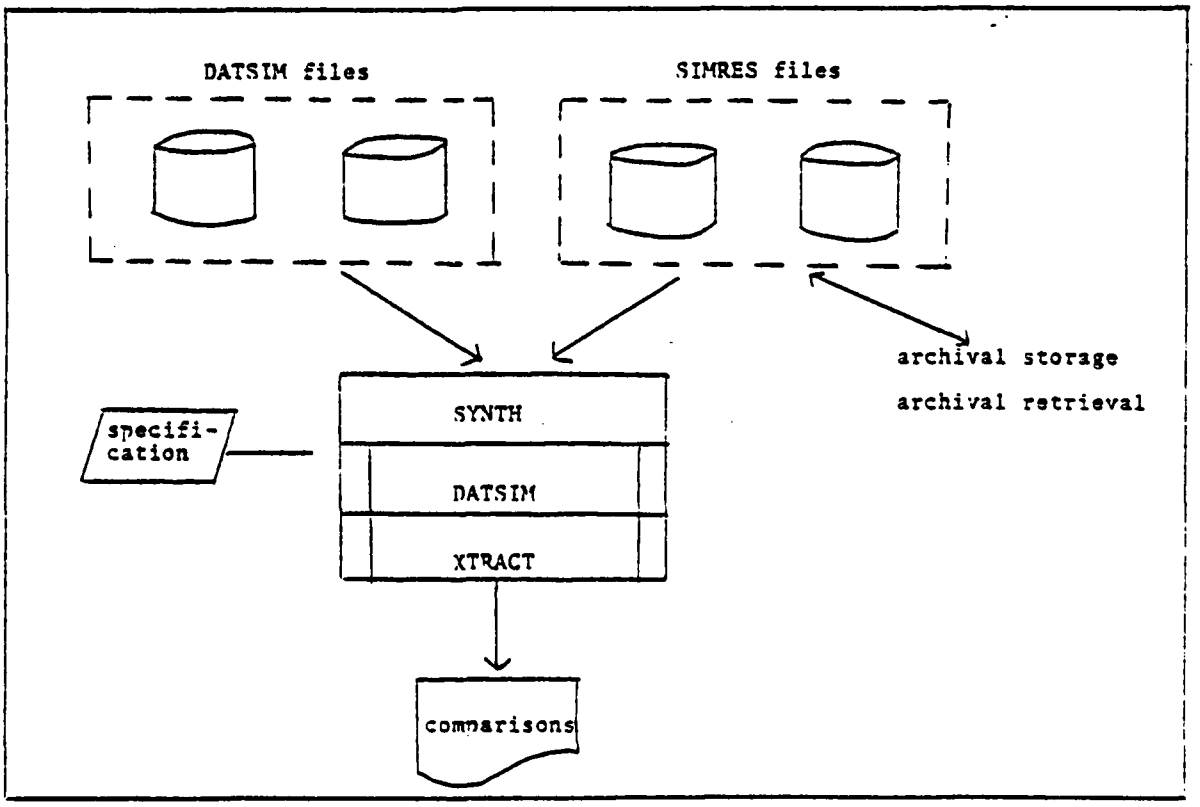

FIGURE 3.3 - PRODUCTION OF COMPARISONS

IV - THE PACKAGES

The packages are the lower level of the system. Beside answering a particular application, their role is to solve a problem in a general way. Each package is made up of several procedures accomplishing a precise task. The packages presented here are the following:

- SIMRES : generation of the SIMRES files;
- XTRACT : operation of the SIMRES files;
- DATSIM : generation and operation of the DATSIM files.

4.1 THE SIMRES PACKAGE

The SIMRES package aims, on the one hand, to keep on one single file all the information relative to a simulation and on the other, to provide self-descriptive files, or files that carry the necessary information to describe their organization. By proceding this way, the integrity of the information is insured (all data relating to one simulation is concentrated in one file) and the system is given a greater flexibility when faced with changes (the organization of the file varies, the key is in its description).

4.1.1 DESIGN OF THE RESULTS FILES

The different simulation models describe the evolution of a laser pulse in a space of n dimensions. The value of n, the number of dimensions, depends on the model. To each dimension corresponds an axis identified by a name and by units. The simulation programs results are functions defined on the reals:

$$f_i = \mathbb{R}^{di} \rightarrow \mathbb{R}$$

where $i = 1,2,\ldots,M$ (M = number of functions)

$$0 \leq d_i \leq N$$ (N = number of dimensions of the simulation space).

For instance, in the ICFS model involving a 4 dimension space defined by the STASTIC, ETA, RHO and TAU axes, the O POWER function depends on the STATISTIC, ETA and TAU axes ($N = 4$ and $d_{O\ POWER} = 3$).

The functions assessed by the simulation programs correspond to continuous phenomena. But the fact of using a computer makes it important to make them discrete. Thus, the points at which a function has to be assessed is determined by associating them to a sampling grid. When only one sampling grid is used for all the functions, it can be said that this grid constitutes the discrete space in which the simulation evolves.

It would be very costly to keep, for each value of a function, the value of its points of assessments. It is thus of prime importance to find a more compact method to describe the sampling grids.

The simplest sampling grid is the linear orthogonal grid which can be described by giving for each of the axes that make up that grid, a starting point, an increment and the number of points on the axis. Figure 4.1 shows such a grid.

However, the linear orthogonal grid offers little flexibility. Thus, in order to follow more adequately the phenomenon under study, there would be a need for a grid where the distance between the points, instead of being uniform, is smaller in certain areas than in others. This will define a finer grid where the phenomenon is more interesting. Such a grid is said to be "nonlinear orthogonal" and can be described by keeping for each of the axis the value of the chosen point: see figure 4.2.

Moreover, there may be a need for a grid even more adapted to the phenomenon under study, for instance for a grid without the constraints of orthogonality. In this case, the coordinate of the grid associated to an axis depends on the value on that axis and possibly on the values on other axes. A grid in $\mathbb{R}^N$ can thus be described by N sampling functions fe_1, fe_2,..., fe_n each of these functions depending of an axis or on several axes for its assessment. What is stored to describe the grid is then the values of the functions. Thus, in figure 4.3, which illustrates a nonlinear orthogonal grid, the sampling grid fe_Y, depending only on the Y axis, is completely described by a 7 points vector and the function fe_x, depending on axes x and y, is described by a matrix of 7x7 points.

This last method is the most advantageous and thus, it is the one most used here. In fact, this method permits the description of grids as general as possible while avoiding the redundancy of the information at the level of the values of the points on the axes. For this method, the use of space is proportional to the "complexity" of the sampling functions.

The definition of a sampling grid often requires that the points be sufficiently close together and sufficiently numerous to assure the stability of the numerical techniques used. Thus, it is possible to store more information than is required to visualize the phenomena. Even more, it is possible that the results files may not be kept on the same disk unit: for instance, the complete Cartesian laser model assures four functions for more than a billion points (7 points for the STATISTIC axis x 300 for the ETA axis x 95 for the X axis x 95 for the Y axis x 64 for the TAU axis) which is far beyond the space capacity of a disk.

It is thus essential to reduce the volume of data to be put on file. This is done by introducing a selection mechanism which chooses those points of a sampling function for which the data is effectively being stored. This selection is done by specifying the number of the starting point and an increment in number of points. This simple way of proceding, together with an as precise a grid as is required gives enough flexibility to make a pertinent choice of data for storage.

4.1.2 USAGE OF THE SIMRES PACKAGE

The procedures of the SIMRES package create the SIMTMP files (SIM for simulation and TMP for temporary) which will later be converted to SIMRES files. These procedures are:

- SIMDEB : initialization of the package;
- SIMAXE : definition of the axes;
- SIMECH : definition of the sampling functions;
- SIMFCT : definition of the functions;
- SIMSEL : definition of the selectors;
- SIMVAL : writing of the values;
- SIMAVC : positioning of the selectors;
- SIMFIN : end of processing.

Figure 4.4 is a diagram showing the sequence of the package procedure calls and the uses of the special parameters, that is: those which identify the axes, the sampling functions, the results functions and those which build the dependencies between the sampling functions and the axes, between the results functions and the sampling functions. All this is explained more fully in the following paragraphs.

The SIMDEB procedure initializes the writing process of a SIMTMP file and records the identification and the main characteristics of the simulation. The parameters of the procedure are the following:

- ULSIM : unit number of E/S associated to the SIMTMP file;
- ULPRNT: unit number of E/S associated to the print file;
- IORI : name of the program creating the SIMTMP file;
- IVER : program version;
- NOSIM : simulation number;
- NBAXE : axes number;
- NBECH : number of the sampling functions;
- NBFCT : number of results functions.

Figure 4.5 shows an example of a program when 3 functions in a 2 dimension space is assessed. For this example, the call corresponding to SIMDEB would be the following:

```
CALL SIMDEB (1,6, 'SIMUL', '1.0', 1, 2, 2, 3)
```

The SIMAXE procedure is used to declare each of the axes defining the simulation space. The order in which the axes are declared determines the order in which the SIMVAL procedure will receive the values of the functions. The procedure receives in parameter the following information:

- IDAXE : the axis identifier;

- NPTAXE: the number of points of the axis;

- UNITAX: the MKSA units used for the graduation of the axis (meters, seconds, ...);

- EXPUNT: the exponent affecting the units, for instance: if UNITAX = 'seconds' and EXPUNT = -6, we have microseconds;

- FACUNT: the multiplying factor affecting the units.

The received information is recorded in the SIMTMP files. In exchange, the procedure initializes the NUMAXE parameter (number of the axis) which identifies the axis in the SIMRES and DEPAXE (axis dependency) package which will mark the dependency of a sampling function with regards to an axis. It is important to note here that the value given to the DEPAXE parameter is in the power of two, thus the dependencies can be combined by addition. For example, the calls for SIMAXE will be the following:

```
SIMAXE ('x', 7, 'METERS', -2, 1.0, NUMAXX, DEPAXX)

SIMAXE ('y', 8, 'METERS', -2, 1.0, NUMAXY, DEPAXY)
```

The SIMECH declares to the SIMRES package the sampling function. The procedure receives in parameter:

- IDFECH : the identifier of the sampling function;

- NUMAXE : the number of the axis to which the function applies;

- DEPAXS : dependency in term of the axes of the sampling function, DEPAXS = $\sum_{k \in \{i\}}$ DEPAXE$_k$
  where k corresponds to the axes of which depends the function and {i} is the body of available dependencies for the axes.

In exchange, the procedure initializes the NUMFEC parameter (number of the sampling function) which identifies the sampling function when recording its values and the DEPFEC parameter (dependency of the sampling function) which will be used to mark the dependency of a results function as to a sampling function. In the example, the calls to SIMECH would be:

```
SIMECH ('XFC', NUMAXX, DEPAXX + DEPAXY, NUMFCX, DEPFCX)

SIMECH ('YFC', NUMAXY, DEPAXY, NUMFCY, DEPFCY)
```

The SIMFCT procedure defines a results function (as opposed to a sampling function). The procedure receives in parameter the identifier of the function (IDFCT) and its dependency in term of sampling functions (sum of the value type DEPFEC fedback by SIMECH). The NUMFCT parameter returns the number of the function: it is the number that must be used in the calls to SIMVAL to identify the values of a function. Thus, in the example used here, the three functions would be defined as follows:

```
SIMFCT ('ENER', DEPFCX + DEPFCY, NUMFEN)

SIMFCT ('PEAKX', DEPFCY, NUMFPX)

SIMFCT ('PEAKY', DEPFCX, NUMFPY)
```

The procedure SIMSEL changes the value of lack of selectors of an axis for one or several functions. By their absence, all the points of an axis are selected. The parameters of the SIMSEL procedure are the following (there is no exit parameters):

- TABFCT : vector containing the numbers of the functions;

- DIMTAB : give the number of elements in TABFCT;

- NUMAXE : number of the axis for which the selectors are to be changed;

- DEBSEL : number of the first selected point;

- INCSEL : increment for the selected points.

It must be noted that changing the selectors of an axis affects only those functions whose numbers have been received by SIMSEL. Thus, in our example, the following call:

```
SIMSEL (NUMFEN, 1, NUMAXY, 1, 2)
```

implies that the values of function ENER will be kept only for 1 of 2 points of the Y axis, but this does not touch the PEAKX function which also depends on the Y axis.

The SIMPAR procedure allows the addition to the SIMTMP file of the simulation parameters; in that way, the data needed to identify the simulation always comes with the results. The procedure receives the following information:

NAME : parameter identifier;

TYPE : complete code giving the type of the parameter (0 for complete, 1 for real, ...);

VALUE : list of values of the parameter (vectorial parameters are allowed);

NBELEM : number of elements in VALUE array.

Thus, in our example, there will be the two following calls:

```
SIMPAR ('PHI', 1, 20.0, 1)

SIMPAR ('THETA', 1, 45.0, 1)
```

The SIMVAL procedure writes the values of the sampling functions or results functions. The SIMRES package awaits the values of the functions in an order which is induced by the axes declaration, the last declared axis varies first. As there is no order among the functions, and as each function can evolve at its own rythm, it is expected that the values of a same function are dispersed in the SIMTMP file. It is thus necessary that the SIMVAL procedure precedes each block of values by a label identifying the function and the length of the block. It is also the SIMVAL procedure which controls the application of the selectors (thus it may happen that SIMVAL is called and that nothing is written on the SIMTMP file). The parameters of the procedure are the following ones:

- NOFCT : number of the sampling or result function;

- TABVAL: list of values;

- NBVAL : number of values in TABVAL.

Figure 4.6 gives a valid scenario for one example showing the use of the SIMVAL procedure.

The SIMAVC procedure was conceived to make pre-positioning and in that way contravene the order imposed by the writing of the values of the functions. The procedure changes the context of the required functions by replacing the numbers of the last points of the axes that have been recorded by numbers entered in parameters. This "skip" is noted in the SIMTMP file by a special label. Thus this procedure avoids loading the SIMTMP file with unusable values where it is impossible to correctly assess one or several functions. The parameters of this procedure are as follows:

- TABFCT : list of functions numbers for which the context is to be changed;

- NBFCT : number of functions;

- TABIND : list of the numbers of the points on the axes for each declared axis;

- NBIND : number of values in TABIND.

The SIMFIN procedure, which has no parameter, must be called on to terminate the generation of the SIMTMP file. This procedure adds an end of file mark to the SIMTMP file.

4.1.3 CONVERSION OF SIMTMP TO SIMRES

The SIMTMP file is a sequential file in which the position of the values associated to the different functions depends on the order in which they are written. The dispersion of the information in the SIMTMP file makes the search for the values of a function quite long and complex. The SIMNET program (SIM for simulation and NET for cleaning) has thus been created to convert a SIMTMP file to a direct access file in which the values of a same function will be in consecutive locations. This new file format is the SIMRES format.

Figure 4.7 shows the functioning of the SIMNET program. It is possible to create a file where the values of each function are pooled because the SIMRES program knows the number of values of each function and can thus assess the locations where the writing is to be made. For this, a memory zone is divided in as many buffers as there are functions on the SIMTMP file. The size of each buffer is determined in such a way as to minimize the number access to the disk. The program reads the SIMTMP file sequentially, pools the "bits" of functions in the appropriate buffer and, when the buffer is full, it is written at its place in the SIMRES file.

The size of the memory zone required for proper functioning has made it necessary to opt for a special conversion program rather than directly writing the results in the SIMRES format. It has thus been deemed preferable to have a program using a large working area during a short time spread, rather than adding this time to simulation programs already quite loaded and using already too much time.

4.2 THE XTRACT PACKAGE

The XTRACT package allows the extraction of information from the SIMRES file. The package procedure can be divided into three sub-groups. The first sub-group includes the EXTDEB procedure which initializes the XTRACT package. The second includes the procedures which extract the descriptive information, that is the information written by the SIMAXE, SIMECH, SIMFCT and SIMPAR procedures. These are procedures that work more or less alone. Finally, the procedures of the last sub-group extracts the values of the function of a SIMRES file, that is the information written by the SIMVAL procedure. These procedures are interdependent and they follow a rigorous sequence.

4.2.1 THE EXTDEB PROCEDURE

The EXTDEB procedure initializes the package and opens the SIMRES file on which the other procedures will work. It is thus essential to call the EXTDEB procedure before trying to extract any information from the SIMRES file. The procedure gets as parameter the name of the SIMRES file and the number of logical unit of E/S associated to the printing file. In exchange, the procedure gives the following information: the name of the program generating the SIMRES file, the version number of this program, the sequential number of the file and the computer on which this file has been generated.

4.2.2 PROCEDURE OF EXTRACTION OF THE DESCRIPTIVE INFORMATION

This sub-group is composed of the following procedures:

- EXTTIM : gives the date and the hour of the generation of the SIMRES file;
- EXTNOM : gives the axes identifiers, the sampling functions, the result functions or of the parameters;
- EXTAXE : gives the characteristics of an axis;
- EXTECH : gives the characteristics of a sampling function;
- EXTFCT : gives the characteristics of a results function;
- EXTPAR : gives the characteristics of a parameter.

It is important to note here the particular role played by the EXTNOM procedure, which provides the identifiers of different objects (axes, functions, parameters). The characteristics of those objects could be later called up by the appropriate procedure.

The running of each procedure is relatively easy. The input parameters identify the needed information. This information is extracted from the SIMRES file and returned to the caller through the output parameters. Figure 4.8 gives a list of the parameters of each of procedures of this sub-group.

4.2.3 PROCEDURE FOR THE EXTRACTION OF THE RESULTS FUNCTIONS

The procedures which extract the values not only locate and retrieve the information on the SIMRES file but they also have a mechanism which splits the data to be extracted in sub-groups or pages. At this point, the extraction loop allows the routine to receive data page by page. This mechanism has three steps.

The first step consists in establishing the field of extraction, i.e. the set of evaluation points for which a value of a given function is needed. This specification is done by indicating the name of the function and by giving, for each of the axes on which the function depends, a list of selection intervals. Each selection interval is defined by the number of the first and the last point of the interval and by an increment. The special value, in this case 0, allows us to choose all the points of an axis. For instance, for function A which depends on axis X, we can choose the points 1 to 20 by sets of 5 and the points 22 to 30 by sets of 2. The order of the presentation of the axes is important because it induces the nesting order of the extraction loops. Moreover, the choice of the selection intervals must take into account the points for which the requested function has been assessed and written in the SIMRES files.

The second step establishes the segmentation of the extraction field and the specification of the tuples configuration needed. The segmentation of the extraction field is done

by giving the number of axes that must vary to form a page. These varying axes are always the last to be declared, and they are called the internal axes. It is thus the external axes, those left aside, which will define the loops extracting the different pages. Figure 4.9 gives an example showing the extraction field and the segmentation of a function.

The information fedback by an "elementary" extraction has a list of tuples of the form (<value of the results function>, <value of the sampling function 1>, ..., <value of the sampling function M>) and a list giving, for each non-identified axis in the tuple, the value of the point where the extraction has taken place. In the case of orthogonal grids, the tuples must be composed of the value of the function followed by the value of the internal axes points. The list of the axes points should give the value of the external axes points. Thus the varying data is separated from the fixed data, this avoids redundancies. However, this is not always the case. In fact, when the grids are not orthogonal, it is possible that even the internal axes may have different points for each of the values of the results function. In order to hold the possible different cases and to permit a maximum of flexibility, the XTRACT package works either by the explicit specification of the composition of a tuple or by a specification by default where all happens as if in an orthogonal grid. The explicit specification of a tuple is done by giving a list of the axes for which we need the values of the point in the tuple. In this case, the identification of the points of the other axes is done when possible in the list of the axes points (i.e. as this list gives only one point per axis, if 1 axis varies, the value is indicated as 1E300). Figure 4.10 shows the example of figure 4.9 and the organization of the tuples and the list of axes points.

The third and last step consists in calling the extraction procedure as many times as needed by the segmentation. The role of the package here is to control the evolution of the loops dealing with the external axes, to retrieve the data making up a page on the SIMRES file and to organize the tuples and the list of axes points according to the required configuration.

One option of the XTRACT package gives as an added information the minimums and the maximums of the functions and axes making up a tuple.

Indispensable for graphic applications, this piece of information can easily be obtained if the minimums and maximums can be assessed on one page. But this is not always the case. There may be a need for the minimums and maximums for a larger set of values: for example, for the field of extraction or even for all the SIMRES file. In these cases, the application program must make a special extraction run to assess the minimums and maximums. This task has therefore been given to the XTRACT package which will do it in the most efficient way.

In terms of application, by obtaining the minimums and maximums, it is possible to establish a scale to express the values obtained in the tuples. The XTRACT package can assess the minimums and maximums on three specific fields defining three types of scales: the global scale, the local scale and the standard scale. The global scale is defined by all the values whether selected or not from an axis or a function. The local scale is defined by the values of an extraction page. And finally, the standard scale is defined by the field of extraction either by taking the whole field or by taking a sub-set of this field. In this latter case, the sub-set is delimited by an axis, and each time the counter of the axis is incremented (i.e. there is a change of point), the minimums and maximums of the points covered by the interior axes must be reassessed. Figure 4.11 gives an example of the different scales.

The EXTRAC, EXTSEL, EXTDEF and EXTTUP procedures show how the work described above can be processed.

The extraction process starts with the EXTRAC procedure. This procedure specifies the function from which we would like to extract the values. It gets in parameter the identifier of the function. It outputs NBAXES a complete parameter giving the number of axes on which depends the function and IERR indicating, and if it exists, the number of the detected error.

Second, the EXTSEL defines the field of extraction. A call on the EXTSEL procedure indicates for an axis on which the function depends, the number of the points for which we need the values of the function. This procedure must be called NBAXES times and the order in which the axes are presented is important for the definition of the extraction loops. The procedure receives the following parameters:

- NAME : the axis identifier;
- SELAXE : list of selection intervals, one selection interval is made up of either 3 values (the first selected point, the last selected point and an increment) or the value 0 (all points are selected);
- NBSEL : gives the number of intervals in SELAXE.

The procedure outputs the following data:

- NPTSEL : indicates the total number of points chosen on the axis;

- FIXE : the boolean value which is realized if the value of the points on the axis does not depend on other axes, i.e. if the grid is orthogonal in relation to that axis;

- IERR : in case of error, writes the number of the error.

Third, comes the EXTDEF procedure which defines the configuration of a page, the composition of a tuple and the type of scale needed. The procedure receives the following data:

- NBDIM : defines the cut by giving the number of axes that must be made to vary to obtain a tuple page (the innermost axes vary first);

- TABAXE : explicitly specifies the contents of a tuple by giving the list of axes which make up the tuple. This chart is only used if NBAXE > 0;

- NBAXE : if this parameter is less than 0, then the option by default is applied and the tuples are made up of the value of the function followed by the deepest NBDIM axes. If not, then the tuples are made up of the value of the function and of the NBAXES axes declared in TABAXE;

- TYSECH : is a chain of characters which gives the type of the requested scale. The possible values are: none, global, local, standard;

- AXEECH : specifies, in the standard scale case, an axis which limits the scope of the scale: i.e., the field of the standard scale is then defined only on the axes deeper than that axis.

The procedure outputs NBEXT the number of pages necessary to cover all the field of extraction and IERR indicating if an error has been detected.

Finally, it is the EXTTUP which carries out the extraction of the information and the computations of the scales. Usually, this procedure should be called up NBEXT times so that all the field of extraction is covered. The parameters of this procedure are the following:

- TABVAL : the array containing the tuples. For a given extraction, the structure of the array is TABVAL (DIMTUP, NPT_1, ..., NPT_M) where DIMTUP is the number of the value making up the tuple, NPT_1 the number of points selected on the deepest axis, ..., NPT_M the number of points selected on the least deep axis making the page;

- DIMTAB : input parameter giving the total dimension in number of TABVAL words;

- TABIND : gives the numbers which identify the non-varying axes;

- TABVAX : gives the value of the points on the non-varying axes;

- DIMIND : input parameter giving the dimension of the TABIND and TABVAX arrays;

- TABECH : array giving the minimums and maximums for the function and the axes making up the tuple;

- DIMECH : input parameter giving the number of TABECH columns (there is always 2 lines, one for the minimum and one for the maximum);

- IERR : indicates the presence of an error.

Figure 4.12 shows the call sequence of the EXTRAC, EXTSEL, EXTDEF and EXTTUP procedures. As can be seen, it is possible to define the cut of a field of extraction, the configuration of the tuples and the type of required scale and then to restart the extraction of the values.

4.3 THE DATSIM PACKAGE

When a group of entities (or objects) have the same information fields, the DATSIM package stores these fields, or a sub-set of these fields, in a same direct access file thus creating a kind of data bank. In this data bank, the model, that is: the necessary information needed to operate the file, specifically the description of the fields of information, is kept in the file heading. The recording of the data bank is made up of the information field of one entity. By giving a sequence number to the different entities and an identifier to the different information fields, it is possible to construct keys which will identify in a unique manner the different recordings.

In the DATSIM file, an entity can then have as many recording as there are information fields. When applicable however, the DATSIM package avoids an excessive proliferation of recordings by defining a value by default for an information field. At this moment, all the active entities (an entity may be non-active) of the data bank must have the same information fields. If the recording of an active entity does not show up in the data bank, then it has a value by default.

In the context of the laser modeling project, the DATSIM package keeps on disk a summary of the SIMRES files. It is thus possible to concentrate in one file, information which would have been otherwise dispersed in several files and only a small part of this information would have fit on disk (the major part of the SIMRES files would be filed away on magnetic tape).

The summaries of the SIMRES files produced by a laser simulation program are regrouped in a same DATSIM data bank. A simulation is an entity at the level of the data bank, and the simulation sequence number (which is also the SIMRES file number) identifies the recordings belonging to a same simulation. The information fields written in the DATSIM files are: some general information on the simulation, the parameters of the simulation and the values of the results functions usually implicated in a comparison.

The components of the DATSIM package can be divided into two sub-groups. The first is made up of programs which generate and modify a heading of a DATSIM file. The second sub-group is made up of the procedures that allow the running in reading and writing mode of a DATSIM file.

4.3.1 GENERATION AND MODIFICATION OF A DATSIM FILE

The generation phase of a DATSIM file is done in two steps. First, the generated file holds in its heading only the data needed for an empty DATSIM file. Next, the description of the data that can be recorded in the file is added to the heading. It is preferable to write from the beginning the description of all the information fields, however it is also possible to make additions to an already operational DATSIM file, that is: a file which contains other data than the descriptive ones.

The DATCRE generates the base of a DATSIM file. This program reads in the input file the generic name of the entities composing the data bank, namely the name of the simulation program producing the SIMRES files which feed the data bank. The base of a DATSIM file includes the identifier of the current version of the DATSIM package, the generic name of the entities, the sequence number of the last entity for which data has been recorded, that is 0, and the number of information fields described in the heading, which is also 0.

The DATEDI program adds to a DATSIM file heading the description of the information fields that can be recorded in the files. The input file of the DATEDI program include, in first line, the command ADD or MODIFY. This command indicates to the DATEDI program whether it is a first addition to the heading (command ADD) or of a subsequent addition (command MODIFY). The description of the different information fields is found later in free form in the input file. This description includes the field identifier, the field class, the type of values of the field (complete, real, boolean, chain of characters), the number of values by default that follow (possibly 0), and finally the list of values by default (possibly empty). The information field class is an identifier known by DATSIM (through an interchangeable table) which allows the pooling and the organization of the information.

For security reasons, the DATEDI program procedes by two runs. In the first run, the data is validated. If no error is detected, then the program runs the data one more time and writes the data in the heading of the DATSIM file. This way, it is possible to avoid situations where an error invalidates work already done. Figure 4.13 gives an example of data for the DATEDI program. It is to be noted that the number of values by default in no way fixes the number of the values associated to a field: the same field could include a varying number of information from one entity to another.

4.3.2 OPERATION OF A DATSIM FILE

The procedures that run a DATSIM file are:

- DATDEB : starting of a DATSIM file;
- DATNOM : returns the list of indentifier of the information fields;
- DATINF : returns the characteristics of an information field;
- DATLIR : reading of a recording;
- DATECR : writing of a recording;
- DATACT : activation or non-activation of an entity;

- DATFIN : closing of a DATSIM file.

The information and the space necessary for the manipulation of a DATSIM file are concentrated in a control block entered as a parameter at the different procedures of the package. This way, an application program can work on several DATSIM files at the same time on the condition of having a control block for each file.

Following is an overview of the operation of each of the package procedures.

The DATDEB procedure is called upon to start a DATSIM file and to initialize the control block associated to this file. Any attempt to work with a DATSIM file without starting first with DATDEB will be an error. The procedure will then receive as parameter the name of DATSIM file to be started, the control block, and the size in number of words of the control block (the suggested size is 2500 words). The procedure returns part of the information composing the base of the heading, in other words, the generic name of the entities making up the file, the sequence number of the last recorded entity and the number of fields described in the heading.

The DATNOM procedure obtains the list of the information fields identifiers. This list is taken from the DATSIM file heading. The parameters of the procedure follow:

- DATBLK (input) : control block of the DATSIM file;
- TABNOM (output): chart containing the information fields identifiers;
- DIMTAB (input) : size of TABNOM;
- NBNOMS (output): number of identifiers placed in TABNOM.

The DATINF procedure obtains the characteristics of an information field. The parameters of this procedure are:

- DATBLK (input) : control block of the DATSIM file;
- NOM (input) : identifier of field of which we need the characteristics;
- CLASSE (output): class of information;
- TYPE (output) : type of value of the information field;
- TABDEF (output): chart giving the values by default (if there are no values by default for the field, the chart will be empty);
- DIMTAB (input) : size of TABDEF;
- LGDEF (output) : number of elements placed in TABDEF;
- IERR (output) : gives 0 if there are no errors, if not, it gives the number of the error.

The DATLIR procedure reads the recording of a DATSIM file, that is, it gives access to the values contained in the information field of a given entity. If the entity exists (i.e. if its sequence number is smaller than the number of the last recorded entity in the file) and if it is active, the procedure assembles the key (entity number and field identifier) and orders the reading of the recording. If the recording exists, then all it does is to transfer it to the caller. If not, then the procedure verifies if there is a value by default for the field, and if it faids one, it returns it. In case the data required does not exist at all, an error number is returned to the application program. Figure 4.14 shows schematically the running just described. The parameters are as follows:

- DATBLK (input) : control block of the DATSIM file;
- NUMSIM (input) : entity number (in this case, it is a simulation number);
- NOM (input) : field of information identifier;
- TABVAL (output): field of information values;
- DIMTAB (input) : size of TABVAL;
- DIMVAL (output): number of values read and returned in TABVAL;
- IERR (output) : gives 0 if there is no error. If not, it gives the error number.

The DATECR procedure can add a recording to a DATSIM file. First, the procedure verifies if the entity at hand is new, in this case it must update the number of the last recorded entity in the file. If it is an already recorded entity, it must see if it is active, as there should be no access to the information field of a non-active entity. If all works well until this step, then the procedure checks to see if there is no values by default for the requested field. If none exists, then the recording is written in (in some cases, it will be a rewriting). If however there is a value by default, then there must be a comparison between the values by default and those received for the field. If they are equal, nothing is written in the file, and the previous recording is deleted. If they are not equal, then the recording is written into the file or the previous recording is replaced by the new one. Figure 4.15 shows schematically how this is done. The different parameters of the procedure are as follows:

- DATBLK (input) : control block of the DATSIM file;
- NUMSIM (input) : entity number for which an information field is to be written;
- NOM (input) : information field identifier;
- VALEUR (input) : chart containing the field values;
- DIMVAL (input) : number of values in the VALEUR chart;
- IERR (output) : gives 0 if there are no errors, if not, gives the number of the error.

The DATACT procedure specifies the state of an entity in the DATSIM file, in other words, an entity can be active or non-active. The recordings of a non-active entity cannot be retreived but they are not destroyed. Thus by reactivating a non-active entity, we can have access to its recordings. The parameters of this procedure are as follows:

- DATBLK (input) : control block of the DATSIM file;
- NUMSIM (input) : number of the entity that has to be modified;
- ACTIF (input) : boolean parameter with its true values if the entity is active, and its false value if it is non-active.
- IERR (output) : gives 0 if there are no errors, if not, gives the number of the error.

Finally, the DATFIN procedure terminates the operation of the DATSIM file. It is imperative to call the DATFIN procedure because the buffer associated to the DATSIM file must be cleared. The only parameter of this procedure is DATBLK, the control block of the DATSIM file that is to be closed.

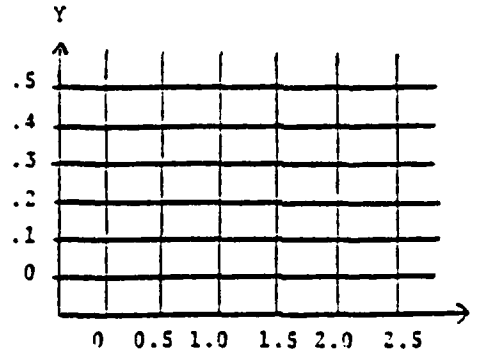

Information to describe the grid

AX	Number of points	Starting point	Increment
X	6	0.0	0.5
Y	6	0.0	0.1

FIGURE 4.1 - LINEAR ORTHOGONAL GRID

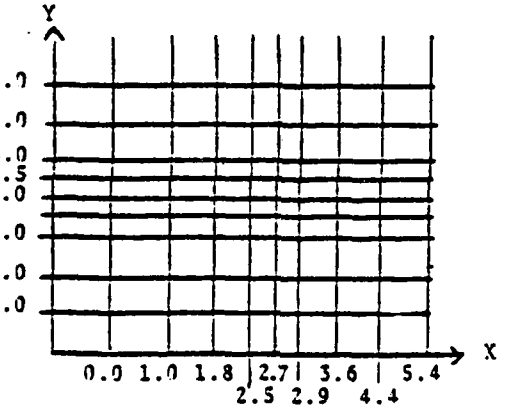

Information to describe the grid

Axis X 9 points

0.0	1.0	1.8	2.5	2.7	2.9	3.6	4.4	5.4

Axis Y 9 points

0.0	1.0	2.0	2.5	3.0	3.5	4.0	5.0	6.0

FIGURE 4.2 - NONLINEAR ORTHOGONAL GRID

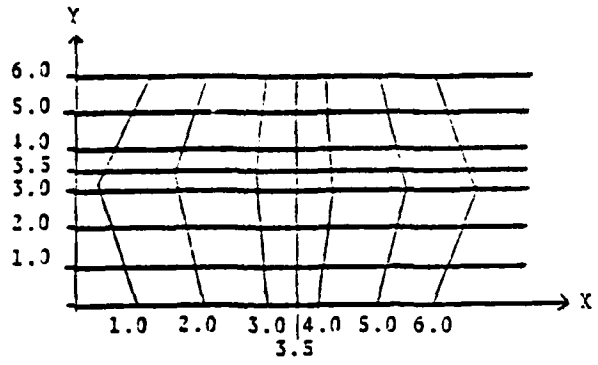

Information to write the grid

fe_y (Y) 7 points

1.0	2.0	3.0	3.5	4.0	5.0	6.0

fe_x (X, Y) 49 points

0.8	0.6	0.4	0.3	0.4	0.6	0.8
1.85	1.7	1.55	1.48	1.55	1.7	1.85
2.45	2.9	2.85	2.82	2.85	2.4	2.95
3.5	3.5	3.5	3.5	3.5	3.5	3.5
4.05	4.1	4.15	4.17	4.15	4.1	4.05
5.15	5.3	5.45	5.52	5.45	5.3	5.15
6.2	6.4	6.6	6.7	6.6	6.4	6.2

FIGURE 4.3 - NON ORTHOGONAL GRID

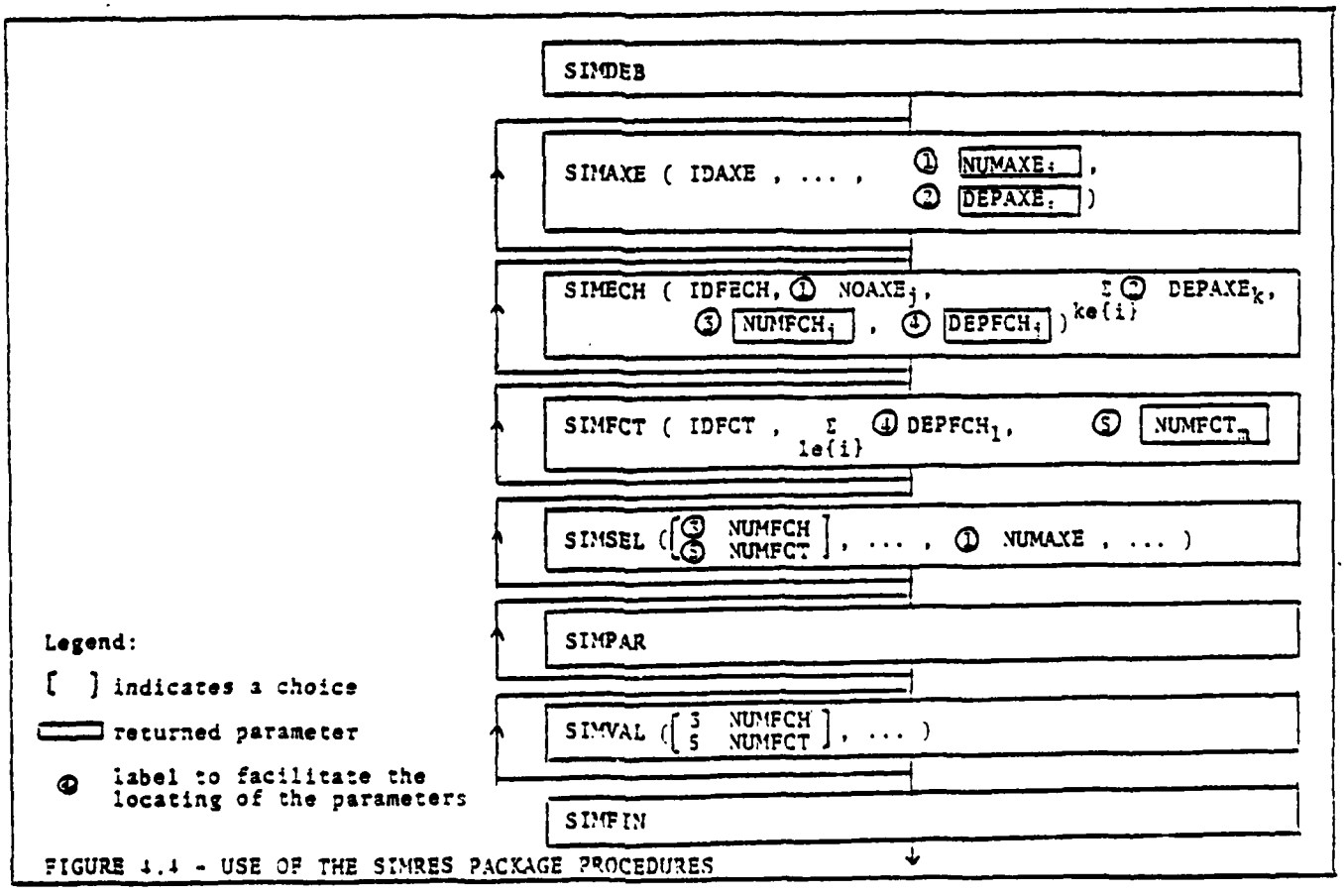

FIGURE 4.4 - USE OF THE SIMRES PACKAGE PROCEDURES

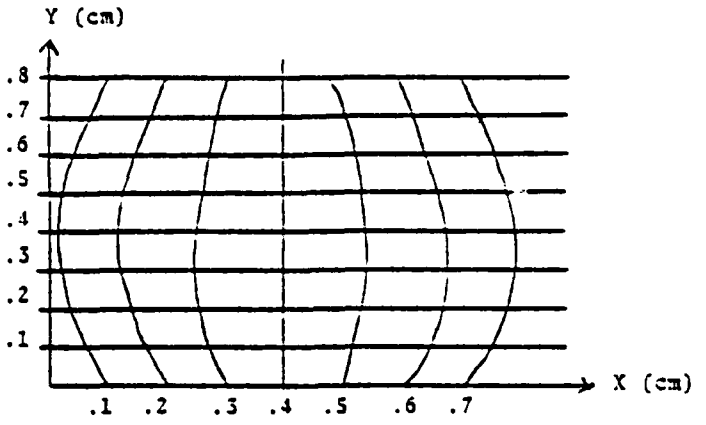

Axes	NB. Points	Units	Exp.	Factor
X	7	meters	-2	1.0
Y	8	meters	02	1.0

Sampling functions

fe_x (X, Y)
fe_y (Y)

Results functions

ENER (X, Y)	i.e.	ENER (fe_x, fe_y)
PEAKX (Y)		PEAKX (fe_y)
PEAKY (X)		PEAKY (fe_x)

Selection

axis Y one point out of 2 for ENER { parameters { PHI = 20.0 ; THETA = 45.0

FIGURE 4.5 - CONTEXT DEFINITION TO ILLUSTRATE THE USE OF SIMRES PACKAGE PROCEDURES IN A PROGRAM

```
      REAL  ENERY (8),
            PEAKX,
            PEAKY (8),
            AXEY (8),
            AXEX (7),

      :

      <Establish axis Y>
      call SIMVAL (NUMFCY, AXEY, 8)
      DO 10 IX = 1,7

      <Establish a column of axi X>
      call SIMVAL (NUMFCX, AXEX, 8)
      DO 20 IY = 1,8
      ENERY (IY) = ...

   20 continue
      call SIMVAL (NUMFEN, ENERY, 8)
      PEAKX = MAX (ENERY, 8)
      call SIMVAL (NUMFPX, PEAKX, 1)

      <asses partial PEAKY>

   10 continue
      call SIMVAL (NUMFPY, PEAKY, 1)
```

FIGURE 4.6 - USE OF SIMVAL PROCEDURE

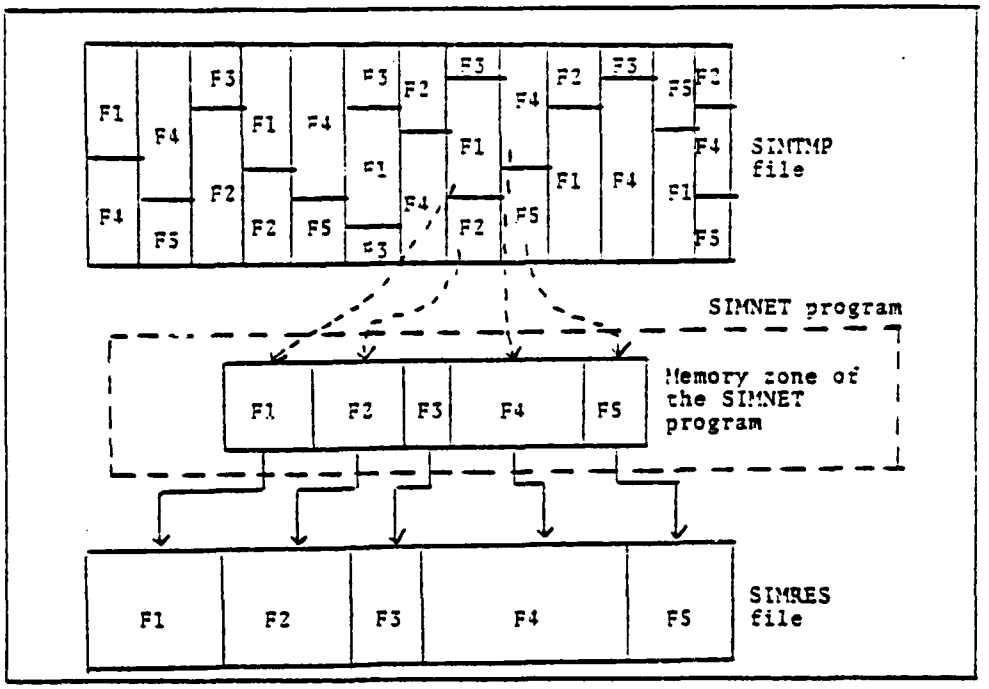

FIGURE 4.7 - CONVERSION OF A SIMTMP FILE INTO A SIMRES FILE

Procedure	Parameter	Description
EXTTIM	DATE (output)	Date of generation of the file
	HOUR (output)	Hour of generation of the file
EXTNOM	KIND (input)	Indicates which identifier is needed AXE → AXES ECH → sampling functions FCT → results functions PAR → parameters
	TABNOM (output)	List of identifiers
	DIMTAB (input)	Size of TABNOM
	NBNOMS (output)	Number of identifiers put in TABNOM
EXTAXE	NAME (input)	Axis identifier
	UNITS (output)	Type of units of the axis
	EXPO (output)	Exhibitor affecting the units
	FACT (output)	Factor affecting the units
	RESOL (output)	Number of resolution points on the axis (not to be mistaken with the number of selected points)
EXTECH	NAME (input)	Identifier of the sampling function
	AXEREP (output)	Identifier of the axis associated to the function
	AXEDEP (output)	Boolean array giving the dependencies of the function as to each of the axes (1)
	DIMDEP (input)	Dimension of AXEDEP
EXTFCT	NAME (input)	Identifier of the results functions
	ECHDEP (output)	Boolean array in which the I element indicates whether the function depends on the Ith sampling function
	AXEDEP (output)	Boolean array in which the I element indicates if the function depends on the Ith axis
	DIMDEP (input)	Dimension of ECHDEP and AXEDEP
EXPAR	NAME (input)	Identifier of the parameter
	TYPE (OUTPUT)	Code indicating the type of parameter (0: complete, 1: actual, ...)
	TABVAL (output)	Value of the parameter (can be a vector)
	DIMTAB (input)	Dimension of TABVAL
	NBVAL (output)	Number of effective value in TABVAL

(1) The order of the elements is that in which they have been declared.

FIGURE 4.8 - PARAMETERS OF THE PROCEDURES EXTRACTING DESCRIPTIVE INFORMATIONS FROM A SIMRES FILE

AD-A127 502 TRANSVERSE AND QUANTUM EFFECTS IN SUPERFLUORESCENCE; 3/3
PUMP DYNAMICS FOR TH.. (U) POLYTECHNIC INST OF NEW YORK
BROOKLYN DEPT OF MECHANICAL AND A.. F P MATTAR
UNCLASSIFIED 11 APR 83 POLY-M/AE-83-4 ARO-16800.19-PH F/G 20/6 NL

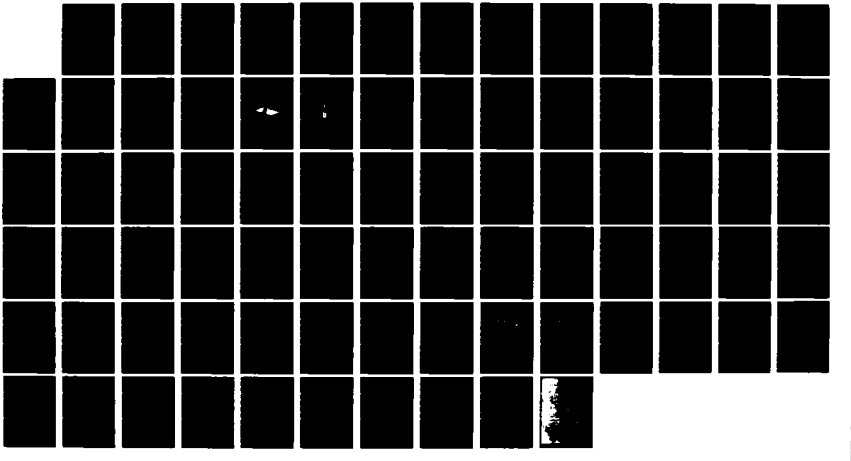

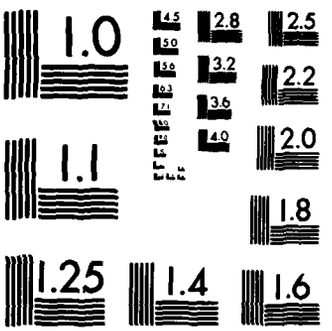

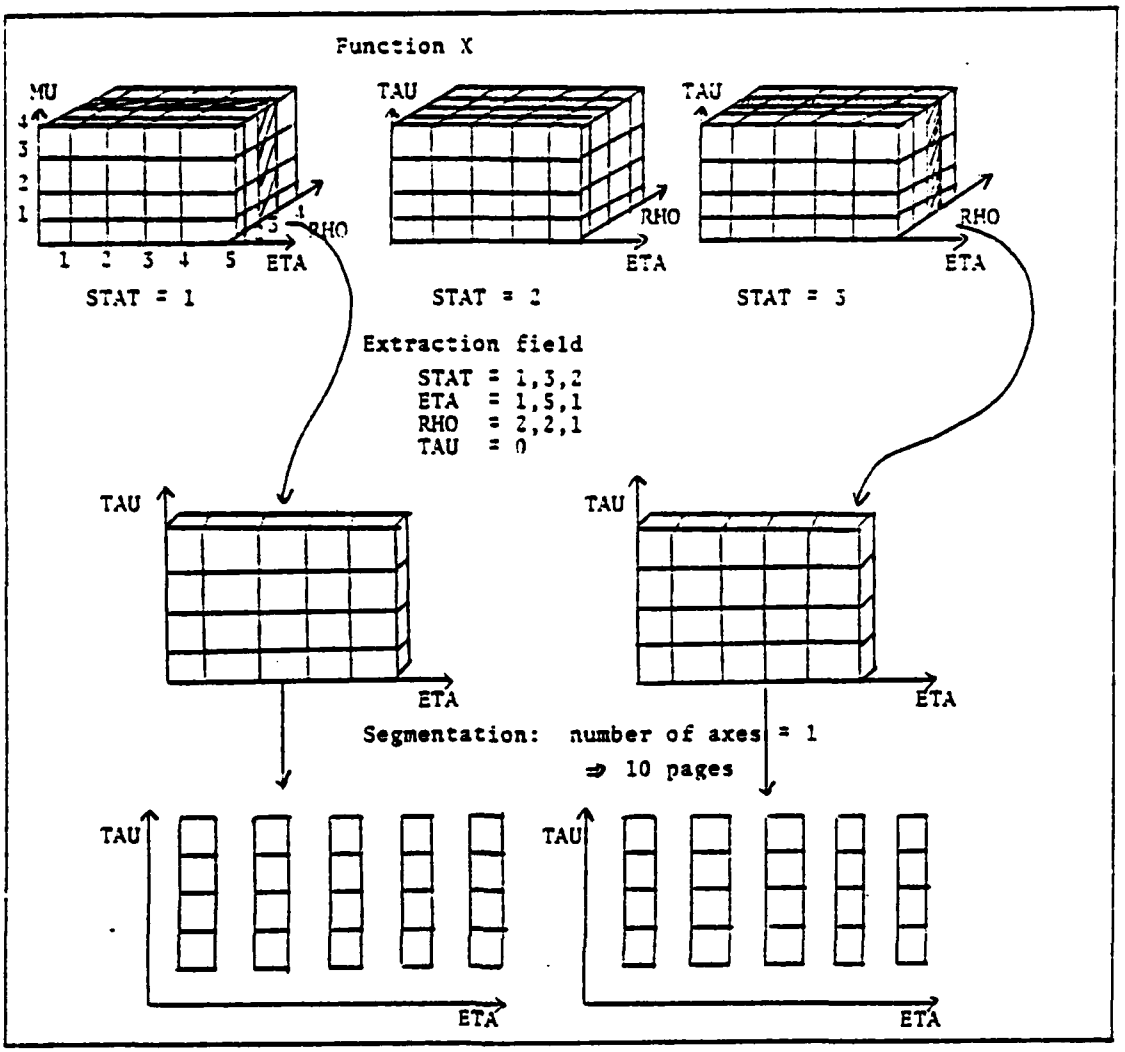

FIGURE 4.9 - EXTRACTION FIELD AND SEGMENTATION OF A FUNCTION

Function A depending on axes STAT, ETA, RHO, TAU

Extraction field: STAT = 1,3,2
ETA = 1,5,1
RHO = 2,2,1
TAU = 0

Number of axes on a page: 1

A) Option by default

Tuples

	Value A	point 1 TAU
1 page	"	" 2 "
	"	" 3 "
	"	" 4 "

List of axes points

point 1 STAT
point 1 ETA
point 2 RHO

B) Specification of Tuple = (TAU, ETA, STAT)

Tuples

Value A	Point 1 TAU	Point 1 ETA	Point 1 RHO
"	" 2	" 1	" 1
"	" 3	" 1	" 1
"	" 4	" 1	" 1

List of axes points

Point 2 RHO

FIGURE 4.10 - TUPLE COMPOSITION AND LIST OF AXES POINTS

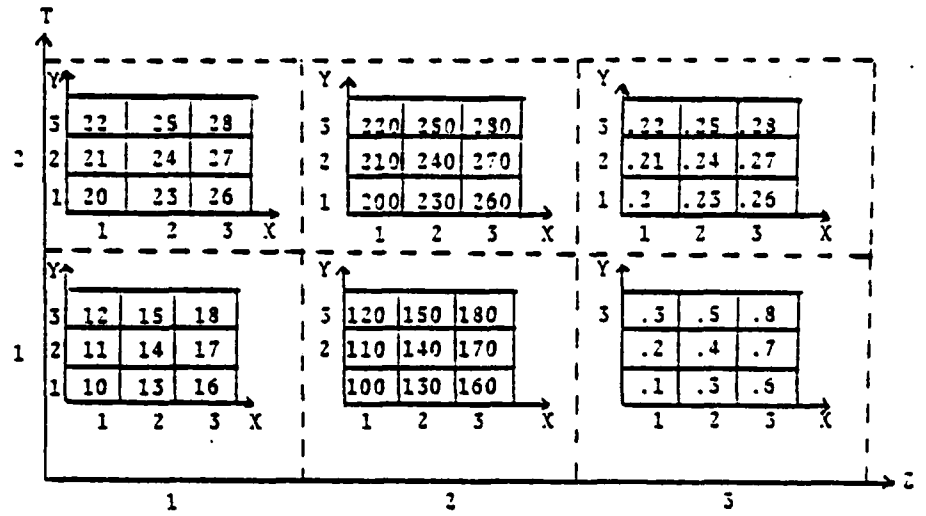

Function A depends on axes Z, T, X and Y

Field of Extraction: Z = 1,3,2
T = 0
X = 1,3,2
Y = 0

Page comprises 1 axis

Global scale

	Fct A	Y
min	.1	1
max	280	3

Local scale: will change at each page extraction

ex. page 1 Z = 1, T = 1, X = 1

	Fct A	Y
min	10	1
max	12	3

page 2 Z = 1, T = 1, X = 3

	Fct A	Y
min	16	1
max	18	3

etc. ...

Standard scale

	Fct A	Y
min	.1	1
max	22	3

Standard scale: with Z as axis implying a reevaluation of the minimums and maximums

Z = 1

	Fct A	Y
min	10	1
max	23	3

Z = 2

	Fct A	Y
min	.1	1
max	.2	3

FIGURE 4.11 - EXAMPLE SHOWING THE DIFFERENT SCALES

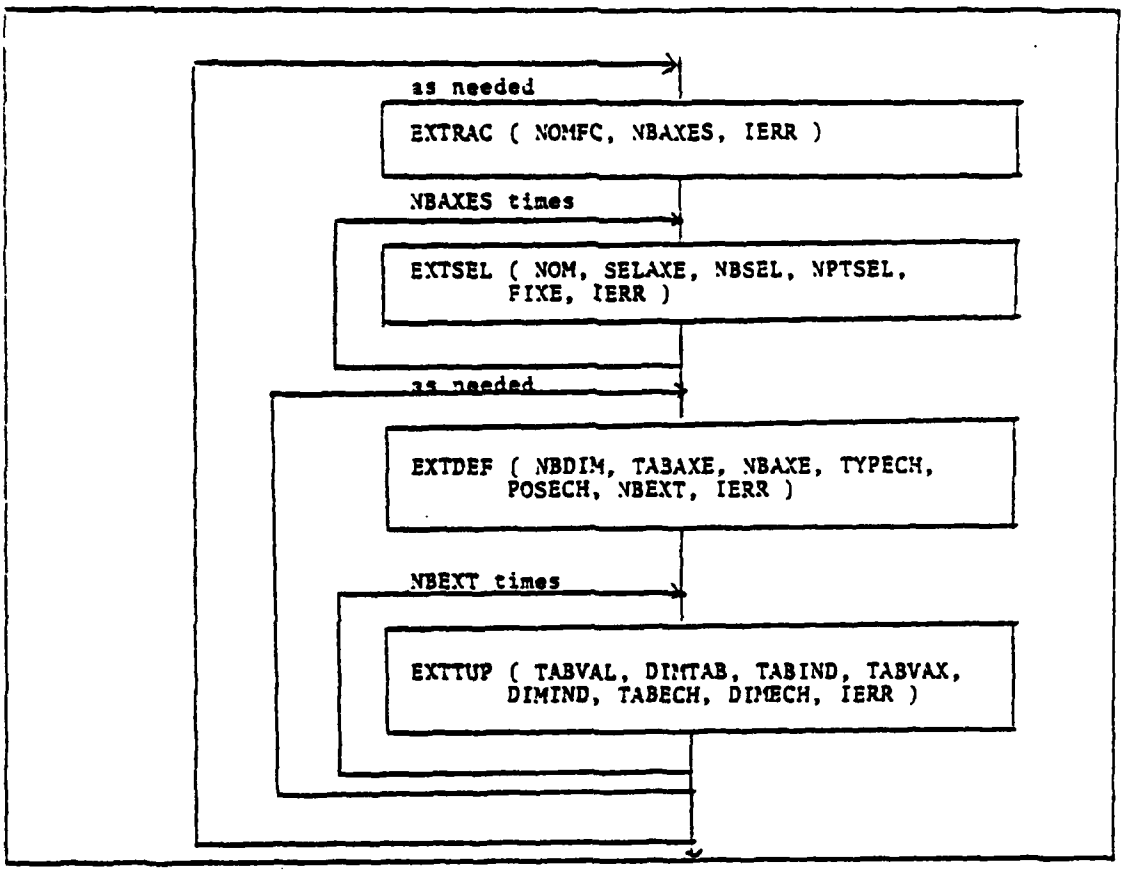

FIGURE 4.12 - CALL SEQUENCE OF THE PROCEDURES PRODUCING THE RESULTS FUNCTIONS EXTRACTION

```
ADD
NBRUNS      BASE      COMPLETE    1       1
JSAVE       BASE      COMPLETE    1       300
MSAVE       BASE      COMPLETE    1       32
KSAVE       BASE      COMPLETE    1       64
C1          BASE      REAL        1       0.08
TBRHO       BASE      REAL        1       4.236669
IGV         BASE      COMPLETE    1       1
PHI0        BASE      REAL        1       3.1417817
AKAP        PHYSIQUE  REAL        0
FSKA        PHYSIQUE  REAL        0
DATE        TEMPS     CHAIN       0
ETAPTS      AXE       REAL        5       1.0  2.0  3.0  4.0  5.0
RHOPTS      AXE       REAL        4       0.0  0.1  0.2  0.3
DUREE       SYNTH     REAL        0
ENER        SYNTH     REAL        0
```

FIGURE 4.13 - EXAMPLE OF DATA FOR A DATEDI PROGRAM

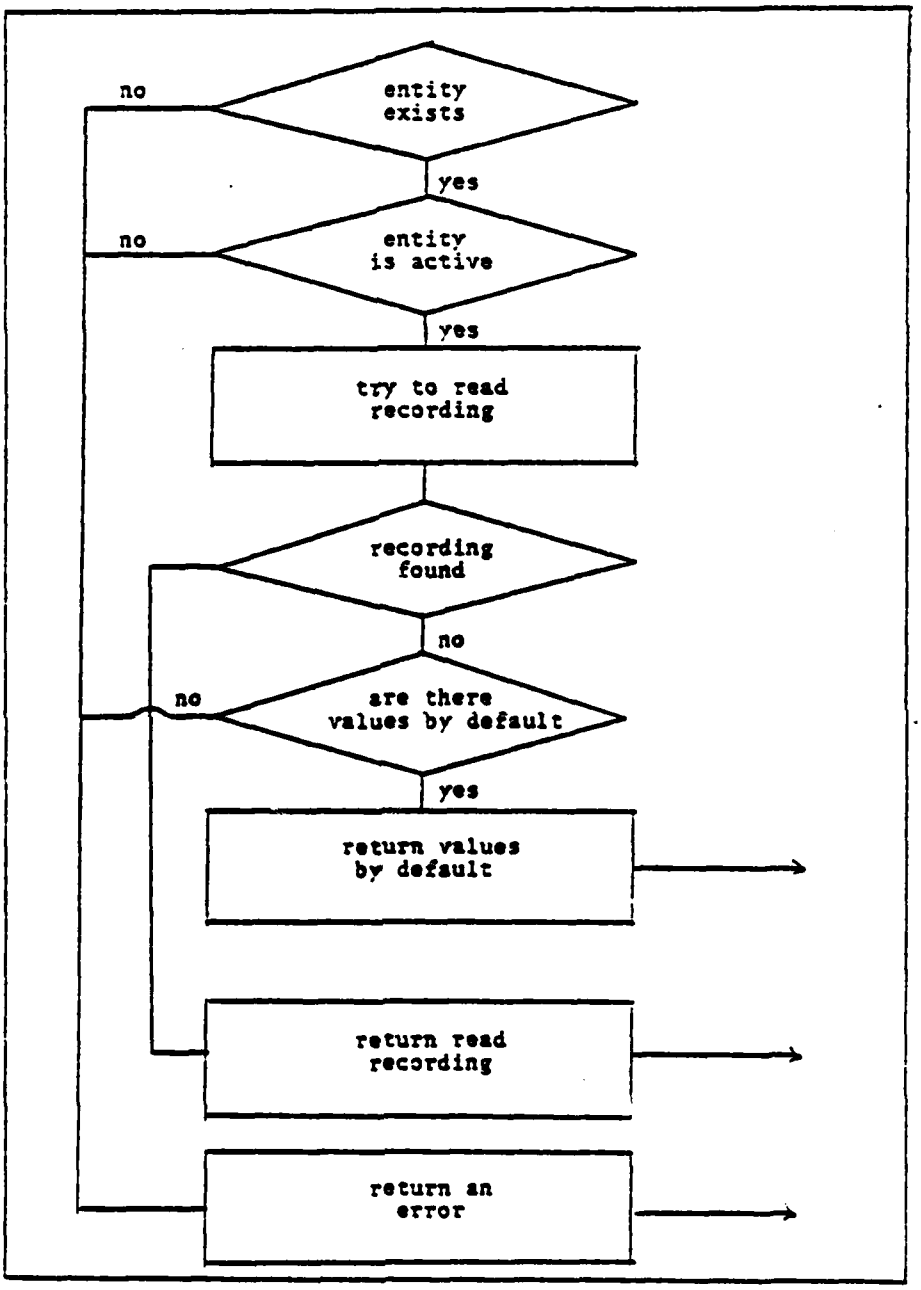

FIGURE 4.14 - RUNNING OF THE DATLIR PROCEDURE

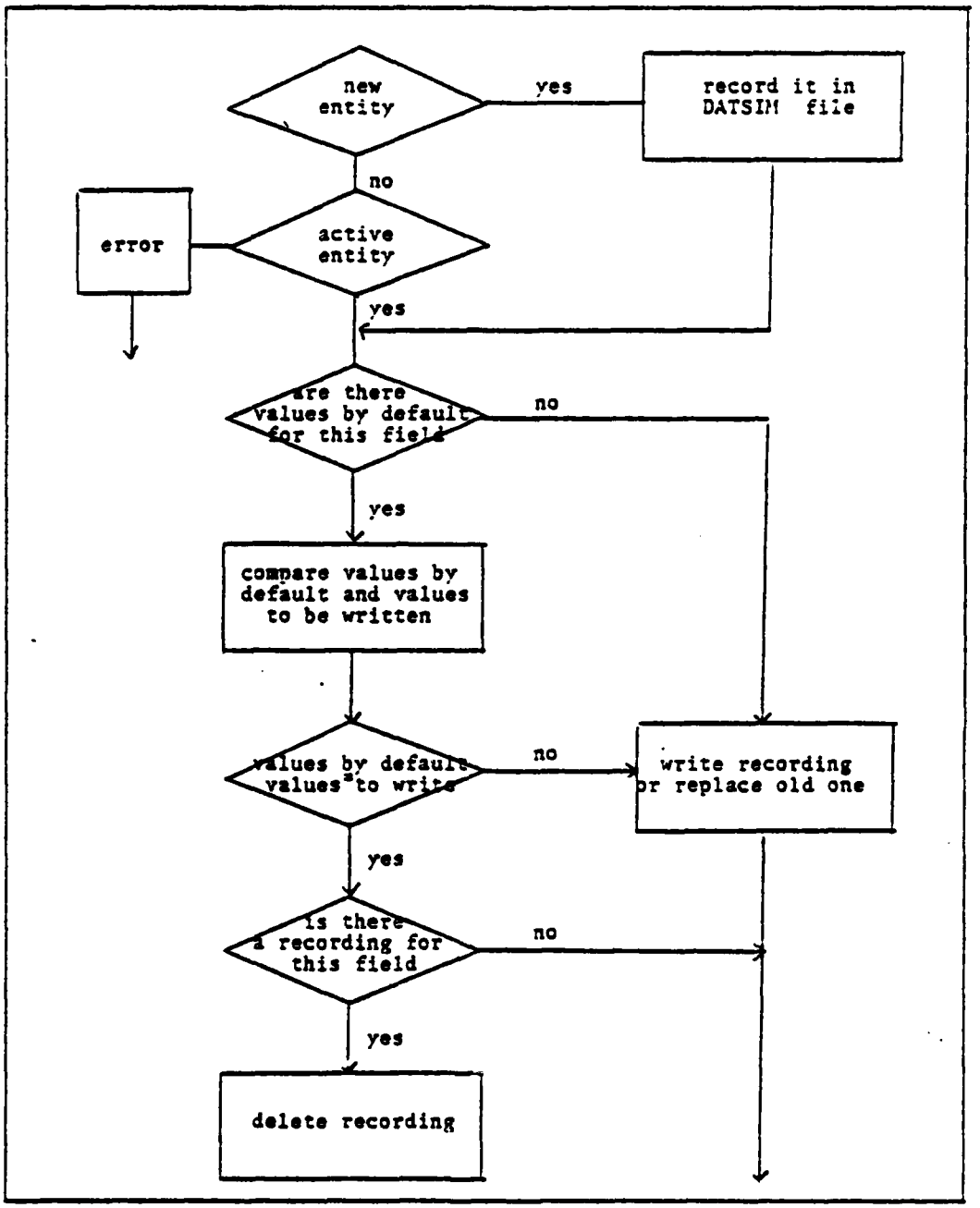

FIGURE 4.15 - RUNNING OF DATECR PROCEDURE

V - APPLICATION PROGRAMS

This section deals with the programs in the system that go beyond the frame of application in the laser model building project. These are the DEFPARM, DESRES and SYNTH programs created to treat in a general way a specific application. These also use the SIMRES, XTRACT and DATSIM software. All the examples in this chapter derive from the only source we have: the laser model building project.

5.1 THE DEFPARM PROGRAM

The DEFPARM program is an interactive tool which defines the FORTRAN NAMELISTs. A program generation of the NAMELISTs is a good way to validate them (syntactically) and to avoid certain trivial errors. DEFPARM is a program of general application but by referring to the laser modelbuilding project to describe its operation, the explanations will be more concrete.

In the DEFPARM program, the NAMELISTs are defined by statements that follow a specific syntax. A set of statements establishes the parameters of a group of simulations dealing with a particular phenomenon. These simulations differ only by the value of a limited number of parameters, all the other parameters being fixed. It is because of these fixed parameters that the information can be condensed and the syntax made more concise.

A statement specifies the value or values associated to a block of parameters. A block of parameters is made of one parameter or a group of interdependent parameters (varying conjointly). For example, A = 0 shows that a parameter has a given value. If the parameter is to be given several values or that there be a simulation for each of these values, the values are separated by a comma, A = 0,1,2. To specify that a group of parameters are interdependent, forming one whole, parenthesis are used. The values associated to the parameters are also put between parenthesis. The order of the elements in such a group is of major importance, and the order of the parameters induces the order of the values. Moreover, there must be as many values in each group of values as there are parameters in the reference group. Thus the following group of parameters can be defined as: (A,B) = (0,1), (1,1).

Vectorial parameters are put between brackets and the different values are separated by a comma: thus A = [0,1,2] or B = [1]. The specific values of the parameters need not have the same number of elements; thus: A = [1,2], [1,2,3], [1,2,3,4]. But the order of the values is important as it corresponds to the order of the elements in the vector.

The statements are separated by semi-colons and an empty statement ends the specification of a group of simulations. The following specifications can be written as: A = 1; B = 1,2; C = 0,1;;

The syntactic cards corresponding to the above mentioned syntax are shown in figure 5.1. It is possible to go from the specification of a family of simulations to the exhaustive lists of parameters of each simulation forming this family by making a Cartesian product between the values given to the parameters, or a group of parameters, by the different statements. Thus, the specification:

```
A = 1,2;
(B,C) = (0,0), (1,1);
D = -1,1;;
```

can create eight simulations (only the changes in the values of a parameter are noted in the following list).

Number	A	B	C	D
1	1	0	0	-1
2				1
3		1	1	-1
4				1
5	2	0	0	-1
6				1
7		1	1	-1
8				1

There are four principal steps to the execution of the DEFPARM program. The first step is initialization. The user indicates for which simulation program he needs the NAMELISTs. The DEFPARM program will find in the corresponding DATSIM file the number of the last encoded simulation and of the possible parameters for the simulation. The DEFPARM program will thus know which number to give to the new simulation and can verify the parameter identificators that the user could eventually give it.

The second step is the specification of the simulation families. This can be done in two optional parts: first: the DEFPARM program will provide the specification of another simulation, second, the user will give his own parameter specification. In other words, the user can:

1 - define nothing,
2 - define a base with the parameters of another simulation,
3 - give his own specification to a simulation family,
4 - define a base and add to it his own specification.

Figure 5.2 illustrates the second case and figure 5.3, the third case (the fourth case is a grouping of the second and third cases). It is important to note here that the data given by the user are in free form and that the errors found on a line will be flagged for correction.

The third step is a correction phase which can be repeated as often as necessary. First, the program lists, in a condensed form, the values of the parameters for each defined simulation, then it asks the user if he needs to correct these values, (this is in fact the only kind of correction allowed). If the user wants to get into the correction mode, the program will question him on each group of parameters. The program writes the group of parameters, using the same input syntax and the user answers either by a semi-colon (list of empty values) to indicate no correction or by a new list of values which will replace those held by the program. The correction phase will end either when all the groups of parameters held by the program have been run for the user or when the user writes a period instead of a list of values. The program will then list the new values of the parameters for each of the simulations and again offers the user the correction phase. This procedure is repeated until the user has finished his corrections. Figure 5.4 shows the correction phase associated to the data entered on figure 5.3.

Finally, the fourth step is the production of the NAMELISTs Fortran and the storing in the appropriate DATSIM file the number of the simulation of the data is has just produced. Figure 5.5 gives the NAMELISTs products for the specification of figures 5.3 and 5.4.

5.2 THE DESRES PROGRAM

The DESRES program generates the drawings of the functions stored on SIMRES type files. It reads the specification of the drawing, validates it and, if no error is detected, executes it. The program can function in both the interactive mode and the batch mode.

The drawing specification is done by a special language using all the possibilities of the XTRACT software. This language separates the information necessary for the definition of the drawing into four levels: program, simulation, function, drawing. In here, the information is interleaved, that is: if the information is the same for all levels, it is not necessary to redefine them to give other drawing specification.

The user must give the name of the program which has produced the SIMRES files to be drawn. This identifier will be the prefix used to build the SIMRES files identifiers to be localized. Following is the interaction between the user and the DESRES program (what the program writes is underlined).

PROGRAM: LRICFS

For the simulation, the user specifies a list of simulation numbers to be drawn. These numbers will be the suffixes needed to retrieve the SIMRES files. The syntax of this list of numbers conforms to the following rules: a list of numbers is made of any sequence of numbers and of sets of numbers separated by a comma and, finally, a set is defined by two numbers separated by a dash. Thus for SIMULATIONS: 1-5, 10,12, what is needed is simulations 1,2,3,4,5,10 and 12.

For a function, the user indicates which function must be drawn and specifies the field of extraction, that is, the set of evaluation points for which the value of the function on the SIMRES files is to be extracted. The function to be drawn is specified by an identifier. The field of extraction is specified by giving the list of points to be selected on each of the axes defining the function. These points must evidently coincide with those stored on the SIMRES files. A list of points is made of a sequence of point labels and of selection sets separated by commas. A selection set includes the label of the first chosen point, the label of the last chosen point and, optionally, of an increment. If this increment is absent, the default increment is used: its value is 1. The special symbols $ and * used instead of the label point signify the first and last points stored in the SIMRES files respectively. Finally, the key word TOUS (ALL) can be used instead of a list to signify that all the points of the axis present in the SIMRES files are selected. For example:

```
FUNCTION:  ENERGY
     SELECT STAT = TOUS (ALL)
     SELECT ETA  = (1,71,10),76,101
     SELECT RHO  = (1,*,2)
     SELECT TAU  = ($,*)
```

For the drawings, the user must indicate the scale and kind of drawing needed. The scale is specified by indicating one of the following identifiers: GLOBALE (the scale is for the whole file), LOCALE (the scale is for a given drawing), STANDARD (the scale is for the extraction field). If the chosen scale is the STANDARD scale, the user can also add, between parenthesis, the name of an axis to limit the scope of the scale to the axes within this axis. For instance, if a function depends on the STAT, ETA, RHO and TAU axes, and if the scale is limited to the standard scale on the ETA axis, this scale will be evaluated for the ETA, RHO and TAU axes only and there would be as many standard scales as there are points on the STAT axis. Section 4.2 gives more details on the nature of the different scales. The kind of drawing is indicated by the following identifier: PLOT 3D (surface drawings), PLOT 2D (curve drawings), CONTOUR (level curves) and PROJEC (2 dimension projection of a sub-array of curves describing the surface of a 2 variable function). The kind of drawing requested will induce a segmentation on the extraction field. Thus, one action can produce several plots; that is as many plots to empty the extraction field. An example of scale specification and type of drawing follows:

SCALE: STANDARD
DRAWING: PLOT 3D

The DESPES program will loop at the deepest level, that of drawing, then ask the user to specify a scale and a type of drawing. To get out of a level: enter an empty line or write the key word FIN (END). The user goes to the other level and here, it is possible to define this level or getting out of it. Figure 5.5 shows a complete example of a specification for the DESRES program.

In the interactive mode, the DESRES program analyzes the user's request and indicates as soon as possible the syntactical errors (data in the wrong format) and the invalid specifications (the requested function does not exist ...). The program then asks the user to hold some specification in order to continue its execution. When it is a submission by batch mode, when an error is detected, the running is stopped but the syntactical analysis can continue.

To execute a drawing specification, the SIMRES program must first localize the SIMRES files to be treated. These files are opened one at a time and the information showing the function to be plotted, the field of extraction, the composition of the tuples and the type of scales is given to the XTRACT software. This information recovered by the EXTTUP procedure is processed by the appropriate plotting procedure (PLOT 3D, PLOT 2D, CONTOUR, PROJEC). The program repeats this operation until all the requests have been fulfilled or until a non-retrievable error occurs.

Figures 5.7 to 5.11 show the different graphic output of the DESRES program. Figure 5.7 shows the list of parameters identifying the plotted simulation. Figure 5.8 shows the plot drawn by PLOT 3D for a 2 variable function. Figure 5.9 shows the curves set by the CONTOUR procedure for the same function. Figure 5.10 shows a projection of this function as produced by PROJEC. And finally, figure 5.11 shows the plot produced by PLOT 2D for a function which varies as to one axis.

5.3 THE SYNTH PROGRAM

The SYNTH program permits the synthesis of the information of many distinctive simulations in order to study a specific phenomenon. This synthesis is done by selecting the pertinent simulations necessary to draw out a specific phenomenon and by comparing one or several functions of these simulations. In its final version, the SYNTH program should allow the user to specify the phenomenon to be studied with the help of a predicate (studying the effect of a parameter in function of another, or studying the effect of such or such a model). The SYNTH program would find which simulations will satisfy the predicate. However, for a first version (still being developed), it is better to ask the user to identify the simulation to be compared. The SYNTH program thus verifies the validity of the comparison, makes up the headings identifying the work done and makes the comparisons.

There are three possible fields for comparisons:

- inside one simulation,
- between specific simulation produced by a same model (same simulation program),
- between simulation produced by different models.

With comparisons done inside the same simulation, it is the variation of an axis which will provide the criterion for a comparison: it is the position on the axis which is studied. Often, the comparison will deal with the repetitive axis, in other words, an axis which does not define the space of the simulation but which induces repetition of the stored information: this is specifically the case with the models with several lasers (where a "laser" axis will store information on the different lasers) and the model including statistics (where a "statistic" axis will store the different repetitions of the simulation).

The comparisons of simulations produced by the same model permits the study of the effect of parameter variation on a given model. For instance, it is possible to study the effect of a parameter by choosing simulations that are distinguished from each other only by the different values given to this parameter.

The comparison of simulations produced by different simulations brings out the impact of the models. This type of comparison is very complex as the different models do not necessarily use the same parameters. The SYNTH program must thus use equivalence tables between the parameters of the different model to judge the validity of a comparison and to make up a valid heading.

The functions to be compared can either be vectorial (a simulation produces a curve) or scalar (a simulation produces a point on a curve). The vectorial function can be used with the three types of comparison. According to the case, the curves of the comparisons are thus identified by the varying axis, by the distinguishing parameters, by the changing model. The scalar function can be used only in comparisons with simulations produced by a same model. Thus, the effect of a group of parameters can be studied in terms of another. In this case, the simulations providing the points of a curve are distinguished from one another by a group of parameters A defining the horizontal axis of the comparison. The comparison thus involves several curves distinguished from one another by a group of parameters B, group B does not include any of the parameters of A.

The specification of the required type of comparison is done in two steps: first, by indicating which function is to be compared and which are its selectors, second, by indicating the simulations involved in each comparison making up the series. A series is a group of comparisons which have logical bonds and which make up a more or less exhaustive study of a given phenomenon.

In the first step of the specification of a series of comparisons, the user must indicate the identifier of the required function. Next, the user must indicate the name of the axis, its type and the specification of the selected points for each of the axes on which the function depends. There are four possible types to characterize an axis and each type is shown by a letter (S, G, C or M). The specification of the selected points is done by a list of point numbers, and a set of selection separated by commas (in fact, it is the same syntax of the DESRES program, cf. section 5.2). This first step is ended when the user writes a semicolon instead of a name of axis. For instance:

The S type indicates an axis used to select points of evaluation of the function to be compared. This is the "by default" type, and the symbol S can be omitted. Thus, the function O POWEP is selected for all the points on the TAU axis evaluated at point 1 of axis STAT and at point 71 of axis ETA (what the SYNTH program writes is underlined):

```
FUNCTION   O POWER
    STAT = S,1
     ETA = S,71
     TAU = *
       ;
```

The G type corresponds of an axis giving many comparisons, that is providing comparisons for each of the points selected on the axis. Thus, the following specification:

```
FUNCTION   O POWEP
    STAT = 1
     ETA = G,61,71
     TAU = *
       ;
```

indicates that 2 comparisons of the function O POWER are needed, one for point 61 on the ETA axis and another for point 71.

Type C corresponds to a comparison axis, that is, the impact of this axis on the function to be compared. There can be only one comparison axis for a given function. For instance, the specification:

```
FUNCTION   O POWEP
    STAT = C (1,7,1)
     ETA = 71
     TAU = *
       ;
```

indicates that the comparison contains the function O POWER seven times, once for each of the points selected on the STAT axis.

Finally, type M shows that the user would like to compare the arithmetic mean of the function rather than the function itself. When M qualifies an axis, it means that the arithmetic mean of the function for the points selected on the axis must be evaluated. Thus, in the case of

```
FUNCTION   O POWER
  STAT = M,(1,7)
   ETA = 71
   TAU = *
     ;
```

the user must compare the average of the seven function O POWER selected on the STAT axis.

By analyzing the specification of the first step, the SYNTH program is already able to know some of the user's intentions and thus to determine which informations must be provided at the second step. In other words, if a type C axis is already known, the SYNTH program will automatically know that the comparison is done inside the same simulation and will expect only one simulation number per comparison. Moreover, if the specification of the points selected determine a scalar function (i.e. FUNCTION WIDTH STAT = M,(1,7) ETA = 71), the SYNTH program will conclude that the user wants to study the impact of a group of parameters on another group of parameters. In this case, the SYNTH program must ask the user to specify a list of parameters. Each of the parameters on this list will be used one after the other to define the points of the horizontal axis (axis x) which corresponds to the different simulations that make up the curves to be compared. For instance, in the following case:

```
PARAMETERS FOR AXIS X:  TBRHO, FARUSKA, INVFRNL
```

The program will produce three series of comparisons, one using the values of the TBRHO parameter to form axis x, another using the FARUSKA parameter and finally one using the INVFRNL parameter.

The second major step for the definition of the work to be done comes when the series of comparisons are specified. A series includes one or several comparisons making up a logical whole, that is studying the same phenomenon. The SYNTH program produces a heading for each series of comparisons, showing the changes of parameters, of models, or of points on the axes for each of the involved simulations.

Depending on the kind of study, a comparison is made up of one or many simulations, and each simulation is identified by a model and a simulation number (one or several blank spaces separate the two elements). In order to avoid a repetition of the name of the model, the SYNTH program lets the user define, at the beginning of a series of simulation, a model by default.

To end a series of comparisons, the symbol period is used. At this moment, it is possible to redefine another series using the same function specification, or even to return with another point at the level of function specification.

What happens after this identification by "model by default" depends on the type of comparison that the user requires.

If the comparison deals with the same simulation, the program asks the user to indicate the simulation used for each comparison. The following example illustrates a series of these comparisons showing the variations produced by the STAT axis.

```
FUNCTION   O POWER
  STAT = C,(1,7)
   ETA = 71
   TAU = *
MODEL BY DEFAULT:  LR1CFS
SIMULATION:  100
SIMULATION:  101
SIMULATION:  102
SIMULATION:   .
MODEL BY DEFAULT:   .
FUNCTION:   .
```

When the comparison studies the impact of certain parameters or of the model on a vectorial function, the SYNTH program will ask the user to give the numbers (at least two) of the simulations making up each comparison in the series. In the following example is defined a series of two comparisons involving three simulations, then a series of one comparison involving three simulations of different models.

```
FUNCTION   O POWER
  STAT = M,(1,7)
   ETA = 7
   TAU = *
     ;
MODEL BY DEFAULT:  LR1CFS
SIMULATIONS:  100,101,102
SIMULATIONS:  110,111,112
SIMULATIONS:   .
```

```
MODEL BY DEFAULT:  LR1CFS
      SIMULATIONS:  100,LR1PS 5,LR1P4S 2
      SIMULATIONS:  .
MODEL BY DEFAULT:  .
         FUNCTION:  .
```

Finally, when the comparison involves a scalar function, the SYNTH program asks the user, first, to indicate the simulations making up the curves, then to indicate which curves make up the comparison (it is possible to define one curve only). The following example shows a series of two comparisons involving three and two curves respectively.

```
         FUNCTION:  WIDTH  (pulse width)
             STAT = M,(1,7)
              ETA = 71
MODEL BY DEFAULT:  LR1CFS
SIMULATIONS MAKING UP THE CURVE
#1:  100,101,102
#2:  103,104,105
#3:  106,107,108
#4:  109,110
#5:  111,112
#6:  .
CURVES MAKING UP THE COMPARISON
#1:  1,2,3
#2:  4,5
#3:  .
MODEL BY DEFAULT:  .
         FUNCTION:  .
```

By and large, the SYNTH program functions by processing the series of comparisons one by one. Syntactical verifications are done as the specifications are entered. When the definition of a series of comparison is completed, the program verifies the validity of what is requested. If there are no errors at this level, the program makes up the heading of the series. The data needed for this operation comes on the one hand from the series specification that defines the type of comparison requested and, on the other, from the DATSIM files which provide the values of the simulations parameters to be compared. A specific heading is given to each comparison in order to identify each plot. Finally, the comparisons are generated, and the value of the functions to be compared comes either from the DATSIM files (if it contains the needed information) or from the SIMRES files.

Figure 5.12 shows the heading of a series of comparisons, in which the impact of parameters IGVA, IGVB and IGVN on the vectorial function E*R*DR are studied. Figure 5.13 shows a comparison of this series. Figure 5.14 shows the heading of a series of comparisons showing the impact of parameter G1AO in terms of parameter SB on a scalar function. Figure 5.15 shows a comparison of this series.

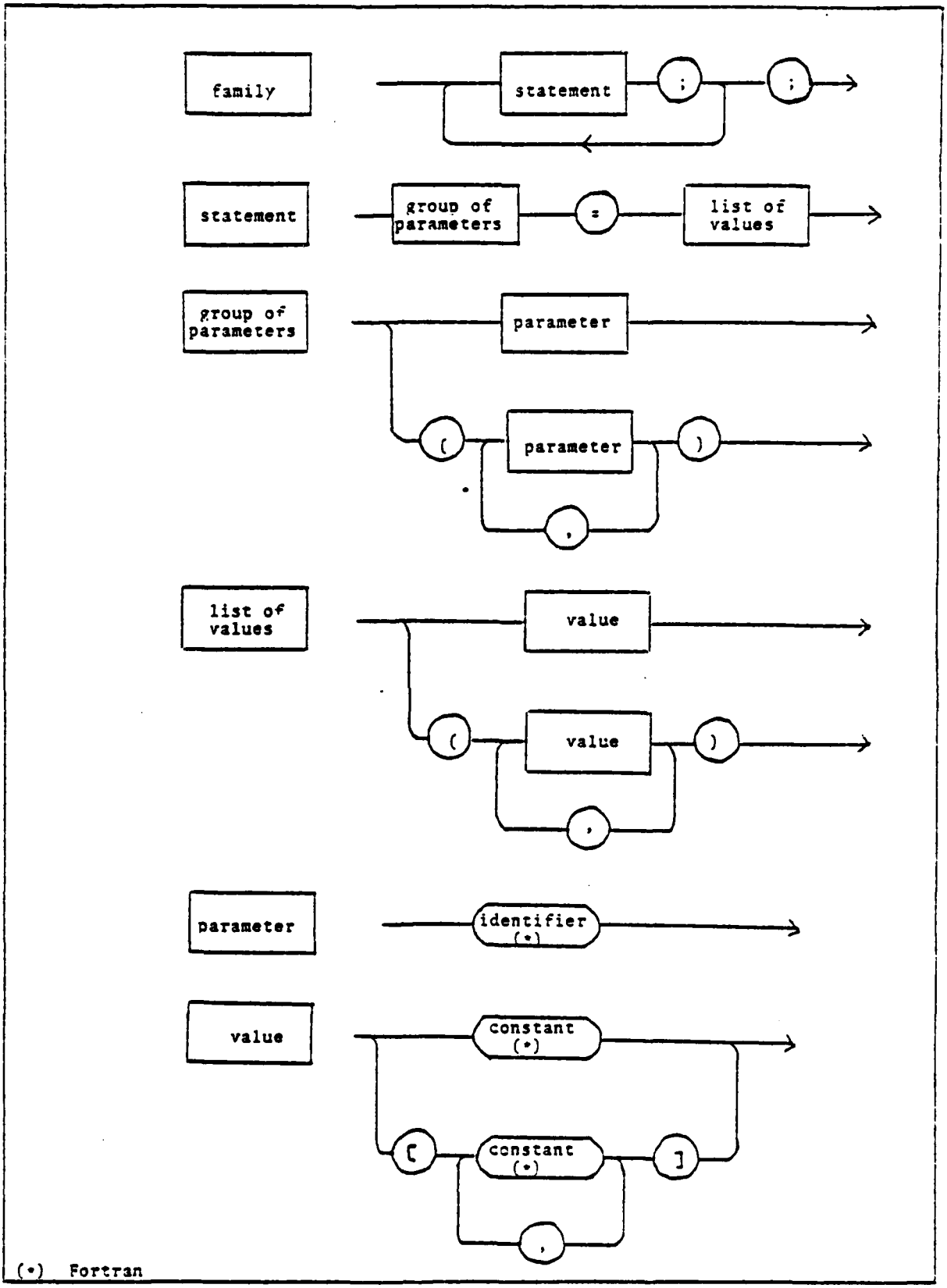

FIGURE 5.1 - SYNTACTICAL CARDS FOR THE SPECIFICATION LANGUAGE FOR THE SIMULATION FAMILIES

```
-PROGRAM DEFPARM 1.0
-HAPPY TO HELP YOU!
-LOAD THE PARAMETERS OF A PREVIOUS SIMULATION ? (YES/NO)
>yes
-GIVE THE NUMBER OF THIS SIMULATION
>312
-LOOKING FOR SIMULATION  312 WAIT A MOMENT PLEASE
-BE PATIENT I'M DOING MY BEST!
-ENTER PARAMETERS AND THEIR VALUES
>;

    -  Program output
    >  User's input
```

FIGURE 5.2 - CREATION OF A BASE FROM PARAMETER VALUES OF A PREVIOUS SIMULATION

```
-PROGRAM DEFPARM 1.0
-HAPPY TO HELP YOU!
-LOAD THE PARAMETERS OF A PREVIOUS SIMULATION ? (YES/NO)
>no
-LOOKING FOR THE NUMBER OF THE NEXT SIMULATION
-WAIT A MOMENT PLEASE
-ENTER PARAMETERS AND THEIR VALUES
>idimen= 1;
>(     ideltaa , ideltab. ) =
>(    1, 1    ) ;
>(    0, 0    ) ;
>toto = ab
-TOTO = AB
-****
-ERROR NUMBER:  12
-THE GIVEN PARAMETER IS UNKNOWN
I.E. WAS NOT FOUND IN THE LIST OF PARAMETERS USED IN PREVIOUS SIMULATION)
-PLEASE RETYPE LINE FROM THE BEGINNING
>sla0 = 125.0 , 250.0, 375.0 ;
>tbrhoa = 4.236669, 8.7;;

    -  Program output
    >  User's input
```

FIGURE 5.3 - USER'S SPECIFICATION OF A FAMILY OF SIMULATIONS

```
SIM#      IDIMEN      IDELTAA      IDELTAB      GLAO      TBRHOA

 649      1           1            1            125.0     4.236669
 650                                                      8.7
 651                                            250.0     4.236669
 652                                                      8.7
 653                                            375.0     4.236669
 654                                                      8.7
 655                  0            0            125.0     4.236669
 656                                                      8.7
 657                                            250.0     4.236669
 658                                                      8.7
 659                                            375.0     4.236669
 660                                                      8.7

>CORRECTIONS (YES/NO) ?

-yes

-FOR MODIFICATION ENTER NEW VALUE(S) OF PARAMETER(S) LISTED
-";" MEANS NO MODIFICATION
-"." MEANS END OF MODIFICATION
-NUMBER OF THE FIRST SIMULATION
>;
-IDIMEN =
>;
-(IDELTAA,IDELTAB) =
>(1,1),(2,2);
-GLAO =
>.
SIM#      IDIMEN      IDELTAA      IDELTAB      GLAO      TBRHOA

 649      1           1            1            125.0     4.236669
 650                                                      8.7
 651                                            250.0     4.236669
 652                                                      8.7
 653                                            375.0     4.236669
 654                                                      8.7
 655                  2            2            125.0     4.236669
 656                                                      8.7
 657                                            250.0     4.236669
 658                                                      8.7
 659                                            375.0     4.236669
 660                                                      8.7

>CORRECTIONS (YES/NO) ?

-no
```

FIGURE 5.4 - CORRECTION PHASE OF THE DEFPARM PROGRAM

```
$DATA NUMBER=649,
IDIMEN=1,IDELTAA=1,IDELTAB=1,G1AO=125.0,
TBRHOA=4.236669,
$
$DATA NUMBER=650,
IDIMEN=1,IDELTAA=1,IDELTAB=1,G1AO=125.0,
TBRHOA=8.7,
$
$DATA NUMBER=651,
IDIMEN=1,IDELTAA=1,IDELTAB=1,G1AO=250.0,
TBRHOA=4.236669,
$
$DATA NUMBER=652,
IDIMEN=1,IDELTAA=1,IDELTAB=1,G1AO=250.0,
TBRHOA=8.7,
$
$DATA NUMBER=653,
IDIMEN=1,IDELTAA=1,IDELTAB=1,G1AO=375.0,
TBRHOA=4.236669,
$
$DATA NUMBER=654,
IDIMEN=1,IDELTAA=1,IDELTAB=1,G1AO=375.0,
TBRHOA=8.7,
$
$DATA NUMBER=655,
IDIMEN=1,IDELTAA=2,IDELTAB=2,G1AO=125.0,
TBRHOA=4.236669,
$
$DATA NUMBER=656,
IDIMEN=1,IDELTAA=2,IDELTAB=2,G1AO=125.0,
TBRHOA=8.7,
$
$DATA NUMBER=657,
IDIMEN=1,IDELTAA=2,IDELTAB=2,G1AO=250.0,
TBRHOA=4.236669,
$
$DATA NUMBER=658,
IDIMEN=1,IDELTAA=2,IDELTAB=2,G1AO=250.0,
TBRHOA=8.7,
$
$DATA NUMBER=659,
IDIMEN=1,IDELTAA=2,IDELTAB=2,G1AO=375.0,
TBRHOA=4.236669,
$
$DATA NUMBER=660,
IDIMEN=1,IDELTAA=2,IDELTAB=2,G1AO=357.0,
TBRHOA=8.7,
$
..
```

FIGURE 5.5 - NAMELISTS PRODUCTS OF THE DEFPARM PROGRAM

```
PROGRAM:  LR1CFS
    SIMULATIONS:  1-5, 7, 12
        FUNCTION:  Energy
        select STAT = TOUS (ALL)
        select ETA  = (1, 71, 10)
        select RHO  = (1, *, 2)
        select TAU  = ($, *)
             SCALE  : STANDARD
              PLOT  : PLOT 3D
             SCALE  : STANDARD
              PLOT  : CONTOUR
             SCALE  : FIN (END)
        FUNCTION:  O POWER
        select STAT = TOUS
        select ETA  = (1, 71, 10)
        select TAU  = ($, *)
             SCALE  : STANDARD (STAT)
              PLOT  : PLOT 2D
             SCALE  : FIN (END)
        FUNCTION:  FIN
    SIMULATIONS:  FIN
PROGRAM:  FIN
```

FIGURE 5.6 - PLOT SPECIFICATION FOR THE DESPES PROGRAM

DOUBLE LASER SIMULATION

NUMERO = 626.

LASER: A

PARAMETERS

LASERA	= 1.	LASERB	= 1.
PHIOA	= .31417817E+01.	PHIOB	= .31417817E+01.
PHI2A	= 0.0.	PHI2B	= 0.0.
IBCA	= 1.	IBCB	= 1.
IBCA2	= 0.	IBCB2	= 0.
C1A	= .632E-03.	C1B	= .8E-01.
IGVA	= 1.	IGVB	= 1.
G1A0	= .75E+01.	G1B0	= .226E+03.
G1AFCT	= .1E+01.	G1BFCT	= .1E+01.
IGVFCTA	= 0.	IGVFCTB	= 0.
TBRH0A	= .42366695E+01.	TBRH0B	= .42366695E+01.
IRAN0A	= 0.	IRAN0B	= 0.
SIGNA	= -.99E+00.	SIGNB	= -.1E-03.
IDELTAA	= 0.	IDELTAB	= 1.
DANA	= 0.0.	DANB	= 0.0.
GAMMAA	= .1E+01.	GAMMAB	= .1E+01.
SA	= .1E+01.	SB	= 0.0.
TBHA	= .5E+00.	TBHB	= .5E+00.
RKAPPAA	= 0.0.	RKAPPAB	= 0.0.
TAUOA	= .7E+01.	TAUOB	= .7E+01.
T1NINVA	= .125E-01.	T1NINVB	= .125E-01.
T2NINVA	= .142857E-01.	T2NINVB	= .142857E-01.
PHISTOA	= 0.0.	PHISTOB	= 0.0.
ISTPHIA	= 0.	ISTPHIB	= 0.
CURVA	= 0.0.	CURVB	= 0.0.
RKPLONA	= 0.0.	RKPLONB	= 0.0.
IDISTRA	= 0.	IDISTRB	= 0.
EPSILNA	= .1E+01.	EPSILNB	= .2E-03.
T2NINVC	= .142857E-01.	IOCN	= 0.
TAUSF	= .4E+01.	TAUOCT	= .9E+01.
WINCOW	= .21E+02.	IDIMEN	= 3.
KSAVE	= 64.	MSAVE	= 32.
JSAVE	= 300.	JSTEP	= 4.
HA	= .1786714286714 3E-01	HB	= .625E-03.
NA	= 32.	NAT	= 57.
INLR	= 1.	NSRUNS	= 1.
IST	= 2.	ISR	= 2.
IPUMPSH	= 0.	ILEVEL	= 1.

FIGURE 5.7 - LIST OF PARAMETERS IDENTIFYING THE PLOTTED SIMULATION

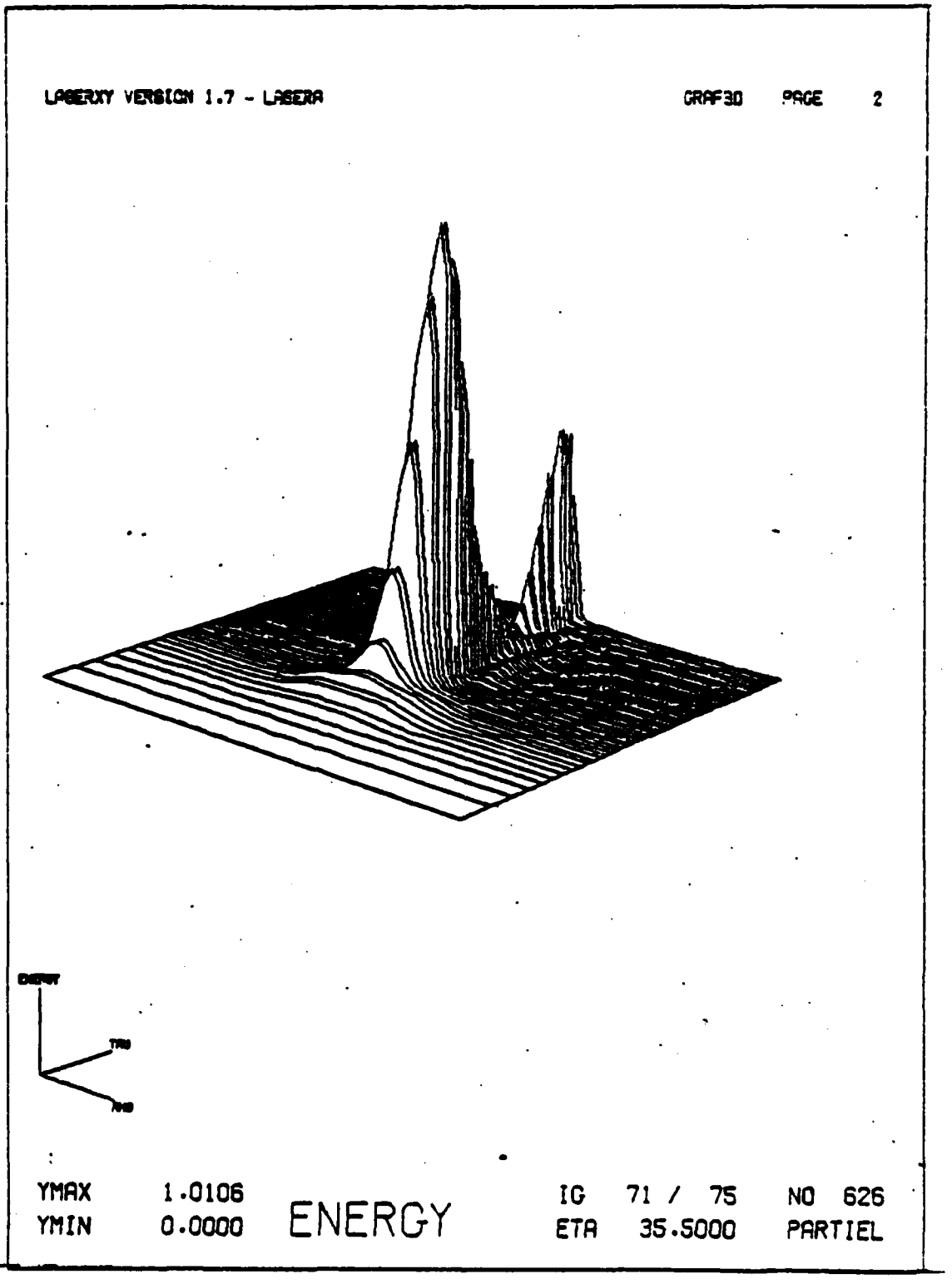

FIGURE 5.8 - PLOT DRAWN BY PLOT 3D FOR A 2 VARIABLE FUNCTION

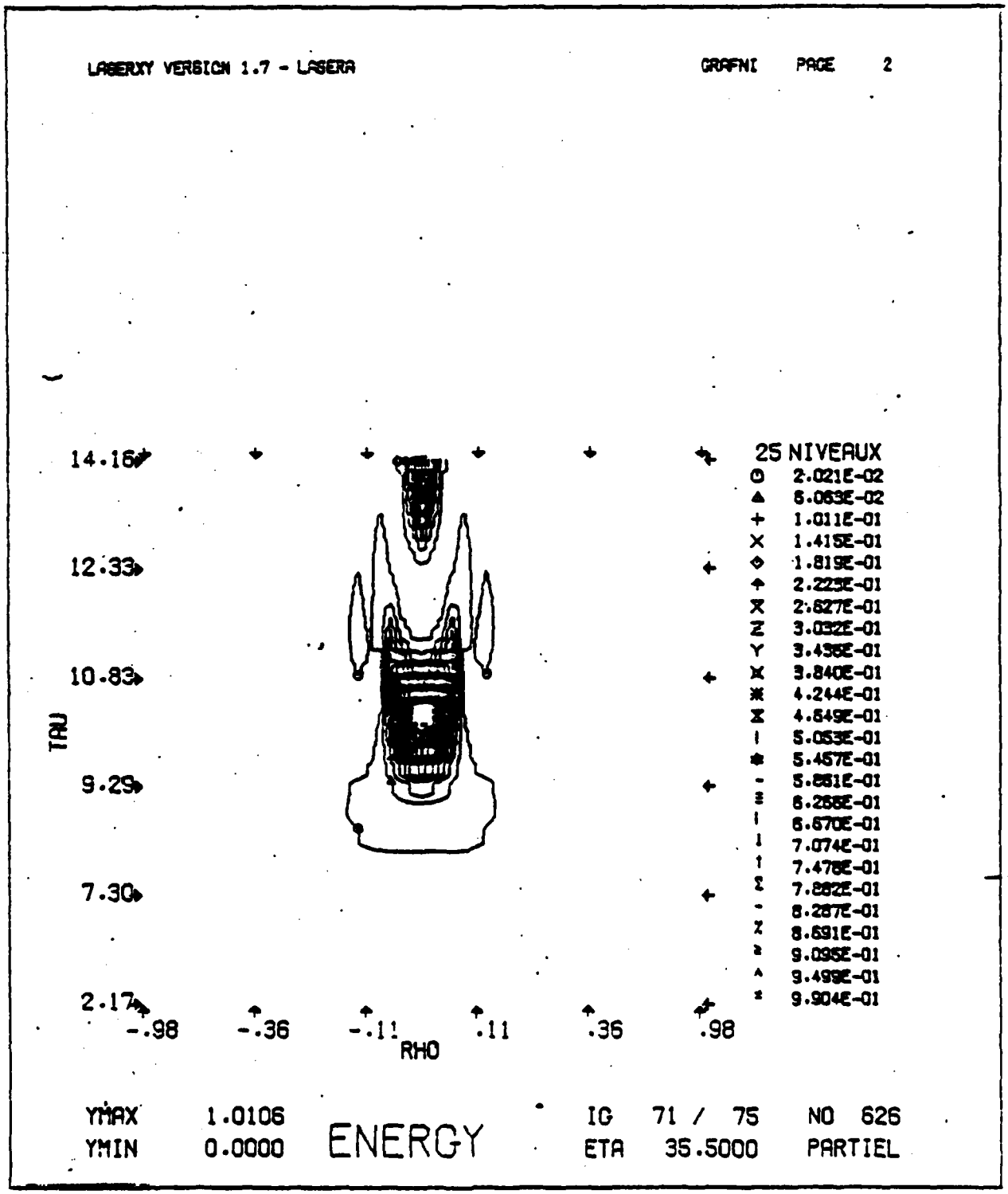

FIGURE 5.9 - CURVES SET BY THE CONTOUR PROCEDURE FOR A 2 VARIABLE FUNCTION

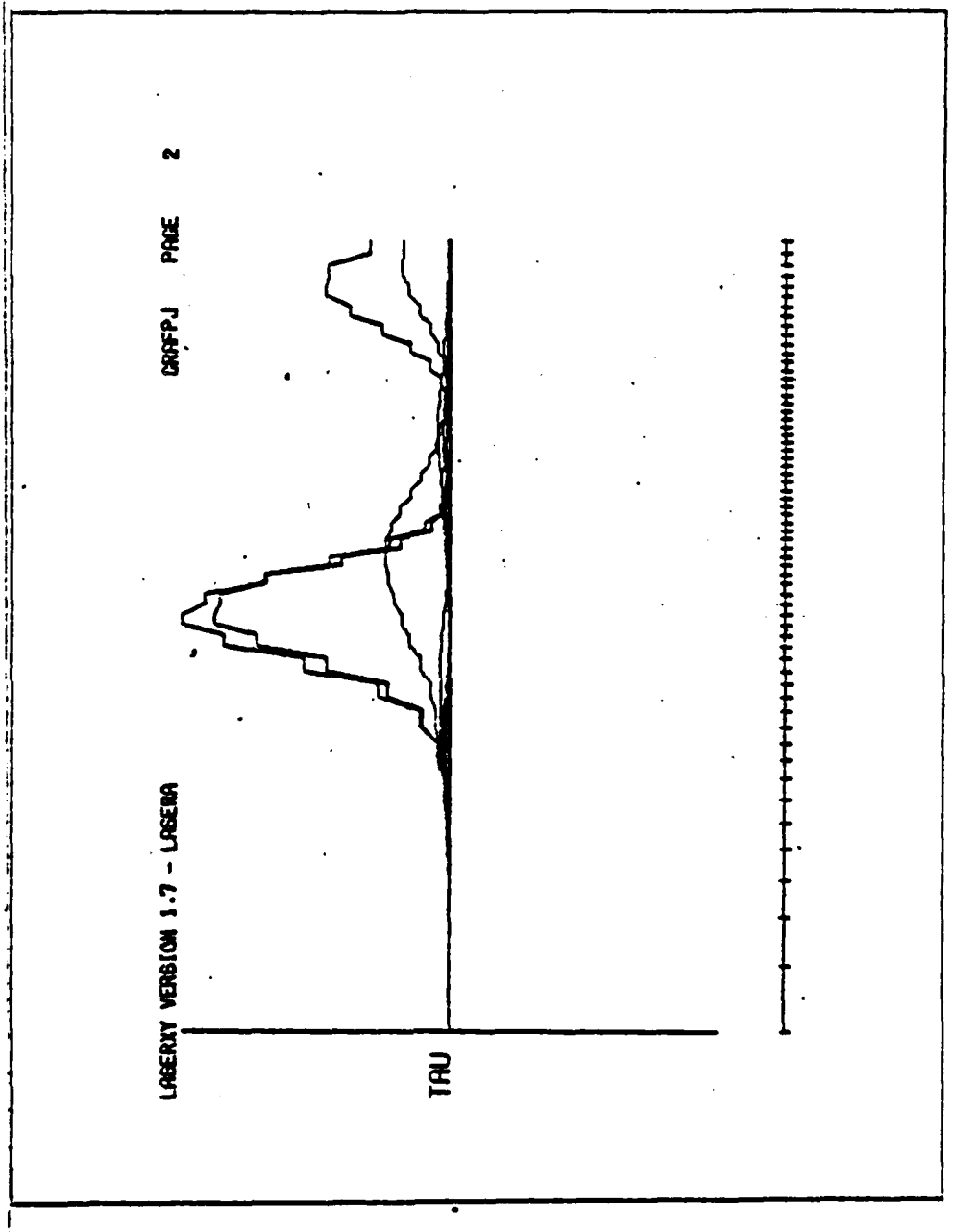

FIGURE 5.10 - PROJECTION OF A 2 VARIABLE FUNCTION AS PRODUCED BY PROJEC

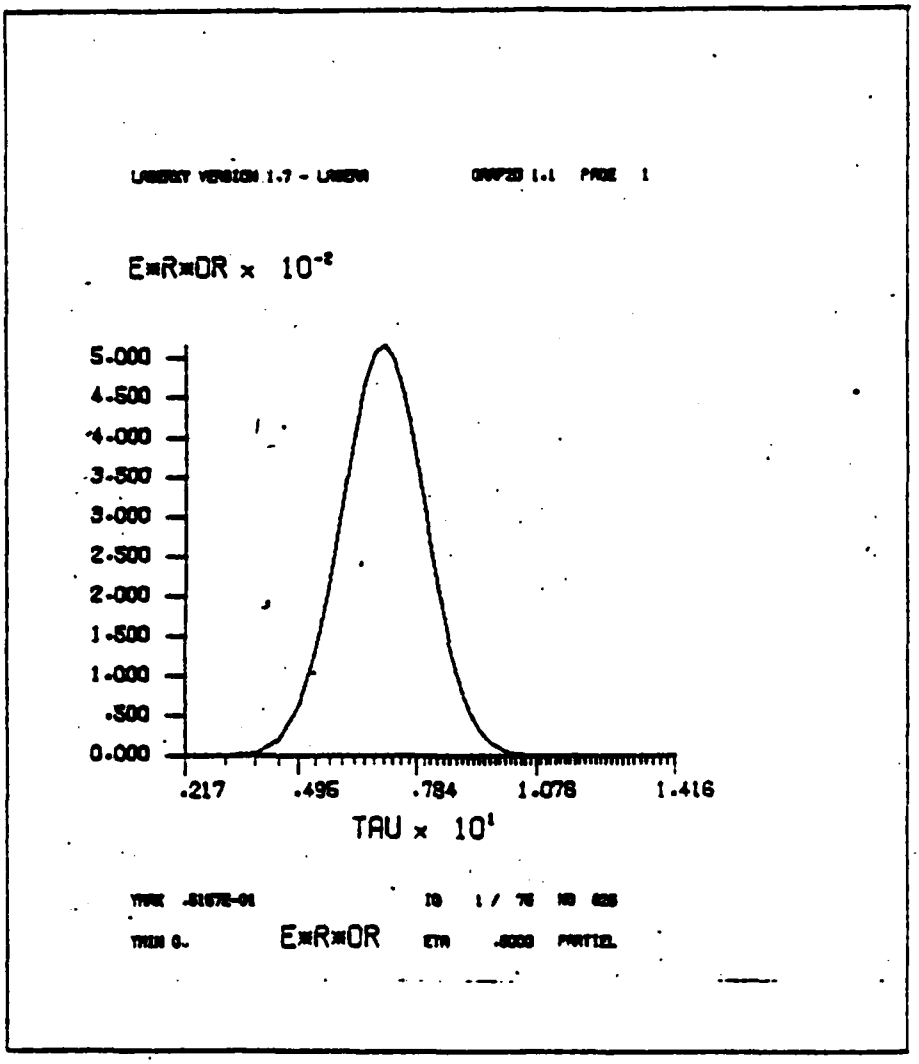

FIGURE 5.11 - PLOT PRODUCED BY PLOT 2D FOR A FUNCTION WHICH VARIES AS TO ONE AXIS

COMPARISON

SERIE 95 (NUMBER 1)
WITH NORMALIZATION

NUMBER	IGVA	IGVB	IDGN
410.	1.	1.	0.
580.	0.	0.	0.
584.	0.	0.	1.

```
LASERA  = 1,                          LASERB  = 1,
PHIOA   = .3141782E+01,               PHIOB   = .3141782E+01,
PHI2A   = 0.0,                        PHI2B   = 0.0,
IBCA    = 1,                          IBCB    = 1,
IBCA2   = 0,                          IBCB2   = 0,
C1A     = .632E-03,                   C1B     = .8E-01,
G1AO    = .75E+01,                    G1BO    = .275E+03,
G1AFCT  = .1E+01,                     G1BFCT  = .1E+01,
IGVFCTA = 0,                          IGVFCTB = 0,
TBRHOA  = .4236669E+01,               TBRHOB  = .4236669E+01,
IRANDA  = 0,                          IRANDB  = 0,
SIGNA   = -.99E+00,                   SIGNB   = -.1E-03,
IDELTAA = 1,                          IDELTAB = 1,
DWNA    = 0.0,                        DWNB    = 0.0,
GAMMAA  = .1E+01,                     GAMMAB  = .1E+01,
SA      = .1E+01,                     SB      = 0.0,
TBWA    = .5E+00,                     TBWB    = .5E+00.
RKAPPAA = 0.0,                        RKAPPAB = 0.0,
TAUOA   = .7E+01,                     TAUOB   = .7E+01,
T1NINVA = .125E-01,                   T1NINVB = .125E-01,
T2NINVA = .14286E-01,                 T2NINVB = .14286E-01,
PHISTDA = 0.0,                        PHISTDB = 0.0,
ISTPHIA = 0,                          ISTPHIB = 0,
CURVA   = 0.0,                        CURVB   = 0.0,
RKPLONA = 0.0,                        RKPLONB = 0.0,
IDISTRA = 0,                          IDISTRB = 0,
EPSILNA = .1E+01,                     EPSILNB = .1E-02,
T2NINVC = .14286E-01,                 TAUSF   = .4E+01,
TAUOCT  = .9E+01,                     WINDOW  = .21E+02,
IDIMEN  = 3,                          KSAVE   = 64,
MSAVE   = 32,                         JSAVE   = 300,
JSTEP   = 4,                          HR      = .17857E-01,
HS      = .625E-03,                   NA      = 32,
NAT     = 57,                         INLR    = 1,
NBRUNS  = 1,                          IST     = 2,
ISR     = 2,                          IPUMPSH = 0,
ILEVEL  = 1,                          BETAA   = .474E-02,
BETAB   = .22E+02,                    FARUSKA = .8608E-01,
FARUSKB = .394886013E+03,             INFRNLA = .11344E-01,
INFRNLB = .1435949E+01,               LGPHIOA = .3723432E+01,
LGPHIOB = -.3723432E+01,              IGVNEGA = 0.0,
IGVNEGB = 0.0,                        IGVPOSA = -1,
IGVPOSB = -1,                         LGPHSQA = .13863943E+02,
LGPHSQB = .13863943E+02,              ING1ASQ = .17778E-01,
ING1BSQ = .13E-04,                    INVG1AO = .133333E+00,
INVG1BO = .3636E-02,                  G1AOSQ  = .5625E+02,
G1BOSQ  = .75625E+05,                 INVC1A  = .1582278481E+04,
INVC1B  = .125E+02,                   RCG1AO  = .2738613E+01,
RCG1BO  = .18583124E+02               AKAPPAA = .6170670064E+04,
AKAPPAB = .48748294E+02,              TAURA   = .713489E+00,
TAURB   = .19459E-01,                 TAUSA   = .822756009E+03,
TAUSB   = .177267E+00,                GLRA    = .8508E-01,
GLRB    = .384886013E+03,             ALPHAA  = .25E+00,
ALPHAB  = .9166667E+01.
```

FIGURE 5.12 - HEADING OF A SERIES OF COMPARISONS IN WHICH THE IMPACT OF PARAMETERS IGVA, IGVB AND IGVN ON THE VECTORIAL FUNCTION E*R*DR ARE STUDIED

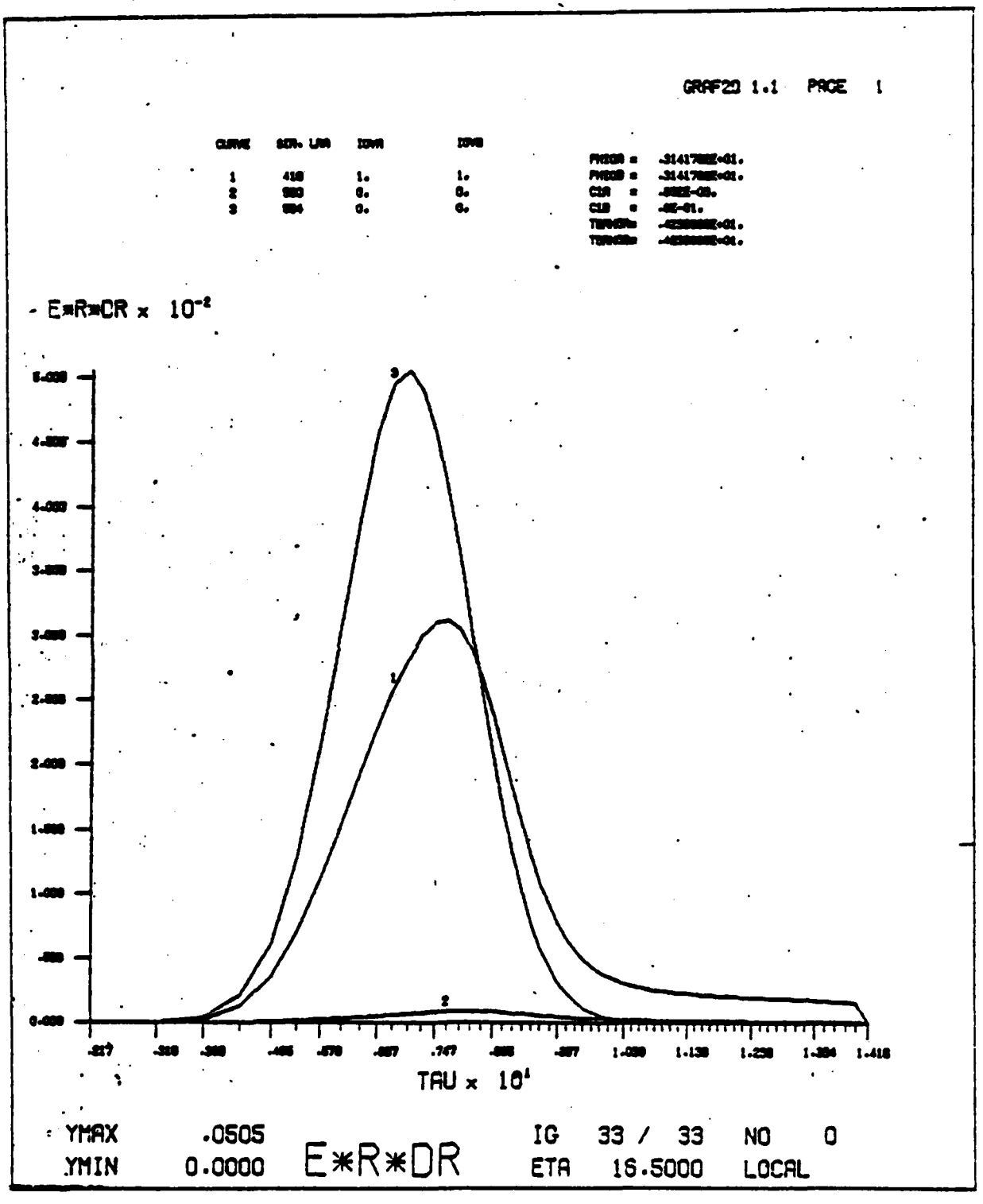

FIGURE 5.13 - COMPARISON OF A SERIES OF COMPARISONS IN WHICH THE IMPACT OF PARAMETERS IGVA, IGVB AND IGVN ON THE VECTORIAL FUNCTION E•R•DR ARE STUDIED

COMPARISON

7. G1AO VS SB (CF. COMPARISON 07)

A) CONSTANT PARAMETERS

PARAMETER	VALUE	PARAMETER	VALUE
LASERA	= 1	LASERB	= 1
PHIOA	= 3.1417817	PHIOB	= 3.1417817
PHI2A	= 0.0	PHI2B	= 0.0
IBCA	= 0	IBCB	= 0
IBCA2	= 0	IBCB2	= 0
C1A	= .08	C1B	= .000632
IGVA	= 1	IGVB	= 1
G1BO	= 6.25	G1AFCT	= 1.0
G1BFCT	= 1.0	IGVFCTA	= 0
IGVFCTB	= 0	TBRHOA	= 4.236669
TBRHOB	= 4.236669	IRANDA	= 0
IRANDB	= 0	SIGNA	= -1.0
SIGNB	= -1.0	DWNA	= 0.0
DWNB	= 0.0	GAMMAA	= 1.0
GAMMAB	= 1.0	SA	= 0.0
TBWA	= .5	TBWB	= .5
RKAPPAA	= 0.0	RKAPPAB	= 0.0
TAUOA	= 7.0	TAUOB	= 7.0
T1NINVA	= .0125	T1NINVB	= .0125
T2NINVA	= .0142857	T2NINVB	= .0142857
PHISTDA	= 0.0	PHISTDB	= 0.0
ISTPHIA	= 0	ISTPHIB	= 0
CURVA	= 0.0	CURVB	= 0.0
RKPLONA	= 0.0	RKPLONB	= 0.0
IDISTRA	= 0	IDISTRB	= 0
EPSILNA	= .001	EPSILNB	= 1.0
T2NINVC	= .0142857	IDGN	= 0
TAUSF	= 4.0	TAUOCT	= 9.0
WINDOW	= 21.0	IDIMEN	= 3
KSAVE	= 64	MSAVE	= 32
JSAVE	= 300	JSTEP	= 4
HR	= .017857142857	HS	= .000625
NA	= 32	NAT	= 57
INLR	= 1	NBRUNS	= 1
IST	= 4	ISR	= 2
IADRHO	= 0	IPUMPSH	= 0
ILEVEL	= 1		

B) PARAMETERS VARYING ON A CURVE

	G1AO
1.	225.0
2.	275.0
3.	325.0

C) PARAMETERS VARYING BETWEEN CURVES

CURVE	SB
1	1.0
2	2.0
3	3.0

D) SIMULATIONS USED IN CURVES

CURVE	SIMULATIONS		
1	498	501	504
2	345	351	357
3	348	354	360

FIGURE 5.14 - HEADING OF A SERIES OF COMPARISONS SHOWING THE IMPACT OF PARAMETER G1AO IN TERMS OF PARAMETER SB ON A SCALAR FUNCTION

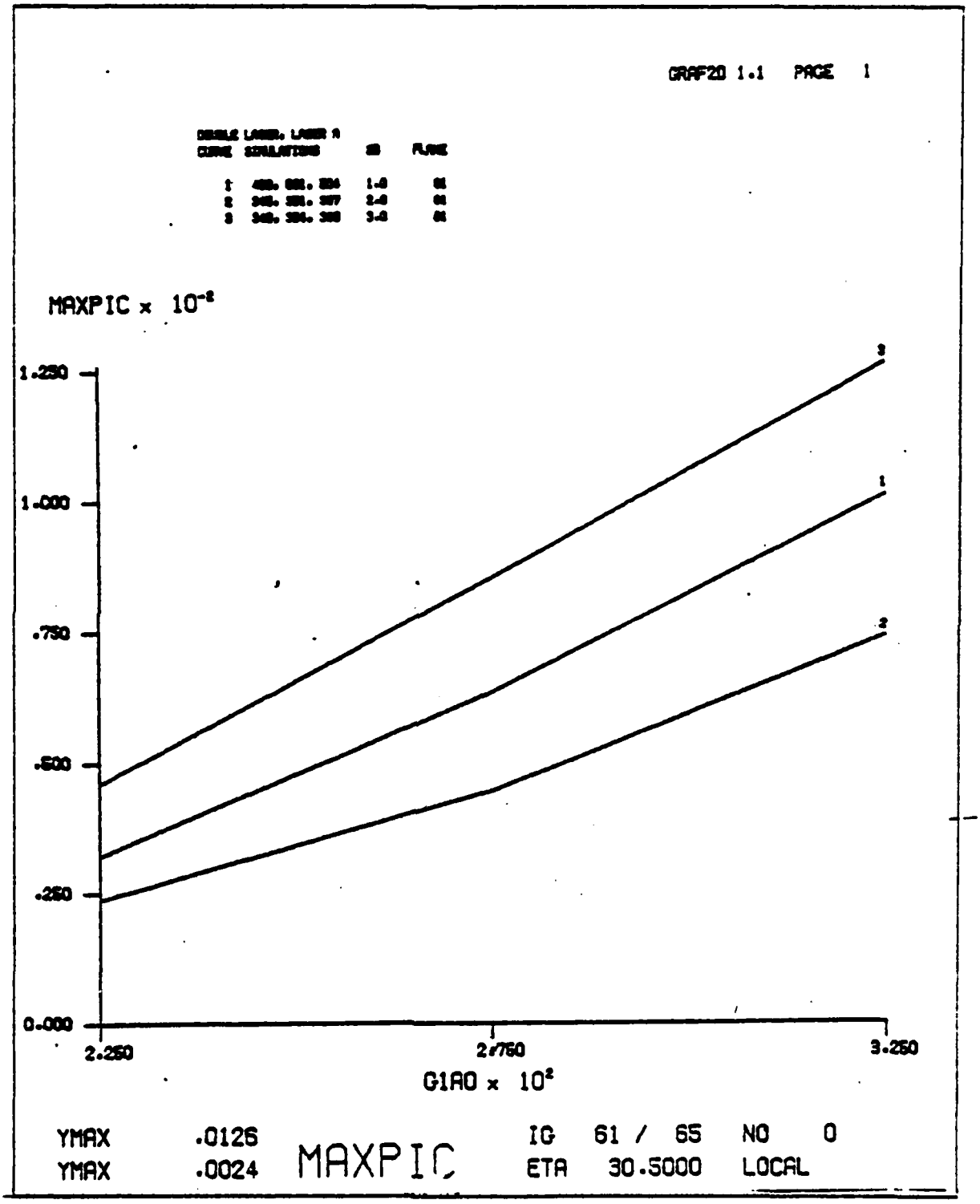

FIGURE 5.15 - COMPARISON OF A SERIES OF COMPARISONS SHOWING THE IMPACT OF PARAMETER GIAO IN TERMS OF PARAMETER SB ON A SCALAR FUNCTION

VI - THE LASER PROGRAMS

Even though the laser simulation programs do not in themselves form the core or the basis of the system presented here, they remain nevertheless its fundamental motivation. It should be noted that the different softwares and programs making up the system are general enough to process several different problems. The SIMRES for instance can process any program using numerical integration for result calculations. Therefore, it seemed necessary to devote a whole chapter to discuss the production and resolution problems faced in the laser simulation programs.

It will not be possible to give here a detailed explanation of the physics and the numerical techniques used to solve the diverse differential equations in these programs. These two aspects will only be touched on descriptively in order to place the programs in their proper context.

This chapter is divided in four parts:

1 - the first part is a summary description of the programs with an overview of their particular techniques,

2 - the second part deals with the general characteristics of the programs: documentation, modularity, etc.,

3 - the third discusses the problems of validity and reliability of the programs,

4 - the last part shows how the problems created by the constraints of memory were resolved and how the performance of the programs was increased.

6.1 DESCRIPTION OF THE LASER SIMULATION PROGRAMS

Even though each program is essentially different from the other, all the programs use similar numerical techniques to solve the nonlinear propagation equations (Maxwell) and the atomic equations (Bloch). These equations are solved simultaneously by a dynamic predictor/corrector algorithm: the predictor used generally is the explicit method of the middle point (Euler's modified formula), the corrector used is the trapezoid.

Moreover, nonlinearly defined axes (transverse axes, temporal axes) are used in order to increase the efficiency of the predictor/corrector algorithm. These axes determine a non-uniform multi-dimensional meshing that show, around the focal point along the propagation axis, the interesting phenomena of the beam. Depending on the choice and the nature of the phenomena studied, this non-uniform meshing can be calculated statistically either at the beginning of the simulation or redefined locally as the simulation is in progress (dynamic adaptation) to check the rapid changes in self-focusing.

The names of the laser simulation programs follow these conventions:

a - the prefix LR means LaseR;

b - the number following the prefix indicates the number of lasers used in the simulation;

c - the letter immediately following this number shows the implication of radial symmetry (C for Cylinder, thus one transverse axis) or its absence (P for Parallelepiped, thus two transverse axes, x and y);

d - the letters or numbers that follow denote the principal characteristics of the program.

Also, the axes used in the different programs are designated as follows:

- longitudinal axis of the cylinder or parallelepiped: axis z;

- radial symmetry axis of the cylinder: axis r;

- Cartesian transverse axes of the parallelepiped: axis x and axis y;

- temporal axis: axis t;

- axis of frequencies: axis ω.

Following is the description of the laser simulation programs already integrated in the system and using the SIMRES software to produce the simulation results.

1) The LR1CFS program (F for frequency and S for statistics): the simulation is defined by the z, r, t, ω axes. The model is based on the scalar wave equation coupled to the two-level resonant atomic system without degeneracy. This program offers the following options:

- the possibility of inclusion of the transverse effects (activation of the r axis of the cylinder): this shows the increase in the inhomogeneities and the importance of the nonlinear dispersion and the nonlinear absorption;

- the possibility of inclusion of the quantum fluctuations in the medium initiation for superfluorescence evolution (activation of statistics calculations);

- possibility of inclusion of the "extended" Doppler effects (activation of the ω axis associated with the atomic system).

It is also possible to include in this simulation all these possibilities at the same time.

2) The LR1PS program (S for statistics): the simulation is defined by the z, x, y, t axes. This model is essentially the same as the one used in LR1CFS without the inclusion of the extended Doppler effects into the program. The following characteristics should be noted however:

- the transverse axes x and y are only defined for the positive quadrant: i.e., the x axis is defined from 0.0 to xmax and the y axis is defined from 0.0 to ymax;

- the transverse effects on one axis can be activated without necessarily activating the transverse effects on the other axis;

- the maximal delimiter chosen on the x axis (xmax) can be different from the maximal delimiter (ymax) on the y axis: this allows for a larger choice of situations.

3) The LR1P4S program (S for statistics and 4 to indicate that the transverse axes cover the four quadrants): the simulation is defined by the z, x, y and t axes. This model is identical to the one used in the LR1PS program except for the two following points:

- the transverse effects cannot be removed: i.e., the x axis is necessarily defined from -xmax to xmax and the y axis is defined from -ymax to ymax;

- the minimal and maximal delimiters of the two axes are equal to one another, i.e., -xmax = -ymax and xmax = ymax.

4) In the LR12C program, the simulation is defined by the z, r, t axes. This model is based on two scalar equations of the propagation movement defined by 2 intense ultra-wave laser beams propagating simultaneously through a gas of three-level atoms. This model shows the interaction between the two beams and how they influence each other. This program allows for the possibility of inclusion of the transverse effects on the simulation.

The following programs are not yet integrated to the system but will soon be added to the four programs described above.

5) The LR2CFS program (F for frequency and S for statistics): the simulation is defined by the z, r, t, ω axes. The model used here is essentially the same as the one described in LR2C except that, as in the LR1CFS program, it offers the following options:

- the possibility of including transverse effects;

- the possibility of including statistical calculation (quantum fluctuations);

- the possibility of including the extended Doppler effects.

When this program will be integrated to the rest of the system, it will completely replace the LR2C program.

6) The LR1CC program (C for chemistry): this simulation is defined by the z, r, t axes. The model is similar to that used in the LR1CFS program but with a more refined atomic configuration system to allow for a six of ten levels of absorption. This model thus permits the study of the effects of coherent propagation in the multi-level atomic configuration such as Europium.

7) The LR1PH program (H for hydrodynamic): the simulation is defined by the z, x, y axes. This model is based on a hydrodynamic formulation. In order to avoid the oscillatory behavior resulting from the decomposition of the electrical field into its real and imaginary parts, it is necessary to describe the field by using the modulus and the phase, or equivalently, by using the field energy and the transverse gradient of its phase. The evolution of the beam can thus be seen as a flowing fluid whose density is proportional to the field energy and whose velocity is proportional to the gradient of the phase. This description leads to a generalized Navier-Stockes equation of motion for a compressible fluid subjected to an internal potential which depends solely and nonlinearly on fluid density and its derivatives.

8) The LR1CP program (P for plasma): the simulation is defined by the z, r axes. This is based on a simplified LR1CFS program: the transient effect is eliminated and the temporal variation is disregarded, what is calculated here is the asymptotic effects and adiabatic approximation response of the atomic field (off-resonance). The nonlinear field is characterized by an analytical susceptibility where the light-matter interaction is instantaneous (unlike the model used by the LR1CFS program). This nonlinearity is cubic in nature: thus the Kerr effect. However, this effect can be corrected and limited by a saturation or even by a nonlinear exponentiality. The laser can therefore describe the evolution of the electromagnetic field in a plasma medium governed by these kinds of nonlinearities.

9) The LR1PP program (P for plasma): the simulation is defined by the z, x and y axes. It is essentially the same model as the one described in 8) but without the radial simmetry.

10) The LR1CT program (T for transistor): the simulation is defined by the z, r and tφ axes. The model used here is based on the following approach: when two waves going in opposite directions (a forward wave and a backward wave) interact coherently with each other and with a medium resonant to the pulse frequency, this pulse adapts itself longitudinally and transversely during the simulation. The dynamic cross-coupling of these two waves appears explicitely in a two-mode equation analogous to the traditional one-mode Bloch equation describing the two-level absorption system. The variation of phase and the amplitude of the linear field polarized in the transverse direction are described by two wave equations, one for each mode: forward travelling propagation and backward travelling propagation. The equations derive from the Maxwell equation comprising the transverse and transient phase variations. φ denotes the spatial frequency harmonies associated with the standing wave nature of the field.

The algorithm used to solve these equations is a generalization of Moretti's scheme for the integration of the Euler equation of compressible flow. It is an explicit algorithm which demands a simultaneous integration along the t axis for both waves and which also takes into consideration the directional derivations to check the mutual influence of the two waves while respecting the law of forbidden signals. The program thus allows a unified simulation of the soliton collision, of the two-wave superfluorescence and of the optical instability phenomena in a nonlinear Fabry Perot cavity.

11) The LR1CI program (I for implicit): the simulation is defined by the z, r and t axes. The model used here is similar to those used for the LR1CFS and the LR1CC programs, however this model uses an implicit efficient algorithm with dynamically adapting grids: to achieve a greater stability and a greater exactitude, in many cases, the algorithm is obtained by expressing the variable on the left side of a given equation in terms of an integral on the variables on the right side of that equation. The field equation solution is determined in terms of average quantities that varies less rapidly than the original variables. Every mesh point is determined with the associate neighboring points: the resulting triadiagonal Bloch matrix is solved by recurrence method.

The program offers the possibility of studying the influence of diffraction, of density variation and of the inertial response in a multi-level system for a large number of experimental parameters.

6.2 GENERAL CHARACTERISTICS OF THE LASER SIMULATION PROGRAMS

Several problems arise from the frequent modifications, from the handling by different users and from the transportation and implantation of these programs into other computers. These problems can be summarized as follows:

- general comprehension of the programs;
- detailed comprehension of the code;
- ease of program modification;
- transportability of the programs.

In order to answer all these requirements, the programs must adhere to certain basic criteria which make their manipulation and maintenance easier; these are:

- the documentation of the programs;
- the use of standard FORTRAN;
- the modularity of the programs.

It is important to point out here that all the laser simulation programs as well as the softwares presented here adhere to these requirements.

6.2.1 DOCUMENTATION

Following is presented the complete description of these programs when dealing with the above mentioned requirements of general comprehension.

- the principal program includes a summary description of the model used and a complete description of its algorithm;
- all the physical parameters (program data) are adequately reported;
- each subroutine of the program has a detailed description of its role in the program and, if need be, of its algorithm;
- the code of the principal program is reported in its smallest detail;
- all the global variables of the program (i.e. variables in the commons) and specific to the subroutines, as well as their parameters, are explicitely described as per their usage.

Not only is a proper and extensive documentation a time-saving device but it also allows a more detailed analysis of the program at hand.

6.2.2 TRANSPORTABILITY

The laser simulation programs can be installed on different kinds of computers, therefore they must be easily transportable. As a general rule, and whenever possible and feasible, these programs are coded in standard Fortran (ANSI).

Thus all the programs use identifiers (i.e. names of subroutines, variables, parameters, etc.) with at the most six alphanumeric characters: in fact, most Fortran programs installed in computers other than CDC or CRAY do not permit more than the maximum six characters allowed by the standard Fortran. Nevertheless, some non-standard statements, such as GOTO, the PROGRAM declaration, the indices in form of expression, etc., can also be used because most Fortran language processor accept these statements.

It is worth noting that the use of standard statements was promoted by the criterion of majority. The only exception to this is the BUFFER IN and BUFFER OUT used for pagination done for efficiency. More information about this will be given in section 6.4.

6.2.3 MODULARITY

The first advantage of modularity is the simplicity and clarity it brings to the program; that is: in the laser simulation programs, a subroutine performs only one precise task. For example: the CIDTAU subroutine of the LRICFS program deals with the calculations of the temporal axis and of its derivatives. The second advantage of modularity resides in the ease of introducing additions, modification or corrections to the program. In fact, when a program has been cut into simple functional and independent modules, its model can be refined (thus a new code) without upsetting all its structure. Moreover, any modification to the program will remain localized (i.e. modifying a numerical integration algorithm for a function) and its effects will be better understood; in other words, the risks of unexpected errors, produced by these modifications, will be considerably diminished.

Following is the general diagram of the LRICFS program (figures 6.2.1, 6.2.2 and 6.2.3).

6.3 MANAGEMENT CONTROL AND VALIDITY OF THE RESULTS

Two interdependent problems result from the relatively frequent modification to the laser simulation programs, whether these modifications are for the improvement of the performance or for refining the models at hand. These problems are:

- the minimization of errors due to modifications to the program;
- verification of the validity of the results.

6.3.1 HANDLING AND MANAGING THE PROGRAMS

All the laser simulation programs are controlled by the CDC UPDATE program which produces program libraries. Thus it is possible to keep a complete inventory of the programs and to retrieve anterior versions as each new modification to the programs generates a new version.

This method offers the advantage of:

- controlling the results: one is certain that a specific result was produced by a precise version of the program and the relevance of this result is verified in its production context;

- controlling all the modifications effected to the program over a period of time. It is thus possible to have a detailed verification of the code if there is a need to check the compatibility of certain results with others, previously produced.

Another advantage resides in the fact that all the laser simulation programs are centralized on the same file. Moreover, because it is necessary to use the UPDATE program to make any modification or addition to these programs, their manipulation must be very precise. It follows that the errors (accidental destruction of files, presentation of a wrong program), and the proliferation of more or less similar programs (i.e. different versions) stored on several different files are kept to a minimum, this in spite of the fact that a programmer always tends to create working space by using several files.

Given its facility and its great security, this practice has encompassed all the programs and software presented in this paper.

6.3.2 RELIABILITY OF THE PROGRAMS AND VALIDITY OF THE RESULTS

Validity of the results is one of the trickiest problems to deal with. Usually, a semantically faulty program will blow up, sometimes however the program will run till the end and produces completely wrong results. A program using integration techniques with slow evolving numerical values may be quite resistant to such minor errors as the use of a wrong constant in an equation or a wrong sign. The problem is then to recognize the wrong results.

The surest way of verifying the validity of the results is to test the program with previously obtained results known as valid. There is the possibility that the results obtained in the new version may not be strictly identical to the previous results (results are said to be identical when, for a given function and a given point, all the significant numbers are identical) however these may not be necessarily wrong. Indeed, if any modification to the program dealt with the numerical algorithm, or even with the order of certain calculations, the results will be slightly different (for example, only the first significant n numbers in the two versions agree). It is thus necessary to establish a percentage below which the results may be considered as valid and above which these can be seen as doubtful.

Moreover, one test only may be quite inadequate when dealing specifically with the reliability of the programs. With the introduction of modifications to the statistics of the LRICPS program for instance, it will be necessary to determine whether the new version will function with or without the transverse effects, with or without frequencies. A minimum of four tests will be necessary in order to ascertain the proper running of the program. According to the importance of the modifications carried out, it is important to choose the most exhaustive set of tests to cover all the possible effects of the modifications on the model used in the program. The validity of the results will thus be verified in <u>all</u> cases (i.e. for any set of parameters).

This testing procedure with the mechanism of using other versions in program libraries establishes a consistency between the results of the different versions of the same program.

6.4 CONSTRAINTS OF THE LASER SIMULATION PROGRAMS

Like many other programs, those of laser simulation fall under two major constraints:

- the memory available on a computer, and

- the efficiency of the programs.

6.4.1 MEMORY

Two main factors must be dealt with, first:

- the rather small memory of the computer these programs run on: for example, depending on the equipment, the memory of the CYBER computers series 170 may vary between $300K_8$ and $400K_8$ words;

- the variable size of the programs are determined by the number of words sampled on the axes that define the simulation.

One of the smallest programs, the LRICPS, will be used to show the importance of these two factors. This program depends on the following four axes:

- the z axis: longitudinal axis of the cylinder

- the r axis: radial axis (of symmetry) of the cylinder

- the t axis: temporal axis

- the ω axis: frequency axis.

Let us call E the electromagnetic field and DE the field derivative in connection to z: these two quantities depend explicitely on the z, r and t axes. For the purpose of this discussion, the ω axis will not be used. Moreover, if L is the current plane associated with the z axis and i is that associated with the r axis, and if k is the current point associated with the t axis; when the used predictor is considered (modified mid-point method) then: $E(L,i,k) = E(L-2,i,k) + (\Delta z/2) \times (DE(L-1,i,k) + DE(L,i,k))$; as can be seen, the three planes L-2, L-1, L of E and the two planes L-1 and L of DE must be kept. It should be noted that the quantities of E and DE are complex (i.e. one word must be counted for the real part and one word for the imaginary part).

With these informations, the size of the program can be assessed. Let us consider the following three cases:

a) 32 points on the r axis and 64 points on the t axis;

b) 64 points on the r axis and 128 points on the t axis;

c) 64 points on the r axis and 192 points on the t axis.

The code and other variable will occupy a total of $50K_8$ words.

Following are the calculations to find out the size of the programs:

a) required memory for E and DE: $(3+2)x2x32x64 = 50K_8$ words; total memory required: $50K_8+50K_8 = 120K_8$ words;

b) required memory for E and DE: $(3+2)x2x64x128 = 240K_8$ words; total memory required: $50K_8+240K_8 = 310K_8$ words;

c) required memory for E and DE: $(3+2)x2x64x192 = 360K_8$ words; total memory required: $50K_8+360K_8 = 430K_8$ words.

Depending on the number of points on the axes, it can be noted that the size of the very same program may fluctuate surprisingly. With facilities that can deal only with $300K_8$ to $400K_8$ words, like in cases b and c, there will be serious problems to face. Moreover, certain programs without the radial symmetry hypothesis, like the LR1PS, require a far greater memory. In the LR1PS program, where the quantities of E and DE depend explicitely on the z, x, y and the t axes, with 32 points on each of the transverse axes (x and y) and 64 points on the t axis, there is a need for $2400K_8$ words (i.e. $(3+2)x2x32x32x64$). This is indeed a major problem for most installations.

Nevertheless, the laser simulation programs have some common characteristics:

- the size of the programs in a function of the quantities of E and DE;

- the size needed by the programs in concentrated in two quantities E and DE (from 50% to 98% of the total size, depending on the program);

- the numerical integration uses a purely sequential algorithm in all the programs (i.e. inner loops structures).

One simple and direct way of solving the problem of memory is to use the computer disks to compensate the central memory; these disks have a great capacity to store information. Thus, as the calculations of the E and DE quantities proceed by successive iterations on the planes (z axis), the values of the quantities of E and DE, for a given plane are stored on a disk (writing operation), when these values are needed for prediction or corrections calculations of a given point of the r axis at given point on the t axis, all that is needed is to retrieve them from the disk (reading operation): this procedure is called pagination.

More precisely, the planes L-2, L-1 and L of E and the planes L-1 and L of DE will be associated to five binary files sequentially manipulated by the Fortran statements BUFFER IN and BUFFER OUT (writing and reading). What remains now is to define the buffers associated to the five files and to manipulate the values these deal with.

At this point, there is a need to distinguish two categories of programs:

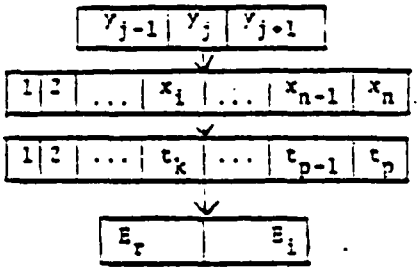

where y_j: jth line on the matrix
n : total number of points on x axis
p : total number of points on t axis
x_i: ith point on x axis
t_k: kth point on t axis
E_r: real part of E
E_i: imaginary part of E

The control of this buffer is similar to the one described in 1) but there is no need here to manipulate the sections of the x axis as all the line fits in the buffer. However, to control the three lines of the buffer, it is necessary to define the supplementary pointers. For the same reasons, the buffer associated to the files holding the values of DE on the L-1 plane will have a similar structure but it will have only the two lines y_{j-1} and y_j. All the other buffers for E and DE will control only one y_j line at a time.

As in 1), the pointers on the files are used to go from plane to plane, yet the solution here is not as versatile. The main problem here is the great size of the buffers. In fact, for 32 points on the x axis and 64 points on the t axis, the size of the buffer controlling the three lines will be of $3x2x32x64 = 30K_8$ words. Keeping in mind the fact that there are several buffers, and considering the memory needed by the code and the other variables (nearly $70K_8$ words for the LR1PS program), there will be $160K_8$ words for LR1PS. By changing the number of points on the axis, it will be easy to reach the $300K_8$ words of the computers used here.

Finally, it is necessary to note that in the two solutions presented here, only four buffers are needed instead of five, even though there are five files to control. In fact, as there is never any need for the values of E on the L-2 plane and for the L-1 plane simultaneously (the L-2 plane is used for prediction and the L-1 for correction). It is possible to use the same buffer to control the two files associated to these planes for the values of E.

6.4.2 EFFICIENCY

The pagination of the laser simulation programs may be the first source of inefficiency. In fact, it is slower to read or write a word on a disk than to accede to an address in core memory (primary storage). In order for the pagination not to affect the performance of the program to a great extent, the following rules have been adopted:

- using buffers large enough to minimize the access to the disk;
- using the statements BUFFER IN and BUFFER OUT to read and write the buffers on file, these statements are three times faster than equivalent binary statements READ and WRITE;
- using pointers for the control of files and buffers in order to avoid unnecessary manipulations (displacements of the values in the buffers, transfer of values from one file to another, etc.);
- non-usage of auxilary panels for calculations (these will be done directly in the buffers) in order to avoid supplementary transfers.

Beside pagination, other points dealing with the efficiency of the programs must be checked:

- given the inner loops structure of this kind of programs, it is necessary to avoid the transfer of variables as parameters in the subroutines called for by the inner loops. For example, each variable transferred in parameter in the C1DRVE (or C1DRVP) subroutine of the LR1CPS program will increase the total running time of the program by 0.5%, and if this subroutine has 10 variables transferred in parameters, the running time of the program will be increased by 5%: this is quite significant.
- It is necessary to minimize the number of divisions and multiplications in the equation used in the subroutines of the inner loops. This can be done, when possible, by linking all the constant terms for each point of the same axis and by storing the result in a panel subject to this axis. In that way, it will be possible to replace many multiplications and divisions by one multiplication and one address calculation (access to the element in the panel).

For example, the running time of the LR1CPS program without storing the pagination mechanism goes from 500 seconds (on a CYBER 173) to 350 seconds but with the storing of the pagination mechanism, the gain is of 30%.

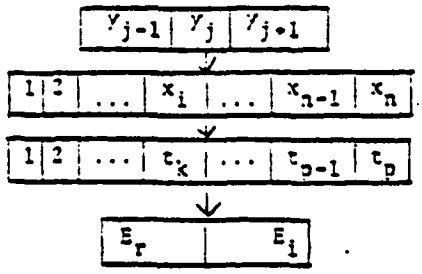

where y_j: jth line on the matrix
n : total number of points on x axis
p : total number of points on t axis
x_i: ith point on x axis
t_k: kth point on t axis
E_r: real part of E
E_i: imaginary part of E

The control of this buffer is similar to the one described in 1) but there is no need here to manipulate the sections of the x axis as all the line fits in the buffer. However, to control the three lines of the buffer, it is necessary to define the supplementary pointers. For the same reasons, the buffer associated to the files holding the values of DE on the L-1 plane will have a similar structure but it will have only the two lines y_{j-1} and y_j. All the other buffers for E and DE will control only one y_j line at a time.

As in 1), the pointers on the files are used to go from plane to plane, yet the solution here is not as versatile. The main problem here is the great size of the buffers. In fact, for 32 points on the x axis and 64 points on the t axis, the size of the buffer controlling the three lines will be of $3x2x32x64 = 30K_8$ words. Keeping in mind the fact that there are several buffers, and considering the memory needed by the code and the other variables (nearly $70K_8$ words for the LR1PS program), there will be $160K_8$ words for LR1PS. By changing the number of points on the axis, it will be easy to reach the $300K_8$ words of the computers used here.

Finally, it is necessary to note that in the two solutions presented here, only four buffers are needed instead of five, even though there are five files to control. In fact, as there is never any need for the values of E on the L-2 plane and for the L-1 plane simultaneously (the L-2 plane is used for prediction and the L-1 for correction). It is possible to use the same buffer to control the two files associated to these planes for the values of E.

6.4.2 EFFICIENCY

The pagination of the laser simulation programs may be the first source of inefficiency. In fact, it is slower to read or write a word on a disk than to accede to an address in core memory (primary storage). In order for the pagination not to affect the performance of the program to a great extent, the following rules have been adopted:

- using buffers large enough to minimize the access to the disk;
- using the statements BUFFER IN and BUFFER OUT to read and write the buffers on file, these statements are three times faster than equivalent binary statements READ and WRITE;
- using pointers for the control of files and buffers in order to avoid unnecessary manipulations (displacements of the values in the buffers, transfer of values from one file to another, etc.);
- non-usage of auxilary panels for calculations (these will be done directly in the buffers) in order to avoid supplementary transfers.

Beside pagination, other points dealing with the efficiency of the programs must be checked:

- given the inner loops structure of this kind of programs, it is necessary to avoid the transfer of variables as parameters in the subroutines called for by the inner loops. For example, each variable transferred in parameter in the C1DRVE (or C1DRVP) subroutine of the LR1CPS program will increase the total running time of the program by 0.5%, and if this subroutine has 10 variables transferred in parameters, the running time of the program will be increased by 5%: this is quite significant.
- It is necessary to minimize the number of divisions and multiplications in the equation used in the subroutines of the inner loops. This can be done, when possible, by linking all the constant terms for each point of the same axis and by storing the result in a panel subject to this axis. In that way, it will be possible to replace many multiplications and divisions by one multiplication and one address calculation (access to the element in the panel).

For example, the running time of the LR1CFS program without storing the pagination mechanism goes from 500 seconds (on a CYBER 173) to 350 seconds but with the storing of the pagination mechanism, the gain is of 30%.

Terms used in the diagrams

eta: longitudinal axis of the cylinder
rho: transverse axis of the cylinder (symmetry axis)
tau: temporal axis t
dwn: frequency axis w (associated to the material)
material: polarization P (complex quantity) and energy W
E : electromagnetic field (complex quantity)
DE : field derivation in terms of eta (complex quantity)
L : Lth plane on the eta axis
i : ith point on the rho axis
k : kth point on the tau axis
Euler formula: E(L,i,k) E(L-1,i,k) zXDE(L-1,i,k)
Modified Euler formula: E(L,i,k) E(L-2,i,k) (zX2)XDE(L-1,i,k)
Trapezoid method: E(L,i,k) E(L-1,i,k) (z/s)X(DE(L,i,k)DE(L-1,i,k)
PHI0, PHI2: initial tilting angles used in material calculation
Statistics: indicate that depending on certain distributions, the PHI0 and PHI2 angles will be randomly generated

Key to figures

**********: sub-routine contents

= = = = = =: loop on the number of laser simulations; (sta)

_ _ _ _ _ _: loop on the eta axis

----------: loop on the rho axis

__________: loop on the tau axis

.... loop on the dwn axis

The loops on the sta, rho and dwn axes are optional, i.e. it depends on the activation of certain effects in the simulation.

FIGURE 6.2.1 - GENERAL DIAGRAM OF THE C1IUVW SUB-ROUTINE

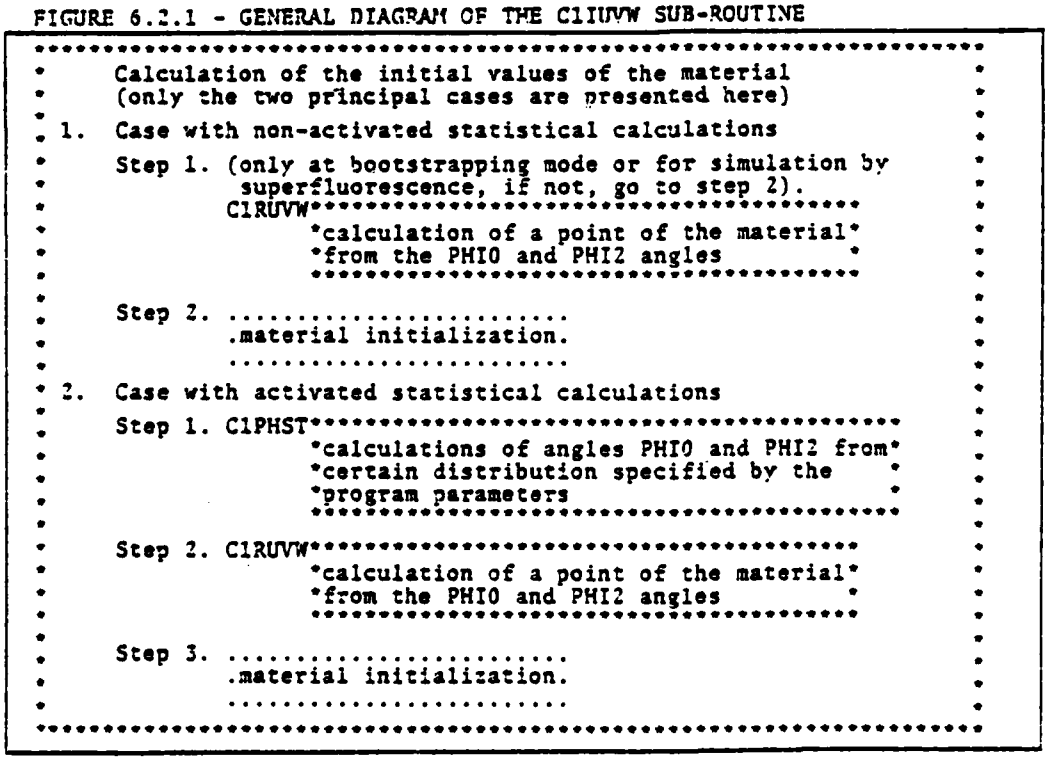

FIGURE 6.2.2 - GENERAL DIAGRAM OF THE C1INTG SUB-ROUTINE

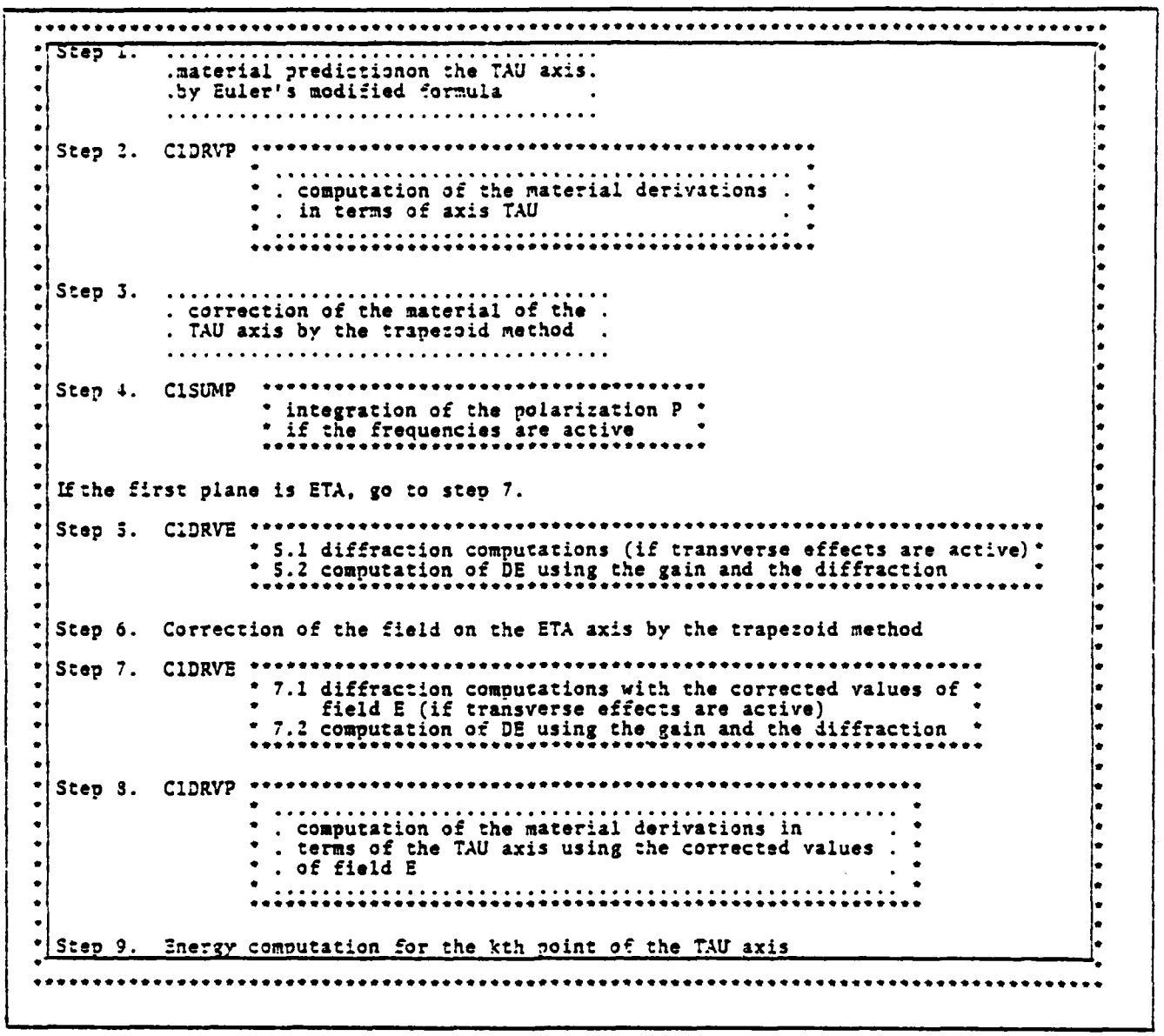

FIGURE 6.2.3 (cont'd)

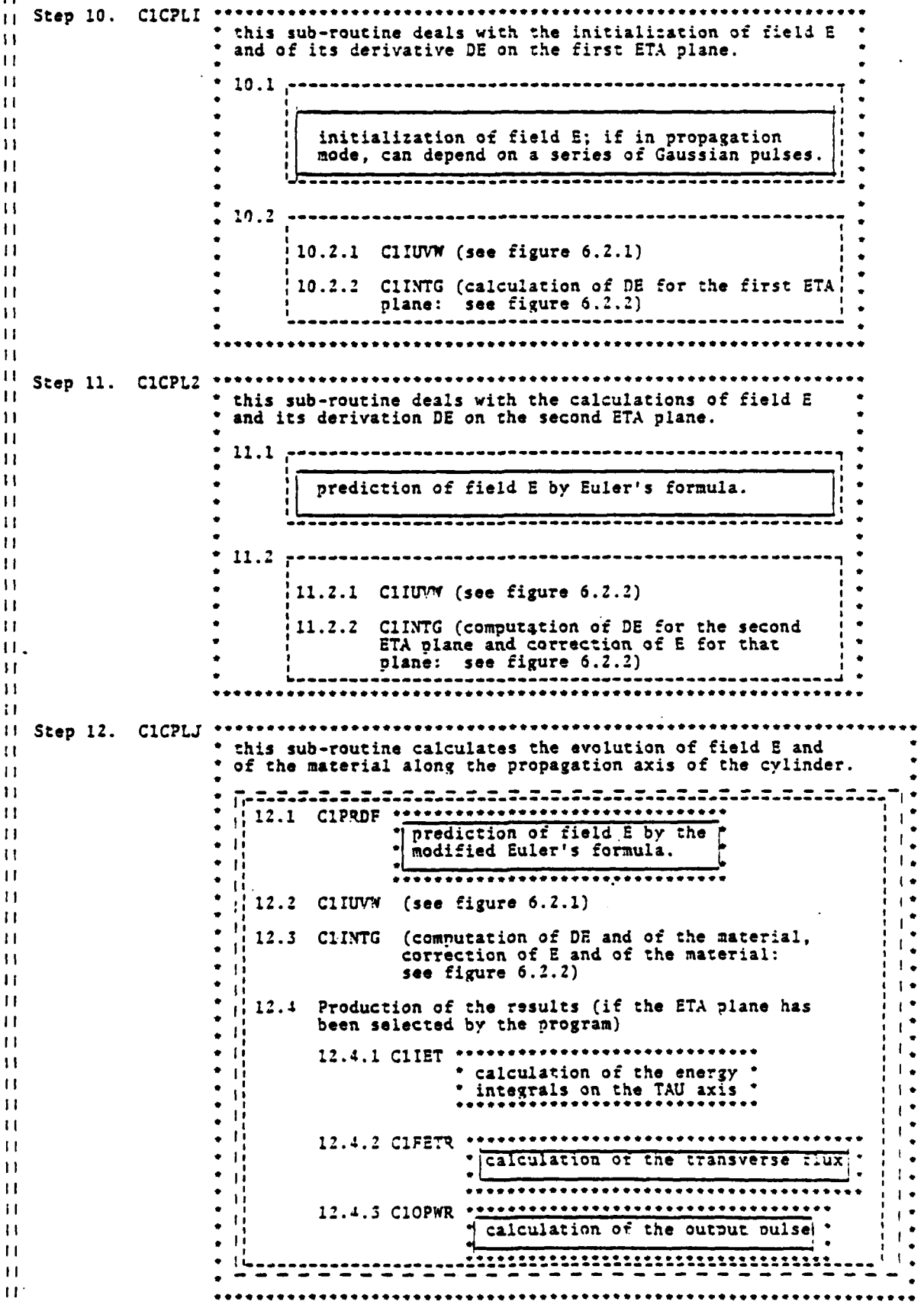

FIGURE 6.2.3 - GENERAL DIAGRAM OF THE LRICFS PROGRAM

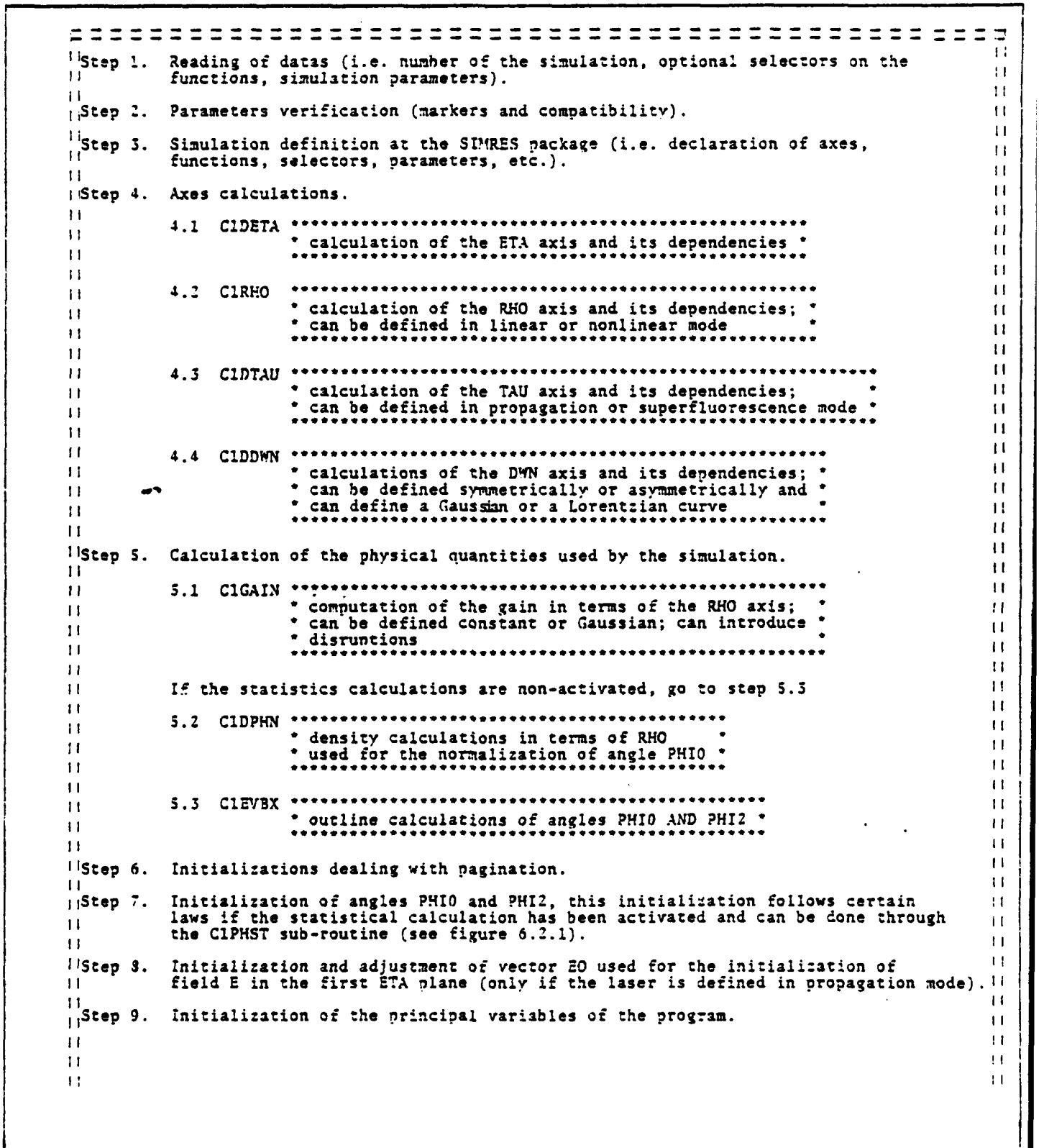

FIGURE 6.2.3 (cont'd)

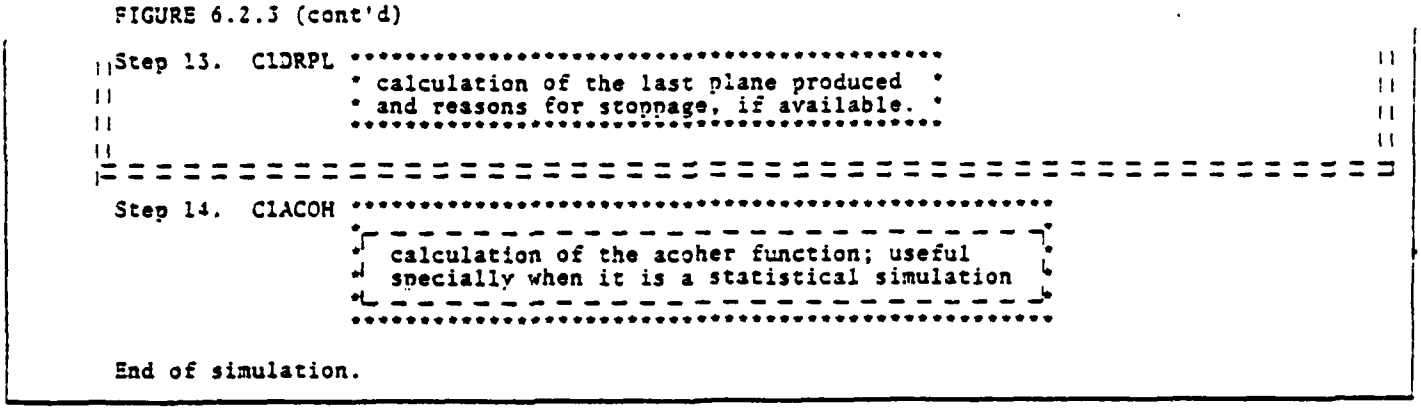

VII - CONCLUSION

It is noteworthy to state at this point that the functioning part of the system corresponds to the packages in section IV and to an appreciable part of the laser simulation programs presented in section VI (LR1CFS, LR2CFS, LR1PS, LR1P4S, LR1CP, LR1PP). The programs of application DEFPARM, DESRES and SYNTH are still being developed, however DEFPARM and DESRES are already in use.

In conclusion, it would be of value to review our objectives and to examine how the software developed for the laser model building project answered our expectations.

With respect to modularity, it is evident at this stage that a considerable effort has been extended to divide the work into concrete jobs and to limit these different jobs into procedures or groups of procedures. By their very definition and by their conception, these packages constitute evident examples of modularity. This modularity can be also found in the step by step division of the programs of application.

As to flexibility, there was an effort, all along the conception of the new system, to identify the problems of general concern by liberating us of the specific constraints of the laser project in order to concentrate on the fundamental aspects of the tasks at hand. It follows that the softwares thus developed have enough flexibility to be adapted to the different situations arising within the same laser model building project or even to be adapted to other projects where to results are functions and where there is a sufficient quantity of results to justify a data bank.

The question of security is more difficult to evaluate. Nevertheless, the use of techniques such as data validation, exhaustive tests during the set up period, etc., increase the security aspects of the programs. Moreover, splitting up the work into modules facilitates the inception and set up of the programs and contributes to their strength. Finally, the fact of using these programs in the context of production makes it easier to test them and to find their loopholes.

As to efficiency, it is clear that the development of more complex laser models has forced us to take into consideration of execution time and memory requirements. For instance, the direct access to the SIMRES and DATSIM files has increased the efficiency of the application programs and made them more amenable to use in the interactif. Moreover, the use of pagination in the laser modeling programs has cut down the size of the programs, and facilitates their use on computer with limited memory.

Much attention was given to transportability in order, on the one hand, to execute certain laser programs on computers more powerful than those at our disposal, and on other, to use our auxiliary software in other projects. To make the software more transportable, we have chosen to write it FORTRAN IV and to respect the ANSI standard. Moreover, we have isolated in procedures the instructions or portions of code that are particular to a given environment (like the files direct access subroutines) thus making it easy to locate what is to be modified in order to transfer the software to another system.

With respect to documentation finally, we have established and tried to follow a strict standard for the programs comments. We expect to publish (internal publication) a technical report and a user's manual for the different packages and the programs dealt with in this document.

ACKNOWLEDGEMENTS

This work would not have been possible without the help of several people who have given us technical help and who have stimulated and enlightened us with their invaluable advice. Not least among them are Dr. J. Teichman, Dr. R. Zahar and Dr. W. Armstrong. By their hospitality, they have made this project possible at the Université de Montréal.

As to the Physics, Dr. Farres P. Mattar wishes to acknowledge the extensive discussions with Prof. G. Moretti, Dr. J. Herrman, Dr. B.R. Suydam, Dr. J. Fleck and Dr. R.E. Francoeur who have helped in the development of the computational algorithms used in the laser programs.

The collaboration of C. Goutier, M. Béliveau and M. Lavoie with regards to the development of the productions system is greatly appreciated.

We also wish to thank Miss D. Reid for the translation of the first three sections and Miss W. Bashour for the translation of the last three sections of this document originally written in French. The skilful typing of Miss L. Leclair is commended with pleasure.

BIBLIOGRAPHY

Software for the Laser Project

1. P. CADIEUX, M. CORMIER, Y. CLAUDE, C. GOUTIER and F.P. MATTAR, Proc. of The Twelfth Annual Pittsburgh Conference of Modeling and Simulation, Ed. W.G. Vogt and M.H. Mickle, published by Instrument Society of America (May 1981), p. 1527.

Cylindrical Laser

2. F.P. Mattar and M.C. NEWSTEIN, Proc. Seventh Conf. on Numerical Simulation of Plasma, Courant Inst., New York Univ. (June 1975), p. 225.

3. F.P. MATTAR, Adaptative Stretching & Rezoning as Effective Computational Techniques for Two Level Paraaxial Maxwell-Bloch Simulation, Tech. note 03, Laboratory for Laser Energetics, University of Rochester, Rochester, N.Y.

Adaptative Rezoning

4. F.P. MATTAR, Appl. Phys. 17, 53 (1978).

5. F.P. MATTAR and M.C. NEWSTEIN, Comp. Phys. Comm. 20, 139 (1980).

Implicit Laser

6. F.P. MATTAR, Proc. of Ninth Conf. of Numerical Methods in Plasma, Monteray, Calif. (June 1978), Lawrence Livermore Lab. Tech. Rep. LLL 78-004.

Hydrodynamic Laser

7. F.P. MATTAR, J. TEICHMAN, L. BISSONNETTE and R.W. MacCORMACK, Proc. of Second Int'l Symp. on Gas Flow and Chemical Lasers, Ed. by J. Wendt, Western Hemisphere Pub. (1979).

8. F.P. MATTAR and J. TEICHMAN, Comp. Phys. Comm 22, 1 (1981).

Transistor Laser

9. F.P. MATTAR, Proc. of Eleventh Congress for the International Commission for Optics, Ed. J. Besca, Madrid (1979).

10. F.P. MATTAR, G. MORETTI and R.E. FRANCOEUR, Comp. Phys. Comm. 23, 1 (1981).

Double Laser

11. F.P. MATTAR and J.M. EBERLY, Proc. of the Physics and Chemistry of Laser-Induced Processes in Molecules, Edimburgh (1978), Ed. K.L. Kompa and S.C. Smith, 61, Springer-Verlag.

Others

12. F.P. MATTAR and B.R. SUYDAM, A Novel Rezoned Implicit Algorithm for Coherent Propagation in Multi-Level System, Polytechnic Institute of New-York Aerodynamics Lab., Tech. Report (1982).

13. F.P. MATTAR, in Optical Bistability, Ed. C.M. Bowden, M. Ciftan and H.R. Robl, Plenum Press, New York (1981), p. 503.

F.P.1

IEEE International Quantum Electronics Conference
Munich (1982), Abstracts Digest Appl. Physics
Dec (1982) Springer Verlag

LIGHT CONTROL BY LIGHT WITH AN EXAMPLE IN COHERENT PUMP DYNAMICS, PROPAGATION, TRANSVERSE & DIFFRACTION EFFECTS IN THREE-LEVEL SUPERFLUORESCENCE

FARRES P. MATTAR*
Mechanical and Aerospace Engineering Department
Polytechnic Institute of New York, Brooklyn, NY 11201, USA, and
Spectroscopy Laboratory, Massachusetts Institute of Technology
Cambridge, MA 02139, USA, Telephone: (617) 253-7700

and
C. M. BOWDEN

Research Directorate, US Army Missile Laboratory, US Army
Missile Command, Redstone Arsenal, AL 35898, USA
Telephone: (205) 876-3342

ABSTRACT

A model and results are presented which describe copropagational coherent pump dynamics and evolving superfluorescence (SF). Specification of certain pump pulse initial conditions results in specific SF characteristics, as recently observed in CH_3F and Ba.

* Partially supported by the U. S. Army Research Office, the U. S. Office of Naval Research, the U. S. Science Foundation and Battelle Columbus Laboratories.

LIGHT CONTROL BY LIGHT WITH AN EXAMPLE IN COHERENT PUMP DYNAMICS, PROPAGATION, TRANSVERSE & DIFFRACTION EFFECTS IN THREE-LEVEL SUPERFLUORESCENCE

FARRES P. MATTAR*
Mechanical and Aerospace Engineering Department
Polytechnic Institute of New York, Brooklyn, NY 11201, USA
and Spectroscopy Laboratory, Massachusetts Institute of Technology
Cambridge, MA 02139, USA, Telephone: (617) 253-7700

and

C. M. BOWDEN
Research Directorate, U.S. Army Missile Laboratory, U.S. Army
Missile Command, Redstone Arsenal, AL 35898, USA
Telephone: (205) 876-3342

SUMMARY

Recently developed computational methods, are used to evaluate for the first time the dynamic longitudinal and transverse reshaping associated with the concomitant propagation of two light beams in a three-level medium. Neither the mean field theory [1] nor the adiabatic following [2] or even the rate equation [3] approximations have simplified this analysis. Instead, the full Maxwell-Bloch [4,5] equations with phase and diffraction effects [6] included are solved rigorously, using self-consistent numerical methods [7].

A new concept in nonlinear light matter interactions is introduced: The results obtained for the first time display the conditions under which an injected light pulse of a given frequency can be used to shape and control a second light pulse of a different frequency coupled through the nonlinear three-level medium. Thus, a specific aspect of the phenomenon of light control by light is demonstrated [8].

The model has been applied to double coherent transients (i.e., double self-induced transparency) and to the pump dynamics effects in superfluorescence (SF).

The goal of this paper is to illustrate how the output characteristics of the collective spontaneous emission of the SF pulse [9] (such as delay time, pulse width, peak intensity, shape, etc.) can be controlled, deterministically, by appropriately selecting certain initial and boundary conditions for the injected pump pulse.

---

* Partially supported by the U.S. Army Research Office, the U. S. Office of Naval Research, the U.S. Science Foundation and Battelle Columbus Laboratories.

With the exception of Bowden and Sung [10], all theoretical work has dealt exclusively with the relaxation process from a prepared state of complete inversion in a two-level manifold of atomic energy levels, and thus do not consider the dynamic effects of the pumping process. Yet, all reported experimental work has utilized optical pumping on a minimum manifold of three atomic [11-13] or molecular [14-15] energy levels by laser pulse injection into the nonlinear medium, which subsequently superfluoresces. (Note that the two-level analysis is only valid for $\tau_R >> \tau_p$, where τ_R is the characteristic SF time and τ_p is the pump pulse temporal width, and has not been realized over the full range of reported data).

Our analysis extends ~~Contrary to~~ Bowden and Sung's analytical treatment, we do not confine our solution to the mean field regime and the linearized short time regime but have adopted the semiclassical model advanced by Feld and co-authors [16] where both transients and propagation effects are rigorously studied. Quantum fluctuations [17-19] are not discussed in the treatment; instead, a classical uniform (not random) tipping angle concept is used for initiating the polarization to simulate the fluorescence initiation. The latter method is well-established for both two- and three-level [20-21] propagation calculations. Since transverse effects are also considered, the obtained results also extend the pumpless analysis that previously modelled the Cs experiment [22].

In particular, it is shown that the injected coherent pump initial characteristics, such as on-axis area, temporal and radial width (and associated gain-length-Fresnel number), and shape alter the SF pulse characteristics. The effects of changing the effective gain [23] of either the SF or the pump transition and the density of active atoms are also studied.

For sufficiently large effective gain and/or large input pump area, the two light pulses overlap and the two-photon processes (RCR-resonant coherent Raman) make strong contributions to the mutual pulse development.

Dependencies of this type have been recently observed in methyl fluoride [24] and in barium [25]. Futhermore, under other conditions, we obtained a SF pulse of temporal width much less than that of the pump even though the two pulses temporally overlap. This calculation agrees qualitatively with the results of recent experiments in mode locked CO_2 pumped CH_3F [26].

o- F.P. Mattar Twelfth Pittsburgh Annual Modeling & Simulation conf (1979), Pittsburgh, Inst. Soc. of Am

REFERENCES

[1] R. Bonifacio and L.A. Lugiato, Phys. Rev. A11, 1507 (1975); and A12, 587 (1975).

[2] D. Grischkowsky, M.M.T. Loy and P.F. Liao, Phys. Rev. A12, 2514 (1975).

[3] A. Javan, Phys. Rev. 107, 1579 (1957).

A.M. Clogstar, J. Phys. Chem. Solids 4, 271 (1958).

R.L. Panock and R.J. Temkin, QE 13, 425 (1977).

[4] S.L. McCall and E.L. Hahn, Phys. Rev. 183, 457 (1967).

[5] R.G. Brewer and E.L. Hahn, Phys. Rev. A11, 1641 (1975).

[6] F.P. Mattar and M.C. Newstein, IEEE J. Quantuum Electron 13, 507 (1977).

[7] F.P. Mattar, Appl. Phys. 17, 53 (1978); F.P. Mattar and M.C. Newstein, Comput. Phys. Commun. 20, 139 (1980).

[8] F.P. Matter and C.M. Bowden, Topics of Current Physics: Multiple Photon Dissociation of Polyatomic Molecules, ed. C.D. Cantrell, Springer Verlag, 1982.

[9] R.H. Dicke, Phys. Rev. 93, 99 (1954).

[10] C.M. Bowden and C.C. Sung, Phys. Rev. A18, 1558 (1978); and A20, 2033 (1979).

[11] M. Gross, C. Fabre, P. Pillet and S. Haroche, Phys, Rev. Lett. 36, 1035 (1976).

[12] A. Flusberg, F. Mossberg and S.R. Hartmann, Cooperative Effects in Matter and Radiation, ed. C.M. Bowden, D.W. Howgate and H.R. Robl (Plenum Press, 1977) p. 139.

[13] H. M. Gibbs, Q.H.R. Vrehen and H.M.J. Hickspoocs, Phys, Rev. Lett. 39, 547 (1977).

[14] N. Skribanowitz, I.P. Herman, J.C. MacGillivray and M.S. Feld, Phys. Rev. Lett. 30, 309 (1973).

[15] J.J. Ehrlich, C.M. Bowden, D.W. Howgate, S.H. Lehnigk and T.A. DeTemple, Coherence and Quantum Optics IV, ed L. Mandel and E. Wolf (Plenum Press), 1978, p. 923.

[16] J.C. MacGillivray and M.S. Feld, Phys. Rev. A14, 1169 (1976).

[17] F. Haake, J. Haus, H. King, G. Schroder and R. Glauber, Phys. Rev. Lett. 45, 558 (1980).

[18] D. Polder, M.F.H. Schuurmans and Q.H.F. Vrehen, Phys. Rev. A19, 1192 (1979).

[19] F. Hopf, Phys. Rev. A20, 2064 (1979).

[20] M.S. Feld and J.C. MacGillivray, Coherent Nonlinear Optics, ed. M.S. Feld and V.S. Letokhov (Springer Verlag, 1980).

[21] J.R.R. Leite, R.S. Scheffield, M. Ducloy, R.D. Sharma and M.S. Feld, Phys. Rev. A14, 1151 (1976).

[22] F.P. Mattar, H.M. Gibbs, S.L. McCall and M.S. Feld, Phys. Rev. Lett. 46, 1123 (1981).

[23] F.P. Mattar and M.C. Newstein, Cooperative Effects in Matter and Radiation, ed. C.M. Bowden, D.W. Howgate and H.R. Robl (Plenum Press, 1977) p. 139.

[24] A.T. Rosenberger and T.A. DeTemple, Phys. Rev. A24, 868 (1981).

[25] A. Crubellier, S. Liberman, D. Mayou, P. Pillet and M.G. Schweighofer, Optics Lett. 7, 16 (1982).

[26] T.A. DeTemple, Private Communication.

DISTORTIONS OF A CW LIGHT BEAM PROPAGATING THROUGH GAS : SELF-LENSING AND SPATIAL RINGINGS

Martine Le Berre

Laboratoire des Signaux et Systèmes, Plateau du Moulon, 91190 Gif/Yvette, France

and

Farrès P. Mattar*

Laboratoire de Photophysique Moléculaire du CNRS, Bâtiment 213, 91405 Orsay, France
and Spectroscopy Laboratory, Massachusetts Institute of Technology,
Cambridge, Massachusetts 02139, Etats-Unis

and

Elisabeth Ressayre and Andrée Tallet

Laboratoire de Photophysique Moléculaire du CNRS, Bâtiment 213, 91405 Orsay, France.

Abstract

Transverse effects on the profile of an intense off-resonant cw light beam, propagating through a gazeous cell of length ℓ, are numerically displayed in both cases of the very small absorption length ($\alpha^{-1} \ll \ell$) and the intermediate case ($\alpha^{-1} \sim \ell$). As predicted by the theory, self-focusing and spatial ringings are obtained. Moreover for $\alpha\ell \sim 1$, these distorsions generally appear as a recurrent process.

Introduction

The profile of a cw light beam with an on-axis input intensity I_o was analytically shown to exhibit unusual distortions when propagating through an off-resonance optically thick absorber [1], such as

$$\alpha\ell >> I_o/I_s >> 1 , \quad \text{(Case I)} \quad . \tag{1}$$

The quantity α^{-1} denotes the off-resonance absorption length and I_s is the saturation intensity for a homogeneously broadened atom,

$$\alpha\ell = \frac{2\pi N \mu^2}{c\hbar} \frac{T_2}{1 + \delta^2 T_2^2}$$

$$I_s = (1 + \delta^2 T_2^2) / T_1 T_2 . \tag{2}$$

Within the framework (1), an approximate treatment [1] of the normalized Maxwell equation for a cw electric field with envelope $\varepsilon(\rho,z)$

$$(-i \nabla^2_T + \frac{\partial}{\partial Z}) \varepsilon(\rho,z) = -\frac{\alpha}{2} F \left(\frac{1 - i\delta T_2}{1 + |\frac{\mu}{\hbar}\varepsilon(\rho,z)|^2 / I_s}\right) \varepsilon(\rho,z) \tag{3}$$

displayed the formation of one or several concentric transverse rings of light after some propagation, either inside the cell or in the free space. Moreover self-focusing was also predicted for a blue-shifted excitation in spite of strong absorption losses. In Eq. (2), T_2 denotes the homogeneous lifetime and δ is the detuning between the atomic pulsation ω_a and the driving field pulsation ω_o. The undimensionnal variable ρ is the radial variable r scaled to the input beam waist r_o and Z is the axial variable z scaled to the diffraction length,

$$z_d = \frac{1}{2} r_o^2 \frac{\omega_o}{c} . \tag{4a}$$

* Partially supported by the US Army Research Office DAAG29-79-C0148; on extended leave of absence from Polytechnic Institute of New York.

The Fresnel number F for an absorption length is

$$F = \alpha z_d \ . \tag{4b}$$

It measures the ratio between the diffraction length and the absorption one and it was shown to be the check parameter for transverse effects in transient phenomena like S.I.T[2] and superfluorescence [3]. For large F, the loss (or gain) due to the atomic medium prevails on the diffraction loss while in the opposite case (F < 1) the diffraction losses generally prevent S.I.T. and superfluorescence [2,3].

In the present study governed by Eqs.(1) and (3), the balance between the diffraction and the atomic response, and then the shape of the intensity profile depend not only on F but also on I_o/I_s and δT_2. The analytical treatment just assumes that the beam experiences two regimes : from the entrance in the cell to a transition abcissa z_{NL}, the diffraction is taken as negligeable ($z_{NL} << z_d$). Through the cell, the wave-front undergoes distortions because of the interplay of nonlinearities and absorption only. It follows that at z_{NL} the wave-front is encoded, carrying away knowledge of the nonlinearities of the medium. Afterwards the driven intensity becomes so weak that the diffraction only causes further distortions of the beam, like in free space propagation. In summary the encoding of the wave-front results from the propagation equation

$$\frac{\partial}{\partial z}\,\mathcal{E}(\rho,z) = -\frac{2}{T}\,\frac{F(1 - i\,\delta T_2)}{1 + |\frac{\mu}{\hbar}\mathcal{E}(\rho,z)|^2/I_s}\,\mathcal{E}(\rho,z), \tag{5}$$

for any $0 < z < z_{NL}$, while self-focusing and multiple ringings arise from the diffraction equation

$$(-i\,\nabla^2_T + \frac{\partial}{\partial z})\,\mathcal{E}(\rho,z) = -2F(1 - i\,\delta T_2)\,\mathcal{E}(\rho,z) \quad , \tag{6}$$

which describes the distortion of the encoded envelope

$$\mathcal{E}(z_{NL},\rho) = \mathcal{E}_o(\rho)\; e^{-\frac{1}{2}(1 - i\,\delta T_2)\,(\alpha z_{NL} + [\frac{\mu}{\hbar}\mathcal{E}_o(\rho)]^2/I_s)} \tag{7}$$

for any $z \gtrsim z_{NL}$. The abcissa z_{NL} which locates the transition between the two regimes was found to obey approximately the law [1]

$$z_{NL} \simeq \frac{1}{\alpha}\,(\frac{I_o}{I_s} + 1) \tag{8}$$

that implies

$$\frac{I_o}{I_s} << F \tag{9}$$

when using Eq.(4) together with the inequality $z_{NL} << z_d$. Actually, Ineq.(9) is only a necessary condition for the diffraction to be negligible. A more detailed analysis showed that, near resonance, a sufficient condition for the diffraction to be negligible is

$$(\frac{I_o}{I_s})^3 << F \qquad (\delta T_2 \lesssim 1) \quad . \tag{10}$$

This latter condition can be generalized to large detunings, such as

$$\frac{1}{2}\,\delta T_2\,(\frac{I_o}{I_s})^2 << F \qquad (\delta T_2 >> 1). \tag{11}$$

In this paper we first present the results of a numerical simulation which confirm the validity of the theoretical model (case I). In a next section we extend our numerical study

to the case of weaker absorber, such as

$$\alpha \ell \sim I_o/I_s \sim 1 \qquad \text{(Case II)} , \tag{12}$$

for which there is presently no available analytical model. For such media the numerical calculations display the formation of several rings inside the cell for sufficiently large values of either F or δT_2. Experiments realized by Gibbs and Rushford [*] in the conditions (12) for some δT_2 as higher as 10^2, 10^3 and small F ~ 0.15 exhibited many transverse ringings. They will be discussed in details elsewhere.

Case I $(\alpha \ell >> I_o / I_s >> 1)$

In this section we compare the analytical calculations (Eqs.(5)-(7)) performed within the framework defined by Ineqs. (1) and (11) with the numerical solution of the field amplitude which obeys the full reduced Maxwell equation (2).

The input cross-section will be assumed to be gaussian. Both analytical and numerical transverse shapes of the intensity are plotted on Fig. 1 as the beam propagates, first inside the vapor cell ($0 \leq z \leq \ell = 0.03$) and next in the free space to ten times the cell length. The parameters $I_o/I_s = 2.31$, $\delta T_2 = +5$, $\alpha \ell = 4$ and $F = 29.3$ have been chosen in order to satisfy the conditions (1) and (11). Fig. 1 displays the good agreement between the analytical profile (broken lines) with the numerical one (full lines). Let us notice that the ringings take form after the transition point $z_{NL} = 0.025$ cm, and even only outside the cell. For z larger than the diffraction length the numerical solution exhibits a substructure of ringings for the two lateral large rings.

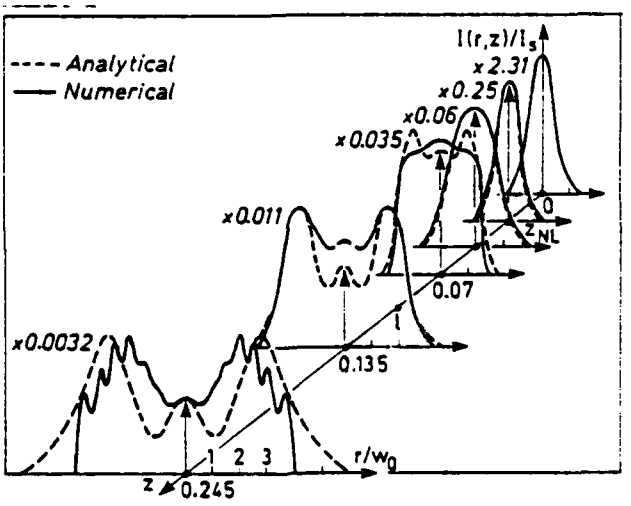

Figure 1. Transverse reshaping $I_o/I_s = 2.31$, $\alpha \ell = 4$, $\delta T_2 = +5$, $z_d = 0.22$ cm, $F = 29.5$, $\ell = 0.03$ cm, $z_{NL} = 0.025$ cm.

In Fig. 2 the parameters are the same as in Fig. 1 except for F = 8.8 . In this latter case, the inequality (11) is not satisfied. This explains why the analytical curves do not fit the numerical ones. At z_{NL}, the theoretical profile exhibits a narrowing of the beam waist of magnitude of order $\sqrt{I_s/I_o}$, resulting from the nonlinear absorption while the numerical profile exhibits defocusing due to the diffraction. This discrepancy between the two descriptions clearly shows that the diffraction strongly works before z_{NL}. The encoding model is no more valid. Fig. 3 illustrates the behaviour of the on-axis intensity as a function of z for $z < z_{NL}$, with the same parameters as in Fig. 1 and Fig. 2, respectively. For large F, the analytical curve given by the squared-modulus solution of Eq.(5) agrees with the numerical one deduced from Eq.(3), that confirms the validity of the encoding approach. For smaller F, as yet pointed out in Fig. 2, the diffraction cannot be neglected.

Fig. 4 displays the propagation for smaller Fresnel number, F = 1.25 where the analytical treatment does not hold in any case. The parameters I_o/I_s, δT_2 and $\alpha \ell$ are those of Fig. 2 but the absorption length (together with the cell length) is seven times larger than in Fig. 2 or the diffraction length is seven times smaller in Fig. 4 than in Fig. 2. The beam widely defocuses since the very beginning of the cell and the ringings appear inside the cell, even for penetration smaller than z_{NL}. Let us point out that even though

strong diffraction effects, the nonlinearities of the medium still work to give rise to ringings.

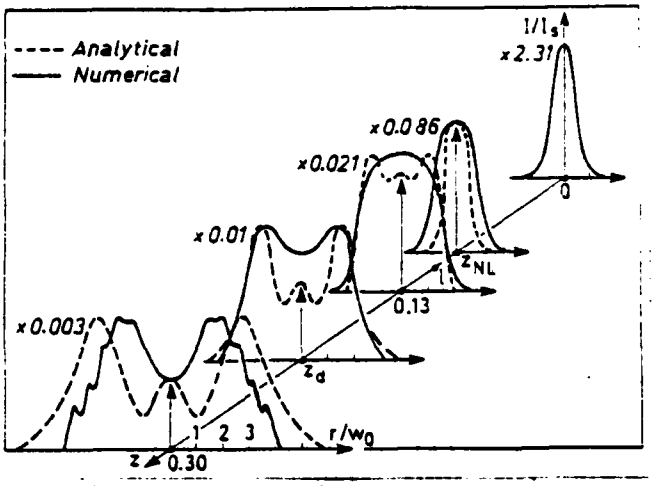

Figure 2. Transverse reshaping; same parameters as in Fig. 1, except F = 8.8, ℓ = 0.1 cm, z_{NL} = 0.08 cm/

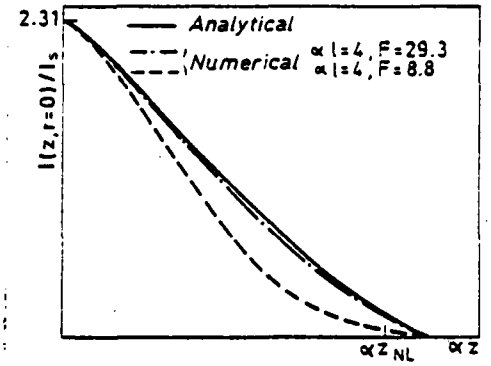

Figure 3. On axis intensity as a function of z. The full lines correspond to the analytical treatment and the dotted lines to the numerical integration of Eq.(5) with F = 29.5 and F = 8.8, respectively.

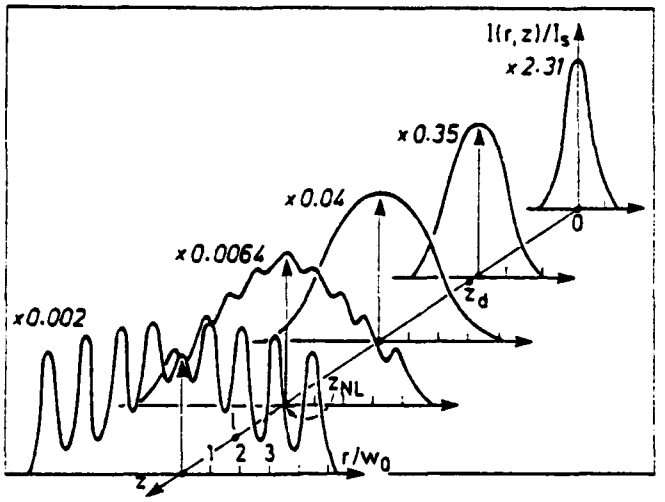

Figure 4. Transverse reshaping, same parameters as in Figs. 1 and 2, except F = 1.25, ℓ = 0.7 cm, z_{NL} = 0.6 cm.

Case II ($\alpha\ell \sim I_o/I_s \sim 1$)

The case treated in this section is quite different from the situation encountered in the previous section. In the present situation, the Fresnel number, $F = \alpha z_d$, is of magnitude of order the cell Fresnel number, $\mathcal{N} = z_d/\ell$, which generally does not exceed some units, for propagation of visible light in cells with reasonable lengths. From another hand, if an encoding of the beam was feasible, a strong non linear phase modification would be expected only for large values of the product of (I_o/I_s) by δT_2 (see Eq.(7)). The conjunction of the three relations

$$\frac{I_o}{I_s} \sim 1 \quad , \quad \delta T_2 \frac{I_o}{I_s} >> 1 \quad , \quad F \sim \mathcal{N} \sim 1 \qquad (13)$$

implies that the condition for encoding (Eq.(12)) cannot be realized. The encoding of the beam before z_{NL} would be viewed for very large $\mathcal{N}$ ($F \equiv \alpha \ell \mathcal{N}$).

Moreover the present case is still different from the situation for which analytical treatment of self-focusing was made ($\alpha \ell \ll I_o/I_s \ll 1$) [5]. In this latter case, the condition $I_o/I_s \ll 1$ allows to approximate the term $(1 + |(u/\hbar)\,\varepsilon(z,r)|^2/I_s)^{-1}$ in the right hand member of Eq.(2) by $(1 - |(u/\hbar)\,\varepsilon(z,r)|^2/I_s)$ and then to relate self-focusing to a cubic index [3].

Up to now, no analytical treatment is attempted in the conditions (13). Only a computer-simulation appears presently to turn out the transverse effects. The figures (5 - 9) exhibit some features of the distortion of an input gaussian profile as a blue shifted light beam through the gas and then through the vacuum. Fig. 5 displays a quasi

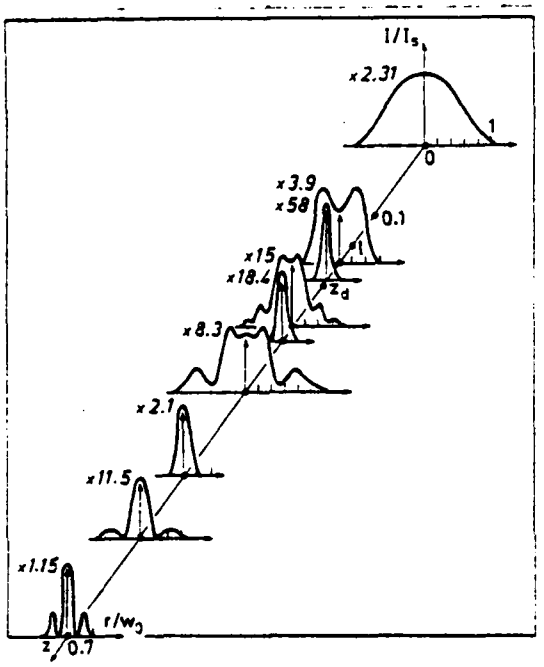

Figure 5. Intensity profile. $I_o/I_s = 2.31$ $\alpha\ell = 2$, $\delta T_2 = -60$, $z_d = 0.22$ cm, $F = 2.9$, $\ell^2 = 0.15$ cm.

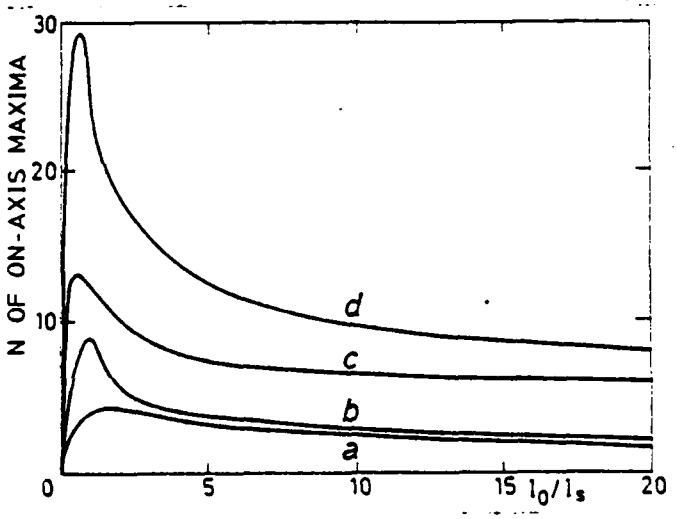

Figure 6. Number of on-axis maxima as a function of I_o/I_s, for same parameters as in Fig.5, and for different T_2 a) -60, b) -120, c) -250, d) -500.

periodicity of the transverse patterns exhibiting self-focusing followed by ringings. This recurrence results from the variation of the factor $(1 + |(u/\hbar)\,\varepsilon(z,r)|^2/I_s)^{-1}$, which alternatively behaves either like $(1 - |(u/\hbar)\,\varepsilon(z,r)|^2/I_s)$ for small intensities or $(I_s/|(u/\hbar)\,\varepsilon(z,r)|^2)$ near the focus. When the driven intensity $I(z,r)/I_s$ is much smaller than unity, the gas behaves like a cubic medium, giving rise to self-lensing. This self-focusing causes so large $I(z,r)/I_s$ that $(1 + |(u/\hbar)\,\varepsilon(z,r)|^2/I_s)^{-1}$ practically vanishes, giving rise to ringings (Case I), and so on ... . Fig. 6 exhibits the number of the successive foci corresponding to the recurrent lensing phenomenom, for given ℓ and α^{-1}, as a function of I_o/I_s, and for different atomic densities. The two regimes for small or strong input intensities are clearly differentiated. The figures 7 and 8 display the variation of the maximum intensity $I(z_\ell)/I_o$ and its location z_ℓ as a function of I_o/I_s, for same parameters as Fig. 7. Let us notice that, as a result of the absorption of the diffraction losses, the absolute maximum is located at the first focus. For I_o/I_s smaller than unity, the magnitude of z_ℓ strongly decreases as I_o/I_s increases [3], reaches a minimum for I_o/I_s smaller or of order unity and then slowly increases with I_o/I_s.

The numerical analysis also shows that ringings appear inside a cell with $\alpha\ell > 1$ if the product $F\,\delta T_2$ is high enough, in Fig. 5 with a large F (~ 3) and $\delta T_2 = -60$, and in Fig. 9 with a small F (~ 0.15) and larger $\delta T_2 = -1200$. The case of Fig. 9 was thoroughly studied in relationship with experiments of Gibbs and Rushford and will be published elsewhere. Let us only point out that the ringings disappear for large pene-

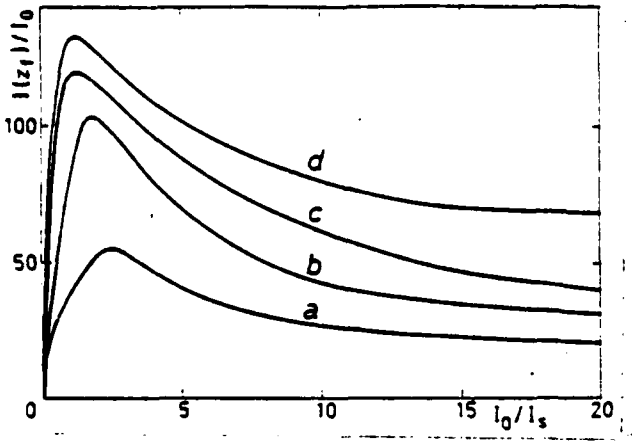

Figure 7. On-axis intensity at the focus as a function of I_o/I_s for same parameters as in Fig. 6.

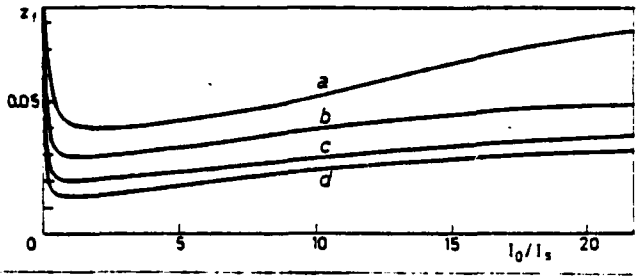

Figure 8. First focus as a function of I_o/I_s for same parameters as in Figs. 6 and 7.

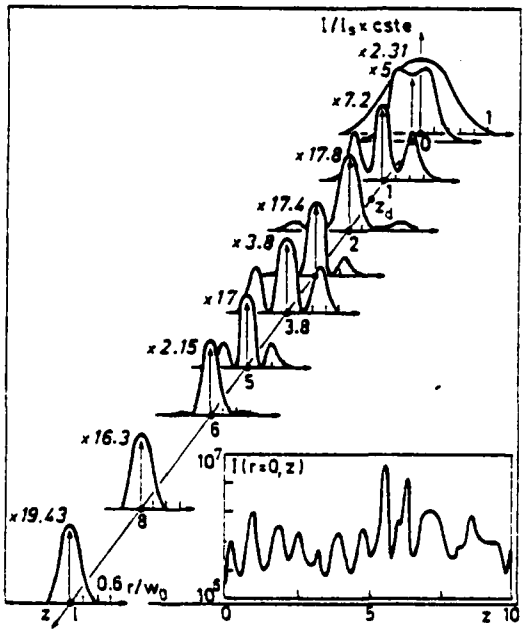

Figure 9. Transverse reshaping and on-axis intensity. I_o/I_s = 2.31, $\alpha\ell$ = 1, δT = -1200, z_d = 1.26 cm, F = 0.14, ℓ = 10 cm.

tration. The behaviour of the patterns for large z seems to make possible the filamentation of the beam. Self-trapping in the unusual conditions of Case II will be also discussed elsewhere.

References

1. Le Berre, M., Ressayre, E. and Tallet, A., Phys. Rev. A25, pp. 1604-1618. 1982 ; ibidem in Proceedings of the Lasers'81 conference, to be published.

2. Gibbs, H.M., Bolger, B., Mattar, F.P., Newstein, M.C., Forster, G., and Toschek, P.E., Phys. Rev. Lett. 37, pp. 1743- 1746.1976.

3. Mattar, F.P., Gibbs, H.M., McCall, S.L., and Feld, M.S., Phys. Rev. Lett. 46, pp. 1123-1126. 1981.

PHYSICAL REVIEW A VOLUME 27, NUMBER 1 JANUARY 1983

Coherent pump dynamics, propagation, transverse, and diffraction effects in three-level superfluorescence and control of light by light

F. P. Mattar
Aerodynamics Laboratory, Mechanical and Aerospace Engineering Department, Polytechnic Institute of New York, Brooklyn, New York 11201 and Laser Spectroscopy Laboratory, Massachusetts Institute of Technology, Cambridge, Massachusetts 02139

C. M. Bowden
Research Directorate, United States Army Missile Laboratory, United States Army Missile Command, Redstone Arsenal, Alabama 35898

(Received 1 June 1982)

A model is presented for the dynamical evolution of superfluorescence from an optically pumped three-level system. The full propagation, transverse, and diffraction effects are taken into account. With the use of a previously developed algorithm, a computational simulation was constructed from this model and results are presented and discussed. In particular, it is shown that the injected coherent pump-pulse initial characteristics, such as on-axis area, temporal and radial width and shape, can have significant deterministic effects on the superfluorescent pulse delay time, peak intensity, temporal width, and shape. Thus, by specifying certain initial properties of the injected pump pulse, the superfluorescent pulse can be shaped and altered. The results predict the conditions under which an injected light pulse of a given frequency can be used to generate, shape, and control a second light pulse of a different frequency via a nonlinear medium, thus demonstrating a new aspect of the phenomenon of light control by light.

I. INTRODUCTION

Superfluorescence[1] is the phenomenon whereby a collection of atoms or molecules is prepared initially in a state of complete inversion and then allowed to undergo relaxation by collective, spontaneous decay. Since Dicke's initial work,[2] there has been a preponderance of theoretical and experimental work dealing with this process.[3]

With the exception of the more recent work of Bowden and Sung,[4] all theoretical treatments have dealt exclusively with the relaxation process from a prepared states of complete inversion in a two-level manifold of atomic energy levels and thus do not consider the dynamical effects of the pumping process. Yet, all reported experimental work[5-10] has utilized optical pumping on a minimum manifold of three atomic or molecular energy levels by laser pulse injection into the nonlinear medium, which subsequently superfluoresces.

It was pointed out by Bowden and Sung[4] that for a system otherwise satisfying the conditions for superfluorescent (SF) emission, unless the characteristic super-radiance time[1] τ_R is much greater than the pump-pulse temporal duration τ_p, i.e., $\tau_R \gg \tau_p$, the process of coherent optical pumping on a three-level system can have dramatic effects on the SF. This is a condition which has not been realized over the full range of reported data.[3]

In this paper, we present calculational results and analysis for the effects of coherent pump dynamics, propagation, transverse, and diffraction effects on SF emission from an optically pumped three-level system. The full, nonlinear, copropagational aspects of the injected pump pulse, together with the SF which evolves, are explicitly treated in the calculation. Not only do our results relate strongly to previous calculations and experimental results in SF, but we introduce and demonstrate a new concept in nonlinear light-matter interactions, which we call light control by light. We show how characteristics of the SF can be controlled by specifying certain characteristics of the injection pulse in the regime $\tau_p > \tau_R$.

In Sec. II, the model upon which the calculation is based is presented, and the algorithm used in the simulation is outlined. Results of the calculation are presented and discussed in Sec. III. Section IV is used to summarize the results and cite implications and to discuss future work.

II. MODEL FOR THREE-LEVEL SUPERFLUORESCENCE

The model upon which the calculation is based is composed of a collection of identical three-level

atoms, each having the energy-level scheme shown in Fig. 1. The $1\leftrightarrow 3$ transition is induced by a coherent electromagnetic field injection pulse of frequency ω_0 nearly tuned to the indicated transition. The properties of this pumping pulse are specified initially in terms of the initial and boundary conditions. The transition $3\leftrightarrow 2$ evolves by spontaneous emission at frequency ω. It is assumed that the energy-level spacing is such that $\epsilon_3 > \epsilon_2 \gg \epsilon_1$ so that the fields at frequencies ω_0 and ω can be treated by separate wave equations. The energy levels $2\leftrightarrow 1$ are not coupled radiatively due to parity considerations.

Further, we neglect spontaneous relaxation in the $3\leftrightarrow 1$ transition, and spontaneous relaxation in the $3\leftrightarrow 2$ transition is simulated by the choice of a small, but nonzero, initial transverse polarization[11] characterized by the parameter $\phi_0 \sim 10^{-3}$. Our results do not depend upon nominal variations of this parameter. The initial condition is chosen consistent with the particular choice of ϕ_0 (see the Appendix) with nearly all the population in the ground state and the initial values of the other atomic variables chosen consistently[4,12] according to the initial equilibrium properties of the system.[13] The full statistical treatment of the quantum initiation process with resulting temporal fluctuations will be presented in a future development. Thus, the results presented here are to be regarded as expectation values or ensemble averages.

We use the electric-dipole and rotating-wave approximations and couple the atomic dipole moments to classical field amplitudes which are determined from Maxwell's equations. The Hamiltonian which describes the field-matter interaction for this system comprising N atoms[4] is

$$\mathcal{H}=\hbar\sum_{r=1}^{3}\sum_{j=1}^{N}\epsilon_{rj}R_{rr}^{(j)}-\frac{i\hbar}{2}\sum_{j=1}^{N}\{\Omega^{(j)}R_{32}^{(j)}\exp[-i(\omega t-\vec{k}\cdot\vec{r}_j)]-\Omega^{(j)*}R_{23}^{(j)}\exp[i(\omega t-\vec{k}\cdot\vec{r}_j)]\}$$
$$-\frac{i\hbar}{2}\sum_{j=1}^{N}\{\omega_R^{(j)}R_{31}^{(j)}\exp[-i(\omega_0 t-\vec{k}_0\cdot\vec{r}_j)]-\omega_R^{(j)*}R_{13}^{(j)}\exp[i(\omega t-\vec{k}_0\cdot\vec{r}_j)]\}\ . \tag{2.1}$$

The first term on the right-hand side (rhs) of Eq. (2.1) is the free atomic system Hamiltonian with atomic level spacings ϵ_{rj}, $r=1,2,3$; $j=1,2,\ldots,N$. The second term on the rhs describes the interaction of the atomic system with the fluorescence field associated with the $3\leftrightarrow 2$ transition, whereas the last term on the right in (2.1) describes the interaction between the atomic system and the coherent pumping field. The fluorescence field and the pumping field have amplitudes $\Omega^{(j)}$ and $\omega_R^{(j)}$, respectively, in terms of Rabi frequency, at the position of the jth atom, $\vec{r}_j$. The respective wave vectors of the two fields are $\vec{k}$ and $\vec{k}_0$, and the carrier frequencies are ω and ω_0. It is assumed that the electromagnetic field amplitudes vary insignificantly over the atomic dimensions and that all of the atoms remain fixed during the time frame of the dynamical evolution of the system.

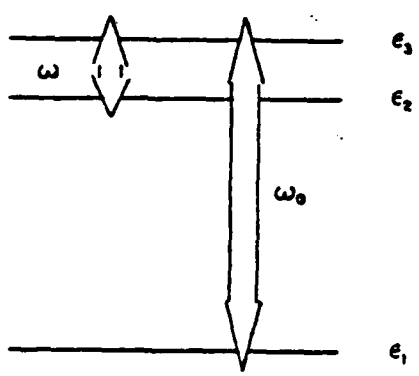

FIG. 1. Model three-level atomic system and electric field tunings under consideration. For the results reported here, the injected pulse is tuned to the $1\leftrightarrow 3$ transition.

The atomic variables in (2.1) are the canonical operators[4] $R_{kl}^{(j)}$ which obey the Lie algebra defined by the commutation rules[14–16]

$$[R_{ij}^{(m)},R_{ik}^{(n)}]=R_{ik}^{m}\delta_{ij}\delta_{mn}-R_{ij}^{(m)}\delta_{ik}\delta_{mn}\ , \tag{2.2}$$

where $i,j=1,2,3$; $m,n=1,2,\ldots,N$. The Rabi rates $\Omega^{(j)}$ and $\omega_R^{(j)}$ are given in terms of the electric field amplitudes $E^{(j)}$ and $E_0^{(j)}$, respectively, and the matrix elements of the transition dipole moments $u_{32}^{(j)}$ and $u_{31}^{(j)}$ by

$$\Omega^{(j)}=\frac{E^{(j)}u_{32}^{(j)}}{\hbar}\ , \tag{2.3a}$$

$$\omega_R^{(j)}=\frac{E_0^{(j)}u_{31}^{(j)}}{\hbar}\ , \tag{2.3b}$$

where we have considered only one linear polarization for the two fields and propagation in the positive z direction.

It is convenient to canonically transform (2.1) to remove the rapid time variations at the carrier frequencies ω and ω_0 and the rapid spatial variations due to the wave vectors $\vec{k}$ and $\vec{k}_0$. We assume that the field envelopes $\Omega^{(j)}$ and $\omega_R^{(j)}$ vary much more slowly than the periods ω^{-1} and ω_0^{-1}, respectively. In the transformed representation, we are thus deal-

ing with slowly varying field amplitudes and atomic operators. The desired unitary transformation U, such that

$$\mathscr{H}_T = U\mathscr{H}U^{-1}, \tag{2.4}$$

is given by

$$U(t) = \prod_{j=1}^{N} \exp[i\lambda_a^{(j)}(t)R_{33}^{(j)}] \exp[i\lambda_b^{(j)}(t)R_{22}^{(j)}], \tag{2.5}$$

where

$$\lambda_a^{(j)}(t) = \omega_0 t - \vec{k}_0 \cdot \vec{r}_j, \tag{2.6a}$$

$$\lambda_b^{(j)}(t) = [(\omega_0 - \omega)t - (\vec{k}_0 - \vec{k}) \cdot \vec{r}_j]. \tag{2.6b}$$

If (2.5) is applied to (2.1) and the commutation rules (2.2) are used, we get for the canonically transformed Hamiltonian $\mathscr{H}_T$,

$$\mathscr{H}_T = \hbar \sum_{j=1}^{N} \Delta^{(j)} R_{33}^{(j)} + \hbar \sum_{j=1}^{N} \delta^{(j)} R_{22} - \frac{i\hbar}{2} \sum_{j=1}^{N} (\Omega^{(j)} R_{32}^{(j)} - \Omega^{*(j)} R_{23}) - \frac{i\hbar}{2} \sum_{j=1}^{N} (\omega_R^{(j)} R_{31}^{(j)} - \omega_R^{*(j)} R_{13}^{(j)}), \tag{2.7}$$

where

$$\Delta^{(j)} = \epsilon_{33}^{(j)} - \omega_0, \quad \delta^{(j)} = \epsilon_{22}^{(j)} + \omega - \omega_0, \quad \epsilon_{11} = 0. \tag{2.8}$$

The equations of motion for the atomic variables are calculated from (2.7) according to

$$\dot{R}_{kl}^{(j)} = \frac{i}{\hbar}[\mathscr{H}_T, R_{kl}^{(j)}]. \tag{2.9}$$

By imposing the canonical transformation defined by (2.5) we, in fact, transformed to a slowly varying operator representation which is consistent with the slowly varying envelope approximation to be imposed later on in the Maxwell's equations coupled to the hierarchy of first-order equations (2.9).

If (2.7) is used in (2.9), the following hierarchy of coupled nonlinear equations of motion is obtained for the atomic variables:

$$\dot{R}_{33}^{(j)} = -\tfrac{1}{2}(\Omega^{(j)} R_{32}^{(j)} + \Omega^{*(j)} R_{23}^{(j)}) - \tfrac{1}{2}(\omega_R^{(j)} R_{31}^{(j)} + \omega_R^{*(j)} R_{13}^{(j)}) - \gamma_{\parallel}(R_{33}^{(j)} - R_{33}^{(e)}), \tag{2.10a}$$

$$\dot{R}_{22}^{(j)} = +\tfrac{1}{2}(\Omega^{(j)} R_{32}^{(j)} + \Omega^{*(j)} R_{23}^{(j)}) - \gamma_{\parallel}(R_{22}^{(j)} - R_{22}^{(e)}), \tag{2.10b}$$

$$\dot{R}_{11}^{(j)} = +\tfrac{1}{2}(\omega_R^{(j)} R_{31}^{(j)} + \omega_R^{*(j)} R_{13}^{(j)}) - \gamma_{\parallel}(R_{11}^{(j)} - R_{11}^{(e)}), \tag{2.10c}$$

$$\dot{R}_{32}^{(j)} = -i\delta^{(j)} R_{32}^{(j)} - \tfrac{1}{2}\Omega^{*(j)}(R_{22}^{(j)} - R_{33}^{(j)}) - \tfrac{1}{2}\omega_R^{*(j)} R_{12}^{(j)} - \gamma_{\perp} R_{32}^{(j)}, \tag{2.10d}$$

$$\dot{R}_{12}^{(j)} = -i\delta^{(j)} R_{12} + \tfrac{1}{2}(\Omega^{*(j)} R_{13} + \omega_R^{(j)} R_{32}) - \gamma_{\perp} R_{12}^{(j)}, \tag{2.10e}$$

$$\dot{R}_{13}^{(j)} = -i\Delta^{(j)} R_{13}^{(j)} - \tfrac{1}{2}\Omega^{(j)} R_{12} + \tfrac{1}{2}\omega_R^{(j)}(R_{33}^{(j)} - R_{11}^{(j)}) - \gamma_{\perp} R_{13}^{(j)}. \tag{2.10f}$$

In Eqs. (2.10), we have added phenomenological relaxation $\gamma_{\parallel}$ and dephasing $\gamma_{\perp}$ and taken these to be uniform, i.e., the same parameters for each transition. For the diagonal terms $R_{kk}^{(j)}$ the equilibrium values are designed as $R_{kk}^{(e)}$, the same for all atoms.

We shall treat the Eqs. (2.10) from this point as c-number equations, i.e., expectation values. Further, we assume that all the atoms have identical energy-level structure and also, we drop the atomic labels j, so it is taken implicitly that the atomic and field variables depend upon the spacial coordinates x, y, and z, as well as the time t.

It is convenient to introduce a new set of real variables in terms of the old ones. We let

$$W_{kl} = R_{kk} - R_{ll}, \quad k > l \tag{2.11a}$$

$$R_{kl} = \tfrac{1}{2}(U_{kl} + iV_{kl}), \quad k > l \tag{2.11b}$$

where U_{kl}, V_{kl}, and W_{kl} are real variables, and $U_{kl} = U_{lk}$, $V_{kl} = V_{lk}$,

$$\Omega = X + iY, \tag{2.11c}$$

$$\omega_R = X_0 + iY_0, \tag{2.11d}$$

where X, Y, X_0, and Y_0 are real variables.

If the transformation (2.11) is applied to (2.10), the resulting equations of motion for the real variables $\{W_{kl}, U_{kl}, V_{kl}\}$ are

$$\dot{W}_{31} = -\tfrac{1}{2}\{XU_{32} - YV_{32}\} - \{X_0 U_{31} - Y_0 V_{31}\} - \gamma_{\parallel}(W_{31} - W_{31}^{(e)}), \tag{2.12a}$$

$$\dot{W}_{32} = -\{XU_{32} - YV_{32}\} - \tfrac{1}{2}\{X_0 U_{31} - Y_0 V_{31}\} - \gamma_{\parallel}(W_{32} - W_{32}^{(e)}), \tag{2.12b}$$

$$\dot{U}_{32}=+\delta V_{32}+XW_{32}-\tfrac{1}{2}(X_0U_{12}-Y_0V_{12})-\gamma_\perp U_{32}\,, \tag{2.12c}$$

$$\dot{V}_{32}=-\delta U_{32}-YW_{32}+\tfrac{1}{2}(X_0V_{21}+Y_0U_{21})-\gamma_\perp V_{32}\,, \tag{2.12d}$$

$$\dot{U}_{31}=-\Delta V_{31}-\tfrac{1}{2}(XU_{21}+YV_{21})+X_0W_{31}-\gamma_\perp U_{31}\,, \tag{2.12e}$$

$$\dot{V}_{31}=+\Delta U_{31}-\tfrac{1}{2}(XV_{21}-YU_{21})-Y_0W_{31}-\gamma_\perp V_{31}\,, \tag{2.12f}$$

$$\dot{U}_{21}=-\delta V_{21}+\tfrac{1}{2}(XU_{31}-YV_{31})+\tfrac{1}{2}(X_0U_{32}-Y_0V_{32})-\gamma_\perp U_{21}\,, \tag{2.12g}$$

$$\dot{V}_{21}=+\delta U_{21}+\tfrac{1}{2}(XV_{31}+YU_{31})-\tfrac{1}{2}(X_0V_{32}+Y_0U_{32})-\gamma_\perp V_{21}\,. \tag{2.12h}$$

In obtaining Eqs. (2.12), we have made use of the invariant $\mathrm{tr}R=I$

$$I\equiv R_{11}^{(j)}+R_{22}^{(j)}+R_{33}^{(j)}\,. \tag{2.13}$$

It is noted that $\dot{I}=0$ is satisfied identically in (2.10a)—(2.10c) for $\gamma_{\|}\to 0$. For $\gamma_{\|}\neq 0$, the condition (2.13) together with (2.10a)—(2.10c) constitutes the statement of conservation of atomic density, i.e., particle number.

Equations (2.12) are coupled to Maxwell's equations through the polarizations associated with each transition field. It is easily determined that the Maxwell's equations in dimensionless form in the rotating-wave and slowly varying envelope approximations can be written in the following form:

$$\mathcal{F}_p^{-1}\nabla_\rho^2\begin{bmatrix}-\bar{X}_0\\ \bar{Y}_0\end{bmatrix}+\frac{\partial}{\partial\eta_p}\begin{bmatrix}\bar{Y}_0\\ \bar{X}_0\end{bmatrix}=d\begin{bmatrix}-U_{31}\\ V_{31}\end{bmatrix}, \tag{2.14a}$$

$$\mathcal{F}_s^{-1}\nabla_\rho^2\begin{bmatrix}-\bar{X}\\ \bar{Y}\end{bmatrix}+\frac{\partial}{\partial\eta_s}\begin{bmatrix}\bar{Y}\\ \bar{X}\end{bmatrix}=d\begin{bmatrix}-U_{32}\\ V_{32}\end{bmatrix}, \tag{2.14b}$$

where the variables $\bar{X}$, $\bar{Y}$, $\bar{X}_0$, $\bar{Y}_0$ are the same as those defined in (2.11c) and (2.11d), but in units of $\gamma_\perp$. In the above equations, we have assumed cylindrical symmetry, thus

$$\nabla_\rho^2=\frac{1}{\rho}\frac{\partial}{\partial\rho}\left[\rho\frac{\partial}{\partial\rho}\right].$$

The first term on the left-hand side in (2.14a) and (2.14b) accounts for transverse effects with normalized radial coordinate $\rho=r/r_p$, where r is the radial distance and r_p is a characteristic spatial width. In (2.14), $\eta_{p_s}=zg_{\mathrm{eff},p_s}$, where g_{eff,p_s} is the on-axis effective gain

$$g_{\mathrm{eff},p_s}=\frac{\begin{bmatrix}\omega_0\\ \omega\end{bmatrix}\begin{bmatrix}\mu_{32}\\ \mu_{31}\end{bmatrix}^2 N}{n\hbar c}T_2\,, \tag{2.15}$$

where N is the atomic number density (assumed longitudinally homogeneous), and n is the index of refraction assumed identical for each transition wavelength. The quantity

$$d=\frac{N(r)}{N_0} \tag{2.16}$$

governs the relative radial population density distribution for active atoms. This could have variation, say, for an atomic beam. Equations (2.14) are written in the retarded time τ frame where

$$\tau=t-nz/c\,.$$

From this point on, the dot in Eqs. (2.12) is taken to be $\partial/\partial\tau$. Finally, the first factors on the first terms on the lhs in (2.14) are the reciprocals of the "gain-length" Fresnel numbers defined by

$$\mathcal{F}_{p_s}\equiv\frac{2\pi r_p^2}{\lambda_{p_s}g_{\mathrm{eff}}^{-1}_{p_s}}\,. \tag{2.17}$$

It is seen from (2.14) that for sufficiently large Fresnel number $\mathcal{F}$ the corrections due to transverse effects become negligible. The gain-length Fresnel numbers $\mathcal{F}$ are related to the usual Fresnel numbers $F=2\pi r_p^2/\lambda L$, where L is the length of the medium, by

$$\mathcal{F}/F=g_{\mathrm{eff}}L\,, \tag{2.18}$$

i.e., the total gains of the medium. In the computations, diffraction is explicitly taken into account by the boundary condition that $\rho=\rho_{\max}$ corresponds to completely absorbing walls.

The initial conditions are chosen to establish a small, but nonzero transverse polarization for the $3\leftrightarrow 2$ transition with almost the entire population in the ground state. This requires the specification of two small dimensionless parameters $\epsilon\sim 10^{-3}$ for the ground-state initial population deficit, and $\delta\sim 10^{-3}$ for the tipping angle for the initial transverse polarization for the $3\leftrightarrow 2$ transition. The derivation for the initial values for the various matrix elements is presented in the Appendix, and the results are given by (A22), (A23), and (A28)—(A33).

III. CALCULATION RESULTS AND ANALYSIS

Calculational methods developed earlier[17] and discussed elsewhere[18,19] were applied to the model presented in Sec. II to compute the effects on SF pulse evolution for various initial conditions for the injected (pump) pulse. The results presented here demonstrate many facets of the control and shaping of the SF signal by control of the input signal initial characteristics. The material parameters chosen for these calculations are arbitrary, but correspond roughly to those for optically pumped metal vapors in the regime $\tau_p > \tau_R$.

Thus, although the simulation inherently yields numerically accurate results for particular experimental design, the results reported here must be taken as qualitative. Our main purpose here is to demonstrate and analyze specific correlations between the initial and boundary conditions associated with the injected pump pulse and characteristics of the SF pulse which evolve. In many of the cases which follow, rules are established through the analysis which can be used to predict quantitative results for any particular experimental conditions. Our choice of particular initial and boundary conditions has been motivated in part by processes which may have been operative in experiments which have been reported[5-10] and in part by the feasibility of experimental selection or specification. In connection with the latter, we demonstrate the control of one light signal by another via a nonlinear medium, thus imparting nonlinear information transfer and pulse shaping of the SF from specific initial and boundary conditions associated with the pump injection signal.

Figure 2 shows results of the numerical calculation for the transverse integrated intensity profiles for the copropagating SF and injected pulses at a penetration depth of $z=5.3$ cm in the nonlinear medium. These profiles correspond to what would be observed with a wide aperture, fast, energy detector. The pumping pulses are labeled by capital letters, and the corresponding SF pulses are labeled by the corresponding lower case letters. Each set of curves represents a different initial on-axis area for the pump pulse, i.e., curve A is the reshaped pump pulse at $z=5.3$ cm which had its initial on-axis area specified as $\theta_p=\pi$, and curve a is the resulting SF pulse which has evolved. All other parameters are identical for each set of pulses. The initial conditions for the atomic medium is that nearly all the population is in the ground state ϵ_1 at $\tau=0$, and a small, but nonzero macroscopic polarization exists between levels ϵ_3 and ϵ_2. These two conditions are specified by two parameters ϵ and δ, respectively, and we have chosen $\delta=\epsilon=10^{-3}$ self-consistently as

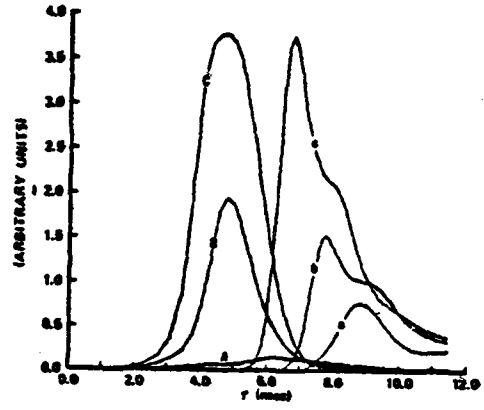

FIG. 2. Radially integrated normalized intensity profiles for the SF and injected pulse at $z=5.3$-cm penetration depth for three different values for the initial on-axis injection pulse area θ_p. The SF pulses are indicated by a, b, and c, whereas the corresponding injected pump pulses are labeled A, B, and C. The injected pulses are initially Gaussian in r and τ with widths (FWHM) $r_0=0.24$ cm and $\tau_p=4$ nsec, respectively. The level spacings are such that $(\epsilon_3-\epsilon_1)/(\epsilon_3-\epsilon_2)=126.6$. The effective gain for the pump transition $g_p=17$ cm^{-1} and that for the SF transition $g_s=291.7$ cm^{-1}. The gain-length Fresnel numbers for the two transitions are $\mathcal{F}_p=16\,800$ and $\mathcal{F}_s=2278$. The relaxation and dephasing times are taken as identical for all transitions and are given as $T_1=80$ nsec and $T_2=70$ nsec, respectively. The injected pulse initial on-axis areas are (A) $\theta_p=\pi$, (B) $\theta_p=2\pi$, and (C) $\theta_p=3\pi$.

specified in the Appendix. These initial conditions are uniform for the atomic medium and are the same for all results reported here. Notice that we have neglected spontaneous relaxation in the pump transition $1\leftrightarrow3$ relative to the SF transition $3\leftrightarrow2$. This is justified owing to our choice of relative oscillator strengths (see Fig. 2 caption).

These results clearly indicate the coherence effect of the initial pump-pulse area on the SF signal which evolves. Notice that the peak intensity of the SF pulses increases monatonically with initial on-axis area for the pump pulse. This is caused by self-focusing due to transverse coupling and propagation. For instance, a 2π-injection pulse would generate a very small SF response compared to an initial π-injection pulse for these conditions at relatively small penetration z, or for the corresponding case in one spatial dimension. Even so, the peak SF intensity is approximately proportional to the square of the pump-pulse initial on-axis area, whereas the delay time τ_D between the pump-pulse peak and the corresponding SF pulse peak is very nearly inversely proportional to the input pulse area. The temporal SF pulse width at full width at half maximum (FWHM) τ_s is approximately invariant with respect

to the injection pulse area.

Since the average values of τ_D and the peak SF intensity are important quantities for interpreting experimental results with theories of SF[1,2,11], the manner in which the pump-pulse coherence and initial on-axis area affects these quantities is seen to be of extreme importance in any analysis.

Figure 3 shows the effect upon the SF pulse of variation in the intitial temporal width at half maximum intensity for the pumping pulse. As the initial temporal width of the injected pulse τ_w becomes smaller, the SF delay time τ_D increases, whereas the peak SF intensity decreases, and the SF temporal width τ_s remains very closely fixed.

It is clear from these results that there exists an approximate linear relationship between the time delay τ_D, between the peak SF intensity and the corresponding pump-pulse intensity, and the initial temporal width τ_p of the pump pulse.

This linear relationship is shown in Fig. 4, where the time delay τ_D is plotted versus the corresponding pump-pulse initial temporal width, from Fig. 3. These results generate the following empirical formula for τ_D as a function of τ_p:

$$\tau_D = 0.375\tau_R[\ln(4\pi/\phi_0)]^2 - 4\tau_R\gamma_\perp(\gamma_R/4\gamma_\perp - 1)\tau_p , \tag{3.1}$$

where[20]

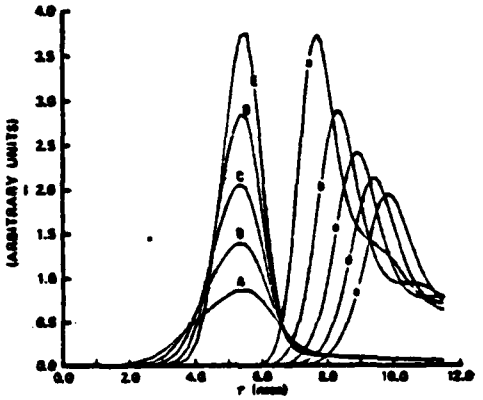

FIG. 3. Radially integrated normalized intensity profiles for the SF and injected pulses at $z=5.3$-cm penetration depth for five different values for the initial temporal width of the injected pulse. The initial on-axis area of the injected pulse is $\theta_p=\pi$, and the pump transition and SF effective gains are $g_p=17.5$ cm^{-1} and $g_s=641.7$ cm^{-1}, respectively. All other parameters except for the Fresnel numbers are the same as those for Fig. 2. The injected pulse initial temporal widths at half maximum are (A) $\tau_p=4$ nsec, (B) $\tau_p=3.3$ nsec, (C) $\tau_p=2.9$ nsec, (D) $\tau_p=2.5$ nsec, and (E) $\tau_p=2.2$ nsec.

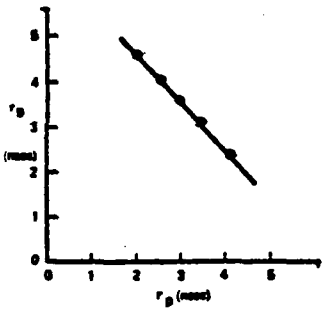

FIG. 4. Delay time τ_D of the SF peak intensity from the corresponding pump-pulse peak intensity vs the pump-pulse initial full temporal width at half maximum intensity τ_p according to Fig. 3.

$$\tau_R = \frac{2T_2}{g_s z} \tag{3.2}$$

is the characteristic superfluorescence time,[1,3] and ϕ_0 is a parameter adjusted to give a best fit to the calculational results. For the case treated here, $\tau_R=41$ psec, $T_2=70$ nsec, and $\phi_0=10^{-8}$, and the Fresnel number $F=1.47$.

The relation (3.1) is at least in qualitative agreement with the analytical prediction made in Ref. 4(b), Eq. (5.1), based upon mean-field theory. The first term in (3.1) was chosen to conform with the quantum-mechanical SF initiation result.[21] The quantity ϕ_0 can be interpreted as the "effective tipping angle" for an equivalent π-initial impulse excitation, i.e., for $\tau_p \to 0$, which initiates subsequent superfluorescence. It is to be noted that the value for ϕ_0 is dependent upon our choice of δ (see the Appendix); however, τ_D varies less than 25% for order-of-magnitude changes in δ for $|\delta| < 10^{-2}$. The choice of δ is simply an artificial way of instigating the semiclassical numerical calculation, and reasonable variations in its value do not strongly affect the results. The physical parameter is, then, ϕ_0, which, interpreted on the basis of (3.1), is generated through the dynamics caused by the pumping process and represents quantum SF initiation. The full statistical treatment for three-level superfluorescence with pump dynamics included will be presented in another publication.[22]

These results emphasize the importance of the initiating pulse characteristics in SF pulse evolution, and the effect of SF pulse narrowing with approximate pulse shape invariance by increasing the initial temporal width of the injected pulse. It is emphasized that all other parameters, including the initial value for the injected pulse on-axis area, are identical among these sets of curves.

The initial radial width r_0 of the injected pulse

was varied and the effect upon the SF pulse evolution is shown in Fig. 5. There is clearly indicated an optimum value for r_0 for which the SF peak intensity is a maximum and the SF temporal width τ_s is a minimum. If the relation (2.18) is used in conjunction with the values of the parameters given in Fig. 5 and its caption, it is seen that optimization occurs for a value for the conventional Fresnel number F_s for the SF transition $F_s \approx 1$. Thus from (2.18) and $F_s = 1$, we have

$$\mathcal{F}_s = g_s z_{max} \tag{3.3}$$

for the gain-length Fresnel number. Since $F_s \sim 1/z$, the implication is that Eq. (3.3) gives the penetration depth z_{max} at which the SF peak intensity reaches a maximum in terms of the ratio $\mathcal{F}_s/g_s$. Since this takes both transverse and diffraction explicitly into account as well as propagation, this is indeed a profound statement.

Further insight into the implication of (3.3) can be obtained by considering a one-spacial dimension analogy. If the linear field loss is taken to be entirely due to diffraction, then the one-dimensional linear loss κ corresponding to the two-dimensional case specified by $\mathcal{F}_s$ is given by

$$\kappa_s = \frac{\lambda_s}{2\pi r_0^2} . \tag{3.4}$$

Then, from (2.17),

$$\mathcal{F}_s = \frac{g_s}{\kappa_s} \tag{3.5}$$

is the effective gain g_s to loss κ_s ratio. From the condition (3.3),

$$z_{max} = (\kappa_s^{-1}) , \tag{3.6}$$

i.e., z_{max} is the penetration depth at which the SF peak intensity is a maximum and corresponds to one effective diffraction length, as defined by (3.4). Carrying the one-dimensional analogy one step further, (3.5) used in (2.18) gives

$$F = (\kappa z)^{-1} . \tag{3.7}$$

From (3.5) and (3.7) we have exhibited the significance of the Fresnel numbers $\mathcal{F}$ and F in terms of diffraction loss, i.e., $\mathcal{F}$ can be thought of as gain to loss ratio, Eq. (3.5), whereas F can correspondingly be thought of as the reciprocal of the strength of the diffraction loss, Eq. (3.7).

The effect on SF pulse evolution of variation of the initial radial shape of the initiating pulse is shown in Fig. 6. The shape parameter ν is defined in terms of the initial condition for the pump transition field amplitude $\omega_R(r)$:

$$\omega_R(r) = \omega_R(0)\exp[-(r/r_p)^\nu] . \tag{3.8}$$

Thus for $\nu = 2$, the initial amplitude of the injected pulse is radially Gaussian, whereas for $\nu = 4$, it is radially super-Gaussian. We see from the results presented in Fig. 6 that as the initial radial shape of the injected pulse becomes broader, i.e., larger values for ν, the peak intensity of the SF pulse generated becomes larger, and the width τ_s and delay time τ_D, diminish. It is emphasized that all other parameters, including the initial values for the radial and temporal widths are invariant among these sets of curves.

Thus if the initial radial shape of the injected pulse is modulated from one injection to the next, the SF temporal width and delay time τ_D are correspondingly modulated as well as the SF peak intensity. Correspondingly, the coherence and initial radial shape of the pump pulse cannot, with validity, be ignored in interpretation of SF experiments in terms of τ_s and τ_D.

Whereas the initial on-axis area for the pumping pulse was $\theta_p = 2\pi$ for the results shown in Fig. 6, the identical conditions and parameters were imposed, but the initial on-axis pump-pulse area was changed

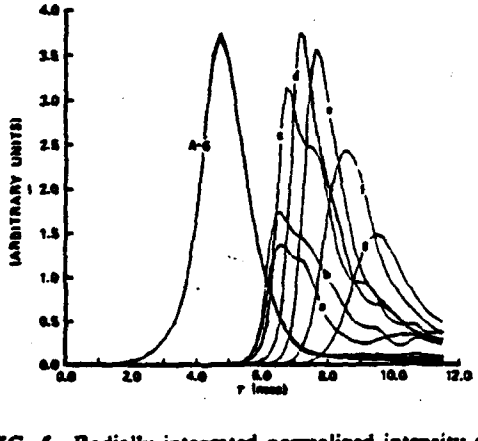

FIG. 5. Radially integrated normalized intensity profiles for the SF and injected pulses at $z = 5.3$-cm penetration depth for seven different values for the injected pulse initial radial width at half maximum r_0. The initial on-axis area θ_p of the injection pulse is $\theta_p = 2\pi$; the SF effective gain $g_s = 758.3$ cm^{-1}, and the pump transition effective gain $g_p = 14.6$ cm^{-1}. All other parameters are the same as for Fig. 2. The initial radial widths at half maximum for the injected pulses are (a) $r_0 = 0.57$ cm, (b) $r_0 = 0.43$ cm, (c) $r_0 = 0.24$ cm, (d) $r_0 = 0.18$ cm, (e) $r_0 = 0.15$ cm, (f) $r_0 = 0.11$ cm, and (g) $r_0 = 0.09$ cm. The corresponding geometrical Fresnel numbers are (a) $F_s = 8.46$, (b) $F_s = 4.79$, (c) $F_s = 1.47$, (d) $F_s = 0.85$, (e) $F_s = 0.57$, (f) $F_s = 0.35$, and (g) $F_s = 0.21$.

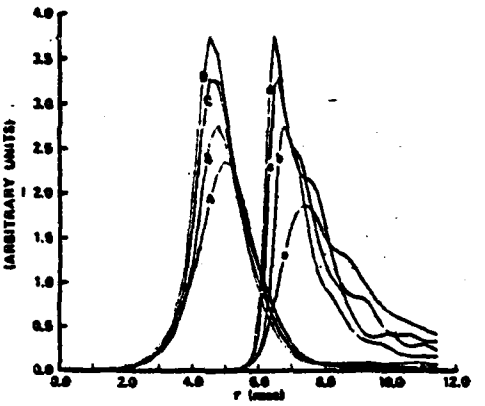

FIG. 6. Radially integrated normalized intensity profiles for the SF and injected pulses at $z=5.3$-cm penetration depth for four different values for the injected pulse initial radial shape parameter ν (see text). The initial on-axis area θ_p of the injected pulse is $\theta_p=2\pi$, and the SF effective gain $g_s=758.3$ cm^{-1}, whereas the effective gain for the pump transition $g_p=14.6$ cm^{-1}. All other parameters are the same as for Fig. 2. The initial radial shape parameters for the injected pulses are (A) $\nu=1$, (B) $\nu=2$, (C) $\nu=3$, and (D) $\nu=4$.

to $\theta_p=3\pi$, and the results are shown in Fig. 7. It is seen that the major effect of changing the initial on-axis area from 2π to 3π is to cause more ringing in the SF pulses and to modify the pump-pulse temporal reshaping as is noted by comparing Fig. 7 with Fig. 6.

The response of SF pulse evolution to changes in the initial temporal shape of the injection pulse is shown in Fig. 8, which compares the effect of a

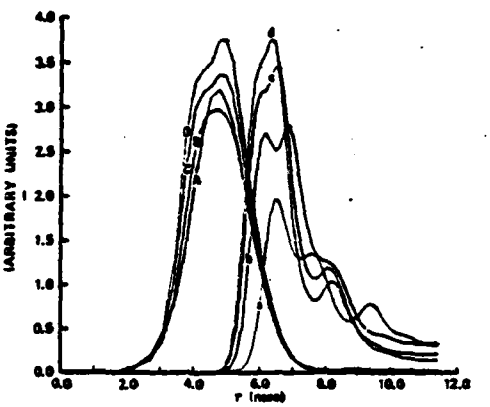

FIG. 7. Radially integrated normalized intensity profiles for the SF and injected pulses at $z=5.3$-cm penetration depth for four different values for the injected pulse initial radial shape parameter ν (see text). The initial on-axis area θ_p of the injected pulse is $\theta_p=3\pi$. All other parameters are the same as for Fig. 6.

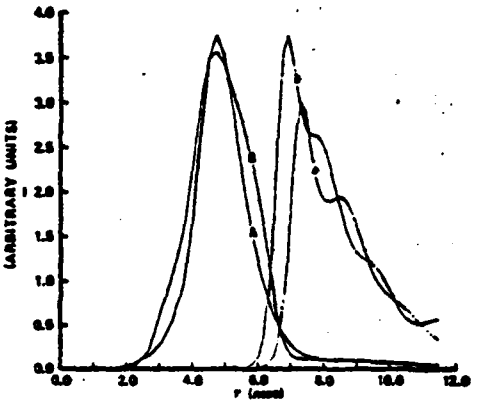

FIG. 8. Radially integrated normalized intensity profiles for the SF and injected pulses at $z=5.3$-cm penetration depth for two different values for the injected pulse initial temporal shape parameter σ (see text). The initial on-axis area θ_p of the injected pulse is $\theta_p=2\pi$, and the SF effective gain $g_s=641.7$ cm^{-1}. All other parameters are the same as for Fig. 5(c). The initial radial shape parameters for the injected pulses are (A) $\sigma=2$ and (B) $\sigma=4$.

Gaussian initial temporal shape for the pump pulse, identified by the temporal shape parameter $\sigma=2$ with that of a super-Gaussian identified by $\sigma=4$. As for the radial distribution discussed previously, the temporal shape parameter σ is defined in terms of the initial condition for the pump transition field amplitude $\omega_R(\tau)$,

$$\omega_R(\tau)=\omega_R(0)\exp[-(\tau/\tau_p)^\sigma]\,. \tag{3.9}$$

Again, it is seen that the broader initial pump pulse causes an increase in the peak SF intensity and a reduction in the delay time τ_D and SF pulse width τ_s.

Whereas the results of Fig. 8 correspond to an initial on-axis area $\theta_p=2\pi$ for the pump pulse, the results of Fig. 9 correspond to identical conditions and values for the parameters as those for Fig. 8, except that the initial on-axis area for the injection pulse is $\theta_p=3\pi$.

The effect of changing the effective gain for the SF transition g_s and hence the relative oscillator strength between the SF transition and the pump transition is demonstrated in the results of Figs. 10–13. Each of these figures corresponds to a different on-axis initial area θ_p for the injection pulse. Consistent among the entire set of results is that increasing the effective gain g_s results in a nearly linear increase in the SF peak intensity as well as decrease in the delay time τ_D. Also, the smaller area initiating pulse causes a narrower SF pulse to evolve and with apparently less ringing.

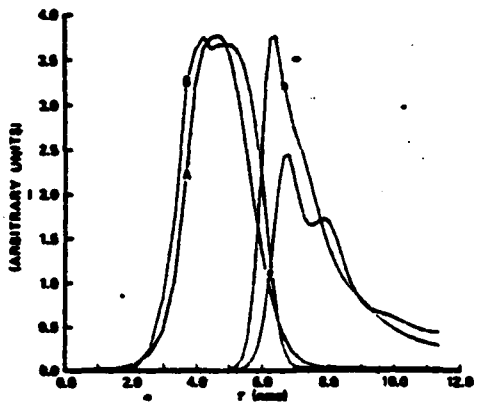

FIG. 9. Radially integrated normalized intensity profiles for the SF and injected pulses at $z=5.3$-cm penetration depth for two different values for the injected pulse initial temporal shape parameter σ (see text). The initial on-axis area θ_p of the injected pulse is $\theta_p=3\pi$. All other parameters are the same as for Fig. 8. The initial radial shape parameters for the injected pulses are (A) $\sigma=2$ and (B) $\sigma=4$.

Figure 14 shows the effect of variation of the density ρ of active atoms. The effective gains g_s and g_p are changed proportionally, corresponding to a density variation ρ. The ratio of the SF intensities is $I_c/I_b=1.76$ and $I_b/I_a=2.06$; these ratios are larger than the corresponding density ratios squared, $(\rho_c/\rho_b)^2=1.40$ and $(\rho_b/\rho_a)^2=1.49$. This difference from the predictions from previous theories of

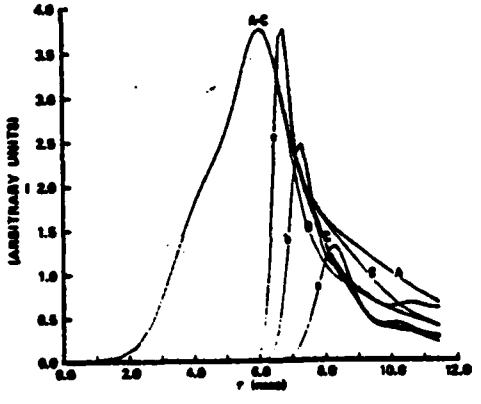

FIG. 10. Radially integrated normalized intensity profiles for the SF and injected pulses at $z=5.3$-cm penetration depth for three different values for the SF transition effective gain g_s. The on-axis initial area θ_p for the injected pulse is $\theta_p=\pi$. All other parameters are the same as those for Fig. 5(c). The SF transition effective gain is (a) $g_s=525.0\ \text{cm}^{-1}$, (b) $g_s=641.7\ \text{cm}^{-1}$, and (c) $g_s=758.3\ \text{cm}^{-1}$.

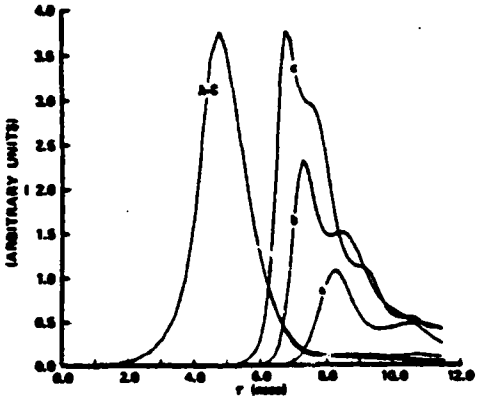

FIG. 11. Radially integrated normalized intensity profiles for the SF and injected pulses at $z=5.3$-cm penetration depth for three different values for the SF transition effective gain g_s. The on-axis initial area θ_p for the injected pulse is $\theta_p=2\pi$. All other parameters are the same as for Fig. 10.

SF[1-3] may be due to self-focusing, especially since the values of the effective gains used in this case are quite high. However, the ratio of the temporal widths τ_s, FWHM, are within 15% of the corresponding inverse ratios of the densities; the same is true for the delay time τ_D of the SF intensity peak with respect to the pump intensity peak. These results compare qualitatively reasonably well with the mean-field predictions for SF in two-level systems initially prepared in a state of complete inversion.[1]

A comparison of the effects upon the injection pulse of variation in oscillator strengths between the

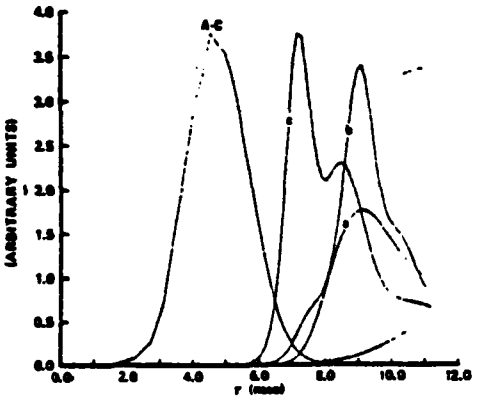

FIG. 12. Radially integrated normalized intensity profiles for the SF and injected pulses at $z=5.3$-cm penetration depth for three different values for the SF transition effective gain g_s. The on-axis initial area θ_p for the injected pulse is $\theta_p=3\pi$. All other parameters are the same as for Fig. 10.

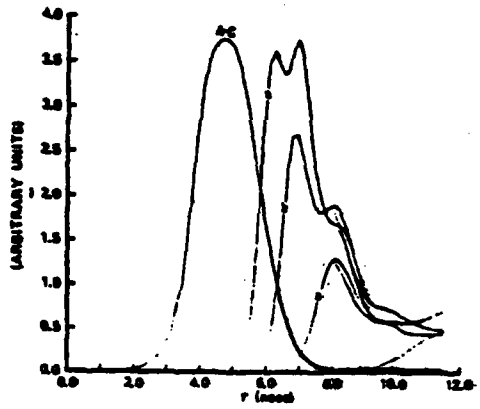

FIG. 13. Radially integrated normalized intensity profiles for the SF and injected pulses at $z=5.3$-cm penetration depth for three different values for the SF transition effective gain g_s. The on-axis initial area θ_p for the injected pulse is $\theta_p=4\pi$. All other parameters are the same as for Fig. 10.

SF and pump transition (variation of g_s) as contrasted to effects upon the pump pulse of a density variation (variation of both g_p and g_s proportionally) is given in Figs. 15 and 16, respectively. It is seen that the respective effects in the pump-pulse reshaping are quite distinct. The variation in oscillator strengths, Fig. 15, essentially causes "hole burning"

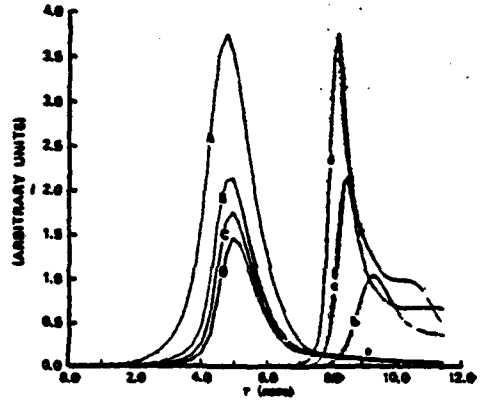

FIG. 14. Radially integrated normalized intensity profiles for the SF and injected pulses at $z=5.3$-cm penetration depth for three different values for the density ρ of atoms. The on-axis initial area θ_p for the injected pulse is $\theta_p=2\pi$. Except for the effective gains and Fresnel numbers, the values for all other parameters are the same as for Fig. 5(c). For each set of curves, the gain values are (b) $g_s=525.0\ \text{cm}^{-1}$, $g_p=26.3\ \text{cm}^{-1}$; (c) $g_s=641.7\ \text{cm}^{-1}$, $g_p=32.1\ \text{cm}^{-1}$; and (d) $g_s=758.3\ \text{cm}^{-1}$, $g_p=37.9\ \text{cm}^{-1}$. The corresponding Fresnel numbers are (b) $\mathcal{F}_p=25\,992$, $\mathcal{F}_s=4100$; (c) $\mathcal{F}_p=31\,724$, $\mathcal{F}_s=5010$; and (d) $\mathcal{F}_p=37\,456$, $\mathcal{F}_s=5922$.

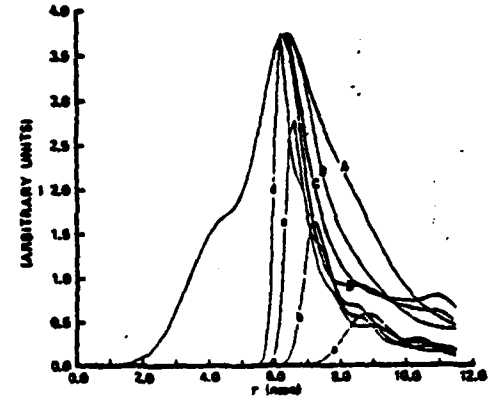

FIG. 15. Radially integrated normalized intensity profiles for the SF and injected pulses at $z=5.3$-cm penetration depth for four different values for the SF transition effective gain g_s. The initial on-axis area for the injected pulse is $\theta_p=\pi$, and the effective gain for the pump transition $g_p=17.5\ \text{cm}^{-1}$. Except for the effective gain g_s, all other parameters are the same as those for Fig. 5(c). The SF transition effective gain g_s for each set of curves is (a) $g_s=291.7\ \text{cm}^{-1}$, (b) $g_s=408.3\ \text{cm}^{-1}$, (c) $g_s=525.0\ \text{cm}^{-1}$, and (d) $g_s=641.7\ \text{cm}^{-1}$.

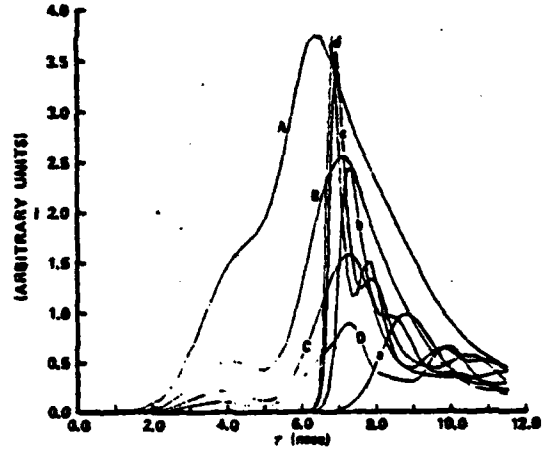

FIG. 16. Radially integrated normalized intensity profiles for the SF and injected pulse at $z=5.3$-cm penetration depth for four different values for the density ρ of atoms. The on-axis initial area θ_p for the injected pulse is $\theta_p=\pi$. Except for the effective gains and Fresnel numbers, the values for all other parameters are the same as for Fig. 5(c). For each set of curves, the gain values are (a) $g_s=291.7\ \text{cm}^{-1}$, $g_p=17.5\ \text{cm}^{-1}$; (b) $g_s=408.3\ \text{cm}^{-1}$, $g_p=24.5\ \text{cm}^{-1}$; (c) $g_s=525.0\ \text{cm}^{-1}$, $g_p=31.5\ \text{cm}^{-1}$; and (d) $g_s=641.7\ \text{cm}^{-1}$, $g_p=38.5\ \text{cm}^{-1}$. The corresponding Fresnel numbers are (a) $\mathcal{F}_p=17\,296$, $\mathcal{F}_s=2278$; (b) $\mathcal{F}_p=24\,212$, $\mathcal{F}_s=3188$; (c) $\mathcal{F}_p=31\,130$, $\mathcal{F}_s=4100$; and (d) $\mathcal{F}_p=38\,048$, $\mathcal{F}_s=5010$.

in the following edge of the pump pulse, whereas the variation in density, Fig. 16, affects the whole pump pulse. This contrast has an analogy as an inhomogeneous, Fig. 15, as opposed to a homogeneous, Fig. 16, effect on the pump pulse. This effect might be used for the purposes of pulse shaping under suitable conditions.

Shown in Fig. 17 is the transverse integrated SF pulse intensity versus retarded time τ (curve 2) together with the transverse integrated pump-pulse intensity versus τ (curve 1) for a gain and propagation depth chosen so that the pulses temporally overlap. Under these conditions the two pulses strongly interact with each other via the nonlinear medium, and the two-photon processes (resonant, coherent Raman—RCR), which transfer populations directly between levels ϵ_2 and ϵ_1, make strong contributions to the mutual pulse development.[4] The importance of the RCR in SF dynamical evolution in an optically pumped three-level system was pointed out for the first time in Ref. 4. Indeed, the SF pulse evolution demonstrated here has greater nonlinearity than SF in a two-level system which has been prepared initially by an impulse excitation. What is remarkable is that this is an example where the SF pulse temporal width τ_s is much less than the pump width τ_p even though the two pulses temporally overlap, i.e., the SF process gets started late and terminates early with respect to the pump time duration. Pulses of this type have been observed[23] in CO_2-pumped CH_3F.

The remaining figures are isometric representations of pump-pulse and SF pulse copropagation and interaction via the nonlinear medium. These figures exhibit details of the dynamic mutual pulse reshaping, self-focusing and defocusing during SF buildup.

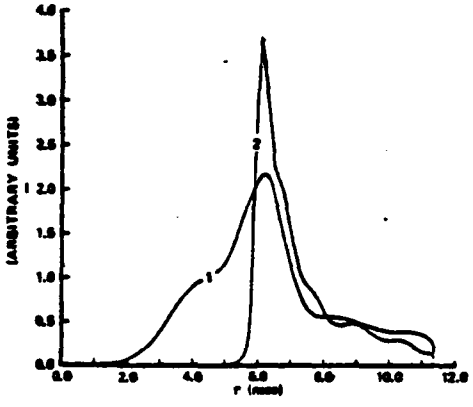

FIG. 17. Radially integrated intensity profiles, in units of Rabi frequency, for the SF (2) and injected pulse (1) at a penetration depth of $z=5.3$ cm. The effective gain for the pump transition and the SF transition are $g_p=17$ cm^{-1} and $g_s=641.7$ cm^{-1}, respectively. The initial on-axis area for the injected pulse is $\theta_p=\pi$. All other parameters are the same as for Fig. 2.

The pulse intensities as functions of the radial coordinate ρ and retarded time τ are presented in Figs. 18 and 19 for two different penetrations $z=4.4$ cm and $z=5.3$ cm, respectively, into the high gain medium. The injected pulse is initially radially and temporally Gaussian. Both the pump pulse and the SF pulse are seen to exhibit considerable self-defocusing with ringing following the main SF peak. At the larger penetration, Fig. 19, a large postpulse appears in both the pump and SF pulse propagation. This is due to energy feedback from the SF to the pump transition. The postpulses overlap, and so the two-photon RCR effects are active and quite significant in the dynamic evolution and coupling between the pump and SF pulses. This effect is due entirely to the coherence in the dynamical evolution of the system.

Portrayed in Figs. 20 and 21 are isometric representations for the radial and temporal dependence of the copropagating injected and SF pulses for two different initial shape distributions for the pump pulse. In the first case, Fig. 20, the initial temporal distribution of the injected pulse is Gaussian, whereas the initial radial distribution is characterized by the parameter $\nu=3$, Eq. (3.8). It is observed that the injected pulse has undergone considerable reshaping, due to propagation, to a more Gaussian radial distribution, and the SF pulse exhibits strong self-defocusing in the wings of the tail region. In the second case, Fig. 21, the initial radial distribution of the injected pulse is Gaussian, whereas the initial temporal distribution is half-Gaussian, with the sharp temporal cutoff on the following temporal half-section of the pulse. The SF pulse rises extremely sharply, in comparison to the other cases analyzed, and tapers off with strong self-defocusing indicated in the wings of the pulse tail. Pump pulses of this type are generated using a plasma switch[10] and the corresponding SF pulses with steep rise have been observed.

IV. CONCLUSIONS

The effects presented here clearly demonstrate the coherence and deterministic effects on SF pulse evolution of injection pump-pulse characteristics and conditions in the regime $\tau_p < \tau_R$. It is suggested that effects of the type discussed here may have in fact been operative in SF experiments and their results which were published earlier.[5-10] The pump pulse was taken as purely coherent in these calculations. To determine whether or not effects of the nature

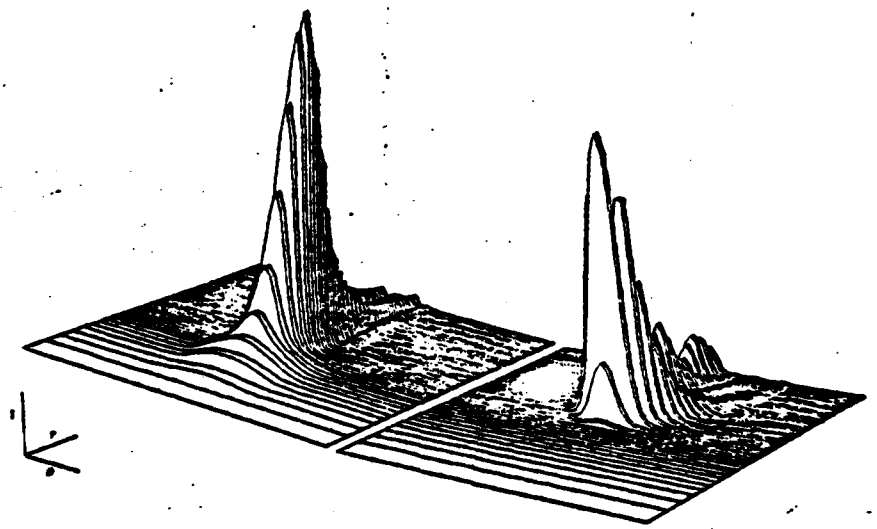

FIG. 18. Pulse intensity I as a function of the radial coordinate ρ and retarded time τ at penetration $z=4.4$ cm. The injected pump pulse is in the upper left, and the SF pulse, which is generated, is in the lower right. The parameters are the same as for Fig. 3(A).

reported here are indeed operative in a given experiment, it is crucial to determine the degree of coherence of the pumping process as well as its temporal duration.[4]

Furthermore, and perhaps of greater importance, we have demonstrated the control and shaping of the SF pulse which evolves by specification of particular initial characteristics and conditions for the pumping pulse which is injected into the nonlinear medium to initiate SF emission. These manifestations and others of the same class we call the control of light by light via a nonlinear medium. This phenomenon constitutes a method for nonlinear information encoding, or information transfer, from

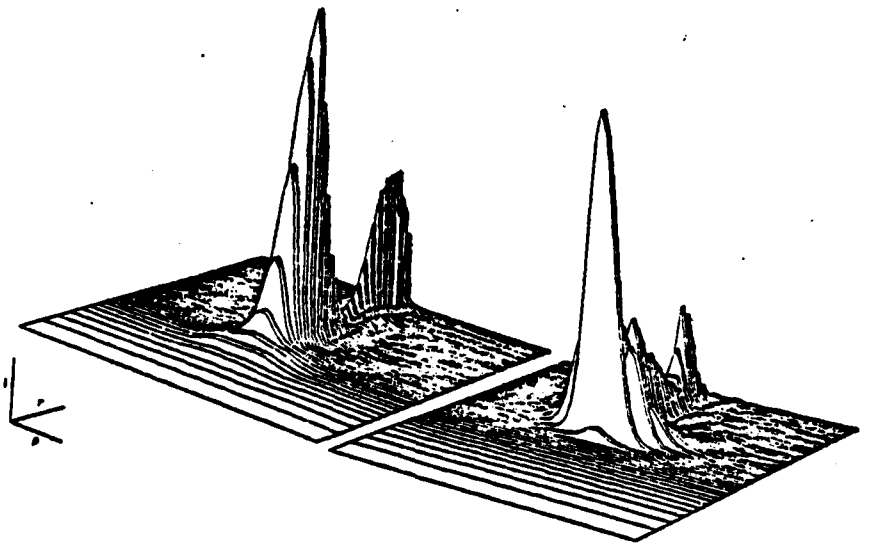

FIG. 19. Pulse intensity I as a function of the radial coordinate ρ and retarded time τ at penetration $z=5.3$ cm. The injected pump pulse is in the upper left, and the SF pulse, which is generated, is in the lower right. The parameters are the same as for Fig. 18.

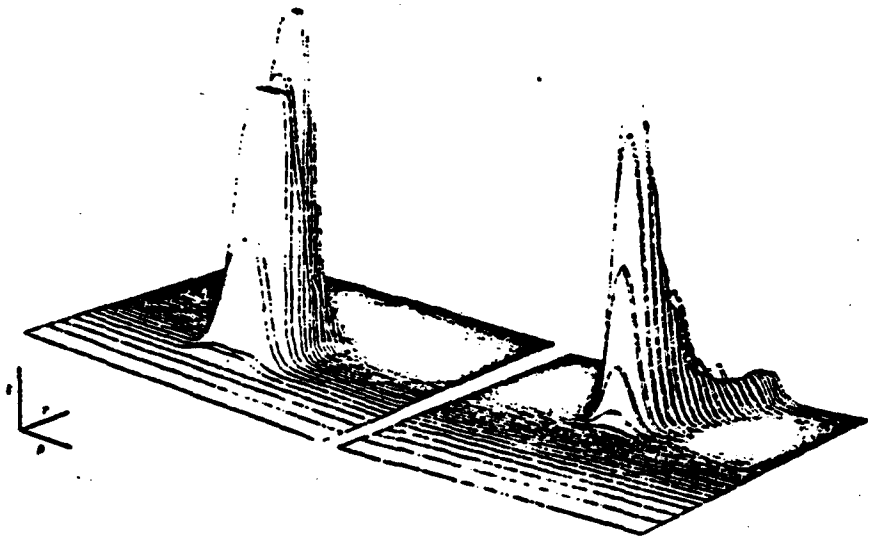

FIG. 20. Pulse intensity I as a function of the radial coordinate ρ and retarded time τ at penetration $z=5.3$ cm. The injected pump pulse is in the upper left, and the SF pulse, which is generated, is in the lower right. The parameters are the same as for Fig. 14(b) except that the initial on-axis area for the injected pump pulse is $\theta_p=3\pi$ and the initial radial shape parameter is $\nu=3$ (see text).

the injection pulse initial characteristics to corresponding SF pulse characteristics which evolve due to propagation and interaction in the nonlinear medium.[22]

Work is now in progress to incorporate the effects of quantum statistics of the SF spontaneous relaxation process.[22] We are in the process of further determination and analysis of the nonlinear interac-

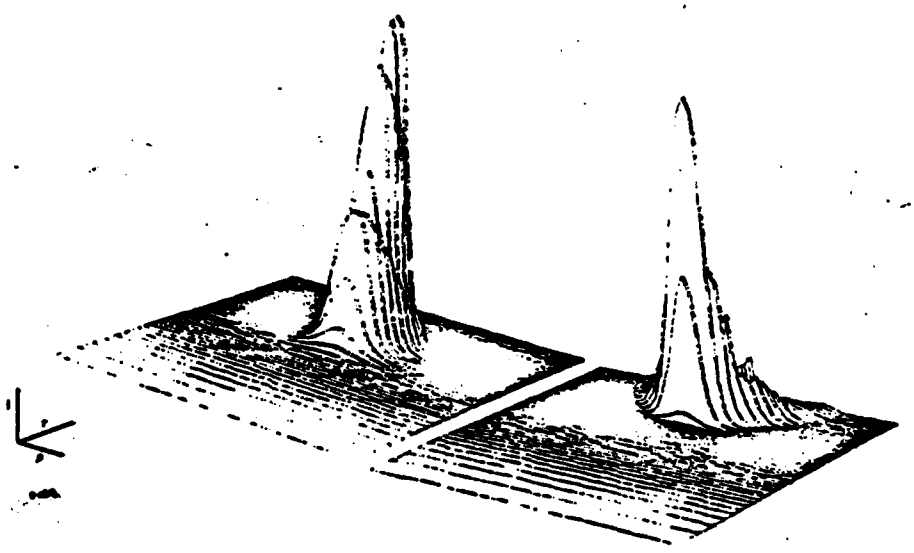

FIG. 21. Pulse intensity I as a function of the radial coordinate ρ and retarded time τ at penetration $z=5.3$ cm. The injected pump pulse is in the upper left, and the SF pulse, which is generated, is in the lower right. The parameters are the same as for Fig. 6(B) except that the initial on-axis area for the injected pulse is $\theta_p=3\pi$, and the initial temporal shape of the injected pulse is half-Gaussian with the sharp temporal cutoff on the following, i.e., increasing τ, side of the pumping pulse.

tion between two copropagating pulses resonantly, as well as nonresonantly, interacting by a nonlinear medium.

ACKNOWLEDGMENTS

The programming assistance of Y. Claude and M. Cormier is gratefully acknowledged. The work of F. P. M. was partially supported by the U. S. Army Research Office, Battelle Columbus Laboratories, and the Office of Naval Research.

APPENDIX

We must choose the initial conditions self-consistently. We wish to establish a small, but nonzero, uniform initial transverse polarization δ for the $3\leftrightarrow 2$ transition. For self-consistency, this corresponds to initial population depletion ϵ of the ground-state population, consistent with (2.13) and Eqs. (2.10).

In terms of initial population number N_k,

$$W_{32}=N_3-N_2\,, \tag{A1}$$

$$W_{31}=N_3-N_1\,. \tag{A2}$$

We choose

$$N_1=1-\epsilon\,, \tag{A3}$$

ϵ small and positive and impose the ansatz

$$U_{32}=p\sin\delta\sin\phi_s\,, \tag{A4}$$

$$V_{32}=p\sin\delta\cos\phi_s\,, \tag{A5}$$

and let

$$p=\epsilon,\quad N_2/N_3\ll 1\,. \tag{A6}$$

The condition (A6) means essentially that $N_3\approx\epsilon$ and $N_2\approx 0$. Equations (A1), (A4), and (A5) under condition (A6) become

$$U_{32}\approx\epsilon\delta\sin\phi_s\,, \tag{A7}$$

$$V_{32}\approx\epsilon\delta\cos\phi_s\,, \tag{A8}$$

$$W_{32}\approx\epsilon\cos\delta\,. \tag{A9}$$

Our uniform initial conditions are just the conditions which led to the linearized mean-field equations in the small fluorescence signal regime of Ref. 4, Eqs. (4.14c)–(4.14f). Initially, the pump field amplitude $\omega_R=0$, and these equations of motion become

$$\dot{R}_{13}=-i\alpha A_T R_{12}\,, \tag{A10}$$

$$\dot{R}_{32}=-2i\alpha A_T^{\dagger}R_3\,, \tag{A11}$$

$$\dot{R}_{12}=-2i\alpha A_T^{\dagger}R_3\,, \tag{A12}$$

$$\dot{A}_T=-i\alpha R_{23}-\kappa A_T\,, \tag{A13}$$

and A_T is the initial fluorescence field amplitude, $\alpha=g_{eff}\gamma_\perp$, and κ is the linear fluorescence field loss. We let

$$R_3\equiv\tfrac{1}{2}W_{32}\,,$$

and initially,

$$\kappa A_T\gg\frac{\partial A_T}{\partial t}\,. \tag{A14}$$

The condition (A14) in (A13) gives

$$A_T=-\frac{i\alpha}{\kappa}R_{23}\,. \tag{A15}$$

Using (A15) and (A14) to eliminate the field amplitude A_T from Eqs. (A10)–(A13), we get

$$\dot{R}_{31}=-\frac{\alpha^2}{2\kappa}R_{21}R_{32}\,, \tag{A16}$$

$$\dot{R}_{12}=\frac{2\alpha^2}{\kappa}R_{13}R_{32}\,, \tag{A17}$$

$$\dot{R}_{32}=\frac{\alpha^2}{\kappa}W_{32}R_{32}\,. \tag{A18}$$

Dividing (A17) by (A16),

$$\frac{dR_{12}}{dR_{31}}=-4\frac{R_{13}}{R_{21}}\,. \tag{A19}$$

Integrating (A19),

$$R_{13}^2=-\tfrac{1}{4}R_{12}^2\,, \tag{A20}$$

where the constant of integration has been set equal to zero. Thus

$$R_{13}=\frac{i}{2}R_{12}\,. \tag{A21}$$

In terms of the real variables defined by (2.11b), and using (A21), we get

$$U_{21}=-2V_{32}\,, \tag{A22}$$

$$V_{21}=2U_{32}\,. \tag{A23}$$

From the initial conditions (A1)–(A6),

$$W_{32}\equiv\cos\eta=-1+2\epsilon\,. \tag{A24}$$

Thus

$$\eta=\cos^{-1}(2\epsilon-1)\,, \tag{A25}$$

and

$$U_{31}=\sin\eta\sin\phi_p\approx\eta\sin\phi_p\,, \tag{A26}$$

$$V_{31}=\sin\eta\cos\phi_p\approx\eta\cos\phi_p\,. \tag{A27}$$

We have, therefore, using (A9),

$$W_{32}=\epsilon\ , \tag{A28}$$

$$W_{31}=2\epsilon-1\ , \tag{A29}$$

$$U_{32}=\epsilon\delta\sin\phi_s=0\ , \tag{A30}$$

$$V_{32}=\epsilon\delta\cos\phi_s=\epsilon\delta\ , \tag{A31}$$

since we must choose the phase ϕ_s such that $\sin\phi_s=0$. We have

$$U_{31}=\eta\sin\phi_p\ , \tag{A32}$$

$$V_{31}=\eta\cos\phi_p \tag{A33}$$

with η given by (A25) and ϕ_p chosen arbitrarily.

[1]R. Bonifacio and L. A. Lugiato, Phys. Rev. A 11, 1507 (1975); 12, 587 (1975).

[2]R. H. Dicke, Phys. Rev. 93, 99 (1954).

[3]See papers and references in *Cooperative Effects in Matter and Radiation*, edited by C. M. Bowden, D. W. Howgate, and H. R. Robl (Plenum, New York, 1977).

[4](a) C. M. Bowden and C. C. Sung, Phys. Rev. A 18, 1558 (1978); (b) 20, 2033 (1979).

[5]N. Skribanowitz, J. P. Herman, J. C. MacGillivray, and M. S. Feld, Phys. Rev. Lett. 30, 309 (1973).

[6]H. M. Gibbs, Q. H. F. Vrehen, and H. M. J. Hikspoors, Phys. Rev. Lett. 39, 547 (1977).

[7]Q. H. F. Vrehen, Ref. 3, p. 79.

[8]M. Gross, C. Fabre, P. Pillet, and S. Haroche, Phys. Rev. Lett. 36, 1035 (1976).

[9]A. Flusberg, F. Mossberg, and S. R. Hartmann, Ref. 3, p. 37.

[10]A. T. Rosenberger and T. A. DeTemple, Phys. Rev. A 24, 868 (1981).

[11]N. E. Rehler and J. H. Eberly, Phys. Rev. A 3, 1735 (1971).

[12]F. T. Hioe and J. H. Eberly, Phys. Rev. Lett. 47, 838 (1981).

[13]J. R. R. Leite, R. S. Sheffield, M. Duclay, R. D. Sharma, and M. S. Feld, Phys. Rev. A 14, 1151 (1976).

[14]R. Gilmore, *Lie Groups, Lie Algebras, and Some of Their Applications* (Wiley, New York, 1974), Chap. 6, Sec. 2.

[15]R. Gilmore, C. M. Bowden, and L. M. Narducci, Phys. Rev. A 12, 1019 (1975).

[16]R. Gilmore, C. M. Bowden, and L. M. Narducci, in *Quantum Statistics and the Many-Body Problem*, edited by S. B. Trickey, W. R. Kirk and J. W. Dufty (Plenum, New York, 1975).

[17]F. P. Mattar and M. C. Newstein, Ref. 3, p. 139.

[18]F. P. Mattar, in *Optical Bistability*, edited by C. M. Bowden, M. Ciftan, and H. R. Robl (Plenum, New York, 1981), p. 503; in *Proceedings, Tenth Simulation and Modeling Conference, Pittsburgh, 1978*, edited by W. Vogt and M. Mickle (Instrument Society of America, Pittsburgh, 1979).

[19]F. P. Mattar, H. M. Gibbs, S. L. McCall, and M. S. Feld, Phys. Rev. Lett. 46, 1123 (1981).

[20]R. Friedberg and S. R. Hartmann, Phys. Rev. A 13, 495 (1976).

[21]F. Haake, J. Haus, H. King, G. Schroder, and R. Glauber, Phys. Rev. Lett. 45, 558 (1980); D. Polder, M. F. H. Schuurmans, and Q. H. F. Vrehen, Phys. Rev. A 19, 1192 (1979).

[22]C. M. Bowden and F. P. Mattar (unpublished).

[23]T. A. DeTemple (private communication).

PHYSICAL REVIEW A VOLUME 27, NUMBER 3 MARCH 1983

Quantum fluctuations and transverse effects in superfluorescence

E. A. Watson* and H. M. Gibbs
Optical Sciences Center, University of Arizona, Tucson, Arizona 85721

F. P. Mattar
Aerodynamics Laboratory, Polytechnic Institute of New York, Brooklyn, New York 11201
and Spectroscopy Laboratory, Massachusetts Institute of Technology, Cambridge, Massachusetts 02139

M. Cormier and Y. Claude
Laboratoire de Modelisation Numerique, Département d'Informatique,
Université de Montréal, Montréal, Québec, Canada H3C 3J7

S. L. McCall
Bell Laboratories, Murray Hill, New Jersey 07974

M. S. Feld
Spectroscopy Laboratory and Physics Department, Massachusetts Institute of Technology,
Cambridge, Massachusetts 02139
(Received 15 September 1982)

Superfluorescence emission profiles are computed using one-way coupled Maxwell-Bloch equations. Transverse effects are included in the full three-spatial-dimension case as well as in the cylindrical-symmetry case. Initiating quantum fluctuations are approximated by a random polarization source with a completely random phase and root-mean-square tipping angle of $2/\sqrt{N}$, where N is the number of atoms in each volume element. These fluctuations reduce the tail of the output obtained with transverse effects alone. In fact, the fluctuations in output pulse shapes encompass the Cs data of Gibbs, Vrehen, and Hikspoors. The standard deviation for the delay time is found to be (12.5±4)% for Fresnel number of 0.8 compared with the value (10±2)% recently measured by Vrehen and der Weduwe, also for Cs. Inhomogeneous-broadening effects are also included in some simulations.

I. INTRODUCTION

Previous simulations of superfluorescence[1–6] have included quantum fluctuations[7–15] or transverse effects[16] but never both until recently. This article reports simultaneous treatment of both of these effects in the presence of inhomogeneous broadening and evaluates their significance.

Superfluorescence (SF) is the process by which coherent emission occurs from an ensemble of two-level atoms initially in an inverted state in the absence of driving external radiation. The emission begins by incoherent spontaneous emission; only the geometry of the inverted medium leads to directed emission. The quantum initiation process leads to large ($\simeq$10%) macroscopic fluctuations in the temporal and spatial shapes of the SF pulses emitted by a system of 10^8 initially inverted atoms.

Recently, two groups[8–15] have studied theoretically the quantum initiation of SF, including propagation effects in the plane-wave approximation. Quantum effects occur during the very beginning of the pulse evolution when the problem is still linear. During the later nonlinear evolution when the number of photons in important modes is large, the dynamics can be described accurately semiclassically, i.e., with coupled Maxwell-Bloch equations.[4,5] The quantum initiation is then described by a statistical ensemble of initial conditions for Maxwell-Bloch solutions. One can adopt for each volume element an initial polarization source with random phase ϕ and with tipping angle θ_0 which is a bivariate Gaussian with rms value $2/\sqrt{N}$, where N is the number of atoms in a given volume element. There are two experiments that indicate that θ_0 is about $2/\sqrt{N}$; they show that injected pulses must have input pulse areas larger than θ_0 in order to shorten the SF delay time.[17,18] Uniform plane-wave Maxwell-Bloch solutions have been calculated by Haake *et al.* for hundreds of such statistical initial conditions.[15] These yield about 12% for the standard deviation $\sigma(\tau_D)/\bar{\tau}_D$ in the delay time in good agreement with the expression $2.3/\ln N$ derived by Polder *et al.*[10] Vrehen and der Weduwe[19] have measured (10±2)%

for Fresnel number $F=0.8$, $(6\pm2)\%$ for $F=4$, and $<4\%$ for $F=18$, where $F=\pi r_p^2/\lambda L$, r_p is the radius of the initial inversion density at half maximum, L is the sample length, and λ is the SF wavelength. Note that the plane-wave theoretical value of $\sigma(\tau_D)$ is in good agreement with the $F=0.8$ experimental value. However, the lack of ringing is not accounted for. One might hope that this would be so in that a single-mode plane-wave theory was always justified by noting that $F\sim1$ has enough diffraction loss to favor single-mode emission without introducing excessive losses. This article contains the first[20,21] calculations of SF in which both quantum initiation and transverse effects are included; we find satisfactory agreement with experiment. Inclusion of inhomogeneous broadening further improves the agreement.

An earlier paper[16] presented a study of transverse effects in superfluorescence in the absence of statistics. In those simulations, a one-way-propagating small-area pulse irradiated a population-inverted medium under conditions of cylindrical symmetry. Within those simplifying assumptions, propagation and cylindrical transverse effects were fully taken into account. It was found that transverse effects couple together atoms in various parts of the beam, so that they tend to emit at the same time and, hence, largely remove the strong ringing[22] so prominent in the plane-wave simulations. In fact, rather good agreement was found with the Cs data[23] by using simulation densities somewhat higher than the measured ones. Also the simulated pulses trailed off more slowly than the observed ones. Finally, the simulations predicted large ringing for a small detector placed in the center of the Fresnel-number-1 ($F=1$) SF output. The primary objective of this paper is to show how the various refinements of the propagation model lead to an increasingly accurate description of the observed SF pulse shapes, delays, jittering, and fluctuations.

II. APPROXIMATIONS AND NUMERICAL TECHNIQUES

The basic assumptions of these calculations are one-way propagation and initiation by a polarization randomized in a particular way. Previous studies[5,24] indicate that interference effects between forward- and backward-evolving SF pulses are quite insignificant for the small tipping angles θ_0 ($\lesssim10^{-4}$ rad) usually encountered in experiments. At large θ_0 ($\simeq10^{-1}$ rad), the interference can reduce the tail by several percent.

To reduce the computer costs, the first calculations described a geometry with cylindrical symmetry (one transverse dimension). Subsequent calculations have been extended to the more complex case where azimuthal symmetry is absent and two transverse dimensions are required. The latter model is needed to describe short-scale-length phase and amplitude fluctuations which result in multiple-transverse-mode initiation and lead to multidirectional output with hot spots. This effect is only important in samples with Fresnel numbers of order unity or larger, since diffraction singles out a smooth phase front in small-F samples.

The polarization is assumed to be random in phase relative to the coherent emission which eventually evolves. The probability $P(u,v)$ that the transverse polarization has components u and v is a Gaussian distribution

$$P(u,v)du\,dv=\frac{1}{\pi\delta^2}\exp[-(u^2+v^2)/\delta^2]du\,dv, \tag{1}$$

where

$$\delta=\langle\theta^2\rangle^{1/2}=2/\sqrt{N}, \tag{2}$$

for the quantum initiation to be properly represented.[9,10,25] The angular brackets denote an ensemble average. Equation (2) is easily checked using

$$u^2+v^2=\theta^2\sim\sin^2\theta\sim\theta^2 \tag{3}$$

for small θ as assumed here; then

$$P(\theta^2)d\theta^2\simeq\frac{1}{\delta^2}e^{-\theta^2/\delta^2}d\theta^2. \tag{4}$$

The probability that θ^2 is less than θ_0^2 is

$$\int_0^{\theta_0^2}P(\theta^2)d\theta^2=1-e^{-\theta_0^2/\delta^2}, \tag{5}$$

so that Eq. (5) can be set equal to $1-R$, where R is a random number between 0 and 1. This leads to

$$\theta_0=\frac{2}{\sqrt{N}}\left[\ln\frac{1}{R}\right]^{1/2}. \tag{6}$$

When the population-inverted medium is divided into smaller volume elements, N in Eq.(6) is replaced by the number of atoms in each volume element, i.e.,

$$\theta_0^i=\frac{2}{\sqrt{N_i}}\left[\ln\frac{1}{R}\right]^{1/2} \tag{7}$$

is the initial tipping angle for the ith volume element containing N_i atoms. The smaller the volume element the larger the initial tipping angle and the fluctuations for that element, but also the smaller their effect.

The random numbers used in Eq. (7) and in randomizing ϕ between 0 and 2π are obtained from a table of random numbers. The starting address

the table is changed at the beginning of each run. The equations of motion are

$$\frac{\partial \mathscr{E}}{\partial z} - i(4FL)^{-1}\nabla_T^2 \mathscr{E} = \frac{4\pi^2}{\lambda}\mathscr{P}, \tag{8a}$$

$$\frac{\partial \mathscr{P}}{\partial \tau} + \frac{\mathscr{P}}{T_2} = \frac{\mu^2}{\hbar} n \mathscr{E}, \tag{8b}$$

$$\frac{\partial n}{\partial \tau} + \frac{n - n^e}{T_1} = -\mathrm{Re}\frac{\mathscr{P}\mathscr{E}^*}{\hbar}, \tag{8c}$$

where $\mathscr{E}$ and $\mathscr{P}$ are the slowly varying complex amplitudes of the electric field and polarization, respectively; n is the inversion density and can initially sustain transverse variations, and n^e its equilibrium value; $\tau = t - z/c$ is the retarded time; μ is the transition dipole moment matrix element; and T_1 and T_2 are the population-relaxation and polarization-dephasing times. Diffraction is taken into account by the Laplacian term

$$\nabla_T^2 \mathscr{E} = (1/\rho)(\partial/\partial\rho)\rho\partial\mathscr{E}/\partial\rho,$$

or

$$(\partial^2\mathscr{E}/\partial\xi^2 + \partial^2\mathscr{E}/\partial\zeta^2),$$

where

$$\rho = r/r_p,\ \xi = x/r_p, \text{ and } \zeta = y/r_p.$$

The boundary conditions are $\nabla_T \cdot \mathscr{E} = 0$ (where $\mathscr{E}$ is the electric field) on the axis ($r = 0$ or $x = y = 0$) and at $r = \infty$ (or $x = y = \infty$). Equations (8) are numerically integrated with $\mathscr{P} = \mu n_0 \sin\theta_0^l \exp(i\phi_0^l)$ and $n = n_0 \cos\phi_0^l$; θ_0^l is defined by Eq. (7) and ϕ_0^l is uniformly randomly distributed between 0 and 2π. For computational efficiency, the temporal and radial grids are adaptive nonlinear, i.e., nonlinear with parameters determined by the computer noting the evolution of the pulse.[26]

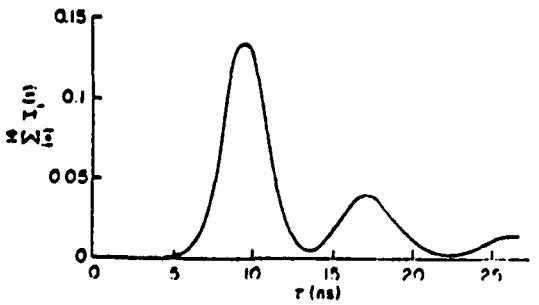

FIG. 1. Intensity as a function of time for the average of 14 output pulses in the plane-wave case with quantum fluctuations such that $(\theta_0^l)^{1/2} = 1.69 \times 10^{-4}$ rad and $n_0^0 = 11.8 \times 10^{10}$ cm^{-3}.

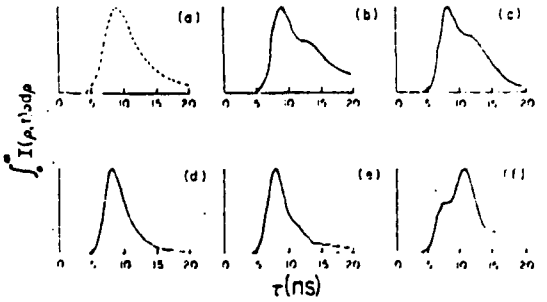

FIG. 2. Intensity integrated over the transverse cylindrical coordinate as a function of time for single trajectories. (a) Cs data for $n_0^0 \simeq 7.6 \times 10^{10}$ cm^{-3}. (b) Simulation with transverse effects, but no fluctuations: $n_0^0 = 18.2 \times 10^{10}$ cm^{-3}, $\theta_0 = 1.37 \times 10^{-4}$ rad, and Fresnel number $F = 1$. (c)–(f) Simulations with transverse effects and fluctuations for $n_0^0 = 18.2 \times 10^{10}$ cm^{-3}, $(\theta_0^2)^{1/2} = 1.37 \times 10^{-4}$ rad, and $F = 1$.

The simulation parameters (except as noted) were essentially those of the Cs single-pulse experiment,[21] namely, $\lambda = 2.931\ \mu$m, $L = 2$ cm, $T_1 = 70$ ns, $T_2 = 80$ ns, $\tau_R = 8\pi\tau_0/3n_0^0\lambda^2 L$, $\tau_0 = 551$ ns, $n_0^0 = 1.8 \times 10^{11}$ cm^{-3}, and $F = 1$. The initial gain profile is Gaussian, i.e., $n_0(r) = n_0^0 \exp[-(r/r_p)^2 \ln 2]$, so the spatial width is narrower for smaller F, but the peak gain remains the same.

III. SIMULATION RESULTS

A. SF pulse shapes

Figure 1 is a summation of 14 output pulses in the plane-wave case with quantum fluctuations. The ringing is still very pronounced so quantum

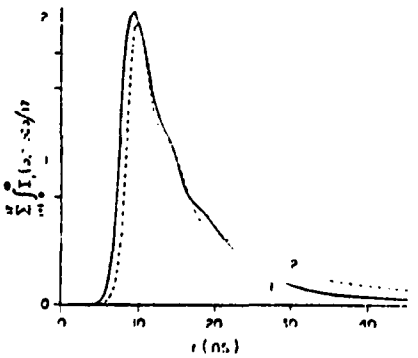

FIG. 3. Effect of fluctuations on the average pulse shape. Average over 17 trajectories with fluctuations (solid curve) has a slightly shorter delay and a smaller tail than the dashed curve with no fluctuations and a uniform θ_0. Here, $n_0^0 = 18.2 \times 10^{10}$ cm^{-3}, $(\theta_0^2)^{1/2} = 1.37 \times 10^{-4}$ rad, and $F = 0.32$.

the table is changed at the beginning of each run. The equations of motion are

$$\frac{\partial \mathcal{E}}{\partial z} - i(4FL)^{-1}\nabla_T^2 \mathcal{E} = \frac{4\pi^2}{\lambda}\mathcal{P}, \tag{8a}$$

$$\frac{\partial \mathcal{P}}{\partial \tau} + \frac{\mathcal{P}}{T_2} = \frac{\mu^2}{\hbar} n \mathcal{E}, \tag{8b}$$

$$\frac{\partial n}{\partial \tau} + \frac{n - n^e}{T_1} = -\mathrm{Re}\frac{\mathcal{P}\mathcal{E}^*}{\hbar}, \tag{8c}$$

where $\mathcal{E}$ and $\mathcal{P}$ are the slowly varying complex amplitudes of the electric field and polarization, respectively; n is the inversion density and can initially sustain transverse variations, and n^e its equilibrium value; $\tau = t - z/c$ is the retarded time; μ is the transition dipole moment matrix element; and T_1 and T_2 are the population-relaxation and polarization-dephasing times. Diffraction is taken into account by the Laplacian term

$$\nabla_T^2 \mathcal{E} = (1/\rho)(\partial/\partial\rho)\rho\partial\mathcal{E}/\partial\rho,$$

or

$$(\partial^2\mathcal{E}/\partial\xi^2 + \partial^2\mathcal{E}/\partial\xi^2),$$

where

$$\rho = r/r_p,\ \xi = x/r_p, \text{ and } \zeta = y/r_p.$$

The boundary conditions are $\vec{\nabla}_T \cdot \vec{\mathcal{E}} = 0$ (where $\vec{\mathcal{E}}$ is the electric field) on the axis ($r = 0$ or $x = y = 0$) and at $r = \infty$ (or $x = y = \infty$). Equations (8) are numerically integrated with $\mathcal{P} = \mu n_0 \sin\theta_0' \exp(i\phi_0')$ and $n = n_0\cos\phi_0'$; θ_0' is defined by Eq. (7) and ϕ_0' is uniformly randomly distributed between 0 and 2π. For computational efficiency, the temporal and radial grids are adaptive nonlinear, i.e., nonlinear with parameters determined by the computer noting the evolution of the pulse.[26]

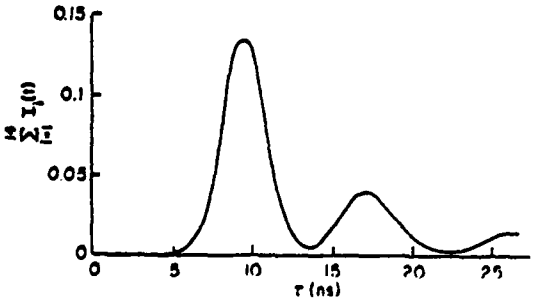

FIG. 1. Intensity as a function of time for the average of 14 output pulses in the plane-wave case with quantum fluctuations such that $\langle\theta_0^2\rangle^{1/2} = 1.69\times10^{-4}$ rad and $n_0^0 = 11.8\times10^{10}$ cm^{-3}.

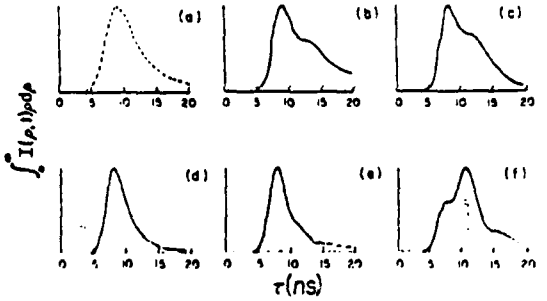

FIG. 2. Intensity integrated over the transverse cylindrical coordinate as a function of time for single trajectories. (a) Cs data for $n_0^0 \simeq 7.6\times10^{10}$ cm^{-3}. (b) Simulation with transverse effects, but no fluctuations: $n_0^0 = 18.2\times10^{10}$ cm^{-3}, $\theta_0 = 1.37\times10^{-4}$ rad, and Fresnel number $F = 1$. (c)–(f) Simulations with transverse effects and fluctuations for $n_0^0 = 18.2\times10^{10}$ cm^{-3}, $\langle\theta_0^2\rangle^{1/2} = 1.37\times10^{-4}$ rad, and $F = 1$.

The simulation parameters (except as noted) were essentially those of the Cs single-pulse experiment,[23] namely, $\lambda = 2.931$ μm, $L = 2$ cm, $T_1 = 70$ ns, $T_2 = 80$ ns, $\tau_R = 8\pi\tau_0/3n_0^0\lambda^2 L$, $\tau_0 = 551$ ns, $n_0^0 = 1.8\times10^{11}$ cm^{-3}, and $F = 1$. The initial gain profile is Gaussian, i.e., $n_0(r) = n_0^0\exp[-(r/r_p)^2\ln 2]$, so the spatial width is narrower for smaller F, but the peak gain remains the same.

III. SIMULATION RESULTS

A. SF pulse shapes

Figure 1 is a summation of 14 output pulses in the plane-wave case with quantum fluctuations. The ringing is still very pronounced so quantum

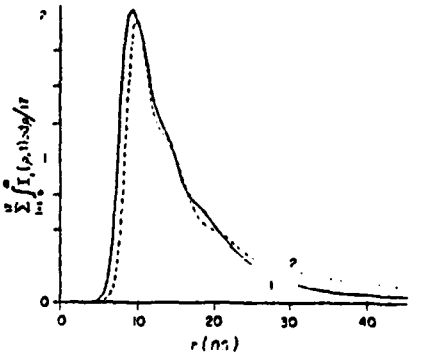

FIG. 3. Effect of fluctuations on the average pulse shape. Average over 17 trajectories with fluctuations (solid curve) has a slightly shorter delay and a smaller tail than the dashed curve with no fluctuations and a uniform θ_0. Here, $n_0^0 = 18.2\times10^{10}$ cm^{-3}, $\langle\theta_0^2\rangle^{1/2} = 1.37\times10^{-4}$ rad, and $F = 0.32$.

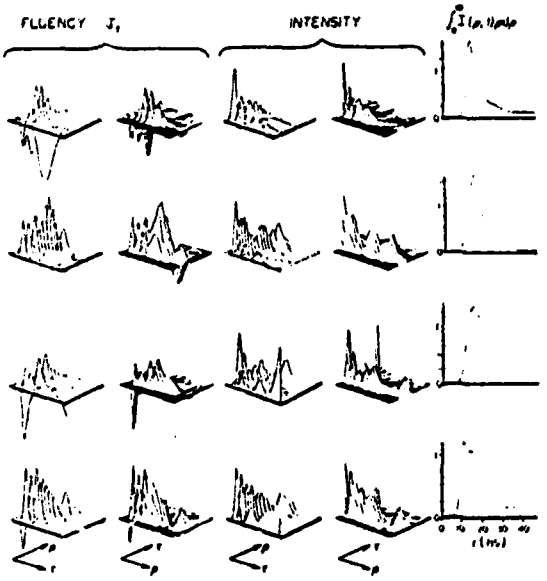

FIG. 4. Transverse energy current J_T and intensity are plotted isometrically for four shots in a statistical ensemble. In some of the shots the phase curvature is such that the associated energy flux flows inwardly; i.e., the transverse energy current is negative, which could lead to self-focusing. Inward energy flow never occurred for simulations using a homogeneous initial tipping angle (without quantum initiation) for any value of the Fresnel number. Here, $n_0^0 = 9.5\times10^{10}\,\mathrm{cm}^{-3}$, $F = 1.49$, and $10^4\langle\theta_0^2\rangle^{1/2} = 2.15$, 1.63, 1.79, and 1.16 rad, respectively, from top to bottom. Note the fluctuations in peak maximum and its associated delay in the output integrated over ρ (last column).

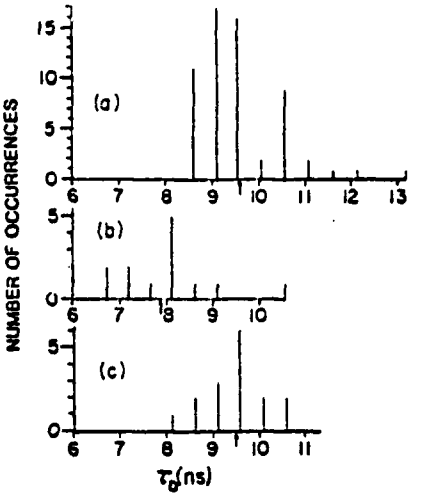

FIG. 5. Histogram showing the number of occurrences of a particular delay time. Points do not occur at integral values of τ_D because of the nonlinear time mesh. (a) Plane-wave case for $n_0^0 = 11.8\times10^{10}\,\mathrm{cm}^{-3}$ and $\langle\theta_0^2\rangle^{1/2} = 1.69\times10^{-4}$ rad. (b) and (c) Cylindrical-symmetric transverse case for $n_0^0 = 18.2\times10^{10}\,\mathrm{cm}^{-3}$, and $\langle\theta_0^2\rangle^{1/2} = 1.37\times10^{-4}$ rad. (b) $F = 1$. (c) $F = \pi^{-1}$. Each arrow denotes $\bar{\tau}_D$.

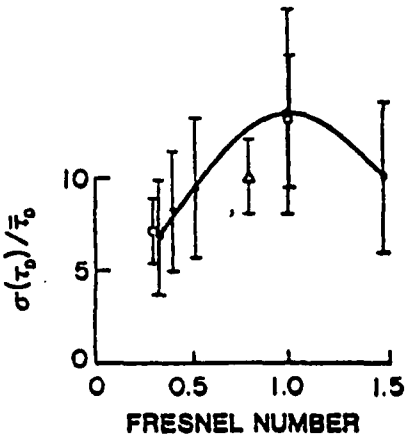

FIG. 6. Fresnel-number dependence of the uncertainty in delay time normalized to the average delay. Points are as follows: ●, seven trajectories with $n_0^0 = 9.5\times10^{10}\,\mathrm{cm}^{-3}$ and $\langle\theta_0^2\rangle^{1/2} = 1.89\times10^{-4}$ rad; □, $n_0^0 = 18\times10^{10}\,\mathrm{cm}^{-3}$ and $\langle\theta_0^2\rangle^{1/2} = 1.37\times10^{-4}$ rad, for 13 trajectories for $F = 1$, and for 16 trajectories for $F = \pi^{-1}$; Δ, experimental value for 468 trajectories. A peak close to $F = 1$ can be argued as follows: For small F, strong diffractive coupling reduces fluctuations in the overall output. For large F, so many transverse modes compete that a good average is obtained on every shot. For $F \simeq 1$, competition of a few modes is maximal, resulting in large fluctuations. Meaningful calculations for large F require an increasing number of transverse steps, and so we avoid the large-F region.

fluctuations alone do not remove it.[15] Figure 2(b) illustrates the fact that, for $F = 1$, transverse effects alone do largely remove ringing.[16] Figures 2(c) through 2(f) show that transverse effects and quantum fluctuations together result in fluctuating output pulses with very little ringing that encompass the published Cs pulse shapes [one is shown in Fig. 2(a)]. Figure 3 illustrates that on the average (17 runs) the tail of the pulse is lower with fluctuations than without.

Figure 4 displays isometric plots of the SF intensity and its associated fluency ($J_T = |\mathcal{E}|^2\partial\Phi/\partial\rho$), where Φ is the phase of the electric field as a function of ρ and τ for four elements of the statistical ensemble. One finds that the transverse energy current J_T occasionally flows inwardly causing hot spots in the output beam as was sometimes observed in the Cs experiments. The previous transverse calculations[16] involving a uniform tipping angle never displayed inward transverse energy flow. Figure 4

also shows the radially integrated output SF intensity as a function of τ for the four shots of the statistical ensemble.

B. Delay-time fluctuations

Figure 5(a) is a histogram showing the fluctuations in delay time τ_D (τ at pulse peak) when quantum fluctuations are included in the plane-wave approximation. These 57 runs yield

$$\frac{\sigma(\tau_D)}{\bar{\tau}_D} \equiv \frac{\left[\sum_{i=1}^{N}(\tau_D^i-\bar{\tau}_D)^2/N\right]^{1/2}}{\bar{\tau}_D}\left[1\pm\frac{1}{\sqrt{N-1}}\right]$$

$$=(9.9\pm1.3)\%$$

compared with 12% from the formula $2.3/\ln N$ derived by Polder *et al.*[10] and from numerical simulations of a larger number of trajectories.[15] Figures 5(b) and 5(c) are similar histograms for cylindrical-symmetry transverse simulations for $F=1$ and $F=\pi^{-1}$, respectively;

$$\sigma(\tau_D,F=1)/\bar{\tau}_D=(13.0\pm3.6)\%$$

for 13 trajectories and $(7.2\pm1.8)\%$ for $F=\pi^{-1}$ and 16 trajectories. Figure 6 summarizes the Fresnel-number dependence over the range $F=0.3-1.5$. The curve is drawn through the points to guide the eye. Because the same starting point was used in the same random-number table for the five closed circle points, the Fresnel number dependence of $\sigma(\tau_D)/\bar{\tau}_D$ is probably determined much better than the error bars would suggest. The curve yields $(12\pm4)\%$ for $F=0.8$ compared with $(10\pm2)\%$ reported by Vrehen and der Weduwe for Cs.[19] Drummond and Eberly have more extensive calculations of $\sigma(\tau_D)$ for $F=1-16$.[21(b)]

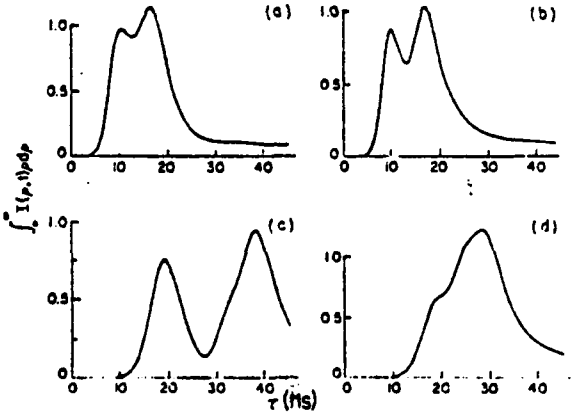

FIG. 7. Phase waves. Fluctuations can result in the second peak exceeding the first. $n_0^0=9.5\times10^{10}$ cm^{-3}. (a) $F=1.49$, $\langle\theta_0^2\rangle^{1/2}=1.21\times10^{-4}$ rad; (b) $F=1.49$, $\langle\theta_0^2\rangle^{1/2}=1.24\times10^{-4}$ rad; (c) $F=0.165$, $\langle\theta_0^2\rangle^{1/2}=2.22\times10^{-4}$ rad; (d) $F=0.165$, $\langle\theta_0^2\rangle^{1/2}=1.79\times10^{-4}$ rad.

Figure 7 illustrates a difficulty encountered in calculating $\sigma(\tau_D)$. Occasionally, the first "peak" is not the highest peak. If one uses the second peak for determining τ_D for just one trajectory in a set of 10, the value of $\sigma(\tau_D)$ is dominated by that one trajectory. Consequently, in Fig. 6, τ_D is measured to the first peak even if it is only an inflection on the lead-

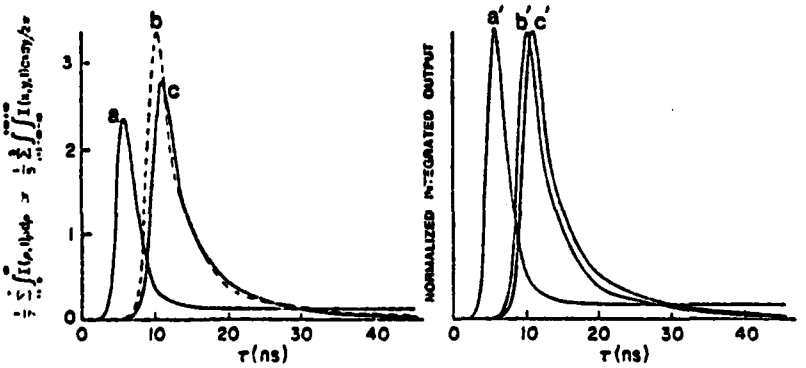

FIG. 8. Effect of Cartesian vs cylindrical geometry for the sum over shots of the transversely integrated intensity for quantum-fluctuation calculations. Curve a holds for $F=1.37$ for a Cartesian geometry. $F=0.11$ for both curves b and c; curve b involves cylindrical geometry while curve c is Cartesian (parallelepiped). Note that the delay with $F=1.37$ (curve a) is shorter than the delay with $F=0.11$ (curve c), just as it was for cylindrical geometry and no fluctuations (Ref. 16): Strong diffraction increases the delay because of energy lost transversely, but the tail is greatly reduced because the diffraction makes the sample superfluoresce as a unit. Curves a'–c' show the same curves normalized for pulse-shape comparisons. $n_0^0=18.2\times10^{10}$ cm^{-3} and $\langle\theta_0^2\rangle^{1/2}$ is about 1.56×10^{-4} rad.

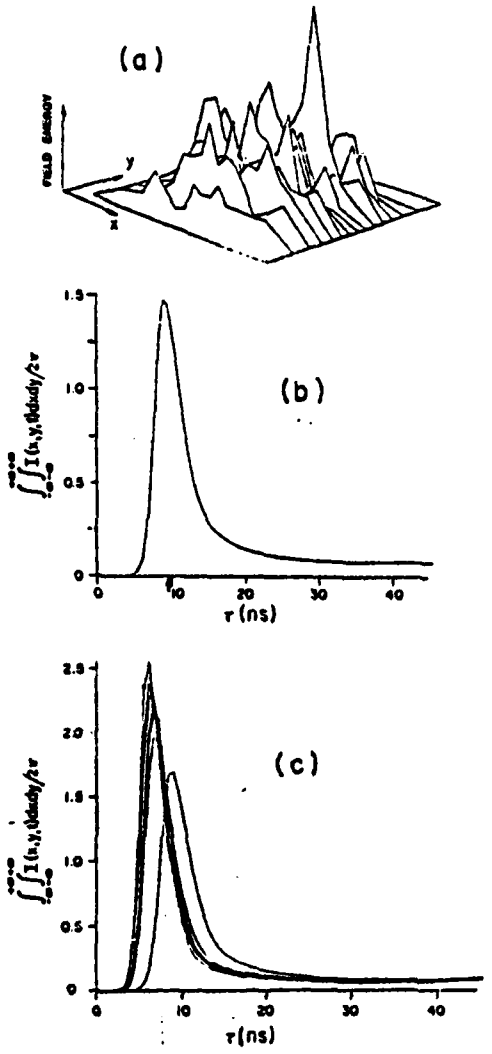

FIG. 9. Transverse fluctuations for a full three-spatial-dimension calculation with quantum initiation. (a) Field energy is displayed isometrically at a time near the peak of the pulse [see arrow, Fig. 9(b)]. In (b) the transversely integrated energy is displayed. (c) Comparison of seven output energy profiles. $F=1.37$, $n_0^0=18.2\times10^{10}$ cm $^{-3}$, and $(\theta_0^2)^{1/2}=1.56\times10^{-4}$ rad. Actually (a) and (b) were calculated for $L=1.86$ cm and (c) for $L=2$ cm.

ing edge of the pulse as in Fig. 7(d). Trajectories as unusual as those of Fig. 7 occurred perhaps once in every 20 to 30 trajectories, and they can be interpreted as phase waves discussed by Hopf.[13]

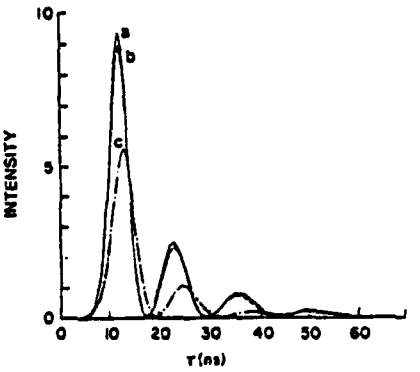

FIG. 10. Effects of inhomogeneous broadening in the uniform plane-wave case with homogeneous initial tipping angle. a: $T_2^*=\infty$. b and c: $T_2^*=32$ ns in the formulas (for b) $g(\Delta\omega)=(T_2^*/\pi)\exp[-[T_2^*(\Delta\omega)/\sqrt{\pi}]^2]$ and (for c) $g(\Delta\omega)=(T_2^*/\pi^{3/2})\{1+[T_2^*(\Delta\omega)/\sqrt{\pi}]^2\}^{-1}$ corresponding closely to the value in the Cs experiment. Notice that including T_2^* damps the field energy amplitude and reduces the tail. Delay is also affected slightly. $n_0^0=9.5\times10^{10}$ cm $^{-3}$ and $\theta_0=1.89\times10^4$ rad.

C. Full three-dimensional quantum fluctuations—Cartesian geometry

The cylindrical symmetry was removed to allow fluctuations in all three spatial dimensions. This permits treatment of the large-Fresnel-number case in which there may be competition between transverse modes not possessing cylindrical symmetry. This additional degree of freedom has little effect on pulse shapes integrated over transverse dimensions (Fig. 8), but it elucidates fluctuations in SF angular distributions (Fig. 9). For small Fresnel number the diffraction term strongly couples the various parts of the beam, and so the beam behaves as a unit. On the other hand, the output for large Fresnel number

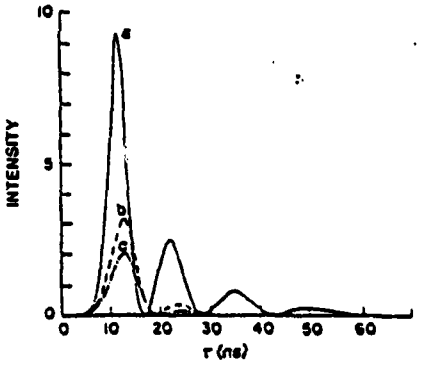

FIG. 11. Removal of ringing by inhomogeneous broadening. Parameters: Same as Fig. 10 with $T_2^*=0.67$ ns.

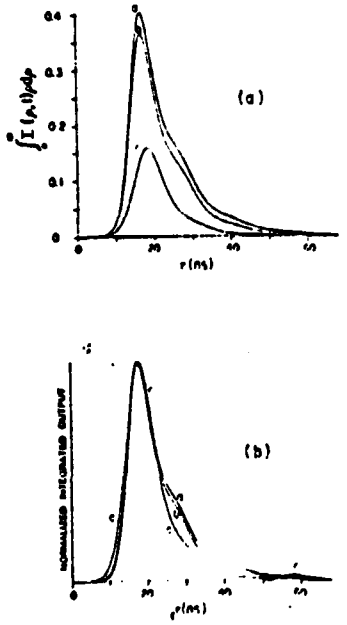

FIG. 12. Transverse effects and inhomogeneous broadening. Parameters: Same as Fig. 10 except that transverse effects ($F=0.27$) are now considered. Including T_2^* in the Cs simulation is seen to be a small refinement which does suppress the tail slightly. (a) Relative integrated outputs. (b) Normalized integrated outputs with peaks shifted to coincide with each other to simplify pulse-shape comparisons.

is completely irregular and highly asymmetrical [see Fig. 9(a) for the energy isometric near the peak of the output pulse]. This is owing to the loose coupling between the various portions of the beam as well as the short-scale fluctuations. Nevertheless, Fig. 9(b) shows that the (transversely) integrated output signals remain smooth, as observed by the detector in the experiment. Figure 9(c) compares seven different outputs showing quantum fluctuations in the full three-dimensional Cartesian case.

D. Inhomogeneous broadening

Fluctuations in the medium initiation and inhomogeneous[27] broadening in the plane-wave limit have been calculated by Haake, Haus, King, Schröder, and Glauber.[14] Their results show that simulations, including both inhomogeneous broadening (T_2^*) and fluctuations but ignoring transverse effects, do not explain the absence of ringing in the Cs data. Without fluctuations or transverse effects, Fig. 10 shows that $T_2^* \simeq 32$ ns as in the Cs data has little effect on the ringing. Elimination of ringing is shown in Fig. 11 using a T_2^* almost as short as τ_{SF}. Figure 12 shows that adding $T_2^* = 32$ ns to the previous simulations including fluctuations and transverse effects changes the pulse shapes very little.

IV. CONCLUSIONS

The addition of quantum fluctuations in the initial conditions of SF calculations does not greatly alter the general shape of the total output pulse integrated over the transverse dimension. It does result in noticeable macroscopic pulse-shape fluctuations similar to those observed. Although fluctuations prevent prediction of a single-shot pulse shape, by examining many single-shot calculations one finds that fluctuations reduce the on-axis ringing and the tail, on the average, improving the agreement with existing Cs data. The standard deviation in delay time is consistent with the measured value, but the uncertainties in both the simulations and experiments are large. The existing Cs data are encompassed by the changes in output pulse shapes calculated including both fluctuations and transverse effects. The plane-wave predictions fail for all Fresnel numbers, large or small, so the strong ringing computed[22] for small-area pulse propagation in an inverted medium is not expected in superfluorescence.

ACKNOWLEDGMENTS

The authors would like to acknowledge useful discussions with F. A. Hopf, J. V. Moloney, R. Glauber, F. Haake, and C. M. Bowden, and partial support from the U. S. Army Research Office (Grant Nos. DAAG29-79-C-0148 and F49620-80-C-0022) and the National Science Foundation.

---

*Present address: P.O. Box 5147, Kirtland A.F.B., New Mexico 87185.

[1]R. H. Dicke, Phys. Rev. 93, 99 (1954).
[2]J. H. Eberly and N. E. Rehler, Phys. Lett. A 29, 142 (1969); N. E. Rehler and J. H. Eberly, Phys. Rev. A 3, 1735 (1971).
[3]R. Bonifacio, P. Schwendimann, and F. Haake, Phys. Rev. A 4, 302 (1971); 4, 854 (1971); R. Bonifacio and

L. A. Lugiato, *ibid.* 11, 1507 (1975); 12, 587 (1975).
[4]N. Skribanowitz, I. P. Herman, J. C. MacGillivray, and M. S. Feld, Phys. Rev. Lett. 30, 309 (1973).
[5]J. C. MacGillivray and M. S. Feld, Phys. Rev. A 14, 1169 (1976); 23, 1334 (1981).
[6]Reviews of SF: M. S. Feld and J. C. MacGillivray, in *Coherent Nonlinear Optics*, edited by M. S. Feld and V. S. Letokhov (Springer, Berlin, 1980), p.7; Q. H. F. Vrehen and H. M. Gibbs, in *Dissipative Systems in Quantum Optics*, edited by R. Bonifacio (Springer, Berlin, 1981), p.11; M. F. H. Schuurmans, Q. H. F. Vrehen, D. Polder, and H. M. Gibbs, in *Advances in Atomic and Molecular Physics*, edited by D. R. Bates and B. Bederson (Academic, New York, 1981), p. 168.
[7]V. Degiorgio, Opt. Commun. 2, 362 (1971).
[8]F. Haake, H. King, G. Schröder, J. Haus, R. Glauber, and F. Hopf, Phys. Rev. Lett. 42, 1740 (1979).
[9]R. Glauber and F. Haake, Phys. Lett. 68A, 29 (1978).
[10]D. Polder, M. F. H. Schuurmans, and Q. H. F. Vrehen, Phys. Rev. A 19, 1192 (1979).
[11]F. Haake, Phys. Rev. Lett. 41, 1685 (1978).
[12]F. A. Hopf and E. A. Overman II, Phys. Rev. A 19, 1180 (1979).
[13]F. A. Hopf, Phys. Rev. A 20, 2064 (1979).
[14]F. Haake, J. Haus, H. King, G. Schröder, and R. Glauber, Phys. Rev. Lett. 45, 558 (1980).
[15]F. Haake, H. King, G. Schröder, J. Haus, and R. Glauber, Phys. Rev. A 20, 2047 (1979).
[16]F. P. Mattar, H. M. Gibbs, S. L. McCall, and M. S. Feld, Phys. Rev. Lett. 46, 1123 (1981).
[17]Q. H. F. Vrehen and M. F. H. Schuurmans, Phys. Rev. Lett. 42, 224 (1979).
[18]N. W. Carlson, D. J. Jackson, A. L. Schawlow, M. Gross, and S. Haroche, Opt. Commun. 32, 350 (1980).
[19]Q. H. F. Vrehen and J. J. der Weduwe, Phys. Rev. A 24, 2857 (1981).
[20]F. P. Mattar, *Proceedings of the European Conference on Atomic Physics, Heidelberg, 1981*, edited by J. Kowalski, G. Zuputlitz, and H. G. Weber (European Physical Society, Geneva, 1981), Vol. VA; *Laser Spectroscopy V*, edited by B. Stoicheff *et al.* (Springer, Heidelberg, 1982); U. S. Army Research Office Workshop on Coupled Nonlinear Oscillators, Los Alamos, 1981 (unpublished); *Proceedings of the Los Alamos Conference on Optics, Los Alamos, 1981* (Society of Photo-optic Instrumentation Engineers, Bellingham, Washington, 1981), Vol. 288, pp. 364–371; E. A. Watson, H. M. Gibbs, F. P. Mattar, M. Cormier, S. L. McCall, and M. S. Feld, J. Opt. Soc. Am. 71, 1589 (1981).
[21](a) P. D. Drummond and J. H. Eberly, J. Opt. Soc. Am. 71, 1588 (1981); (b) Phys. Rev. A 25, 3446 (1982).
[22]S. L. McCall, PhD. thesis, University of California, Berkeley, 1968 (unpublished); D. C. Burnham and R. Y. Chiao, Phys. Rev. 188, 667 (1969).
[23]H. M. Gibbs, Q. H. F. Vrehen, H. M. J. Hikspoors, Phys. Rev. Lett. 39, 547 (1977). The first recognition of the importance of dynamic transverse effects in explaining the absence of ringing in the Cs data is difficult to pinpoint for certain, but it was discussed repeatedly in 1976 and 1977 by the present authors, MacGillivray and Vrehen, and mentioned in this paper and by H. M. Gibbs, Q. H. F. Vrehen, and H. M. J. Hikspoors, in *Laser Spectroscopy*, edited by J. L Hall and J. L. Carlsten (Springer, New York, 1977). Independently, E. Ressayre and A. Tallet [Phys. Rev. Lett. 37, 424 (1976); Phys. Rev. A 15, 2410 (1977)] conclude that superfluorescence cannot be described accurately by a one- or two-mode model, i.e., geometrical and propagational effects are essential to a quantitative description. Already in Ref. 4 a simple loss term was introduced to account for diffractive losses. In 1977 MacGillivray and Feld showed that a Gaussian average of plane-wave solutions removes most of the ringing but results in a much longer tail than observed (private communication to H. M. Gibbs). Reference 2 also discusses the importance of geometrical factors and diffraction.
[24]R. Saunders and R. K. Bullough, in *Cooperative Effects in Matter and Radiation*, edited by C. M. Bowden, D. W. Howgate, and H. R. Robl (Plenum, New York, 1977).
[25]Strickly speaking, Ref. 10 derives $\theta_0=(2/\sqrt{N})[\frac{1}{8}\ln(2\pi N)]^{1/2}$ which increases $2/\sqrt{N}$ by a multiplicative factor of 1.59 for $N=10^8$ resulting in a 9% decrease in delay.
[26]For more details on the numerical techniques see F. P. Mattar, Appl. Phys. 17, 53 (1978); M. Cormier, Y. Claude, P. Cadieux, and F. P. Mattar, *Proceedings of the International Conference on Lasers, December, 1981*, edited by C. B. Collins (STS, MacLean, Virginia, 1982), pp. 1055–1115; F. P. Mattar and M. C. Newstein, Comput. Phys Commun. 20, 139 (1980).
[27]Effects of inhomogeneous broadening upon SF emission have been calculated much earlier using various approximations. See E. Ressayre and A. Tallet, Phys. Rev. Lett. 30, 1239 (1973); R. Jodoin and L. Mandel, Phys. Rev. A 9, 873 (1974); and Refs. 3 and 5 above.

Unclassified

SECURITY CLASSIFICATION OF THIS PAGE (When Data Entered)

REPORT DOCUMENTATION PAGE		READ INSTRUCTIONS BEFORE COMPLETING FORM
1. REPORT NUMBER 3	2. GOVT ACCESSION NO.	3. RECIPIENT'S CATALOG NUMBER
4. TITLE (and Subtitle) Transverse effects light-matter interaction: superfluorescence and optical Bistability		5. TYPE OF REPORT & PERIOD COVERED Final Sept.79 to Jan. 31, 83 6. PERFORMING ORG. REPORT NUMBER
7. AUTHOR(s)		8. CONTRACT OR GRANT NUMBER(s) DAAG 29-79-C-0148
9. PERFORMING ORGANIZATION NAME AND ADDRESS Polytechnic Institute of New York 333 Jay Street, Brooklyn, NY 11201		10. PROGRAM ELEMENT, PROJECT, TASK AREA & WORK UNIT NUMBERS DRXRO-PR P-16800-P
11. CONTROLLING OFFICE NAME AND ADDRESS U. S. Army Research Office Post Office Box 12211 Research Triangle Park, NC 27709		12. REPORT DATE 11 April '83 13. NUMBER OF PAGES
14. MONITORING AGENCY NAME & ADDRESS(if different from Controlling Office) Office of Naval Research, RR NY Area Office, 750 Broadway, N.Y. 10003		15. SECURITY CLASS. (of this report) Unclassified 15a. DECLASSIFICATION/DOWNGRADING SCHEDULE

16. DISTRIBUTION STATEMENT (of this Report)

Approved for public release; distribution unlimited.

17. DISTRIBUTION STATEMENT (of the abstract entered in Block 20, if different from Report)

18. SUPPLEMENTARY NOTES

The view, opinions, and/or findings contained in this report are those of the author(s) and should not be construed as an official Department of the Army position, policy, or decision, unless so designated by other documentation

19. KEY WORDS (Continue on reverse side if necessary and identify by block number)

Rigorous Simulation Transverse Quantum Initiation Superflorescence; Comform Cs data: Control of Light at a given frequency by a light injected at another frequency; optical bistability algorithm encompassing diffraction, full transient, absorption, dispersion, and standing wave effects

20. ABSTRACT (Continue on reverse side if necessary and identify by block number)

Two and Three-Level Superfluoresence Calculations and an algorithm for Optical Bistability

I. Methodology

Computational methodologies were developed to treat rigorously (i) transverse boundary in an inverted (amplifying) media; (ii) to treat quantum fluctuations in an initial boundary conditions in the light-matter interactions

DD FORM 1 JAN 73 1473 EDITION OF 1 NOV 65 IS OBSOLETE

UNCLASSIFIED

SECURITY CLASSIFICATION OF THIS PAGE (When Data Entered)

problem; (iii) construct a two-laser three-level code to study light control by light effect; (iv) construction of a data base that (a) would manage the production of different types of laser calculations: cylindrical, cylindrical with atomic frequency broadening, cartesian geometry; all of the above with quantum mechanical initiation), (b) allow parametric comparison within the same type of calculations, by establishing a unifying protocol of software storage, of the various refinements of the model could be contrasted among themselves and with experiment; (v) construct an algorithm for counterbeam transient studies for optical bistability and optical oscillator studies.

II. Physics

A. Transverse effects were shown to be inherent to the problem of superfluorescence. By refining the propagational model advocated by Feld, we were able to simulate correctly Gibbs, et al's Cs data for the first time. The mean field approach was shown not to directly relevant to the Cs data. The interplay of quantum fluctuations and transverse dynamic effects lead to Fresnel variation of the time delay statistic in conformity with experiments.

B. The previously studied as totally independent effects superradiance and swept-gain superradiance were shown to be strongly related to and to evolve assymptotically from the first one to the second one. Output energy stabilization was obtained by balancing the gain (from the inverted medium) with the dynamic diffraction loss (from the finiteness of the beam).

C. The Study of three-level systems exhibited that injected coherent-pump initial characteristic (such as on-axis area, temporal and radial width and shape) injected at one frequency can have significant deterministic effects on the evolution of the superfluorescence at another frequency and its pulse delay time, peak intensity, temporal width and shape. The importance of Resonant Coherent Roman processes was clearly demonstrated in an example where the evolving superfluorescence pulse temporal width τ_s is much less than the reshaped coherent pump width τ_p eventhough the two pulses temporarily overlap (i.e., the superfluorescence process gets started late and terminates early with respect to the pump time duration). The results of the three-level calculations are in quantitative agreement with observations in CO_2 pumped CH_3F.

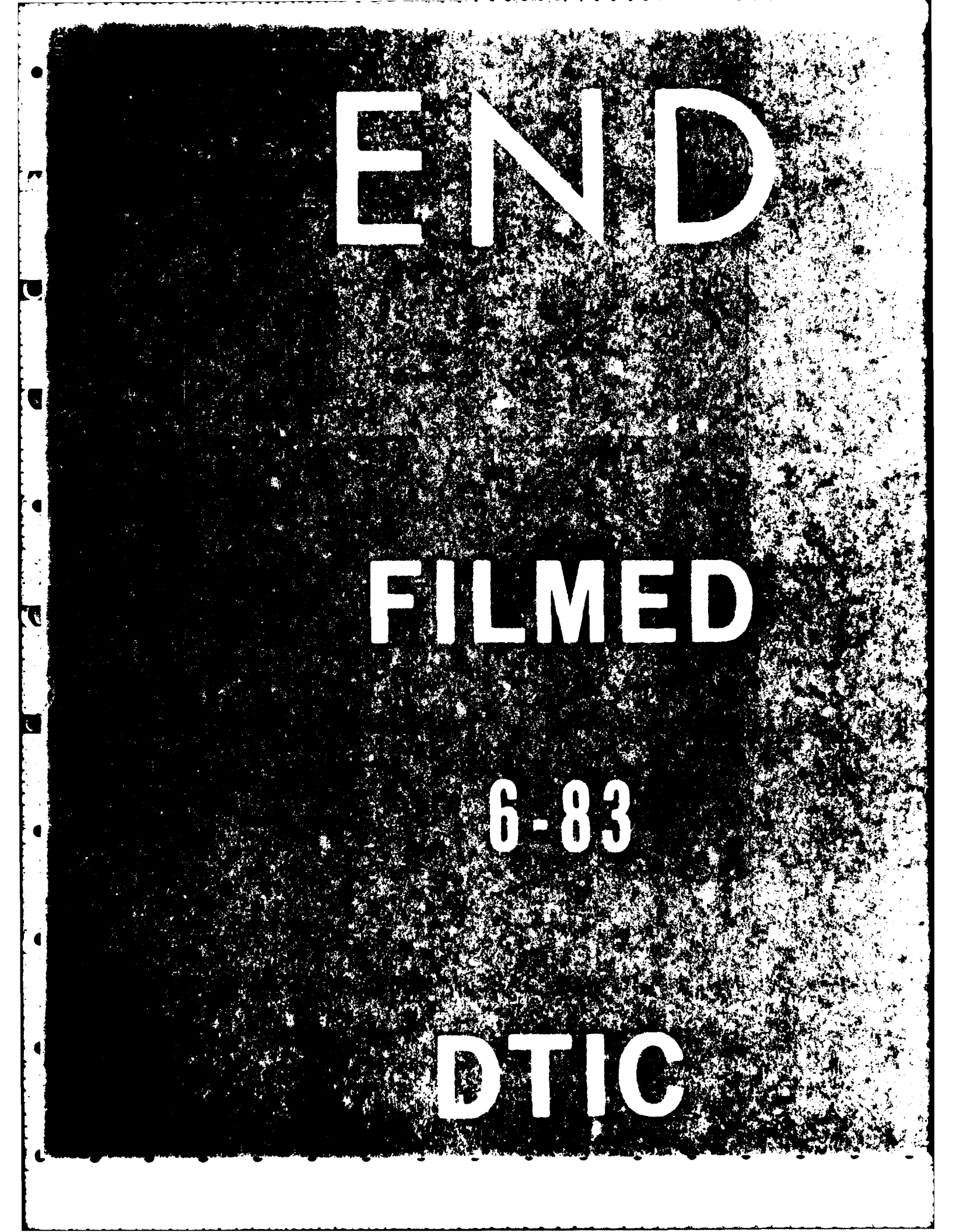
END
FILMED
6-83
DTIC